The characterisation of the flavocytochrome P450-CPR fusion enzymes CYP505A30 from *Myceliophthora thermophila* and CYP102A1 from *Bacillus megaterium*.

A thesis submitted to The University of Manchester for the degree of Doctor of Philosophy in the Faculty of Life Sciences.

2015

George Baker

List of Contents:

List of Figures:

List of Tables:

Word count: 96,100

List of Abbreviations:

$(NH_4)_2SO_4$:	Ammonium sulphate
Δ-ALA:	5-aminolevulinic acid
1/4/5-PhIm:	1/4/5-Phenylimidazole
2YT:	Yeast Extract Tryptone Medium
Å:	Angstrom
A:	Absorbance
ADP:	Adenosine diphosphate
BM3:	CYP102A1, Cytochrome P450 BM3
BSTFA:	N,O-Bis(trimethylsilyl)trifluoroacetamide
$CaCl_2$:	Calcium chloride
CCD:	Charge-coupled device
CO:	Carbon monoxide
CPR:	Cytochrome P450 Reductase
Da:	Dalton
ddH_2O:	Distilled, deionised water
DNA:	Deoxyribonucleic acid
DEAE:	Diethyl aminoethyl (cellulose/Sepharose)
dNTP:	Deoxynucleotide triphosphate
DSF:	Differential scanning fluorimetry
DTT:	Dithiothreitol
EC:	Enzyme Commission
E. coli:	*Escherichia coli*
EDTA:	Ethylenediaminetetraacetic acid
EM:	Electron Microscopy
EPR:	Electron Paramagnetic Resonance spectroscopy
FAD:	Flavin adenine dinucleotide
FMN:	Flavin mononucleotide
Fdx:	Ferredoxin
FLDR:	Flavodoxin reductase
Fldx:	Flavodoxin
FNR:	Ferredoxin $NADP^+$ reductase
HD:	Heme domain
HPLC:	High Performance Liquid Chromatography
HQ:	Hydroquinone
HS:	High-spin
HSQC:	Heteronuclear Single Quantum Coherence
IPTG:	Isopropyl β-D-thiogalactopyranoside
kbp:	kilobase pair (DNA)
K_d:	Dissociation constant
kDa:	kiloDalton

KPi:	Potassium phosphate (buffer)
LCMS:	Liquid Chromatography-Mass Spectrometry
SEC-MALLS:	Size Exclusion Chromatography–MultiAngle Laser Light Scattering
LB:	Luria Bertani medium
LS:	Low-spin
MALLS:	MultiAngle Laser Light Scattering
M_w:	Molecular weight
MS:	Mass Spectrometry
MT1:	CYP505A30 from *Myceliophthora thermophila*
NAD(P)H:	Nicotinamide adenine dinucleotide (phosphate), reduced form
$NAD(P)^+$:	Nicotinamide adenine dinucleotide (phosphate), oxidised form
NCBI:	National Centre for Biotechnological Information
Nm:	Nanometre
NMR:	Nuclear Magnetic Resonance
NO:	Nitric oxide
NOESY:	Nuclear Overhauser Effect Spectroscopy
NOS:	Nitric oxide synthase
NPG:	N-palmitoylglycine
OD_{600}:	Optical density at 600 nm
P450:	Cytochrome P450
PCR:	Polymerase Chain Reaction
PDB:	Protein Data Bank
Pfu:	*Pyrococcus furiosus* DNA polymerase
pK_a:	Acid dissociation constant
QCL:	Quick Change Ligation
Q-Sepharose	Quaternary amino Sepharose
$R_{h:}$	Hydrodynamic radius
RPM:	Revolutions per minute
Rz:	Reinheitzahl (Ratio of heme Soret absorbance to A_{280} value)
SDS-PAGE:	Sodium dodecyl-sulfate polyacrylamide gel electrophoresis
SQ:	Semiquinone
TAE:	Tris Acetic acid Buffer
TEM:	Transmission Electron Microscopy
TB:	Terrific Broth
T_m:	Melting temperature
TROSY:	Transverse relaxation-optimised spectroscopy
UV:	Ultraviolet
v/v:	Volume to volume
WT:	Wild type (enzyme/gene)
w/v:	Weight to volume

Abstract

The University of Manchester, George Baker, PhD Biochemistry

The characterisation of the flavocytochrome P450-CPR fusion enzymes CYP505A30 from *Myceliophthora thermophila* and CYP102A1 from *Bacillus megaterium*.

September 2015

High catalytic activity and a broad substrate range are characteristic of P450 fusion enzymes of the CYP102A class. P450 BM3 (CYP102A1, BM3) is a paradigm for the P450 fusion enzymes and is accredited with the highest monooxygenase activity in the P450 superfamily, a property which has led to its engineering and exploitation for biotechnologically valuable oxidation reactions. Initial research in the thesis focused on characterisation of a novel P450-redox partner fusion enzyme from the thermophilic fungus *Myceliophthora thermophila* (CYP505A30, $P450_{MT1}$). Sequence alignments revealed a P450 domain and a diflavin P450 reductase domain with high sequence similarity to BM3's domains (41% and 31% amino acid identity, respectively). The purified 118 kDa protein is soluble and exhibits characteristic P450 spectral properties, giving a Soret absorption shift to 450 nm upon binding CO to its ferrous heme iron. Binding titrations of intact P450 MT1 and its expressed P450 (heme) domain with fatty acid substrates and imidazole-based inhibitors revealed type I (blue) and II (red) Soret shifts, respectively, typical of other members of the P450 superfamily, and enabled determination of substrate binding constants. HPLC analysis confirmed stoichiometric amounts of bound FAD and FMN cofactors. Subsequent kinetic and biochemical studies included stopped-flow kinetic experiments showing that NADPH-dependent reduction of P450 MT1's FAD cofactor occurs with a rate constant of ~150 s^{-1} at 20 °C. P450 MT1 has an unconventional substrate hydroxylation profile for saturated fatty acids. It hydroxylates these substrates predominantly at positions ω-1, ω-2 and ω-3. However, an unusual property of this enzyme is observed in its strong preference (~85% of total converted product) for either the ω-1 or the ω-2 position on odd and even chain length fatty acids, respectively. However, it displays higher selectivity for branched chain fatty acids over straight chain fatty acids, e.g. for the substrate *iso*-myristic acid, similar to BM3's properties. Other work done focused on biophysical characterisation of the model P450-reductase fusion enzyme P450 BM3 from *Bacillus megaterium*. A combination of alternative structural techniques to X-ray crystallography were used to characterise the enzyme. More specifically, electron microscopy (EM) and nuclear magnetic resonance (NMR) were used to gain greater insights into the intimate associations of the enzyme monomers in BM3's dimeric structure. These studies led to the first structural insights into how P450 BM3's dimeric complex is organised. Dimerisation in BM3 arises predominantly from self-association of the enzyme's FAD domains, and wild-type and mutant BM3 FAD domain forms were also characterised. Key FAD domain mutations that prevented intra-/inter-monomer disulphide bond formation facilitated the crystallization and determination of the FAD domain structure, the final part of the BM3 enzyme to have its three dimensional structure resolved. Data reported in this thesis give new insights into the biochemistry of biotechnologically important P450 monooxygenase enzymes from mesophilic and thermophilic microorganisms.

Declaration

The author declares that no portion of the work referred to in this thesis has been submitted in support of an application for another degree or qualification of this or any other university or other institute of learning.

Copyright Statement

Acknowledgements

First and foremost I would like to thank my supervisor, Professor Andrew Munro, for believing in me and giving me the opportunity to undertake a PhD. I would have a very different attitude towards scientific research were it not for his encouragement and guidance throughout this project. The past four years have flown by thanks to the Munro group, I'll always appreciate the camaraderie and I hope that many of us will remain friends.

Special thanks go to Dr. Hazel Girvan whose patience and advice were invaluable, you have my sincere gratitude. I also wish to thank Dr. Kirsty Mclean who was extremely supportive with her encyclopaedic knowledge and positive attitude. Acknowledgements must extend to the rest of the Molecular Enzymology group within the MIB, not only for help and advice in the lab, but also for the great memories and friendships made.

The support of my advisor, Professor David Leys, can't go without mention. He was a source of new ideas for the project and always provided me with astute feedback.

Last, but by no means least, I would like to thank my family for their utmost belief in me and who, even during the hardest of times, stood by me with interest, enthusiasm and pride.

Chapter 1: Introduction

1.1 Enzyme Classes

The contemporary understanding of enzymes is that they are functional biocatalysts that enable organisms to control the flow of molecules to their advantage, allowing beneficial reactions to proceed very rapidly when compared to reactions that offer no selective advantage to that organism. They are able to increase the natural reaction rate by up to 24 orders of magnitude, e.g. as seen for uroporphyrinogen decarboxylase [1].

Over 5000 types of biochemical reactions have been attributed to enzymes [2]. Enzymes that perform similar reactions tend to share structural properties in conserved catalytic sites and have similar tertiary folds. Table 1.1 depicts the current classification of enzymes in 6 main groups divided by function according to the Nomenclature Committee of the International Union of Biochemistry and Molecular Biology (NC-IUBMB) [3].

Table 1.1 The present classes of known enzymes. The major classes of enzymes are shown along with the broad reaction types that they catalyse and examples of their group. While some enzymes may catalyse a variety of reaction types listed below they are classed according to their more prevalent reaction chemistry.

EC no.	Enzyme Class	Reaction	Example
1	Oxidoreductases	Electron transfer	Cytochromes P450
2	Transferases	Transfer of functional groups	Transaminases
3	Hydrolyases	Chemical bond hydrolysis	Lipases
4	Lyases	Bond breakage excluding hydrolysis	Uroporphyrinogen decarboxylase
5	Isomerases	Isomer conversion catalysis	Cyclases
6	Ligases	Linkage of two macromolecules	DNA ligases

1.2 Oxidoreductase enzymes

The Nomenclature Committee of the International Union of Biochemistry and Molecular Biology (NC-IUBMB) designated the oxidoreductase class of enzymes as EC.1, a category containing over 6000 enzymes [3]. As their name implies, this group of enzymes act as

intermediaries in the transfer of electrons from a donor to an acceptor and can employ certain cofactors to aid their role. These cofactors can be tightly (occasionally covalently) bound to the enzyme, such as flavin mononucleotide (FMN) and flavin adenine dinucleotide (FAD), e.g. in human CPR, where the protein backbone shields these cofactors and is able to modulate their redox potential, binding stability and selectivity (Figure 1.1, right) [4]. Flavin cofactors can accept up to 2 electrons with their redox states being: oxidised, 1-electron-reduced semiquinone (SQ) and (fully) 2-electron-reduced hydroquinone (HQ) states.

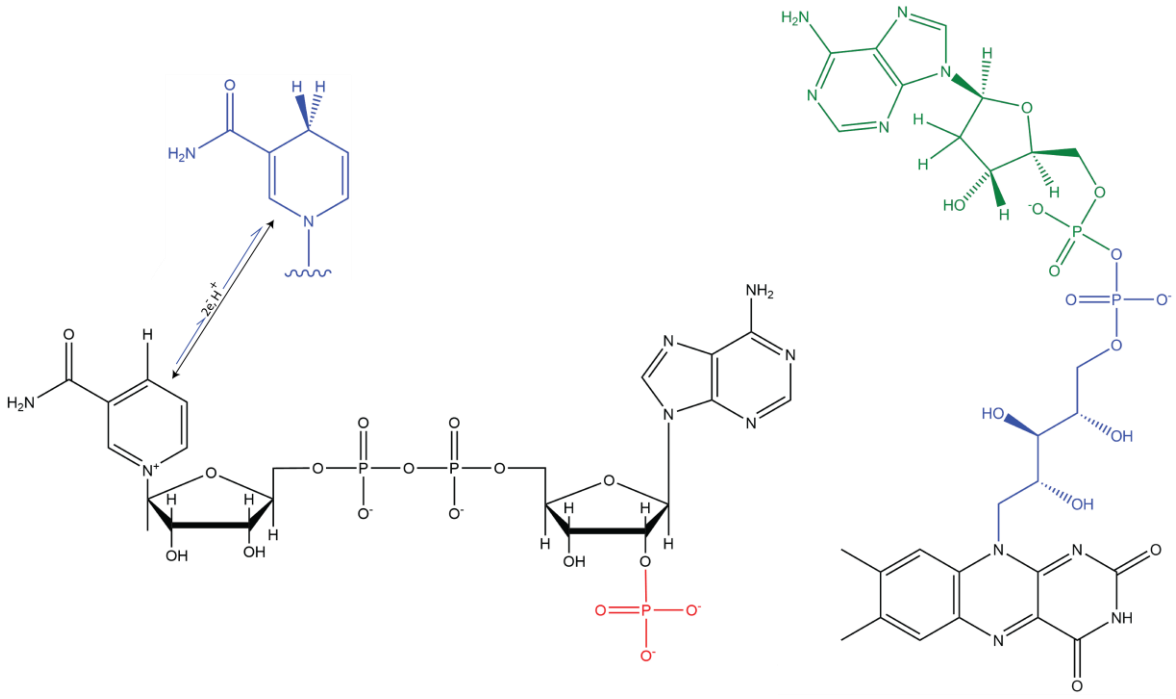

Figure 1.1 Schematic diagrams of cofactor structures. The coenzyme nicotinamide adenine dinucleotide phosphate ($NADP^+$/NADPH) is shown on the left. The phosphate group (red) is absent on the nicotinamide adenine dinucleotide (NAD^+/NADH) cofactor. Shown in blue are the changes in the nicotinamide portion of the cofactor upon accepting a hydride equivalent ($2e^-$, H^+) to form NADPH from $NADP^+$. The cofactor flavin adenine dinucleotide (FAD) is shown on the right. The isoalloxazine ring is shown in black attached to an adenine nucleotide moiety (green) via a phosphodiester linkage (blue). The related cofactor, flavin mononucleotide (FMN, riboflavin phosphate) does not have the adenine nucleotide moiety (green).

Transiently-bound cofactors, or coenzymes, such as nicotine adenine dinucleotide (NAD^+ or NADH according to whether its nicotinamide ring is oxidised or reduced, respectively) and nicotine adenine dinucleotide phosphate ($NADP^+$ or NADPH) are a common source of electrons for oxidoreductase enzymes (Figure 1.1, left).

The reduced forms of these coenzymes, NADH and NADPH are able to supply 2 electron equivalents and a proton via hydride (H^-) transfer. Upon donating their electron equivalents the coenzymes are converted to their oxidised forms $NAD(P)^+$.

Metal ions are also used by oxidoreductases, e.g. Cu, Fe and Mo ions which can be coordinated by amino acid side chains or present in complexes such as the Fe-containing protoporphyrin-heme group. Hemes are often tightly bound to their proteins and such cofactors are called prosthetic groups. Certain hemes also become covalently bound to their proteins (detailed in Section 1.3). Further examples are the iron sulfur clusters. Iron can be found in a variety of complexes with inorganic sulfur atoms, e.g. [2Fe-2S] and [4Fe-4S], which are commonly bound to the enzyme through cysteine residues and by inorganic sulfur. Occasionally, histidine residues replace cysteines in Rieske-type [2Fe-2S] clusters (Figure 1.2).

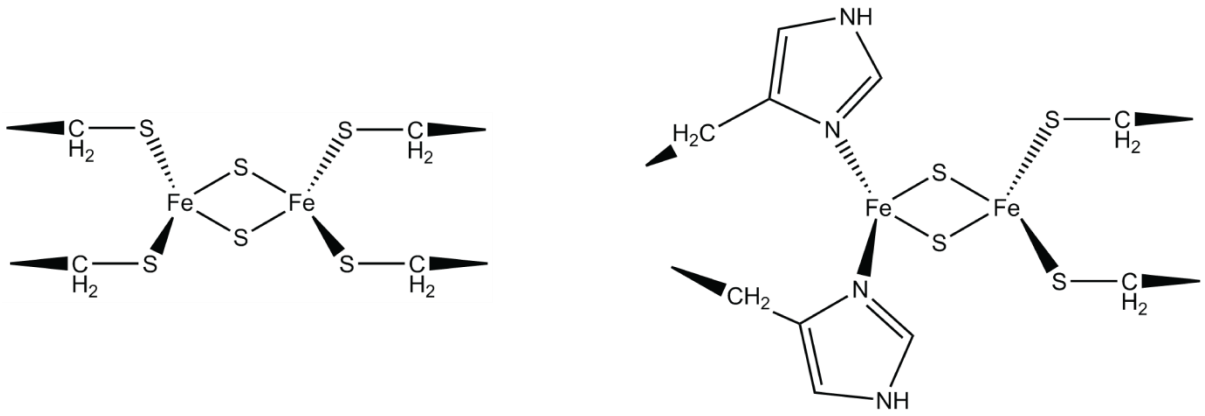

Figure 1.2 Schematic diagram of two enzyme-bound [2Fe-2S] iron sulfur clusters. The standard ligation of a [2Fe-2S] cluster by four cysteine residues is shown on the left and the Rieske-type ligation with two cysteine and two histidine residues is shown on the right.

The iron atoms in iron sulfur clusters can exist in different redox states to one another (typically the ferric and ferrous states) [5]. Ferredoxins all contain iron sulfur clusters and are involved in the transfer of electrons to and from a variety of oxidoreductase enzymes (Section 1.12). Rieske-type ferredoxins are components of ubiquinol cytochrome *c* reductases in bacterial and mitochondrial respiratory chains, and are involved in the degradation of aromatic compounds through dihydroxylation reactions (e.g. phthalate dioxygenase) [6].

These cofactors and prosthetic groups mentioned all act as electron shuttles within oxidoreductase enzymes. The reduction potentials of these redox centres are a measure of their electron affinity, they are a governing factor which determine the overall direction of electron flow; electrons will flow from a more negative potential to a more positive potential. Electron transport is also governed by Dutton's "ruler" which dictates that the distance between redox centres is inversely proportional to the rate of electron transfer (ET) between them such that ET at 4Å occurs at 10^{-10} s^{-1} while at 10Å ET is slower by a factor of 10,000 at 10^{-6} s^{-1}, and the maximum distance for ET within a protein medium is 14Å [7,8]. The "nature" of the intervening medium, the most difficult parameter to quantify, also regulates electron transfer.

In oxidoreductase enzymes BM3 and NOS electrons flow from NADPH through redox centres FAD, FMN and heme as depicted in Figure 1.3.

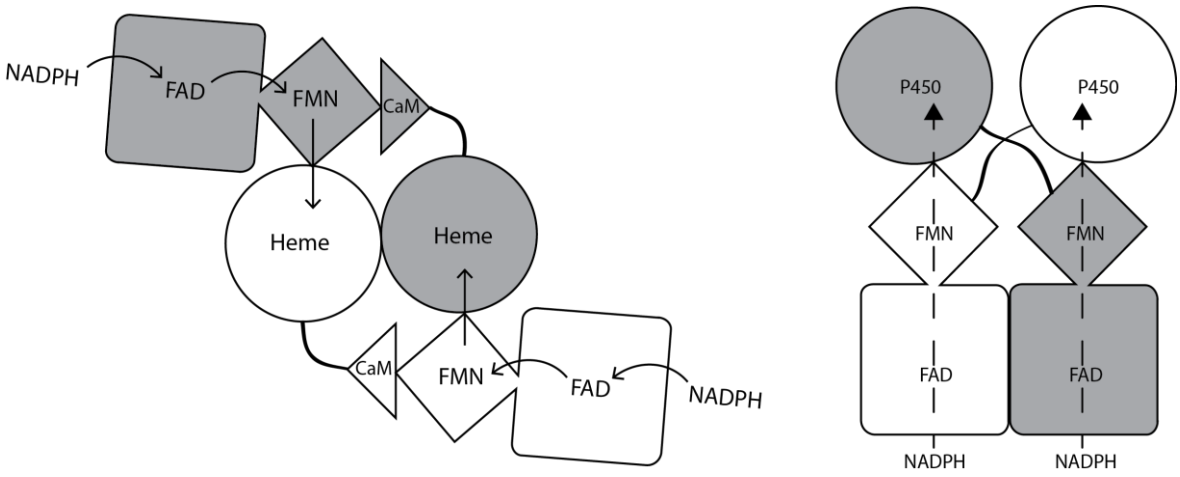

Figure 1.3 Schematic of putative inter-monomeric electron transfer pathways in oxidoreductase enzymes nitric oxide synthases (NOSs) and flavocytochrome P450 BM3. The domains of different monomers are coloured white and grey and inter-monomeric (FMN_1 to $heme_2$) electron transfer is displayed by arrows in each model. iNOS (left) dimerises solely through its heme oxygenase domains (adapted from Siddhanta et al. [9]). The model of BM3 (right) is shown with predominant FAD domain association (adapted from Girvan et al. [10]).

In many oxidoreductase enzymes, namely oxygenases and oxidases such as BM3 and NOSs, the final reductant is molecular oxygen. Molecular oxygen is relatively stable at room temperature and pressure and is the second most abundant gas on earth.

While oxygen is thermodynamically a strong oxidant, its reduction is kinetically unfavourable. Oxygen exists in a triplet (ground) state at room temperature and the energy barrier (E_{act}) to its singlet state must be overcome for its reactivity to be both kinetically and thermodynamically feasible (Figure 1.4). These oxidoreductase enzymes have evolved to be good catalysts to overcome this barrier by coordinating molecular oxygen to allow its successive reduction to a more reactive singlet species (outlined in Section 1.11 for P450s).

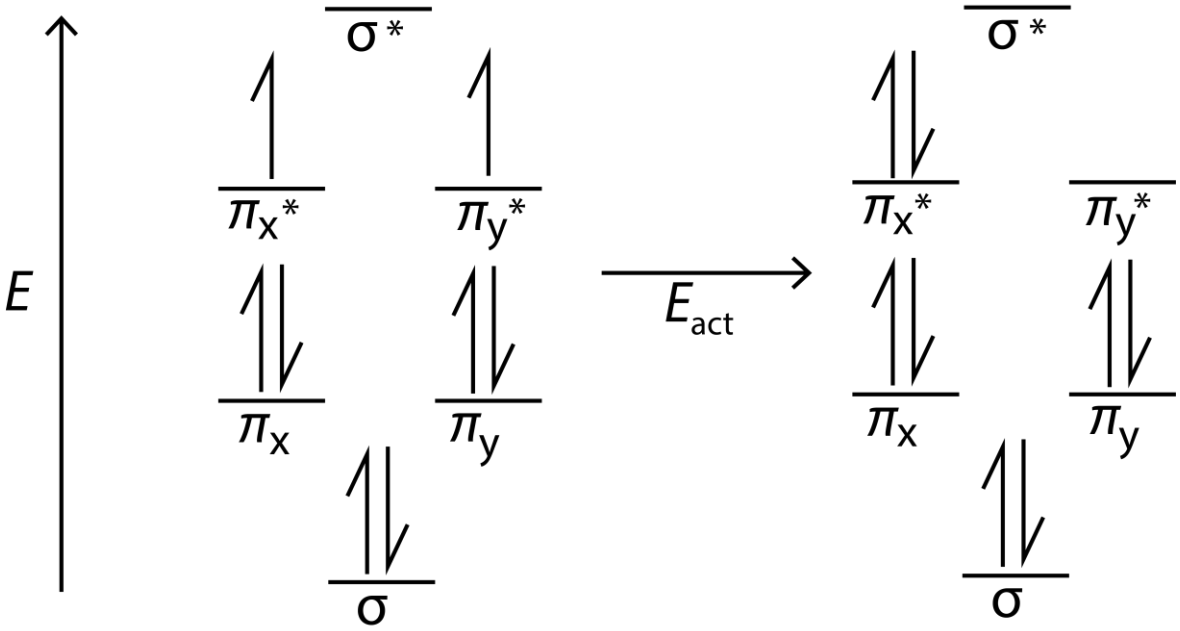

Figure 1.4 Orbital arrangement of oxygen triplet and singlet quantum states. The electrons that occupy the 2p orbitals shown here are depicted as half arrows for the triplet state (left) and singlet (right) diradical states of oxygen. The energy level (*E*) of each orbital are relative and the activation energy (E_{act}) of triplet state to singlet state is 22 kcal/mol [11].

1.3 Hemoproteins

Classes of metalloenzymes containing a heme prostethic group are collectively known as hemoproteins. The heme iron is the enzyme's catalytic centre and the driving force behind these enzymes' reaction chemistries. The biosynthesis of heme is a well-known 8-step pathway involving the synthesis of 5-aminolevulinic acid (δ-ALA) from starting components glycine and succinyl CoA (Figure 1.5). Two molecules of δ-ALA are required by ALA dehydrogenase for the synthesis of porphobilinogen (PBG) which is converted to uroporphyrinogen III (UPG) via PBG deaminase and UPG synthase involving a

hydroxymethyl bilane intermediate. The decarboxylation of UPG by UPG decarboxylase forms coproporphyrinogen III followed by two oxidative decarboxylations to yield protoporphyrinogen IX, its dehydrogenation to generate protoporphyrin IX, and finally iron chelation produces heme (ferroprotoporphyrin IX) [12].

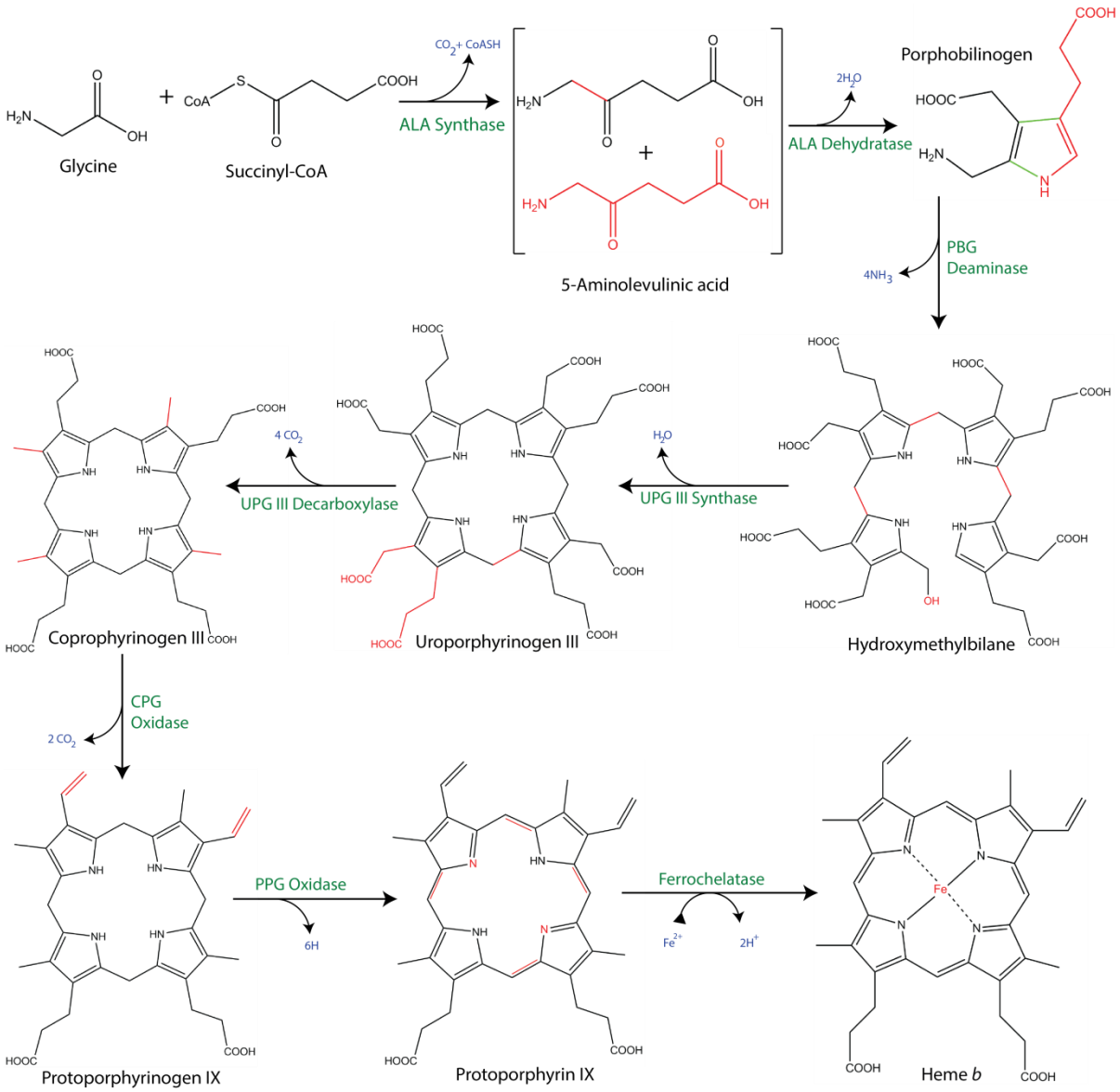

Figure 1.5 Heme biosynthesis pathway. The compounds involved are labelled in black along with their structure. The enzymes at each of the 8 steps are labelled in green and the by-products are coloured blue. Structural changes associated with the product of each step are depicted in red. The generation of porphobilinogen requires two molecules of 5-aminolevulinic acid and the second molecule is coloured red to emphasis its position in porphobilinogen.

More recently, however, an alternate heme biosynthesis was discovered some bacteria and archaea involving the use of a siroheme, a prosthetic group in sulfite and nitrite reductases, as an early iron-chelated intermediate [13].

A tetrapyrrole ring with pyrrole nitrogens coordinating an iron at the centre via 4 planar bonds makes up the fundamental structure of the heme prosthetic group, leaving a maximum of two more axial positions where other ligands (e.g. amino acids, water and diatomic gases) can bind the iron, depending on the particular heme type and factors such as the iron oxidation state and the environment around the heme. The binding of heme to its protein scaffold may be covalent or non-covalent and the structure of the heme cofactor and the nature of its peripheral substituent groups enable heme cofactors to be divided into classes. The nature of the heme structure and its ligands influences the thermodynamic and catalytic properties of the hemoprotein, as does its protein scaffold. These factors all contribute to the diversity of hemeproteins, as represented in Figure 1.6. Different functional groups at carbon positions: C3, C8 and C18 account for the 8 types of heme currently found in nature; heme A, B, C, D, *I*, *m*, O, and S. Lactoperoxidase (LPO) is a heme *I*-containing glycoprotein and forms a part of the mammalian peroxidase superfamily. It catalyses the oxidation of halides to produce antimicrobial agents in exocrine secretions such as milk, tears and saliva [14,15].

Cytochrome *c* oxidase (CCO) is a large membrane-bound enzyme complex and the final component of the respiratory chain in eukaryotic mitochondria and bacteria. CCO contains two heme A cofactors (heme *a* and heme a_3), and two copper centres (Cu_A and Cu_B) which receive and transport electrons derived from reduced cytochrome *c* and, in a concerted 4-electron process, reduce molecular oxygen to water, the last step in cellular respiration [16]. Depicted in Figure 1.6 (left) is the heme and copper binuclear centre responsible for oxygen reduction in CCO. The CCO heme A (heme a_3) shown is coordinated by a histidine (with the other axial position vacated for interaction with O_2) and has a high potential (E°) of 230-360 mV vs NHE for heme Fe^{3+} reduction to Fe^{2+} [17]. Nitric oxide synthase (NOS) enzymes also reduce molecular oxygen, but without a binuclear centre. NOS catalyses the N-oxidation of arginine (Figure 1.6, middle) to citrulline in two steps, using a cysteine thiolate coordinated heme iron to bind and reduce dioxygen to facilitate the attack of a reactive iron-oxo species to form first N-hydroxyarginine, and then citrulline and nitric

oxide (NO), with H_2O produced as a by-product. The NOS cysteine-ligated heme B has a redox potential of ~ -270 mV vs NHE for heme Fe^{3+} reduction to Fe^{2+} [18].

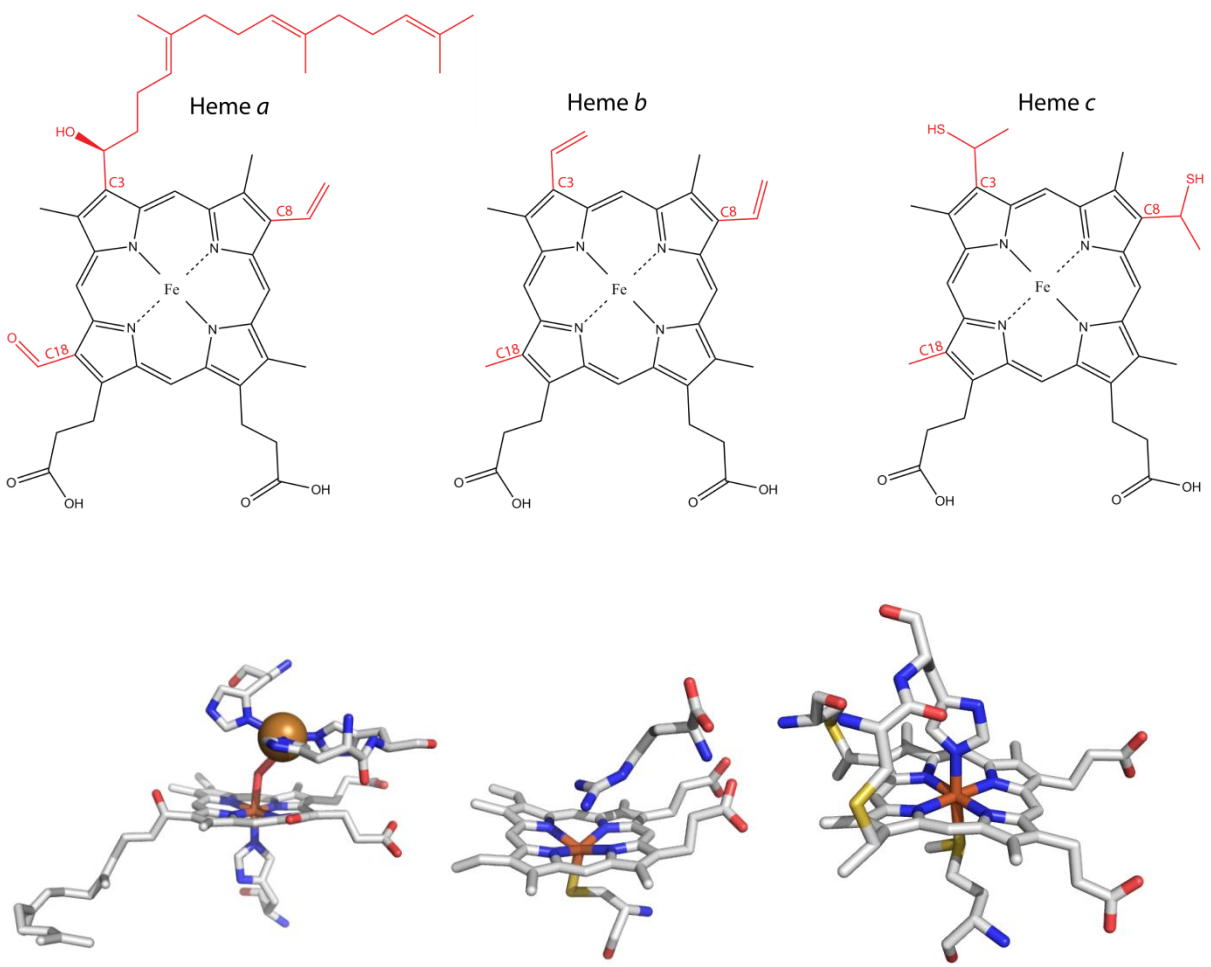

Figure 1.6 Structures of hemes A, B and C. The heme structures are drawn in the upper panel, showing selected numbered substituent groups, and covalent attachments to a hydroxyethylfarnesyl group in the case of heme *a*, and thioether linkages to protein cysteine residues in heme *c*. In the lower panel, selected active site details are shown for cytochrome *c* oxidase (CCO, left), nitric oxide synthase (NOS, centre) and cytochrome *c* (right), with these proteins binding heme *a*, heme *b* and heme *c*, respectively. Elements are coloured as follows: carbon (grey), oxygen (red), nitrogen (blue) and sulphur (yellow). Heme iron and its axial and equatorial bonds are shown in orange. Cu^{2+} is shown as an orange sphere in the binuclear active site of CCO, with dioxygen (in red) bridged between the metal ions (PDB code: 1OCC). In the centre panel, *L*-arginine is shown in the active site of NOS, with cysteine thiolate as the proximal ligand to the heme iron (PDB code: 1NOD). In the right hand panel, His and Met act as axial ligands to the heme *c*, with two vinyl groups esterified to cysteine residues in the protein to covalently link the cofactor to the protein scaffold (PDB code: 1HRC).

While NOS and CCO both function to bind and reduce oxygen, their heme iron midpoint potentials vary substantially ($\Delta E = \sim 1$ V), highlighting important differences in their heme structures and axial heme ligation that influence their heme reduction potential. Similar to NOS, hemoglobin (not shown) has an axially histidine-ligated heme *b* cofactor and a redox potential of +137 mV vs NHE [19] Cytochrome *c*, unlike the other proteins mentioned, does not bind oxygen, instead having two axial amino acid ligands (His and Met) to the heme iron, and is involved in electron transport to CCO. Cytochrome *c*'s heme is covalently bound to the protein scaffold via cysteine thioether bonds, depicted in Figure 1.6 (right), which affords it increased stability [20]. Cytochrome *c* does not bind oxygen and instead is involved in oxidoreductase (electron transfer) reactions over a range of reduction potentials across ~1 V [21].

1.4 The Cytochrome P450 Superfamily

The cytochromes P450 (P450s or CYPs) are a ubiquitous heme enzyme "superfamily" that span all kingdoms from viruses, the most basic of lifeforms to higher organisms such as mammals [22,23].

The P450s are oxidoreductase enzymes that catalyse the reductive scission of molecular oxygen that is bound to their heme iron, and the insertion of one of the oxygen atom into their substrates, with the other atom of O_2 reduced to water:

$$RH + O_2 + 2H^+ + 2e^- \rightarrow ROH + H_2O$$

Figure 1.7 The P450 monooxygenation reaction. Using hydroxylation as the example of P450 chemistry, the substrate (RH) undergoes oxidation into a hydroxylated product (ROH) through the reductive activation of O_2 bound to the P450 ferrous heme iron. The further reduction and protonation of the Fe^{2+}-O_2 species produces a reactive iron-oxo species that hydroxylates the substrate, with the other atom of oxygen from O_2 reduced to form water. Electrons are typically obtained from NAD(P)H via one or more redox partners, while protons are delivered from active site amino acids.

The cytochromes P450 bind a heme *b* (protoheme IX) prosthetic group, which underpins the P450 chemistry. The heme's protoporphyrin ring coordinates an iron atom at its centre via four nitrogen ligands. The ferric iron binds axially to the P450 metalloprotein via a thiolate ligation to a proximal cysteine residue. Cysteinate coordination and the electron donating character of the thiolate bond is crucial for the activity of the P450 monooxygenases [24]. Until recently, the conserved cysteine proximal ligand was considered the only invariant amino acid of this superfamily [25].

P450 enzymes missing the conserved cysteine residue are few, and the absence of a thiolate ligation almost certainly inactivates oxygen activation and substrate oxidation. In the case of the *Aspergillus nidulans* PpoC, it has been suggested that this particular P450 enzyme domain is non-catalytic in the absence of a proximal cysteinate ligand, and is conserved for reasons of structural stability of its fused dioxygenase/peroxidase domain [26].

The last bond to the heme iron is the distal ligand, which is reserved for a water ligand in the ferric, substrate-free, low-spin resting states of many P450s (although some P450s may be predominantly pentacoordinate, high-spin in their cellular substrate-free states). The distal water is then displaced on binding a substrate to make way for oxygen binding in the distal position that is essential for the catalytic cycle to proceed (covered in Section 1.11). The removal of the 5^{th} axial water ligand also usually favours the conversion of the P450 heme iron from a low-spin to a high-spin ferric state. In many cases, this results in a large positive shift in the reduction potential for the Fe^{3+}/Fe^{2+} couple of the heme iron, which facilitates electron transfer from a redox partner. This may be an important regulatory

mechanism that ensures electron transfer occurs only when a substrate is bound, and thus ensures efficient coupling of oxygen reduction to substrate monooxygenation with minimal production of oxygen radical species (superoxide and peroxide) [27].

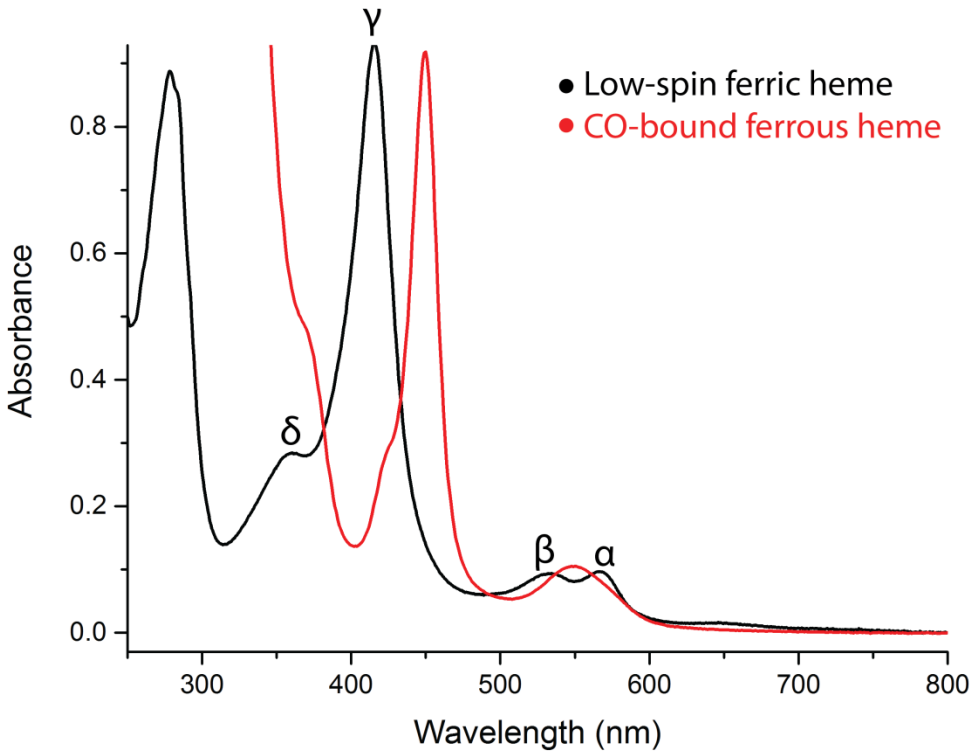

Figure 1.8 Absorption spectra for cytochrome P450 and its ferrous-CO complex. The UV-visible spectrum of a low-spin ferric (Fe^{3+}) P450 (black line, 9 µM) with labelled Soret (γ) peak at ~418 nm, δ peak at 360 nm and associated α and β features (Q band) at 567 nm and 532 nm, respectively. The CO-bound ferrous (Fe^{2+}) state is shown in red, with hallmark P450 Soret shift to 450 nm and 364 nm just visible under the saturated dithionite absorbance <350 nm. The Q band merges to a single peak at 550 nm typical of ferrous heme upon reduction. The spectra shown are for the CYP505A30 P450 MT1 heme domain (MT1 HD, described later in this thesis). A small shoulder originating from the inactive (thiol-coordinated) P420 form of MT1 is visible at ~420 nm in the spectrum of the ferrous-CO complex.

The heme-complexed iron gives P450 enzymes distinct spectral features in the UV-visible region. In the low-spin ferric state, aside from the protein band at ~280 nm, they have heme-specific absorption bands in the range from 300-600 nm. These are the distinctive Soret (gamma, γ) band at ~420 nm, which is the most intense heme absorption band; a shorter wavelength delta (δ) band at ~360 nm; and two longer wavelength alpha (α) and beta (β) bands, collectively known as the Q bands between 500-600 nm (Figure 1.8).

Changes in the heme environment (e.g. influenced by changes in heme iron redox and spin-state) perturb its spectral features, allowing straightforward analysis of heme ligation and also spin state (Section 1.10).

Independent, concurrent reports from Klingenberg [28] and Garfinkel [29] showed the first glimpse of this unusual enzyme class isolated in the microsomal fractions of pig and rodent liver in 1958. The name P450 is an abbreviation derived from 'Pigment with absorption at 450 nm', which signifies the distinctive absorption band that acts as a fingerprint for identifying members of the superfamily. The P450 band arises on CO binding to Fe(II) in the heme prosthetic group (Figure 1.8) which converts the 420 nm, ferric Soret band to produce two bands at ~364 and ~450 nm [30], the latter one enabling the distinction of P450s from other proteins, excluding 3 classes of hemoproteins: NOSs, chloroperoxidases and protein H450, which are closely related to P450s and share the feature of a substantially red-shifted Soret band in their ferrous-CO complexes [31–33]. The subsequent 67 years of P450 research in a range of fields has revealed the diversity of the P450 gene "superfamily", along with numerous examples of their catalytic properties, diversity of substrate recognition, structural and spectroscopic properties, enzyme mechanisms and biotechnological/biomedical applications (Figure 1.9).

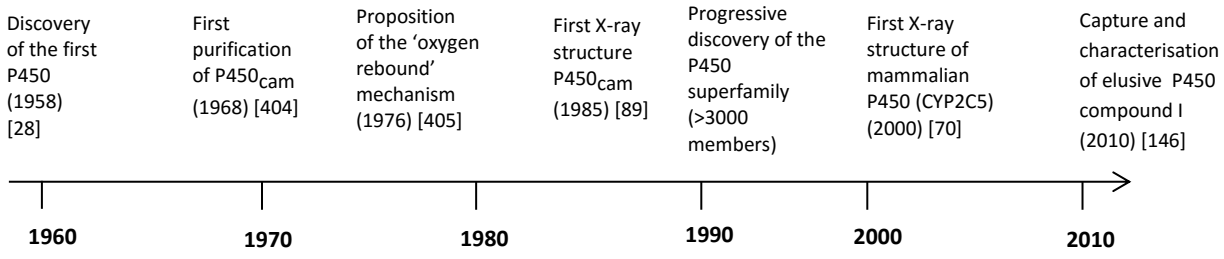

Figure 1.9 Schematic diagram illustrating the timeline of selected breakthroughs in cytochrome P450 chemistry.

1.5 Evolution of the Cytochrome P450 Superfamily

The evolution of the cytochromes P450 and the P450 superfamily diversification is linked to atmospheric oxygen composition driven speciation [34]. P450 are among the oldest

known enzymes, dating as far back as 3.5 billion years ago (BYA), and evidence shows that all known P450s have a common prokaryotic ancestor [35] which may have originally functioned as a nitroreductase or endoperoxidase isomerase under anaerobic conditions [36]. Around 2.7 BYA, cyanobacteria started photosynthesising and releasing oxygen, but it wasn't until 2.4 BYA that it was present in the atmosphere in significant amounts when P450s could have been utilised by early lifeforms as a defence against oxygen toxicity [34]. Corresponding to this time period is the advent of eukaryotes and afterwards the first major expansion of P450s into mitochondrial and microsomal variants, which may have metabolised endogenous compounds such as fatty acids and cholesterol to maintain the membranes present in eukaryotic cells (e.g. the CYP11 and CYP4 families) [37].

The next major expansion of P450 families occurred around 800 million years ago (MYA) when several steroid-synthesising P450s arose (e.g. CYP19, CYP21 and CYP27) [38]. The Cambrian period (541-485 MYA), which followed shortly after an unprecedented increase in atmospheric oxygen, saw the emergence of multiple animal phyla and the divergence of the CYP1 and 2 P450 families from the steroid synthesising and endogenous compound metabolising families; and their emerging as exogenous compound (xenobiotic) metabolising P450s [37]. Around 400 MYA, the xenobiotic metabolising P450 families greatly expanded and radiated further into other CYP families (e.g. CYP3 and CYP6).

This marks an interesting time for both evolution and xenobiotic P450 family expansion, as around 400 MYA aquatic organisms began to colonise land and as a consequence were introduced to toxic plant allelochemicals for the first time, along with exposure to hydrocarbon-based chemicals in the earth's atmosphere, both thought of as drivers of P450 family diversification [38,39]. The expansion and diversification of the P450 superfamily at this stage in evolution was influenced greatly by their recurrent co-evolution in animals to detoxify plant allelochemicals, and their recruitment in plants to produce novel toxins, which has been described as plant-animal "warfare".

Phylogenetic analysis of cytochrome P450 genes show that they are among the most rapid to evolve and studies have estimated the evolutionary unit range to be between 2 and 4 million years (depending on the sequence) [38].

Table 1.2 Evolutionary and atmospheric oxygen content concordances with P450 superfamily developmental history. CYP family divergence is represented alongside a chronological timeline of major evolutionary events and atmospheric oxygen concentration.

MYA	(%) Atmospheric O_2 Content	Biological Development	P450 Superfamily Divergence
3500	0	Evidence of life (prokaryotes)	First ever CYP
2000	>5	Advent of the eukaryotes	Eukaryotic CYP enzymes combat oxygen toxicity
1000	>5	Animal-plant divergence	Mitochondrial and microsomal CYPs
800	>5	Ediacaran biota (trilobites)	P450s used in steroid hormone production
650-450	~12	Divergence of animalia, arrival of invertebrates and land colonisation	CYP1 and 2 separate from CYP17 and 21 and all diverge further. Xenobiotic degrading P450s evolve against plant toxins
370-230	~35	Amphibia, reptiles and bird-mammal divergence	CYP2D diverges from CYP2 and radiates
120-0	~25	Mammalian divergence	CYP1A1 and 1A2 diverge. P450 superfamily now composed of over 1000 families

1.6 Classification of P450s

The P450 superfamily currently encompasses over 21000 enzymes in over 1000 families [40] and, due the enzyme group's prevalence, a nomenclature system was devised in 1987 by Nebert *et al.* to accommodate the growing number of *CYP* genes and P450 enzymes

identified [41]. The first tier of classification was for CYP (Cytochrome P450) families, divided numerically. e.g. CYP1, CYP2 etc, and containing only highly related members with 40% or greater amino acid identity. The subfamily division sets apart those P450s that share over 55% amino acid identity (and likely highly similar substrate specificity and reactivity), and these members were assigned additional alphabetical characters e.g. CYP1A, CYP1B, followed by individual numbers according to the time of discovery (e.g. CYP1A1, CYP1A2 etc) [35]. Due to the recent surge in gene discovery, this system with strict parameters for sequence similarity eventually became outdated and was replaced by a more lenient, alphanumerically similar one based on the clustering on phylogenetic trees; CYP1-49 and CYP300 are assigned to animals, CYP51-69 and CYP501-699 to lower eukaryotes, CYP71-99 and CYP701-999 to plants, and finally CYP101-299 and CYP1001-2999 to bacteria (not taking into account reserved CYP ranges) [23]. Dr. David Nelson (University of Tennessee) maintains the 'The Cytochrome P450 Homepage' which contains all the known P450 amino acid sequences with their associated CYP codes [23].

1.7 Major cytochrome P450 reactions

The cytochrome P450 superfamily are classed as mixed function oxidases due to the fact that they catalyse both the oxidation of NAD(P)H and of the P450 substrate during their reactions. The P450s catalyse a wide range of reactions, including those summarised in Table 1.3. Their copious substrate portfolio (>200,000) span nearly every class of organic molecule [42].

The hydroxylation of saturated fatty acids at the ω-terminus is an example of a typical P450 oxidation reaction, e.g. as catalysed by the members of CYP102A subfamily (notably P450 BM3 from *Bacillus megaterium* – CYP102A1) at subterminal (ω-1 to ω-3) positions [43]. P450s are clearly not limited to aliphatic fatty acid hydroxylation, as some P450s accept and hydroxylate polycyclic aromatic substrates, e.g. eukaryotic CYP1A1 [44]. Nor are they limited to hydroxylation at the ω-position, as seen e.g. for *Bacillus subtilis* CYP152A1, an unusual "peroxygenase" P450 that uses hydrogen peroxide to form a reactive heme iron-oxo species (bypassing NAD(P)H and a P450 redox partner system) to catalyse fatty acid hydroxylation at the β carbon [45,46]. While hydroxylation may be the

most common reaction in the P450 literature, it is only one example in the diverse reaction chemistry of P450s, important examples of which are illustrated in Table 1.3 below [47].

Table 1.3 Prevalent P450 Reaction Chemistry.

	Reaction type	Description	Example P450
1	Carbon hydroxylation	Oxidising C-H bond to C-OH	CYP102A1 [48]
2	Heteroatom release	N, O, S and C dealkylation	CYP2B1 [49]
3	Heteroatom oxygenation	N- and S- oxidation, dehydrogenation and deamination	CYP3A4 [50]
4	Epoxidation	Oxidation across unsaturated C-C bonds	CYP2E1 [51]
5	Heme suicidal destruction	Inactivation by a porphyrin ring-binding enzymatic product	CYP2B4 [52]
6	1,2-Group migrations	Molecular rearrangement	CYP74A1 [53]

Dealkylation at N, O, S and C atoms are also carried out by P450s. CYP51 enzymes C-dealkylate sterols (e.g. the fungal sterol demethylases that are the targets of azole drugs such as ketoconazole) and the human liver enzyme CYP1A2 catalyses the N-demethylation of caffeine [54,55]. N- and S- oxidation and dehydrogenation reactions are commonly carried out by liver CYPs in the Phase I clearance of pharmaceuticals, e.g. in the deamination of amphetamine by CYP2C3 [56]. Epoxidation is a common P450 reaction for unsaturated fatty acids and other compounds, e.g. the epoxidation of olefins by CYP2B4 and polycyclic aromatic epoxidation reactions done by CYP1A1 and CYP1B1 enzymes [51,57]. A non-concerted epoxidation may lead to 'heme suicide' by pyrrole nitrogen alkylation through a reactive intermediate formed during the oxidation mechanism [58].

While these common P450 reactions are diverse they usually follow the typical mono-oxygenation route involving activation of molecular oxygen and the utilisation of electrons donated by P450-redox partners (Covered in detail in Section 1.12). Several other chemical outcomes are also found in P450 reactions across nature, including isomerization, reduction, nitration and C-C bond formation [59].

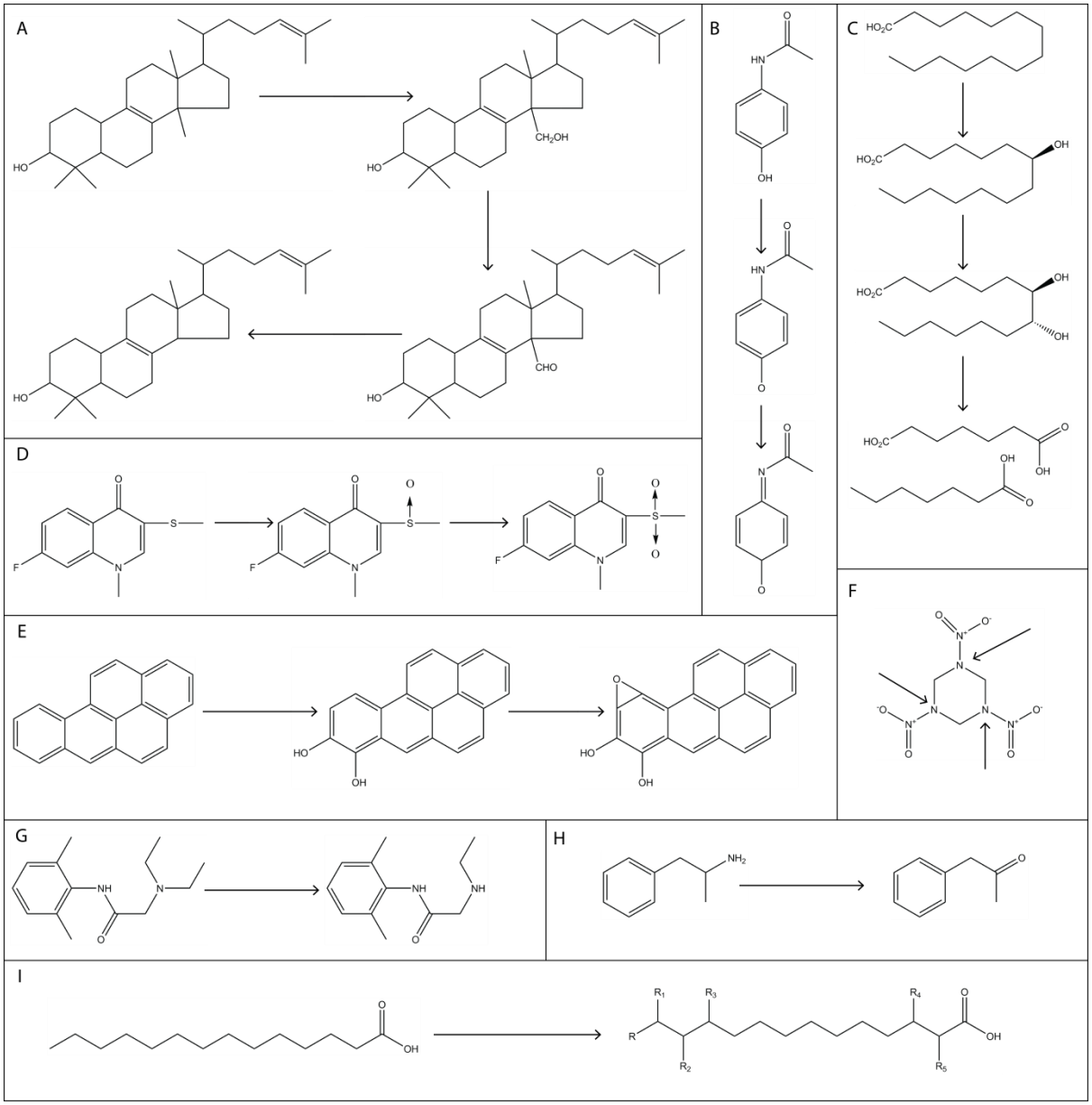
A
HO
CH2OH
CHO
B
HN
OH
O
C
HO2C
OH
D
S
F
N
E
HO
OH
F
G
NH
N
H
NH2
I
R
R1
R2
R3
R4
R5

Figure 1.10 Exemplary P450 reaction chemistry. The major classes of the diverse P450 chemistry repertoire are represented in panels A through I. **A**, Demethylation through successive oxidation of lanosterol to ergosterol by fungal sterol demethylase CYP51 [60]. **B**, N-dehydrogenation of acetaminophen (paracetamol) to iminoquinone, likely by human liver P450 CYP2E1 [61,62]. **C**, C-C bond cleavage of myristic acid through successive hydroxylation by CYP107H1 P450 BioI from *B. subtilis* [63]. **D**, S-oxidation of the heart-failure drug flosequinan by human P450 CYP3A2 [64]. **E**, Epoxidation after successive hydroxylation of polycyclic aromatic benza[a]pyrene by mammalian P450 CYP1A1, leading to the generation of carcinogenic epoxide products [57]. **F**, Reductive denitration of RDX explosive by the P450-flavodoxin fusion CYP177A1 XplA from *Rhodococcus rhodochrous* at sites indicated by arrows [65]. **G**, N-deethylation of the antiarrhythmic drug lidocaine by rat liver P450s CYP2B1 and CYP2B2 [66]. **H**, Deamination of amphetamine by rabbit P450 CYP2C3 [56]. **I**, Hydroxylation of the saturated fatty acid, myristic acid. R1-R3 indicate the ω-1, ω-2 and ω-3 positions hydroxylated by the CYP102A1 (P450 BM3) enzyme from *B. megaterium* [67]. R is the ω position hydroxylated by eukaryotic CYP4 P450s [68]. R4 and R5 indicate the fatty acid α and β positions hydroxylated by CYP152A1 ($P450_{\beta S\beta}$) from *B. subtilis* [46]. Adapted from Munro et al. [59].

1.8 The Diverse Physiology and Distribution of Cytochromes P450

It has been stated previously that the P450 superfamily spans all the major kingdoms, including Archaea, and they have been shown to catalyse a large number of reactions, both biosynthetic and degradative [47]. The evolution and diversification of P450s point towards their complexity and to a broad range of important physiological roles.

1.8.1 Human P450s

Even before the discovery of P450s, the capacity of mammalian tissue to break down nonpolar xenobiotics was already recognised, despite the responsible agent(s) remaining unknown. There are presently 58 human CYP genes divided into 18 subfamilies, with the most abundant families being CYP1, 2, 3 and 4 [69]. They are typically expressed as membrane-bound monomers in the endoplasmic reticulum, although a group of steroid synthesising/metabolising P450s are also found in the mitochondrial inner membrane [70].

P450s certainly have a central role in drug metabolism, being responsible for 90% of phase I metabolism of xenobiotics in humans While a number of CYPs have been shown to take part in metabolising drugs in the liver, CYP2D6 is a key player, responsible for 25% of all xenobiotic metabolism in the human liver. However, CYP3A4 is the most promiscuous human P450 isoform and is responsible for ~50% of xenobiotic metabolism [71,72]. While P450s play a prominent role in drug detoxification, these activities stemmed from their original functions in endogenous substrate metabolism, and only represents a fraction of their capabilities. Roles for P450s have been established in a range of developmental processes, such as cell proliferation, transcriptional regulation and apoptosis induction [73–75]. They have been implicated in early embryonic development (with CYP1A1 expressed only 12 hours after fertilisation) and P450s involved in steroid synthesis are also induced early on in development [76]. P450-controlled metabolism of vitamin D is responsible for the maintenance of calcium homeostasis through vitamin D-activated calcium channels [77]. Sterol biosynthesis is an especially important P450 role in human metabolism and, as one example, CYP17A1 is responsible for the production of glucocorticoids and androgens in the adrenal glands [78].

1.8.2 Plant P450s

Plant P450s comprise the largest group in the P450 superfamily, with 5,100 members divided into 127 families, and with one particular family, CYP71, representing over half of all higher plant CYPs [79].

CYPs account for 1% of all plant protein coding genes, a proportion matched only by transcriptional and regulatory proteins. Plant CYPs are essential in the biosynthesis of membrane sterols and cell wall lignin, carotenoids for photosynthesis and hormones for plant signalling [80]. P450s in consumer crops are routinely genetically modified to increase the crop yield and to enhance resistance to pesticides/herbicides [81,82].

1.8.3 Bacterial P450s

The biodiversity of bacterial P450s, with over 1000 sequences catalogued, comes partially from their requirement to enable the host bacterium to metabolise different carbon sources,

and they are thus implicated in a variety of functions, including fatty acid and alkane hydroxylation and in the oxidative degradation of herbicides and explosives [83–85]. While initial interest in P450s was in mammalian systems, due to their roles in e.g. sterol synthesis and xenobiotic breakdown, the solubility of bacterial P450 systems makes them attractive enzymes that are more amenable to biochemical and structural studies than their membrane-bound mammalian counterparts [86]. Bacterial P450s are often exploited for biotechnological and pharmaceutical use due to their soluble nature (the N-terminal, membrane spanning anchor region present in eukaryotic P450s is absent from bacterial and archaeal P450s), the diversity of their reaction chemistry and their amenability to redesign. As an example, CYP107A1 from *Saccharopolyspora erythraea* is involved in the biosynthesis of erythromycin, the first macrolide antibiotic and still part of the World Health Organization's list of essential medicines [87,88].

Important early structural and mechanistic work was done on the "model" P450 enzyme $P450_{cam}$ (CYP101A1) from *Pseudomonas putida*, which was the first P450 to be crystallized and have its structure determined – providing an important "template" for what proved to be a common P450 fold. $P450_{cam}$ has also been an important model used for the isolation and characterization of short-lived intermediate species in the general P450 catalytic cycle (Figure 1.13) [89,90]. $P450_{cam}$ has also been extensively mutated to explore the roles of various amino acids important for P450 catalytic function, and has been rationally redesigned to oxidise the non-natural substrate pentachlorobenzene (PeCB), an environmental contaminant [91]. Much work has gone into the engineering and application of P450 BM3 (a catalytically efficient *Bacillus megaterium* cytochrome P450-redox partner fusion enzyme) for the production of human drug metabolites [92,93]. P450 BM3 is also an important model enzyme in the P450 superfamily, particularly in light of its fused redox partner being a homologue of the diflavin reductase enzyme that supports the function of the human microsomal P450 enzymes (NADPH-cytochrome P450 reductase) [94].

1.8.4 Fungal P450s

The 399 families of fungal P450s make these the most diverse compared to the P450 families belonging to other kingdoms [35]. This diversity of fungal P450s comes from the

need to degrade exogenous chemicals from plant matter for survival [95]. As an example, the CYP53 family members are widely distributed in 2 major fungal phyla: the Ascomycota and the Basidiomycota, due to the crucial roles they play in overcoming plant defences [96]. The CYP53 family enzymes catalyse the *para*-hydroxylation of benzoic acid and other natural plant antifungals, e.g. salicylic acid [97,98]. Other bioprocesses involving fungal P450s can range from the synthesis of cholesterol-lowering drugs such as lovastatin by $P450_{LovA}$ from *Aspergillus terreus*, to corticosteroid production by CYP509C12 in *Rhizopus oryzae* [99,100] Only the CYP51 and CYP61 families are conserved among fungi and their functions are in ergosterol production for membrane integrity [101,102]. For this reason, CYP51 and CYP61 are drug targets for azole inhibitors, which bind in their active sites and coordinate to the heme iron in the distal position to inactivate P450 function [103].

1.8.5 Viral P450s

In 2004 the 1.2 Mbp genome of *Acanthamoeba polyphaga mimivirus* (APMV), the largest known virus, was sequenced and the mimivirus was found to contain 2 putative *CYP* genes [104]. This was an extraordinary discovery as, of the 4,854 viral genomes sequences listed on the NCBI, no other *CYP* ORFs have been observed [105]. The YP_142886 mimivirus gene was designated *CYP5254A1*, and encoded a P450 of 486 amino acids that is homologous to CYP37B1, a nematode P450 with 25% amino acid sequence identity. The YP_143162 gene was designated *CYP5253A1*, and encoded a P450 of 709 amino acids as a putative P450 fusion enzyme with an N-terminal P450 domain homologous to the CYP51 protein from *Leishmania major*, with 23% amino acid sequence identity [22]. The C-terminal domain of CYP5253A1 is a domain of unknown function (DuF) with 26% amino acid identity to the glycosyl transferase HI4320 from *Proteus mirabilis* [22]. The evidence for mimiviruses having evolved prior to cellular life raises some interesting questions about the evolutionary origins of P450s. However, these viral P450s have likely resulted from horizontal gene transfer from its amoebic hosts, or from one of the scores of other parasitic bacterial endosymbiont hosts it infects, most of which have a high number of cytochrome P450 genes [104,106].

1.9 Cytochrome P450 Structure

The first P450 enzyme to be crystallised was CYP101A1, a camphor hydroxylase from *Pseudomonas putida* (P450cam) in 1985 [89]. P450cam was also the first bacterial P450 to be discovered and as a soluble protein presented great advantages for ease of purification and analysis over insoluble, membrane-bound mammalian P450s [107,108]. The structure of the BM3 heme domain (the first 472 residues of the 1048 amino acid flavocytochrome) was the next P450 structure to be solved, and in both substrate-free [109] and later substrate-bound forms, revealing a long and hydrophobic substrate access channel that could be occupied by long chain fatty acid substrates [110]. These substrate-free and substrate-bound BM3 heme domain structures revealed distinctive P450 conformations, suggesting that structural rearrangement occurs to accommodate the substrate. However, even though a palmitoleic acid-bound form of the BM3 heme domain was clearly in a "substrate bound'' conformation, the mode in which the substrate interacted with the heme was evidently non-productive. The ω-terminus of the fatty acid remained distant from the heme, with the carboxylate group of the substrate interacting with Arg47 and Tyr51 at the mouth of the active site, and with the ω-end of the substrate too far from the heme to enable the relevant ω-1 to ω-3 carbons to be hydroxylated by a reactive iron-oxo species on the heme. Thus, it appears that BM3 crystallises in a 'pre-catalytic' state, with its substrate too distant from the heme to permit its hydroxylation. Movement of the substrate from this position is clearly required to enable its oxidation. Using temperature-jump spectroscopy experiments, it was later demonstrated that substrates in the active site could occupy a proximal site which is close enough to the heme to permit oxidation and also a distal site 7.5 Å from the heme, as seen in substrate-bound crystal structures [111]. Recently, however, crystal structures of P450 BM3 heme domain mutants bound to omeprazole revealed occupancy of this drug substrate in the 'proximal site', 3.9-4.1 Å from the heme iron [93]. The crystal structures of A82F and A82F/F87V BM3 heme domain mutants have a well-defined conformation for omeprazole, which would also explain their high regioselectivity observed in oxidation reactions of this drug.

Members of a particular P450 family share less than 40% amino acid sequence identity with P450s from a different P450 family (often much lower identity). However, the basic P450 structural folds and topology are conserved [112]. The P450 fold is made up of two subdomains, the larger (α domain) contains mainly α-helices and the smaller (β domain)

has a substantial β-sheet content [113]. The α-helix rich subdomain comprises several helices (identified by consecutive letters) including the distal I-helix that spans the protein and makes close approaches to the heme, including residues important for substrate interactions and for protonation of heme iron-oxo species. The most highly conserved feature, however, is the so-called heme binding sequence found on the β subdomain with the sequence FxxGx(H/R)xCxG [114], where the cysteine residue is the invariant thiolate proximal ligand essential for catalytic activity, and where "x" signifies variability in the amino acid present at this position [115]. The phenylalanine (Phe393 in P450 BM3) is important in making interactions with the thiolate-iron bond and various F393 mutants were shown to have substantial effects on the heme iron redox potential [116]. The amide (NH) groups of the residues neighbouring the invariant cysteine thiolate moderate its negative charge, which causes an increase in reduction potential of the ligated heme iron [117]. This reduction potential modulation via peptide NH hydrogen bonding has also been observed in other heme containing monooxygenases, such as nitric oxide synthase (NOS) and chloroperoxidase (CPO) [118,119].

The most affected regions of the P450 BM3 heme domain structure upon substrate binding are the F- and G- helices and the inter-helical F/G loop [120]. In Figure 1.11 the Asp217-Asp255 salt bridge is stabilised in the substrate-bound form, while the Lys224-Asp255 residues also shown form a salt bridge in the substrate-free form. The movement of the F- and G-helices upon substrate binding accompany the active site adopting a 'closed' conformation where it becomes quite solvent inaccessible [121].

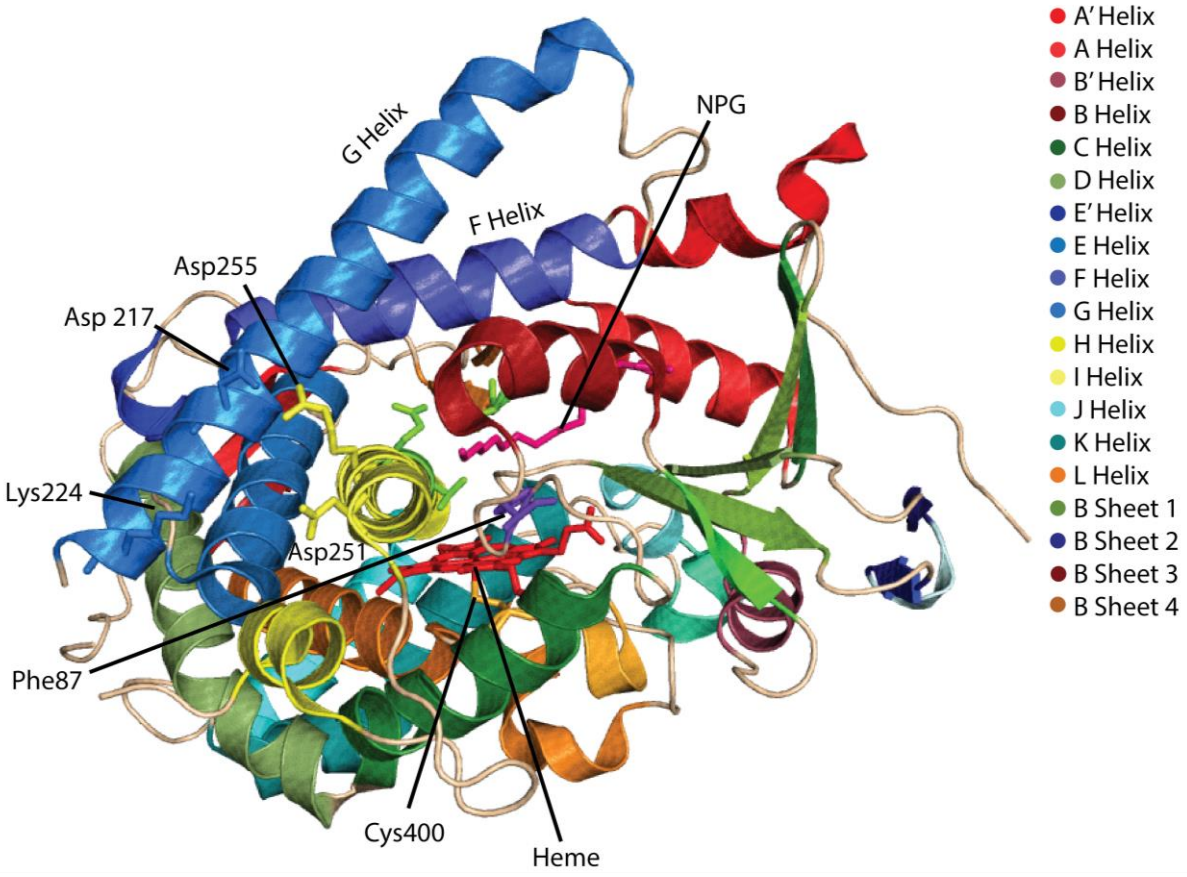

Figure 1.11 An Exemplary P450 Structure. The N-palmitoylglycine (NPG)-bound P450 domain structure (PDB code 1JPZ) of the *Bacillus megaterium* flavocytochrome P450 BM3 is shown [122]. The major α-helices are individually colour coded in the legend and labelled A-L, following the standard nomenclature, while the β-sheets are coloured by group [123]. The P450 structure is orientated for looking along the I helix (yellow). The heme cofactor (red) is shown with a cysteine proximal ligand (orange) and the bound NPG molecule in pink. Some residues affected upon substrate binding are also labelled: Phe87 perpendicular to the heme is shown in purple, while residues involved in salt bridge disruption (Lys224 – Asp251) and formation (Asp217 – Arg255), which are responsible for conformational changes in the I helix, are also labelled. Glu267 and Thr268 (unlabelled) on the I helix are shown coloured green, and are crucial as a proton relay system that protonates heme iron-oxo species (ferric-peroxo and then ferric-hydroperoxo) to facilitate compound I formation and oxidative catalysis.

In the substrate-free 'open' form the I-helix has a 13° kink arising from a water molecule inserted between the backbone carbonyl and amide groups of Ile263-Glu267 and Ala264-Thr267 [122]. Substrate binding is accompanied by disruptions in I-helix hydrogen bonding and pivotal water molecules allow new hydrogen bonds to form directly between Ile263-Glu267 and Ala264-Thr267 [124]. The displacement of the distal-ligated water

molecule (Wat500) upon this structural rearrangement allows dioxygen binding to ferrous heme iron, following the first electron transfer from the redox partner. Another water molecule (Wat501) is coordinated between the dioxygen ligand and the amide group of Thr268 (Figure 1.11). This threonine is highly conserved in P450s and stabilises the hydrogen bonding network that allows the proton deliver events to heme iron-oxo species required for oxygen scission. This altered bonding rearrangement and accompanying water displacements results in the straightening of the I-helix, now only bent by 5° (Figure 1.11) [122].

The ligand-induced open and closed conformations in BM3 are analogous to the previously identified conformational changes in P450cam, including the conformational changes in the I-helix and resultant hydrogen bonding network redistribution [125]. However, the substrate-associated structural changes are more substantial in the P450 BM3 heme domain. In P450cam, binding to its redox partner putidaredoxin (Pdx) occurs in the 'open' conformation and causes structural rearrangement of certain substrate recognition sequences (SRS) including the F-G loop and I helix [126].

The BC loop is often disordered in P450s structures and changes in its organization are associated with substrate binding and recognition processes. The Phe87 residue in BM3 (Figure 1.11) is located on this loop and has its side chain parallel to the heme. The Phe87 side chain rotates by ~90° upon substrate binding [110]. Mutations to the Phe87 residue have effects on substrate specificity and particularly on regioselectivity in P450 BM3. For instance, the F87V mutant increased the proportion of 14(S)-15(R)-epoxidation of arachidonic acid from 20% to 100% [127].

1.10 P450 Heme Iron Spin State and Associated Redox Potential Changes

Heme iron has its outer 3d-orbital electrons split into 2 e_g and 3 t_{2g} orbital groups. In its resting state the heme iron is coordinated by 6 ligands in an octahedral conformation, which is responsible for a large energy difference between e_g and t_{2g} orbitals known as the octahedral energy splitting (ΔG), shown in Figure 1.12. This energy difference is ligand-dependent and can be measured [128]. P450 inhibitors (e.g. cyanide and azoles) are strong field ligands and π-acceptors which increase the splitting compared to the native water distal ligand. The energy difference is such that it is more energetically economical to spin

pair 4 electrons in the lower energy t_{2g} orbital than to have 2 in the higher energy e_g orbital. The resulting spin value (S) is ½ (2 x 0 + 1 x (+½)) – i.e. ((no. of e_g orbitals x electrons occupying them) + (no. of unpaired electrons in t_{2g}). This gives a value of S = ½, which gives the ferric low-spin heme iron a paramagnetic property.

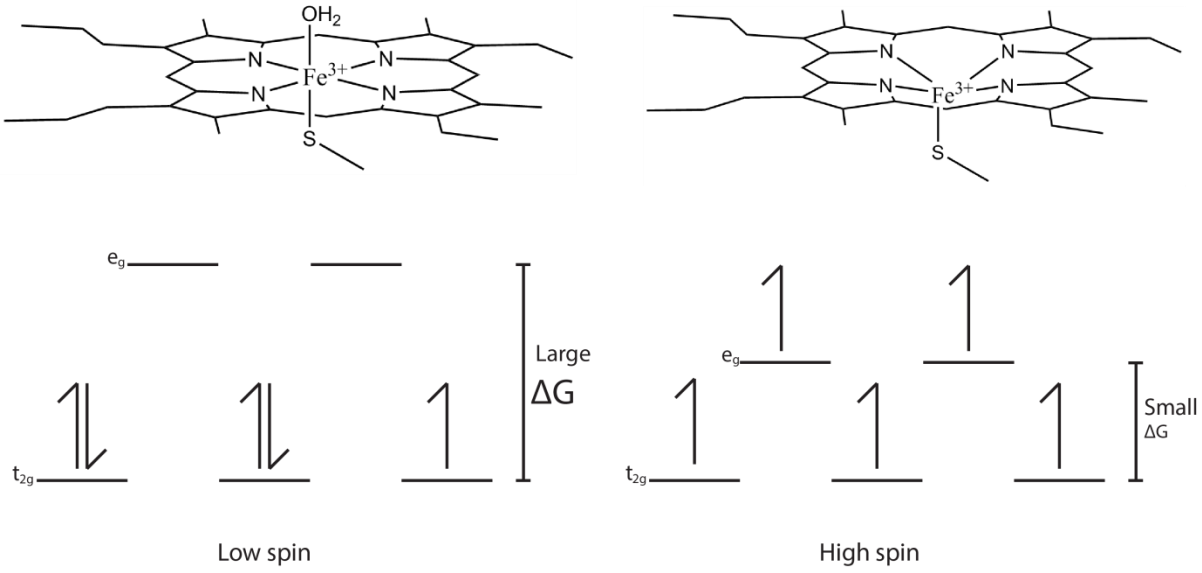

Figure 1.12 Heme iron (Fe^{3+}) d-orbital arrangement. The low-spin P450 heme iron (S indicates a cysteine thiolate ligand) in an octahedral conformation (top, left) is shown above a diagrammatic representation of its electronic configuration (bottom, left), where all of its 5 valence electrons occupy the low energy t_{2g} orbitals and its spin value (S) = ½. Substrate-induced water displacement alters the heme iron ligation state, shifting it to high-spin with an S value of 5/2. This pentacoordinated conformation (bottom, right) has the 5 electrons equally distributed among orbitals, as the energy barrier between the orbital groups (t_{2g} and e_g) is now lower than the spin-pairing energy.

In the initial step of the catalytic cycle (explained below in Section 1.11), a substrate displaces the water ligand and the heme iron becomes pentacoordinated. This change in conformation lowers the energy splitting difference (ΔG) as the heme iron shifts from low- to high-spin with an S value of 5/2 (5 x (+½)). The ΔG is now lower than the electron pairing energy and so the electrons become evenly distributed among the higher and lower energy orbitals (Figure 1.12), resulting in all the orbitals having single electron occupancy and a single orientation of spin state.

In its substrate-free, low-spin resting state the P450 heme iron redox potential is ~-300 mV vs. SHE, regulated by the distal cysteine thiolate ligand; while related heme proteins with a distal histidine ligand, e.g. myoglobin, have a higher redox potential at ~60 mV [19,129]. The electronegative cysteine thiolate has a greater electron "push" effect than the histidine nitrogen, which increases the electron density in the porphyrin ring, which in turn reduces the propensity for the heme iron to accept electrons (due to electrostatic repulsion) and accounts for its lower resting redox potential.

The binding of substrates to P450s displaces the 6^{th} axial water ligand from the heme iron and the associated change from low- to high-spin causes a radius expansion of the Fe^{3+} heme iron, which moves out of the plane of the heme and closer to the proximal cysteine thiolate ligand. This altered heme environment alters the iron redox potential, making it easier to reduce.

EPR and Mössbauer spectroscopic techniques have been used to characterise the spectral changes observed upon P450 heme iron spin shift, giving insights into the contributions from substrate and iron-ligation on spin state [130,131]. Mössbauer spectroscopy is a very sensitive technique able to report on the electric and magnetic interactions of the iron nucleus through sensitive measurements of the energy absorbed upon γ-ray exposure [131]. Initial Mössbauer spectroscopy carried out in P450s characterized the parameters for substrate-free and camphor-bound P450cam, and a mixture of high- and low-spin heme iron was shown in the latter form [132]. EPR spectroscopy allows the measurement of energy separation between spin-states (Figure 1.12) which is crucial for defining distal heme ligands and their effect on the heme plane and electronic environment [133].

1.13 The Cytochrome P450 Catalytic Cycle

Enzymes in the P450 superfamily perform a multitude of important biochemical reactions, as previously discussed. The most common and well-characterised reaction is C-H bond hydroxylation, and the breakdown of the 8-step P450 catalytic cycle considered to underpin this and other P450 activities (Figure 1.13) is as follows:

1. Substrate binding

   Preceding substrate binding, the typical P450 heme ferric iron (Fe^{3+}) is hexacoordinated with a water molecule in the 6^{th} (distal) ligand position, and the heme is planar relative to its 4 heme-pyrrole nitrogen bonds. Its 3d electrons are in a low energy resting state (S = ½).

   Effective P450 substrates displace the distal water ligand upon active site entry. This loss of the water ligand converts the ferric iron into a pentacoordinated state and, due to a change of atomic radius, it occupies a 'sunken' position out of the plane of the protoporphyrin ring towards the proximal cysteinate ligand [123]. This change in ligand coordination is also manifested as a shift in its electrons from a low- to a high-energy (low-spin to high-spin) state accompanied by a significant increase in reduction potential, typically around 140 mV [129], the importance of which will be discussed in the description of the following step.

   Associated with this heme iron coordination and electronic energy state change towards high-spin, a defining feature for P450 enzyme behaviour, is the heme Soret band shift to a lower wavelength (~390 nm), known as a type I shift [134].

   Conversely, most inhibitors and strong binding axial ligands (e.g. imidazole, and CO in the case of the ferrous heme iron), cause the heme iron electrons to occupy a low-spin system in a hexacoordinated state, resulting in a red shift of the Soret band to higher wavelengths, known as type II shift (e.g. to ~424 nm in the case of imidazole binding to ferric P450 heme iron) [134].

2. Initial heme reduction step

The aforementioned increase in oxidation potential upon axial water ligand displacement by substrate binding makes more favourable the single electron reduction of ferric heme iron (Fe^{3+}) to the ferrous (Fe^{2+}) state by its redox partner [135]. This avoids the unnecessary transfer of electrons to the heme iron in the P450 substrate-free form, and the wastage of electrons from NAD(P)H in non-specific oxygen reduction (to form either superoxide, peroxide or water according to which point in the catalytic cycle there is non-productive "collapse" of a particular iron-oxo species) [136].

3. Oxygen binding to ferrous heme iron

Only after stage 2 is O_2 is able to bind (to the ferrous heme iron). This increase in affinity can be attributed in part to their spin-spin interaction energies, the product of the two quantum spin numbers, being the dominant force in the oxygen binding process [137]. The ferrous iron has an unpaired electron in the d_Z^2 orbital with sufficient energy to spin pair with an odd electron in the oxygen antibonding orbital [138].

The pentacoordinated ferrous heme iron has a great affinity for small electronegative π-acceptor ligands like molecular oxygen, and their binding returns the heme iron to its planar, hexacoordinated state and forms a nucleophilic ferrous-oxo intermediate [139]. The highly electronegative oxygen is able to pull an electron from the heme iron to form a ferric (Fe^{3+})-superoxo species which is isoelectronic with the ferrous-oxo form.

4. Second heme reduction step

The highly oxidizing ferric (Fe^{3+})-superoxo species generated in the preceding step is able to receive the second and final electron transferred from the redox partner to form a ferric (Fe^{3+})-peroxo heme complex. The now doubly reduced species has one electron on the oxygen atom and the other delocalised on the cysteinate ligand [140]. This step and the initial electron transfer step are considered to be the slowest in the entire P450 catalytic cycle.

5. Initial proton delivery step (Compound 0 formation)

The ferric-peroxo species readily accepts a proton to form a ferric (Fe^{3+})-hydroperoxo species known as Compound 0 [141]. A "shortcut" to this species can be achieved using the so-called "peroxide shunt" method – whereby H_2O_2 (or other organic peroxides) can be used to convert a ferric heme iron directly to compound 0 (Figure 1.13). However, this is typically an inefficient process and peroxide-dependent destruction of the heme competes with the productive pathway. Compound 0 production directly from H_2O_2 and ferric heme iron is used naturally by peroxygenase P450s and is discussed later in the thesis. X-ray crystallographic studies on $P450_{cam}$ and kinetic studies on P450 BM3 have implicated the E267 and T268 residues (a highly conserved amino acid "acid-alcohol" pair in the I-helix of P450 monooxygenases) in proton donation to the ferric-peroxo intermediate to form Compound 0 [142,143]. The threonine reside also stabilises the ferric-hydroperoxo species and functions in the second proton delivery to form Compound I (following section) while the glutamate residue may aid this process through the stabilisation of the water network in the active site, and potentially as a conduit for proton transfer to the iron-bound dioxygen [144,145].

6. Second proton-to-heme delivery and accompanying water loss (Compound 1 formation)

The second protonation of oxygen causes intramolecular oxygen bond splitting and the subsequent loss of a water molecule, resulting in the formation of a ferryl (Fe^{4+})-oxo species responsible for substrate oxidation, the (until recently) elusive Compound I [146].

Compound I is able to abstract a hydrogen from the substrate via the oxygen rebound mechanism (Figure 1.14, Section 1.11.1) to form a caged substrate radical and a ferryl (Fe^{4+})-hydroxy species known as Compound II [147,148].

7. Product formation and 8. Product release/water re-binding

The substrate radical formed quickly attacks Compound II, which results in the formation of a new bond to the hydroxyl group and thus forms a transiently heme-bound hydroxylated product [149]. The cycle is completed with water or substrate replacing the oxidised product, which quickly diffuses out of the active site once generated.

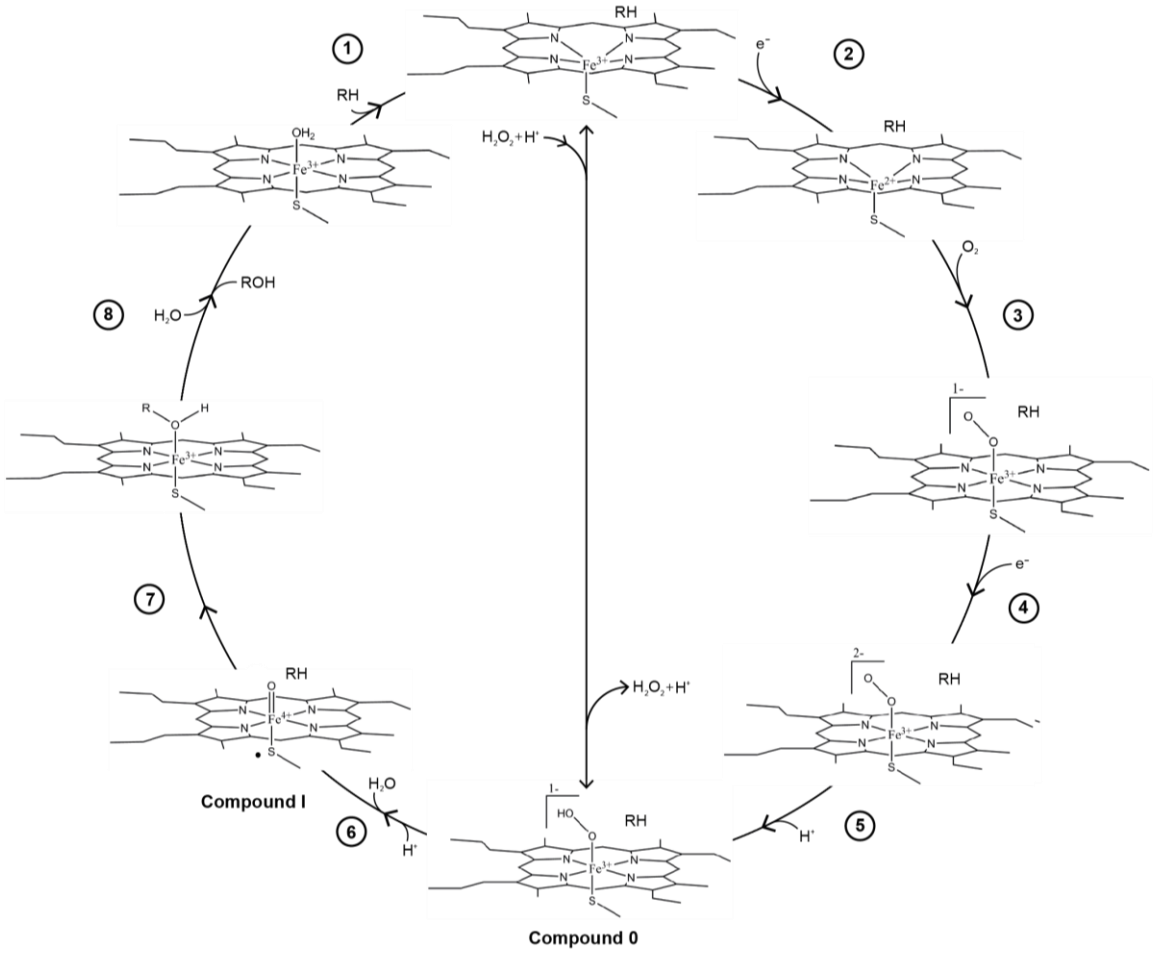

Figure 1.13 The P450 catalytic cycle and peroxide shunt pathway. The 8 distinct steps of the now fully characterised P450 catalytic cycle are shown numbered, and are referred to and described in the text. The protoporphyrin ring is accurately represented with the four nitrogen atoms emphasised and with the Fe and S representing heme iron and cystein(at)e sulfur in their various states. Substrate and product are shown as RH and ROH, respectively. The peroxide shunt is shown and discussed later. Steps 7 to 8 and the oxygen rebound mechanism, including the active species, are explained below.

1.11.1 The Final Solution to the Active Species Question: Elucidation of Compound I

As early as 1978, Groves obtained kinetic isotope effect (KIE) data that pointed to a ferryl-oxo complex as the active species responsible for C-H bond activation via hydrogen abstraction in the P450 catalytic cycle [148] and using the oxygen radical rebound mechanism (Figure 1.14), which was consistent with a previously proposed mechanism for metal-oxo intermediates [150].

A computational model proposed a 2-state reactive pathway involving a high-spin quartet state and a low-spin doublet state ferryl-oxo species [151]. The mechanism suggested that the high-spin species was responsible for the hydrogen abstraction via the oxygen rebound mechanism, further supporting the prevalent theory.

Compound I has unpaired electrons in its heme d-orbitals, making it detectable by EPR and ENDOR spectroscopy as shown in a close P450 relative, chloroperoxidase (CPO) [152]. CPOs have polar residues in their active site which stabilise anionic peroxo species, increasing their half-lives and making them more easily detectable compared with the hydrophobic lipid-binding active sites in P450s.

A variety of experiments using EPR and ENDOR in combination with flash freeze-quenching and slow reacting halo-substrates were employed to achieve concentrations of compound I high enough for accurate detection. A species identified as compound I and apparently identical to the one in CPO was reported [153,154]. However, the species detected were later shown to likely arise from iron-nitrosyl complexes [155,156].

Investigations into catalytically active species via X-ray crystallography elucidated the entire catalytic cycle of horseradish peroxidase (HRP) including compound I, which added to evidence supporting the use of the same radical rebound mechanism in P450s as in HRP. However, a similar experiment involving P450cam failed to unequivocally characterise compound I, but gave further insights into its formation [125,157].

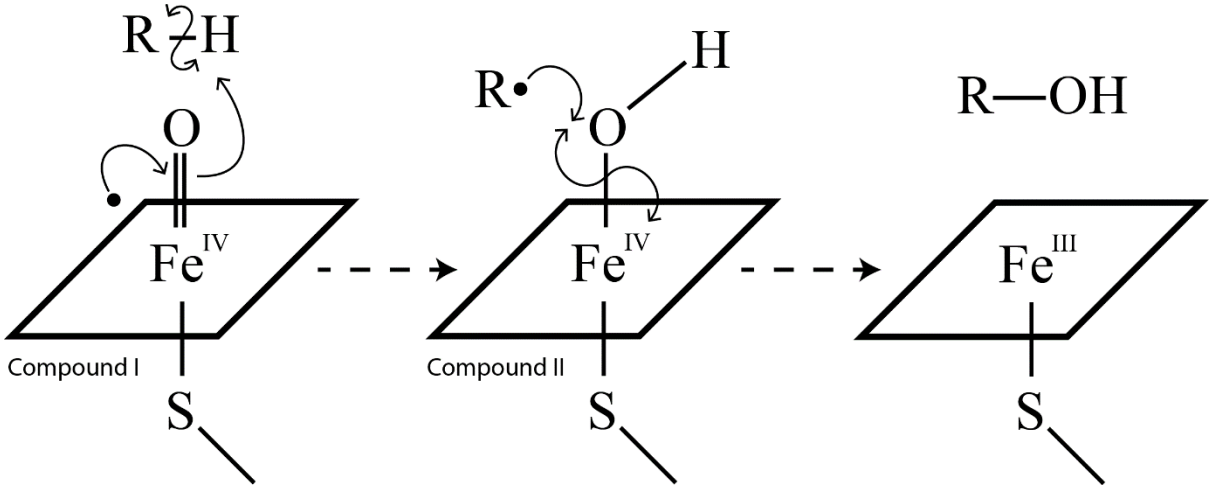

Figure 1.14 The oxygen rebound mechanism for aliphatic bond activation by cytochrome P450. The porphyrin ring is shown as a parallelogram with iron oxidation state in roman numerals and the S indicating thiolate ligation of the heme iron. Compound I (left) with a porphyrin π radical abstracts a hydrogen from the substrate (RH) by heterolytic cleavage of the R-H bond to produce a substrate radical and the ferryl (Fe^{4+})-hydroxo species known as compound II (middle). The substrate radical generated rebounds onto compound II, resulting in bond formation with the OH group, forming the ROH product and returning the heme iron to its resting high spin (Fe^{3+}) state (right).

Ultimately it was Rittle and Green who successfully managed to take a *bona fide* "snapshot" of compound I [146]. Using highly purified CYP119A1 from the thermoacidophilic crenarchaeon *Sulfolobus acidocaldarius* they managed to obtain a 70% yield of compound I after mixing the ferric CYP119A1 protein with *m*-chlorobenzoic acid (a peroxide donor) at 4 °C. Using Mössbauer and EPR techniques, they were able to categorically confirm compound I formation.

1.11.2 Rate Limiting Steps in the P450 Catalytic Cycle

Early work using P450s in rat liver microsomes pointed towards the 1st and 2nd electron delivery steps from P450-redox partners as the major contributors to catalytic rate limitation in P450s [158,159]. This may be generally accepted for P450s, but is obviously too simplistic, as it would imply that all P450 reactions would then proceed at a similar rate, which is clearly not the case [47,160]. Contributions from other steps in the catalytic cycle (Section 1.11), e.g. the binding of the substrate, oxygen binding step, protonation

steps and product release rate constants, all uniquely affect P450 reaction rates. In particular, substrate binding and orientation steps along with product dissociation (particularly if the product retains high affinity for the active site) are likely to be influential in many cases [161].

1.11.3 The Peroxide Shunt and Alternative P450 Mechanisms

Some P450s are able to use an alternate source of electrons/protons/oxygen which can obviate the need for redox partners (Section 1.12). P450 peroxygenases can utilise hydrogen peroxide to directly form compound 0, bypassing the initial steps of the classical P450 catalytic pathway (Figure 1.13). In most P450s this route can often lead to low turnover rates, destruction of the heme and protein oxidation, due to the inefficiency of this process and as observed with P450cam [162]. The bacterial CYP152 family, however, has apparently evolved to use the peroxide shunt pathway naturally, and members were shown to safely exploit this pathway, without excessive heme destruction. $P450_{SP\alpha}$ from *Sphingomonas paucimobilis* and $P450_{BS\beta}$ from *Bacillus subtilis* use this 'peroxide shunt' to catalyse the hydroxylation of long chain fatty acids near-exclusively at the α-position and predominantly at the β-position, respectively [45,46]. P450 OleT from the same family is also able to decarboxylate long chain fatty acids into their n-1 terminal olefins using this peroxide-dependent pathway [163].

Fungal nitric oxide reductase P450s ($P450_{nor}$ enzymes) also use an alternate mechanism to reduce nitric oxide. The coordination of a nitric oxide (NO•) molecule to the heme iron directly inhibits P450 enzymes in most cases. However, the nitric oxide reductase CYP55A1, which is responsible for NO detoxification in the fungus *Fusarium oxysporum*, can bind and reduce NO• to N_2O in the absence of oxygen and redox partners [164]. It does so by directly binding NAD(P)H in the active site to facilitate hydride transfer directly to an NO•, with a second NO• molecule bound to the heme iron, allowing a very fast reductive reaction that produces N_2O with a catalytic rate of $>10^3$ s^{-1} [165]. The basic amino acid residues R64 and R174 in P450nor form a positively charged pocket that enable binding to NAD(P)H [166].

Some P450 reactions have been reported to proceed via intermediates earlier in the catalytic cycle than compound I. For example, P450 TxtE from *Streptomyces*

turgidiscabies catalyses nitration of tryptophan using both O_2 and NO in the biosynthesis of the pytotoxin thaxtomin. The proposed pathway uses the ferric-superoxo species (Step 3, Figure 1.13) to oxidise NO to NO_2•, which is then responsible for the nitration of a tryptophan substrate bound in the P450 active site [167]. In a distinct P450 system, The ferric-peroxo intermediate (Step 4, Figure 1.13) is proposed to be responsible for the last of the three-oxidation steps in the oxidative demethylation of sterols by the 14α-demethylase P450 enzymes (CYP51 family) [168]. The fungal sterol demethylases are examples of this class, and are inhibited by the azole class of drugs.

The ferrous and ferrous-oxy species (Steps 2 and 3, Figure 1.13) appear unlikely electron donors due to their low heme-iron potential of approximately -300 mV [129] and tight O_2 affinity. However, P450s have been shown to catalyse the reduction of a number of substrates, e.g. tetrachloromethane by P450cam [169] and glyceryl trinitrate by CPY3A [170].

1.12 Redox Partners

Electron transfer underpins many of the most fundamental functions necessary for cellular life. The flavodoxin/ferredoxin $NADP^+$ oxidoreductase (FLDR/FNR enzymes) family members, participate in many important biological redox chains, e.g. in photosynthesis, facilitating the transfer of electrons between ferredoxin/ferredoxin reductase (Fd/FNR) and the cellular cofactor NADP(H). However, certain FNR-type flavoproteins do catalyse reactions other than pure electron transfer, for example the Baeyer-Villiger monooxygenases, a related family of FAD/NADPH-dependent (type I) or FMN/NADH-dependent (type II) monooxygenases, catalyse the oxidation of linear or cyclic ketones into esters or lactones, respectively, using a mechanism with some similarities to that of the P450s [171,172].

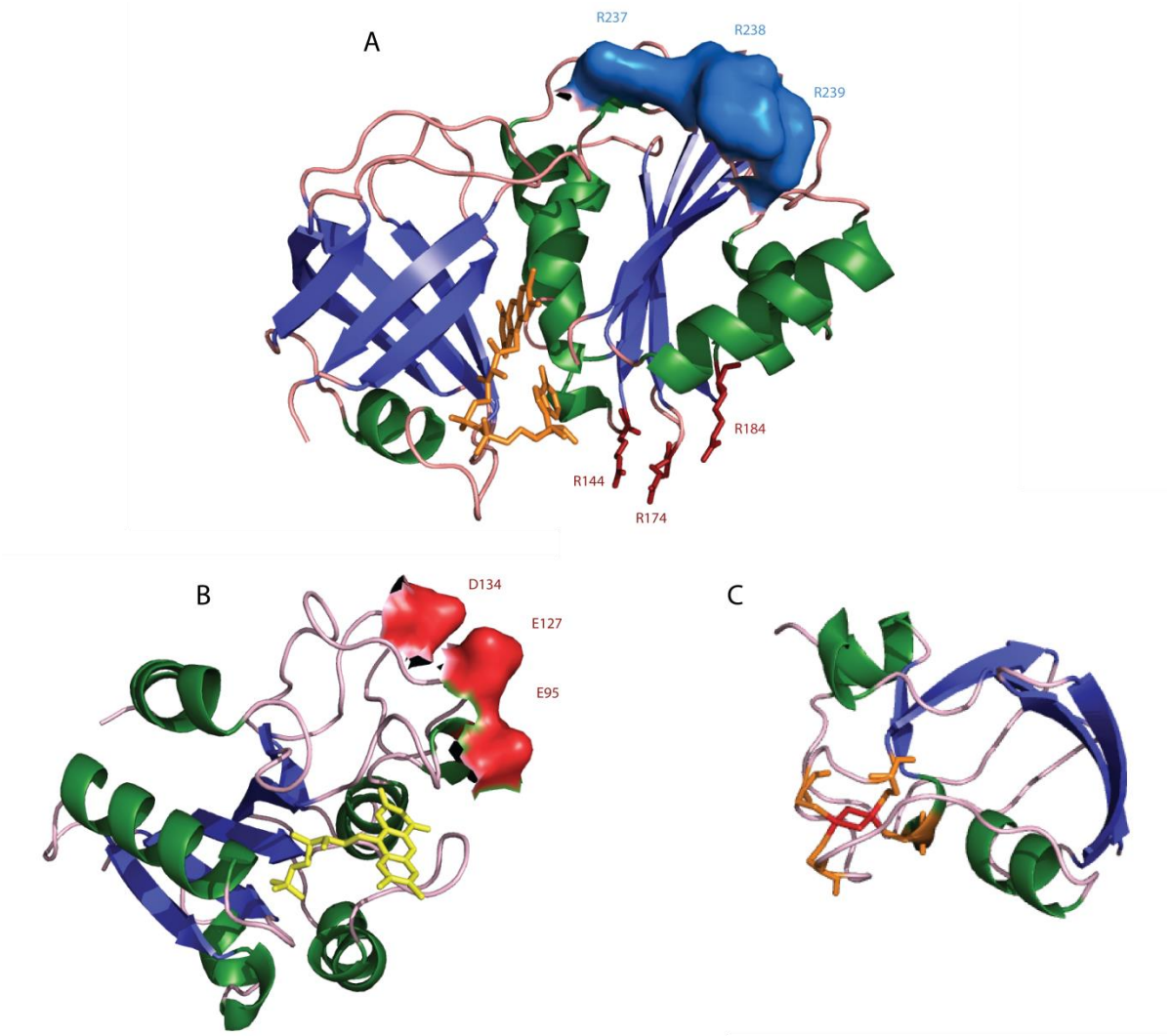

Figure 1.15 The structures of *E. coli* flavodoxin and flavodoxin reductase, and of *S. oleracea ferredoxin*. The secondary structures of these proteins are shown with a common design. The α-helices are coloured green, the β-sheets are in blue and the loop conformations are in pink. **Panel A**: The *E. coli* flavodoxin reductase (FLDR) structure (1FDR) with bound FAD cofactor in orange. Arginine residues R144, R174 and R184, shown in red, are important in binding NADPH and in facilitating efficient hydride transfer to the FAD, while surface residues R237, R238 and R239, shown in blue, facilitate ionic bonding with FLD. The Rossmann-like fold is the β-sheet arrangement on the right hand side of the structure. **Panel B**: The *E. coli* flavodoxin structure (1AHN) with bound FMN in yellow. Glutamate residues E95 and E127 and aspartate residue D134, shown in red, bind to the surface arginine residues (R237, R238 and R239) in FLDR. **Panel C**: the spinach (*Spinacia oleracea*) ferredoxin structure (1A70) with the bound iron sulfur cluster (2Fe-2S) in red and its 4 coordinating cysteine residues (C39, 44, 47 and 77) coloured orange.

The cytochrome P450 reductase (CPR), phthalate dioxygenase reductase (PDOR), glutathione reductase (GR), nitrate reductase (NR) and sulfite reductase (SiR) enzymes are all members of the FNR family [173–177]. Across these groups, a consistent protein fold

consisting of two contiguous domains occurs: an N-terminal flavin cofactor-binding subdomain and a NAD(P)(H)-binding subdomain, which are linked to the C-terminal flavodoxin/ferredoxin redox partner domain (Figure 1.15). The N-terminal domain binds an FAD cofactor (FMN in the case of PDOR) and provides the site for binding to NAD(P)(H), which is composed of multiple beta-strands in a Rossmann-type fold [178]. Both flavin- and NAD(P)(H)-binding domains are conserved in all members, with the specific cofactor-binding regions being particularly well conserved. In the *E. coli* flavodoxin reductase (that resembles the N-terminal, FNR domain of the above listed enzymes), a series of arginine residues (R144, R174 and R184) all participate in the binding of NADP(H). R174 is the most highly conserved residue among this trio in FNR proteins, as it interacts with the 2'-phosphate moiety of NADP(H), which confers NADPH preference over NADH [179].

The transfer of electrons between proteins such as FLDR and FLD in *E. coli* is governed in part by the electrostatic forces between surface amino acids at the binding sites of cognate redox partners. The positively charged surface arginine residues (R237, R238 and R239) on FLDR (Figure 1.15) facilitate ionic bonding with FLD through its negatively charges surface residues (E95, E127 and D124) [180].

The rate of electron transfer is also influenced by the difference in redox potential between the acceptor and donor species, the distance between these cofactors, and the nature of the interstitial medium between the redox centres [181]. The electron transfer rate constant and protein-protein interactions may both be affected by conformational changes associated with protein-protein interactions, NADP(H) binding and the redox state of the cofactors.

The NADPH-flavodoxin reductase in *E. coli* (FLDR) is known to reduce both Fd and FLD proteins, and is thus involved in important roles including the flavodoxin-dependent reduction of methionine synthase, pyruvate-formate lyase, ribonucleotide reductase and biotin synthase [182–185].

For flavodoxin, the surface residues that compose its binding interface with FLDR overlap with those that form the interaction interface between the fused FAD/NADPH-binding and FMN-binding domains of methionine synthase (a diflavin reductase, like cytochrome P450 reductase) [186]. This system is analogous to the 2Fe-2S-binding putidaredoxin (Pd), which is able to bind and abstract electrons from its FAD-binding redox partner putidaredoxin reductase (PdR), and also to bind to and deliver electrons to P450cam, but

cannot bind to both partner proteins simultaneously (i.e. it works by forming consecutive binary complexes with its partners – shuttling between them) [187,188]. P450cam follows the same mechanism outlined in Section 1.11 to oxidise its camphor substrate to 5-*exo*-hydroxycamphor, which requires the successive delivery of two single electrons in two temporally distinct events [123]. To achieve this outcome and enable P450cam compound I-dependent camphor hydroxylation, the P450cam-Pd-PdR system would have to achieve four productive collisions and up to three dissociations per turnover, which clearly has potential to affect the overall rate constant for the substrate hydroxylation reaction. From a genetic perspective, the P450cam, Pd and PdR genes are all encoded on the same plasmid in *Pseudomonas putida*. However, similar genetic co-location does not normally occur in eukaryotic systems. For examples the genes for the numerous microsomal CYPs and their cognate CPR are widely separated in the genome, although the encoded enzymes localise to microsomes. Protein sequence studies led to the proposal that the evolutionary origin of CPR-type genes (including the diflavin reductase methionine synthase) is from the fusion of bacterial-like flavodoxin (FLD) and FNR/FLDR genes, with which they shares a high degree of similarity [189]. This is also the case for the CPR-like reductase domains in fusion proteins including flavocytochrome P450 BM3 from *Bacillus megaterium* (and related CYP102A family enzymes) and the mammalian NOSs [190,191].

1.12.2 Cytochrome P450 Redox Partner Diversity and Classification

P450 enzymes can be divided into groups based on their cognate redox system. Early on in P450 research, 2 classes were used to classify the superfamily, as only a relatively small number of P450s were being studied. Class I are the bacterial, NADH-dependent systems with 3 soluble components (Figure 1.16). The first example of the class I system was the P450cam system from *P. putida*, in which electron transfer occurs from NADH to the FAD-containing putidaredoxin reductase (PdR), which in turn passes 2 electrons (1 at a time) to the iron-sulfur cluster-binding putidaredoxin (Pd). The Pd then transfers two single electrons to P450cam to form first the ferrous form and then (after binding of oxygen) the ferric-peroxo species [107]. A variant of the class I system has been observed in *Citrobacter braakii* where $P450_{cin}$ (CYP176A1) oxidizes cineole, and also in *B. subtilis* where $P450_{BioI}$ (CYP107H1) is able to catalyse fatty acid hydroxylation. In these systems, homologous (in both cases) and heterologous (for $P450_{BioI}$) NADPH-dependent

FLDR/FLD redox partners are used for productive catalysis [192,193]. Thus, these systems can use a soluble FMN-containing flavodoxin in place of a ferredoxin (Fdx). However, the true physiological role of $P450_{BioI}$ is likely to be in the 3-step oxidative cleavage of a long chain fatty acid attached to an acyl carrier protein (ACP) and delivered to the P450 through formation of a loaded ACP-P450 complex. The relevant product from the reaction is considered to be the C7 diacid pimelic acid, an intermediate in the biotin synthesis pathway [194].

Class II eukaryotic redox partner systems are usually NADPH-dependent systems with 2 membrane-bound components; an FAD- and FMN-containing CPR and the P450 enzyme, both localised to microsomal membranes (Figure 1.16). Domains homologous to the FLDR and flavodoxin (Fldx) proteins are naturally fused in the CPR enzyme that supports the function of microsomal P450s [186]. Many eukaryotic P450s operate class II redox partner systems, including CYP2C5 which is involved in progesterone metabolism [70]. Mammalian adrenal mitochondrial systems are involved in steroid synthesis, e.g. CYP11A1 which converts cholesterol to pregnenolone [195]. However, mitochondrial P450s are supported by an NADPH-dependent, FAD-binding adrenodoxin reductase (ADR) and a 2Fe-2S ferredoxin (adrenodoxin, AD). These were initially classified into the wider class I system, but can also allocated to a class III system, as shown in Figure 1.16.

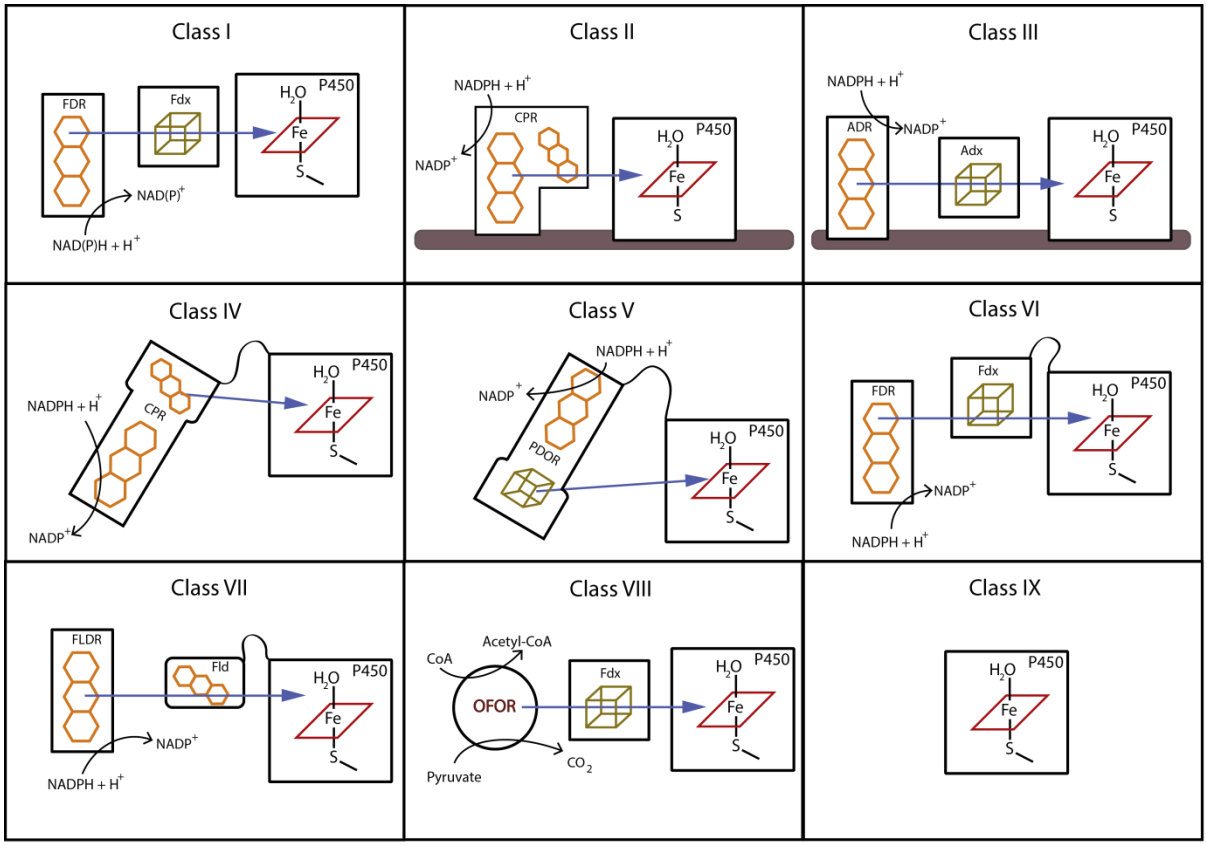

Figure 1.16 A schematic representation of diverse P450 systems and their redox partners. Abbreviations: FDR – NAD(P)H-dependent, FAD-containing ferredoxin reductase; Fdx – ferredoxin; CPR – NADPH-dependent FAD- and FMN-containing P450 reductase; ADR – adrenodoxin (ferredoxin) reductase; Adx – adrenodoxin (ferredoxin), PDOR – FMN- and 2Fe2S cluster-binding phthalate dioxygenase reductase; OFOR – 2-oxo-acid-ferredoxin oxidoreductase; Fld – FMN-containing flavodoxin. The P450 is represented in with the iron surrounded by a porphyrin ring as a red parallelogram in a ferric state, with a distal water and proximal cysteinate ligands. Each box represents a labelled P450 class with electron transfer depicted as a blue arrow passing from the left-most protein to the right-most protein, and with hydride transfer from NAD(P)H to the relevant protein as a black arrow. In class II and III the membrane is depicted as a thin brown cylinder. All classes are referred to in Section 1.12.2. Adapted from Hannemann et al. [196].

The advances in whole genome sequencing techniques in the past decades have uncovered many new P450 redox systems, such that their current classification system is not exhaustive and (due to the rate at which novel P450s and new redox partner and non-redox partner systems are discovered) the classification systems in the literature are currently proving inconsistent and incomplete. Figure 1.16 displays 9 known classes of P450s and their redox partners (including P450s that bypass redox partners).

With the discovery of P450 BM3 from *Bacillus megaterium* in 1986, the first cytosolic P450-CPR fusion, the first exception to the established 2-class rule arose (Class IV, Figure 1.16) [67]. *CYP102A1* encodes a single polypeptide with an N-terminal P450 domain and a C-terminal CPR-like reductase domain separated by a short linker region. This fusion arrangement affords BM3 the highest catalytic rate recorded for a monooxygenase enzyme at 17,000 min^{-1} with arachidonic acid [197]. The first FMN-to-heme electron transfer, the likely major contributor to rate limitation in BM3, is ~223 s^{-1} at 25 °C, which is threefold higher than the reported CPR FMN-to-P450 electron transfer rate in CYP2B4 of ~80 s^{-1} [198,199]. The CPR domain of BM3 is also primed for rapid electron transfer, with hydride transfer from NADPH to the FAD cofactor occurring at >700 s^{-1} at 25 °C. [198]. The rapid electron transfer from the CPR through to the BM3 heme domain is in part due to its tethered P450 and CPR domains, enabling frequent productive collisions within the BM3 dimer that underpin its high monooxygenase activity [59].

More examples of the class IV system have been characterised since the discovery of P450 BM3. Notably, another two members of the CYP102A family: CYP102A2 and A3 were discovered in *Bacillus subtilis* and shown to be sub-terminal (ω-1 to ω-3) fatty acid hydroxylases, similar to P450 BM3 [43]. Class IV fusion enzymes have also been found in lower eukaryotes, including the membrane-associated fatty acid hydroxylase P450foxy (CYP505A1) from *Fusarium oxysporum* [200]. Gene sequencing techniques have uncovered many eukaryotic CYP505 family members of the class IV fusion enzyme type, including CYP505A2 from *Neurospora crassa* and CYP505B1 from *Fusarium verticilloides*, a putative hydroxylase involved in production of the mycotoxin fumonisin [201]. Importantly, the entire genome sequencing of the ascomycete fungus *Myceliophthora thermophila* led to the identification of CYP505A30 (P450 MT1) and its characterisation is detailed in Chapters 3 and 4 of this thesis.

The next type of P450-partner fusion identified by genome analysis was a P450-PDOR fusion (i.e. a P450 fused to a Phthalate Dioxygen OxidoReductase) in a *Rhodococcus* species [202]. This class V (Figure 1.16) fusion enzyme has some similarities to the class I system, being composed of an N-terminal P450 domain covalently attached to a NAD(P)H-dependent FMN- and 2Fe-2S cluster-containing reductase [203]. A few Class V members from the CYP116B family have now been expressed and characterised, e.g. CYP116B1, a thiocarbamate-herbicide degrading enzyme from *Cupriavidus metallidurans*

[204]. The class IV and V members comprising P450 BM3 and CYP116B1 and their homologues represent *bona fide* P450-reductase fusions that are self-sufficient, requiring only substrate, molecular oxygen and NAD(P)H to function [205].

The CYP51FX enzyme from *Methylococcus capsulatus* represents class VI in Figure 1.16. It is an N-terminal sterol 14α-demethylase P450 fused to a C-terminal 3Fe-4S ferredoxin, which obtains electrons from an NADPH-dependent ferredoxin reductase (FDR) [206]. The Royal Demolition Explosive (RDX)-metabolising XplA (CYP177A1) from *Rhodococcus rhodochrous* is a class VII fusion consisting of an N-terminal FMN-containing flavodoxin and a C-terminal P450 domain [84,207]. Classes VI and VII described here are 'partial' fusions in that they still need the assistance of a separate redox partner, an NADPH-dependent FDR in these cases, to reconstitute P450 function.

CYP119A1 from the thermophilic archaeon *Sulfolobus solfataricus*, used to identify compound I as described in Section 1.11.1, is shown in Class VIII in Figure 1.16. CYP119A1 interacts with a unique pyruvate-dependent 2-oxo-acid-ferredoxin oxidoreductase (OFOR) and functions using pyruvate and a source of electrons in place of NAD(P)H for catalysis [208,209].

Class IX in Figure 1.16 covers independent P450 domains that do not require a formal redox partner, fused or otherwise. They can be cytosolic and bind directly to their electron donating cofactor, such as P450nor which catalyses the conversion of 2 molecules of NO to N_2O using NADPH bound to the enzyme; or not require electrons for catalysis at all, such as CYP74A, an allene oxide synthase which catalyses substrate conversion using an intramolecular electron transfer system. This class can also embrace those P450s that have evolved to utilise the peroxide shunt (such as OleT), as described in Section 1.11.3 [53,165].

Novel, uncharacterised P450 fusions to other redox and likely non-redox partners have been uncovered recently by genome sequencing, but remain unclassified in the current P450 systems. For example, a P450-CAD (a P450 fused to a cinnamyl alcohol dehydrogenase-like module from *Streptomyces ghanaensis*) and P450-BDOR (a P450 fused to a benzoate dioxygenase reductase from *Burkholderia* sp. CCGE1002) characterized at Manchester (Dominika Luciakova, PhD thesis, University of Manchester [210]). These enzymes, like CYP505A30 described in this work and many other

uncharacterised putative P450-fusions, represent the untapped potential of these new types of catalyst, many of which would be expected to have catalytic rates much faster than other multicomponent P450 redox systems. Analysis of the structure and function of these novel fusion systems should also help to understand the evolutionary drive for their development, along with their physiological roles in their host organisms.

1.12.3 P450 electron transfer pathways

P450cam is an extensively studied model P450 (a camphor hydroxylase from *Pseudomonas putida*) with a "class I" redox partner arrangement consisting of three individual soluble components (P450cam, Pdx and PdR) where the electron transfer (eT) between them is coupled with their interactions. The FAD-containing putidaredoxin reductase (PdR) receives two electrons from NADH to form the fully reduced FAD hydroquinone (HQ) with the reduction potential midpoint for the two electron transfer at -268 ± 10 mV in the presence of NAD^+ at a 1:1 molar ratio with PdR, as measured by thin-layer cell electrochemical spectroscopy [211].

The midpoint potential of the PdR FAD measured in the absence of NAD^+ is -369 ±10 mV, significantly more negative than the midpoint potential of its physiological electron donor $E^{0'}_{NAD+/NADH}$ = -320 mV [211,212]. The binding of NAD^+ to PdR modulates the redox potential of the FAD cofactor upon binding to mediate eT between the two. $NADP^+$ has a similar effect on adrenodoxin reductase (AdR) (class III, Figure 1.16), the reductase component of the class I-like redox system for the mitochondrial P450s, positively shifting its 2-electron reduction potential by ~94 mV [213]. The 2Fe-2S putidaredoxin (Pdx) protein facilitates sequential single eT reactions between PdR and P450cam. A ping-pong mechanism for binding has been ruled out for transient sequential binding as the P450cam and PdR binding regions on Pdx overlap [211,214]. The binding of P450cam to Pdx shifts its 1-electron midpoint potential from -240 mV to -196 mV [215]. These examples demonstrate how the binding and interactions of key components in the eT pathway favourably influence the redox potentials towards heme reduction. Substrate binding to P450 enzymes also plays a part in the regulation of eT to P450s (Section 1.10) and camphor binding to P450cam shifts its electron potential from -330 mV to -173 mV, thermodynamically favouring electron transfer and heme reduction by Pdx when P450cam is substrate-bound [215].

Human CPR and other related class II redox partner members contain two flavin cofactors, FAD and FMN, which facilitate efficient eT from their physiological two-electron donor, NADPH (by hydride transfer), to membrane-associated P450s. These 2 flavin cofactors can hold a maximum of 4 electrons, while the typical class I redox partners can hold a maximum of 3 electrons.

In human CPR (and likely in most other CPRs) the binding of NADPH is associated with a "swinging" motion of a single amino acid residue, W676. In its oxidised state, the tryptophan residue sits with its indole ring parallel to the *re*-face of the isoalloxazine ring, shielding the flavin. Upon NADPH-binding (which involves several interactions with the adenine dinucleotide and phosphate parts of the molecule), the tryptophan side is displaced from the face of the flavin, enabling the nicotinamide ring of NADPH for to access the flavin to allow hydride transfer to the FAD [173,216]. The mutation of the tryptophan residue in this position to alanine is accompanied by a ~1000-fold switch in cytochrome *c* reduction specificity (k_{cat}/K_M) from NADPH to NADH, indicating the important role that this phylogenetically conserved aromatic residue play in selectivity for NADPH over NADH [217].

The 2-electron midpoint potential for NADPH-dependent electron (formally hydride) transfer to CPR are quite negative at E^0 = -283 mV ($FAD_{OX/SQ}$) and -382 mV ($FAD_{SQ/HQ}$), but their midpoint is similar to that for the physiological donor NADPH (-320 mV) [218]. In CPR (and other diflavin reductases, including BM3) three conserved residues are involved in binding the cofactor and regulating hydride transfer from NADPH to the FAD cofactor. These form a 'catalytic triad' in proximity to the NADPH-binding site [219]. Catalytic studies on WT and mutant forms of rat CPR implicate these residues (S456, D674 and C629) in stabilising $NADP^+$ after hydride transfer and in the binding and orienting of the nicotinamide ring for efficient electron transfer [219].

The standard midpoint potentials of the individual human CPR FMN redox states are separated by ~200 mV as the $FMN_{OX/SQ}$ midpoint at -66 mV, which is much more positive than that of the $FMN_{SQ/HQ}$ (-269 mV). This results in the CPR enzyme stabilising the 1-electron reduced blue (neutral) semiquinone *in vivo*, and *in vitro* during potentiometric titrations [218]. During catalysis, the FMN cofactor shuttles between the semiquinone and hydroquinone states, the latter being the heme reducing species due to its more negative potential. Following hydride transfer from NADPH to the physiologically relevant (FMN

semiquinone) form of the enzyme, the FAD_{HQ} reduces the FMN_{SQ} to FMN_{HQ}, and becomes oxidised to FAD_{SQ}. The immediate electronic environment of the flavins stabilises their semiquinone states and an extensive hydrogen bond network enables electron tunnelling through the 3.5-4.5 Å which separates them in the "closed" state of the enzyme, as observed in the first crystal structure for the rat CPR enzyme [173]. The reduction of the P450 ferric heme iron by the FMN_{HQ} results in the formation of a disemiquinone CPR state. The FAD_{SQ} then donates an electron to FMN_{SQ} to form FAD_{OX}/FMN_{HQ}. The FMN hydroquinone species is responsible for the 2nd and ultimate eT to the ferrous-oxy heme iron, returning the CPR system to its resting state of FAD_{OX}/FMN_{SQ} [220]. The total number of electrons passing through eukaryotic CPRs per cycle can be represented as: 1-3-2-1 or [FAD_{OX}/FMN_{SQ} – FAD_{HQ}/FMN_{SQ} – FAD_{SQ}/FMN_{HQ} – FAD_{SQ}/FMN_{SQ} – FAD_{OX}/FMN_{HQ} – FAD_{OX}/FMN_{SQ}].

P450 BM3 is a class II redox system analogue, with a CPR-like reductase domain and an N-terminal P450 domain connected by a short polypeptide linker. The CPR domain of BM3 binds equimolar amounts of FAD and FMN and shares 35% amino acid sequence identity with human CPR. However, its flavin reduction potentials and therefore eT mechanisms differ significantly [221]. Firstly, in its resting state both flavins occupy their fully oxidised forms, unlike eukaryotic CPR. In fact the $FMN_{OX/SQ}$ couple is more negative at -240 ± 5 mV than is the $FMN_{SQ/HQ}$ at -193 ± 5 mV [27,222].

It is the red (anionic) semiquinone that is stabilised over the blue (neutral) semiquinone as in human CPR, although this form is not long-lived in BM3. A loop structure positioned over the *re*-face of the FMN cofactor is responsible for the stabilization of the red (anionic) FMN semiquinone species in P450 BM3. The loop forms a rigid β-turn which places an asparagine residue over the N5 nitrogen (Figure 1.17) that is able to stabilise the red semiquinone species [223]. Human CPR, on the other hand, has a conserved glycine reside in this position which is absent in BM3 [223]. This extra residue affords the loop structure greater flexibility, which in turn allows the glycine carbonyl group to stabilise the blue semiquinone species with a hydrogen bond to the N5 amide group [224].

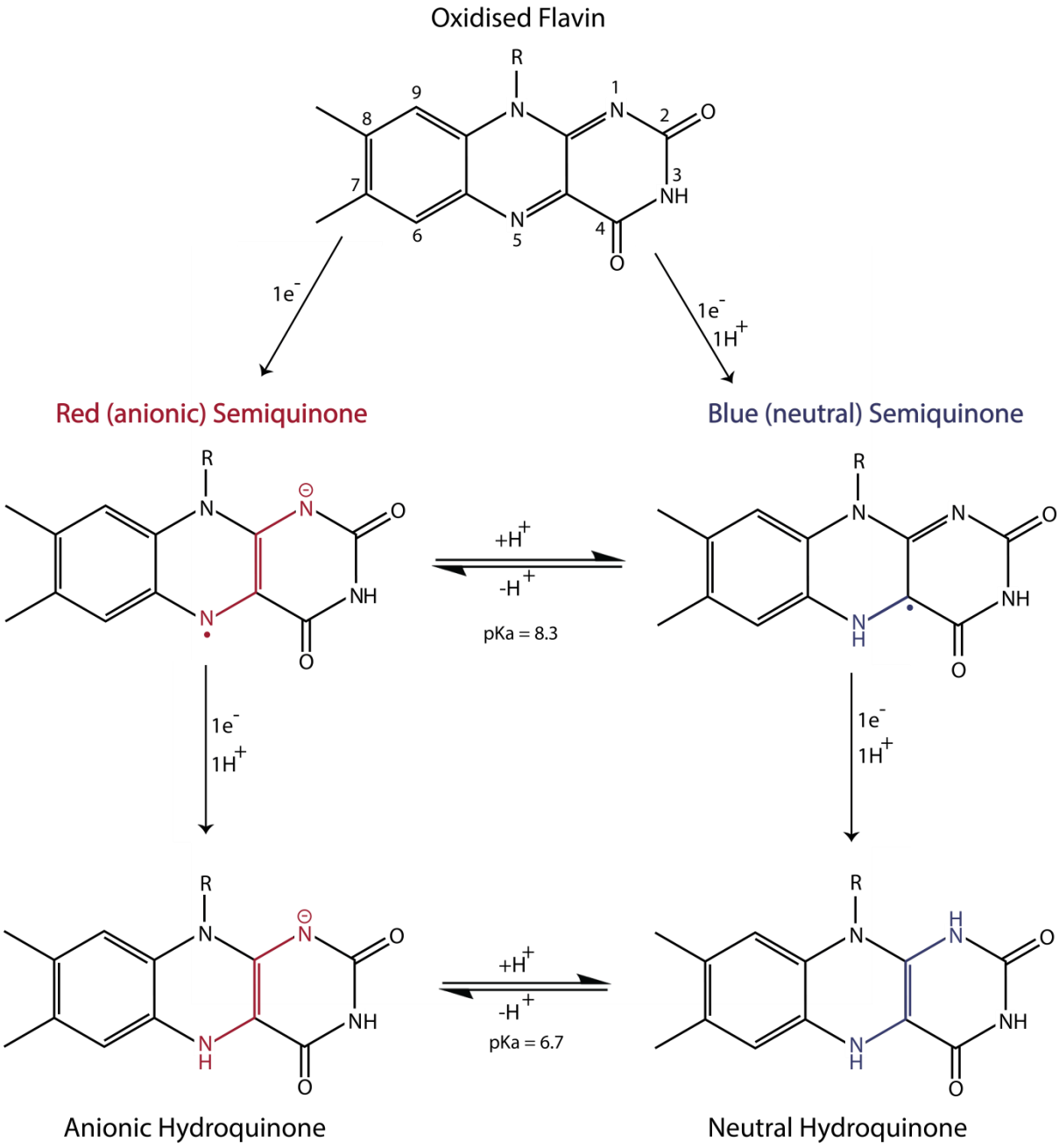

Figure 1.17 A schematic representation of flavin oxidation states. The sequential steps in single electron reductions of a flavin molecule from an oxidised state to a semiquinone state are shown. The semiquinone is either a protonated blue (neutral) or unprotonated red (anionic) semiquinone, coloured appropriately. These are in turn reduced by $1e^-/1H^+$ to form anionic hydroquinone and neutral hydroquinone respectively, coloured to match their parent semiquinone. The pK_a for the interconversion between the two semiquinone and hydroquinone species in solution is also shown. Based on Das and Sligar [220].

It is the red (anionic) FMN semiquinone species that is responsible for heme reduction in BM3, unlike the FMN hydroquinone species in human CPR. The total number of electrons passing through P450 BM3 per cycle can be represented as: 0-2-1-0 or [FAD_{OX}/FMN_{OX} – FAD_{HQ}/FMN_{OX} – FAD_{SQ}/FMN_{SQ} – FAD_{SQ}/FMN_{OX} – FAD_{OX}/FMN_{SQ} – FAD_{OX}/FMN_{OX}] [225].

The midpoint potentials for FAD in the isolated CPR domain of BM3 measured in the absence of NADPH are -372 ± 4 mV and -292 ± 4 mV for $FAD_{OX/SQ}$ and $FAD_{SQ/HQ}$, respectively. Just as for PdR with Pdx/P450cam, the potential for its 1st electron reduction is ~12 mV more negative than the midpoint potential of its physiological electron donor NADPH of $E^{0'}_{NADP^+/NADPH}$ = -320 mV [212]. It is likely that the binding of NADPH to the CPR domain of BM3 modulates its reduction potential much in the same way as in PdR. Studies on human CPR, including kinetic assays involving analysis of the interactions of NADP(H) and various analogues along with computational modelling techniques have shown that the structural changes induced upon NAD(P)H binding can affect flavin redox potentials by up to 58 mV [226].

1.13 P450 BM3 and other P450 Fusions

Flavocytochrome P450 BM3 (BM3) from *Bacillus megaterium* became the first P450-reductase fusion enzyme to be characterised in 1986 by Narhi and Fulco [67]. The 118 kDa enzyme is composed of an N-terminal P450 domain tethered to a C-terminal diflavin reductase, with 35% amino acid sequence identity to human CPR. It was originally described as "catalytically self-sufficient", only requiring NAD(P)H, oxygen and substrate for catalysis [227]. BM3 has the fastest P450 monooxygenase activity ever reported at 17,000 min^{-1} with arachidonic acid [197]. The fused nature of BM3 is thought to be, in part, responsible for such a high catalytic rate with its FMN-to-heme eT measured at ~250 s^{-1} using stopped-flow absorption spectroscopy. By comparison the eukaryotic CPR FMN-to-heme eT rates were reported as ~80 s^{-1} for CYP2B4 [199]. However the eT from NADPH through the flavin cofactors is much faster in BM3 than in human CPR. The k_{lim} for the eT from NADPH to the BM3 FAD domain was measured at 364 ± 25 s^{-1} compared with 20 s^{-1} and ~30-60 s^{-1} in human and rat CPR, respectively [228–230].

This short distance of ~4 Å between the two eukaryotic CPR domain (in the "closed" state of the enzyme) flavins theoretically allows for inter-flavin eT in the order of ~10^{-10} s^{-1} to occur. However, laser-flash photolysis (LFP) and temperature-jump (T-jump) relaxation experiments have measured comparably slower eT at ~36 s^{-1} and 55 s^{-1} respectively in eukaryotic CPR enzymes. These rate constants would be too low to support reported rates of steady-state catalysis in P450 BM3, suggesting that inter-flavin electron transfer is substantially faster in BM3 [7,8,231,232]. Studies involving analysis by pH dependence and using kinetic isotope effects (KIEs) have shown that the pre-steady-state reduction of CPR by NADPH is not gated by proton transfer, implying that conformational protein dynamics are responsible for controlling inter-flavin eT [233].

Recently, the inter-flavin eT in human CPR was monitored using stopped-flow Förster resonance energy transfer (FRET) studies. This allowed for time-based and spatial analysis of CPR domain dynamics to be collected alongside UV-Vis kinetics [234]. These studies show that the movement of the CPR domain from an 'open' to a 'closed' conformation occurred with a rate constant of 47.9 ± 1.1 s^{-1} measured by FRET (with a flavin separation increased to 86 Å in the open state [235]) and the inter-flavin eT rate constant was measured at 66.9 ± 4.4 s^{-1}, which are comparable to the rate constants obtained using T-jump and LFP studies [234]. These data collectively show that inter-flavin eT in human CPR is rate-limiting and point towards BM3 and other kinetically superior diflavin reductases, e.g. CPR from *Artemisia annua* with initial hydride transfer measured at ~500 s^{-1} at 6 °C, having evolved towards more rapid inter-flavin eT [59,236].

Sedimentation experiments using analytical ultracentrifugation methods suggested that BM3 existed in solution in a mixed oligomerisation state of monomer, dimer, trimer and some higher order species [237]. These studied pointed towards the FAD domain as the site of dimerisation in BM3 [237].

Eukaryotic nitric oxide synthases (NOSs) were initially recognised to have both structural and mechanistic similarities with BM3. NOSs are fusion enzymes composed of an N-terminal heme-binding oxygenase domain structurally distinct from P450s, and covalently linked to a CPR-like reductase domain [238]. Like P450s, however, the heme *b* in the oxygenase domain of NOS enzymes is cysteine thiolate-ligated and coordinates a distal water ligand in its resting state, which is replaced during catalysis by molecular oxygen that binds to the ferrous form of the enzyme. Similarly to the P450s, the delivery of two

successive electrons either side of oxygen binding produces reactive iron-oxo species that activate the enzyme to first hydroxylate *L*-arginine to *L*-hydroxyarginine and then, in a second catalytic cycle, to convert *L*-hydroxyarginine to *L*-citrulline and nitric oxide (NO) [239]. NOSs have also evolved to minimise auto-inhibition by the binding of NO to the ferric and ferrous states of their heme iron that occur during the catalytic cycle.

Early work on NOSs enzymes demonstrated that they were catalytically active as dimers, with inter-monomeric eT occurring from the FMN domain of one monomer to the heme domain of the other (FMN_1-to-$heme_2$) within the dimeric NOS complex [9]. Intra-monomer eT in BM3 was also investigated due to the aforementioned similarities with NOSs. Two non-functional BM3 mutants were prepared: (i) A264H, a hexa-coordinated and inactive heme domain mutant with His264 coordinating the heme iron in the distal position and (ii) G570D, an FMN-depleted BM3 mutant. Upon mixing these separate, catalytically-inactive mutants, ω-1 hydroxylase activity with lauric acid was regained, conclusively demonstrating that inter-monomeric eT occurs via FMN_1-$heme_2$ as in NOSs [240].

Two further CYP102A members were identified in 2001 from the organism *Bacillus subtilis* [241]. CYP120A1 and CYP102A3 share >50% amino acid identity with BM3 and also catalyse fatty acid hydroxylation near the ω-terminal end of their substrates. However, they show altered stability and regioselectivities compared to one another and to P450 BM3 [43,242]. Chimeragenesis experiments were carried out by Eiben et al., swapping selected gene segments between CYP102A family members to create a library of novel variants with altered substrate specificity to the parent enzymes [243]. The most stable chimera had a T_m of 56 °C compared to BM3 with a T_m of 49 °C, and showed activity towards non-natural substrates in parent enzymes e.g. the drugs verapamil and astemizole [243].

The first eukaryotic BM3 homologue was discovered as early as 1996, when CYP505A1, P450foxy from the fungus *Fusarium oxysporum*, was described [244]. P450foxy has 36% amino acid sequence identity to BM3 and is also composed of 2 distinct domains, an N-terminal P450 domain tethered to a C-terminal CPR-like reductase [244]. P450foxy also hydroxylates fatty acids, but with a regioselective preference for ω-2 hydroxylation [200]. P450foxy was found to be membrane-associated, although it lacks a distinct transmembrane region and thus membrane association occurs using other hydrophobic

regions in the enzyme [200]. Since the discovery of P450foxy, several other members of the CYP505 clan have been discovered, the majority of which belong to the CYP505A subfamily, including P450MT1 (CYP505A30) characterised in this thesis (Figure 1.18).

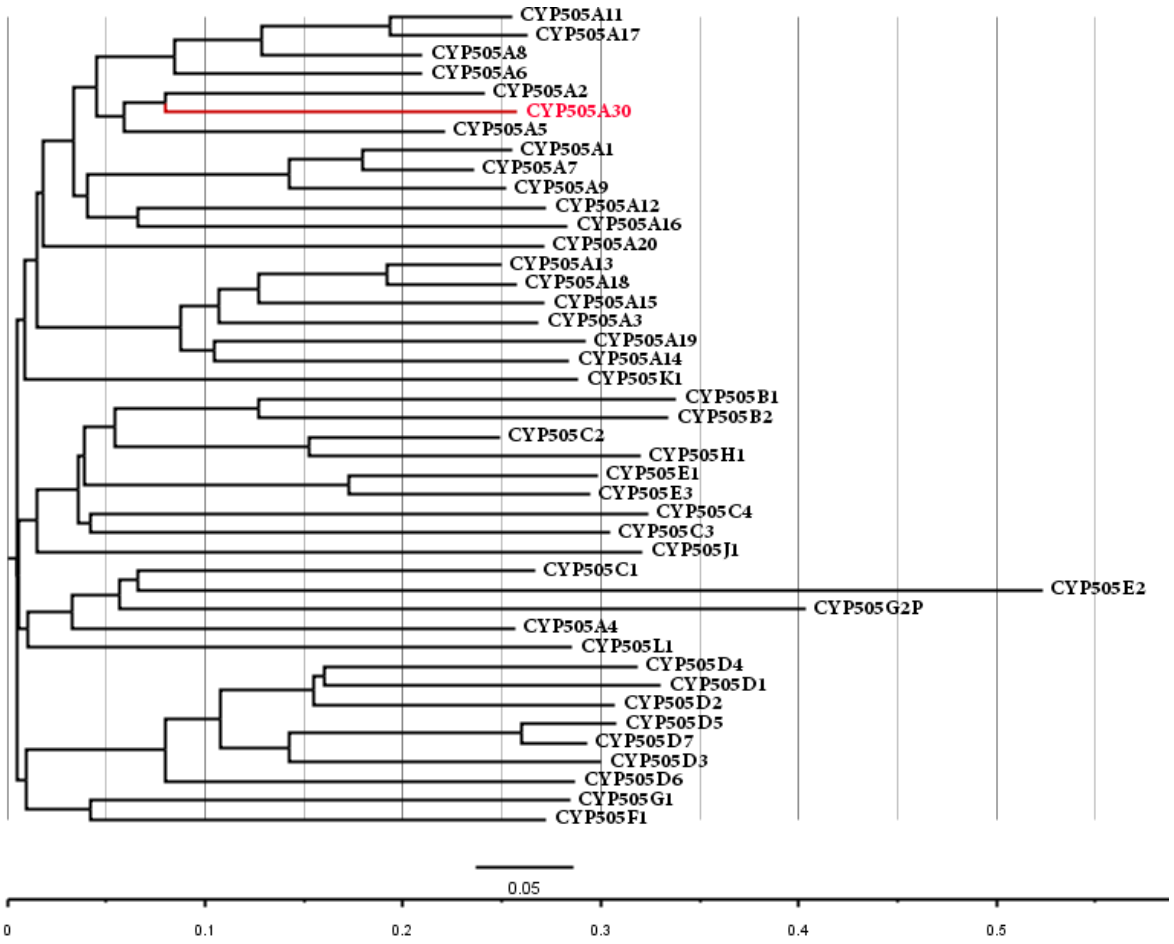

Figure 1.18 Phylogenetic tree showing the majority of sequenced members of the fungal CYP505 family. CYP505A30 is shown in red. The figure was made using FigTree phylogenetic software [245].

1.14 Biotechnological applications of BM3 and other P450 enzymes

The cytochrome P450 monooxygenases have shown great potential and malleability in the synthesis of high value chemicals, due to their capacity to selectively hydroxylate an ever-increasing portfolio of substrates [246]. The options to improve or change the activity, stability and also the substrate selectivity of P450s by selective mutation make them promising candidates in biotechnological applications. Despite the potential of P450s, the drawbacks of enzyme use in industrial settings limit their application, e.g. the need for the expensive external cofactor NAD(P)H, coexpression/purification of stoichiometric amounts of redox partners and, of course, protein stability. These issues currently limit the use of P450s to whole-cell catalysis in industrial processes [247].

In the case of P450 BM3, the effects of mutations to certain residues on binding propensity and catalytic activity with a number of non-natural substrates, e.g. alkanes, gastric proton pump inhibitors (PPIs) and steroids, have been extensively studied [248].

Butler et al. identified certain ‘gatekeeper” residues in the active site of BM3, mutations to which allow for altered substrate specificity and reactivity [93]. The A82F point mutant BM3 enzyme displayed omeprazole (OMP) binding and its turnover to 5-hydroxyomeprazole, the same position of oxidation as occurs with the main human OMP P450 metaboliser, CYP2C19 [93]. The A82F/F87V double mutant displayed even greater binding affinity for OMP and further oxidised it to 5-COOH OMP, which is also a recognized human OMP metabolite [93].

A single substitution mutation, L437A, in P450 BM3 was able to distort its active site sufficiently to allow the binding to larger substrates, including the steroid compound trimethyl estriol [249]. A further 4 mutations allowed the binding of testosterone and progesterone to the variant BM3 enzyme [249]. Kille et al. reported on an F87V substitution mutant allowing the stoichiometric production of 2β- and 15β-hydroxytestosterone [250]. Iterative combinatorial active-site saturation and subsequent library screening developed 2 quadruple mutants, KSA-2 and KSA-14 with the ability to regioselectively (>96%) hydroxylate testosterone at the 2β- or 15β- positions, respectively [250].

In 2003, Peters et al. generated 6 BM3 mutants with activity towards alkanes through 5 rounds of directed evolution involving 11 substitution mutations [251]. The 9-10A-

A328V BM3 mutant was able to hydroxylate octane to *S*-2-octanol with 40% enantiomeric excess (ee) at a rate of ~400 min^{-1} [251]. Further directed evolution work towards alkane oxidation with BM3 by the same group identified a BM3 mutant, 35-E11, with 17 residue substitutions in the P450 domain, which exhibits a 250 TTN (total turnover number, i.e. the estimated total number of reactions performed by each enzyme molecule) for the conversion of ethane to ethanol [252].

There are also many P450s that naturally make high value compounds, such as opioids, anti-malarials and statins (detailed below). The pairing of these P450s with efficient reductase partners is a crucial step in P450 biotechnology research efforts and often involves genetic manipulation to construct artificial fusion P450s to streamline expression and increase catalytic efficiency.

Opiates are commonly used as analgesics in the treatment of pain, accounting for a worldwide annual production of >1 million tons with a global market of over 10 billion USD in 2007 [253]. Currently, the vast majority of opioids and derivatives are produced from harvesting the opium poppy *Papaver somniferum*, which often leads to supply insecurity and inefficiency. The biosynthesis of morphine in this poppy species is a 17-step pathway starting at tyrosine, and the common backbone of pentacyclic morphinine alkaloids features 5 chiral carbons, which have thus far hindered a synthetic route to these important and valuable compounds.

Recent efforts from synthetic biology approaches have managed to recreate the above pathway in three parts. Dueber et al. produced a biomanufacturing platform in yeast able to convert glucose to (*S*)-reticuline, the first part of the morphine biosynthesis platform [254]. Fossati et al. were then able to go from the (*R*)-reticuline intermediate all the way to morphine [255]. All the genes involved in these two biosynthesis pathways for morphine production had previously been isolated, except for a single gene responsible for (*S*)-reticuline epimerisation to (*R*)-reticuline [256]. Recently, two different groups independently identified a P450 fusion enzyme responsible for (*S*)- to (*R*)-reticuline conversion (Figure 1.19) [257,258].

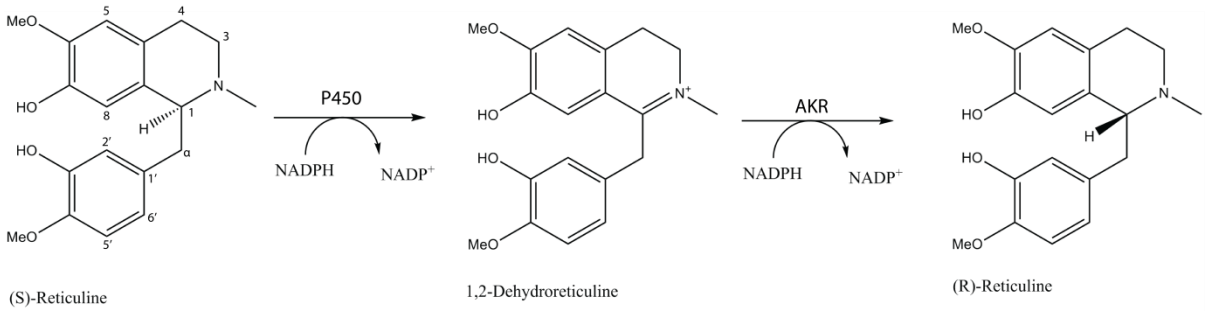

Figure 1.19 The proposed 2-step epimerisation of (*S*)-reticuline to (*R*)-reticuline catalysed by CYP82Y2 from *Papaver somniferum*. The carbons are numbered on the (*S*)-reticuline structure (right) and these carry throughout the reaction. The P450 domain of CYP82Y2 is responsible for the 1st dehydrogenation step to form the 1,2-dehydroreticuline intermediate, while the aldo-keto reductase domain catalyses the final step of the reaction by reduction of the intermediate to form (*R*)-reticuline.

The CYP82Y2 P450-AKR (aldo-keto reductase) fusion protein in *P. somniferum* is responsible for the epimerisation reaction of (*S*)-reticuline to (*R*)-reticuline via a 1,2-dehydroreticuline intermediate. The P450 domain is responsible for the dehydrogenation of the C1 carbon of the (*S*)-reticuline which forms 1,2-dehydroreticuline, while the AKR domain is responsible for the re-hydrogenation of the intermediate to form the required (*R*)-reticuline epimer. The CYP82Y2 gene has only been reported in alkaloid-producing *Papaver* species, suggesting that the evolutionary step was both relatively recent and a key reaction for morphinan biosynthesis [257].

Malaria is responsible for over half a million deaths annually and the control of this disease has proven difficult due to the emergence of multi-drug resistant (MDR) *Plasmodium falciparum* strains [259]. The World Health Organization (WHO) recommends therapeutic use of artemisinin, a sesquiterpene lactone endoperoxide from *Artemisia annua* L. Artemisinin is effective against MDR malaria, but in short supply. As full chemical synthesis was too difficult and costly, a semi synthetic route to artemisinin production has been developed as a cost effective alternative [260]. Ro et al. engineered *Saccharomyces cerevisiae* to produce artemisinic acid via a relatively simple 3-stage genetic manipulation process:

1. Engineering of the farnesyl phosphate (FPP) biosynthesis pathway to increase FPP production and decrease its use in sterols.
2. Amorphadiene synthase (ADS) gene addition to convert FPP to amorphadiene
3. CYP71AV1 gene introduction to convert amorphadiene to artemisinic acid through a 3-step oxidation process (Figure 1.20)

All of the artemisinic acid was extruded from the yeast cells, making for a simple purification process, and facilitating the conversion of artemisinic acid to artemisinin using photochemistry or by chemical production of singlet oxygen [260,261].

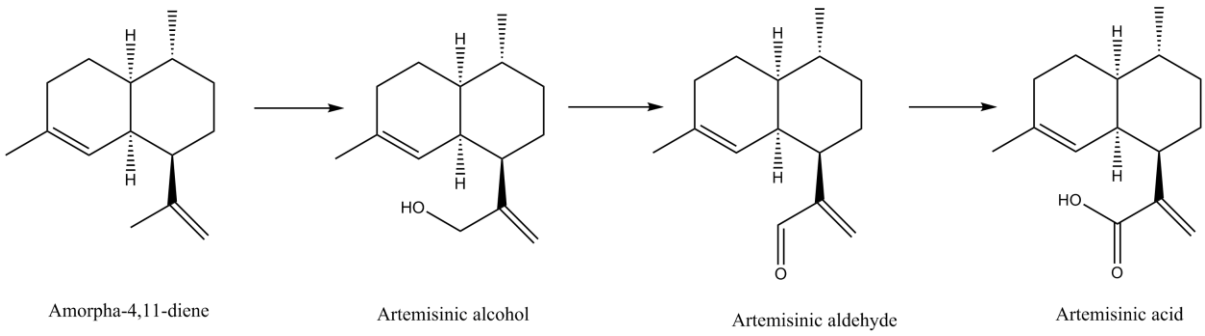

Figure 1.20 The three-step co-oxidation of amorphadiene to artemisinic acid by CYP71AV1 in *A. annua L.* The three oxidation steps are all carried out by the CYP71AV1 enzyme. The artemisinic alcohol is in fact oxidised into a diol which converts to the aldehyde via a non-enzymatic process.

The high titres of 100 mg/L for the artemisinic acid produced via this route were not high enough to be a commercially viable alternative to the current production process.

Advances made to this production route by Westfall et al. included overexpressing all the genes in the FPP biosynthesis pathway [262]. This, however, led to a bottleneck at the amorphadiene intermediate stage and they focused on increasing its production to a value of 40 g/L and on finalising artemisinin production via a synthetic route.

Paddon et al. improved upon this pathway further by the addition of three genes encoding cytochrome b_5, alcohol dehydrogenase and aldehyde dehydrogenase [261]. Cytochrome b_5 aids CYP71AV1 in the first oxidation step of amorphadiene to artemisinic alcohol, while the alcohol dehydrogenase and aldehyde dehydrogenase (ADH1 and ALDH1) catalyse the

oxidation steps to produce the artemisinic aldehyde and artemisinic acid, respectively (Figure 1.20). This allowed for the production of artemisinic acid in greatly increased quantities (~25 g/L) [261]. The process of using singlet oxygen developed by Paddon et al. enabled a simplified and scalable conversion of artemisinic acid to artemisinin for industrial production [261].

Statins are a class of drugs that lower cholesterol by inhibiting cholesterol biosynthesis and by decreasing the levels of low density lipoproteins (LDL) in the bloodstream [263]. They are the most prescribed drugs for lowering LDL-cholesterol and act primarily via inhibition of the 3β-hydroxy-3-methylglutaryl CoA (HMG CoA) reductase, the rate-limiting enzyme in the cholesterol synthesis pathway. Pravastatin is produced industrially via a two-step process involving an initial fermentation of *Penicillium citrinum* which naturally produces the statin compactin. Following a pH increase and neutralisation, the compactin is hydroxylated at the C-6 position in *Streptomyces carbophilus*. $P450_{sca-2}$ in *S. carbophilus* is responsible for this stereospecific hydroxylation and the overall process has a yield of 70% [264].

McLean et al. took a different approach to achieve a pravastatin yield of >95% via a one-step fermentation process [265]. This involved further engineering and optimising/preparing a 50 g/L penicillin-producing *P. chrysogenum* strain for compactin production by deleting the penicillin biosynthesis genes and an esterase that was responsible for converting over half the compactin produced into an inactive deacylated form. Following this process, the *CYP105AS1* gene from *Amycolatopsis orientalis* was identified as a compactin hydroxylase and genetically modified to produce the $P450_{prava}$ enzyme that catalyses stereo-specific hydroxylation of compactin. The $P450_{prava}$ gene was then fused to a PDOR reductase to provide a catalytically self-sufficient enzyme, and this facilitated an increase in the production of pravastatin over its inactive epimer (6-*epi*-pravastatin) by a ratio of 96:4 in *P. chrysogenum*, with production titre values of 6 g/L at pilot scale.

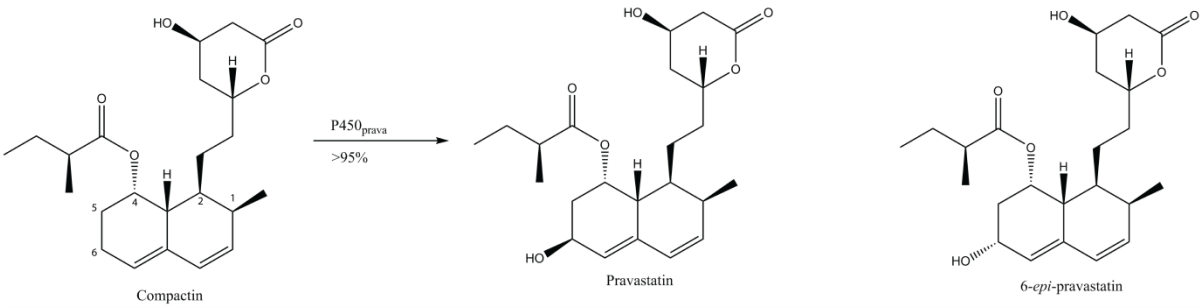

Figure 1.21 Hydroxylation of compactin to pravastatin by P450prava. $P450_{prava}$ is able to hydroxylate compactin (left) to pravastatin (middle) by hydroxylation at the C-6 position. The $P450_{prava}$ (an engineered version of *A. orientalis* CYP105AS1) preferentially produces pravastatin over its inactive epimer 6-*epi*-pravastatin (right) in a ratio of 96:4.

P450 OleT (CYP152L1) from a *Jeotgalicoccus* bacterial species was recognised as a relative of the peroxygenase enzymes $P450_{SP\alpha}$ and $P450_{BS\beta}$, the two best characterized peroxygenases that are known as fatty acid hydroxylases. OleT was shown to have decarboxylation activity on long chain fatty acids to produce their n-1 terminal alkenes, and its crystal structure was determined in both substrate-free and fatty acid-bound forms [266]. While OleT operates efficiently using H_2O_2, it can also use redox partner systems to drive catalysis. Further optimisation of its catalytic performance in alkene production was facilitated by using putidaredoxin and putidaredoxin reductase redox partners, achieving increased product titre values of up to 0.93 g/L [267]. These terminal alkenes can serve as ‘drop in’ biofuels, completely interchangeable with conventional fuels and providing no apparent barrier to an environmentally-friendly alternative to diesel.

Chapter 2: Materials and Methods

2.1 Materials and gene constructs

Unless otherwise stated, all reagents were purchased from Sigma Aldrich (Poole, UK) to the highest grade available. The *CYP505A30* gene was codon optimised, custom synthesised and subcloned into the pUC57 vector by Genscript (Cherwell, UK). The *CYP102A1*/pET14b and *CYP102A1HD*/pET14b constructs were donated by Dr. Christopher Butler (University of Manchester) and all the FAD domain constructs (WT FAD, C120A FAD, C120A/C999A FAD in pET11a) were donated by Dr Kirsty McLean from the University of Manchester, and are described in [268].

2.1.1 Bacterial cell strains

DNA manipulation and protein expression studies were carried out in a number of different *E. coli* strains. XL10-Gold and BL21-Gold (DE3) were purchased from Stratagene-Agilent (Cheale, UK), while Novagen (London, UK) supplied NovaBlue (NB), Rosetta (DE3), HMS174 (DE3) and C41 (DE3) strains. BL21-CodonPlus (DE3) was kindly donated by Dr Edward McKenzie, Protein Expression Facility Manager (University of Manchester).

Table 2.1 Relevant cell strain, supplier and genotype information.

Cell Strain	Supplier	Original Strain	Genotype
XL10-Gold	Stratagene	/	Tet^R, Δ(mcrA)183, Δ(mcrCB-hsdSMR-mrr)173, endA1, supE44, thi-1, recA1, gyrA96, relA1, lac, Hte, [F´ proAB, $lacI^qZ\Delta M15$, Tn10(Tet^R, Amy, Cam^R)]
BL21-Gold (DE3)	Novagen	B834	F^-, ompT, gal, dcm, lon, $hsdS_B(r_B^- m_B^-)$, λ(DE3 [lacI, lacUV5-T7 gene 1, ind1, sam7, nin5])
NovaBlue	Novagen	K12	endA1, hsdR17 ($rK12^-$ $mK12^+$), supE44, thi-1l, recA1, gyrA96, relA1, lac, F′[$proA^+B^+$, $lacI^qZ\Delta M15$::Tn10], (TetR)
Rosetta (DE3)	Novagen	B834	F^-, ompT, hsdSB(RB^- mB^-), gal, dcm, λ(DE3 [lacI, lacUV5-T7 gene 1, ind1, sam7, nin5]), pLysSRARE (Cam^R)
HMS174 (DE3)	Novagen	K12	F^-, recA1, hsdR ($rK12^-$ $mK12^+$),(DE3), (Rif R)
C41 (DE3)	Lucigen	B834	F^-, ompT, hsdSB (rB^- mB^-), gal, dcm
BL21-CodonPlus (DE3)	Stratagene	B834	argU (AGA, AGG), ileY (AUA), leuW (CUA)

Table 2.2 Reference table for the genotype-associated phenotype and its significance in *E. coli* strains.

Genotype	Phenotype and significance
Amy	Expresses amylase allowing for amylose utilisation.
Cam^{R}	Chloramphenicol resistance.
Dcm	DNA cytosine methylase mutation: unmethylated DNA preparation
DE3	Lysogen encodes T7 RNA polymerase used to induce overexpression in T7-driven systems.
endA1	Endonuclease 1 which improves plasmid yield
F	Host does (F') or does not (F^{-}) contain the F plasmid: A self-transmissible, low-copy plasmid used for the generation of single-stranded DNA when infected with M13 phage.
gal	Mutation in galactose metabolism pathway, cells cannot grow on galactose.
gyrA96	DNA gyrase mutation, confers resistance to nalidixic acid.
hsdR	Inactivation of *Eco* endonuclease activity which abolishes *Eco* restriction but not methylation, for efficient transformation of cloned unmethylated DNA from PCR amplifications.
hsdS	Inactivation of Eco site-recognition activity. Both restriction and methylation of certain sequences are deleted from the strain. If you transform DNA from such a strain into a wild type strain, it will be degraded.
Hte	Allows high transformation efficiency with large plasmids (mechanism unknown).
lac	Overproduction of the lac repressor protein
lon	Deletion of the lon protease, decreases the degradation of recombinant proteins
$m_{B/K}^{+/-}$	The (B/K) defines the strain lineage. The +/- indicates whether the strain does or does not encode the modification (methylation) system.
mcr	Inactivation of pathway that cleaves methylated cytosine DNA and which is used to identify and destroy foreign (unmethylated) DNA.
ompT	Indicates that the *E. coli* lack an outer membrane protease which reduces degradation of heterologous strains and recovery of intact recombinant proteins
proAB	Mutation in the proline biosynthesis pathway, cells require an exogenous source of proline for growth.
$r_{B/K}^{+/-}$	The (B/K) defines the strain lineage. The +/- indicates whether the strain does or does not encode the restriction system.
recA1	Mutation in a DNA-dependent ATPase that is essential for recombination and general DNA repair, which results in reduction of plasmid recombination and increases plasmid stability.
relA1	Allows RNA synthesis in absence of protein synthesis.
Rif^{R}	Confers resistance to rifampicin.
supE44	Suppression of the amber (UAG) stop codon by inserting glutamine.
Tet^{R}	Confers resistance to tetracycline.
thi	Mutation in thiamine metabolism, cells require an exogenous source of thiamine for growth.
tn10	Tetracycline resistance gene.

2.1.2 Enzymes

All restriction enzymes used: BamHI, NdeI, HincII, KpnI and NcoI were supplied by New England Biolabs (NEB, Hertfordshire, UK) for cloning and diagnostic digests. T4 DNA ligase was also supplied by NEB and was used for all DNA ligations unless stated. Cytochrome *c* (bovine heart) from Sigma-Aldrich (Poole, UK) was used in all steady-state kinetic assays reported in this thesis.

2.2 Media and buffer preparation

2.2.1 Growth media

All growth media used were prepared according to the manufacturer's instruction, dissolved in distilled, deionised water (ddH_2O) and sterilised by autoclaving prior to use. Luria broth (LB), Terrific broth (TB) and 2-YT Broth were supplied by Formedium (Hunstanton, UK). EnPresso B Defined Nitrogen-free medium was bought from BioSilta (St Ives, UK) and M9 minimal medium was prepared according to Maniatis et al. [269]. M9 medium and EnPresso B Defined Nitrogen-free medium were both used in growing ^{15}N labelled protein for NMR studies.

Table 2.3 Composition of *E. coli* growth media. Components were as described by the relevant manufacturer or protocol. All media were made up to a pH of 7.0 at 25 °C. YE stands for yeast extract.*

LB	g/L	TB	g/L	2-YT	g/L	M9	g/L
Tryptone	10	**Tryptone**	12	**Tryptone**	16	**Na_2HPO_4**	12.5
YE	5	**YE**	24	**YE**	10	**KH_2PO_4**	7.5
NaCl	0.5	**KH_2PO_4**	9.4	**NaCl**	5	**Glucose**	4
		K_2HPO_4	2.2			**$(^{15}NH_4)_2SO4$**	1
						$MgSO_4.7H_2O$	0.24
						$CaCl_2.2H_2O$	0.02
						Thiamine	0.01
						Trace elements	**

*The formula for EnPresso B Defined Nitrogen-free media is not freely available.
**Trace elements are listed in Appendix 7.2. 1 mL were added to every 1 L medium after autoclaving.

2.2.2 Antibiotics and supplements

All antibiotics and supplements used in media as in Table 2.4 were supplied by Sigma Aldrich (Poole, UK).

Table 2.4 Table of antibiotics and supplements used in growth media. Detailed are the stock concentration, (final) concentration in the medium and the composition of the diluent.

Antibiotic/ Supplement	Stock Concentration (mg mL^{-1})	Diluent	Final Concentration (µg mL^{-1})
Carbenicillin	50	ddH_2O	50 µg mL^{-1}
Ampicillin	50	ddH_2O	50 µg mL^{-1}
Rifampicin	10	0.17 M NaOH in 67% MeOH	10 µg mL^{-1}
Tetracycline	5	50% v/v EtOH/ddH_2O	12.5 µg mL^{-1}
Chloramphenicol	34	EtOH	34 µg mL^{-1}
IPTG	238	ddH_2O	0 – 1 mM*
Δ-ALA	59	ddH_2O	0 – 1 mM*

*The concentrations of IPTG and ΔALA used for protein expression and to promote P450 heme incorporation were optimised for each enzyme experimentally.

2.2.3 Agar plate media

37 g/L LB-agar (Melford Laboratories, UK) solutions were autoclaved. Once below 50 °C the appropriate antibiotic stocks were added to the liquid agar in volumes appropriate to reach twice the final concentrations listed in Table 2.4 Before the agar solidified, the mixture was poured into sterile agar plates (~20 ml/plate) and left to cool in aseptic conditions.

2.2.4 Agarose gels

10 mg/ml (1% w/v) agarose gels were prepared by weighing out the correct amount of agarose (Duchefa Direct, USA) and dissolving it into the desired volume of 1x TAE (Tris-acetic acid-EDTA) buffer. The resultant solution was microwaved until the agarose had completely dissolved. Once below 50 °C, 0.01% (v/v) SYBR Safe DNA gel stain (Thermo Fisher, Loughborough UK) was mixed in the liquid agar before pouring the mixture into a pre-made case with a comb inserted for the desired volume and number of wells.

2.2.5 Buffers

2.2.5.1 Phosphate buffer

1 M stocks of potassium dihydrogen phosphate (KH_2PO_4) and dipotassium hydrogen phosphate (K_2HPO_4) were made in ddH_2O to the concentrations required. The dibasic solution was titrated into the monobasic solution until the desired pH of the KPi buffer was obtained. Lysis buffer (50 mM KPi at pH 8.0) and buffer A (50 mM KPi at pH 7.0) were made in this way.

2.2.5.2 2',5'-ADP Sepharose purification buffers

The appropriate volumes of 50 mM KH_2PO_4 and K_2HPO_4 stock solutions were mixed to prepare a 50 mM KPi buffer of pH 7.0. Purification of the target protein by 2',5'-ADP Sepharose chromatography involved a wash step with 10 mM 5'-AMP in this buffer and an elution step with 200 mM 5'-AMP in the same buffer. Both solutions were made by weighing out the correct amounts of solid 5'-AMP and dissolving it in the required final volume of buffer B (50 mM KPi, 200 mM KCl buffer, pH 7.0 at 4°C).

2.2.5.3 Imidazole buffer

The appropriate volumes of 50 mM KH_2PO_4 and K_2HPO_4 stock solutions were mixed to prepare a 50 mM KPi buffer, pH 8.0. Solid potassium chloride was added to 90% of the final volume required to give a 200 mM KCl concentration, and the solution was then made up to the final volume with glycerol and the pH adjusted to 8.0 as required. Glycerol was added to make up the buffer to the final volume. For the various washing, elution and cleaning steps involved in the P450 protein purification by nickel chromatography, a 250 mM imidazole stock solution was made by weighing out the correct amount of imidazole and dissolving it directly into the same buffer. This 50 mM KPi, 200 mM KCl, 250 mM imidazole buffer at pH 8.0 (buffer C) was diluted with imidazole-free nickel buffer to produce other buffers with different imidazole concentrations in the range required for use in nickel chromatography purification (0 – 250 mM).

2.2.5.4 Enzyme assay buffer

A 50 mM KPi buffer, pH 7.0 was prepared as described above. KCl was weighed out and added to 90% of the final volume required to give a 200 mM final KCl concentration

(buffer B). Buffer B was then made up to the final volume and the pH readjusted if required. This buffer was used in the majority of assays carried out for all enzymes used.

2.2.5.5 Tris EDTA buffer

Tris base and EDTA were weighed out and dissolved in ddH_2O at 4 °C to 80% of the final volume required for 50 mM Tris base and 1 mM EDTA concentrations. Concentrated hydrochloric acid was used to adjust the pH to 7.0 at 4 °C (the pH of Tris buffer is temperature sensitive), before the solution was made up to the final volume with ddH_2O (buffer D).

KCl was added to Tris buffer to make solutions required for protein elution procedures using ion exchange chromatography (IEC) with various resins. The appropriate amount of KCl was weighed out and added to 90% of the final volume buffer, and the volume was adjusted to the final volume and any pH adjustment made as described above. After KCl addition, the solution was refrigerated at 4 °C.

Table 2.5 Buffer composition reference table.

Buffer Name	Composition	pH
Lysis Buffer	50 mM KPi	8.0
Buffer A	50 mM KPi	7.0
Buffer B	50 mM KPi, 200 mM KCl	7.0
Buffer C	50 mM KPi, 200 mM KCl	8.0
Buffer D	50 mM Tris	7.0

2.3 Experimental procedures

2.3.1 *E. coli* competent cell preparation

5 ml of sterile 2YT medium were inoculated under aseptic conditions with a surface scraping of frozen cells from a glycerol stock of the desired *E. coli* strain, and the cells were grown overnight (16 – 20 hours) in an orbital incubator at 37 °C and with agitation at 200 rpm. 50 µl of the overnight culture were then inoculated into another 5 ml of fresh 2YT medium under sterile conditions and the cells were again grown at 37 °C and 200 rpm. Once the medium had reached an optical density at 600 nm (OD_{600}) of ~0.6, 1 ml of culture was transferred into a sterile Eppendorf tube and centrifuged in a microfuge at 13,000 rpm for ~30 seconds until the cells were pelleted. The cell pellet was then

resuspended in 500 µl of 50 mM $CaCl_2$ (sterile and chilled at 4 °C). After another round of pelleting and resuspension in 0.5 ml $CaCl_2$, the cell suspension was ready for the plasmid transformation process. If prepared for later use, 15% v/v glycerol was added to the suspension and the cells were stored at -80 °C.

2.3.2 Transformation of plasmid DNA

An aliquot of competent *E. coli* cells was kept on ice for 30 minutes. These cells were either prepared fresh (see section 2.3.1) or taken from glycerol stocks made from the same method, or bought directly as ultracompetent cells ready for use. The choice of strain depended on the desired outcome. For plasmid amplification and eventual use for plasmid preparation (section 2.3.4), Nova Blue and XL21 GOLD cells were selected for their high plasmid copy number. For target gene expression, BL21-Gold (DE3), Rosetta (DE3), HMS174 (DE3), C41 (DE3) strains and BL21-CodonPlus (DE3) strains were used. The DE3 denotes the presence of a dormant λ prophage that allows IPTG-inducible expression of the target gene through its encoding bacteriophage T7 RNA polymerase. 1 µl of a plasmid stock (typically >50 ng) was added to the cells, mixed and left on ice for a further minute. The suspension was then heat shocked at 42 °C for 45 seconds and returned to ice for another minute. Freshly transformed ultracompetent cells were then plated directly onto LB-agar containing the suitable antibiotic and incubated overnight at 37 °C. Competent cells prepared in the laboratory were supplemented with 0.5 ml sterile SOC medium and incubated at 37 °C for 1 hour before plating onto LB-agar plates containing the suitable antibiotic and incubating overnight at 37 °C.

2.3.3 Manufacture of glycerol stocks of transformed *E. coli* strains

Freshly transformed *E. coli* cell strains for gene expression were also stored as glycerol stocks at -80 °C. 5 ml of sterile LB medium with suitable antibiotic were inoculated with a single transformant colony from an LB-agar plate and incubated in an orbital incubator at 37 °C with shaking at 200 rpm until the OD_{600} reached 0.6. 200 µl of this culture was then mixed with 800 µl glycerol in a 1.5 ml Eppendorf and subjected to flash freezing in liquid nitrogen before storage at -80 °C. LB-agar plates containing an appropriate antibiotic could then be streaked directly from these glycerol stocks of transformed *E. coli* cell strains. After overnight incubation at 37 °C, single colonies visible on the plate were then used to inoculate starter cultures (see Section 2.5.1) for protein expression.

2.3.4 Plasmid preparation

Single colonies of either NovaBlue or XL10 Gold *E. coli* strains freshly transformed with plasmids were used to inoculate 5 ml of 2YT medium supplemented with 50 µg/mL carbenicillin. After overnight incubation at 37 °C with orbital shaking at 200 rpm, the culture was pelleted by centrifugation at 13,000 rpm for 1 minute using a desktop centrifuge. A Qiagen Miniprep kit (Qiagen, Manchester UK) was used to extract and purify the plasmid DNA according to the supplied instructions. For a larger scale DNA preparation, a 50 ml overnight culture was used and the aforementioned steps were scaled accordingly. The resultant plasmid DNA was checked for size and purity on a NanoDrop instrument, and by electrophoretic separation a 1% (w/v) agarose gel for 50 minutes at 90 V against a 1 kb Molecular-weight size DNA ladder (NEB, UK). DNA in the gel was viewed using a DNA transilluminator.

2.3.5 Restriction enzyme digests

Restriction enzyme digests were used either to identify a successful genetic modification (diagnostic digests), e.g. a vector and gene ligation, or to excise a gene for further manipulation, e.g. for insertion into another vector or for site-directed mutagenesis (SDM) methods (Section 2.4.2).

DNA samples were resolved on a 1% (w/v) agarose gel prior to the restriction enzyme digest to check the homogeneity of the DNA structure (supercoiled, circular and linear all migrate at different speeds on the gel).

Reaction mixtures contained 400 ng – 1 µg plasmid DNA in a final volume of 50 µl. 1 µl of each HF (High Fidelity) restriction endonuclease was used along with 5 µl (10x) CutSmart buffer (NEB, UK) and the remaining volume was made up with UV-sterilised ddH_2O. The reaction mixture was incubated for 3 hours at 37 °C. 10 µl of 6x DNA loading dye was added to the mixture before loading adjacent to a 1 kb Molecular-weight size DNA ladder (NEB, UK) and electrophoresis at 90 V for 50 minutes on a 1% (w/v) agarose gel. DNA bands in the gel were inspected using a DNA transilluminator.

If one of the separated fragments was to be used for further DNA manipulation, it was physically cut out of the gel and purified using a Gel Purification Kit (Qiagen) to remove

all possible agarose and other contaminants. The isolated DNA fragment was checked for purity and concentration on a NanoDrop instrument.

2.3.6 Ligation reactions

Vector and gene insert DNA were cut using two different and appropriate restriction enzymes, as described in Section 2.3.5. After separation by agarose gel electrophoresis, bands matching the cleaved gene and vector were extracted and purified from the agarose gel using a gel purification kit (Qiagen) using the manufacturer's protocol. The concentration of the extracted DNA was measured using a Nanodrop instrument. Ligation reactions were set up in 1.5 mL microfuge tubes using 1:1, 1:3 and 1:5 vector-to-insert concentrations, with the amount of vector maintained at 100 ng. UV-sterilised ddH_2O was used to make the solutions up to 40 µl and T4 DNA ligase (200 units) was added last to initiate the ligation reactions, with incubation at room temperature for 24 hours.

Ligation products were transformed into competent *E. coli* cells and plated on LB agar containing 100 µg/ml carbenicillin with growth overnight at 37 °C. Transformant colonies were picked and cells were grown overnight in 5 ml LB medium containing 50 µg/ml carbenicillin at 37 °C in an orbital incubator with shaking at 200 rpm. DNA was extracted using a QIAGEN miniprep kit using the manufacturer's protocol.

2.4 Plasmid construct generation

2.4.1 *CYP505A30*/pET15b construct generation

The *CYP505A30*/pUC57 construct was obtained from Genscript (Cherwell, UK), and the *CYP505A30* gene was subcloned into a pET15b vector. The *CYP505A30*/pUC57 and pET15b plasmids were both digested with BamHI and NdeI, as described in Section 2.2.6, followed by dephosphorylation of the 5' and 3' ends of the DNA by CIP (Calf Intestinal alkaline Phosphatase, Sigma-Aldrich, UK) before separating cleavage products on a 1% agarose TAE gel for 50 minutes at 90 V (Section 2.2.2). Bands matching the cleaved *CYP505A30* gene and the pET15b vector were extracted and purified from an agarose gel using a Qiagen gel purification kit (Qiagen, Manchester UK) and the manufacturer's protocol. The concentration of the extracted DNA was measured using a Nanodrop 2000 instrument (Thermo Scientific, Delaware, USA). Ligation reactions were set up as described in Section 2.2.6. To verify correct ligation of the gene into the pET15b vector, a sample of the plasmid was also sent to Source Bioscience in Nottingham for sequencing with T7F, T7R primers and 4 additional synthesised primers (F1-F4, Table 2.6) to verify

that the entire gene was correctly inserted into pET15b with no errors in the nucleotide sequence.

Table 2.6 Oligonucleotide primers used to verify correct CYP505A30 gene sequence. Primer sequences are both shown reading from the 5' to the 3' end.

Primer Name	Sequence
F1	GGCCAGAAGGTGAGTGAT
F2	GGTAGCAATACCGGCACG
F3	TACGTGGAACTGAGTCAGCC
F4	GATGGGTCGTATTGTGCT

2.4.2 Generation of G46X heme domain construct by Site-Directed Mutagenesis (SDM)

The intact WT *CYP505A30* gene construct pET15b was used as the template to generate a heme (P450) domain expression plasmid by introduction of an ochre stop codon (TAA) in place of amino acid Gly463 at the proposed end of the heme domain (the G463X mutant), using the QuikChange Lightning site-directed mutagenesis kit (Stratagene-Agilent UK), as detailed in Tables 2.7 and 2.8 below, and by optimising the suggested parameters for the best PCR results. PCR reaction mixtures were set up in thin walled PCR tubes with 10 ng, 25 ng and 50 ng dsNDA template, as described in Table 2.7.

Table 2.7. PCR reaction mixture composition for stop codon insertion into pET15b/CYP505A30. PCR reaction samples used a series of starting dsDNA template quantities ranging from 10 – 100 ng, while other conditions were kept constant and the final PCR reaction volume was always 50 µl. Pfu Ultra enzyme was added last prior to initiating these reactions.

Reagents	Volume (µl)	Final Concentration
DNA	X	0.2-2 ng/µl
Forward primer	1	2.5 ng/µl
Reverse primer	1	2.5 ng/µl
dNTPS	1	120 µM
QuikSolution	1.5	
UV-sterilised ddH_2O	36.5 – 50	/
10x QCL Buffer	5	1x
Pfu Ultra II DNA Polymerase	1	2.5 U
Final volume	50	

Table 2.8 PCR reaction set up for stop codon insertion into pET15b/*CYP505A30* (8.8 kbp) using Pfu Ultra II Polymerase.

Cycle	Temperature (°C)	Time
1	98	**20 s**
2	98	**20 s**
18x repeat	68	**20 s**
	72	**4.4 min (30s/kb template DNA)**
3	68	**10 m**
Hold	10	∞

The PCR mutagenesis reaction mixtures were prepared and the experimental conditions in Table 2.7 and Table 2.8 were used according to the manufacturer's protocol, and were optimised for the specific template DNA and primers used. Custom designed primers were synthesised according to the QuikChange Lightning Site-Directed Mutagenesis Kit (Agilent, UK) specifications of:

- 25 – 45 bps
- Tm ≥78 °C
- 10 – 15 bps complementary DNA flanking mismatched mutation
- GC base content of >40%
- Terminate in 1 or more G or C bases.

Table 2.9 Oligonucleotide primers used to generate heme domain expressing construct. Primer sequences are both shown reading from the 5' to the 3' end. The inserted ochre (TAA) stop codon is highlighted in bold.

Primer Name	Sequence
G463X F	GTGCTATTCTGCGCGAC**TAA**CTGACCGCGACGGAACT
G463X R	AGTTCCGTCGCGGTCAG**TTA**GTCGCGCAGAATAGCAC

Immediately after the reaction was completed, the PCR products were treated with DpnI, a restriction enzyme that degrades methylated DNA. 1 µl of DpnI (20 U/µl, NEB UK) was added to each PCR reaction tube, and the sample was mixed gently and incubated for 2 hours at 37 °C. DpnI-digested PCR reaction mixtures were transformed directly into XL10-Gold Ultracompetent cells (Section 2.3.2) as described in the QuikChange Lightning kit protocol. DNA extraction was carried out as in Section 2.3.4 and samples of the entire

plasmid constructs were sequenced (Source Bioscience, Nottingham UK) to establish the insertion of the stop codon at the correct position and the absence of non-specific mutations.

2.5 Protein expression

2.5.1 Small scale expression trials for P450 MT1.

Cell strains BL21-Gold (DE3), HMS174 (DE3), C41 (DE3) and Rosetta (DE3) transformed with the CYP505A30/pET15b construct were trialled for P450 MT1 expression and protein solubility. The conditions ware varied sequentially and experiments included use of different (i) growth media (LB, TB and 2YT), (ii) OD_{600} at IPTG induction, (iii) IPTG concentration at induction, (iv) ΔALA concentration at the point of induction, and (v) incubation temperature after induction. Freshly transformed colonies were used to inoculate 5 ml of sterile growth medium in a Universal tube for overnight culture growth. Samples were supplemented with the appropriate antibiotic (Table 2.10) and incubated at 37 °C for 16 – 20 hours with shaking. These overnight cultures were then used to inoculate further small scale expression trial Universal tubes containing 5 ml of the relevant medium and antibiotic (and grown under varying conditions as described above).

Table 2.10 Antibiotic resistances in E. coli strains used for expression trials of P450 MT1. The pET15b vector encodes the AmpR (Δ-lactamase) ampicillin resistance gene, and so 50 µg/ml carbenicillin was also added for plasmid selectivity (100 µg/ml on solid media).

		Concentration (µg/ml)	
Cell strain	Antibiotic	Solid Media	Liquid Media
BL21 (DE3)	/	/	/
HMS174 (DE3)	Rifampicin	20	10
C41 (DE3)	/	/	/
Rosetta	Chloramphenicol	68	34

Samples were incubated at 37 °C in an orbital incubator and shaken at 190 rpm until the culture reached an OD_{600} of 0.4 – 0.8, when target gene expression was induced with 0.4 – 1 mM IPTG (final concentration) and supplemented with 0.4 – 1 mM ΔALA to enhance heme incorporation. Uninduced samples were prepared in identical conditions as a control for leaky expression. 200 µl samples and their OD_{600} were taken at time points 0 – 24 hours after induction to monitor the extent of P450 MT1 expression. Samples were centrifuged for 1 minute at 13,000 rpm on a benchtop centrifuge and the pellets were stored at -20 °C overnight. The cell pellets were then resuspended and incubated for 30 minutes in 200 µl of Bugbuster (Novagen, UK) which causes cell lysis. After further centrifugation at 13,000 rpm on a benchtop centrifuge for 30 minutes, the supernatant or soluble fraction (S) was transferred to another Eppendorf tube and the pellet or insoluble fraction (I) was resolubilised in an equal volume of BugBuster solution. All samples were normalised against their measured OD_{600} values before being electrophoresed on an SDS-PAGE gel alongside an appropriate protein molecular weight marker.

2.5.2 P450 MT1 medium scale solubility trials

Scaled-up 50 ml expression cultures were trialled for P450 MT1 solubility using *E. coli* strain BL21-Gold (DE3) and by varying the growth medium (LB, TB and 2YT, keeping to the best conditions for expression obtained from the small scale trials). After IPTG induction of target gene expression, separate flasks with identical contents were incubated at 18 °C and 25 °C for 20 hours. Thereafter, the bacterial cells were pelleted by centrifugation at 6000 x *g* for 20 minutes at 4 °C and then frozen at -20 °C. Subsequently, the pellets were thawed and resuspended in lysis buffer (Section 2.2.5.1) and supplemented with EDTA-free protease inhibitor cocktail (Roche Applied Science, Mannheim Germany), 100 µg/ml lysozyme (hen egg, Sigma-Aldrich, UK) and DNase I (bovine pancreas, Sigma-Aldrich, UK). Cells were lysed by sonication on ice using a Bandelin Sonopuls GM2600 sonicator (40% amplitude, 44 pulses for 8 s with 40 s between pulses). The supernatant containing soluble MT1 was separated from cell debris by centrifugation (20,000 x *g*, 40 min, 4 °C). Soluble fractions and insoluble fractions at various time points were analysed using SDS-PAGE and the combination of conditions that showed the

highest levels of soluble protein expression were used for the subsequent scale-up of P450 MT1 expression.

2.5.3 Large scale expression of WT P450 MT1 and the G463X P450 MT1 Heme Domain (HD)

The conditions trialled for full length P450 MT1 were kept for its isolated heme domain G463X. Freshly transformed BL21-Gold (DE3) colonies (Section 2.2.4) containing the appropriate construct were used to inoculate 50 ml LB overnight cultures containing 50 µg/ml carbenicillin. 1% v/v of the overnight cultures were used to inoculate between 12 – 36 2 L flasks containing 0.4 L of LB medium (with antibiotic). Cultures were grown at 37 °C for 2 – 3 hours, up to an OD_{600} of 0.6 and with agitation at 200 rpm in an orbital incubator.

At the target OD_{600}, 0.8 mM IPTG was used to induce gene expression and 0.8 mM ΔALA was added to the culture in efforts to increase heme synthesis and incorporation into the intact P450 MT1 enzyme and its heme domain. Thereafter, the temperature was lowered to 25 °C and cells were grown for a further 16-20 hours. The bacterial cells were then recovered by centrifugation at 4 °C (6000 x *g*, 8 min at 4 °C) and then resuspended in 50 ml of lysis buffer per litre of culture in order to remove excess salt and other impurities from residual media and cell extract. The resuspended cultures were pelleted using the same conditions described previously and stored at -20 °C.

2.5.4 Large scale expression of WT P450 BM3, the BM3 HD (Heme Domain) and FAD domain constructs (WT, C773A and C999A Mutants).

The expression of intact P450 BM3, BM3 HD and all three WT and mutant FAD domain constructs was carried out in a similar fashion. Freshly transformed BL21-Gold (DE3) colonies (Section 2.2.4) containing the appropriate construct were used to inoculate 50 ml LB overnight cultures containing 50 µg/ml carbenicillin. 1% v/v of the overnight cultures were used to inoculate 12 – 36 2 L flasks containing 0.4 L LB medium. Cultures were incubated at 37 °C for 2 – 3 hours, up to an OD_{600} of 0.8 and with agitation at 200 rpm in an orbital incubator.

Once the target OD_{600} of 0.8 was reached, target gene expression in the cultures was induced with 1 mM IPTG (but not in the case of the pUC18 WT BM3 construct, where expression occurs from the native *Bacillus megaterium* promoter). Cells were incubated at 37 °C in an orbital incubator at 190 rpm for a further 16 hours and then the cells were pelleted by centrifugation (6000 x *g*, 8 minutes at 4 °C) and resuspended in 50 ml of lysis buffer per litre of culture, as described above. The resuspended cells were then pelleted again in the same conditions used previously, and stored at -20 °C.

2.7 Enzyme purification

2.7.1 Cell lysis by sonication for P450 MT1 and MT1 HD expression cells

The frozen pellets from harvested cells (Section 2.5) were thawed in 25 ml lysis buffer per litre of culture and supplemented with EDTA-free protease inhibitor cocktail, 100 µg/ml lysozyme and DNase I. Cells were lysed by sonication on ice using a Bandelin Sonopuls GM2600 sonicator (40% amplitude, 44 pulses for 8 s with 40 s between pulses). The supernatant containing the expressed enzyme was separated from cell debris by centrifugation (20,000 x *g*, 40 min, 4 °C).

2.7.2 Ammonium sulfate precipitation

Ammonium sulfate precipitation was used to partially purify the target proteins by selective precipitation of other cellular proteins (Section 2.7.1) before the first column purification steps for P450 MT1 and MT1 HD. 176 g of $(NH_4)_2SO_4$ per litre of supernatant (30% w/v) was prepared and added gradually to the supernatant with stirring on ice, prior to a centrifugation step (20,000 x *g*, 30 min, 4 °C).

2.7.3 Purification of P450 MT1

The supernatant after ammonium sulfate precipitation (Section 2.7.2) was dialysed into buffer A (Section 2.2.5.1).The intact P450 MT1 enzyme was partially purified from the

supernatant by mixing with 2',5'-ADP Sepharose resin in 10 mM 5'-adenosine monophosphate (5'-AMP) for 3 hours at 4 °C, before pouring the mixture into an empty column, and washing the resin with 3 column volumes (CV) of 10 mM AMP buffer (Section 2.2.5.2). Partially pure P450 MT1 was eluted with 200 mM 5'-AMP buffer in the same buffer. The eluted protein was pooled, dialysed into buffer D and concentrated by ultrafiltration using Vivaspin ultrafiltration devices (100 kDa molecular weight cut-off [MWCO]). The concentrated solution was loaded onto a pre-equilibrated Q-Sepharose ion exchange chromatography (IEC) column. Elution was achieved by applying a linear gradient of 0-500 mM KCl in buffer D. The fractions containing the purest P450 MT1 solutions were pooled and concentrated by ultrafiltration using a 100 kDa MWCO Vivaspin.

A further purification step by size exclusion chromatography (SEC) in buffer B was done using a Sephacryl S-200 column (26 mm diameter by 60 mL bed volume or 26/60). Intact P450 MT1 fractions were checked for purity by SDS-PAGE, concentrated by ultrafiltration (as described above) to a final concentration of ~800 µM and dialysed into buffer B containing 20% v/v glycerol, before storage at -80 °C. The flavoenzyme concentration was determined spectrophotometrically using an absorption coefficient of ε_{457} = 23,000 M^{-1} cm^{-1} for the oxidized minus sodium dithionite-reduced sample difference spectrum. The coefficient was established by quantification of flavin content as described previously [270]. The concentration of heme-bound P450 MT1 was estimated using ε_{418} = 105,000 M^{-1} cm^{-1} (Section 2.8).

2.7.4 Purification of the P450 MT1 G463X Heme Domain (MT1 HD) and WT P450 BM3

The P450 MT1 (G463X) heme domain and the WT P450 BM3 enzymes were expressed from plasmid vectors that incorporated a His-Tag on their respective N-termini. A similar approach was used to purify both these enzyme, beginning with a nickel affinity column.

Each enzyme was separated from an ammonium sulfate supernatant (see Section 2.7.2) by mixing with Ni-IDA nickel chromatographic medium (Generon, Maidenhead, UK) using 10 mM imidazole in 50 mM KPi buffer at pH 8.0 for 3 hours on a rolling table at 4 °C,

before the resin was poured into an empty column (2 cm x 10 cm). 2 CV of 5 mM imidazole buffer (Section 2.2.5.3) were used to wash the column before elution was achieved with 200 mM imidazole buffer. The eluted proteins were then dialysed into buffer D (Section 2.2.5.5) and concentrated using Vivaspin ultrafiltration devices (30 kDa MWCO for MT1 HD and 100 kDa MWCO for P450 BM3) before being loaded onto a pre-equilibrated Q-Sepharose IEC column. Elution was achieved by applying a linear gradient of 500 mM KCl buffer D. The fractions containing the purest enzyme samples were pooled and concentrated by ultrafiltration. A further purification step by SEC using a Sephacryl S-200 column (as described above) was done in buffer B.

Enzyme fractions were checked for purity by SDS-PAGE, concentrated by ultrafiltration (as described above) and dialysed into 50 mM KPi buffer (pH 7.0) containing 200 mM KCl and supplemented with 20% v/v glycerol prior to storage at -80 °C. The enzyme concentration was determined spectrophotometrically using an absorption coefficient of ε_{418} = 95,000 M^{-1} cm^{-1} for the MT1 HD and ε_{418} = 105,000 $M^{-1}cm^{-1}$ for P450 BM3 (Sections 2.8).

2.7.5 Purification of the P450 BM3 Heme Domain (BM3 HD)

The P450 BM3 HD supernatant (Section 2.7.2) was dialysed extensively into 3 x 5 L of buffer D and loaded straight on to a DEAE Sepharose IEC column that was pre-equilibrated and further washed in the same buffer. Elution was achieved by applying a linear gradient of 500 mM KCl buffer D. Fractions were checked for purity on a spectrophotometer by their Reinheitszahl (Rz) value – corresponding to the 420 nm/280 nm absorbance ratio of the protein (a value of >1.5 indicates a highly purified for the BM3 HD). The purest fractions were pooled and concentrated by ultrafiltration with a 30 kDa MWCO Vivaspin before being buffer exchanged back in 50 mM Tris buffer at pH 7.0 to remove excess salt. After dialysis, the incompletely purified BM3 HD was loaded onto a Q-Sepharose IEC column pre-equilibrated with buffer D. Elution was achieved by applying a linear gradient of 0-500 mM KCl in buffer D. The fractions containing the purest P450 enzyme samples were pooled and concentrated by ultrafiltration with a 30 kDa MWCO Vivaspin. A further purification step by SEC using a Sephacryl S-200 column (as described above) was then done in buffer B.

P450 enzyme fractions were checked for purity by SDS-PAGE, pooled and concentrated. Once concentrated, the protein was dialysed into buffer B and 20% v/v glycerol. The BM3 HD concentration was determined spectrophotometrically using an absorption coefficient ε_{418} = 95 mM^{-1} cm^{-1} (Section 2.8) before storage at -80 °C.

2.7.6 Purification of WT, C120A and C120A/C999A P450 BM3 FAD domain proteins

The supernatant from sonication WT and mutant FAD domain expression cells (see section 2.6) was dialysed in extensively into 3 x 5L buffer D and loaded directly onto a DEAE-Sepharose Fast Flow IEC (50/100) column pre-equilibrated and further washed in the same buffer. Elution was achieved by applying a linear gradient of 0-500 mM KCl in the same Tris buffer. Fractions were checked for purity on a spectrophotometer by their 280 nm/450 nm absorbance value ratio (a value of ~6 is indicative of highly purified FAD domain). The purest fractions were pooled and concentrated by ultrafiltration with a 30 kDa MWCO Vivaspin before being buffer exchanged back into buffer D to remove excess salt.

After DEAE IEC purification, the concentrated eluate was loaded onto a pre-equilibrated Q-Sepharose IEC column and further washed in buffer D. Elution was achieved by applying a linear gradient of 0-500 mM KCl in the Tris buffer. Fractions were checked for purity on a spectrophotometer by their 280 nm/450 nm absorbance values and the purest fractions were pooled and concentrated by ultrafiltration with a 30 kDa MWCO Vivaspin before dialysis back into buffer D.

The concentrated protein samples for the WT, C120A and C120A/C999A FAD domains were loaded onto a Sephacryl S-200 SEC column (16/60) pre-equilibrated in and run using buffer D. Pure fractions were pooled and dialysed into buffer B and 20% v/v glycerol, before concentration of the sample by ultrafiltration in Vivaspin tubes with a 30 kDa MWCO. Once concentrated, the FAD concentrations of the final samples were determined spectroscopically before storage of FAD domains at -80 °C.

Table 2.11 Chromatography columns used in the protein purification.

Column Name	Resin Name	Supplier	Internal Diameter (mm)	Bed Volume (mL)
DEAE	DEAE-Sepharose Fast Flow	GE Healthcare	50	100
Qsepharose	Q-Sepharose Fast Flow	GE Healthcare	26	60
S200	Sephacryl S-200	GE Healthcare	26	60
Nickel	Nickel-IDA Fast Flow	Generon	20	10

2.8 P450 Protein concentration calculation

Cytochrome P450 hemoprotein concentrations were calculated using the Beer Lambert law (equation 1). Absorbance was measured in quartz cuvettes with 1 cm path length in a Varian Cary 50 UV-visible spectrophotometer.

$$A = \varepsilon c l$$

Equation 1. The Beer-Lambert law used for calculating the concentration of light absorbing compounds. A is the measured absorbance, ε is the extinction coefficient at the particular wavelength of the absorbance being measured, c is the sample concentration and l is the path length.

Extinction coefficients for WT P450 BM3, P450 BM3 HD and the FAD domain of BM3 have already been previously determined at ε_{418} = 105 mM^{-1} cm^{-1}, ε_{418} = 95 mM^{-1} cm^{-1} and ε_{450} = 11.3 mM^{-1} cm^{-1} respectively [198,271]. The P450 BM3 HD extinction coefficient of 95 mM^{-1} cm^{-1} was used for MT1 HD. Due to the issues with sub-stoichiometric heme incorporation seen in P450 MT1, two extinction coefficients were used ε_{418} = 105 mM^{-1} cm^{-1} as in WT P450 BM3 and ε_{475} = 23 mM^{-1} cm^{-1}, obtained experimentally in Section 2.10, depending on the experiment.

Purity ratios for enzyme samples used during purification rounds were obtained by comparing their Reinheitszahl (Rz) value (heme absorbance at 418 nm over that of protein aromatic amino acids at 280 nm). Similarly for FAD domain samples, high values for its absorbance at 450 nm over 280 nm denoted high purity.

2.9 Sodium Dodecyl Sulfate Polyacrylamide Gel Electrophoresis (SDS-PAGE) of protein samples

Protein electrophoretic separation using SDS-PAGE gels provides a biochemical means of estimating protein size and evaluating sample purity. The appropriate volume of 2x Loading Dye (100 mM Tris-HCl, pH 6.8, 4% SDS, 0.2% bromophenol blue, 20% glycerol, 200 mM DTT) was added to SDS-PAGE protein samples and mixed prior to heating at 95 °C for 10 minutes. After the heat denaturation step, samples were loaded onto commercially precast Mini-Protean TGX SDS-PAGE gels (Bio-Rad Laboratories, Hertfordshire) and run at 260 V for 24 minutes. When precast gels couldn't be used, e.g. for western blotting (where a thinner gel is required), gels were cast from the recipe below (Table 2.12).

Table 2.12 Components of SDS-PAGE gels. The gels were cast separately, with the Running gel (bottom) allowed to set before casting of the Stacking gel (top). In both cases, all the components were mixed, with ammonium persulfate and TEMED added only immediately before casting (for both the stacking and resolving gels).

Materials	8% Running gel (ml)	5% Stacking gel (ml)
H_2O	4.6	2.1
30% acrylamide mix	2.7	0.5
1.5 M Tris Buffer pH 8.8	2.5	/
1 M Tris Buffer pH 6.8	/	0.38
10% SDS	0.1	0.03
10% Ammonium persulfate	0.1	0.03
TEMED	0.006	0.003
Total volume	10	3

When required, gels were stained with Coomassie Blue stain (0.1% w/v Brilliant blue G-250, 40% v/v EtOH, 10% v/v acetic acid and 50% v/v H_2O) for 30 minutes before destaining with distilled water

2.10 Determination of WT P450 MT1 flavin content by High Performance Liquid Chromatography (HPLC)

A 40 µM sample of P450 MT1 was made in buffer B and quantified using two extinction coefficients, these being ε_{418} = 105 mM^{-1} for the and ε_{456} = 21.2 mM for the combined FAD and FMN flavins [272]. The sample was incubated at 90 °C for 10 minutes to release the flavin cofactors from its reductase domain. Centrifugation at 20,000 x *g* for 5 min separated the soluble flavins from the precipitated, denatured enzyme. A 60 µl sample was loaded onto a reverse phase C18 HPLC column (Ascentis, Sigma-Aldrich UK) in 85% 5 mM ammonium acetate (pH 6.5) and 15% methanol. Separation of FAD and FMN was achieved by increasing the methanol concentration linearly from 15% to 100% in 30 min. Absorbance was monitored at 264 nm. The retention times for FAD and FMN standards (Sigma-Aldrich, UK) were 25.0 minutes for FAD and 27.3 minutes for FMN. Integration of the areas corresponding to the peaks of known amounts of FAD and FMN allowed a standard curve to be generated, and thus for the quantification of the P450 MT1 flavins by integration [273,274]. The concentration of the FAD in the P450 MT1 sample was taken as the most accurate representation of the P450 MT1 concentration from its cofactors. Using the Beer-Lambert law (Equation 1 in Section 2.8) an extinction coefficient of 23 mM^{-1} cm^{-1} at 475 nm was calculated for P450 MT1.

2.11 The Pyridine hemochromogen method for hemoprotein quantification

The pyridine hemochromogen method is a quantitative spectroscopic assay for the determination of heme content in an enzyme solution as first described by Berry and Trumpower [275]. The absorption spectra of the oxidized and reduced forms of the pyridine-ligated heme complex are used to calculate the concentration of heme using the Beer-Lambert law (Section 2.8). An appropriate extinction coefficient for the enzyme can then be deduced from its defined concentration.

UV–visible absorbance spectra in the range from 250-800 nm were recorded for a 3-5 µM enzyme solution before and after the addition of an equal volume of pyridine hemochromagen solution (40% v/v pyridine, 0.8 mM potassium ferricyanide and 200 mM NaOH). Further spectra were recorded after reduction by of a few grains of sodium dithionite.

The enzyme concentration was calculated using the difference in absorbance between the oxidized and reduced spectra at 557 nm (ΔA_{557}) divided by the extinction coefficient of pyridine hemochromagen (ε_{557} = 23.98 mM^{-1} cm^{-1}) [275]. The value obtained was doubled, as the concentration of enzyme was effectively halved after the addition of the equal volume of pyridine solution. Using the absorbance value of the P450 Soret peak in the original enzyme spectrum before pyridine addition and by dividing it by the accurately determined enzyme concentration, the extinction coefficient for the hemoprotein sample could be established.

2.12 Western blot immunodetection of P450 MT1

A whole cell fraction from an *E. coli* protein expression culture sample was taken at a 16 hour time point, following induction of target gene expression at an OD_{600} of 0.6 with 1 mM IPTG. The sample was run on a self-cast SDS PAGE gel (Section 2.9). Protein from the SDS PAGE gel was transferred to a polyvinylidene fluoride (PVDF) transfer membrane (Trans-Blot Turbo Mini/Midi PVDF Transfer Packs, Bio-Rad) pre-soaked in ethanol for 30 s, and then washed in H_2O and soaked in 100 ml Transfer buffer (50 ml 20x NuPAGE Transfer Buffer, 100 ml MeOH and 850 ml H_2O).

The gel and membrane were then placed between 2 sheets of filter paper (pre-soaked in transfer buffer). The filter paper, gel and membrane were fitted into the blotting chamber of an XCell II™ Blot Module (Invitrogen) with pre-soaked blotting pads. The blotting chamber was then filled with transfer buffer and the external chamber with H_2O. A constant voltage of 10 V was applied to the cell for ~16 hours. The PVDF membrane was visualised using a WesternBreeze© Chemiluminescent Immunodetection Protocol. Following this protocol, the PVDF membrane was incubated in 10 ml Blocking solution (1x phosphate buffered saline (PBS)/0.1% Tween 20 (PBS/T) + 5% w/v non-fat dry milk) for 30 minutes on a shaker at room temperature. After washing twice with UV-sterilised dH_2O to remove any residual blocking buffer, the membrane was incubated in 10 ml primary mouse anti-His antibody (Abcam) in 1x PBS/T + 2% milk antibody solution for 1 hour at room temperature on a roller/shaker. The membrane was then washed a further two times with UV dH_2O before incubation with the secondary goat anti-mouse antibody, diluted 1:2000 in the same PBS/T buffer antibody solution. Finally, the secondary

antibody-incubated membrane was further washed twice in dH_2O before being placed on a transparent sheet of plastic, where it was incubated with 2.5 ml of Chemiluminescent substrate for 5 minutes. Excess substrate was then blotted from the membrane before it was covered completely in film. Kodak biomax XAR film was then exposed to the membrane at various times in a darkroom using a Fujifilm FPM 800A developer.

2.13 UV-Visible absorption spectroscopy of P450 enzymes

All UV-visible spectroscopic measurements were obtained using a Cary 50 UV-visible spectrophotometer (Varian Ltd, Oxford, UK) using a 1 cm path length quartz cuvette thermally regulated with a peltier element (Varian) in combination with a pump-driven water cooling system. Typically 4 – 6 µM enzyme in buffer B at a final volume of 1 ml was used for monitoring enzyme spectra in the range of between 250 – 750 nm. A buffer-only sample was used to provide a baseline absorbance spectrum across this range. Spectral data manipulation and analysis were performed using Origin software (OriginLab, Northampton, MA).

UV-visible spectra were recorded for enzymes in their oxidised states, and in their reduced forms using a variety of reducing agents: NADPH, NADH and sodium dithionite (DT). Typically, a final concentration of 200 µM NAD(P)H was used to fully reduce enzyme samples, and in the case of DT, a few grains of solid DT a few grains was usually enough to reduce flavins (though heme reduction sometimes required anaerobic conditions). Carbon monoxide (CO) binding was analysed in enzymes containing a P450 heme domain (P450 BM3, P450 MT1 and their isolated heme domains). The enzyme sample was initially reduced with DT (under anaerobic conditions, as required), prior to CO gas exposure via bubbling in a sealed cuvette. Spectra were recorded for the oxidised, reduced and CO-bound enzyme samples, and scans were recorded at 30 s intervals for 10 minutes after CO bubbling to ensure full conversion. A heme Soret band shift to ~450 nm was confirmation of the formation of a P450 Fe^{2+} – CO complex with a cysteinate proximal ligand. The binding of nitrogen monoxide (NO) was also analysed for P450 heme domain-containing enzymes. A few bubbles of NO gas were bubbled directly into a sealed cuvette containing the oxidised enzyme. Spectra were recorded for the oxidised and NO-bound enzyme sample and scans were recorded at 30 s intervals for 10 minutes after NO bubbling

to ensure full conversion to the NO-bound state. A heme Soret shift to ~436 nm was confirmation of a shift to a Fe^{3+} – NO complex (though likely forming a Fe^{2+} – NO^{+} state) with a cysteinate proximal ligand.

2.14 P450 ligand binding titrations using UV-Visible absorption spectroscopy

Spectral binding titrations of P450 MT1 and MT1 HD were carried out with a range of fatty acid substrates and azole inhibitor ligands (Sigma-Aldrich). Prior to binding titrations, enzyme samples were passed through Lipidex column of dimensions 5 x 1 cm (Perkin Elmer, Cambridge UK) in order to remove any residual lipid retained by the protein from *E. coli* during purification. This was repeated until enzyme recovered from the column was in an extensively low-spin (LS) ferric state. Titrations were performed at 25 °C in buffer B using 1 mL samples containing a final enzyme concentration of 3 – 8 µM in a quartz cuvette. Binding candidates (substrates and inhibitors) were typically made up into stock solutions of 1 – 80 mM in 50% EtOH in the same buffer. Titrations were performed by serial additions of aliquots (0.1-1 µL) of the binding candidates to the enzyme sample (aliquot additions to < 1% of total sample volume). Spectra in the range from 250 – 750 nm were recorded for the ligand-free enzyme and following each addition of substrate using a Cary 60 UV-visible spectrophotometer (Varian). A buffer-only sample was used to provide a baseline spectrum in all cases. Difference spectra at each stage in the titration were obtained by subtraction of the initial ligand-free enzyme spectrum from subsequent spectra collected after each addition of an aliquot of ligand. From the difference spectra, a pair of wavelengths were identified and defined as the absorbance maximum (A_{peak}) and minimum (A_{trough}). The overall absorbance change (A_{max}) was calculated by subtracting the minimum from the maximum absorbance for every spectrum collected after an aliquot addition. Graphs of ($A_{max} - A_{min}$) against [ligand] were potted for each binding candidate and fitted using either a hyperbolic (Michaelis-Menten) function (Equation 2) or by using the Quadratic (Morrison) function for tight binding ligands (Equation 3) in order to determine dissociation constant (K_d) values. The Morrison equation was used in preference when the K_d value was $\leq$ 5x the enzyme concentration. Titrations were repeated in triplicate and the final K_d value was determined from the average values across the three sets. All data fitting was done using Origin software (OriginLab, Northampton, US).

$$A = \frac{A_{max}[L_f]}{K_d + [L_f]}$$

Equation 2 Michaelis-Menten hyperbolic, one-site binding equation. A denotes the measured absorbance, A_{max} the maximum absorbance at ligand saturation, $[L_f$ the concentration of free ligand (L_f = [L_{total}] - [L_{bound}]) at which A is measured and K_d the dissociation constant for L binding to the target protein.

$$A_{obs} = \left(\frac{A_{max}}{2 * E_t}\right) * \left(\left(L_f + E_t + K_d\right) - \left[\left(\left(L_f + E_t + K_d\right)^2\right) - (4 * L_f * E_t)\right]^{0.5}\right)$$

Equation 3 Quadratic (Morrison) equation for tight binding ligands. A_{obs} denotes the measured absorbance at ligand concentration L_f, A_{max} the maximum absorbance at ligand saturation, E_t the total enzyme concentration, L_f the concentration of free ligand (L_f = [L_{total}] - [L_{bound}]) at which A is measured and K_d the dissociation constant for ligand binding to the target protein. This equation was used in cases where tight binding was observed ($K_d \leq 5[E_t]$).

2.15 Multi-Angle Laser Light Scattering (MALLS) studies

Samples of pure protein were made up to 1 – 5 mg/ml in the appropriate buffer, which was extensively filtered and degassed before use. A SE SX200 24/30 chromatography column (GE Healthcare) purification step was necessary before monitoring light scattering using a DAWN HELEOS spectrometer (Wyatt Technology corp., Santa Barbara, CA, USA) at 25 °C. 200 µl enzyme samples were run through the column at a flow rate of 1 ml/min before data were collected at a 1 s interval rate using a K5 cell type and a laser wavelength of 658 nm. The Refractive index (RI) was detected at 633 nm by an Optilab-rEX refractometer, QELS (Quasi-Elastic Light Scattering) determined the hydrodynamic radius (Rh) of the species in the sample and UV absorbance was monitored by a generic UV detector at 280 nm. The average molecular weight moments (Mr) and the protein concentration of the

eluted fractions collected were calculated using ASTRA v.6 software (Wyatt Technology) and fitted with a Zimm model.

To perturb enzyme oligomeric interactions (specifically to reduce disulfide bonds), samples were incubated with 10 mM dithiolthreitol (DTT) prior to loading on the SX200 SEC column. DTT at a final concentration of 1 mM was added to the running buffer used to pre-equilibrate the SEC column and MALLS instrumentation detectors to maintain any solution state disruption. MALLS experiments were initially conducted by Mrs. Marjorie Howard, and later by Ms. Hilda Diana Ruiz Nivia at the Biomolecular Interactions Facility in the Faculty of Life Sciences, University of Manchester.

2.16 Thermofluorescence assay for protein thermal stability analysis

Sypro Orange (SO) (Invitrogen, Life Technologies, CA, USA), used to analyse protein thermal unfolding, was supplied as a 5000x stock solution in anhydrous DMSO and diluted to a 25x working concentration for all samples. Conditions were prepared using 50 mM buffer solutions (Table 2.13) and additives from the JBS Solubility screen kit (Jena Bioscience, Jena, Germany). Samples of P450 MT1 and MT1 HD at concentrations of 1 mg/ml were prepared to a final volume of 25 µl in 96-well thin-wall PCR plate (Bio-Rad Laboratories, CA, USA) sealed with Optical-Quality Sealing Tape (Bio-Rad). The plates were heated in an iCycler iQ RT PCR Detection System (Bio-Rad Laboratories, CA, USA) from 20 to 90 °C in increments of 0.2 °C after 5 second delays for signal stabilization. The fluorescence emission intensities were monitored simultaneously with a charge-coupled device (CCD) camera. The wavelengths measured for excitation and emission of SO were 492 nm and 610 nm, respectively.

Table 2.13 The 24 Jena Bioscience standard buffer solutions used in protein thermal stability assays. Solutions were provided as 50 mM stocks.

Buffer	pH	Buffer	pH
Glycine	3.0	**Ammonium acetate**	7.0
Citric acid	3.2	**MOPS**	7.0
PIPPS	3.7	**Na/K phosphate**	7.0
Citric acid	4.0	**HEPES**	7.5
Sodium acetate	4.5	**Tris**	7.5
Na/K phosphate	5.0	**EPPS**	8.0
Sodium citrate	5.5	**Imidazole**	8.0
Na/K phosphate	6.0	**Bicine**	8.5
Bis-Tris	6.0	**Tris**	8.5
MES	6.2	**CHES**	9.0
ADA	6.5	**CHES**	9.5
Bis-Tris-propane	6.5	**CHAPS**	10.0

Prior to using the buffer screen, a preliminary screening of protein and dye concentrations was performed to determine the optimal signal-to-noise ratio. Thermal unfolding was measured as a function of fluorescence emission at 610 nm to produce a fluorescence melt curve of arbitrary fluorescence units (RFU) against temperature. The melting temperature (T_m) was determined from the peak of the first derivative plot of the fluorescence melt curve.

2.17 P450 MT1 heme binding analysis by Fe^{2+}-CO complex thermal denaturation

The effect of temperature on heme coordination and binding was probed by monitoring heme Fe^{2+}-CO complex stability. 2 – 4 µM P450 MT1 samples were made up to 1 mL in buffer B in a 1 cm path length quartz cuvette. The enzyme sample was initially reduced with DT, prior to CO gas exposure via bubbling in a sealed cuvette as in Section 2.12. Absorbance was monitored on a Cary 50 UV-visible spectrophotometer (Varian Ltd, Oxford, U.K.), thermally regulated with a peltier element in combination with a pump-driven water cooling system. The cuvette was heated in the spectrophotometer from 25 to 60 °C in increments of 2.5 °C with spectra collection after a 30 second delay at each temperature for signal stabilization. Difference spectra were obtained by subtraction of the initial Fe^{2+}-CO spectrum at 25 °C from the spectra collected at each subsequent temperature point. The absorbance maximum (A_{420}) and minimum (A_{450}) from the

difference spectra reflect the decomposition of the cysteine thiolate–heme coordinated state (450 nm) to the cysteine thiol–heme ligation state (420 nm). The overall absorbance change ($\Delta A_{420} - \Delta A_{450}$) was calculated by subtracting the minimum from the maximum absorbance for spectra at each temperature point, and these data were plotted against the applied temperature. The midpoint melting temperature (T_m) was determined from the fitting of these data using the Hill Function (Equation 4).

$$A = \frac{A_{max} T^n}{T_m^{\,n} + T^n}$$

Equation 4 The Hill function adapted to melting temperature determination. In the equation, A is the measured absorbance at applied temperature, A_{max} is the maximal absorbance change, T is the applied temperature, T_m is the apparent melting temperature and n is the Hill coefficient.

2.18 Flavin fluorescence assay for protein thermal stability analysis

The fluorescence change on flavin dissociation from the reductase domain in P450 MT1 was measured in this assay. 7 μM P450 MT1 samples were made up to 1 mL in buffer B in a 1 cm path length quartz cuvette for fluorescence spectroscopy. Fluorescence was monitored on a Cary Eclipse Fluorimeter (Varian Ltd, Oxford, UK), thermally regulated with a peltier element in combination with a pump-driven water cooling system. Flavin fluorescence was measured with excitation at 450 nm and fluorescence emission recorded between 475 nm and 700 nm. The cuvette was heated in the fluorimeter from 15 to 80 °C in increments of 5 °C, with spectra collected after a 30 second delay at each temperature for signal stabilization. The maximum fluorescence emission from the flavins was at 528 nm, and F_{528} data were plotted directly against temperature (°C) to obtaine a fluorescence melt curve of arbitrary fluorescence units at 528 nm (F_{528}) against temperature. The melting temperature (T_m) was determined from the fitting of these data using the Hill Function (Equation 4).

2.19 Electron Paramagnetic Resonance (EPR) spectroscopy of cofactor-binding proteins

Continuous wave Electron Paramagnetic Resonance (EPR) spectra were recorded at narrow and wide range X-band (~9.4 GHz) using a Bruker ELEXSYS E500/E580 EPR spectrophotometer (Bruker GmbH, Rheinstetten, Germany). Temperature control was effected using an Oxford Instruments ESR900 helium flow cryostat coupled to an ITC 503 controller from the same manufacturer. The output of the detector is the g-factor (Equation 5) displayed as the first derivative on a magnetic field strength scale. Derivative spectra were generated from raw microwave absorption data using the Bruker software associated with the EPR spectrophotometer.

$$hv = g\mu_B B_\theta$$

Equation 5 The g-factor equation. In equation 5, h is Planck's constant, v is the operating frequency of the EPR spectrometer (constant), μ_B is the electron Bohr magneton (constant at 9.273 x 10^{-23} Tesla), B is the magnetic field (Tesla) and g is the g-factor.

2.19.1 P450 Heme analysis by EPR

EPR is a powerful diagnostic tool that has been used extensively in the characterisation of P450 enzymes. It is a sensitive technique that can detect paramagnetic species such as heme-bound ferric iron and the changes in iron d-orbital electron configuration associated with ligand binding and other environmental changes.

Spectroscopic data for both WT P450 MT1 and P450 MT1 HD were recorded at 10 K with a microwave power of 0.5-1 mW, 5 – 7 G modulation amplitude and a range of magnetic field strengths up to 4000 G. EPR samples were prepared in Wilmad 4 mm Suprasil EPR quartz tubes (Wilmad-LabGlass, USA). Protein samples were made up to a final concentration of 225 uM in buffer A containing 500 mM KCl, and frozen in liquid nitrogen for analysis.

For ligand-bound samples, P450 enzyme solutions were prepared as above with the addition of arachidonic acid substrate from stock solution to a final concentration of 1 mM. Ligand-free samples had an equal volume of 50 mM KPi (pH 7.0) buffer containing 500 mM KCl added to compensate for the dilution factor. In the case of NAD(P)H-reduced samples, P450 BM3 and P450 MT1 enzyme samples were prepared as above, with the

addition of NADH and NADPH from stock solution to a final concentration of 1 mM. NAD(P)H only EPR samples had an equal volume of buffer A containing 500 mM KCl added to compensate for the dilution factor.

Strong ligands to the P450 heme iron can produce significant shifts associated with changes in heme iron coordination state; while substrates may induce a change in ferric heme iron spin-state equilibrium towards high-spin. However, as EPR spectra were collected at cryogenic temperatures (10 K in the case of heme EPR spectra), the lower energy, low-spin ferric state may dominate over the high-spin state for the substrate-bound P450s (whereas high-spin would be more prevalent at ambient temperature for substrate-bound P450s). The amount of heme in a protein sample was quantified by comparing the doubly integrated area of their g-factor to those of a set of copper solution concentration standards.

2.19.2 P450 MT1 flavin semiquinone analysis by EPR

EPR spectroscopy was used to qualitatively and quantitatively monitor semiquinone formation in P450 MT1 upon incubation with various reductants. Semiquinone flavins are paramagnetic species detectable by EPR spectroscopy, as they possess a single unpaired electron on their isoalloxazine rings.

NAD(P)H was used at a final concentration of 1 mM and sodium dithionite was used in excess. Enzyme samples were incubated with NADPH, NADH and sodium dithionite for 30 seconds, 5 minutes and 10 minutes. Incubation was halted by freezing in liquid nitrogen.

Spectroscopic analysis of flavin semiquinones was done at 77 K with microwave power of 10 µW, a 1 G modulation amplitude and a 50 G sweep width from 3300 G. EPR samples were prepared in Wilmad 4 mm Suprasil EPR quartz tubes. Protein samples were made up to a final concentration of 225 µM in 50 mM KPi (pH 7.0) buffer containing 500 mM KCl. The amount of semiquinone formation was quantified by comparing the doubly integrated area of their g-factor to that of a copper solution concentration standard.

2.20 Redox potentiometry of P450 MT1

Redox titration experiments were performed in an anaerobic glovebox (Belle Technology, Weymouth UK) under a nitrogen atmosphere, with O_2 levels maintained below 2 ppm. All

solutions were degassed by sparging with nitrogen gas prior to experimental use. The protein was applied to a Pharmacia PD-10 desalting column (GE Healthcare) in an anaerobic glove box, pre-equilibrated with degassed 50 mM KPi (pH 7.0) buffer containing 200 mM KCl.

The titrations for substrate-free protein samples were done using the degassed buffer B. Substrate-bound protein titrations used the same sample buffer supplemented with 10% glycerol (v/v) and 1 mM arachidonic acid. The protein solutions were typically at a concentration of ~10-20 µM in 5 mL of titration buffer, and were titrated electrochemically using sodium dithionite as a reductant. Dithionite was delivered in approximately 0.5-1 µL aliquots from concentrated stock solutions (typically ~1-10 mM).

Mediators were added to facilitate electrical communication between the redox centres in the P450 enzyme (heme, FAD and FMN) and the electrode, prior to initiating the redox titration. Typically, 2 µM phenazine methosulfate, 5 µM 2-hydroxy-1,4-naphthoquinone, 0.5 µM methyl viologen, and 1 µM benzyl viologen were included to mediate in the range between +100 and -480 mV vs. the normal hydrogen electrode (NHE). The electrode was allowed a consistent time for equilibration between each dithionite addition (usually about 2 minutes). Spectra from 250-750 nm were recorded using a fibre optic probe immersed in the enzyme solution and attached to a Cary UV-50 Bio UV-visible scanning spectrophotometer. Data manipulation and analysis were performed using Origin software.

For redox titration of WT P450 MT1, absorbance values at 475 nm were plotted against potential to monitor flavin reduction. When using the P450 MT1 HD, to monitor the extent of heme reduction a set of difference spectra were generated from the absolute spectra by subtracting the initial oxidised enzyme spectrum from the spectra taken after each dithionite addition. The overall absorbance change occurring from enzyme reduction was calculated by subtracting the absorbance maximum (A_{peak}) from the minimum (A_{trough}) to give an A_{max} value, which was plotted against the corrected potential. All measured electrode potential readings were corrected relative to the normal hydrogen electrode (NHE) by a factor of +207 mV. Data were fitted to appropriate Nernst equations.

$$A = \frac{(A_{min} + A_{max})10^{\left(\frac{E_{mid}-E}{RTF}\right)}}{1 + 10^{\left(\frac{E_{mid}-E}{RTF}\right)}}$$

Equation 6 The Nernst Equation for a one electron reduction process. In equation 6, A is the measured absorbance value, A_{min} and A_{max} are the minimum and maximum values of absorbance for the fully oxidized and full reduced species, E_{mid} is the midpoint potential when 50% of the sample is reduced, and E is the observed potential at which the absorbance A is recorded. RTF is a combined constant (59 mV at 298 K) encompassing the absolute temperature (K), ideal gas constant (R = 8.314 J mol^{-1} K^{-1}) and Faraday constant (96485 C mol^{-1}), and a conversion factor from natural to base ten logarithms.

$$A = \frac{\left(A_{max}10^{\frac{E^1_{mid}-E}{RTF}}\right) + A_{mid} + \left(A_{min}10^{\frac{E^2_{mid}-E}{RTF}}\right)}{\left(1 + 10^{\frac{E^1_{mid}-E}{RTF}}\right) + 10^{\frac{E^2_{mid}-E}{RTF}}}$$

Equation 7 The Nernst Equation for a two electron reduction process. In equation 7, A is the measured absorbance value, A_{max} and A_{min} are the minimum and maximum values of absorbance for the fully oxidized and fully (2-electron) reduced species, and A_{mid} is the midphase absorbance value for a 1-electron reduced species. E_{mid}^1 is the first midpoint reduction potential, E_{mid}^2 is the second midpoint potential, and E is the observed potential at the measured absorbance A. RTF is a combined constant (29.5 mV for a concerted 2-electron process at 298 K) encompassing the absolute temperature (K), ideal gas constant (R = 8.314 J mol^{-1} K^{-1}) and Faraday constant (96485 C mol^{-1}), and a conversion factor from natural to base ten logarithms.

2.21 Substrate dependent NAD(P)H oxidation using P450 MT1

The steady-state activity of WT P450 MT1 using a range of lipid substrates was determined at 25 °C using a Cary 50 UV-visible spectrophotometer to monitor substrate-dependent NAD(P)H oxidation. The assays contained 20 – 50 nM final enzyme

concentration made up to a volume of 1 mL in buffer B, and incorporated a range of substrate concentrations in 1.5 mL BRAND UV cuvettes.

The reaction was initiated by the addition of NAD(P)H to the cuvette and reaction progress was followed at 340 nm ($\Delta\varepsilon_{340\ (red\text{-}ox)}$ = 6.21 mM^{-1} cm^{-1}). Control samples with no enzyme present were set up to account for any non-enzyme mediated NAD(P)H cofactor oxidation, and these had an equal volume of buffer added to compensate for the absence of enzyme. Parafilm was used to seal the cuvette to allow thorough mixing prior to the collection of kinetic data, typically over a 2 minute reaction duration. Kinetic assays were run in triplicate and the average NADPH oxidation rates were plotted against the substrate concentration. Origin software was used in data fitting to derive K_m and k_{cat} values from steady-state assays using the Michaelis-Menten function (Equation 2).

2.22 Steady-state kinetic studies with P450 MT1 using non-physiological electron acceptors

The steady-state activity of WT P450 MT1 using cytochrome *c* (cyt *c*) and potassium ferricyanide (KFeCN) as electron acceptors was determined at 25 °C using a Cary-300 Bio UV-visible dual-beam spectrophotometer (Varian Ltd, Oxford, UK). The assays contained 20 – 50 nM final enzyme concentration made to a volume of 1 mL in buffer B in 1.5 mL BRAND standard disposable cuvettes. To determine the kinetic parameters (k_{cat} and K_M) for artificial electron acceptors KFeCN and cyt *c*, their concentrations were varied while NAD(P)H concentration was kept at near-saturating (to obtain K_m values for the electron acceptors) and *vice versa* for the electron acceptors (to obtain the NAD(P)H K_m values). Typically, assay concentration ranges of 0 – 200 µM was used for NADPH, 0 – 800 µM for NADH, 0 – 1.5 mM for ferricyanide and 0 – 400 µM for cyt *c* were used when varied, and final concentrations of 500 µM NAD(P)H, 2 mM ferricyanide and 400 µM cyt *c* for substrates kept near-saturating.

To account for non-enzyme mediated reduction of electron acceptors, assays were performed in a dual beam spectrophotometer against a reference cuvette containing the same components but without enzyme, and with the same volume of buffer in place of the enzyme. The reactions were initiated by the simultaneous addition of NAD(P)H to both cuvettes. Cytochrome *c* (horse heart) reduction was measured at 550 nm ($\Delta\varepsilon_{550\ (red\text{-}ox)}$ = 22.64 $mM^{-1}cm^{-1}$), and ferricyanide reduction was measured at 420 nm ($\Delta\varepsilon_{420\ (red\text{-}ox)}$ = 1.02

$mM^{-1}cm^{-1}$). Parafilm was used to seal the cuvette to allow thorough mixing prior to the collection of kinetic data, typically over a 2 minute reaction duration (though initial rates were often taken over much times for faster reaction processes). Kinetic assays were run in triplicate and the average NAD(P)H oxidation rates or cyt *c*/KFeCN reduction rates were plotted against the concentration of either the electron acceptor (KFeCN and cyt *c*) or electron donor (NAD(P)H) being varied. Origin software was used in data fitting to derive K_m and k_{cat} values from steady-state assays using the Michaelis-Menten function (Equation 2).

2.23 Stopped-flow absorption kinetics and photodiode array analysis of kinetic data for P450 MT1

Single wavelength stopped-flow kinetic studies of flavin reduction using NAD(P)H and of the initial flavin-to-heme electron transfer (following Fe^{2+}-CO complex formation) in P450 MT1 were performed using an Applied Photophysics SX.18 MVR stopped-flow spectrophotometer (Leatherhead, UK) under anaerobic conditions (<5 ppm oxygen). Stopped-flow spectral accumulation was acquired using a photodiode array (PDA) detector on the same instrument. All buffers were made anaerobic by filter degassing followed by extensive bubbling with oxygen-free nitrogen gas. P450 MT1 at a concentration of 20 µM (final concentration in stopped-flow mixture of 10 µM) in buffer B was used in all experiments and the concentration of NAD(P)H was always at least 10-fold greater than the concentration of enzyme to ensure pseudo first-order reaction conditions. At least three separate reactions were done for each sample analysed. Observed rate constants for NAD(P)H-dependent flavin reduction and for heme reduction (measured via CO-binding to ferrous heme iron) were obtained by the fitting of the kinetic transients obtained using a double-exponential function and employing Pro-Data SX software (Applied Photophysics).

2.23.1 P450 MT1 flavin reduction by NAD(P)H

P450 MT1 Flavin reduction by NADH and NADPH was monitored at 475 nm, a wavelength selected as the best compromise between the near-maximal absorption for the oxidised flavins and minimal interference from heme Soret peak at ~420 nm. P450 MT1 in

one syringe (20 µM) was made up in anaerobic buffer B. NADPH at concentrations between 0 – 1.2 mM was prepared in the same buffer in a separate syringe.

For analysis of the temperature-dependence of P450 MT1 flavin reduction by NADPH, a final NADPH concentration of 1 mM was used. The built-in instrument temperature probe was used to heat the Sample Handling Unit from 10 to 35 °C in increments of 5 °C and measurements were taken after 30 second delays for system stabilization. Data were collected over 1 s after the initial mixing event, and the first spectrum was recorded 2.6 ms after mixing.

2.23.2 Analysis of flavin-to-heme electron transfer in P450 MT1

The kinetics of P450 MT1 reduction on mixing with NADPH (and binding to CO to form a ferrous-CO complex – which is considered to be a much faster process than electron transfer from NADPH through the ferric heme iron) was monitored by stopped-flow multiwavelength absorption using a photodiode array detector over the wavelength range from 700-250 nm, and analysed with X-scan software (Applied Photophysics Ltd). P450 MT1 in one syringe (40 µM) was made up in buffer B containing 1 mM arachidonic acid and 10% v/v glycerol, and was bubbled extensively with CO gas. NADPH at 400 µM was made up in the same buffer was in a separate syringe. Reactions followed CO binding to reduced P450 MT1 at 450 nm, over time periods of 2 s after the initial mixing event, and the first spectrum was recorded 2.6 ms after mixing.

2.24 P450 MT1-dependent fatty acid turnover, product derivatisation and identification using Gas Chromatography-Mass Spectroscopy (GC-MS)

Each fatty acid substrate was incubated with WT P450 MT1 in the presence of NADPH and the products formed were purified, derivatised and analysed by GC-MS.

<u>Turnover Reactions</u>

Turnover reactions for fatty acid hydroxylation by WT P450 MT1 were carried out at 37 °C with shaking for 30 min in the presence of NADPH.

The reaction mixtures contained:

- 0.1 mM purified WT P450 MT1
- 1 mM fatty acid substrate
- 500 µM NADPH
- 7.76 mM glucose 6-phosphate
- 0.6 mM $NADP^+$
- glucose-6-phosphate dehydrogenase (0.75 units/ml)

in buffer B, made up to a final volume of 2 mL.

Product Purification and Derivatisation

Following the completion of the reactions, protein was precipitated by heating at 100 °C for 10 min and pelleted by centrifugation at 4000 x *g* for 25 min at 10 °C. Hydroxylated fatty acid products were isolated from the supernatant by flowing the sample onto a StrataX SPE column (Phenomenex, Macclesfield, UK). After extensive washing with 2 CV of buffer B, elution of residual substrate and products was achieved by passing 1 CV of 100% methanol through the column, and collecting samples into mass spectrometry vials. Samples were dried down before the derivatisation process in a rotary evaporator. Derivatisation was carried out by adding 0.5 ml N,O-bis(trimethylsilyl)trifluoroacetamide (BSTFA)/0.1 % trichloromethyl silane (Sigma-Aldrich) to the dry sample and incubating at 60 °C for 60 min.

Gas Chromatography-Mass Spectrometry Analysis of Products

Analysis was done using a ThermoFisher DSQ II GC/MS instrument with a 30 m x 0.25 mm x 0.25 µm ZB5MS GC column (Phenomenex). Injection was cold on-column. The oven program was set so that an initial temperature of 50 °C was ramped at 23 °C/min to 310 °C post-injection. Electronic ionization was used, and ions in the range of 40-640 m/z scanned at two scans per second.

2.25 Electron Microscopy (EM) studies on P450 BM3

EM is a useful tool to study large proteins and complexes with molecular weights above 100 kDa. EM was used to acquire structural data on the dimeric form of BM3. Purified P450 BM3 was initially run through a SEC-MALLS column (Section 2.14) using 100 mM Tris buffer (pH 7.0) to obtain a homogeneous BM3 dimer sample, which was then made up to a concentration of 7 µg/mL. Quantifoil CFT400 Cu R2/2 holey carbon grids (Electron Microscopy Sciences, PA, USA) were ionised by glow discharge [276] before sample application and staining in the following sequence:

- Incubation with P450 BM3 sample (70 µg/mL) for 30 s
- Blotting
- 100 mM Tris buffer (pH 7.0) incubation for 30 s
- Blotting
- 2% (w/v) aqueous uranyl acetate pH 4.6 incubation for 30 s
- Blotting
- 100 mM Tris buffer (pH 7.0) incubation for 30 s
- Blotting

Data collection was performed using a FEI Tecnai 12 Bio-Twin Transmission Electron Microscope (FEI Company, OR, USA) operated at 80-120 kV and equipped with an embedded CCD (FEI Company). Electron microscopy data were screened using Fiji/ImageJ software (version 1.46r, National Institutes of Health, MD, USA). Overview images of the holes were inspected and poor regions on the grid were discarded.

A total of 21k particles were refined with by RELION optimisation with C2 symmetry applied to produce a 3-dimensional structure with a resolution volume of 20 Å using the EMAN 2 image processing suite [277,278]. The data collection and modelling was carried out by Dr. Richard Collins (Faculty of Life Sciences, University of Manchester).

2.26 Nuclear Magnetic Resonance (NMR) studies on the P450 BM3 heme domain

2.26.1 1D ^{1}H NMR spectral collection and sample preparation for the BM3 HD

1D ^{1}H NMR spectra were collected for unlabelled BM3 HD expressed as described in Section 2.5.4 and purified as described in Section 2.7.5. 500 µL samples of 500 µM ferric BM3 HD were prepared in buffer A with 10% (v/v) D_2O and were transferred to 5 mm Shigemi tubes (Shigemi Inc, PA, USA) before 1D NMR spectra collection.

A sample of the ferrous BM3 HD was obtained following the reduction of ferric BM3 HD under anaerobic conditions. Ferric BM3 HD was buffer exchanged into degassed buffer A and concentrated before the addition of 10% (v/v) D_2O. A titration of this sample with a concentrated sodium dithionite solution was monitored by UV/vis spectroscopy until the sample was fully ferrous. The ferrous BM3 HD sample was then transferred to a 5 mm Shigemi tube and a degassed layer of mineral oil was placed on top of the sample to prevent its reoxidation. Parafilm was also used to seal the top of the Shigemi tube to slow the diffusion of oxygen into the tube.

1H NMR spectra were recorded at 298 K with excitation sculpting water suppression (1024 scans) on a Bruker 800 MHz Avance III NMR spectrometer with a TCP cryoprobe equipped with z-gradients.

2.26.2 BM3 HD ^{15}N isotopic labelling and expression trials

Large scale (200 mL) cultures of M9 and EnPresso B Defined media (Section 2.2.1) were investigated for BM3 HD expression using BL21-Gold (DE3) and BL21 CodonPlus (DE3) cells to identify the best route to efficient production of labelled protein. 5 mL LB day cultures of BL21-Gold (DE3) and BL21 CodonPlus (DE3) cells freshly transformed with the BM3 HD expression plasmid were set up to analyse the production of the BM3 HD for NMR analysis.

Expression of BM3 HD in M9 medium was carried out as follows: 1% of day cultures were used to inoculate 2 x 100 mL pre-warmed M9 medium with each strain, once the day cultures reached an OD_{600} of 0.2 - 0.4. 50 µg/mL carbenicillin were added along with 0.2 mL of Solution B (which contained 2 g/mL glucose, 1 g/mL $^{15}NH_4Cl$ and 100 µL of trace elements to each flask. The flasks were then incubated in an orbital incubator at 37 °C with shaking at 190 rpm until an OD_{600} of 0.8 was reached, at which point BM3 HD expression in the cells was induced by addition of 0.8 mM IPTG and the growth temperature lowered to 30 °C. After 20-24 hours, the cells were harvested by centrifugation at 4 °C (6000 x *g*, 8 min) before being stored at -20 °C.

Expression of BM3 HD in EnPresso B Defined medium was carried out exactly as described in the supplier's protocol. 4 tablets of Enpresso medium were dissolved in 90 mL sterile water in each of 2x 2L conical flasks by incubation of the flasks in an orbital shaker at 37 °C. 1% of an overnight culture of the BM3 HD expression cells was used to inoculate each flask along with 50 µg/mL carbenicillin. At this point, 50 µl of Reagent A (3000 U/L, Biosilta) were added along with 6 mL of 2.5 g/mL $^{15}NH_4Cl$, before the flasks were incubated in an orbital incubator at 30 °C and with shaking at 190 rpm until the following day (~ 18 hours). The next day, 0.8 mM IPTG was added to each flask to induce protein expression, along with a further 170 µL of Reagent A, while keeping the temperature at 30 °C and shaking at 190 rpm. After 20-24 hours the cells were harvested by centrifugation at 4 °C (6000 x *g*, 8 min) before being stored at -20 °C. The purification of ^{15}N labelled BM3 HD was carried out exactly as for unlabelled BM3 HD, as detailed in Section 2.7.5.

2.26.3 2D ^{15}N TROSY NMR spectra collection and sample preparation for the BM3 HD

2D ^{15}N TROSY NMR spectra were collected for purified ^{15}N labelled BM3 HD. 500 µl samples of 500 µM ferric BM3 HD were prepared in 50 mM KPi buffer (pH 7.0) with 10% D_2O and transferred to 5 mm Shigemi tubes before 1D NMR spectra collection. Samples of BM3 HD for 2D TROSY spectra collection were reduced to the ferrous state, as described in Section 2.26.1.

2D NMR spectra were collected on an 800 MHz Bruker Avance III NMR spectrometer using a TCI (1H-^{13}C/^{15}N/^{2}H) cryoprobe with z gradients at 298 K. The pulse program was a 2D H-1/X correlation via TROSY using sensitivity improvement, and phase sensitivity was achieved using Echo/Antiecho gradient selection [279].

Chapter 3: Expression, purification and characterisation of P450 MT1 (CYP505A30) from *Myceliophthora thermophila.*

3.1.1 Introduction

Cytochrome P450 BM3 is the most widely studied, industrially relevant P450-redox partner fusion enzyme. It has become a model system in the P450 superfamily due to its high catalytic activity and the ability to engineer the enzyme for the oxidation of novel substrates [94].

The large body of structural data for BM3 heme (P450) domain crystal structures [2–4] in both substrate-free and substrate-bound forms have made it possible to rationally redesign the active site to influence its structure and molecular specificity. Selected mutations (e.g. A82F in the active site vicinity and I401P adjacent to the cysteine thiolate heme iron ligand) perturb the conformational state of the heme domain and facilitate binding and oxidative catalysis with new substrates (e.g. omeprazole and ethanol) [5–7].

Despite structures having been solved for each of the individual domains of the flavocytochrome P450 BM3, a crystal structure for the full length, multidomain enzyme remains elusive. Likely reasons for this are the dynamic nature of multidomain proteins and the fact that BM3 is an active dimer in solution [240]. One possible route to a crystal structure, which has had a track record of success for other proteins, is to find a thermophilic homologue which would be more amenable to crystallisation. While such BM3 homologues may be dynamic and flexible at their physiological temperatures, when brought down to e.g. 4 °C for crystallisation, the difference in temperature between physiological and applied conditions (which will be higher for thermophilic than for mesophilic enzymes) should reduce domain movements to a greater extent and thus increase considerably the chances of crystallisation of such proteins [283].

Fusion enzymes are attractive candidates for biotechnological applications as they tend to be better coupled (e.g. less reagent wastage and undesirable product formation), often have faster reaction rates and are easier to produce than their individual counterparts. However, natural (class I or class II) P450 redox systems can also operate with high catalytic rates. A particularly efficient example being $P450_{cam}$, a class I *Pseudomonas putida* P450 that uses putidaredoxin (Pd, ferredoxin) and putidaredoxin reductase (PdR, ferredoxin reductase) partners and catalyses camphor hydroxylation with a k_{cat} of 4,200 min^{-1} [284]. In contrast,

an artificial fusion protein of $P450_{cam}$-PdR-Pd performed less well, with an apparent V_{max} of 600 min^{-1} based on camphor-dependent oxygen consumption [285].

In natural fusion systems, better coupling and faster reaction rates are likely due to increased 'productive collisions' between the individual domains of these enzymes, compared to those of separate P450 and redox partner domains [286]. As described in Section 1.11, P450s require the sequential delivery of 2 electrons for their monooxygenase activity which would require the dissociation of the redox partner in non-fusion P450s to obtain the second electron from a fused domain (e.g. in the case of CPR) or a separate reductase partner. This is one route to uncoupling of electron transfer from oxidative catalysis, as the newly formed ferrous-oxo species (Section 1.11) is relatively unstable and will collapse to release superoxide if not provided with a second electron in a timely manner. BM3 is no exception to this rule, but the fusion system present a very efficient electron transfer system and has the highest reported P450 monooxygenase activity (~17,000 min^{-1} with arachidonic acid) attributed to its P450-CPR fusion arrangement [197].

BM3, however, has relatively low thermostability (which may compromise potential industrial applications) and its relatively weak FMN binding also poses a challenge for biotechnological applications (although cellular FMN levels may ensure near-complete FMN incorporation). BM3's isolated heme domain unfolds at around 63 °C from differential scanning calorimetry (DSC) studies, a T_m that is significantly higher than that for its isolated reductase domain at 48 °C, with the full length enzyme showing optimal catalytic activity at rather lower temperatures (typically BM3 is assayed at ~30-37 °C) [287]. There have been a variety of approaches used with the aim being to increase the overall thermostability of the BM3 fusion protein. However, there have been limited successes with these approaches and activity of the P450 is compromised [288–291].

Among successful routes described in the literature for production of novel P450-CPR fusion enzymes are the generation of chimeric CYP102A fusions with the isolated BM3 heme domain tethered to a more stable reductase domain from its homologues CYP102A2 and A3 from *Bacillus subtilis* [243,290–292]. While the full length enzyme and the heme domain of BM3 are more thermally stable than the comparable segments of these homologues, the reductase domains of CYP102A2 and A3 are more stable than the reductase domain of BM3 [243]. Importantly, Eiben et al. showed that a generated chimera

(T_m = 56 °C) could be substantially more thermostable than its most stable parent enzyme, $P450_{BM3}$ (full-length) with a T_m of 49 °C [243]. The time it takes for these enzymes' activity to fall to half the original value ($t_{1/2}$) was also examined, and interestingly the best chimera shows a $t_{1/2}$ of 100 min at 50 °C which is over 10 times what was observed for BM3 ($t_{1/2}$ = 8 min) [243]. The disparity in apparent thermostability when observed from a structural and activity-determined assay may be explained by the weak binding of FMN observed in the BM3 reductase domain, which could have an added detrimental effect when observing the activity of BM3 at increased temperatures [293].

The chimeric flavocytochromes generated from recombination of a gene fragment library from parent enzymes CYP102A1-A3 showed activity to drugs (Verapamil and Astemizole) not accepted by parent enzymes and increases in stability from a T_{50} of 54.9 °C BM3, the highest of the parent enzymes, to 64.4 °C [291]. A different approach involving the generation of a fusion of the BM3 heme domain (HD) with the sulphite reductase from *Geobacillus stearothermophilus* gave similar results, with increased stability at 49 °C, but oxidation rates of saturated fatty acids (myristic and palmitic acid) and coupling efficiency were negatively affected, possibly indicating that the reductase domain affects structure and activity in the catalytic P450 domain, and that electron transfer from the non-native reductase is less efficient than that from the native reductase [294]. The CYP116B enzymes are a family of phthalate dioxygen reductase fusion enzymes containing a P450 domain fused to an FMN- and 2Fe-2S cluster-containing reductase domain [202]. Artificial fusion constructs comprising the reductase domain of CYP116B enzymes and plant P450 domains have been generated to increase their activity towards metabolites of interest [295]. A similar approach was taken in the single-step biosynthesis of pravastatin in *Penicillium chrysogenum* via an artificial fusion of a modified P450 domain $P450_{prava}$ (a mutated version of an *Amycolatopsis* sp. CYP105AS1 P450) with a CYP116B2 reductase domain [265]. The rationale for using the CYP116B2 reductase over the kinetically faster reductase domain from BM3 was to avoid the problems of dimerization that might be caused by the BM3 reductase, since CYP116B2 and its reductase are monomeric and thus a fusion system using this type of reductase was considered better suited to industrial use and P450 engineering [296].

In efforts to identify new types of P450-CPR fusion enzymes that are more thermostable and potentially more industrially applicable than is the wild-type P450 BM3 enzyme, my approach (as detailed below) was to use CDART, a bioinformatic tool that could identify

P450/CPR fusions with similar domain architecture to BM3 [297]. Work was done to identify potential thermophilic relatives of BM3, based on the types of organisms found to produce CYP102A family-type (BM3-like) and CYP55A family-type (P450foxy-like) P450-CPR fusion enzymes [244]. The most promising gene candidate identified was 'MYCTH_101224A' (NC_016474.1) from the thermophilic fungus *Myceliophthora thermophila*. My rationale was that a BM3 homologue from a thermostable organism could potentially be thermostable and more useful for applications at higher temperatures required for industrial processes. Such enzymes might also have e.g. better flavin incorporation and possibly have faster monooxygenase activity. As discussed above, the thermophilic nature of the *M. thermophila* enzyme identified may also make it more amenable to crystallisation and to structural elucidation for the intact, multidomain enzyme.

The studies reported in this chapter involve the expression and purification of the recombinant, full length P450-CPR fusion enzyme from *M. thermophila* (CYP505A30, abbreviated as P450 MT1) and its isolated heme domain. In this chapter I show that the purified protein has a molecular mass of 118 kDa, as predicted by bioinformatics and similar to the mass of P450 BM3. MT1's spectral properties are typical of a cytochrome P450, with a ferric heme iron Soret peak at 420 nm, shifting to 450 nm upon CO binding to the reduced (ferrous) iron. The binding of a range of fatty acids to MT1 showed type I Soret spectral shifts (to shorter wavelength) indicative of typical P450 substrate-like behaviour, and conversely imidazole derivatives (1- and 4-phenylimidazole and econazole) showed inhibitor-like type II spectral shifts indicative of heme-iron coordination in the distal (6^{th} coordination) position.

Cytochrome P450 BM3 has a CPR-like C-terminal class II reductase system containing both FAD and FMN cofactors. Homology modelling tools also predicted that CYP505A30 has a CPR-like C-terminal reductase domain. HPLC analysis of the cofactors released from purified enzyme confirmed near-stoichiometric amounts of FAD and FMN. While BM3 has full FAD incorporation, its FMN binding is weak at 41 nM due to fewer protein interactions compared with the FAD cofactor, which is more deeply buried inside its domain [298]. BM3 also displays low affinity for this cofactor compared to other structurally similar flavodoxins, e.g. the K_d is 2.4 nM for a flavodoxin from *D. vulgaris*, *and* YkuN and YkuP from *B. subtilis* have FMN K_d values of 14 nM and 25 nM,

respectively [193,299]. In comparison, it was found that P450 MT1 incorporates a substantial amount of FMN into the purified enzyme.

While *Myceliophthora thermophila* is classed as a moderate thermophile that grows optimally between 45-50 °C [300], protein thermostability studies for MT1 using differential scanning fluorimetry shown that the enzyme is not actually stable much beyond this temperature range. However, the stability of the full length MT1 enzyme can be augmented by appropriate choice of buffer and pH, leading to an increase of the T_m by ~10° to 58 °C under optimized conditions. Moreover, BM3 has been shown to be both present and active in solution as a dimer [240] and multiangle laser light scattering studies on MT1 revealed similar results, indicating that is largely dimeric in the solution state.

3.1.2 Retrieval of the CYP505A30 sequence and Bioinformatics analysis

The bioinformatics tool CDART was employed to search the NCBI to find BM3 homologues from diverse organisms. Rather than searching for direct sequence similarity, the algorithm finds protein similarities based on the entry's domain organisation. At the time of the search, the query brought up 1,065 hits with varying degrees of similarity to BM3.

In the list of relatives with conserved domain architecture we identified the gene candidate 'MYCTH_101224A' (NC_016474.1) from the thermophilic fungus *Myceliophthora thermophila*. With the assistance of Prof. David Nelson (University of Tennessee), the eukaryotic P450 domain/P450 reductase domain fusion was classified according to the standard P450 nomenclature system as CYP505A30 (Figure 3.1).

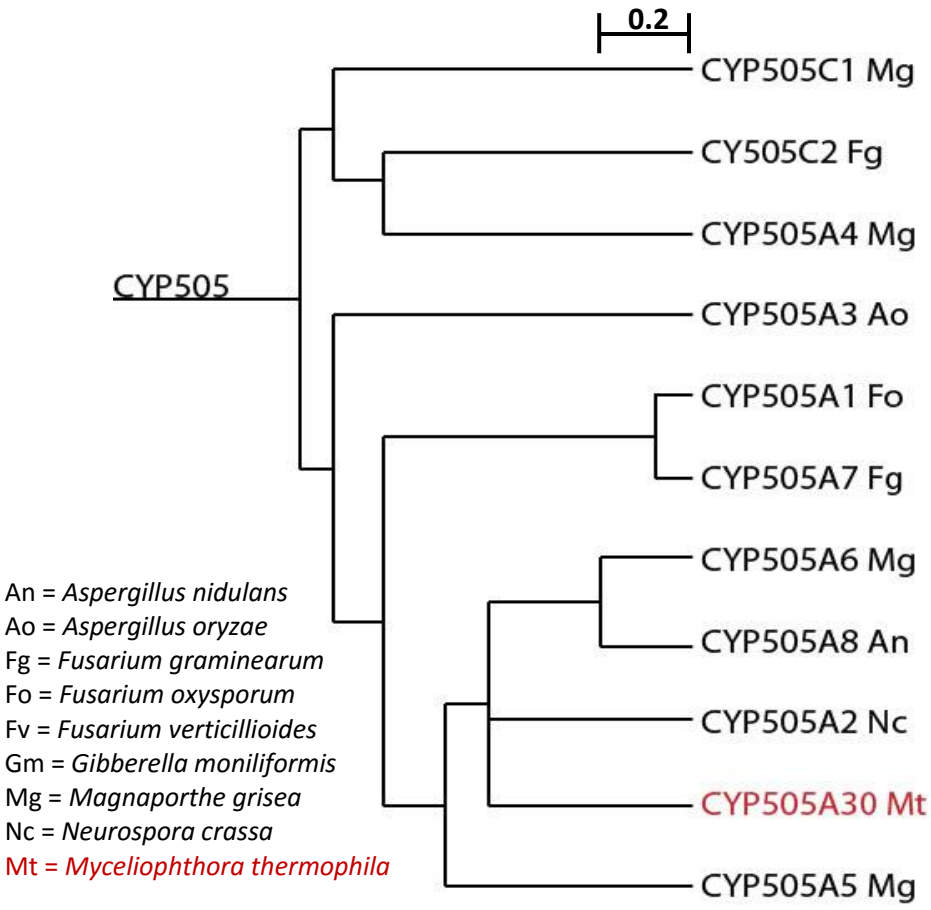

Figure 3.1 Phylogenetic tree of a selection of sequences from the CYP505 family. Each sequence is represented by its formal CYP gene superfamily classification number, followed by the abbreviated name of the organism from which the sequence is derived [41]. The full organism names corresponding to the abbreviated names are found on the key to the left of the tree. The CYP505 sequences were obtained from Prof. David Nelson's website [23] and the image was made using figtree [245]. CYP505A30 is displayed in red.

The *CYP505A30* gene from *M. thermophila* is 3620 bp long and encodes a 1079 amino acid protein (excluding the first methionine residue) which is 30 amino acids longer than BM3 (1048 amino acids excluding the methionine). CYP505A30 showed an overall 36% primary sequence identity to its homologue BM3 and 57% to its orthologue P450foxy (CYP505A1) from *Fusarium oxysporum*, the first characterised P450-CPR fusion enzyme from the CYP505 family [244].

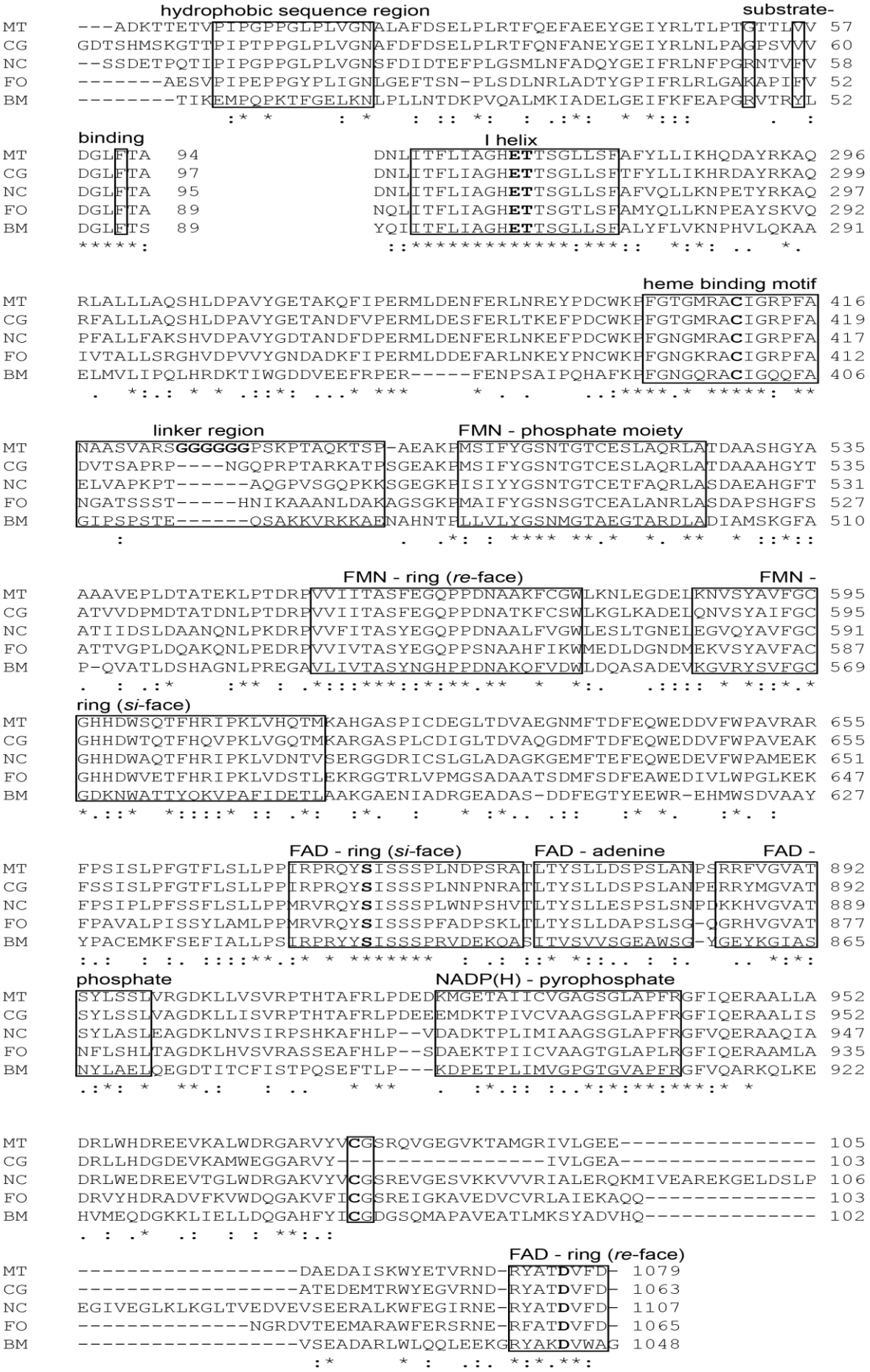
hydrophobic sequence region
substrate-
binding
I helix
heme binding motif
linker region
FMN - phosphate moiety
FMN - ring (re-face)
FMN -
ring (si-face)
FAD - ring (si-face)
FAD - adenine
FAD -
phosphate
NADP(H) - pyrophosphate
FAD - ring (re-face)

Figure 3.2 Protein sequence alignments of selected regions from several P450/diflavin reductase fusion proteins. P450 BM3-like fusion proteins represented are from CG (*Chaetomium globosum*), NC (*Neurospora crassa*), FO (*Fusarium oxysporum*) and BM (*Bacillus megaterium*) and share 80%, 57%, 65% and 36% overall primary sequence identity with that of the CYP505A30 enzyme from MT (*Myceliophthora thermophila*). Boxed amino acid regions are annotated with the motifs they represent and notable individual conserved residues are in bold text. In order of appearance in the protein sequence, the bold MT residues represent: E273 and T268 within the I helix important for proton relay to iron-oxo species in the catalytic cycle; C410 (MT) within the heme binding motif responsible for coordination of the heme iron; and finally S857, C1035 and D1077 (MT) around the FAD isoalloxazine ring that form a 'catalytic triad' involved in NADPH-binding and hydride transfer to the FAD cofactor [301].

CYP505A30 was found to have an ~479 amino acid long N-terminal P450 domain, which contains the sequence FGTGMRA**C**IG (Figure 3.2) consistent with the heme binding motif (FXXGXRX**C**XG) of the cytochrome P450 superfamily, where the cysteine is the proximal thiolate ligand to the heme iron. The P450 domain also contains the conserved I helix region, with residues E273 and T274 present, indicative of a proton relay system to heme iron-oxo species in the P450 catalytic cycle (Introduction 1.11) [144,145]. More specifically, these residues relay protons to the ferric-peroxo and the ferric hydroperoxo intermediates to facilitate dioxygen activation and the formation of the reactive compound I. The numerous crystal structures of BM3 have highlighted a number of key residues important for binding substrates. These include R47 and Y51 which interact with the fatty acid substrate carboxylate tail and are thought to be important determinants of substrate specificity in the CYP102A subfamily enzymes, and F87 which interacts with the terminal methyl group of fatty acids and prevents hydroxylation at the ω-methyl position. In BM3, F87 reorientates on substrate binding and its movement is part of the reorganization process that leads to displacement of the axial water ligand to the heme iron, which in turn results in the type I (high-spin) heme spectral shift that also induces an increase in the reduction potential of the heme iron in the substrate-bound form [27,271]. While P450 MT1 does have a phenylalanine (F92) in the same position as F87 in BM3, it lacks the proposed substrate carboxylate-orientating residues. While this does not necessarily mean that the binding mode for fatty acids is substantially different from that in BM3, it might indicate that fatty acids could penetrate further into the substrate cavity and that MT1 regioselectivity of substrate oxidation could be different to that in BM3.

The C-terminal half of the MT1 comprises ~578 amino acid residues and forms a class II reductase domain (i.e. a cytochrome P450 reductase or CPR) arrangement with predicted

FMN, FAD and NAD(P)H (in order from the N- to C-terminal) binding motifs, as also seen in the P450 BM3 and P450 foxy enzymes (Figure 3.2).

The linker region between the P450 and reductase domains of MT1 is predicted to be ~24 amino acids long, which would be the longest among the fusion enzymes displayed in the alignment in Figure 3.2. Interestingly, the linker contains a 6 x Gly single amino acid repeat (SAAR). SAARs are commonly located in the unstructured regions of proteins [302] and these generally serve one of two functions; molecular recognition and molecular assembly [303,304]. Molecular assembly is a conceivable explanation for this glycine AAR, as the folding of a 120 kDa protein into 3 separate functioning domains each with their cognate prosthetic group is a complex task. However its absence in the other P450-CPR fusion enzymes might also point towards it not being critical for that process. A more plausible explanation for the series of glycine residues may be for the flexibility of the linker region in MT1, which in turn could be essential for the efficient interactions between the different domains of the enzyme.

While bacterial P450s are almost invariably soluble enzymes, most eukaryotic P450s are membrane bound. The P450foxy (CYP505A1) enzyme was shown to be "partially" (~20%) membrane-bound during protein purification [200], and while hydrophobic clustering analysis did not predict a membrane anchor or any long hydrophobic stretches of amino acids in the CYP505A30 sequence, its N-terminal region has a stretch of hydrophobic residues (rich in prolines and glycines) that is not found in BM3 (Figure 3.2). The structural relevance of the residues highlighted in Figure 3.2 are discussed in the next section and are also highlighted in Figure 3.3.

3.1.3 P450 MT1 (CYP505A30) Structural homology modelling

In the absence of any crystal structure data for the intact P450 MT1 or its component domains, the CYP505A30 protein sequence was subjected to analysis using structure prediction and modelling tools in order to visualise and characterise the structural composition of the multidomain enzyme.

Phyre^2 (**P**rotein **H**omology/analog**Y** **R**ecognition **E**ngine V 2.0) was employed to build a 3D model based on sequence alignment and advanced remote homology detection methods

[305]. The Phyre^2-generated model displays a typical P450 heme domain fold with a large component of α-helices (Figure 3.3, top panel). This was expected as the P450 fold remains conserved in members of the P450 family with low sequence identity. The invariant cysteine residue of the MT1 heme domain (C410) is shown in red in panel A, and acts as the proximal axial ligand to the heme iron (not shown). While Phyre^2 is a great tool for visualising the secondary structures of proteins that are yet to be crystallised it, at present, cannot model the binding of prosthetic groups, cofactors and metals, e.g. heme, FAD and FMN as shown here.

In panel B, the residues R47 and Y51 (orange), gatekeeper residue F87 (green) and proton delivery residues E267 and T268 (pink) in BM3's heme domain (1JPZ) are coloured the same as their corresponding residues in MT1's heme domain in panel A. The polar carboxylate tail-orienting residues can be seen interacting with the end of the NPG molecule at the mouth of the active site in the BM3 structure (panel B). The corresponding amino acids in MT1 (panel A) are small and non-polar glycine and valine residues, likely indicating different substrate binding modes by comparison to BM3. MT1's C410, F91, E262 and E263 are otherwise well conserved as the proximal ligand and key residues around the active site.

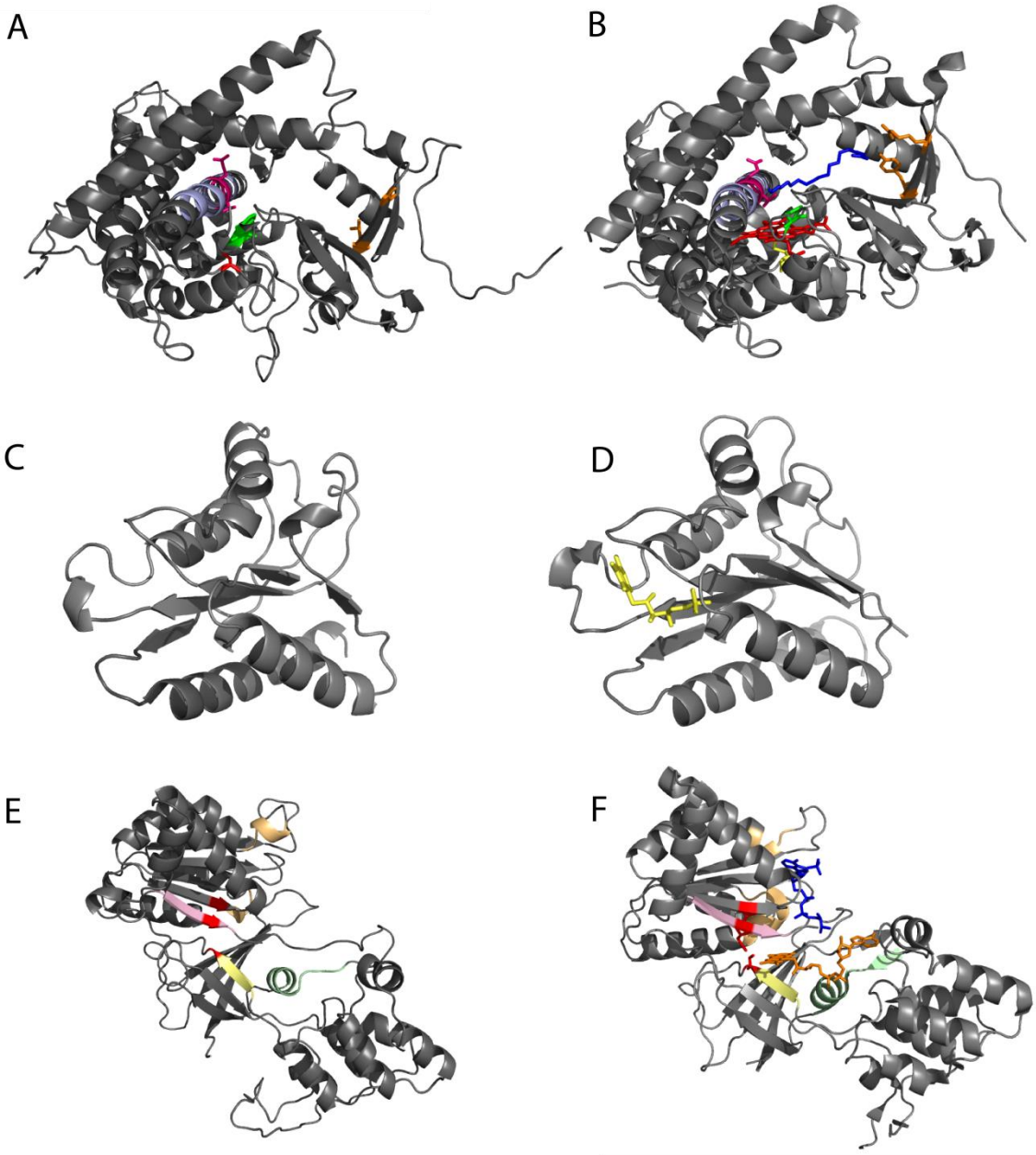
A
B
C
D
E
F

Figure 3.3 CYP505A30 structure modelling. The full length MT1 (CYP505A30) was modelled using Phyre[2]. Panels A and B show the MT1 heme domain (left) alongside BM3's 1JPZ crystal structure (right) displayed in ribbon form. BM3's heme domain is shown bound to NPG (blue), with the heme (red) coordinated by C400 (yellow). Both heme and substrate are absent from the MT1 model (panel A), although its C410 heme thiolate ligand is shown in red. The conserved residues in the I helix of both domains are coloured violet, with BM3's E267 and T274 (pink) shown in stick form. BM3's F87 and the corresponding F91 in MT1 are both coloured green and in stick form. BM3's carboxylate tail orienting residues R47 and Y51 are shown in orange and in stick form, as are the corresponding residues in MT1. The residues V77 to V89 in MT1 and the corresponding residues in BM3 are omitted for a better view of the active sites. Panels C and D show the FMN binding domains of BM3 (1BVY, panel C) and MT1 (panel D). The FMN domains are coloured grey while the FMN cofactor shown bound to the BM3 FMN domain is coloured yellow. MT1's FAD domain (panel E) is presented alongside the $NADP^+$-bound FAD domain of BM3 (4DQL, panel F). The FAD domains are grey with the secondary structures represented in ribbon form. In both cases the FAD *re*-face binding regions are coloured yellow, the FAD *si*-face binding regions are in pink and its adenine binding regions in green. The $NADP^+$ binding regions are coloured pale orange. The catalytic triad residues are represented in stick form and coloured red in both panels. The BM3 FAD domain is shown bound to both FAD (orange) and $NADP^+$ (blue).

MT1's FMN domain (panel C) is composed of 5 parallel β-stands sandwiched by 2 α-helices on either side and shows a highly similar secondary structural arrangement to BM3's FMN domain, which is shown bound to FMN and with the cofactor coloured yellow (panel D) (1BVY).

MT1's FAD domain is shown in panel E, adjacent to the FAD- and $NADP^+$-bound crystal structure of BM3's FAD domain (4DQL, panel F), with the cofactors coloured orange and blue, respectively. The majority of the secondary structures in these domain are coloured grey, save for important regions involved in FAD- and $NADP^+$-binding, which are similarly coloured in both models. The FAD *re*-face binding regions are coloured yellow, the FAD *si*-face binding regions are in pink and the adenine binding regions in green. It should be noted that the homology model of MT1 is lacking an antiparallel β-strand present in BM3's FAD adenine binding region, coloured green. Regions binding $NADP^+$ are coloured pale orange and the catalytic triad of amino acids are represented in stick form and coloured red in panel F.

The high degree of similarity between the structures of these two enzymes is expected, as the predicted model of MT1 is based on the crystal structures of related domains in the NCBI database.

3.1.4 *CYP505A30* gene cluster analysis

Primary sequence analysis and secondary structure homology modelling have already given some insight into the likely role of this enzyme as a catalytically self-sufficient fatty acid NAD(P)H-dependent P450 monooxygenase. The analysis of the position of *MYCTH_101224*, the *CYP505A30* gene, within the *M. thermophila* genome could provide further information into elucidating MT1's true substrate or physiological role. Figure 3.4 shows the position of *MYCTH_101224* in the *M. thermophila* genome.

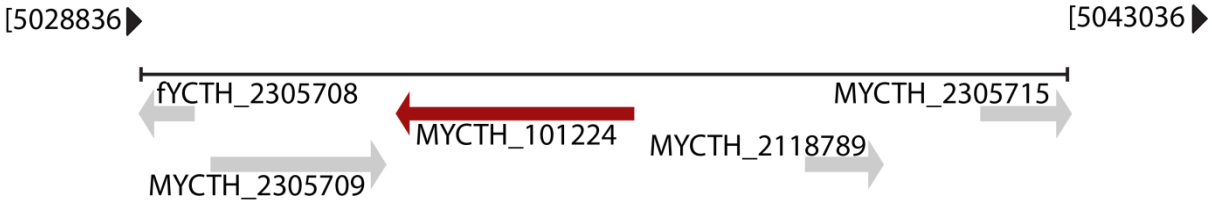

Figure 3.4 Genetic location of P450 MT1. P450 MT1 (encoded by MYCTH_101224) is shown in red and is located on chromosome 3 (NC_016474.1) of *Myceliophthora thermophila*. The location of this gene within chromosome 3 is displayed in the figure (nucleotides 5028836-5043036). KEGG predicts P450 MT1 to be involved in fatty acid degradation and tryptophan metabolism [306]. The 4 other surrounding genes shown are: fYCTH_2305708 – a hypothetical protein, MYCTH_2305079 – a GMC (glucose-methanol-choline)-oxidoreductase, MYCTH_2118789 – a transcription factor and MYCTH_2305715 – a regulatory protein.

MYCTH_101224 is next to *MYCTH_2305079* on *M. thermophila* chromosome 3, and this is a hypothetical choline dehydrogenase gene from the GMC-oxidoreductase family, containing an N-terminal FAD domain and a C-terminal steroid-binding domain. Choline is found in the two most abundant cell membrane phospholipids: phosphatidylcholine and sphingomyelin, possibly implicating both *MYCTH_2305079* and *MYCTH_101224* in membrane composition regulation in *M. thermophila*.

The entire chromosome was submitted to a genome mining tool called antiSMASH that allows the identification of secondary metabolite biosynthesis gene clusters [307]. While the tool did pick up 5 biosynthetic clusters, including one for terpene synthesis,

MYCTH_101224 did not fall within any of them. It was, however, adjacent to a type I PKS (polyketide synthase) cluster for monodictyphenone, as shown below in Figure 3.5.

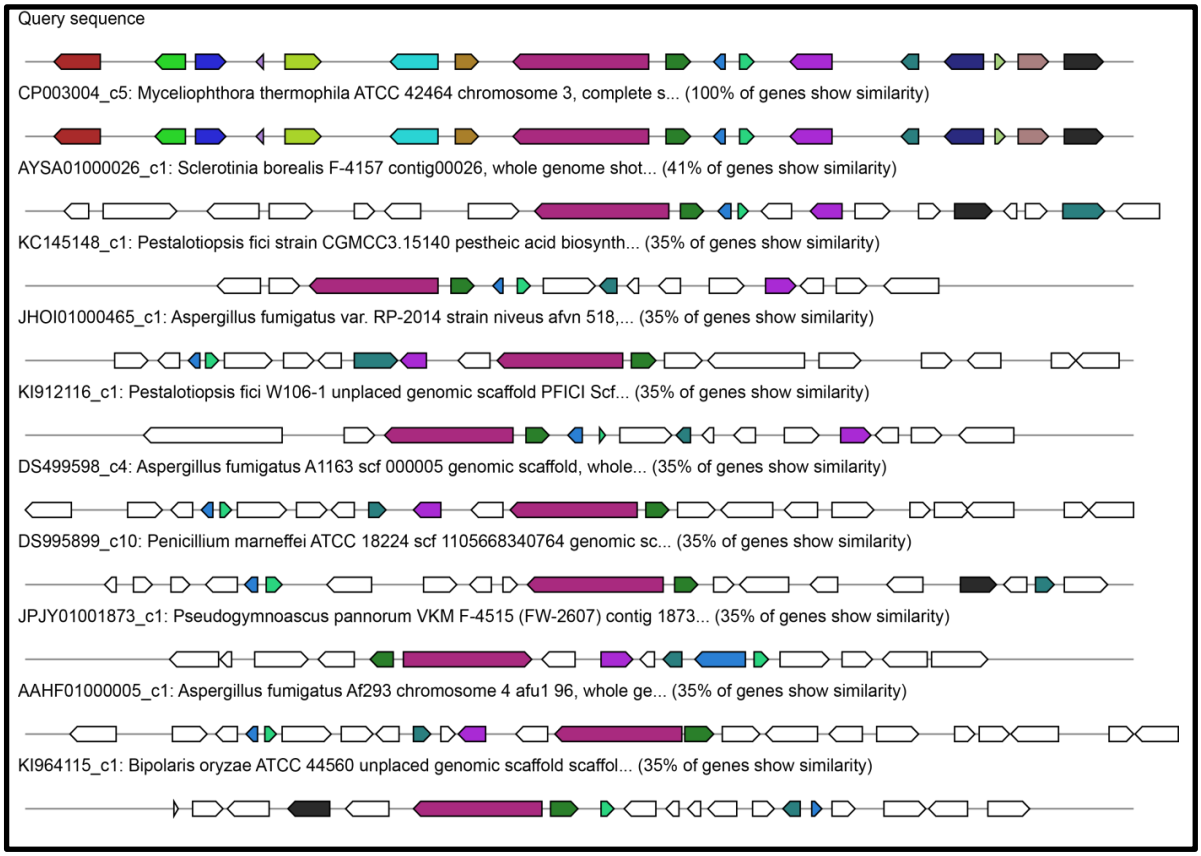

Figure 3.5 AntiSMASH analysis of the P450 MT1 gene cluster. The AntiSMASH search for gene clusters involved in secondary metabolite biosynthesis placed the P450 MT1 gene adjacent to the predicted monodictyphenone type I PKS cluster. The P450 MT1 gene and its orthologues in other organisms are shown in purple with the gene cluster predicted to encode monodictyphenone synthesis located to the left of the MT1 gene in *M. thermophila* and *Sclerotinia borealis* in the top two gene clusters.

PKSs are multi-enzymatic synthases that are involved in the biosynthesis of polyketides, structurally complex molecules with important biological activities, e.g. in the synthesis of tetracycline, erythromycin and lovastatin [308–310]. The biosynthesis of polyketides is analogous to fatty acid synthesis [311,312], but without further studies it is unclear whether the proximity of the *CYP505A30* gene to a proposed monodictyphenone biosynthetic gene cluster implies any role for CYP505A30 in synthesis of a polyketide molecule.

3.2.1 Generation of the expression constructs *CYP505A30*/pET15b and *CYP505A30HD*/pET15b

The codon optimised P450 MT1 gene (*CYP505A30*) was synthesised by Genscript in a pUC57 vector. The *CYP505A30*/pUC57 construct and the empty vector pET15b (5.7 kbp) were both digested with the restriction enzymes BamHI and NdeI, followed by dephosporylation of the 5' and 3'-ends using calf intestinal phosphatase (CIP). Agarose gel electrophoresis was used to resolve and isolate *CYP505A30* (3.2 kbp) from the pUC57 vector and the gene was purified using the Qiagen gel extraction kit protocol before ligation of the gene into pET15b (Methods 2.4.1).

An analytical restriction digest using HincII was done to establish successful ligation of *CYP505A30*/pET15b constructs isolated following *E. coli* cell transformation and plasmid purification. HincII cuts the construct to produce 4 DNA fragments of lengths 3.5, 2.2, 2.0 and 1.0 kbp (Figure 3.6).

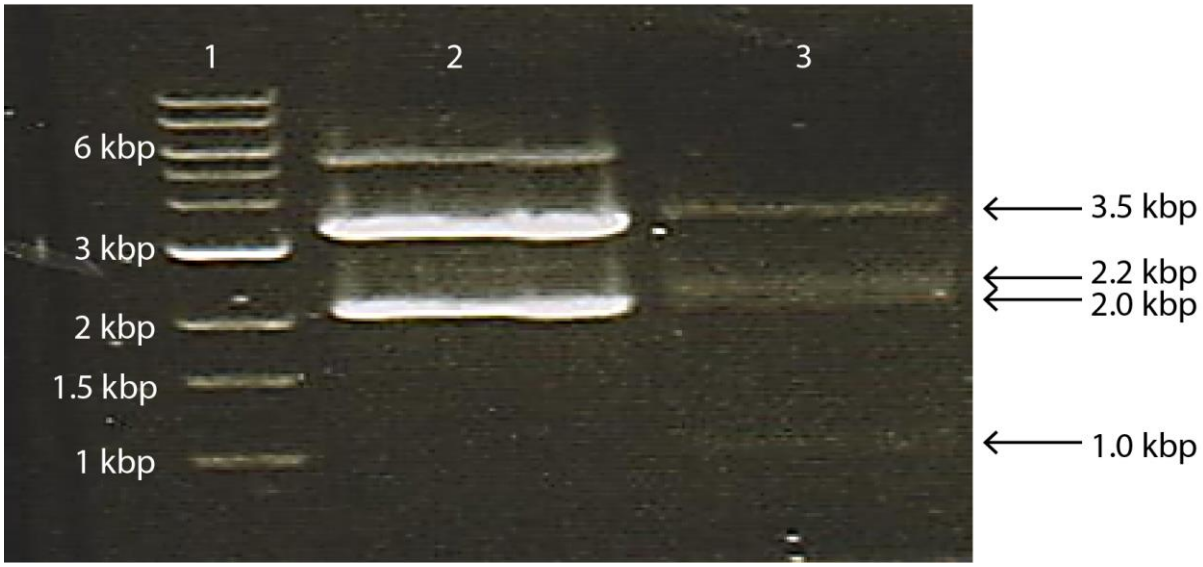

Figure 3.6 A 0.8% agarose gel of a *CYP505A30*/pET15b analytical digest using HincII. Lane 1 = NEB 1 kb DNA ladder (selected band sizes indicated). Lane 2, plasmid isolated from a ligation ratio 1:5 pET15b:*CYP505A30*. Lane 3, plasmid isolated from a ligation ratio 1:5 pET15b:*CYP505A30*. Lane 4, plasmid isolated from a ligation ratio 1:3 pET15b:*CYP505A30*.

Lane 2 has 3 bands, the brightest 2 (at 3.5 and 2.2) likely correspond to correct bands from the digest, but at the expected band at 1.0 kbp is lacking or too faint to see clearly. It also has an additional band between the 5 and 6 kbp marker which corresponds to the linearised

pET15b vector at 5.7 kbp which might point towards a failed ligation process, with the other 2 bands either being the supercoiled plasmid DNA (at 3.5 kbp) and circular, single stranded DNA (at 2.2 kbp); or else the partially HincII digested products of pET15b to produce 3 DNA fragments of lengths: 3.5 kbp, 1.7 kbp and 454 bp.

Lane 3 shows 4 bands which exactly correspond to the DNA fragments expected from a pET15b/CYP505A30 HincII digest. While the intensity of the bands is low, it is enough to discern the top band at 3.5 kbp and the separation between the 2.2 and 2.0 kbp bands. The smallest band is just visible at 1.0 kbp.

Promising plasmid constructs (following analysis by HincII digestion) were sent to Source Bioscience (Nottingham, UK) for sequencing with primers (T7F, T7R and F1-F4) (Methids 2.4.1, Table 2.5), which allowed the sequencing of the entire *CYP505A30*/pET15b gene construct and the validation of the correct cloning (and absence of unwanted mutations) in the cloned P450 MT1 genes.

The G463X heme domain gene in pET15b was generated by the insertion of an ochre stop codon in place of a glycine at position 463, using a QuikChange Lightning mutagenesis kit and primers G463X F and G463R (Methods 2.4.2). The G463X gene was fully sequenced to ensure the presence of the stop codon at the correct location and the absence of undesired mutations, as described above.

3.2.2 Expression and Purification of P450 MT1 and the MT1HD

Expression trials for the full length P450 MT1 protein were carried out in a number of *E. coli* strains: BL21-Gold (DE3), Rosetta (DE3), HMS174 (DE3) and C41 (DE3). The expression of plasmid-borne genes (under control of a T7-lac polymerase/promoter system) in these strains is typically induced by a stable, synthetic analogue of lactose (isopropyl-β-D-thiogalactopyranoside, IPTG). This is achieved through release of repression by IPTG-dependent displacement of the Lac repressor from its operator sequence upstream of both the plasmid-borne MT1 gene and the T7 RNA polymerase gene (present in the bacterial genome as a lambda DE3 phage chromosomal integrant that carries a copy of T7 RNA polymerase, regulated by a lacUV5 promoter to prevent leaky expression). IPTG addition to transformant cultures thus enables both the production of the T7 RNA polymerase and the removal of the Lac repressor to facilitate transcription of the

plasmid-borne MT1 gene. The pET15b plasmid carries the full-length P450 MT1 gene fused to an N-terminal polyHis$_6$-tag. An ampicillin resistance (β-lactamase) gene on pET15b allows for selective growth of successful transformants. Among strains tested for target gene expression, Rosetta (DE3) was the only strain to carry an additional chloramphenicol resistance gene.

Expression trials for intact P450 MT1 were done under varying conditions, including alteration of growth temperature, composition of growth medium, bacterial culture OD_{600} at point of IPTG-induction and IPTG concentration used. Trials were carried out as described in Methods 2.5.1 and 2.5.2 for each expression strain transformant. Small scale 5 ml bacterial cultures were batch screened under all the condition, with samples analysed by SDS-PAGE at various time points during cell growth. Larger 50 ml bacterial cultures were then used in scale-up trials for those transformant strains showing best results from the small scale trials (Figure 3.7). All IPTG-induced *E. coli* transformant cultures showed a band of ~118 kDa (as predicted by bioinformatics), which confirmed the target protein overexpression. No expression was visible in any of the uninduced cultures for any of the strains tested. While P450 MT1 expressed very well in all the media trialled (LB, TB and 2YT), transformants grown in LB had the most P450 MT1 present in the soluble protein fraction. The BL21-Gold (DE3) strain consistently expressed the highest proportion of soluble P450 MT1 protein compared to all other strains tested. However, expression trials with BL21-Gold (DE3) MT1 transformants induced with IPTG at different OD_{600} values (and sampled for protein expression after a further 20 h cell growth) showed very little production of soluble P450 MT1, and little difference compared to non-induced cultures grown under the same conditions (Figure 3.7, left panel). In all cases, a strong band appeared at the predicted molecular weight for P450 MT1 in the insoluble fraction when cells were disrupted using BugBuster™ reagent. The absolute amount of insoluble P450 MT1 produced appeared higher when the heme precursor δ-aminolevilinic acid (ΔALA, 1 mM) was included in the bacterial cultures, and the largest amount was seen with IPTG induction at OD_{600} = 0.6 (Figure 3.7). The effect of concentration of ΔALA addition (0.2, 0.4, 0.6, 0.8 and 1 mM) at the time of IPTG induction was also investigated at lower growth temperature post-induction (20 °C) and at 16 and 20 hours post-induction (Figure 3.7, right panel, only 0.6 and 0.8 mM ΔALA shown). In these cases, the total amount of P450 MT1 produced was decreased but the amount of protein in the soluble fraction was

increased, suggesting that the combination of lower post-induction growth temperature and addition of ΔALA had a positive effect on P450 MT1 protein production.

However, the levels of solubility of P450 MT1 may be questioned, as on the gel shown it is clearly present largely in the insoluble fractions. To investigate further, small scale transformant expression cell lysis experiments were done using a sonicator for bacterial cell disruption (Methods 2.7.1), rather than using the BugBuster cell lysis reagent. Under these cell breakage conditions, the majority of the P450 MT1 P450 protein was found in the soluble fraction (Figure 3.8, right). It was concluded that the aggregated protein found in the insoluble fractions in the preceding experiments was probably due to P450 MT1's intolerance to the SDS detergent present in BugBuster. The BugBuster technique was thus subsequently used only during the screening of small scale (5 ml) bacterial transformant trials as an indicator of solubility of expressed protein, and best conditions identified were then scaled-up in 50 ml cultures with sonication used for cell lysis (Figure 3.8, right).

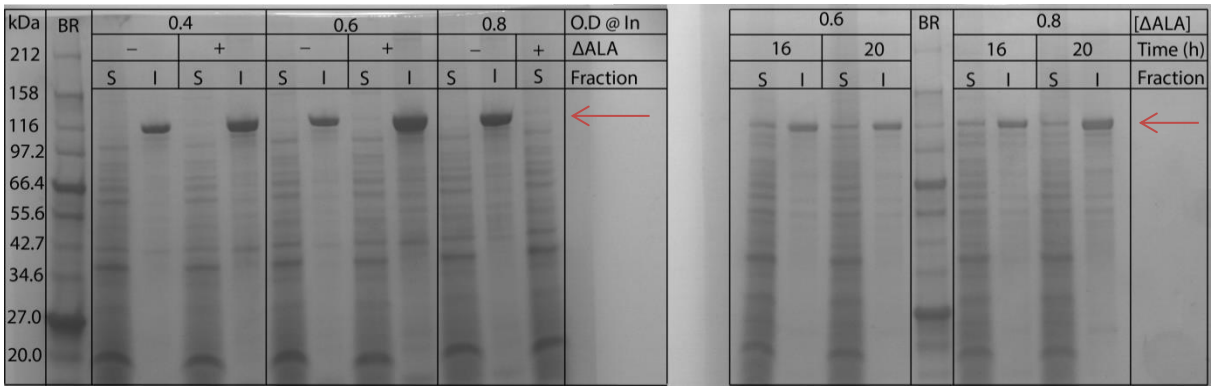

Figure 3.7 Protein expression trials for P450 MT1. The data in the panels are a representative proportion of expression conditions screened. Unstained Protein Marker, Broad Range (2-212 kDa) was used and is annotated as BR in both gels shown. BL21 (DE3) and LB were identified as the optimal strain and growth medium for P450 MT1 expression and are used in both these gels. The left panel shows the soluble (S) and insoluble (I) fractions at different transformant culture OD_{600} values at which IPTG induction was done, both with (+) and without (-) addition of ΔALA (1 mM). All samples shown were taken following 20 hours growth at 37 °C. The right panel shows the varying amounts of soluble and insoluble P450 MT1 following expression cell induction with IPTG (0.8 mM) at an OD_{600} value of 0.6, and with addition of ΔALA (0.6 and 0.8 mM). Samples were taken at 16 and 20 hour time points, this time with bacterial transformant cells grown at 20 °C. A red arrow indicates the position of P450 MT1 protein on the SDS-PAGE gel.

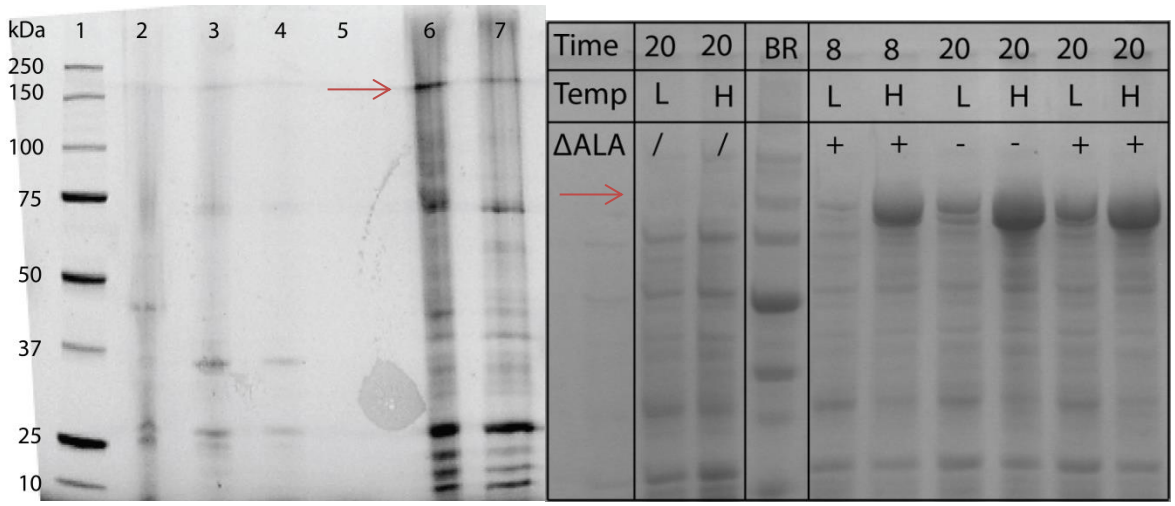

Figure 3.8 Ammonium sulfate precipitation and soluble P450 MT1 expression. The left panel shows the resolubilised fraction of protein from ammonium sulfate precipitation. Lane 1 shows a molecular weight ladder (BIO-RAD Precision Plus^{TM} Unstained Standards 10-250 kDa) and lanes 2- 7 show increasing ammonium sulfate concentrations; Lane 2 – 10%, lane 3 – 20%, lane 4 – 30%, lane 5 – blank, lane 6 – 40% and lane 7 – 50% ammonium sulfate (w/v). The right panel shows a scaled up growth medium expression trial with 50 ml LB cultures of BL21 Gold (DE3) incubated at a high temperature (H) of 25 °C and a low temperature (L) of 18 °C after induction with 0.8 mM IPTG at an OD_{600} of 0.6 with (+) and without (-) 0.6 mM ΔALA. Unstained Protein Marker, Broad Range (2-212 kDa) was used and is annotated as BR in the third lane and the 2 lanes on its left depict uninduced 50 ml cultures incubated at high and low temperature. Cultures were harvested and centrifuges to collect cell pellets (8,000 x *g* for 10 min) at 8 hours and 20 hours after induction, before sonication and SDS-PAGE analysis. A red arrow indicates the position of P450 MT1 protein on the SDS-PAGE gel.

No P450 MT1 expression was seen in uninduced cultures, showing tight regulation by the lacUV5 promoter in pET15b. The culture harvested 8 hours after IPTG induction with ΔALA present at 25 °C showed almost as much P450 MT1 expression as the cultures harvested at 20 hours (Figure 3.8, right). At 20 hours it is evident that more soluble protein is expressed at 25 °C than at 18 °C, but there is no difference between the cultures with and without 0.6 mM ΔALA. There is a significant difference in P450 MT1 expression after 20 hours between the 2 cultures grown at 18 °C with and without 0.6 mM ΔALA.

Following successful P450 MT1 expression trials, BL21-Gold (DE3) *E. coli* cells were used for P450 MT1 production using 0.4 L culture/2 L flask containing LB medium, with cell growth at 37 °C before induction with 0.8 mM IPTG once cells had reached an OD_{600}

of 0.6. 0.8 mM ΔALA was also added at this point to aid with heme incorporation (incomplete heme incorporation is an issue that became clear during purification studies of the P450 MT1 protein). Once induction of the expression of CYP505A3 was done, the cells were grown for a further 16-20 hours at 25 °C, with this lower growth temperature observed to be more conducive to protein folding/heme incorporation and increased levels of protein solubility. This method was also used in subsequent studies for P450 MT1 heme domain (MT1 HD) expression.

After harvest of the bacterial expression cells, cell breakage by sonication was done (Methods 2.7.1), and ~80% of the total P450 MT1 protein was found to be present in the supernatant, with the rest in the insoluble pellet collected after centrifugation of the disrupted cell sample. An ammonium sulfate precipitation step (using ammonium sulfate at up to 30% - Figure 3.8, left) did not affect this ratio and was incorporated into the purification regime immediately after the cell breakage step. The disrupted cell extract was clarified by centrifugation and dialysed into 50 mM KPi buffer (pH 6.5) at 4 °C, prior to the 30% ammonium sulphate step. The soluble fraction was again collected by centrifugation and dialysed into buffer A. Following reduction of sample volume by ultrafiltration using a Vivapsin (100 MWCO), the binding of the P450 MT1 (expressed using the pET15b system with an N-terminal His_6-tag) to nickel-containing resins was investigated. However, the binding was found to be too weak to effectively purify the protein, despite trials with different nickel resins (nickel IDA and nickel NTA) using binding buffers at a range of different pH values and salt concentrations. A western blot (Figure 3.9) using a HexaHis epitope tag antibody as the primary antibody showed that MT1 was expressed with the His_6-tag and that it remained bound after cell lysis. Thus, it appears likely that the His_6-tag is “buried” to some extent in the P450 MT1 protein and inaccessible for effective interaction with the nickel resins.

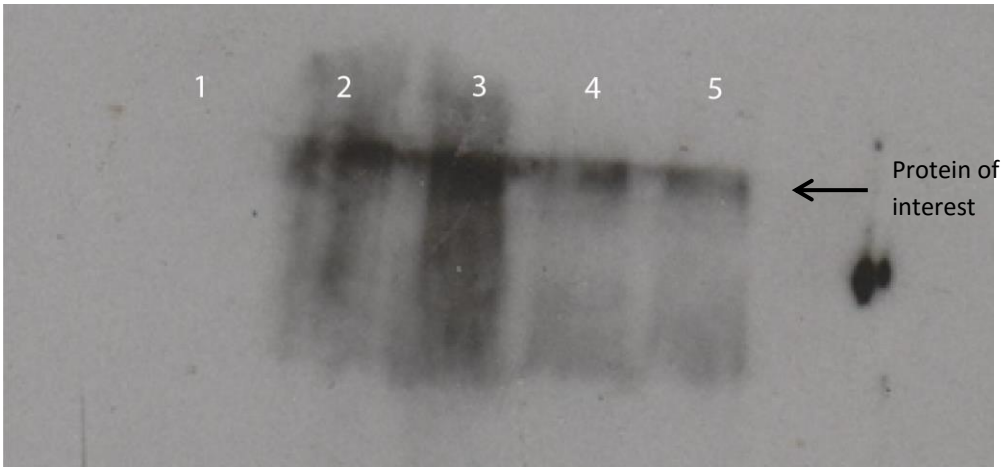

Figure 3.9 Western blot of P450 MT1 in cell extracts. Cell extract was western blotted with a mouse monoclonal antibody raised against a polyHis-Tag. Lane 1 = Molecular weight ladder (not visible). Lanes 2-4 show decreasing *E. coli* transformant cell extract concentrations, all showing single bands corresponding to a ~118 kDa protein and thus indicating the presence of the His_6-tag on the expressed P450 MT1 enzyme.

In view of the inefficiency of P450 MT1 purification using nickel affinity chromatography, the intact P450 MT1 enzyme was instead isolated from the bacterial cell lysate using a 2',5'-ADP Sepharose column (Methods 2.7.3). The supernatant from the expression cell lysate plus 5 mM 5'-AMP was loaded onto the column, before elution of P450 MT1 in buffer B with 20 mM $NADP^+$. This process allowed the collection of ~90% pure P450 MT1 (Figure 3.10, left panel).

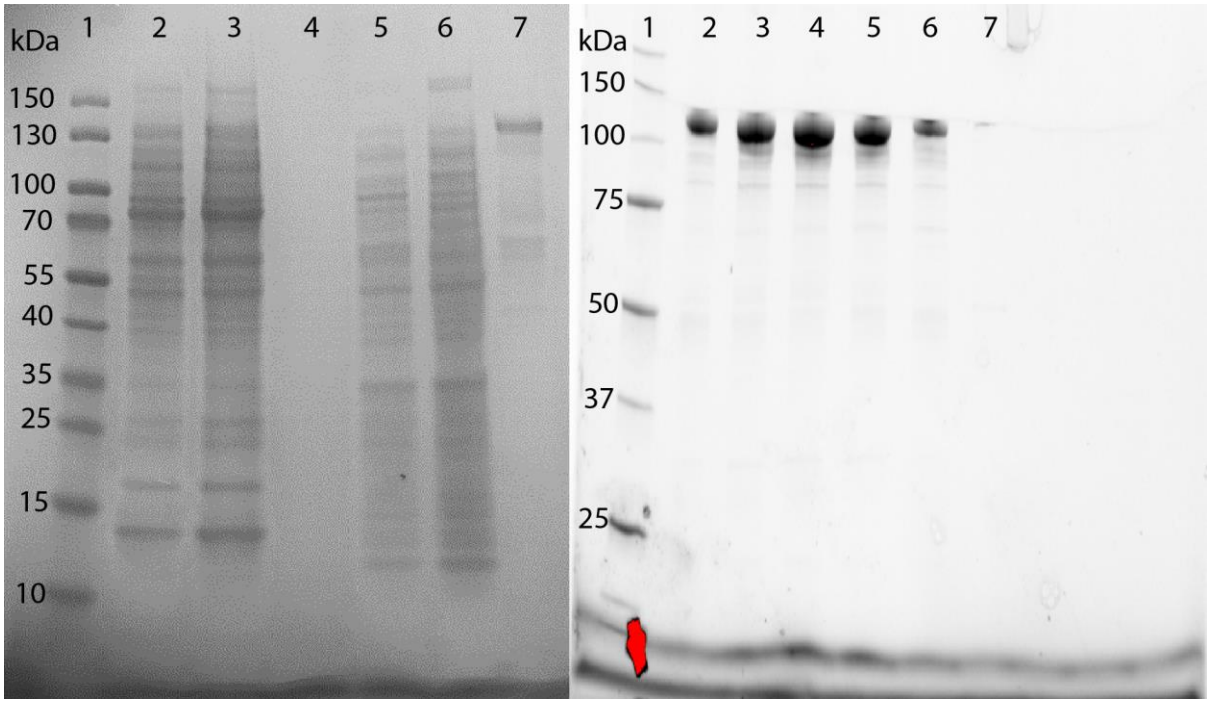

Figure 3.10 Purification stages for *M. thermophila* P450 MT1. SDS-PAGE analysis of 2',5'-ADP Sepharose resin purification samples (left panel) shows a molecular weight ladder (lane 1, PageRuler™ Prestained Protein Ladder, 10 to 180 kDa); the flow-through after loading the 2',5'-ADP Sepharose column with the supernatant from cell lysis (lanes 2 and 3); lane 4 is empty; a wash step with 10 mM 5' AMP (lanes 5 and 6); and P450 MT1 was eluted from the column using 20 mM $NADP^+$, as shown by the band at ~118 kDa (lane 7). The right hand panel shows SDS-PAGE analysis of P450 MT1 fractions from further ion exchange chromatography (IEC) purification using a Sephacryl S200 SE column. Lane 1 shows a molecular weight ladder (BIO-RAD Precision Plus^{TM} Unstained Standards 10-250 kDa) and fractions of purified MT1 from the SE column at ~118 kDa are shown in lanes 2-6.

The eluted P450 MT1 protein was concentrated by ultrafiltration using a Vivaspin (100 MWCO) to a volume of ~0.5 ml, before being dialysed into buffer D to removed excess $NADP^+$ which binds to the reductase domain of MT1.

Following the affinity purification stage, further purification steps were done using IEC Q-Sepharose and Sephacryl S200 SE columns, and were used to achieve homogeneous protein (Figure 3.10, right).

The yield of P450 MT1 from the 2',5'-ADP Sepharose resin was ~30 mg of protein per ml of resin. The binding appeared relatively strong with little amount of the overexpressed

target protein in the flow through and wash fractions. The yield obtained from a larger scale expression culture would be in the range of 10-15 mg per L of culture (Table 3.1).

Table 3.1 Summary of P450 MT1 expression and purification from a 7 L culture (yielding a 41 g pellet).

Purification stage	Total Protein (mg)	P450 MT1 (mg)	Yield (%)	Purification Fold
Crude Extract	7350	220	100	1
Soluble Crude Extract	5670	173.6	79	1.02
2'5' ADP-agarose	69	67.5	31	32.7

Following dialysis, $NADP^+$-free P450 MT1 in buffer D was loaded onto a Q-Sepharose column equilibrated with the same buffer. Proteins were eluted from the column in a KCl gradient of 0 to 500 mM in the same buffer (Methods 2.7.3). After elution, the purest fractions were pooled and concentrated to 100 mg/ml. P450 MT1 protein was loaded onto the Sephacryl S200 SE column after dialysis into buffer B and equilibration of the column in the same buffer. After elution from the S200 SE column, the purest fractions of P450 MT1 were pooled and concentrated to 100 mg/ml in the same buffer by ultrafiltration and stored at -80 °C. Cytochrome P450 protein purity can be assessed spectrophotometrically using the Reinheitszahl (Rz) value, which is the ratio of the heme Soret band absorbance (at ~418 nm for the low-spin hemoprotein) to that of the protein aromatic residues (at 280 nm). This is a common method by which the extent of heme protein purity can be established. For BM3 the Rz value is ~0.6 for the pure flavocytochrome protein. For P450 MT1, this Rz value was lower at ~0.5 (at best), suggesting incomplete heme incorporation, even after taking into account P450 MT1's larger absorbance coefficient at 280 nm (Table 3.2). By comparing the observed Rz ratios of pure samples of BM3 and MT1 against the theoretical $\varepsilon_{420}/\varepsilon_{280}$ ratio (with assumption that the ε_{420} for MT1 is approximately the same as that for P450 BM3), an estimate of the relative heme incorporation could be made. It should be noted that the extent of heme incorporation into P450 MT1 could be improved by the addition of δ-ALA at same time as the IPTG induction step during expression cell growth. However, the extent of heme incorporated into P450 MT1 still varied slightly by

batch-to-batch, and so purity estimates for P450 MT1 by analysis of Rz values were not completely reproducible according to variations in heme incorporation.

Table 3.2 Comparison of Rz ratios and extinction coefficient ratios to determine relevant extents of heme incorporation into P450 BM3 and P450 MT1. With the assumption that the Soret extinction coefficient for P450 MT1 is similar to that determined for P450 BM3, data analysis suggest that (at best) preparations of the P450 MT1 enzyme have ~90% heme incorporation compared to P450 BM3 from *E. coli* expression systems.

	BM3	**MT1**
Rz (A_{420}/A_{280}) of pure protein	0.6	0.5
Rz Ratio (BM3:MT1)	1:0.83	
ε_{418} (mM^{-1} cm^{-1})[93]	105	105
ε_{280} (mM^{-1} cm^{-1}) [313]	118.6	130.9
$\varepsilon_{420}/\varepsilon_{280}$	0.89	0.8
$\varepsilon_{420}/\varepsilon_{280}$ ratio (BM3:MT1)	1:0.9	

The expression protocol designed for intact P450 MT1 was not changed substantially for the MT1 heme domain protein (MT1 HD). The initial step trialled for MT1 HD purification was again nickel affinity. In this case, it was found that the MT1 HD His_6-tag was accessible and the MT1 HD was able to bind to, and to be purified from, nickel affinity chromatography resins. This provides further credence to the hypothesis that the His_6-tag in intact P450 MT1 is inaccessibly buried in the protein. Given that it may be expected that intact P450 MT1 forms a dimer (as is the case for P450 BM3) [240], there is clearly greater potential for the tag to be buried (through interactions with its partner in the dimer) than would be the case for a monomeric enzyme.

Following the binding of the MT1 HD to the Ni-NTA resin, a wash step with 15 mM imidazole ensured that protein contaminants arising from weak binding to the nickel resin were eliminated, and also helped to remove other contaminants from e.g. weak protein-protein interactions to bound MT1 HD. A further wash step with 150 mM imidazole enabled the collection of ~90% pure MT1HD at ~49 kDa, a mass essentially identical to that predicted by the ExPASy pI/molecular weight prediction tools [313].

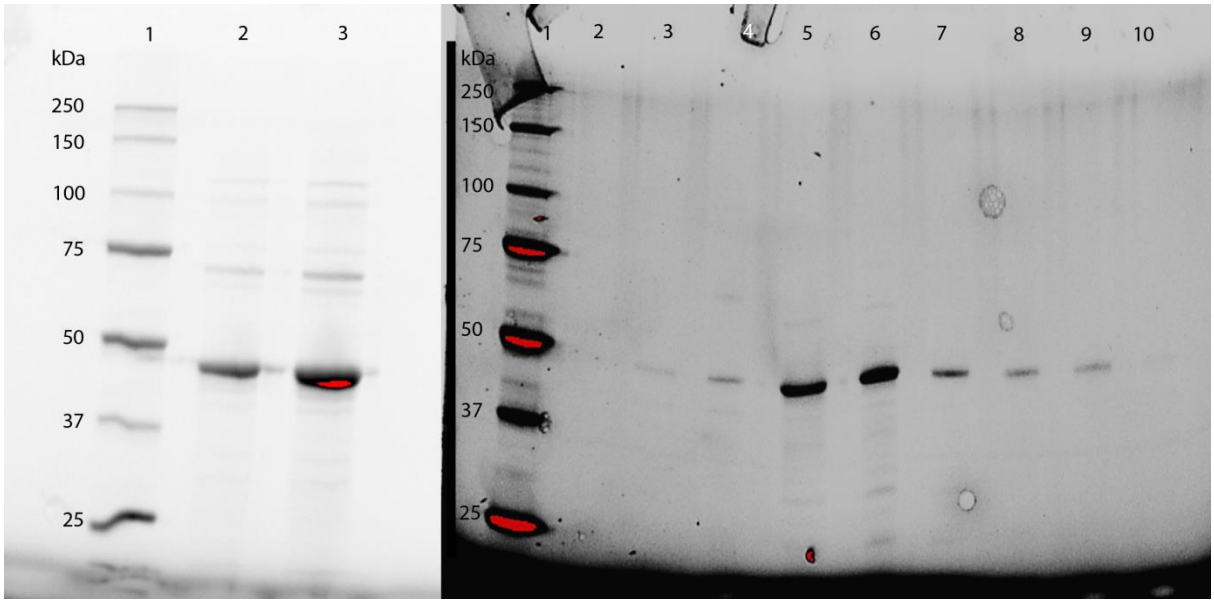

Figure 3.11 Purification stages for the *M. thermophila* P450 MT1 HD. SDS-PAGE analysis of Ni-NTA affinity chromatography fractions (left) shows molecular weight ladder (lane 1, BIO-RAD Precision Plus^{TM} Unstained Standards 10-250 kDa) and the protein bands following washing of the MT1 HD-bound Ni-NTA column with 150 mM imidazole (lanes 2 and 3). The major band in both lanes corresponds to the MT1 HD protein. SDS-PAGE analysis of MT1 HD fractions after further purification using a Sephacryl S200 SE ion exchange column (right) shows the same molecular weight ladder and fractions of purified MT1 HD at ~49 kDa (lanes 2-9) from the SEC column.

Following efficient purification of MT1 HD by Ni-NTA chromatography, the protein was dialysed into buffer B and further purified by IEC using a Q-Sepharose column and SE chromatography using an S200 SE column, as described for the intact P450 MT1 protein. After elution of the MT1 HD protein from the S200 SE column, the purest fractions of MT1 HD were pooled and concentrated to ~50 mg/ml by ultrafiltration using a Vivaspin (50 MWCO), and stored at -80 °C until required for experiments.

3.3 UV-visible spectral characteristics of intact P450 MT1 and the MT1 HD

The distinctive Soret peak of a P450 enzyme provides a convenient spectroscopic tool by which to monitor the heme iron spin state, redox state, and heme iron coordination state changes associated with P450-ligand interactions or other heme environmental effects. These properties provide us with important tools for P450 protein characterisation.

The spectral properties of intact P450 MT1 and the MT1 HD are shown in Figure 3.12 with the ligand-free, ferric (Fe^{3+}) P450 MT1 and MT1 HD proteins represented in solid black lines in all cases.

The effects of reduction of the ferric P450 heme to a ferrous (Fe^{2+}) or a partially ferrous state in both P450 MT1 and MT1 HD by dithionite addition (dashed and dotted lines) are shown in the top panels of Figure 3.12. In Figure 3.12 (panel A), the oxidised P450 MT1 is shown with a Soret peak at 418 nm and distinct flavin band features between 450-500 nm and ~350-400 nm, which slightly obscure the heme delta band at 360 nm and the heme alpha/beta bands at 566/534 nm, respectively. The addition of dithionite (dotted and dashed lines) almost completely bleaches the oxidised flavin contribution to the spectrum. The Soret peak of ferrous heme at 418 nm decreases in intensity and broadens slightly. The alpha and beta bands become more visibly merged near 550 nm, but do not form a single band, possibly due to the formation of a mixture of cysteine thiolate- and cysteine thiol-coordinated ferrous heme iron (and possibly incomplete heme reduction). Spectral contributions from the heme delta band at 360 nm are masked by those from dithionite at 340 nm.

The spectral features of the oxidised MT1 HD (panel B) show a Soret peak at 418 nm, a delta band at 360 nm and alpha and beta bands at 566 nm and 534 nm, respectively, with no flavin contributions (since the reductase domain is absent). The addition of dithionite and reduction of the heme iron causes the Soret band to decrease in intensity and broaden slightly as in full length P450 MT1. The reduced Soret peak is at 412 nm. In absence of the reductase domain, the decreased Soret intensity on reduction cannot be attributed to flavin bleaching, and is instead due to the more complete reduction of the heme iron in this case. The MT1 HD alpha and beta bands merge completely at 544 nm, confirmatory of complete heme reduction. The delta band is again obscured by spectral contribution from the dithionite reductant. Although P450 MT1 was purified with $NADP^+$ and the MT1 HD (G463X construct) using imidazole, extensive dialysis was performed during purification to ensure their removal and exemption from contribution to the resting state heme spectra. This is particularly important in the case of the MT1 HD, where ligation of heme iron by imidazole would influence the position and absorption intensity of the α, β and γ (Soret) bands of the heme.

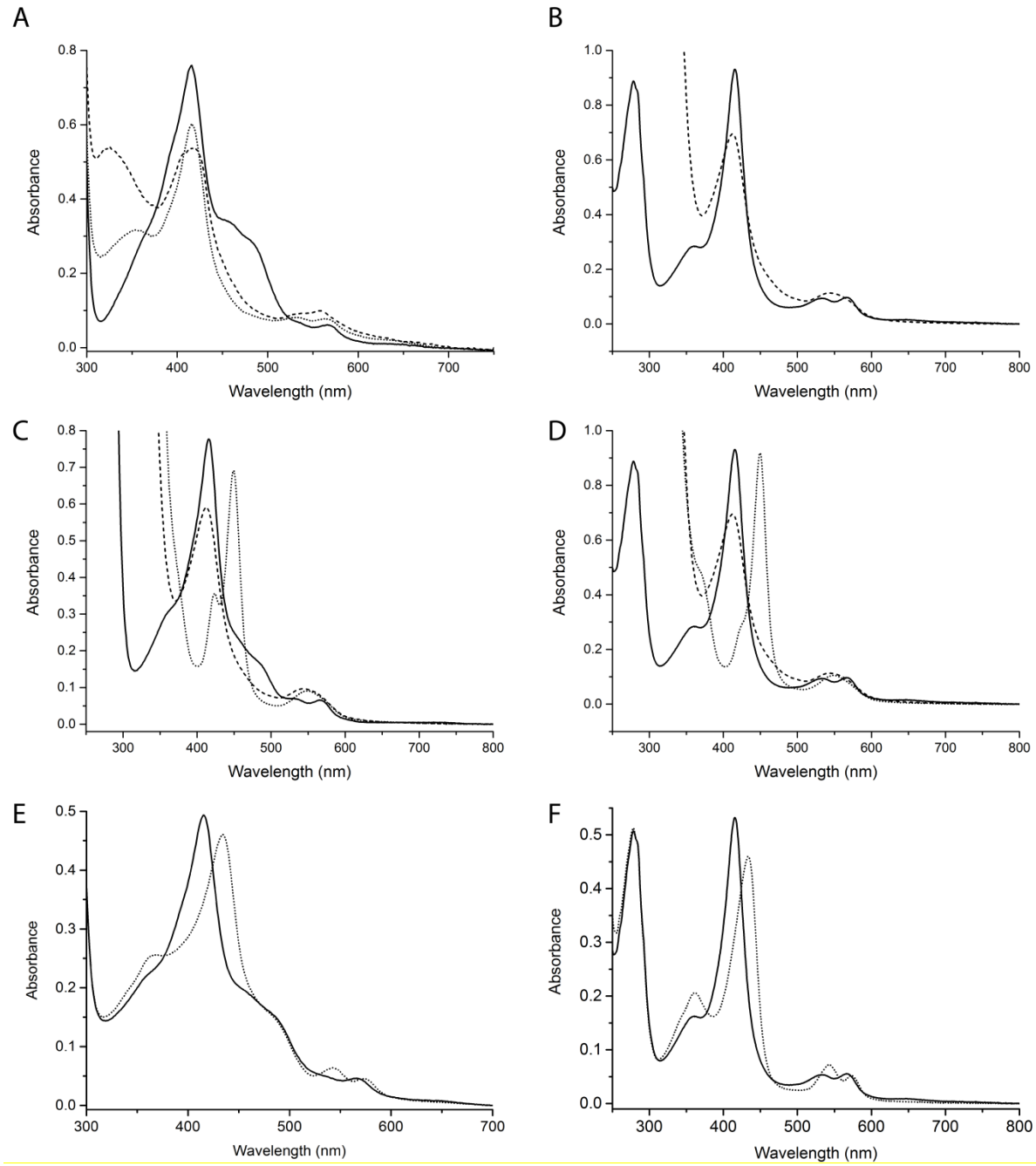
A
B
C
D
E
F
Absorbance
Wavelength (nm)

Figure 3.12 Spectral changes associated with P450 reduction and -ligand interactions and heme environment effects on the intact P450 MT1 and MT1 HD. Panels A and B: spectral changes upon reduction of oxidised P450 MT1 (A, 7 µM) and the MT1 HD (B, 9 µM, thin solid line) on dithionite addition (dotted and dashed lines in the case of P450 MT1, showing different amounts of dithionite added (A), and dashed line in the case of the MT1 HD (B)). Panels C and D: characteristic effects of CO binding to ferrous (Fe^{2+}) heme iron in P450 MT1 (C, 7 µM) and the MT1 HD (D, 9 µM). The solid lines are the oxidised enzyme, the dashed lines represent sodium dithionite-reduced, ferrous enzymes, and the dotted lines the CO-bound ferrous heme species. Panels E and F: spectral changes on NO binding to ferric heme iron in P450 MT1 (5 µM) and the MT1 HD (6 µM). The ferric heme spectra are shown as solid lines, while NO-bound hemes are represented by dotted lines in both cases. Buffer B was used in all cases. In panel C, P450 MT1 has incomplete flavin incorporation due to a purification method used involving elution with high salt instead of $NADP^+$ from the 2'5'-ADP agarose column.

The characteristic P450 shift in the Soret band to 450 nm seen on CO binding to ferrous (Fe^{2+}) heme is observed to be near fully-developed in both the full length P450 MT1 (panel C) and the MT1 HD (panel D, dotted lines in both cases). In these spectra, both P450 MT1 and MT1 HD show complete reduction by dithionite (dashed lines) as evident by their merged alpha and beta bands at 550 nm, which remain in this form in the ferrous, CO-bound spectra (dotted lines). The Soret peaks for the reduced forms of these proteins are at 412 nm for P450 MT1 and for the MT1 HD. This method was found to induce FMN dissociation. The formation of the Fe^{2+}-CO complex at 450 nm is a spectral feature characteristic of almost all P450 enzymes, and confirms P450 MT1's place in the cytochrome P450 superfamily.

The oxidised, nitric oxide (NO)-bound complexes in Figure 3.12 (panels E and F, dotted lines) show the Soret peak for the complex to be blue-shifted Soret to 435 nm, typical of the replacement of a weakly bound water ligand in the distal ligation position for a stronger ligand, and also characteristic for a P450-NO complex. The more pronounced, distinct alpha and beta bands at 575 and 540 nm, respectively, and the increased intensity of the delta band absorbance at 350 nm for both P450 MT1 (panel E) and MT1 HD (panel F) is also characteristic for NO coordination of P450 enzymes.

3.3.1 Ligand binding studies

The heme spectral shifts induced upon ligand binding to P450s can typically be used to infer whether the ligand is substrate- or inhibitor-like, and also to probe into the enzyme's specificity and affinity for certain types of molecules.

The first step of the classical cytochrome P450 catalytic cycle (Section 1.11, Figure 1.11) requires axial ligand water displacement from the ferric heme iron, which increases the reduction potential of the heme iron sufficiently to make the acceptance of an electron from its cognate redox partner energetically feasible [27,314]. Substrates entering the P450 active site are able to displace the distal water ligand which, as a result of the change in coordination of iron from hexa- to penta-coordinated, causes an electronic rearrangement in the ferric heme 3d orbitals from a low-spin to a high-spin state (Section 1.10). This is associated with a shift in the heme Soret absorbance maximum from ~418 nm to ~390 nm (type I shift). Several inhibitory ligands displace the distal water, but then replace the water themselves and become the distal ligand. Examples include imidazole and substituted imidazoles/triazoles (azole drugs) that coordinate to the heme iron via nitrogen atoms. Their binding stabilises or augments the heme iron's low-spin state, and typically causes a Soret absorbance change to longer wavelength (type II shift)

The dichotomous binding modes of typical substrates and inhibitors thus result in distinctive heme Soret shifts, with substrates inducing a type I shift to shorter wavelength and inhibitors a type II shift to higher wavelength. These phenomena enable optical titrations to be done with such molecules to enable determination of their affinity for P450 enzymes. Ligand binding titrations were carried out as outlined in Methods 2.14, with initial studies focusing on the binding of fatty acids as likely substrates for P450 MT1. UV-visible spectral titrations with P450 MT1 were done using a wide range of fatty acids. Spectral titrations produced sets of absolute UV-visible spectra showing type I Soret absorbance changes. From these data, sets of difference spectra were generated by subtracting the initial ligand-free spectrum from a particular fatty acid titration from all subsequent spectra taken after sequential ligand additions. Data shown in Figure 3.13 give examples of substrate titration plots (upper panels) and their respective difference spectral plots (lower panels) for fatty acid titrations with intact P450 MT1 and the MT1 heme domain. From these and related studies, the K_d values for the binding of each substrate were generated by plotting the maximum change in absorbance ($\Delta A_{peak} - \Delta A_{trough}$) in the difference spectra against the relevant concentration of the ligand, and by fitting data to an

appropriate binding function (either a standard hyperbolic function for weaker-binding ligands, or the Morrison [quadratic] equation for tighter-binding ligands) [315].

3.3.2 Substrate binding to P450 MT1

Previously characterised P450 MT1 homologues e.g. P450 BM3 (CYP102A1) and P450 Foxy (CYP505A1) are fatty acid hydroxylases [244,316]. To confirm a similar substrate specificity profile for P450 MT1, a broad range of linear and branched chain fatty acids of varying chain length and saturation were chosen to study their binding mode and affinity for the intact P450 MT1 and the MT1 HD. A set of saturated fatty acids (C10-C18) including decanoic acid (C10), lauric acid (C12), tridecanoic acid (C13), myristic acid (C14), pentadecanoic acid (C15), palmitic acid (C16), heptadecanoic acid (C17) and stearic acid (C18) were titrated with the MT1 enzymes. The branched chain 11- and 12-methyltridecanoic acids (*anteiso* and *iso* myristic acid, respectively), 12- and 13-methylmyristic acids (*anteiso* and *iso* pentadecanoic acid, respectively), and phytanic acid were also identified from previous work on BM3 as strong substrate candidates for MT1 [317]. In addition, N-palmitoylglycine (NPG, a fatty acid amide-linked to glycine) and arachidonic acid (a C_{20} polyunsaturated fatty acid) were also selected based on their high binding affinity and high catalytic rate of oxidation by P450 BM3 [197,271].

UV-visible spectral data sets for 11-methyltridecanoic acid binding to P450 MT1 and MT1 HD are shown in Figure 3.13 together with their respective difference spectra. The substrate-induced low-spin to high-spin change was visible as a shift of the heme Soret band at 415 nm (for both P450 MT1 and MT1 HD) to a shorter wavelength (between 386 and 390 nm) on *anteiso*-myristic acid binding, and this absorbance change was representative of all other sets of substrate-binding spectra with different fatty acids (upper panels in Figure 3.13). The difference spectra (bottom panels) demonstrate the progressive absorbance changes (the directions of which are indicated by black arrows) associated with the type I shift from low- to high-spin. While P450 MT1 and the MT1 HD have different absorbance spectra (due mainly to the absence of the reductase domain and its flavin absorbance contributions in the MT1 HD spectrum) their difference spectra are highly similar. The substrate binding data sets for tridecanoic acid and for its methylated derivatives 11- and 12-methyltridecanoic acid (*anteiso* and *iso* myristic acid, respectively) are shown for P450 MT1 (left) and MT1 HD (right) in Figure 3.14, the data are fitted to appropriate equations to determine the K_d values for binding of the substrates.

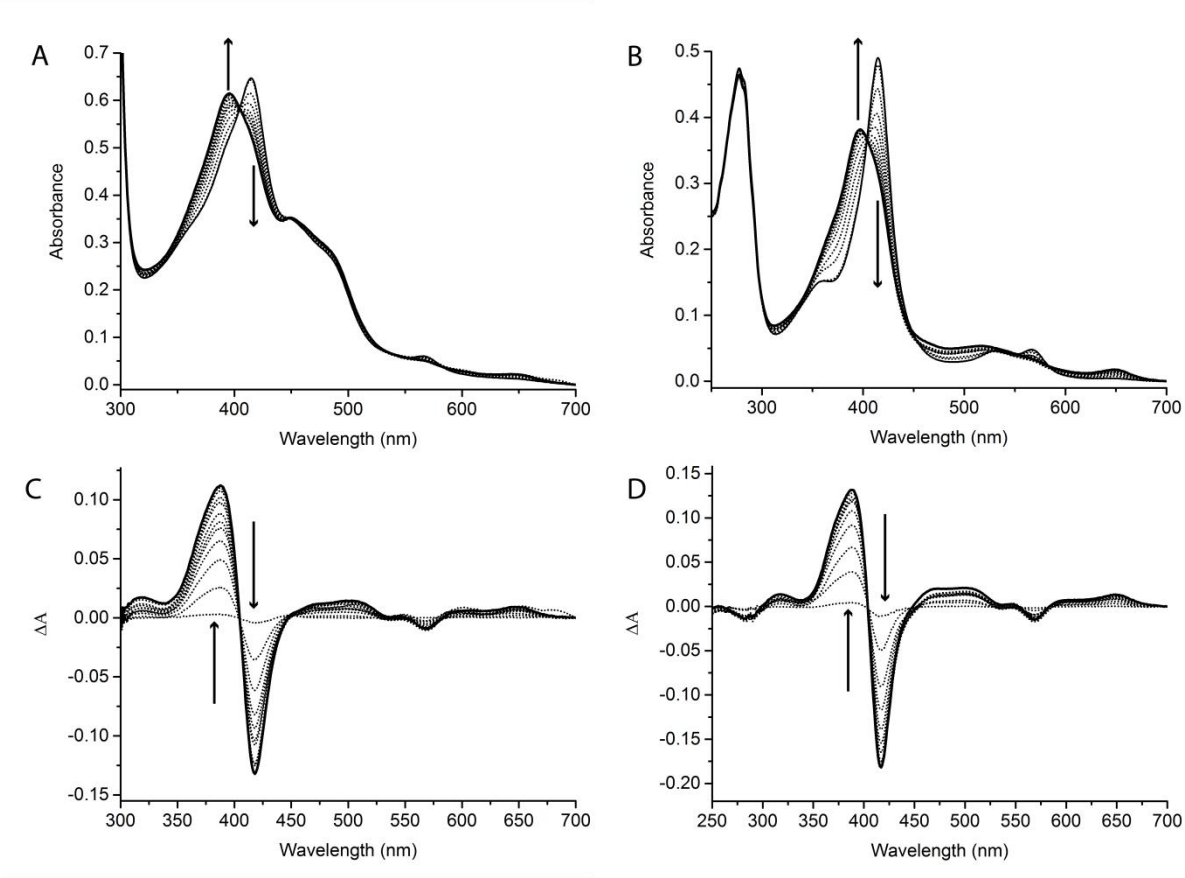

Figure 3.13 Type I absorbance shifts observed upon titration of *anteiso* myristic acid with P450 MT1 and MT1 HD. The top panels display the absolute UV-visible spectra for P450 MT1 (panel A, 6 µM) and MT1 HD (panel B, 5 µM) with the initial absorbance spectrum of the low-spin enzyme represented as a thin solid line and the final absorbance spectra of substrate-bound high-spin spectrum as a thick solid line in both cases. The intermediate spectra are represented as dashed lines, and were recorded after each addition of substrate during the titration (0 – 80 µM). These spectra map the Soret type I peak shift from 415 nm to a lower wavelength (390 nm at near-saturation with the substrate). The bottom panels represents the respective difference spectra for the same titrations with *anteiso* myristic acid acid for P450 MT1 (panel C) and MT1 HD (panel D). The initial spectrum for the substrate-free, low-spin enzymes was subtracted from each of the spectra collected after successive substrate additions (dashed lines) to create the sets of difference spectra, with the final addition showing a near-saturated substrate-bound difference spectrum (thick solid line). Both spectral sets show the concomitant formation of a 388 nm peak and a 418 nm trough, with directions of absorbance change indicated by black arrows, and associated with type I substrate binding. Clear isosbestic points can be seen at 404 nm and 450 nm in both the P450 MT1 and MT1 HD absolute and difference spectra (panels A-D).

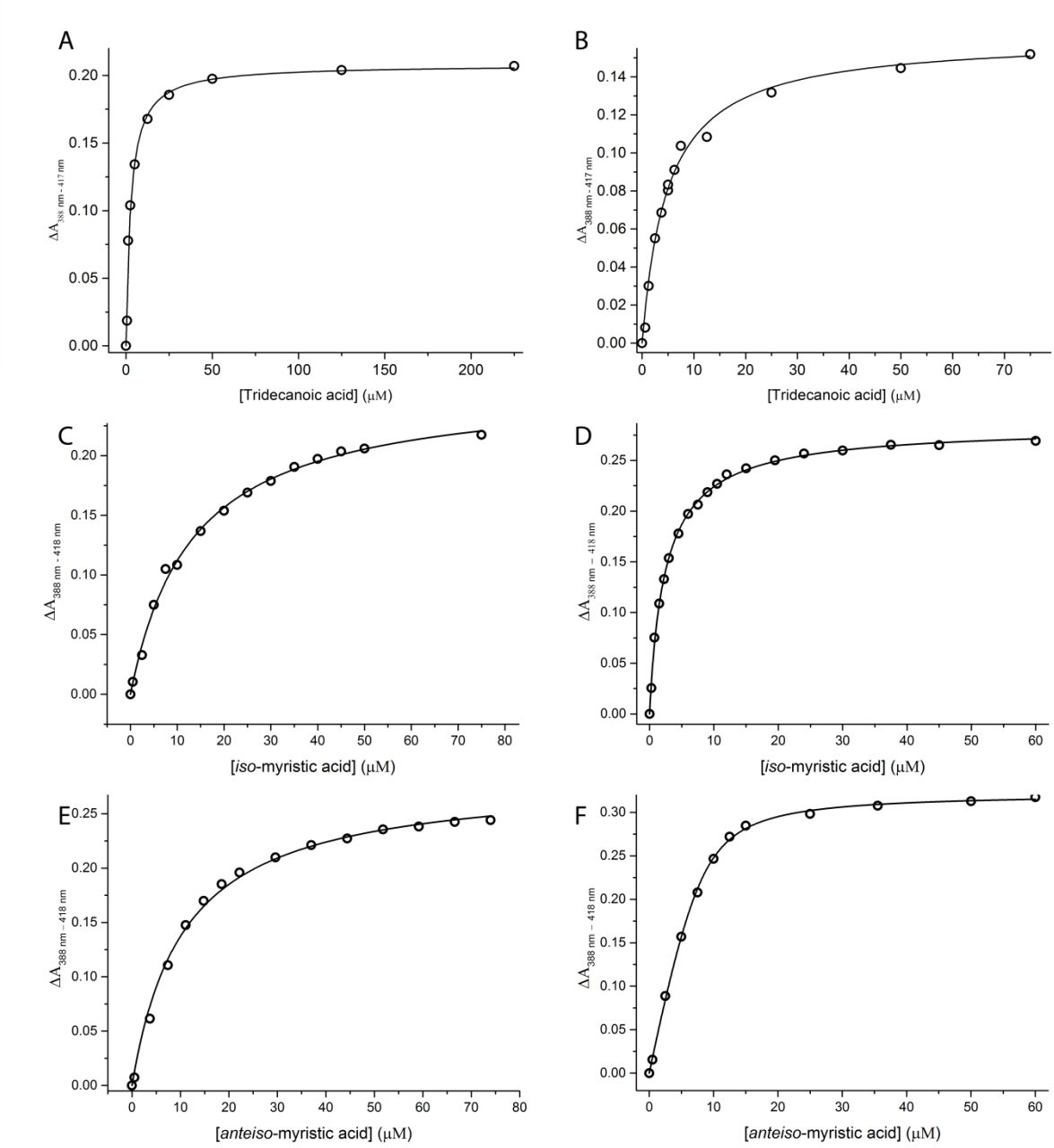

Figure 3.14. Binding titration curves for P450 MT1 and MT1 HD with different fatty acids. The individual panels show data fits from spectral titrations of P450 MT1 (left side panels) and MT1 HD (right side panels) using ~5-7 μM P450 enzymes and three different fatty acid substrates: tridecanoic acid (panels A and B), *iso* myristic acid (panels C and D) and *anteiso* myristic acid (panels E and F). The data points plotted are the maximum changes in absorption ($\Delta A_{388\ nm} - \Delta A_{418\ nm}$) from difference spectra computed from each titration. Data were fitted using either a standard hyperbolic (Equation 2, Methods 2.14) function (panels C and E) or a quadratic (Equation 3, Methods 2.14) function for the tighter-binding fatty acids (panels A, B, D and F). The K_d values determined for these substrates are tabulated along with the K_d values generated for all other substrates trialled in Table 3.3.

Table 3.3 Dissociation constants (Kd values) obtained for a range of fatty acids binding to P450 MT1 and the MT1 HD. The extent of high-spin shift elicited in the P450 MT1 and MT1 HD proteins by each substrate is shown. The K_d values were determined through plotting substrate-induced heme absorption versus applied substrate concentration, and by fitting data using hyperbolic or tight-binding (Morrison) equations, as described in Methods 2.14.

		P450 MT1		**MT1 HD**	
Chain length	Substrate	K_d (μM)	High spin (%)	K_d (μM)	High spin (%)
10	Decanoic acid	21.1 ± 2.0	30	N.D.	N.D.
12	Lauric acid	6.1 ± 0.4	10	9.0 ± 0.9	60
13	Tridecanoic acid	2.7 ± 0.3	65	4.8 ± 0.3	30
13	*iso* myristic acid	13.1 ± 0.8	>95	2.8 ± 0.2	95
13	*anteiso* myristic acid	10.5 ± 0.6	>95	1.1 ± 0.1	95
14	Myristic acid	7.4 ± 0.2	80	3.9 ± 0.3	85
14	*iso* pentadecanoic acid	13.4 ± 0.3	95	4.4 ± 0.2	95
14	*anteiso* pentadecanoic acid	14.3 ± 2	95	4.2 ± 0.4	95
15	Pentadecanoic acid	4.4 ± 0.6	85	1.1 ± 0.3	90
16	Palmitic acid	10.5 ± 0.2	80	1.0 ± 0.4	55
17	Margaric acid	4.1 ± 0.7	10	8.7 ± 0.8	20
18	Stearic acid	11.9 ± 1.0	15	5 ± 0.7	10
20	Arachidonic acid	1.7 ± 0.1	60	0.12 ± 0.01	65
16	N-palmitoylglycine	5.4 ± 0.1	95	2.7 ± 0.8	75
3	Glycerol	47.5 ± 6	20	34.2 ± 4	15
/	TWEEN 20	856 ± 21 nM	60	2.5 ± 0.1 nM	10
/	Cholestenone	0.265 ± 0.088	5	N.D.	N.D.

Some trends emerge from analysis of the comprehensive list of substrate binding data presented in Table 3.3. While all substrates shown bind quite tightly to P450 MT1 and to the MT1 HD (all K_d values <15 μM with the exception of decanoic acid), no obvious preference between saturated, branched chain or other individual fatty acids can be discerned from the K_d values. This has some parallels with the properties of P450 BM3 (CYP102A1), although in this enzyme the affinity for binding saturated fatty acids increases progressively in the chain length range from ~C10 to C16 [43]. Looking at the amount of high-spin heme iron formed on addition of individual substrates, the branched chain fatty acids seem to produce a consistently higher proportion of high-spin heme iron (>90%) in P450 MT1 and MT1 HD, even given their slightly weaker binding to P450 MT1 compared to various other fatty acids tested in this series. It is possible that P450 MT1 may

show a preference for branched chain fatty acids as its natural substrates, as was proposed for the *Bacillus subtilis* CYP102A2 and A3 enzymes [43].

Taking the range of saturated fatty acids alone, differing trends emerge for P450 MT1 and the MT1 HD, as illustrated in Figure 3.15. The MT1 HD binds medium chain length fatty acids (C15 + C16) the tightest, with K_d values increasing from this point with both increasing and decreasing substrate chain lengths (with the exception of C18, which binds ~2-fold tighter than does C17). However, P450 MT1 binds odd chain fatty acids more tightly (K_d values all <5 µM) than even chain fatty acids (in the range from C12-C18), with the even chain fatty acids binding progressively less tightly as their chain length increases in this range.

more strongly than do the even-chain fatty acids.

The isolated P450 domain (MT1 HD) binds more tightly to the majority of fatty acids tested than does the intact P450 MT1 (Table 3.3). This dichotomy between heme domain and full length enzyme substrate binding affinity was observed early on in the case of P450 BM3 and later attributed to the influence the tethered reductase has on the P450 domain conformation in the full length enzyme [286,318]. The FMN domain of BM3 has been shown to interact with a portion of the heme domain (the C and D helices, Chapter 1.9) that has been shown to change conformation upon substrate binding [319]. The removal of the reductase domain could affect the hydrogen bonding network around the distal water in the MT1 HD. This would make the distal water more susceptible to dissociation and the substrates would appear to bind tighter. Moreover, substrate binding has been shown to accelerate steady state reduction of cytochrome *c* by P450 BM3, indicating that conformational changes in the heme domain can affect the structure of the reductase domain [320].

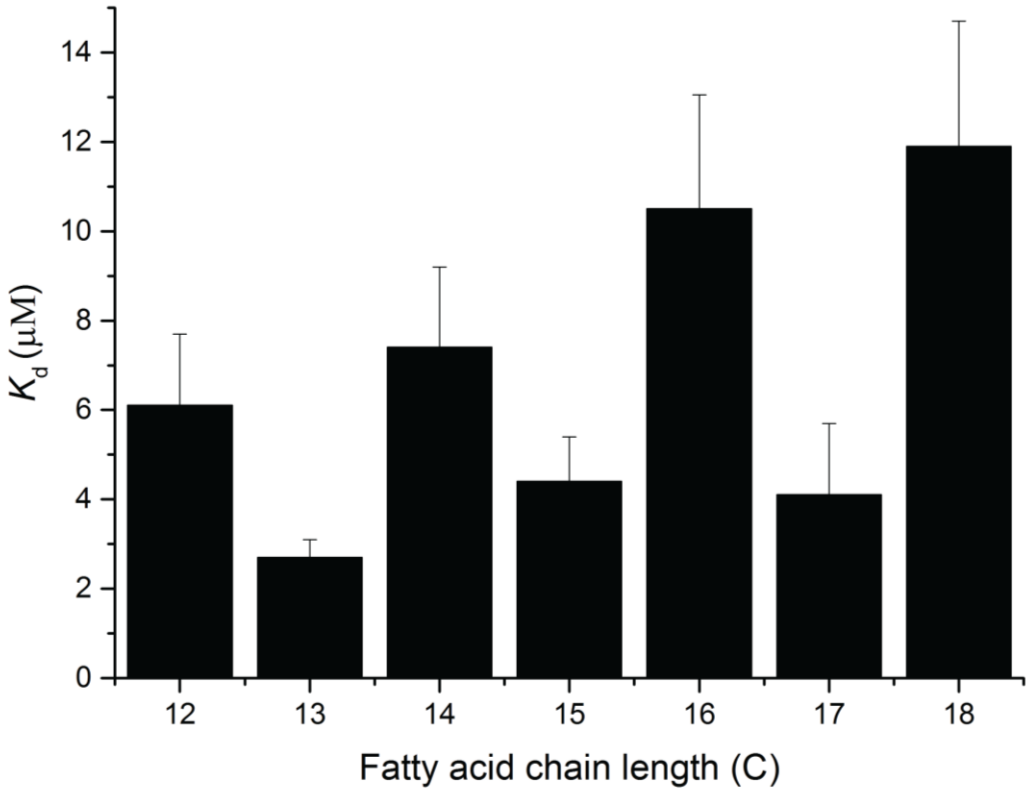
K_d (μM)
0
2
4
6
8
10
12
14
12
13
14
15
16
17
18
Fatty acid chain length (C)

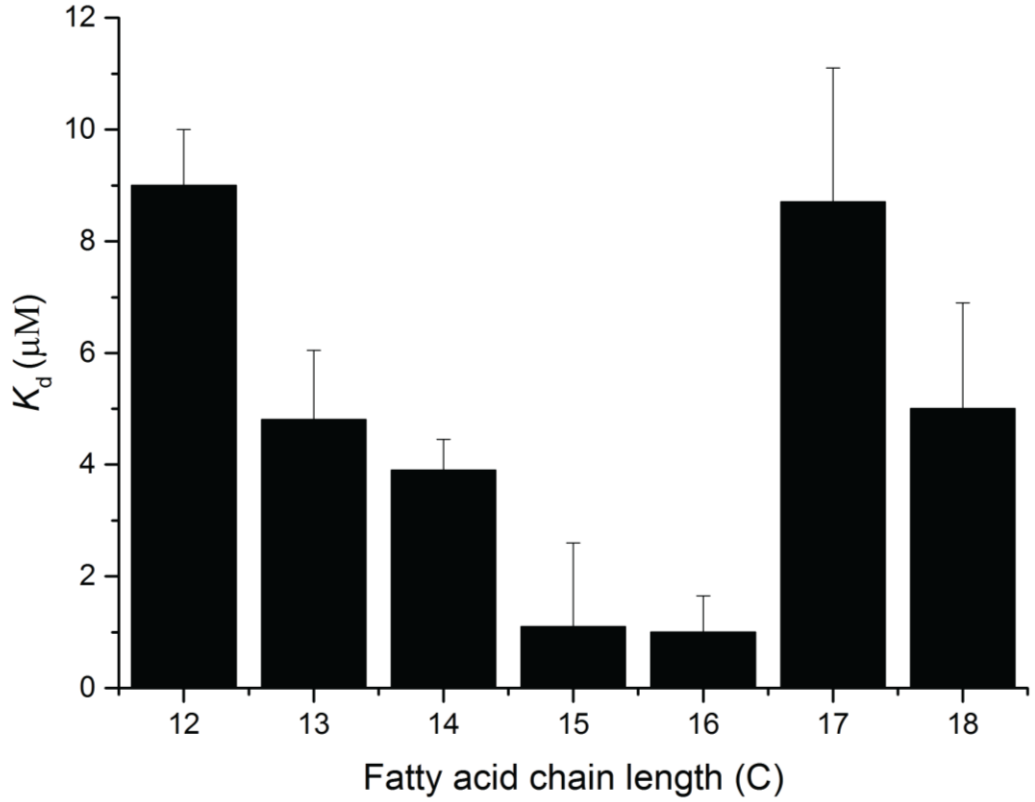
K_d (μM)
0
2
4
6
8
10
12
12
13
14
15
16
17
18
Fatty acid chain length (C)

Figure 3.15 Trends for the binding of saturated fatty acid to P450 MT1 and the MT1 HD. The bar charts are re-plotted from the K_d data shown in Table 3.3. The dissociation constants (K_d values) for a range of saturated fatty acids (C12-C18) are plotted against their chain length for intact P450 MT1 (upper panel) and for the MT1 heme domain (MT1 HD, lower panel). Binding titration was repeated in triplicate for each substrate and the error bars shown here represent the standard deviation. In the case of P450 MT1, an unusual pattern of specificity is seen, where the odd-chain saturated fatty acids consistently bind

Neeli et al. have demonstrated that BM3 is functional as a dimer in solution with its specific activity dropping at protein concentrations below 10 nM, a feature inherently associated with its dimer to monomer conversion, rather than from flavin loss at low concentrations [240]. In the same paper, through an elegant series of stopped flow experiments, they report that electron transfer is intermolecular, i.e. from the FMN of one monomer to the heme domain of the other. This conclusion was reached by showing that fatty acid oxidation was reconstituted by mixing of catalytically inactive oxygenase (A264H) and FMN-depleted (G570D) full length BM3 mutants [240]. This indicated that a functional electron transfer chain was reconstituted in chimeric enzyme, through electron transfer from the functional reductase in the A264H reductase to to the functional heme domain in the G570D mutant. Taking into account that (i) BM3 is active only in its dimeric form with intermolecular heme and FMN domain associations occurring between different monomers, and (ii) that substrate affinity was shown to be altered by interactions between the FMN and heme domains, it can be assumed that the dimeric associations in could also have an effect on substrate binding and selectivity (assuming dimerization at experimental conditions of >10 nM enzyme).

3.3.3 Inhibitor binding to P450 MT1

Many of the major P450 inhibitors in clinical use are compounds with a nucleophilic nitrogen able to displace the P450 distal water molecule and take its place to directly coordinate the heme iron as its 6th proximal ligand [321]. Figure 3.16 shows the structures of the inhibitors used in binding titrations with P450 MT1. Imidazole is a well-known P450 inhibitor. However, its small and polar nature affects adversely its affinity for the typically non-polar active sites of P450s, which in most cases interact with hydrophobic substrates. This means that imidazole affinity for binding most P450s is very weak (in the mM range). The N3 nitrogen in imidazole is the nucleophilic centre of the molecule, and its 2 available electrons are donated to the heme iron to form a covalent bond ligation. 1-

and 4-phenylimidazole have bulky phenyl groups attached at different positions on the imidazole ring, which typically leads to them having higher affinity for P450 active sites, a property which is also reflected in their higher logP (lipophilicity) values (Figure 3.16).

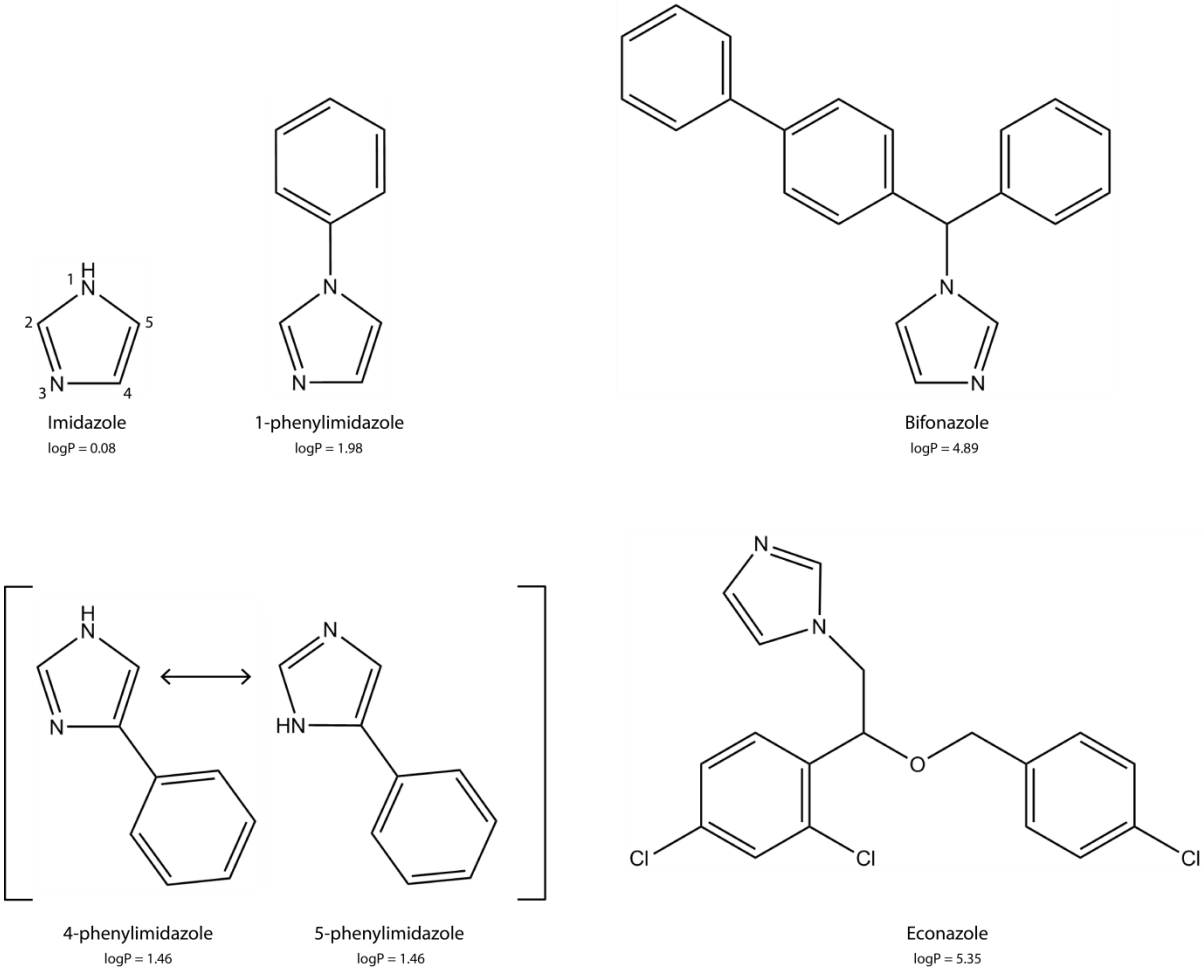

Figure 3.16 Structures of azole inhibitors used in P450 MT1 binding titrations. The imidazole ring is numbered for comparison between other derivative structures shown. The hydrophilicity (logP) values are shown underneath each drug. The lower the value, the more polar the molecule. The tautomerism exhibited by 4- and 5-phenylimidazole is depicted in closed brackets.

1-phenylimidazole has a phenyl group attached to the N1, effectively removing a polar N-H group and replacing it with a less-polar N-Ph group. This results in its higher logP value compared to 4-phenylimidazole, where the N-H group is still present. It can be rationalised that a tighter ligation of 1-phenylimidazole to a P450 heme iron may be attributed to its lower polarity compared to 4-phenylimidazole.

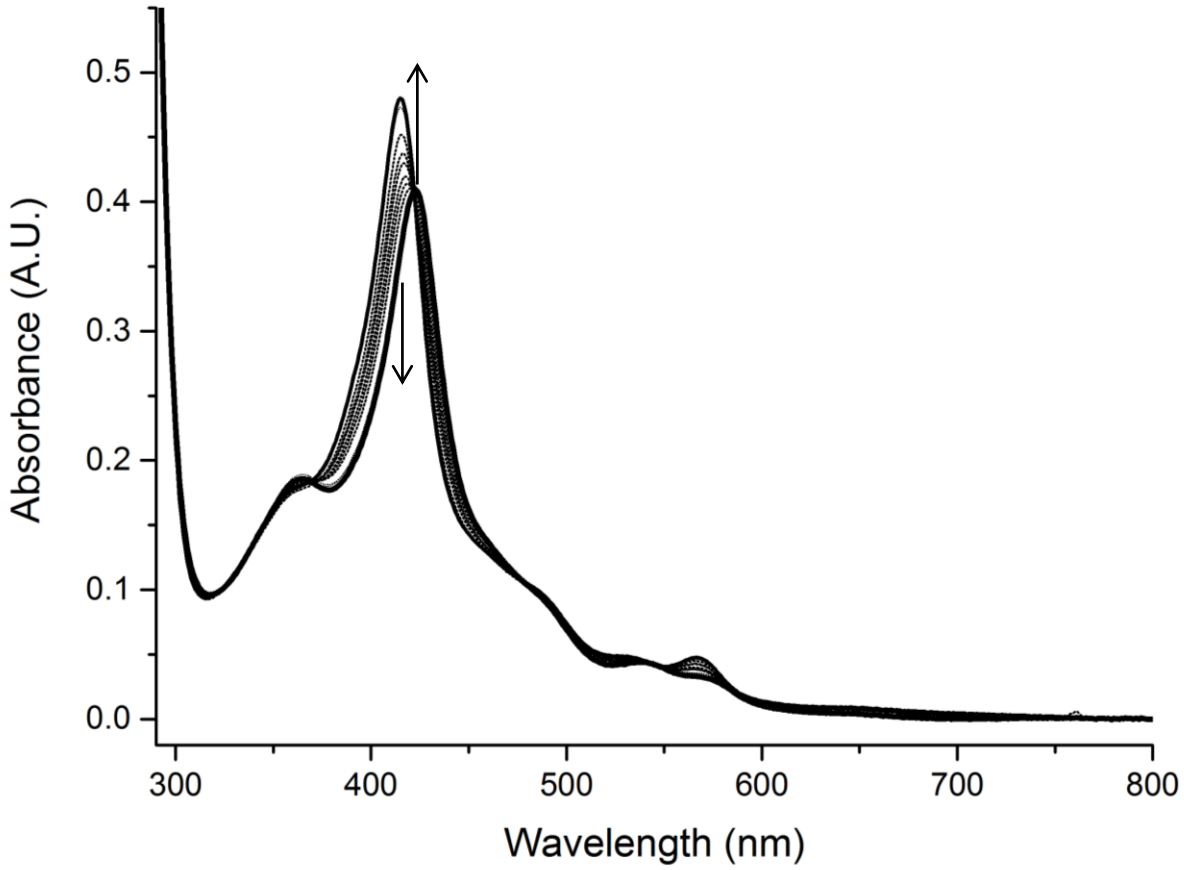

Figure 3.17 UV-visible binding titration of P450 MT1 with bifonazole. A type II Soret absorbance shift (to longer wavelength) is observed upon bifonazole binding to P450 MT1 (~5 µM). Increases in intensity of the alpha and delta bands at 575 nm and 360 nm, respectively, are also seen. The UV-visible spectrum for the ligand-free P450 MT1 is represented as a thin solid line with A_{max} at 415 nm, and the final absorbance spectrum for the near-fully inhibitor-bound form is of lower intensity and is presented as a thick solid line at ~420 nm. The intermediate spectra are represented as dashed lines. Spectra were recorded after each addition of substrate during the titration (0 – 200 µM) and map the Soret type II shift from 415 nm to ~420 nm. All spectra were baselined at 800 nm and black arrows indicate the direction of Soret absorbance changes on inhibitor addition.

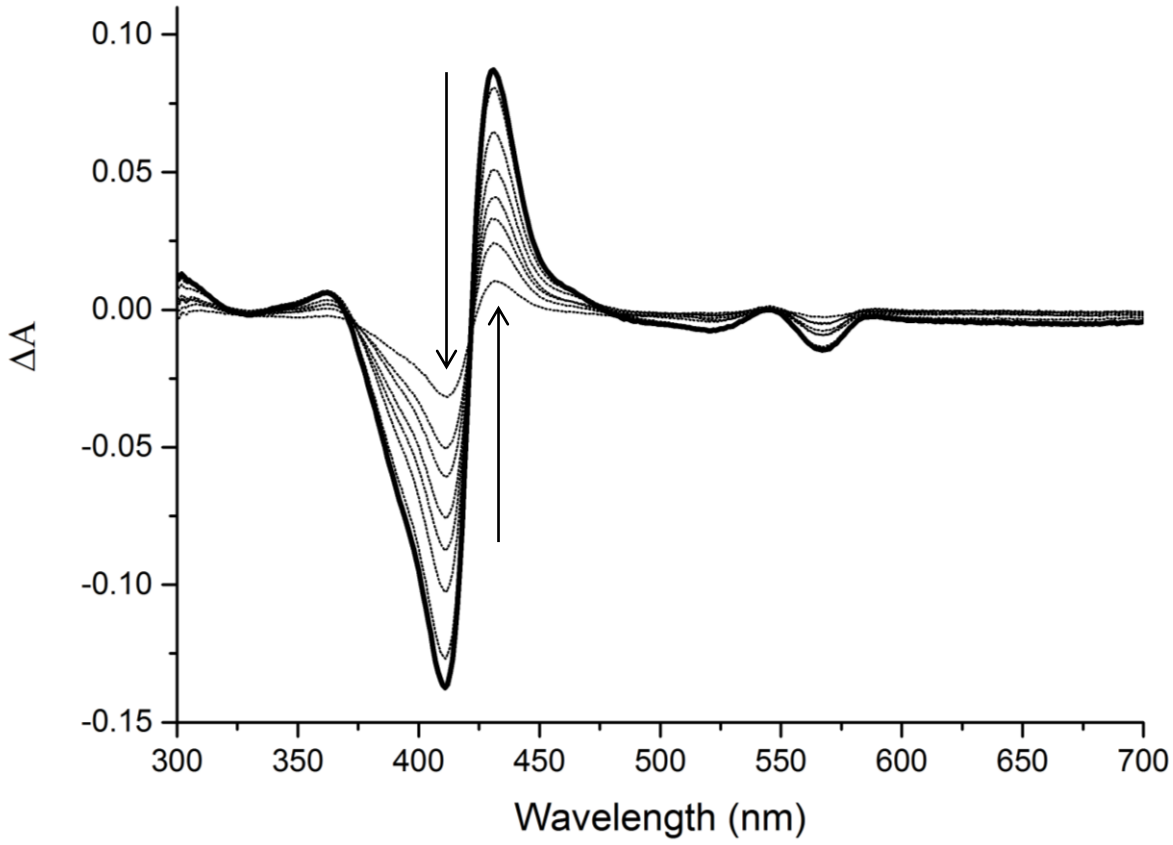

Figure 3.18 Difference spectra from the titration of bifonazole with P450 MT1. The initial absolute spectrum for the ligand-free P450 MT1 was subtracted from all subsequent spectra (dashed lines) recorded after sequential substrate additions to create the set of difference spectra shown. The final difference spectrum (thick solid line) shows a near-saturated inhibitor-bound P450 MT1. The difference spectra show the concomitant development of an ~430 nm peak and an ~412 nm trough, indicated by black arrows, associated with type II inhibitor binding. Clear isosbestic points can be seen at 329 nm, 421 nm and 476 nm.

4-phemylimidazole exists in solution as a mixture of 2 tautomers: 4-phenylimidazole and 5-phenylimidazole [322]. 5-phenylimidazole was shown to ligate heme iron more tightly than 4-phenylimidazole does, as seen in the P450cam structure where 5-phenylimidazole is seen in place of the 4-phenylimidazole [323]. The tighter binding of 5-phenylimidazole to the P450 heme iron may shift the tautomer equilibrium in its favour.

Bifonazole and econazole are both antifungal P450 azole drugs. Microbial P450s make good drug targets and various antifungal azoles were shown to have antibacterial activity against *Mycobacterium tuberculosis* (Mtb) [324]. Selected *CYP* gene knockout studies also highlighted the importance of various P450s to the pathogen's viability and/or survival in

the host [325]. As a result, extensive screening of P450 inhibition through azole drug inhibition has been carried out for the Mtb P450s, and in studies here the inhibitor potency of various azoles was investigated for P450 MT1. Bifonazole and econazole were both shown to bind tightly to P450 MT1, but for these bulky compounds a high logP value does not correlate to tighter binding, as the K_d for bifonazole (logP = 4.89) is lower than that for econazole (logP = 5.35).

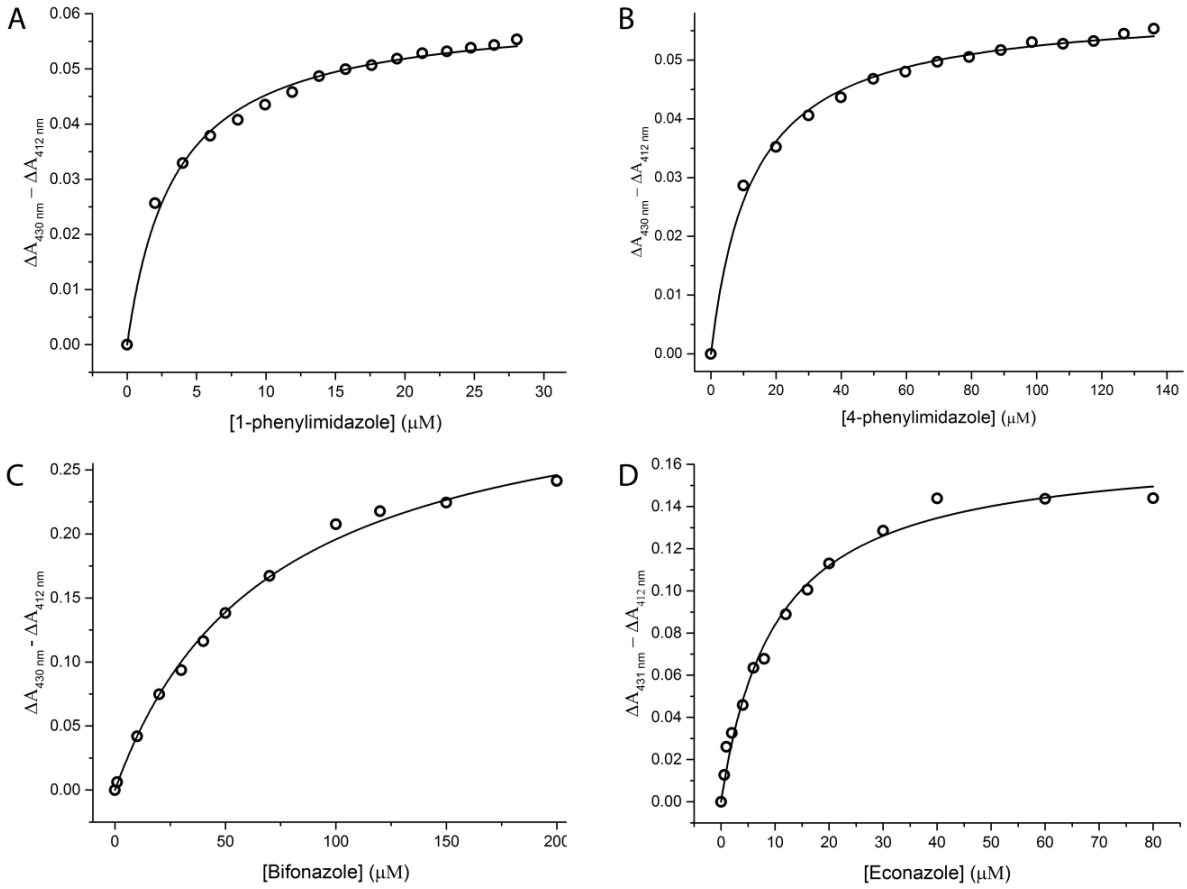

Figure 3.19 Binding curves for P450 MT1 with four different azole inhibitors. P450 MT1 (~5 μM) was titrated with 4-phenylimidazole (panel A), 1-phenylimidazole (panel B), bifonazole (panel C) and econazole (panel D). All graphs show plots of maximal absorption change ($\Delta A_{430\ nm} - \Delta A_{412\ nm}$) from the difference spectra versus the relevant inhibitor concentration (μM) at that point. All data were fitted using a standard hyperbolic function, and K_d values determined were 3.40 ± 0.22 μM (1-phenylimidazole); 12.7 ± 0.8 μM (4-phenylimidazole); 69.1 ± 4.6 μM (bifonazole); and 10.1 ± 0.9 μM (econazole).

Table 3.4 Experimentally obtained dissociation constants (K_d values) for azole inhibitor binding to P450 MT1. The K_d values for azole binding to P450 MT1 are shown alongside the comparable values for their binding to P450 BM3 [271,326,327]. K_d values were determined by spectral titrations as described above and in Methods 2.14. N.D. indicates "not determinable" due to extremely weak affinity in the case of cyanide, and N/A indicates "not available" for BM3 due to econazole and bifonazole being antifungal azole drugs that do not show evidence of binding to P450 BM3.

Inhibitor	**K_d (μM)**	
	P450 MT1	**BM3**
(Sodium) cyanide	N.D.	N.D.
Imidazole	723.1 ± 37.0	535.3 ± 5.2
1-phenyimidazole	3.4 ± 0.2	10.4 ± 0.4
4-phenylimidazole	12.7 ± 0.8	0.9 ± 0.5
Econazole	10.0 ± 0.9	N/A
Bifonazole	69.1 ± 4.6	N/A

3.4 Multi-angle Laser Light Scattering (MALLS) studies of P450 MT1 and MT1 HD proteins

Once the apparent mass of a protein's polypeptide chain has been estimated by SDS-PAGE analysis, MALLS is a useful and complementary technique that can be used to probe the conformational state of the protein in solution, as well as providing estimates of both the size and absolute molecular mass/aggregation state(s) of the species. In this way, MALLS is often used as a prerequisite analytical method for protein sample characterization prior to crystallographic trials, where a fully monodisperse, homogeneous sample is usually crucial for protein crystal formation.

MALLS was used to investigate the oligomerisation state of both P450 MT1 and the MT1 HD. The samples were all analysed in 50 mM KPi buffer, pH 7.0, and under varying salt conditions (Figure 3.20).

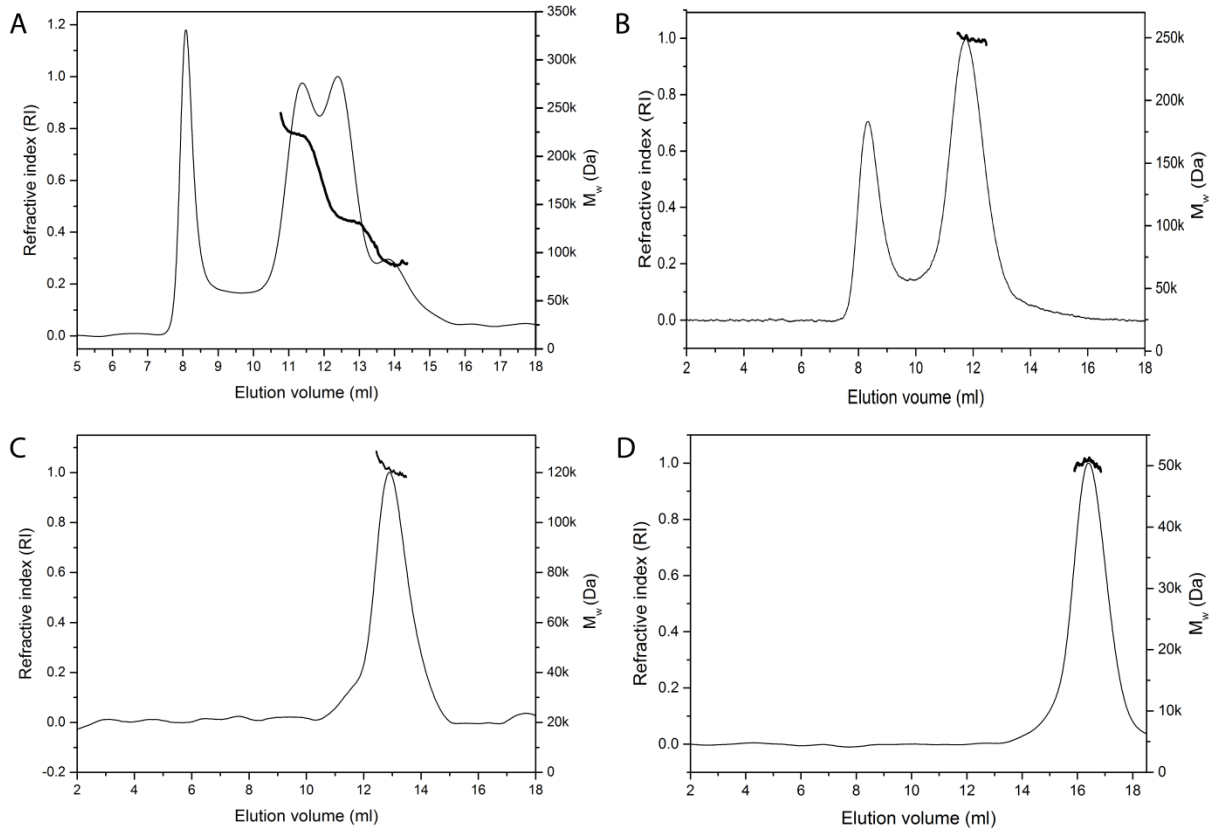

Figure 3.20 MALLS analysis of P450 MT1 and MT1 HD. The x-axes show the elution volume of the protein sample from an 8 ml size exclusion column. The left hand side y-axes show the refractive index (RI), a relative scale of the ability of light (633 nm) to propagate through the sample, plotted as a thin solid line. The right hand side y-axes show the molecular weight (Da) and Zimm fitting of the species in the sample, plotted as a thick solid line. Panel A is a P450 MT1 sample (in 50 mM KPi, 200 mM KCl, pH 7.0) showing 4 peaks: the void volume at 8.5 ml, the dimer species (225 kDa) at ~11.5 ml, the monomer species (138 kDa) at ~12.5 ml and a lower M_w species (85.5 kDa) at 14 ml, showing a polydispersed mixed monomer/dimer composition in solution. Panel B shows a P450 MT1 sample in exactly the same conditions as in panel A (50 mM KPi, 200 mM, pH 7.0) but following a more stringent purification procedure involving decreasing the overall time from cell lysis to pure protein and by removing any sample freezing and thawing steps before sample analysis by MALLS. The 2 peaks correspond to the void volume at 8.5 ml and the dimeric form (249 kDa), here showing a homogeneous, monodispersed dimeric sample. Panel C shows the P450 MT1 monomer fraction from the sample in panel A re-run, this time showing only a monomer peak at 13 ml (121.4 kDa). A peak corresponding to the column void volume is absent in the re-run fractions. Panel D shows a re-run fraction of a sample of the MT1 HD (in 50 mM KPi, 500 mM KCl and pH 7.0) which shows a homogeneous monomer at 16.5 ml (49.8 kDa). The parameters obtained from these MALLS experiments are recorded in Table 3.5.

The MALLS technique involves loading the sample onto an 8 ml SX200 size exclusion column which feeds into the light scattering equipment for detection. Zimm fitting is used to calculate the molecular weight (M_w) and the hydrodynamic radius (R_h) from the data acquired by scattered light from the 658 nm laser hitting the Dawn Helios (Wyatt technologies) detectors. The RI detector measures refractivity from a 633 nm laser, while the absorbance at 280 nm monitors the amount of protein in the sample. Panel A (Figure 3.20) shows a mixed monomer/dimer species for P450 MT1 in solution. The dimer species has an apparent M_w of 220 kDa and an R_h of 6.8 nm. The predicted mass is slightly lower than twice the expected size of the monomer at ~120 kDa. The monomer species on the other hand has a slightly higher M_w at 139 kDa and a higher than expected R_h of 5.8 nm when compared to the dimer. As the monomer and dimer peaks are not fully separated, this interference between the species could account at least partially for the discrepancies in the values obtained. BM3 is functional as a dimer [240], and salt concentration was shown to affect the dimerization state, with higher salt concentrations (>600 mM KCl) favouring the monomeric state (Chapter 5, Section 5.4). The RI peak at ~8 ml is referred to as the 'void', as it corresponds to the volume of the column and is expected for the initial application of samples. There is a further peak at 14 ml with a M_w of 85.5 kDa, which might correspond to the reductase domain of P450 MT1, as BM3 and P450 MT1 are both prone to cleavage at their inter-domain linker region. The affinity column used during the purification procedure is likely also to have retained a cleaved reductase domain (~75 kDa) along with intact P450 MT1, whereas a cleaved heme domain would not be bound to the column.

Panel B (Figure 3.20) shows the MALLS analysis of P450 MT1 under the same conditions as in panel A (50 mM KPi, 200 mM KCl, pH 7.0). The differences in the results between the two sample analyses are likely due to a more rigorous preparation of the sample in panel B, including a shorter purification period with no freezing of the sample before MALLS analysis. This solution shows only one major RI peak aside from the void peak, and has a M_w of 249 kDa corresponding to the dimeric form of P450 MT1 and an R_h of 6.33 nm. These are clearly more accurate values than those obtained from analyses shown in panel A. While the dimer in panel B eluted at ~12 ml, the dimer form in panel A elutes at ~11.5 ml and the slight differences in M_w and R_h between these samples are probably due to peak interference between the partially resolved monomer and dimer forms in the latter sample, as mentioned earlier.

Panel C shows the monomer fraction from panel A re-run through the column, with MALLS showing a homogeneous monomer of 120 kDa, equal to its predicted mass of 120 kDa and with an R_h value of 5.3 nm. While the R_h value for the isolated monomer is lower than for the dimer (and likely reliable), it is still very close to that of the dimer. This could be explained by the fact that the fitting software (Astra, Wyatt technology Corporation) obtains the R_h value for a protein in solution by assuming it is spherical in shape. The monomer did not re-dimerise to any extent, suggesting that the equilibrium for this species is not in favour of the dimer. However there may be some dimer formed, since a small shoulder is observed on the main peak at a lower elution volume.

The MT1 HD was also analysed by MALLS (in 50 mM KPi, 500 mM KCl, pH 7.0). The heme domain was shown to be a homogeneous monomer in solution with a M_w of 49.8 kDa, very close to its predicted molecular weight of 50.0 kDa. The R_h value was obtained at 3.45 nm which is higher than other P450 heme domains (~2.8 nm) of similar size (Chapter 5.4). In studies to date, almost all P450s were shown to be monomeric, even those isolated from dimeric P450-redox partner fusion enzymes, i.e. the P450 BM3 heme domain [328]. However, the P450-like thiolate-ligated heme domains from NOS enzymes are dimers [329]. A conclusion for P450 MT1 is thus that the reductase domain must be responsible for the dimerization we observe for this enzyme – either through self-interactions or through interactions between the individual reductase and P450 domains.

Table 3.5 Molecular weight (Mw) and Hydrodynamic radius (Rh) parameters for P450 MT1 and MT1 HD from MALLS analysis. The MALLS parameters from the P450 MT1 and MT1 HD in Figure 3.20 are recorded here and the superscript lettering indicates their corresponding figure panel.

Oligomeric state	Proportion by weight	M_w (kDa)	Rh (nm)
MT1 dimer^{A}	45.3%	218.4 ± 11	6.8 ± 0.3
MT1 monomer^{A}	44.4%	138.6 ± 5	5.8 ± 0.3
MT1 reductase domain^{A}	10.3%	85.5 ± 4	5.3 ± 0.3
MT1 dimer^{B}	100%	249.0 ± 12	6.9 ± 0.3
MT1 monomer^{C}	100%	121.3 ± 4	5.3 ± 0.3
MT1 HD monomer^{D}	100%	49.9 ± 3	3.6 ± 0.2

3.5 HPLC analysis of flavin cofactors in MT1

The bioinformatics analysis discussed previously identified P450 MT1 as being a diflavin P450 oxidoreductase, and HPLC was thus used to determine the presence and stoichiometry of the flavin cofactors.

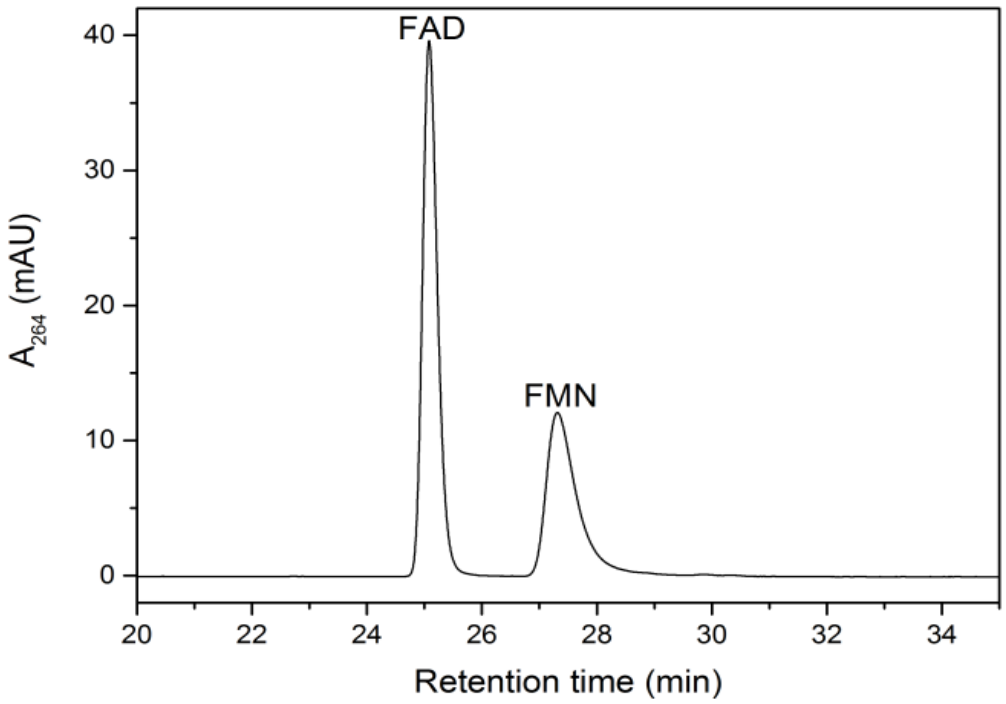

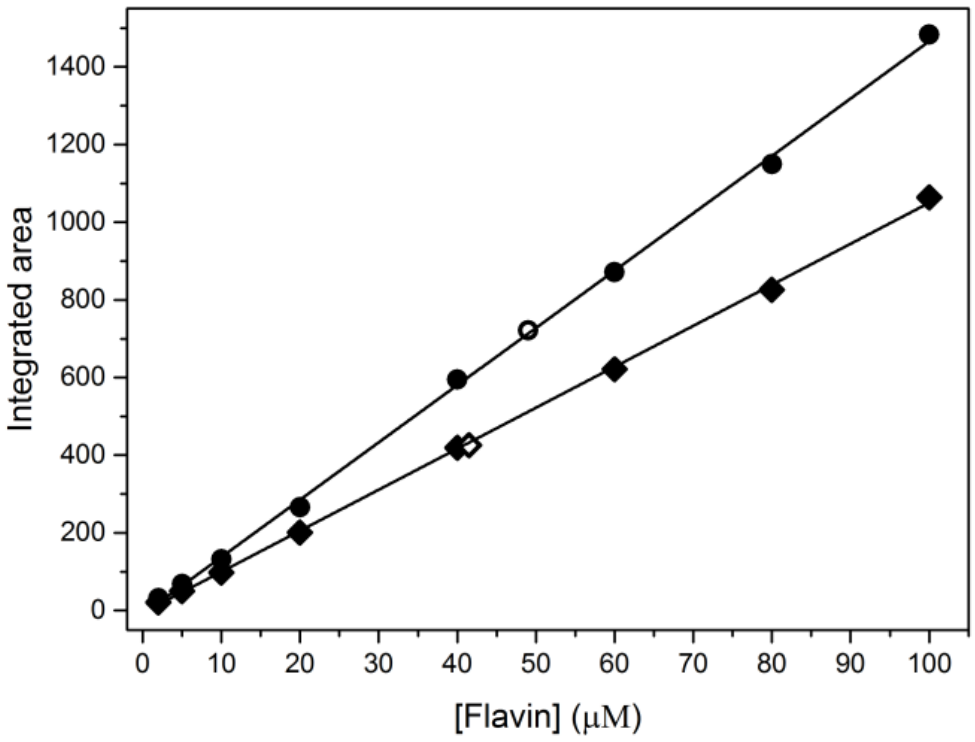

Figure 3.21 HPLC analysis of the flavin cofactors in P450 MT1. The top panel shows separate FAD and FMN peaks from a single P450 MT1 (40 µM) sample eluting at 25.1 min and 27.3 min, respectively. The right hand panel shows the flavin calibration curve established using the integrated areas under the peaks for a range (0–100 µM) of FAD (solid black dots) and FMN (solid black diamonds) standards of known concentrations. The individual FAD and FMN values were fitted to straight lines. The integrated areas of the FAD and FMN peaks (bottom panel) from the P450 MT1 sample were then interpolated on the calibration curve relative to their respective areas (FAD, hollow circle and FMN, hollow diamond) and their corresponding concentrations were found to be 49 µM and 41.5 µM, respectively.

The concentration of the P450 MT1 enzyme sample used for HPLC identification was determined at 46 µM from the 418 nm Soret peak ($\varepsilon_{418\ nm}$ = 105 mM^{-1} cm^{-1} , as used with BM3 [93]) and 50 µM from the 456 nm 'flavin' peak ($\varepsilon_{456\ nm}$ = 24.1 mM^{-1} cm^{-1} used for measuring cytochrome P450 reductase concentration [330]). The small difference in concentration estimates is likely due to incomplete heme incorporation in P450 MT1. Earlier studies revealed that the intensity of the heme Soret band in P450 MT1 (relative to the flavin bands) was lower in P450 MT1 than in P450 BM3, pointing to sub-stoichiometric heme incorporation in the flavocytochrome enzyme.

FMN and FAD standards of known concentrations were run separately to produce a calibration curve (Figure 3.21, bottom panel). The flavins were extracted from the P450 MT1 enzyme sample as described in Methods 2.10, and resolved using HPLC (Figure 3.21, top panel). Comparison of the column retention times of the flavin standards to the HPLC trace from the MT1 sample allowed identification of the separate FMN and FAD peaks, which eluted at 27.3 min and 25.1 min, respectively. The AUC (area under curve) values for the FMN and FAD cofactors extracted from P450 MT1 enabled their concentrations to be established as 41.5 µM and 49 µM, respectively, with reference to the standard curve.

In the case of purified P450 BM3, there have been multiple reports on the weak affinity of FMN compared to FAD, and due to its low incorporation (~70% compared to FAD) the experimental conditions used for BM3 preparation/analysis often include aqueous FMN flavin supplementation to circumvent dissociation of FMN [287,331,332] [13,68,69]. P450 MT1 shows extensive flavin incorporation, with ~85% FMN incorporated compared to FAD, which is expected to be essentially fully incorporated based on its much larger size and its higher affinity for CPR enzymes. These data suggest that a flavin extinction

coefficient of 24.1 mM^{-1} cm^{-1} at 456 nm may be a more reliable indicator of the actual flavoenzyme concentration than by using the coefficient of 105 mM^{-1} cm^{-1} at 418 nm [332].

3.6 P450 MT1 and MT1 HD thermal stability assessment

Full length P450 MT1 and its heme domain (MT1 HD) were subjected to a variety of techniques to assess their thermostability. Most expressed proteins can tolerate temperatures slightly higher than those tolerated by the organism that they originate from. P450 MT1's host organism is *Myceliophthora thermophila*, a moderate thermophile growing optimally between 45–50 °C.

Differential scanning fluorimetry (DSF) measures protein stability using a real time PCR machine to detect the changes in fluorescence when Sypro Orange dye binds to hydrophobic regions of unfolding proteins as temperature is progressively increased (Methods 2.16). DSF data are shown in Figure 3.22 (for intact P450 MT1) and in Figure 3.23 (for the MT1 HD).

The thermally induced unfolding observed for P450 MT1 is irreversible and follows a typical two-state model with a sharp melting transition between the folded and unfolded states (Figure 3.22, left hand panel). P450 MT1 has an unfolding transition (T_m value) of 58 °C in Na/K phosphate, pH 7.0 (the most stabilising condition identified); and this represents the midpoint of protein unfolding for the 120 kDa enzyme (which should form a ~240 kDa dimer). While this could accurately reflect P450 MT1's real T_m, the value is not as high as might have been expected, as by 50 °C, the higher end of its host organism's optimal growth range, it is already partially unfolded. This could be due to differences in the cellular environment compared to buffer conditions used, which were comprehensive but not exhaustive. Another explanation could be that post-translational modifications made by the fungus (and which do not occur in the *E. coli* expression system) further stabilise the P450 MT1 enzyme.

Differential scanning fluorimetry (DSF) is a good tool to screen protein stability over a range of conditions, e.g. different pH and salt concentrations. Figure 3.22 shows the substantial effects that different buffers and pH values can have on P450 MT1's stability. A single pH unit change can increase the T_m of P450 MT1 from 51 °C in Na/K Pi (pH 6.0) by 7° C to 58 °C in Na/K Pi (pH 7.0). It should be noted that, while unfolding of a complex enzyme occurs with a range of energetically distinct events, e.g. with different domains

unfolding at different temperatures, the DSF technique measures the interaction of Sypro Orange with the protein's internal hydrophobic regions as they become solvent exposed. This process can occur uniformly, as seen in Figure 3.22 (left hand panel).

Differential scanning fluorimetry was also used to measure the effects of pH and different buffers on protein unfolding in the MT1 HD (Figure 3.23). The isolated, monomeric MT1 heme domain is a more compact protein than is the dimeric flavocytochrome. However, this does not necessarily mean that it should be a more stable entity than the full length multi-domain P450 MT1. Indeed, the T_m obtained for the unfolding of the MT1 HD (48 °C) was 10° C lower than that for the full length P450 MT1 (58 °C) under the same buffer conditions.

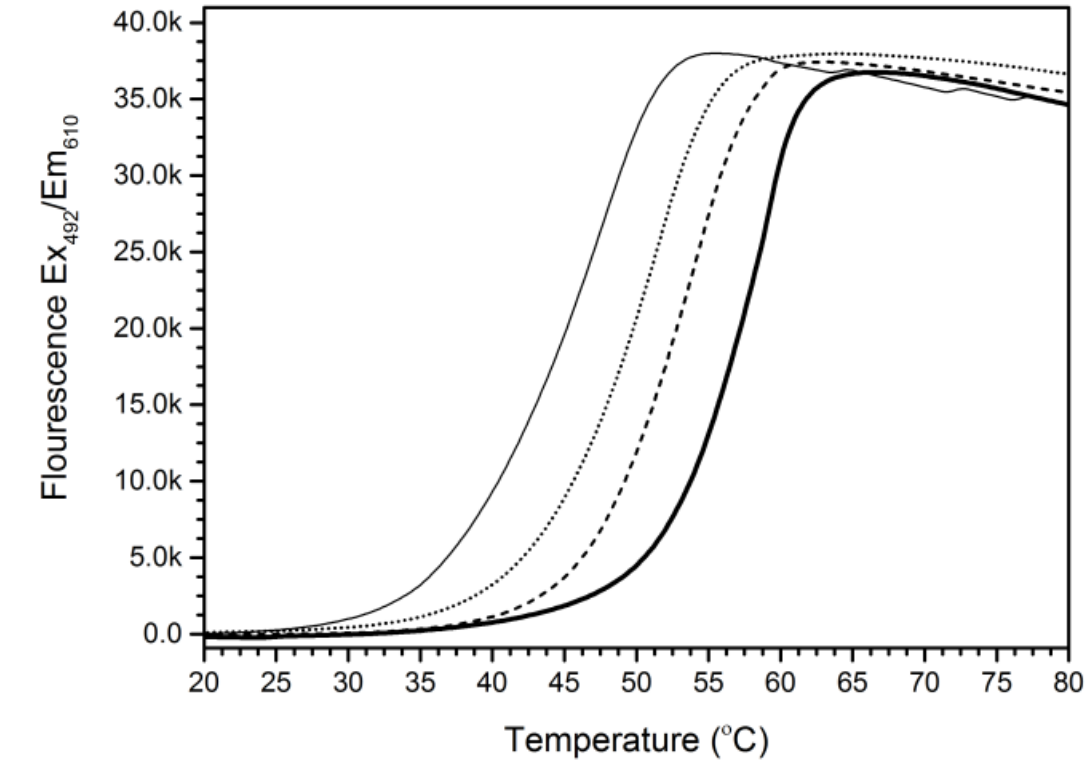
Flourescence Ex_{492}/Em_{610}
40.0k
35.0k
30.0k
25.0k
20.0k
15.0k
10.0k
5.0k
0.0
20 25 30 35 40 45 50 55 60 65 70 75 80
Temperature (°C)

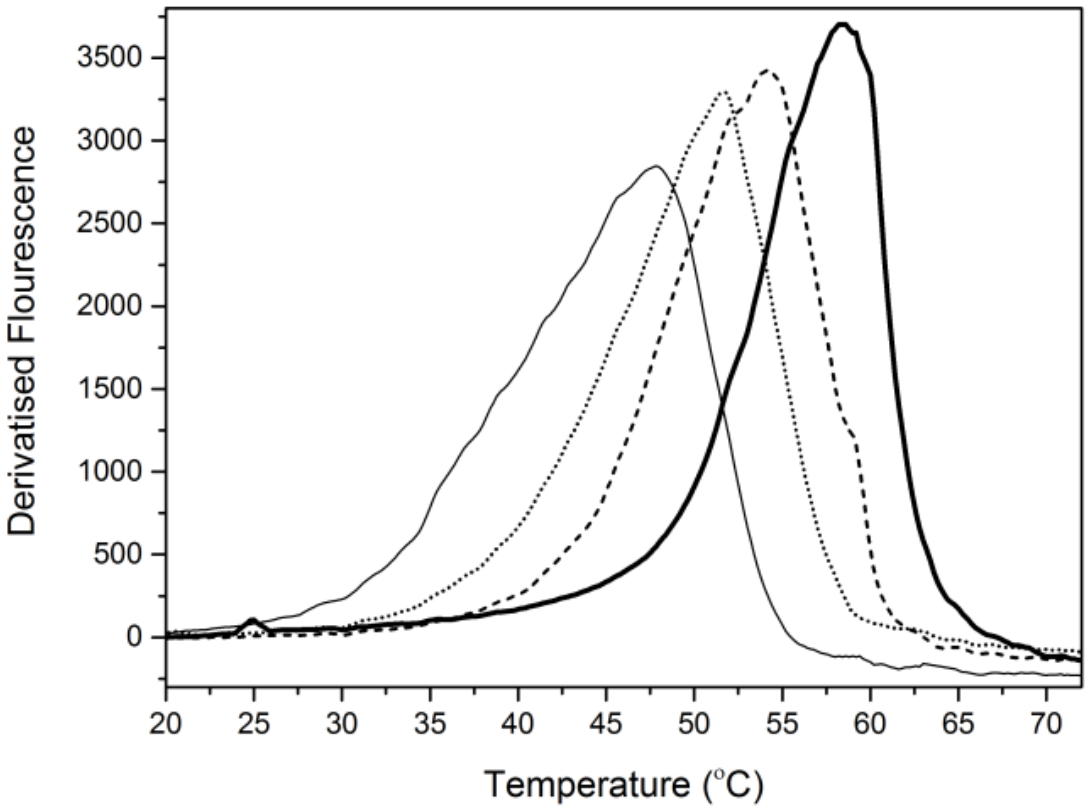
Derivatised Flourescence
3500
3000
2500
2000
1500
1000
500
0
20 25 30 35 40 45 50 55 60 65 70
Temperature (°C)

Figure 3.22 P450 MT1 protein unfolding by differential scanning fluorimetry using Sypro Orange. Unfolding studies were done for P450 MT1 and with analysis of the effects of different buffer and pH conditions on P450 MT1 stability. The top panel shows curves for Sypro Orange fluorescence across a range of temperatures applied. The temperature was ramped at 0.2 °C/min during the experiment. As temperature increases, hydrophobic regions of P450 MT1 become exposed as the protein unfolds and the dye binds and its fluorescence increases. The wavelengths for excitation and emission were 492 and 610 nm, respectively. The different curves show data sets collected in different buffer conditions. These same spectra were derivatised (bottom panel) to highlight the different midpoint unfolding temperature (T_m) values established as peaks. The buffers used were Tris, pH 8.5 (thin solid line) with a T_m of 47 °C; Na/K phosphate, pH 6.0 (dotted line) with a T_m of 51 °C; sodium citrate, pH 5.5 with a T_m of 54 °C (dashed line); and Na/K phosphate, pH 7.0 with a T_m of 58 °C (thick solid line) (in both panels). The fluorescence curves (left hand panel) reach a similar fluorescence maximum before they tail off as dye in complex with the denatured protein begins to precipitate. The full range of buffers and salt conditions used in these experiments are detailed in Methods 2.16 and the respective T_m values are reported in the Appendices 7.3.

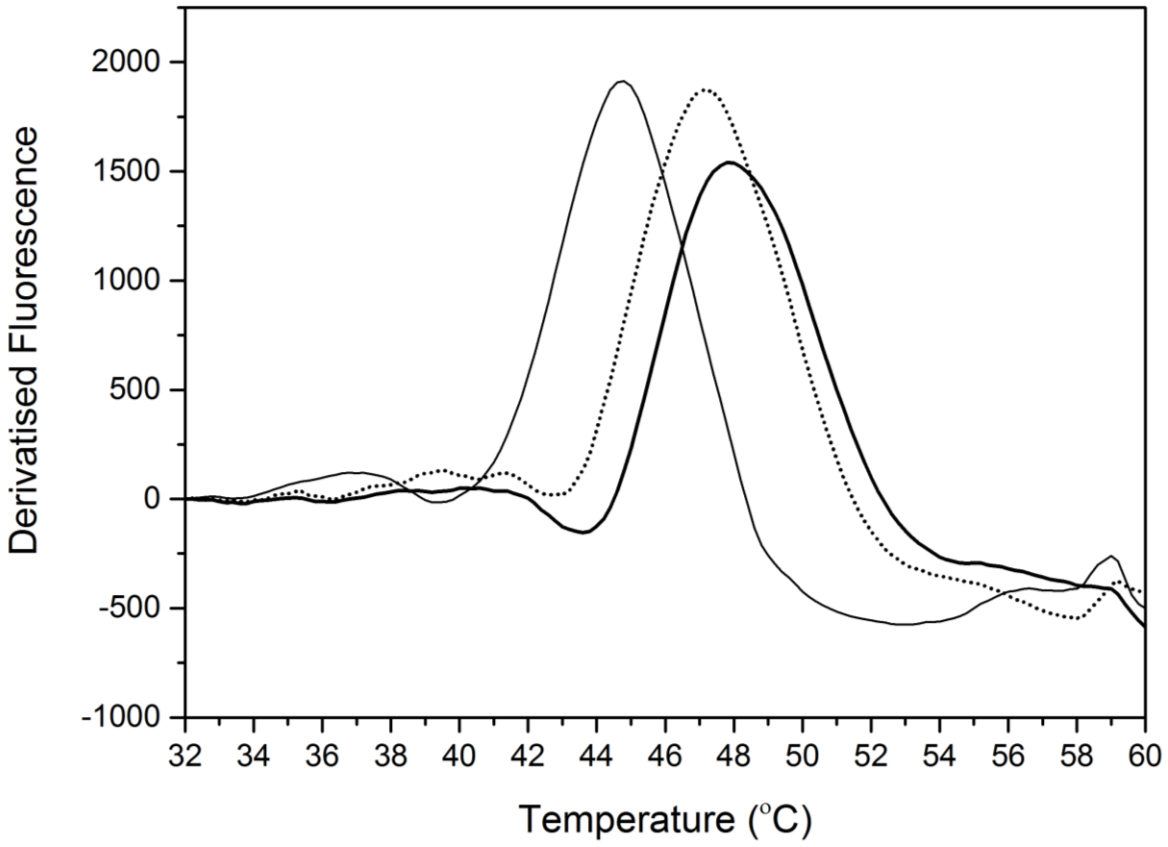

Figure 3.23 Protein unfolding of MT1 HD using differential scanning fluorimetry. Studies were done using Sypro Orange dye fluorescence to monitor MT1 HD unfolding as incubation temperature was progressively increased. Effects of different buffer systems and their pH on the stability MT1 HD were analysed. The image shows derivative curves from MT1 HD DSF curves, with the T_M values seen as the peaks of the curves. The buffer systems illustrated are Tris, pH 8.5 (thin solid line, T_m = 45 °C), Na/K Pi, pH 6.0 (dotted line, T_m = 47 °C) and Na/K Pi, pH 7.0 (thick solid line, T_m = 48 °C). The full range of buffer conditions are recorded in the Methods 2.16 and respective T_m values are listed in the Appendices 7.3.

The rather low T_m values for the isolated MT1 heme domain (i.e. the G463X mutant, MT1 HD) may reflect that, without crucial interactions with its reductase domain, the P450 domain is considerably less stable than is its counterpart in the intact P450 MT1. The interactions made by the heme domain in the P450 MT1 dimer could thus be an important source of stability for this enzyme, and account for the low apparent T_m for the isolated heme domain. Other possibilities for the lower stability of the isolated MT1 HD could be that the stop codon was placed too close to or too far away from the true end of the heme domain. However, the heme domain is readily expressed in *E. coli* and incorporates heme fully.

In further studies, the thermal stability of heme binding in P450 MT1 was also probed through the temperature dependence of decomposition of the Fe^{2+}-CO absorbance at ~450 nm (P450 form) to the P420 form (at 420 nm) (Figure 3.24).

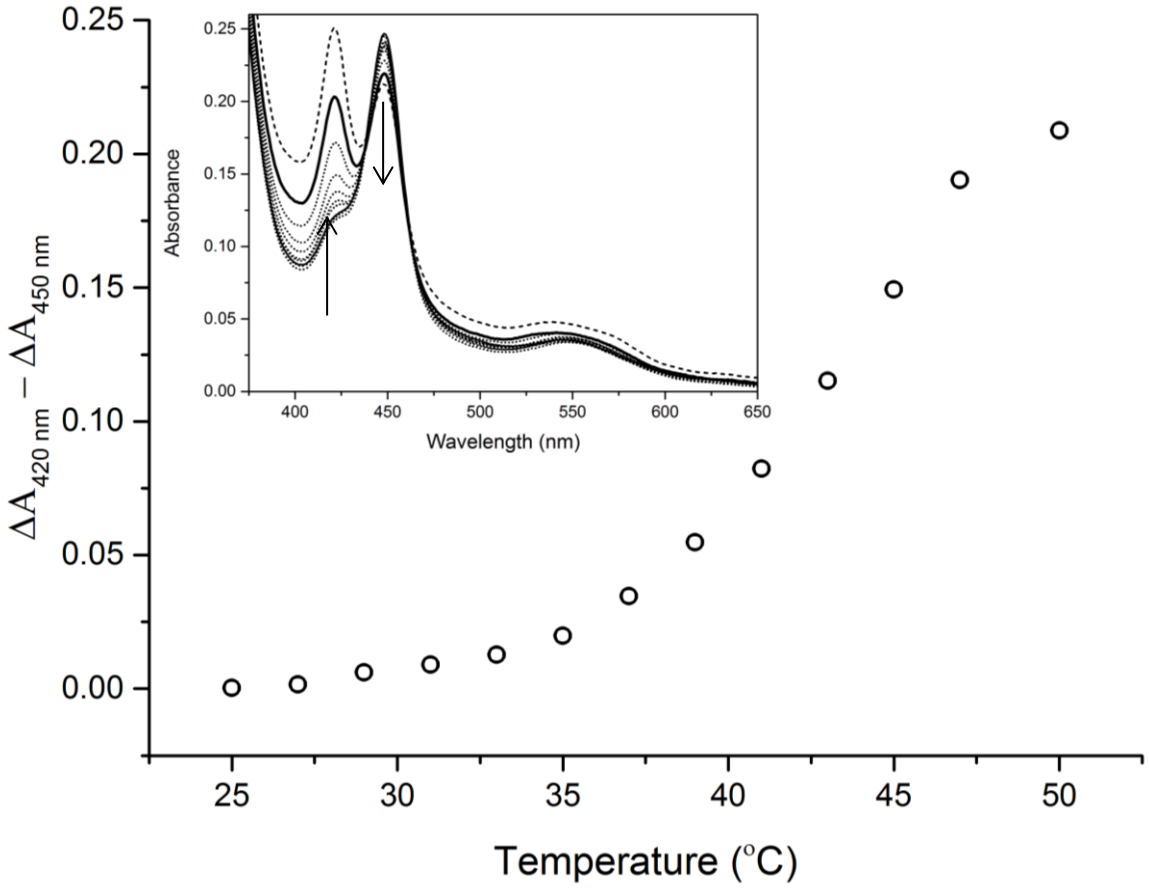

Figure 3.24 Thermal denaturation of P450 MT1 through conversion of the Fe^{2+}-CO form from P450 to P420. The absorbance spectrum of a sample of reduced, CO-bound P450 MT1 (~2.4 µM) in a sealed cuvette was measured consistently as incubation temperature was increased (inset). Difference spectra were obtained by subtracting the initial spectrum (recorded at 25 °C, thin solid line, inset) from subsequent spectra collected at increasing temperatures (dotted lines, inset). The final spectrum was obtained at 50 °C (thick solid line, inset). Maximal absorbance changes (ΔA_{420} minus ΔA_{450}) were plotted against the applied temperature. At higher temperatures, aggregation begins to occur and can be seen in the inset (e.g. the dashed line spectrum taken at 55 °C). For this reason, data points above 50 °C were omitted from the data fit in the main plot.

The P450 Fe^{2+}-CO peak collapse and the concurrent increase in the P420 species at 420 nm reflects the loss of cysteine thiolate heme iron coordination in favour of cysteine thiol ligation. This occurs as a consequence of structural disruption in the MT1 heme domain,

and precedes the dissociation of the heme and its loss from the protein matrix. Points above 50 °C were removed from the data plot as spectra collected at the higher temperatures showed interference from turbidity due to aggregated protein. However, at this temperature there was not any significant dissociation of the heme from the protein. The P450 to P420 thermal collapse clearly precedes any dissociation of heme from the MT1 protein and the full unfolding of the heme domain, which is in accordance with the values of 48 °C and 58 °C for the thermal unfolding of the MT1 HD and intact P450 MT1, respectively, from differential scanning fluorimetry analysis (Figures 3.22 and 3.23).

The changes in fluorescence of P450 MT1's flavins were also analysed as a function of increasing temperature. The fluorescence from the bound flavins changes as they become more solvent exposed and ultimately as they dissociate from the P450 MT1. Data are shown in Figure 3.25.

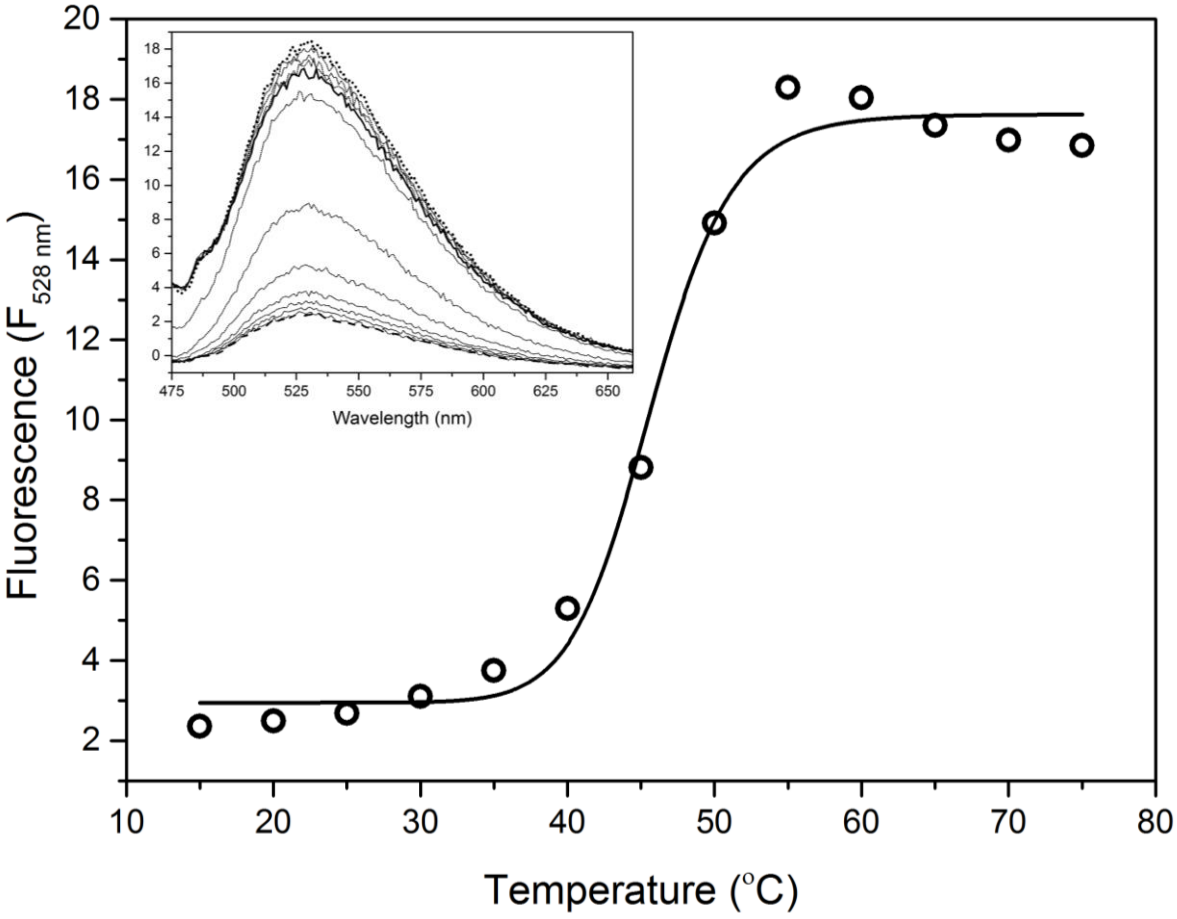

Figure 3.25 Thermal effects on flavin fluorescence in P450 MT1. Flavin fluorescence in intact P450 MT1 was analysed across the temperature range from 15-80 °C in buffer B using 7 µM P450 MT1. Excitation was at 450 nm and fluorescence spectra were recorded between 475 nm and 700 nm. The fluorescence emission spectra collected at different temperatures are shown in the inset. Spectra were monitored from 15 °C (dashed line) at increasing temperature intervals (thin solid lines) up to 80 °C (thick solid line). The maximum fluorescence emission from the flavins was at 528 nm, and F_{528} was plotted against the relevant temperature and data were fitted using the Hill function (Equation 4, Methods 2.17) to give an apparent T_m of 45.7 ± 0.5 °C with an *n* of 16.6 ± 2.9. The inset shows the final fluorescence spectrum (thick solid line) at 80 °C is of lower intensity than the fluorescence spectrum (dotted line) at 55 °C (and is also lower than other emission spectra collected at temperatures between 15 and 90 °C). High temperature is associated with fluorescence quenching, and at high temperature it is also likely that protein aggregation and precipitation affects flavin fluorescence.

As with the influence of elevated temperature on cysteine thiolate protonation and the conversion of the Fe^{2+}-CO complex from the P450 to the P420 state, changes in flavin fluorescence can be important indicators of changes in flavin environment and protein unfolding in the P450 MT1's reductase domain. The apparent T_m of 45.7 °C obtained based on P450 MT1 flavin fluorescence change is lower than that determined using Sypro Orange dye binding (58 °C). However, the flavin fluorescence value obtained is an indicator of the relative stability of the reductase domain in full length P450 MT1 and thus may reflect the lower stability of this domain of the enzyme. The quantum yield (Q_f) of fluorescence is much larger for aqueous FMN (0.27) than it is for FAD (0.032) [333], as the FAD adenine ring dynamically quenches the fluorescence from the isoalloxazine ring, implying that the majority of the fluorescence observed upon protein unfolding of intact P450 MT1 in Figure 3.25 is from FMN cofactor dissociation. However, dynamic quenching of the FAD likely does not occur in protein-bound FAD, where the cofactor adopts a more extended conformation than is the case for the free FAD in solution. FMN binds less tightly to P450 MT1 than does FAD from the HPLC analysis of flavin incorporation (Figure 3.21). The FMN would thus most likely dissociate from the P450 MT1 reductase domain at a lower temperature than does the FAD cofactor. However, the magnitude of flavin fluorescence is affected greatly by the isoalloxazine ring's environment as well as by temperature, and thus it is difficult to establish the state of flavin binding to the MT1 reductase at higher temperatures. Notwithstanding these issues, it is likely that the T_m of 46.6 °C may reflect reasonably accurately that the reductase module of P450 MT1 is less thermostable than the heme domain. Above 55 °C there is a small decrease in fluorescence as the temperature increases. This is likely due to the diminishing of fluorescence at higher temperatures due to alternative routes for energy loss in the excited flavins [334].

3.7 Discussion

This chapter covers the initial biochemical and biophysical analyses of a previously unstudied P450/P450 reductase fusion enzyme (P450 MT1) from the moderately thermophilic fungus *Myceliophthora thermophila*.

The intact P450 MT1 was expressed and purified, and P450 MT1's heme domain (MT1 HD) was also isolated by genetic dissection of the intact P450 MT1 gene through insertion

of a stop codon at the end of the heme domain. This enabled the study of the heme-binding domain in isolation, and without interference from the contributions of the flavins (FMN and FAD) to the UV-visible absorbance spectrum of the heme cofactor. The position of the stop codon at position G463 was determined by performing a sequence alignment of P450 MT1 with other similar P450-CPR fusion enzymes, and by selecting the stop codon position based on that used successfully for the generation of the isolated heme domain from P450 BM3 (CYP102A1).

The characterisations carried out on P450 MT1 and the MT1 HD covered in this chapter include bioinformatics analysis, substrate and inhibitor binding, analysis of mass and aggregation state by MALLS, flavin incorporation by HPLC, and thermodynamic properties (thermal influences on cofactor binding and protein stability). The rationale behind these studies was to identify differences between P450 MT1 and its well-studied homologue P450 BM3, including any advantages/improvements seen for this flavocytochrome enzyme from a moderately thermophilic microorganism. In particular, it was hoped that the P450 MT1 enzyme may exhibit improved catalytic activity, higher stability for biotechnological applications, and a greater propensity to crystallise for ease of structural analysis.

The substrates that exhibited a type I shift on titration with P450 MT1 and its heme domain were similar to those favoured by P450 BM3. That is, P450 MT1 substrates which show binding by heme absorbance perturbation (and catalytic activity – see Chapter 4) were saturated, polyunsaturated and branched chain fatty acids in the chain length range from C12-C18. The physiological role of P450 BM3 is not fully understood, but it is clear that this enzyme efficiently hydroxylates a wide range of fatty acid substrates [94]. As for a number of P450 BM3's substrates, the K_d values for the binding of various lipid substrates to P450 MT1 were quite similar and did not indicate a particular preference for a specific chain length. The extents of high-spin shift (95% and over in some cases) exhibited by the full length P450 MT1 and MT1 HD on binding to various branched chain fatty acids was an interesting property, possibly hinting at these molecules being P450 MT1's true substrates. Only NPG, a synthetic amino acid-derivative fatty acid, elicited a similarly extensive Soret high-spin shift in P450 MT1 (but not as extensive as in the MT1 HD). Branched chain fatty acids are crucial in maintaining membrane fluidity, which is important to organisms which have to withstand a large range of temperatures, particularly thermophiles and mesophiles [335].

P450 MT1 and the MT1 HD showed relatively tight binding of fatty acids compared to *B. megaterium* CYP102A1 (BM3) and *B. subtilis* CYP102A3. However, this is not necessarily a good indication of catalytic activity. For instance, a substrate with tight binding may actually impede enzyme activity by its product having a similarly low K_d and dissociating slowly from the enzyme, so preventing the efficient binding of a new substrate. While BM3 has a very high catalytic activity with arachidonic acid, as previously mentioned [197], CYP102A3 binds this substrate ~5 times tighter than does BM3, but shows only 10% of the activity towards it compared to BM3 [43].

With respect to interactions with inhibitors, P450 MT1 binds tightly to 1-phenylimidazole (3-fold tighter than it binds to P450 BM3), but in the case of 4-phenylimidazole this inhibitor has a K_d value 10-fold lower than that for P450 MT1 [326,327]. These differences in substrate/inhibitor binding suggest that the P450 BM3 and P450 MT1 enzymes have important differences in their active site structures that significantly affect ligand binding. Unlike BM3, P450 MT1 was also shown to bind the large, non-polar econazole and bifonazole antimicrobial drugs relatively tightly, which suggest that P450 MT1's active site can accommodate both large and polar molecules.

The differences in ligand-binding K_d values obtained for P450 MT1 and the MT1 HD suggest that (like intact P450 BM3) the intact P450 MT1 may be present as a dimer in solution, and that dimerization affects P450 domain active site structure and substrate affinity. P450 MT1 was analysed using MALLS, and these studies showed it to be present as a highly monodisperse dimer. It is likely that the dimerization is driven at least in part from the reductase domain, as the MT1 HD was essentially monomeric by MALLS analysis. This phenomenon has been previously reported for its homologue P450 BM3, where the heme domain is monomeric but the intact P450 BM3 is a dimer [240].

Full heme incorporation into P450 MT1 was shown to be an issue from early studies on the enzyme. Alterations were made to the expression and purification protocol and it was found that the Rz value could be increased from 0.3 to ~0.5, but full heme incorporation was not achieved. This finding had implications for the extinction coefficient used to determine the concentration of P450 MT1, ε_{420} = 105 mM^{-1} cm^{-1} (with reference to the BM3 coefficient) which results mainly from the intensity of the low-spin heme Soret peak. Issues with inaccuracy arise here due to incomplete heme incorporation in P450 MT1. HPLC was used to determine the flavin content of P450 MT1, and showed near-

stoichiometric amounts of FAD and FMN bound. The ε_{456} = 24.1 mM^{-1} cm^{-1} coefficient was established as a more consistently accurate route to determining the true enzyme concentration, and was used (see chapter 4) for studies of enzyme kinetics involving electron transfer through the reductase domain of P450 MT1.

Stability studies on both intact P450 MT1 and the MT1 HD used thermal differential scanning fluorimetry to monitor structural stability and perturbations to flavin binding in P450 MT1 (and its heme domain in the former case). A buffer screen showed that P450 MT1 was most stable in Na/K phosphate buffer at pH 7.0 with a T_m of 58 °C, while the MT1 HD in the same conditions exhibits a T_m of 48 °C. Influence of ionic strength (through various conditions with addition of salts) on P450 MT1 thermal stability was also examined, and a trend of increased stability with increasing salt concentration emerged, but was only observed in buffers that otherwise showed lower T_m values. The binding of substrates and inhibitors was also evaluated, and K_d values were determined for a range of different ligands.

The P450 MT1 heme domain had a relatively low T_m (45.7 °C) from DSF studies done using Sypro Orange binding. The T_m of the intact enzyme is much higher, and thus it appears likely that the enzyme is stabilised in its dimeric form and that the heme domain is more stable in intact P450 MT1 through interactions with domains of the other monomer. In the case of P450 BM3, its heme domain has reported T_m values as high as 65 °C [93], although the intact BM3 enzyme's stability is much lower [287]. This appears not to be the case for the MT1 HD, which is less thermostable than the full length enzyme, again pointing to the importance of the dimeric form as the more stable and catalytically relevant state of P450 MT1.

The initial characterisation of the P450 MT1 enzyme outlined in this chapter reveal many of its fundamental thermodynamic, spectroscopic and ligand binding features. Chapter 4 explores other aspects of P450 MT1, including kinetic properties and fatty acid product analysis.

Chapter 4: Biochemical and biophysical characterisation of P450 MT1 (CYP505A30).

4.1 Introduction

After initial studies confirming MT1 as a soluble FAD- and FMN-containing cytochrome P450/diflavin reductase (CPR) fusion enzyme in Chapter 3, a broader set of techniques was employed to further characterise the catalytic properties of P450 MT1. BM3 is widely accepted as the "model" enzyme in MT1's P450-CPR fusion enzyme class. BM3 has also set the benchmark for catalytic rates in these types of P450-CPR enzyme, and indeed it has the highest reported monooxygenase activity of any cytochrome P450 enzyme (285 s^{-1} with arachidonic acid as substrate) [271]. Stopped-flow absorption spectroscopy experiments determined the FMN-to-heme electron transfer rates in BM3 as ~250 s^{-1}, likely identifying this as the major rate-limiting step in the BM3 catalytic cycle [336].

Following from these earlier studies on the P450 BM3 enzyme, kinetic studies on the P450 MT1-dependent oxidation of fatty acid substrates were done in conjunction with stopped-flow absorbance kinetic experiments. These experiments were done to determine (i) the steady-state kinetic parameters (k_{cat} and K_m values) for P450 MT1 in reactions with a range of fatty acid substrates; and (ii) the apparent FMN-to-heme electron transfer rate constant in P450 MT1 in order to compare these values with those of P450 BM3. In studies presented in this chapter, the monooxygenation activity observed for P450 MT1 was found to be far lower than that for P450 BM3 with all the fatty acid substrates tested. From transient kinetic studies, the first FMN-to-heme electron transfer rate constant in P450 MT1 was found to be approximately double that of the rate constant for steady-state NADPH oxidation with NPG and arachidonic acid, suggesting that this step may also make a major contribution to rate limitation in the P450 MT1 enzyme.

The CYP102A family (P450-CPR fusion enzymes) all bind NADPH preferentially over NADH (i.e. have lower K_m/K_d values for NADPH), as does P450 MT1's well characterized orthologue CYP505A1 $P450_{foxy}$ [43,244,337]. P450s MT1's coenzyme specificity for NADPH/NADH was investigated experimentally using steady-state kinetics (with non-physiological electron acceptors) and stopped-flow absorption spectroscopy. As predicted by bioinformatics tools and relationships with other characterized CYP102A and CYP505 enzymes, tighter binding of NADPH over NADH was observed in P450 MT1, accompanied by faster steady-state rate constants with NADPH in P450 MT1.

As in BM3, the electron transfer pathway in the P450 MT1 enzyme starts with NADPH-dependent electron transfer (as a hydride ion) to FAD, and then two single electron transfers from FAD (the hydroquinone and then the semiquinone) through the FMN (using the anionic semiquinone) and finally to the heme iron (Section 1.12, Figure 1.15) [135]. P450 BM3 is a dimer, and electron transfer occurs from the FMN domain of one monomer to the heme domain of the other monomer [240]. In this work, stopped-flow absorbance spectroscopy, redox potentiometry and steady-state kinetic analysis have all been used in efforts to determine the electron transfer rate constants in P450 MT1 and to establish the midpoint potentials of P450 MT1's cofactors. The characterisation of the semiquinones formed on MT1's flavin cofactors features prominently in this chapter, due to the importance of semiquinone formation in the electron transfer pathways of BM3 and other CPR enzymes. In BM3, fully reduced $FADH_2$ shuttles an electron to FMN, resulting in the concurrent formation of two semiquinone species; a neutral, blue FADH semiquinone and a short-lived anionic, red $FMNH^-$ semiquinone (Figure 4.1) [221,338]. In BM3 this red, anionic $FMNH^{\bullet}$ semiquinone is thermodynamically stabilised and is the species responsible for electron transfer to the heme domain [339]. This contrasts with eukaryotic CPR enzymes in which the FMN forms a neutral, blue semiquinone (FMNH) and where it is the fully reduced $FMNH_2$ hydroquinone species that is responsible for heme iron reduction [340]. On the other hand, the FAD cofactor was shown to stabilise a blue, neutral FADH semiquinone in both types of enzyme [27,218].

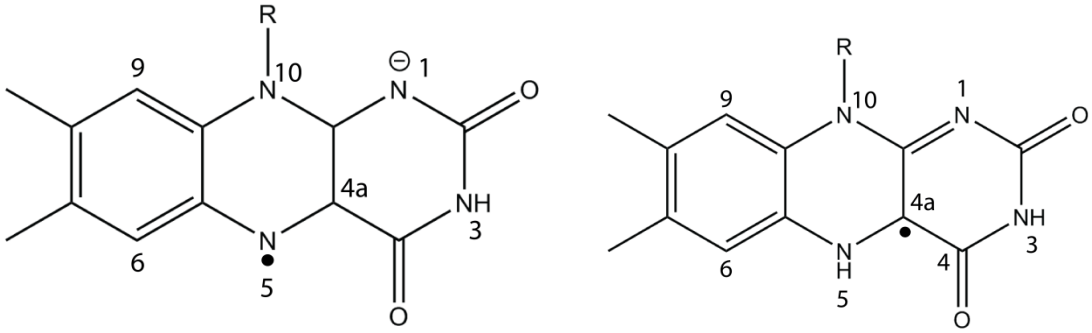

Figure 4.1 Isoalloxazine ring scheme showing the two 1-electron reduced semiquinone species. Ring positions are numbered 1 – 10. Red, anionic semiquinone (left) has a negative charge on its N1 nitrogen and the radical is located at the N5 position on its isoalloxazine ring. Blue, neutral semiquinone has no negative charge associated with it and its radical is located on the 4a carbon. In solution they exist in equilibrium with a pK_a of 8.5 [220].

The difference between red, anionic $FMNH^{\cdot}$ semiquinone stabilisation in the BM3 CPR module and blue, neutral FMNH semiquinone stabilisation in eukaryotic CPR enzymes can be traced to a conserved glycine residue (G141 in human CPR) which is absent in BM3 [173,223]. The increased flexibility in this *re*-face orienting loop allows the 'flipping' of the G141 carbonyl group in CPR to hydrogen bond the NH on position N5 of the ring, stabilising the one electron reduced, blue, neutral semiquinone species; although this interaction is not evident in the oxidised state [224,341]. In contrast, the YNGH loop (Figure 4.2) forms a rigid β-turn with N537 poised for hydrogen bonding to the N5 nitrogen on the FMN ring [223]. This hydrogen bonding would favour the anionic semiquinone over the neutral species and the structural rigidity of the β-turn in BM3 would prevent any conformational change to stabilise the fully reduced hydroquinone species. NMR evidence suggest that the N5 atom moves out of the plane of the isoalloxazine ring to avoid these unfavourable steric interactions, allowing the β-turn to remain in place [298]. Elegant mutagenesis experiments confirmed that the insertion of a glycine residue at this position in BM3 switched its preference to blue semiquinone stabilisation, as in CPR [342]. The deletion of the corresponding glycine residue in NOS, which stabilises the neutral semiquinone as in CPR, had the opposite effect [343].

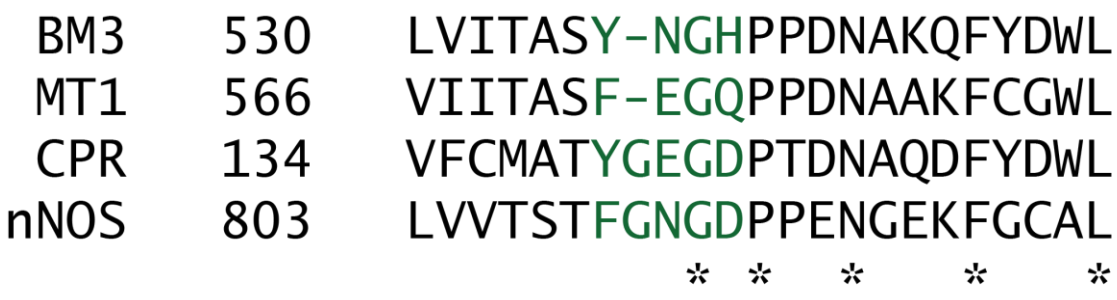

Figure 4.2 Amino acid sequence alignment for the FMN *re*-face binding loop in P450 BM3, P450 MT1, CPR and nNOS. Sequences are shown for P450 BM3 from *B. megaterium*, P450 MT1 from *M. thermophila*, CPR from *Homo sapiens* and neuronal NOS (nNOS) from *Rattus norvegicus*. The residues coloured green compose the loop which orients the *re*-face of the FMN cofactor. Asterisks denote conserved residues in enzymes listed. The otherwise conserved glycine reside is absent in both P450 MT1 and P450 BM3.

Both P450 BM3 and the MT1 P450-CPR fusion enzyme likely have a common ancestor that evolved via the fusion of their three separate domains. That is, the CPR module of these enzymes is considered to originate from the fusion of NAD(P)H-dependent ferredoxin/flavodoxin reductase-like and flavodoxin-like protein-encoding genes to form a CPR [202], followed by the fusion of the respective P450 and CPR genes to form the BM3 and P450 MT1 [205]. While P450 MT1 originates from a eukaryote, its reductase domain has higher sequence identity to that of the prokaryotic BM3 reductase (33%) than to human CPR (29%). P450 MT1 and BM3 show highly conserved sequences involved in flavin cofactor binding (Section 3.1.2). Importantly, P450 MT1, like BM3, lacks a residue corresponding to G141 in eukaryotic CPR enzymes, and thus probably also stabilises a red anionic FMN semiquinone, as opposed to the blue (neutral) FMN semiquinone found in eukaryotic CPRs (Figure 4.2). The catalytically active anionic FMN semiquinone in BM3 may be a more efficient electron transfer mediator (compared to the neutral semiquinone or hydroquinone) which could contribute to its high catalytic activity [342]. The rigidity of the β-turn in BM3 allows the cycling of oxidised and anionic semiquinone states of the FMN cofactor without the need for structural changes in the protein, which would take a larger toll energetically, and this could play a role in BM3's high catalytic activity [271,298]. Additionally, the catalytically inactive, disfavoured hydroquinone FMN oxidation state in BM3 could be a form of control over activity during substrate absence or oxygen depletion [222].

The physiological role of BM3 in *B. megaterium* is not fully understood and, while it is known to bind to and oxidize a range of lipids, the purpose of such reactions *in vivo* remains obscure. Suggestions include roles in oxidation/detoxification of branched chain or polyunsaturated fatty acids [43,197]. Several straight chain fatty acids are known to be substrates of P450 BM3, and the enzyme binds (with induction of a shift of heme iron spin-state towards high-spin) and hydroxylates efficiently a range of saturated fatty acids (~C11-C18) in the ω-1, ω-2 and ω-3 positions. Prior to the characterization of P450 BM3 and its adoption as a model system for eukaryotic P450s and for P450-CPR interactions, the major bacterial model P450 system studied was $P450_{cam}$ (CYP101A1) from *Pseudomonas putida*, the first bacterial P450 to be purified and to be crystallised, leading to the determination of its 3-dimensional structure [89,107]. In $P450_{cam}$, *D*-camphor is undoubtedly its true substrate, as camphor oxidation is well coupled to NADH oxidation through its FAD-dependent putidaredoxin reductase and 2Fe-2S cluster-binding ferredoxin

(putidaredoxin) partner, and since $P450_{cam}$ expression in *P. putida* is also induced by camphor, as is the expression of a suite of other genes involved in camphor metabolism encoded on the transmissible CAM plasmid [344]. Expression of the BM3 (*CYP102A1*) gene may not be induced by straight chain fatty acids, but evidence was presented for the binding of branched chain fatty acids (and other lipids) to the BM3R1 repressor protein in order to displace this protein and enable BM3 gene expression [345]. While *in vitro* studies show some variability in the extent of coupling of NADPH oxidation to hydroxylation of saturated fatty acids, in general BM3 is a highly efficient enzyme and generates substantial amounts of hydroxylated fatty acids from these substrates, confirming that these are likely substrates *in vivo* [346,347].

As discussed above, it has been argued that polyunsaturated fatty acids could be BM3's natural substrates as they do induce expression of *CYP102A1* in *B. megaterium*, and BM3 has its highest reported activity towards the polyunsaturated arachidonic acid (C20:4) [271,348,349]. Selected branched chain fatty acids also show good coupling of NADPH oxidation to substrate oxidation in BM3, accompanied by high *regio*- and *stereo*-specificity of substrate oxidation [350]. They also induce *CYP102A1* gene expression and account for 90% of the fatty acid content in *B. megaterium*, making them very plausible physiological substrates [345,351]. The products formed from saturated and branched chain fatty acids are similar in terms of the ω-1, ω-2 and ω-3 positions being favoured for hydroxylation [350,352], although BM3 can also catalyse epoxidation across double bonds in fatty acids, as reported e.g. in the case of arachidonic acid [197].

The catalytic properties of the P450 MT1 protein were determined with respect to their ability to oxidise a range of fatty acid substrates, and GC-MS was used to determine the products formed and the regioselectivity pattern of substrate hydroxylation observed for *M. thermophila* P450 MT1 in comparison to that observed for the BM3 enzyme. These studies provide further insights into the physiological functions of P450 MT1, as well as some unusual changes in regioselectivity of fatty acid hydroxylation with alteration in chain lengths of saturated lipid substrates.

4.2 Electron Paramagnetic Resonance (EPR) Studies

4.2.1 EPR studies on low spin and high spin ferric heme in MT1 and MT1 HD

EPR studies of CYP505A30 P450 MT1 were conducted to probe its heme and cofactor environment in different conditions. Samples of P450 MT1 were prepared as described in the Methods (Section 2.19) and a saturating amount of substrate (at a concentration at least 5 times their K_d plus the concentration of P450 MT1) was used for the substrate-bound samples.

The substrate-free P450 MT1 spectrum in Figure 4.3 (top) has a typical rhombic trio (g-values = 2.41, 2.24 and 1.92) that is associated with the low-spin cysteine-ligated heme, as seen in all P450s to date [322,353]. While the UV/Visible absorbance spectra for arachidonic acid-bound P450 MT1 showed almost full conversion to high-spin (Section 3.3.2), the EPR spectrum of P450 MT1 with arachidonic acid in Figure 4.3 (bottom) was essentially unchanged compared to the substrate-free form (top). Substrate binding to enzymes under the experimental conditions used with cryogenic EPR temperatures (10 K) might promote substrate dissociation, especially if substrate binding is considered to be thermodynamically favourable. However, perhaps more likely is that at 10 K the low-spin state is favoured regardless of whether substrate is present or not. The g-value of 3.50 is indicative of a contaminating iron species present in the buffer and the g-value of 2.004 denotes the presence of a tiny amount of flavin semiquinone species present in both samples, but to a lesser extent in the arachidonic acid-bound P450 MT1 sample. No exogenous reductant was added to the purified P450 MT1 EPR sample, and so it is assumed that the semiquinone (likely FAD) accumulated during P450 MT1's expression in *E. coli* cells, and that a small amount remained stabilised in the final purified sample. Eukaryotic CPRs often stabilise a blue FMN semiquinone species in their resting state, due to the positive potential for the formation of this species and the poor reactivity of this species with molecular oxygen. The total number of electrons that are cycled through the flavins in these enzymes during their catalytic process are 1-3-2-1 in eukaryotic CPR (resulting from the air-stable FMN semiquinone in the resting state and the FMN hydroquinone as the heme-reducing species) as opposed to the 0-2-1-0 cycle seen in the reductase domain of BM3 (with the anionic FMN semiquinone reducing the hem iron, and a fully oxidised starting form) [117].

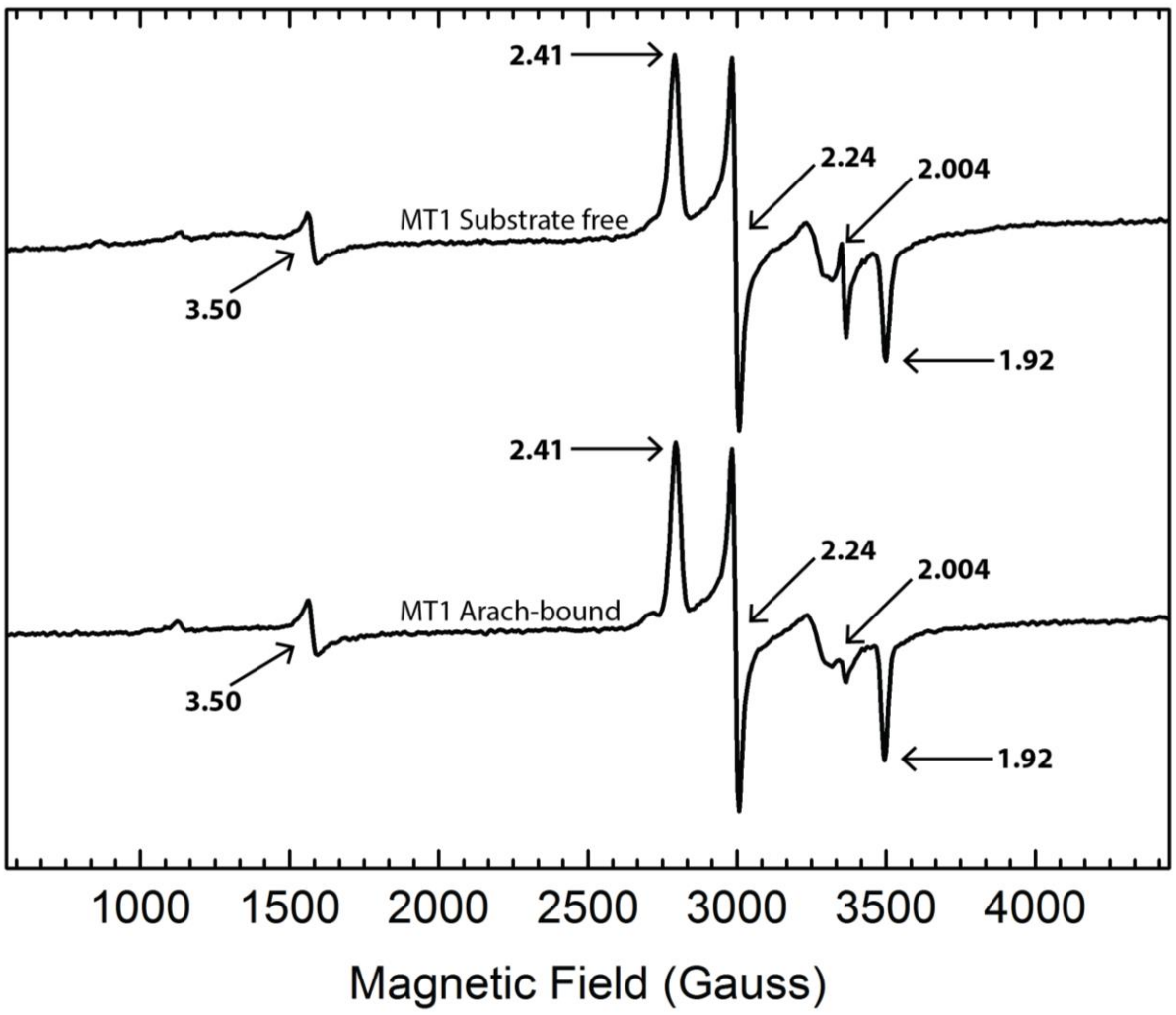

Figure 4.3 EPR spectra of substrate-free and arachidonic acid-bound P450 MT1 samples. The EPR spectrum of substrate-free (top) P450 MT1 sample is almost identical to that for the sample containing 1 mM arachidonic acid ("Arach", bottom). The g-values (labelled for the ferric heme signal) determined for both samples are identical: g_z = 2.41, g_y = 2.24 and g_x = 1.92, indicating a low-spin cysteine thiolate-ligated ferric heme iron. The g-value of 3.50 present at 1500 Gauss is typical of an iron contaminant in the buffer. A small amount of flavin semiquinone with a g-value of 2.004 is observed in both spectra. The concentration of P450 MT1 enzyme in each sample is 225 µM in 50 mM KPi (pH 7.0) buffer containing 500 mM KCl.

The substrate-free EPR spectrum of the MT1 HD in Figure 4.4 (top) displays a small proportion of high-spin heme iron, as seen by its g_z value at 8.01. In the low-spin form, the g_z = 2.41 feature has a shoulder at 2.42, a feature that is absent in the substrate-free EPR spectrum of the full length P450 MT1 (Figure 4.3, top). The EPR spectrum for arachidonic acid substrate-bound form of MT1 HD (Figure 4.4, bottom) also has the shoulder at g_z = 2.42 and a larger, shifted high-spin g_z feature at 8.03, suggesting a slightly greater proportion of high-spin heme iron for the arachidonic acid-bound form of the MT1 HD.

In Section 3.3.2, it was observed that the removal of the reductase domain elicited tighter substrate binding in MT1 HD for all substrates trialled, by an average of ~5.5 µM compared to the full length P450 MT1. The rather tighter binding observed for the MT1 HD suggests that it could have been co-purified with a small amount of bound substrate (more so that for the intact P450 MT1), and this phenomenon may be responsible for the high-spin ferric g-value at 8.01. In this scenario, the substrate would not have been removed from the MT1 HD by the extensive dialysis and hydrophobic column washes (Methods 2.7.4 and 2.13) that successfully achieved the fully low-spin full-length P450 MT1 sample. In the UV/Visible substrate titration experiments (Section 3.3.2), the MT1 HD bound to arachidonic acid (K_d = 120 nM) >10 times tighter than to P450 MT1 (K_d = 1.7 µM). This tighter binding could explain the high-spin component observed in the EPR spectrum of arachidonic acid-bound MT1 HD, but not in the EPR spectrum for P450 MT1. The removal of the reductase domain could also affect the hydrogen bonding network around the distal water in the MT1 HD. This might make the distal water more susceptible to dissociation, even in absence of substrate, which could explain the minor high-spin features seen in the substrate-free MT1 HD spectrum (Figure 4.4, top).

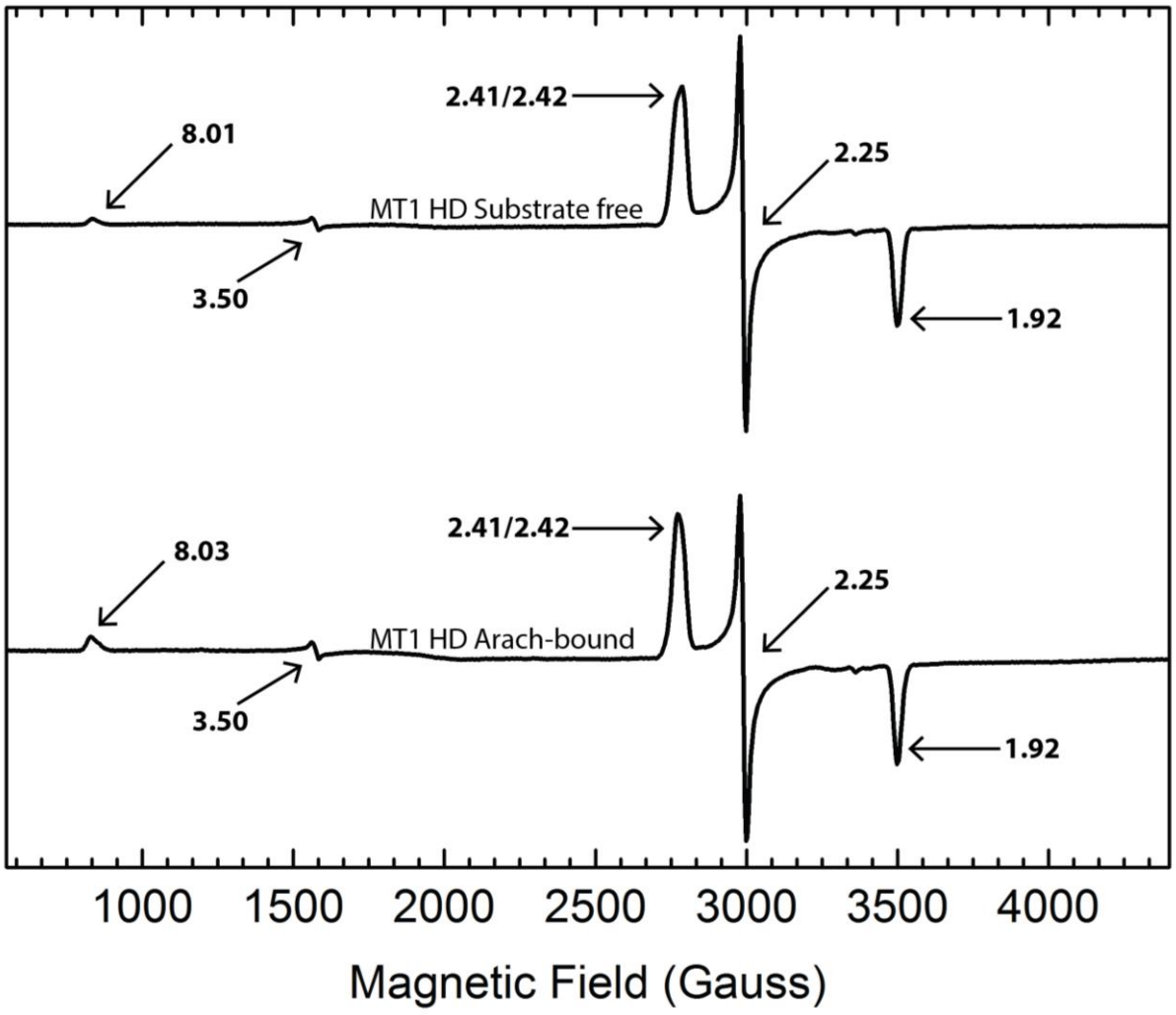

Figure 4.4 EPR spectra for substrate-free and arachidonic acid-bound MT1 HD samples. The substrate free sample of MT1 HD (top) shows characteristic g-values of g_z = 2.41 (shoulder = 2.42), g_y = 2.25 and g_x = 1.92 associated with thiolate-coordinated, low-spin ferric heme iron. The g-value of 8.01 is indicative of a small amount of high-spin heme present in the substrate-free sample. The arachidonic acid ("Arach")-bound sample of MT1 HD (bottom) has identical low-spin g_z, g_y and g_x values to the substrate-free MT1 HD (top). However, it has a slightly larger proportion of a high-spin ferric species with a g-value of 8.03. The signal present at ~1500 Gauss is typical of an iron contaminant in the buffer. The concentration of enzyme in each sample is 225 µM in 50 mM KPi (pH 7.0) buffer containing 500 mM KCl.

4.2.2 Investigation of semiquinone formation in P450 MT1 using EPR

The effects of reductant on semiquinone formation and stabilisation in P450 MT1 was investigated using EPR, as only the semiquinone flavin species are visible in the EPR spectrum, since the technique measures the magnetic dipole of single unpaired electrons. Bioinformatic and HPLC studies (Section 3.1.2 and 3.5) confirmed that the two flavin cofactors (FAD and FMN) are present in stoichiometric amounts in the reductase domain of P450 MT1. The flavins are able to undergo a two state change upon reduction; from fully oxidised flavin to a single electron reduced semiquinone flavin, and from the semiquinone to a two electron reduced hydroquinone (Section 1.12.3).

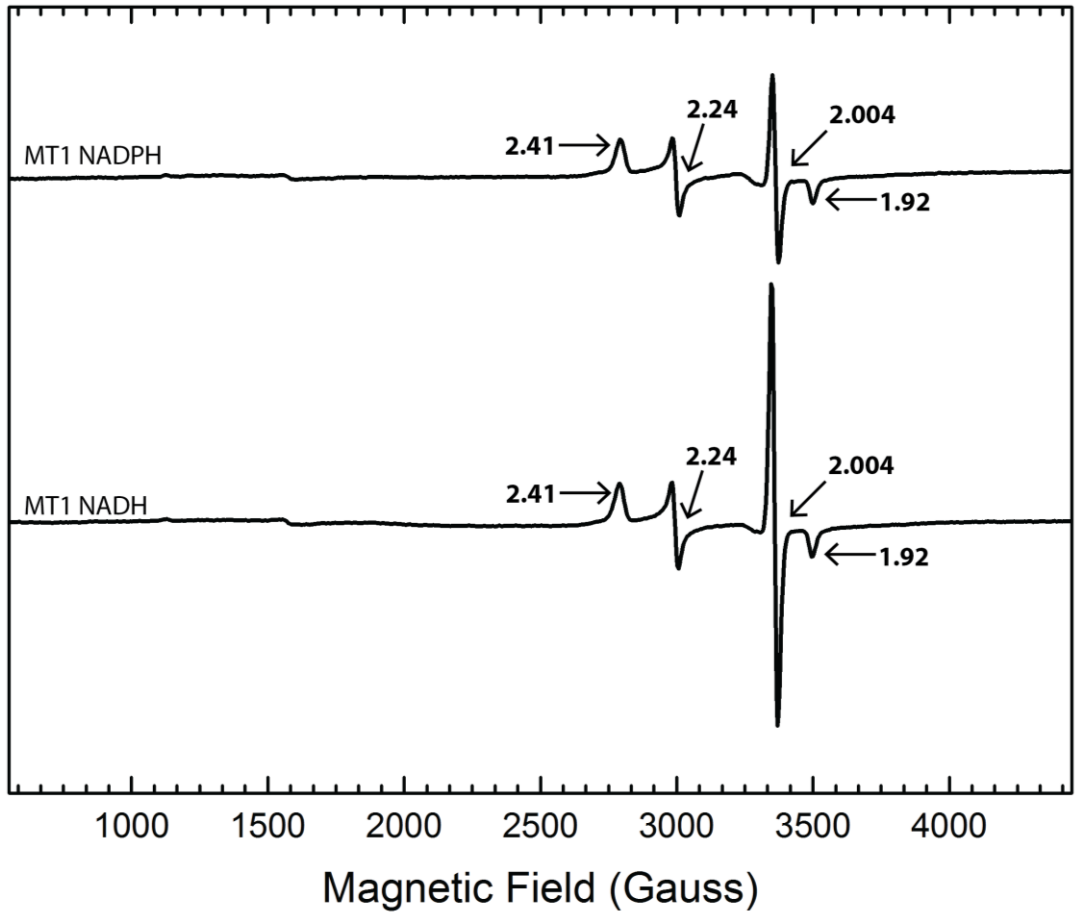

Figure 4.5 EPR spectra of P450 MT1 incubated with NADH and NADPH. Flavin semiquinone signals are present in the EPR spectra for the P450 MT1 samples incubated with both NADPH (top) and NADH (bottom), appearing as derivative signals at 3350 Gauss with a g-value of 2.004. The heme features in both spectra also have identical g-values of 2.41/2.25/1.92 associated with low-spin, cysteine thiolate-ligated ferric heme iron. P450 MT1 was at 225 µM in 50 mM KPi (pH 7.0) buffer containing 500 mM KCl, with NADPH and NADH each added at final concentration of 1 mM.

Figure 4.5 shows semiquinone formation in P450 MT1 on its incubation with NADPH and NADH (labelled). The semiquinone formed in both spectra has a characteristic g-value of 2.004, identical to those seen in Figure 4.1. Reduced (ferrous, Fe^{2+}) heme is EPR silent, but a low-spin heme iron EPR spectrum is clearly seen for both NADPH- and NADH-reduced P450 MT1, which indicates that in absence of fatty acid substrate NAD(P)H cannot reduce the heme iron. The low-spin ferric heme signatures are seen with typical g-values of g_z = 2.41, g_y = 2.24 and g_x = 1.92, and are still present in both spectra in significant amounts.

BM3 exhibits diminished activity if incubated with NADPH in the absence of substrate, a property which has been attributed the "overloading" of the reductase domain with electrons to a 3- or 4-electron reduced state in which the FMN is in the hydroquinone state [67]. EPR analysis of a catalytically active form of BM3 showed two semiquinone species present: a blue, neutral semiquinone and a red, anionic semiquinone [226]. Early redox potentiometry experiments previously confirmed that the FAD forms a blue semiquinone in full length BM3, while later stopped-flow absorbance experiments provided evidence that BM3's isolated FMN forms a transient red, anionic semiquinone, which has been attributed as the catalytically relevant electron transfer species to the heme iron [27,222,339].

The proportion of flavin semiquinone stabilised by P450 MT1 upon incubation with NAD(P)H and also with sodium dithionite was investigated using EPR. Samples of P450 MT1 prepared with excess reductant were incubated for different lengths of time (Methods 2.19.2). Using a copper standard of known concentration in the EPR experiments, the amount of semiquinone formed by P450 MT1 could be quantitatively calculated. The 2 forms of semiquinone have identical g-values of 2.004. However, they can be identified in the first derivative spectra of their EPR spectra by the difference in line widths (G) of their peaks and troughs [354]. Neutral, blue semiquinone has a characteristic 19 G line width, anionic semiquinone has a characteristic 15 G line width, while mixtures of the two semiquinones will have an intermediate G value.

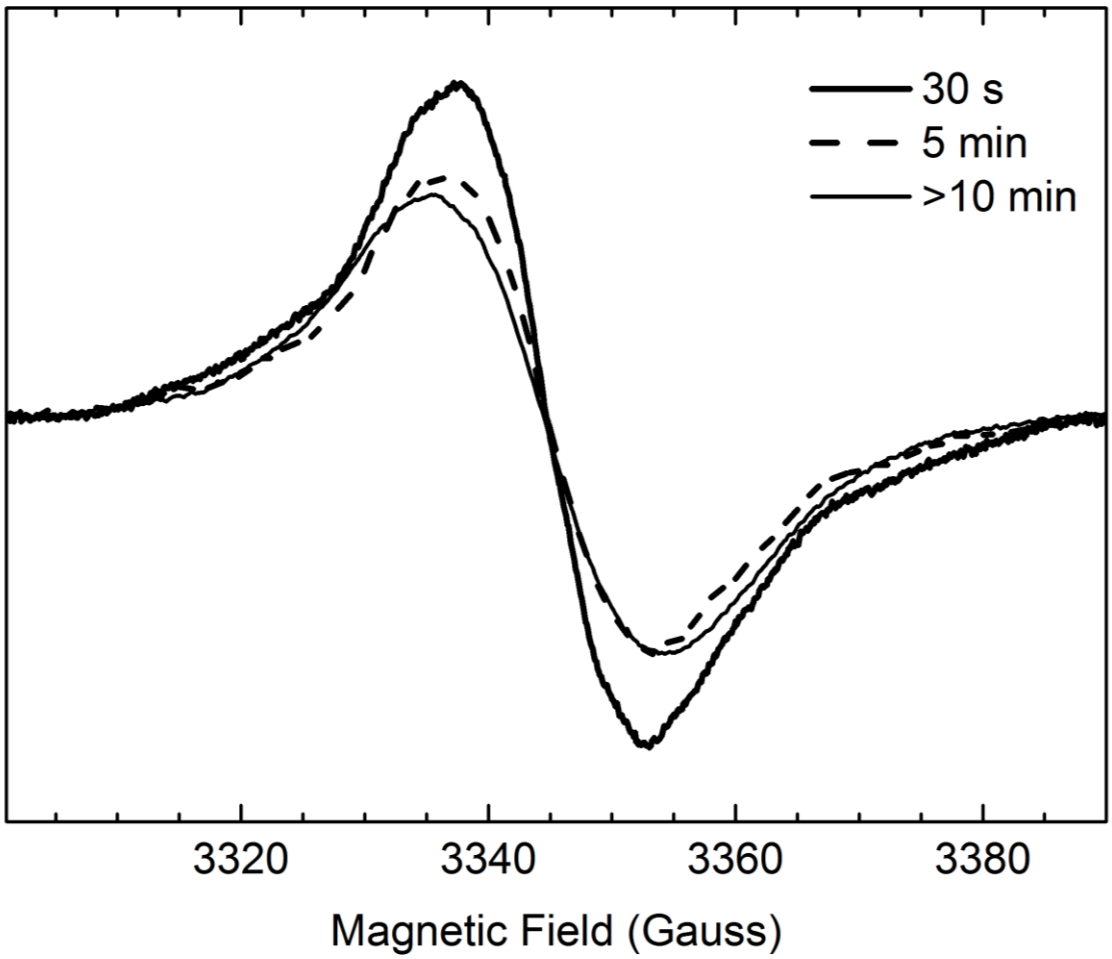

Figure 4.6 Characterisation of P450 MT1 flavin semiquinone by EPR spectroscopy. Overlaid first derivative EPR spectra for P450 MT1 are shown after various incubation times (legend) with NADPH: 30 s (thick solid line), 5 min (dashed line) and >10 min (thin solid line), showing formation of 150.9 µM, 119.9 and 120 µM of semiquinone, respectively. The Gaussian split of the semiquinones formed were 15.83 G, 16.8 G and 19 G for the 30 second, 5 minute and >10 minute sample incubations, respectively. The concentration of enzyme in each sample is 190 µM in 50 mM KPi (pH 7.0) buffer containing 500 mM KCl, and NADPH was present at 2 mM.

The amount and type of semiquinone formed on the incubation of P450 MT1 with NADPH for 30 seconds, 5 minutes and over 10 minutes is shown in Figure 4.6. After 30 s incubation time with NADPH, the first derivative EPR spectrum had a Gaussian split of 16.3 G, indicative of a mixture of blue and red semiquinone and similar to the value obtained for catalytically active BM3 [354]. This suggests that both the FAD and the FMN cofactor are present in their single electron reduced semiquinone states (blue and red, respectively) when active. A similar line width of 16.1 G is observed with NADH

incubation, but not with dithionite incubation which shows semiquinone with a Gaussian split of 14.43 G, typical of only red, anionic semiquinone formation in the sample (Table 4.1). Significant levels of semiquinone were present in all the samples for NADH- and NADPH-reduced P450 MT1, and are comparable to the ones obtained for BM3 [354]. At the 5 minute incubation point, the Gaussian split values for NADPH and NADH still show a mixture of semiquinone species present. However, they are slightly shifted at 16.8 G each as more neutral (blue) semiquinone accumulated. The amount of semiquinone present after a 5 minute incubation with dithionite is greatly reduced at only 0.01 mole semiquinone per mole enzyme, but still apparently formed entirely from red semiquinone. After 10 minutes incubation, it is evident that there is no anionic red semiquinone left in either of the NADPH- or NADH- reduced samples, as both have a Gaussian split of 19 G characteristic of neutral blue semiquinone. This is consistent with the exclusively blue semiquinone in BM3 seen on incubation with NADPH and NADH in absence of substrate, and is attributed to its over-reduced inactive state, and to blue semiquinone on the FAD cofactor [226,354]. There is no semiquinone formed after 10 minutes incubation with dithionite, likely resulting from the formation of the fully reduced hydroquinone species in both the FAD and FMN cofactors, due to dithionite's strong reducing potential.

Table 4.1 A qualitative and quantitative comparison of flavin semiquinone formation in P450 MT1. The table shows the Gaussian split (G) of the first derivative plots and amount of semiquinone (SQ) formed per mole enzyme with varying incubation times for three separate reducing agents. Values in parenthesis denote the qualitative classification of semiquinone species from their Gaussian split value (G) [354]. 'Red' indicates only red, anionic semiquinone present, 'blue' indicates only blue, neutral semiquinone present, while 'int' indicates an intermediates mixture of the two present.

Reducing agent	Incubation time	SQ (mol/mol)	Gaussian split (G)
NADPH	30 s	0.81	16.3 (int)
NADPH	5 min	0.59	16.8 (int)
NADPH	>10 min	0.60	19 (blue)
NADH	30 s	0.79	15.9 (int)
NADH	5 min	0.62	16.8 (int)
NADH	>10 min	0.59	19.1 (blue)
Dithionite	30 s	0.21	14.4 (red)
Dithionite	5 min	0.01	14.4 (red)
Dithionite	>10 min	N.D.	N.D.

4.3 Redox Potentiometry

Redox potentiometry was employed to investigate the reduction potentials of P450 MT1's three bound cofactors: heme, FMN and FAD. The UV/Visible absorbance spectra of the oxidised and reduced forms of these cofactors overlap, as can be seen in Figure 3.12 (Section 3.3), however if their midpoint potentials are distinct enough, then the spectral changes may be deconvoluted.

These studies detailed in Methods (Section 2.20) were performed anaerobically to prevent reoxidation of the enzyme by atmospheric oxygen, and with mediators present to better facilitate electron transfer between the P450 MT1 redox centres, the electrode and the reductant. A UV/Visible spectrum along with the measured reduction potential was recorded initially, and then after each addition of sodium dithionite (a strong reducing agent, E°' = -420 mV) until the enzyme was fully reduced. For all redox potentiometry experiments carried out with substrate, near-saturating conditions of arachidonic acid (>10x the K_d plus the enzyme concentration) in 50 mM KPi (pH 7.0) buffer containing 200 mM KCl supplemented with 10% glycerol. The reduction potential of P450 MT1's flavin cofactors (FMN and FAD) was investigated both in the presence and the absence of substrate (Figure 4.5).

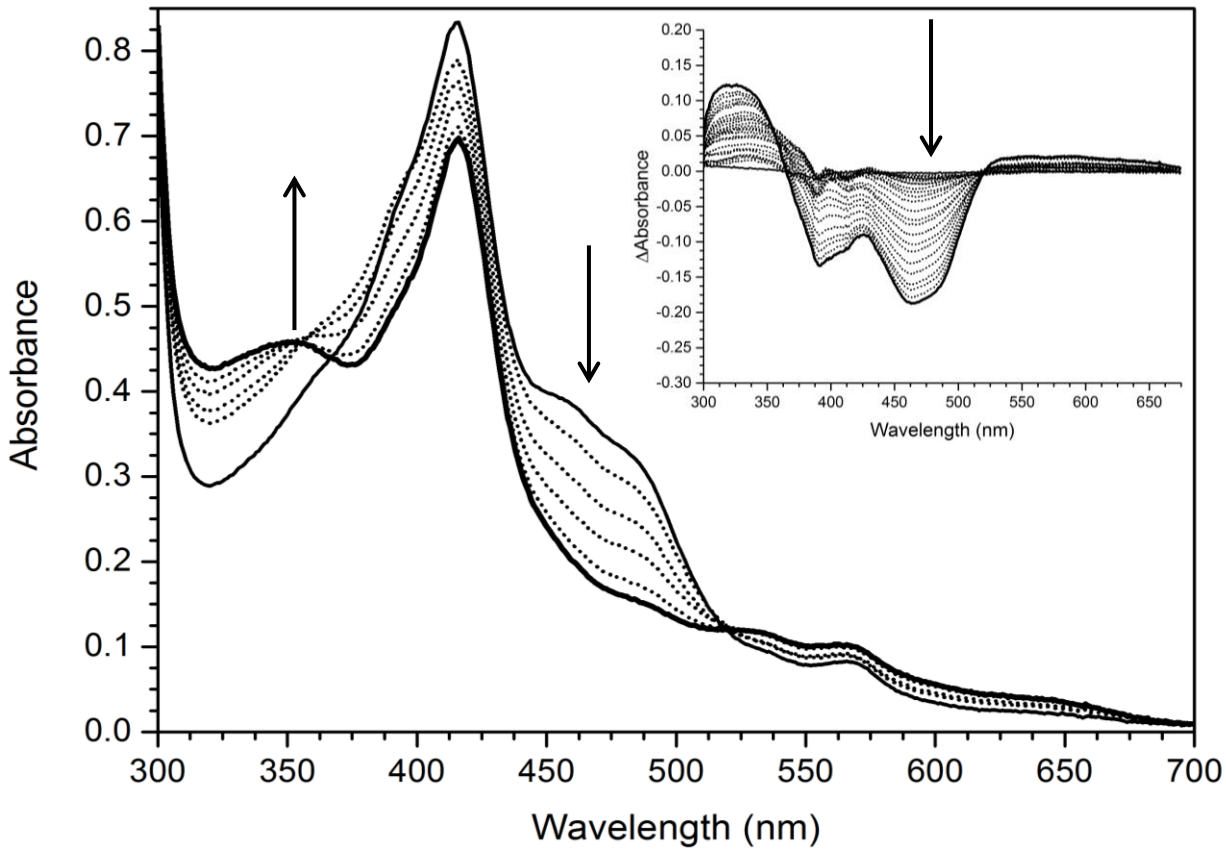

Figure 4.7 UV/visible spectra showing flavin reduction in substrate-free P450 MT1 (~8 µM) during redox titration with sodium dithionite. The decrease in the main flavin absorbance band (360 – 530 nm) is indicated by arrows, as is the increase in dithionite absorbance at 340 nm. No significant heme reduction occurs in the reduction potential range used, as is indicated by the absence of shift of the Soret band, which remains at 416 nm, or in the alpha and beta band region – where these features which remain separate at 566 nm and 534 nm, respectively. The fully oxidised P450 spectrum (thin line) was subtracted from each of the spectra collected after successive dithionite additions (dotted lines) to create the set of difference spectra (inset), with the final addition showing P450 MT1 with its flavins completely almost bleached (thick solid line). The largest absorbance change occurs at ~460 nm and an isosbestic point can be seen at 520 nm, after which there is an absorbance increase over the range from 520 nm to 675 nm.

The difference spectra in Figure 4.7 (inset) show clearly the absorbance change from 360 nm to 520 nm associated with flavin reduction and spectral bleaching. The decrease in absorbance over the flavin reduction range also contributes to the decrease in absorbance of the Soret band at 416 nm, though this is not associated with heme reduction to any significant degree, since the Soret band remains unshifted at 416 nm throughout the titration, as do the alpha and beta bands at 566 nm and 534 nm. The largest absorption change on flavin reduction (at 460 nm) was plotted against reduction potential to give a midpoint potential of -119 mV vs. the normal hydrogen electrode (NHE) (Figure 4.8). The flavins remain near-completely oxidised until approximately -60 mV, but become fully reduced by approximately -180 mV vs. NHE.

The same experiment was repeated using arachidonic acid-bound P450 MT1, which produced an apparent slight decrease in midpoint potential to -125 mV vs. NHE (Table 4.2, data not shown). Substrates are known to positively shift the midpoint potentials of the heme iron closer to those of the flavin cofactors, and the spectral contributions of high-spin, ferric heme iron undergoing reduction could be responsible for the slight despcrepancy between the substrate-free and substrate-bound P450 MT1 flavin midpoint potentials [27]. The dependence of flavin absorbance change on applied potential for the substrate-bound P450 MT1 once again was monophasic and did not resolve individual transitions for the FAD and FMN, or for their 1-electron reduced (semiquinone) forms.

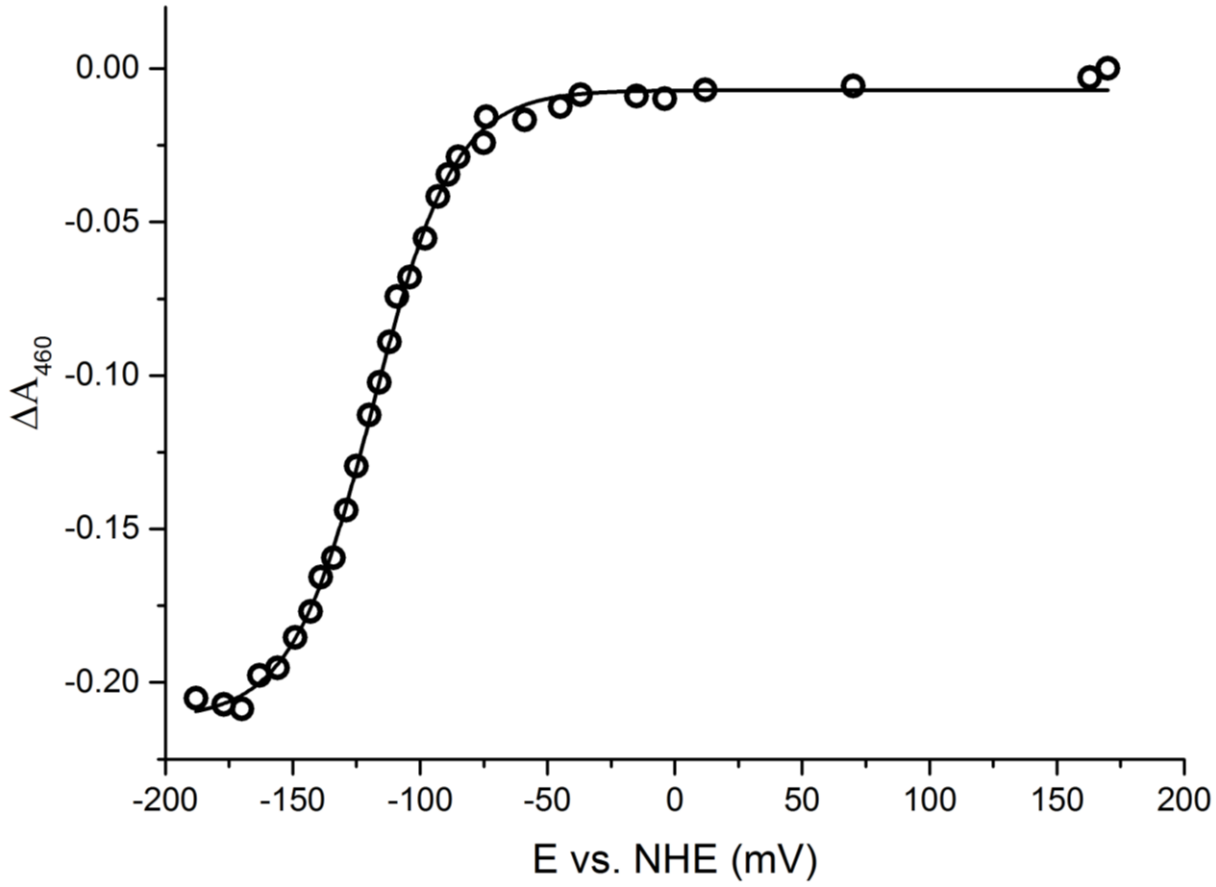

Figure 4.8 Redox potential curve for the reduction of flavins in substrate-free P450 MT1 during sodium dithionite titration. The largest absorbance change observed upon flavin reduction in P450 MT1 was at 460 nm (Figure 4.5, inset), and data at this wavelength were plotted against the NHE-corrected reduction potential. There was an apparently monophasic dependent of ΔA_{460} versus applied potential, and data were fitted using the Nernst equation for 1 electron (Equation 6, Methods section 2.20) to give a midpoint potentials of 119 ± 4 mV.

Thus, the data were fitted using the Nernst equation for a 1-electron process; in this way capturing only the apparent midpoint potential for the complete (4-electron) reduction of both FAD and FMN cofactors. The possibility that the P450 MT1 may be flavin (e.g. FMN) depleted can be discounted, based partly on the large absorbance change associated with reduction of the P450 MT1 flavins, but also on preceding studies showing that both flavins bind tighty to this enzyme. The previsouly described HPLC analysis of CYP505A30 (Section 3.5) confirmed that the reductase domain contained stoichiometric amounts of FAD and FMN, as was predicted from homology recognition software which suggests that the flavin cofactors must titrate in a very narrow window (-50 mV to -180

mV), with their oxidised/semiquinone couples having similar midpoint potentials such that it is impossible to separate them spectroscopically.

The redox potential-dependent changes in the absorbance of the flavin cofactors in P450 MT1 were futher investigated in efforts to resolve their individual midpoint potentials. Using the wavelength of 600 nm to monitor FAD reduction, previously conducted redox potentiometry experiments were able to determine consistent midpoint pointentials for FAD oxidised/semiquinone and semiquinone/hydroquinone couples in intact P450 BM3 and in its isolated FAD and reductase domains [27,218]. A similar approach was attempted with P450 MT1, and absorption at a wavelength of 600 nm (neat the peak absorbance for a blue flavin semiquinone) was plotted against the applied reduction potential, as shown in Figure 4.9.

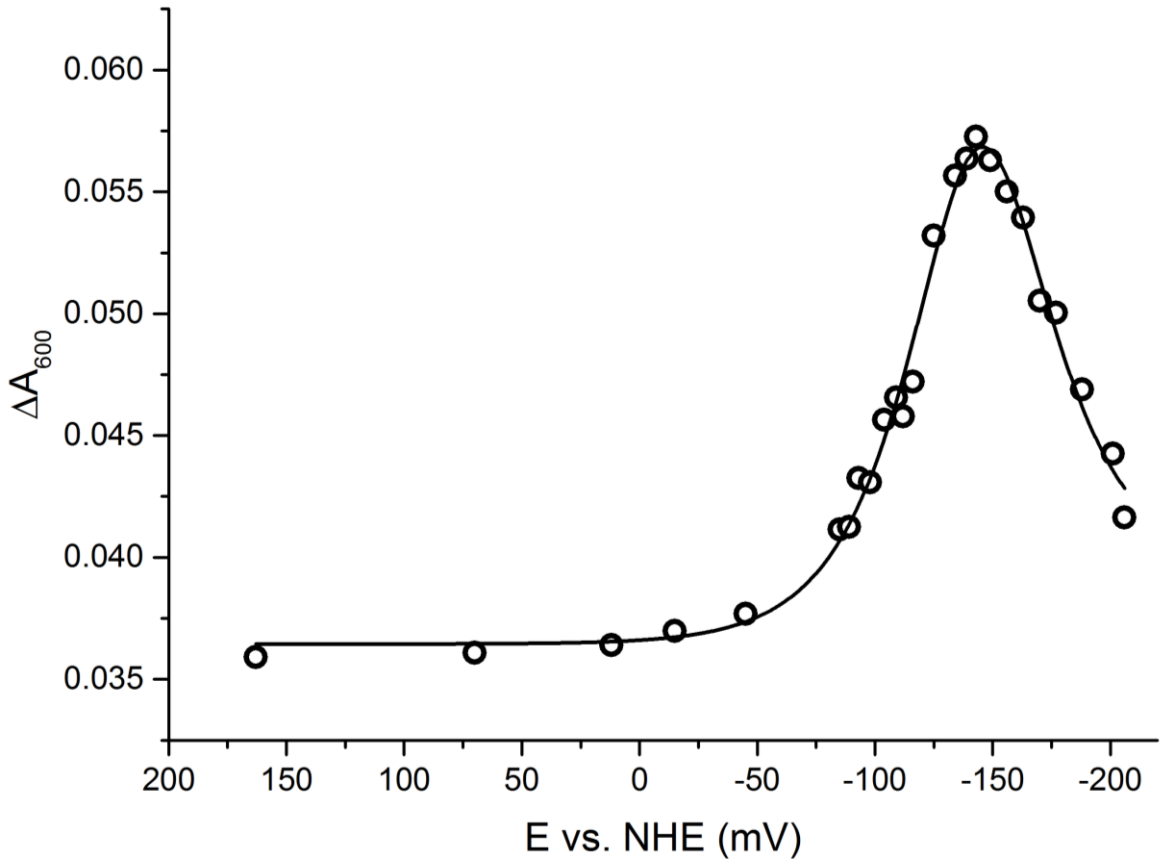

Figure 4.9 Plot of flavin semiquinone absorbance versus applied potential at 600 nm. Neutral semiquinone absorbance is near maximal at 600 nm, and the plot follows the formation and decay of A_{600} versus potential vs. NHE. The data show a biphasic dependence and were fitted using a two electron Nernst equation (Equation 4) with the assumption that only the FAD cofactor forms a blue semiquinone in P450 MT1. Data fitting gave values of E'_1 ($FAD_{ox/sq}$) = -110 ± 24 and E'_2 ($FAD_{sq/hq}$) = -178 ± 21 mV vs. NHE.

Based on the assumption that P450 MT1 behaves like BM3, where the FMN cofactor forms an anionic, red semiquinone (readily converted to the hydroquinone) [222] and the FAD cofactor forms a neutral blue semiquinone [27], the P450 MT1 data obtained were fitted using a 2-electron Nernst equation as with described by Munro et al. [218], to produce two midpoint potentials: E'_1 (FAD) = -110 mV and E'_2 (FAD) = -178 mV vs. NHE; which would correspond to the $FAD_{ox/sq}$ and $FAD_{sq/red}$ couples, respectively, of the FAD cofactor in P450 MT1. These fitted data they fall within the previously detailed bounds of flavin reduction: from -50 mV to -190 mV vs. NHE in Figure 4.8.

To obtain the heme iron midpoint potential and to determine the effect of spin-state on this potential (i.e. by addition of substrate to induce development of high-spin heme iron), the heme UV-visible spectral changes occurring during redox titrations of both substrate-free and substrate-bound forms of the P450 MT1 were analysed. A mid-point potential for the Fe^{3+}/Fe^{2+} heme iron transition in substrate-free P450 HD was obtained (Table 4.2). However, an accurate heme iron mid-point potential for the substrate-bound P450 MT1 redox titration could not be obtained, as this heme potential was too close to that of the flavins and complex simultaneous absorbance changes of flavins and heme occurred. As a consequence, the redox titration experiment was repeated with isolated MT1 HD (Figure 4.10) in the presence (bottom panel) and absence (top panel) of substrate in near-saturating conditions, in order to obtain their respective heme iron mid-point potentials (Figure 4.9), with data tabulated in Table 4.2. Cleaner heme spectral changes were obtained when monitoring MT1 HD heme reduction titration, due to the absence of any flavin contributions.

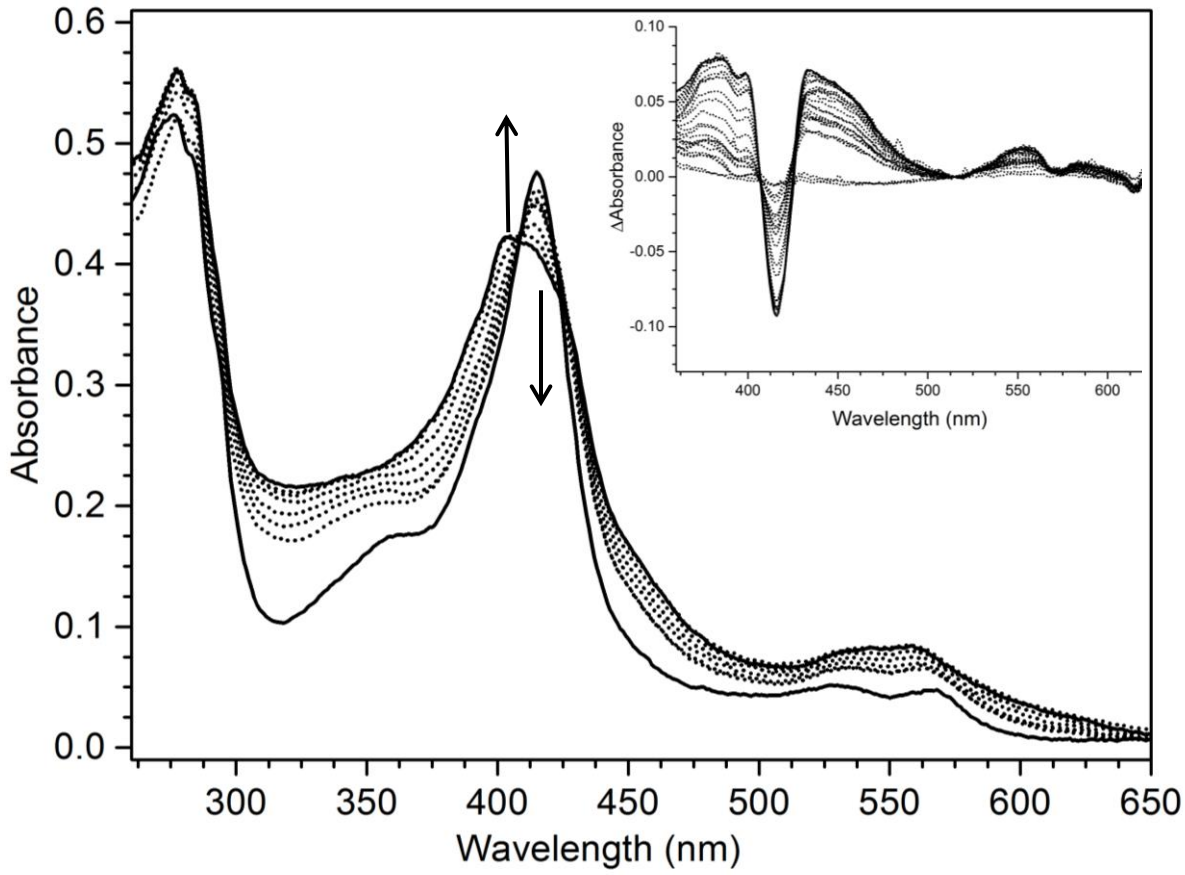
Absorbance
Wavelength (nm)
ΔAbsorbance
Wavelength (nm)

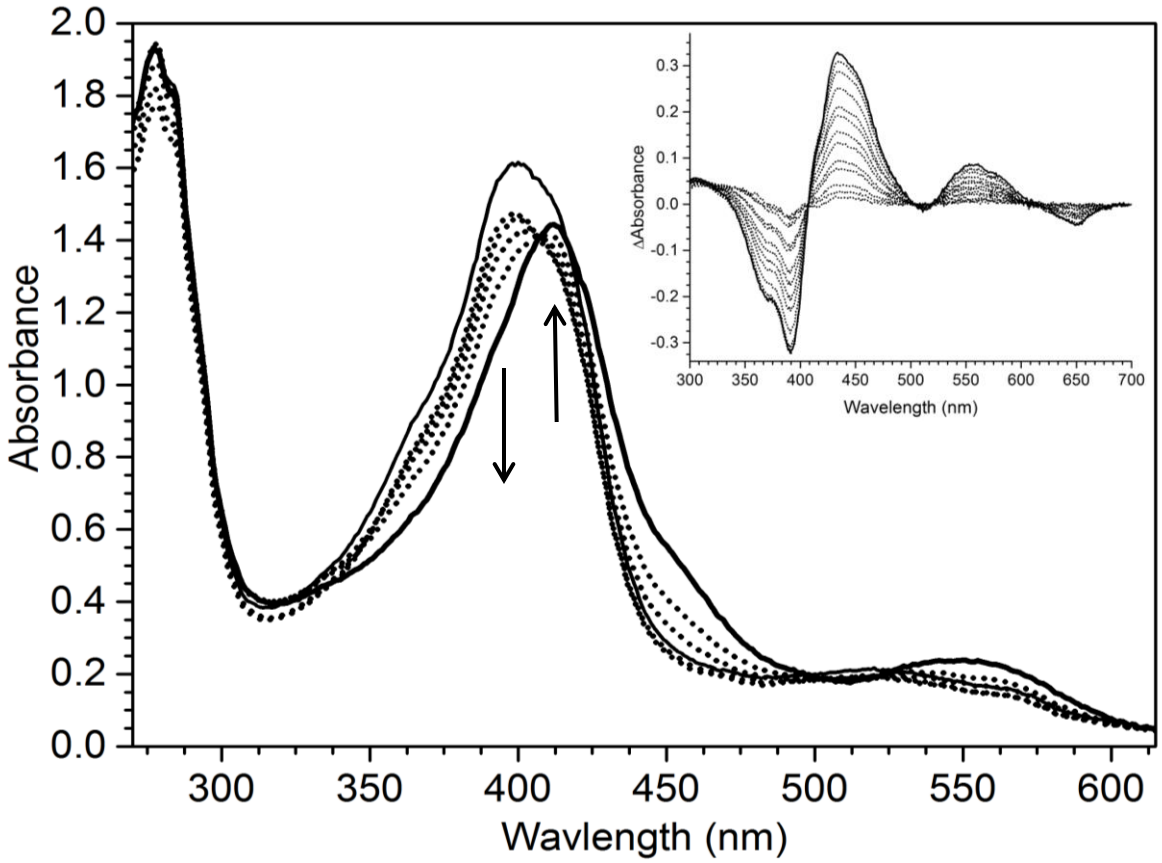
Absorbance
Wavlength (nm)
ΔAbsorbance
Wavelength (nm)

Figure 4.10 UV/Visible spectra and difference spectra from MT1 HD redox titrations following heme reduction in the presence and absence of substrate. The top panel shows substrate-free MT1 HD (thin solid line, 18 µM) with a ferric heme Soret band at 416 nm, which shifts to a major peak at ~403 nm upon reduction by dithionite, as indicated by the arrows, to a near fully-reduced MT1 HD (thick solid line). The dotted lines represent MT1 HD's progressive reduction by sodium dithionite, which absorbs at 315 nm and contributes to the spectra as it accumulates towards the end of the titration. The difference spectra (inset) were obtained by the subtraction of the initial oxidised MT1 HD spectrum from all following spectra (dotted lines) with the final spectrum of the near fully-reduced heme represented as a solid line. The decrease in intensity of the heme Soret at 416 nm and its subsequent shift to 403 nm are visible, as are the effects of the heme Soret broadening upon heme reduction, represented by an absorption increase at ~375–410 nm and at ~430–470 nm in the difference spectra. There are two isosbestic points at 408 nm and 424 nm. The bottom panel shows arachidonic acid-bound MT1 HD (thin solid line, 18 µM) with a type I shifted Soret band at 390 nm, which shifts to 412 nm upon reduction by dithionite, as indicated by the arrows, to form fully-reduced MT1 HD (thick solid line). The dotted lines represent MT1 HD's progressive reduction by sodium dithionite. The difference spectra (inset) were obtained by the subtraction of the initial oxidised MT1 HD spectrum from all following spectra (dotted lines), with the final spectrum of fully reduced MT1 HD represented as a solid line. The decrease in intensity of the substrate-bound heme peak at 390 nm and its subsequent shift to 412 nm are visible, as are the merging of the alpha and beta bands at 560 nm, and the decrease in intensity of the cysteine-to-thiolate high-spin ferric heme charge transfer species at 650 nm on reduction [353]. These absorbance difference changes have clear isosbestic points at 305 nm, 407 nm, 500 nm and 612 nm. There is minimal contribution from a dithionite peak at 315 nm, as the substrate-bound MT1 HD reduction happens early on in the titration.

The redox titration experiments of MT1 HD were carried out in the same way as with P450 MT1. The oxidised, low-spin heme with a Soret band at 416 nm (Figure 4.10, top panel) shifted to 403 nm upon the thiolate-coordinated ferric heme iron reduction to the thiolate-coordinated ferrous state. Heme Soret spectral broadening was also observed upon reduction. The heme does not fully reduce, as the alpha and beta bands at 566 nm and 534 nm do not completely merge. The spectra collected later in the titration are spoiled somewhat by the absorbance contribution from sodium dithionite at 315 nm as it accumulates. Turbidity also contributes to the absorbance background. This effect may have been decreased by addition of the stabilising agent glycerol. However, this could not be added in this case, since it binds to the MT1 HD (and to P450 MT1) and elicits a high spin shift which would affect the measured reduction potential for the substrate-free form. The absorbance shift from 416 nm to 403 nm seen in the difference spectra (Figure 4.10, top, inset), corresponds to the transition of oxidised heme to reduced heme iron, and these

data are plotted against the applied reduction potential in Figure 4.11 to obtain the midpoint potentials for substrate-free and arachidonic acid-bound MT1 HD.

The redox titration experiments for arachidonic acid-bound MT1 HD (Figure 4.10, bottom panel) show a high-spin Soret band at 390 nm for the oxidised, ferric heme (thin, solid line). During the course of the reduction titration with sodium dithionite, the Soret peak shifts to 412 nm as oxidised heme is fully reduced to thiolate-ligated ferrous heme. In its fully reduced form, MT1 HD's alpha and beta bands merge at 560 nm, as previously described (Section 3.3.2). The spectra remain unspoiled by dithionite and turbidity effects compared to the substrate-free titration of MT1 HD (Figure 4.10, top panel) as heme reduction for arachidonic acid-bound MT1 HD occurs early in the titration and since glycerol is present to help stabilise the enzyme. The Soret shift from 390 nm to 412 nm is the maximal change in absorption seen in the difference spectra (Figure 4.10, bottom panel, inset) and these data are plotted against the reduction potential in Figure 4.11 to obtain a midpoint potential for the substrate-bound MT1 HD.

The Soret peak of a thiolate ligated ferrous heme is typically between 407 – 412 nm, as observed in both BM3 and $P450_{cam}$ [27,355]. There is an apparent discrepancy in the position of the ferrous heme Soret peak of 7 nm between that observed for substrate-free MT1 HD at 403 nm and that of arachidonic acid-bound MT1 HD at 410 nm. However, the Soret peak for the apparently fully reduced substrate-free spectra MT1 HD is clearly asymmetric with shoulder features (aside from the maximum at 403 nm) at ~412 nm and 425 nm. The heme is apparently fully reduced by the end of the titration, as evidenced by the end of the redox titration occurring at ~ -375 vs. NHE, compared to the more negative potential of dithionite (~ -420 mV vs. NHE). Thus, the asymmetric nature of the spectra reporting on the ferrous form of substrate-free MT1 HD likely reflect the conversion of the thiolate-coordinated ferric MT1 HD to a ferrous form with mixed thiol/thiolate coordination – i.e. there is partial protonation of the thiolate ligand during heme iron reduction in the substrate free form – giving rise to a mixed proximal coordination state in the ferrous state. Similar conversions from a completely thiolate-coordinated ferric state to a partial or completely thiol-coordinated state have been reported previously – e.g. for the *M. tuberculosis* CYP51B1 and CYP142A1 P450s [356,357]. Further evidence for this conclusion comes from the spectral features in the alpha/beta (Q-band) region. In a thiolate-coordinated, ferrous P450, there is typically fusion of these bands into a single feature with absorption maximum intermediate between those of the ferric alpha/beta

bands. For a ferrous, thiol-coordinated P450 the alpha/beta bands remain distinct, but shift in position. In reduced, substrate-free MT1 HD distinct alpha/beta band features can be seen at ~559 nm and 538 nm, clearly shifted from the positions observed for the ferric, thiolate-ligated P450. However, these new Q-band feature are more rounded and less distinct than would be seen for a fully thiol-coordinated ferrous P450, and thus are again consistent with a ferrous form of the MT1 HD that has mixed thiol/thiolate coordination of the heme iron.

The redox transitions of ferric (Fe^{3+}) to ferrous (Fe^{2+}) heme iron for both the substrate-free and substrate-bound forms of the MT1 HD (shown in Figure 4.11) were monophasic, as expected for redox changes involving one electron reduction of a heme iron. The mid-point potential for the heme Fe^{3+}/Fe^{2+} transition of substrate-free MT1 HD (shown in Figure 4.11, top) was determined at -297 ± 4 mV vs. NHE. This is a more negative than the flavin mid-point potential at -119 mV ± 4 mV vs. NHE and comparable to the one obtained for the intact P450 MT1 at -288 mV vs. NHE (Table 4.2, data not shown), but significantly more positive than the midpoint potential obtained for its homologue P450 BM3 at -368 mV vs. NHE [27]. The data set enabling the determination of the heme iron midpoint potential for the arachidonate-bound MT1 HD is shown in Figure 4.11 (bottom panel), and in this case the heme iron Fe^{3+}/Fe^{2+} potential was determined at -69 ± 3 mV vs. NHE. This is an increase in redox potential of +228 mV from the -297 mV observed in the substrate-free form of the MT1 HD to -69 mV in the arachidonate-bound form. This change is far greater than the difference in heme iron mid-point potential between substrate-free and substrate-bound forms of P450 BM3 (100 – 130 mV) [27].

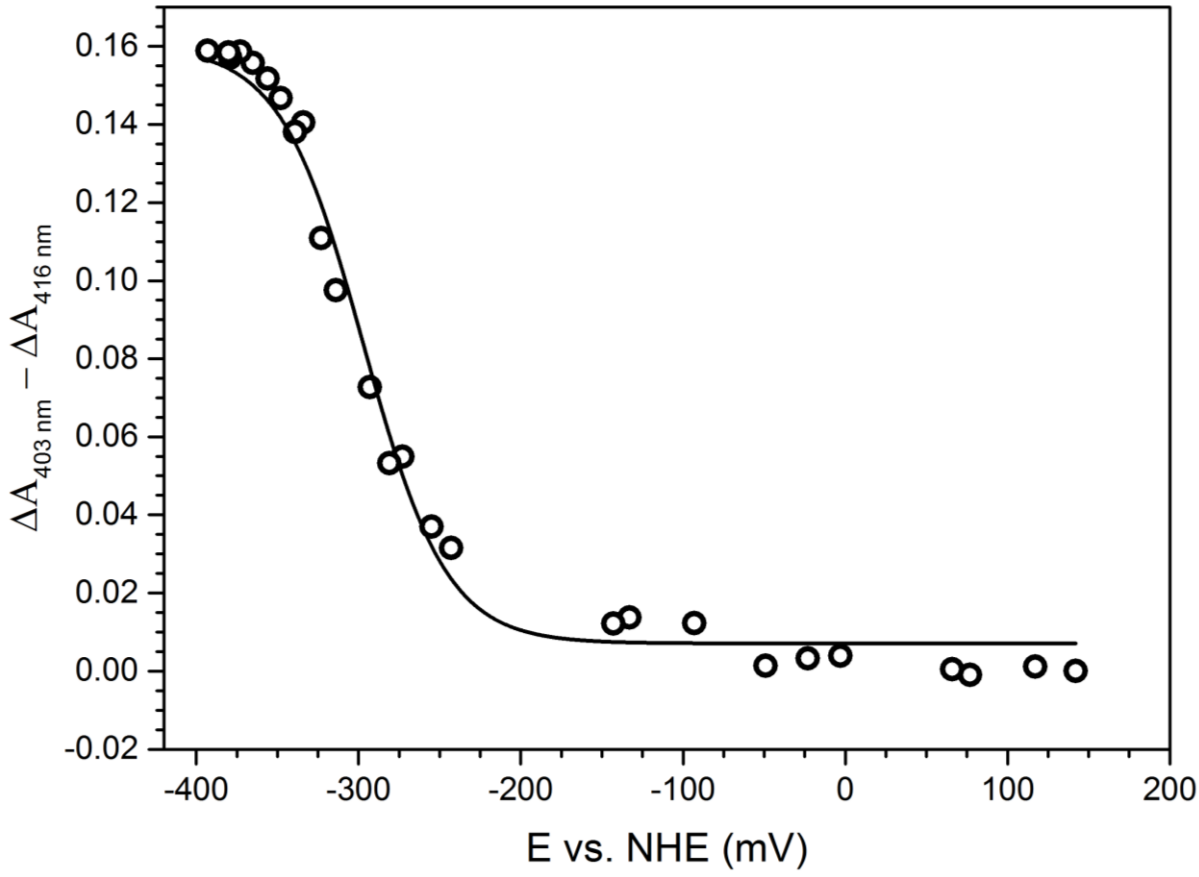
0.16
0.14
0.12
0.10
0.08
0.06
0.04
0.02
0.00
-0.02
$\Delta A_{403\ nm} - \Delta A_{416\ nm}$
-400
-300
-200
-100
0
100
200
E vs. NHE (mV)

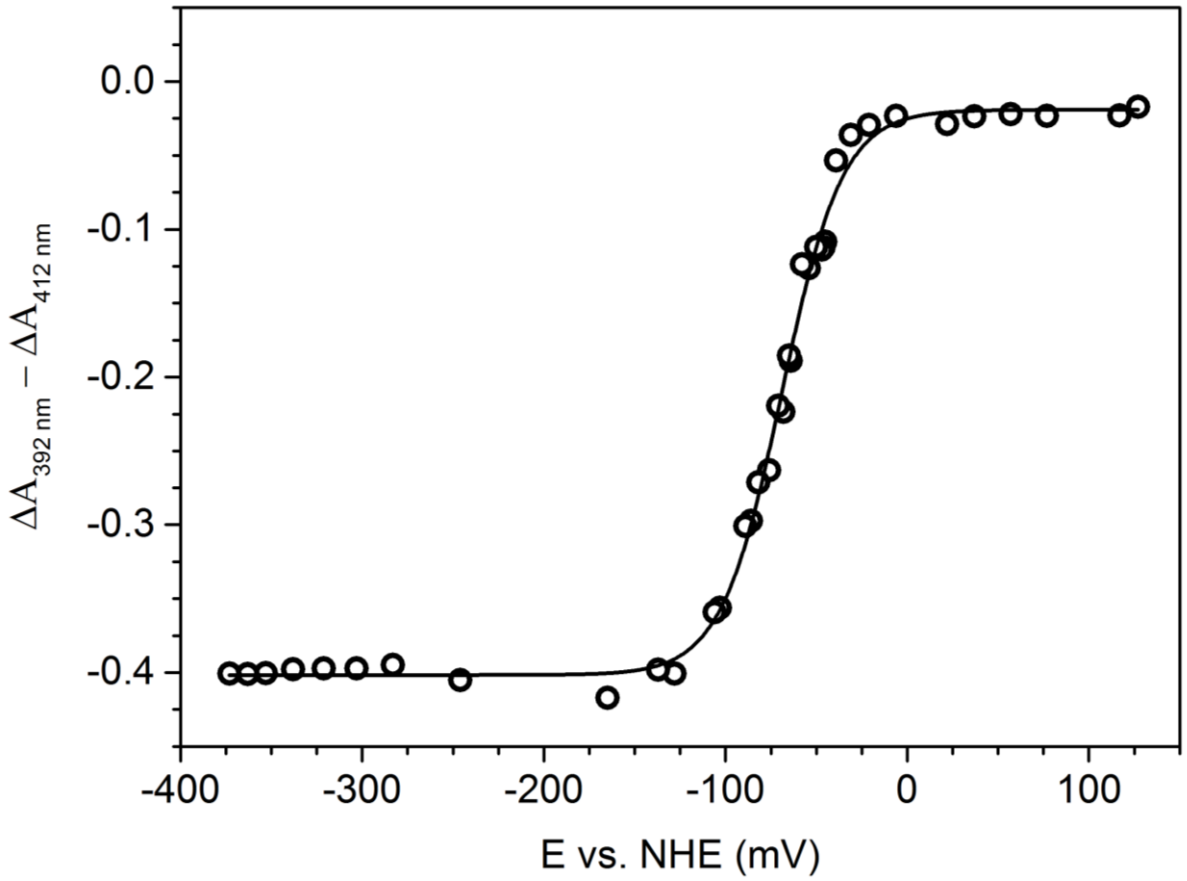
0.0
-0.1
-0.2
-0.3
-0.4
$\Delta A_{392\ nm} - \Delta A_{412\ nm}$
-400
-300
-200
-100
0
100
E vs. NHE (mV)

Figure 4.11 Reductive titration plots for low-spin, substrate-free MT1 HD and high-spin arachidonic acid-bound MT1 HD. The plot of Soret absorbance changes versus applied potential in the top panel are for the substrate-free MT1 HD, and follow the absorbance difference of the oxidised, thiolate-coordinated, low-spin ferric heme Soret band at 416 nm as it shifts to 403 nm upon reduction to ferrous heme with mixed thiolate/thiol coordination. The plot in the bottom panel shows absorbance changes for arachidonic acid-bound MT1 HD, following the absorbance difference of the high-spin heme Soret band at 390 nm as it shifts to 410 nm upon reduction to ferrous heme. The x-axis of both plots in the measured potential corrected against the normal hydrogen electrode (NHE) in mV. The titration curves for both substrate-free and arachidonic acid-bound forms of MT1 HD are monophasic and data are fitted using the Nernst equation for a 1 electron reduction process (Equation 3) to determine the midpoint potentials of -297 ± 4 mV and -69 ± 3 mV respectively. Thiolate proximal coordination of heme iron is retained on reduction of the substrate-bound MT1 HD, but the ferrous, substrate-free MT1 HD has a combination of both thiol- and thiolate-coordinated heme iron.

The apparent difference between the two heme iron potentials for substrate-free and substrate-bound forms of MT1 HD, is substantial at 228 mV. In Figure 4.11 (top panel), the data show that the low-spin heme iron only starts to become reduced after -150 mV vs. NHE, while the high-spin form of MT1 HD (bottom panel) is near-completely reduced to the ferrous form by -100 mV vs. NHE. This displays the ability of substrates to modulate the heme iron's propensity to accept an electron. This modulation of heme potential by a substrate was first observed in $P450_{cam}$, where camphor binding shifts the mid-point potential from -330 mV to -163 mV vs. NHE [355,358]. Putidaredoxin, $P450_{cam}$'s redox partner, has a mid-point potential of -240 mV and therefore electron transfer is only made thermodynamically favourable in the substrate-bound P450 form. This is also observed in P450 BM3, where the midpoint potential of $FMN_{ox/sq}$, responsible for the initial electron transfer to heme iron, is -203 mV vs. NHE and the mid-point potential for the reduction of the heme iron is shifted from -368 mV in the substrate-free form to -239 mV vs. NHE in the arachidonic acid-bound form [27]. This level of substrate control over heme potential prevents the futile cycling of electrons through the heme domain in the absence of substrate. This phenomenon is observed in many P450s besides $P450_{cam}$ and BM3, and is now confirmed also for P450 MT1 [359–361]. The unexpectedly large change in potential between the substrate-free and substrate-bound forms is likely due in part to the change in heme iron coordination state (thiolate to mixed thiol/thiolate) seen in the substrate-free form, in addition to the potential shift caused by the substrate-induced spin-state conversion in the arachidonate-bound form.

Table 4.2 Midpoint reduction potentials (mV vs. NHE) for the flavin and heme cofactors in P450 MT1 and its heme domain. Values were obtained from fitting of heme absorbance data versus applied potential (mV vs. NHE). All values were obtained from titrations in 50 mM KPi buffer, pH 7.0 at 25 ± 2 °C. Data for the low-spin enzyme were obtained in the absence of substrate, and for high-spin form a high concentration of arachidonic acid ("arach", 1 mM at >500-fold its K_d of 1.7 µM) was used to achieve near-saturating conditions. The midpoint potentials for the P450 MT1 flavins encompasses the reduction of both the FAD and FMN cofactors.

Redox Centre	Redox Potential vs. NHE (mV)	
	E'_1	E'_2
Flavins (P450 MT1)	-119 ± 4	
Flavins (P450 MT1) + arach	-125 ± 4	
FAD (P450 MT1)	-110 ± 24	-178 ± 21
Heme (P450 MT1)	-288 ± 5	
Heme (P450 MT1) +arach	N.D.	
Heme (MT1 HD)	-297 ± 4	
Heme (MT1 HD) + arach	-69 ± 3	

4.4 The Steady-State Kinetics of P450 MT1.

4.4.1 Kinetic studies with fatty acid substrates

The kinetics of oxidation of NADPH was followed at a range of substrate concentrations for different fatty acid substrates with P450 MT1. Substrate candidates for steady-state kinetics were selected from successful lipid binding titrations, as the type I shift observed during ligand titrations is a good indication that binding is from a substrate-like molecule (Section 3.3.1). Assays were carried out as described in the Methods section (Section 2.21). The rate of NADPH oxidation was measured by following the decrease in absorbance at 340 nm ($\Delta\varepsilon_{340\ nm}$ = 6.21 mM^{-1} cm^{-1}) for each substrate selected, and at a range of concentrations (typically from ~0.1 – 100 µM). All assays were run in triplicate and the average rate was corrected for enzyme concentration to determine the enzyme-dependent rate constant in each case, which was then plotted against the relevant substrate concentration. The plotted data were then fitted using a hyperbolic function (Equation 2, Methods 2.21), as shown in Figure 4.12. The kinetic constants, k_{cat} and K_M, obtained from all the substrates assayed are presented in Table 4.3.

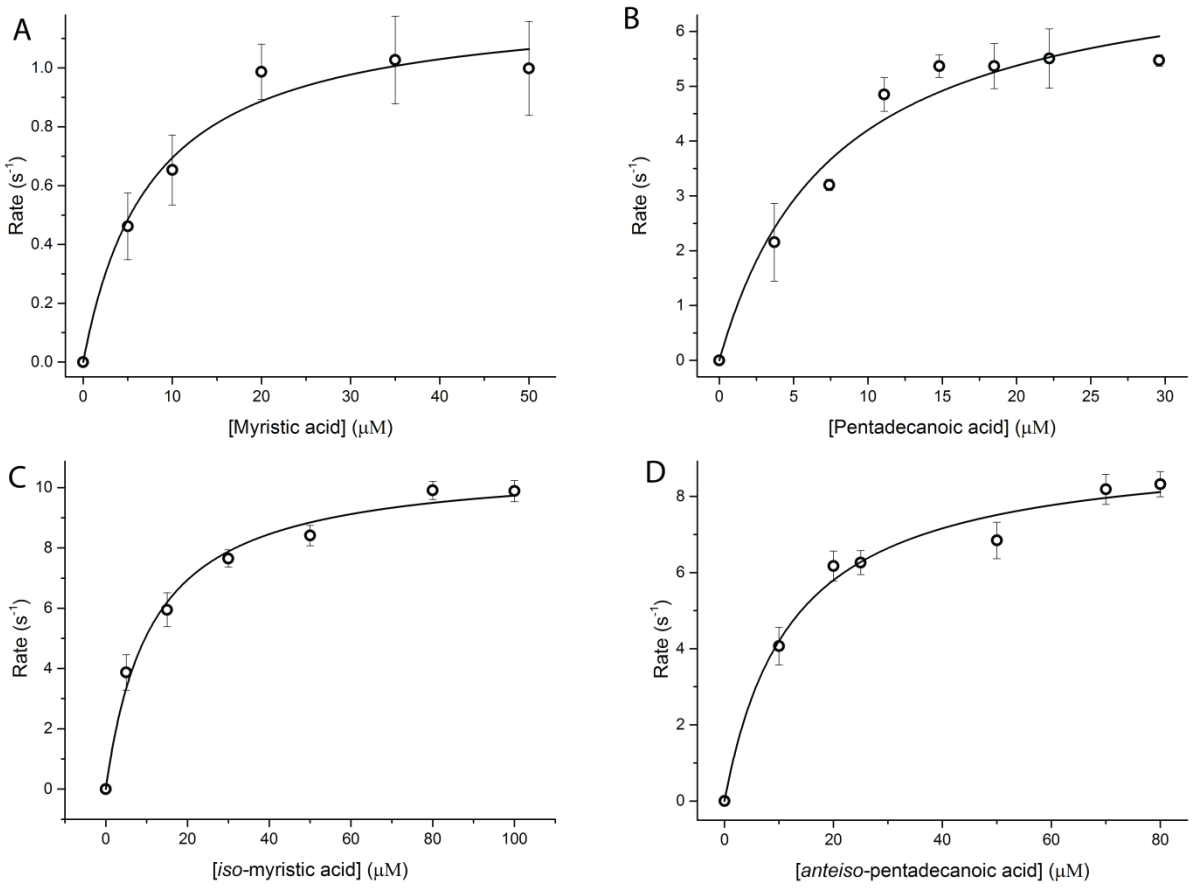

Figure 4.12. Steady-state kinetic curves for the substrate–dependent oxidation of NADPH by P450 MT1. The averaged data points for three assays per concentration point were plotted and the data fitted (black line) using a hyperbolic (Michaelis-Menten) function (Equation 1). Panel A and B show the steady-state kinetic curves for saturated fatty acids myristic acid (14C) and pentadecanoic acid (15C) giving k_{cat} values of 1.2 s^{-1} and 7.5 s^{-1}, and K_M values of 7.7 µM and 7.8 µM, respectively. Panel C and D show the steady-state kinetic curves for the *iso*-myristic acid (12-methyltridecanoic acid) and *anteiso*-pentadecanoic acid (12-methyltetradecanoic acid) substrates, giving k_{cat} values of 10.8 s^{-1} and 9.4 s^{-1}, and K_M values of 11.2 µM and 12.3 µM, respectively. Error bars represent the standard deviation from the averaged data points. The k_{cat} and K_M values obtained from the data fitting for each of the fatty acid substrates are recorded in Table 4.3.

Of the 9 substrate candidates selected, all showed substrate concentration-dependent NADPH oxidation, which suggesting they all bind to and act as substrates for P450 MT1. The substrate giving the highest rate constant was *iso*-myristic acid at 10.8 s^{-1}, although *anteiso*-myristic acid gave only a slightly lower rate constant at 10.5 s^{-1}, and these k_{cat} values are within error of each other. These k_{cat} values are both twice as fast as those for tridecanoic acid at 5.0 s^{-1}, and ten-fold faster than for their skeletal isomer myristic acid (1.22 s^{-1}).

Table 4.3 Kinetic constants (kcat and KM values) for P450 MT1 based on NADPH oxidation in the presence of a range of fatty acid substrates. The values for these rate constants were derived from fitting of data for substrate-dependent NADPH oxidation versus substrate concentration using a hyperbolic function (Equation 1). The error values quoted are taken directly from the fitting function. The K_d values obtained for the same substrates from optical binding titrations (Section 3.3.1) and the k_{cat}/K_M (2^{nd} order rate constant) values are tabulated alongside the kinetic constants for comparison.

Substrate	k_{cat} (s^{-1})	K_M (µM)	K_d (µM)	k_{cat}/K_M (s^{-1} $µM^{-1}$)
Lauric acid	4.8 ± 0.2	21.2 ± 2.4	6.1 ± 0.4	0.22
Tridecanoic acid	5.0 ± 0.3	14.6 ± 2.5	2.7 ± 0.3	0.34
***Anteiso*-myristic acid**	10.5 ± 0.3	8.3 ± 0.8	10.5 ± 0.6	1.26
***Iso*-myristic acid**	10.8 ± 0.4	11.2 ± 1.7	13.1 ± 0.8	0.96
Myristic acid	1.2 ± 0.1	7.7 ± 1.9	7.4 ± 0.2	0.15
***Anteiso*-pentadecanoic acid**	9.4 ± 0.5	12.3 ± 2.3	14.3 ± 2.0	0.75
***Iso*-pentadecanoic acid**	8.0 ± 0.5	12.9 ± 3.5	13.4 ± 0.3	0.62
Pentadecanoic acid	7.5 ± 0.7	7.8 ± 2.1	4.4 ± 0.6	0.96
Arachidonic acid	2.0 ± 0.1	9.2 ± 0.5	1.7 ± 0.1	0.21

Overall, there is a trend for branched chain fatty acids to simulate NADPH oxidation at a higher rate than do their saturated, unbranched counterparts. It was observed during the optical binding titrations that the branched chain fatty acids displayed the highest proportions of type 1 'high spin' optical shift, although their K_d values were not as tight as for other substrates. It was suggested in Section 3.7 that the K_d values are not a good indicator of catalytic activity and, by displaying the K_d values obtained from optical binding experiments alongside the kinetic constants in Table 4.3, no real trend emerges to relate the two values. Catalytic efficiency (k_{cat}/K_M) is also tabulated in Table 4.3 alongside the other kinetic and binding parameters. Larger catalytic efficiency values were obtained for the branched chain fatty acids compared to those with saturated fatty acids, with the notable exception of pentadecanoic acid.

Interestingly, arachidonic acid (which has the highest reported catalytic activity in BM3 [197]) showed a relatively low k_{cat} value for P450 MT1 (2.0 s^{-1}) compared to the other substrates assayed, and despite the high extent of type I Soret shift observed on binding to P450 MT1 (Figure 1.13).

4.4.2. Kinetic studies with artificial electron acceptors

Colorimetric assays were also used to follow absorbance changes associated with the P450 MT1-dependent reduction of the artificial electron acceptors potassium ferricyanide (KFeCN) and cytochrome *c* by NAD(P)H. Ferricyanide is a strong oxidant molecule with a very positive redox potential (E° = +436 mV vs. NHE), making it a proficient electron acceptor molecule for reductase enzymes. Electrons are cycled through the path from NAD(P)H to FAD in P450 MT1, and finally from FAD to the KFeCN. There is the possibility of KFeCN accepting an electron from the FMN cofactor of P450 MT1, following electron transfer from FAD. However, FAD is widely accepted as the preferred electron donor to KFeCN in CPR-type enzymes. Cytochrome *c* (cyt *c*) is a respiratory hemoprotein which also possesses a positive redox potential (E° = +254 mV vs, NHE) and accepts electrons almost exclusively from the FMN cofactor, using the same electron transfer pathway as for BM3 and CPR: NAD(P)H to FAD, FAD to FMN and finally FMN to cyt *c* [301,362,363].

Electron transfer rates could either be followed by measuring the decrease absorbance at 340 nm ($\Delta\varepsilon_{340\ nm}$ = 6.21 mM^{-1} cm^{-1}) associated with substrate-dependent NAD(P)H oxidation, or through the changes in absorbance associated with the reduction of the electron acceptors at 420 nm and 550 nm for ferricyanide and cyt *c*, respectively ($\Delta\varepsilon_{420\ nm}$ = 1.02 mM^{-1} cm^{-1} and $\Delta\varepsilon_{550\ nm}$ = 22.0 mM^{-1} cm^{-1}). The convenient colorimetric assays allow for the measurement of the kinetic properties of P450 MT1 through varying the concentrations of the electron acceptors (while maintaining NADPH or NADH electron donors at near-saturating levels) and *vice versa* in separate assays. All assays were run in triplicate and the average rate constant at each substrate concentration was corrected for enzyme concentration to find the enzyme-dependent rate constant in each case. Depending on the assay, the corrected rate constants were plotted against the concentration of either the electron donor (NADH or NADPH) or the acceptor (ferricyanide or cyt *c*) being varied. The plotted data were then fitted using a hyperbolic function (Equation 1) as in Figure 4.11, and the kinetic (k_{cat} and K_M) parameters for all the steady-state assays are tabulated in Table 4.4.

The steady-state kinetic data presented in Figure 4.13 represent P450 MT1-dependent cytochrome *c* reduction (top panels) and ferricyanide reduction (bottom panels) for both NADPH (left panels) and NADH (right panels). Higher steady-state activity is observed for P450 MT1 reducing ferricyanide (k_{cat} = 43.4 s^{-1} with NADPH and 31.7 s^{-1} with

NADH), than for cytochrome *c* (k_{cat} = 29.7 s^{-1} with NADPH and 29.5 s^{-1} with NADH). This might be expected as ferricyanide should accept electrons earlier in the electron transfer pathway than does cytochrome *c*, i.e. the rate at which electrons can be transferred to cytochrome c may be retarded by the rate at which electrons are transferred from FAD to FMN. Cytochrome *c* reduction might also be more slowly reduced in view of its size (12 kDa) and requirement for appropriate orientation to the P450 MT1 FMN cofactor. However, the cytochrome *c* k_{cat} values remain only slightly lower than those for ferricyanide.

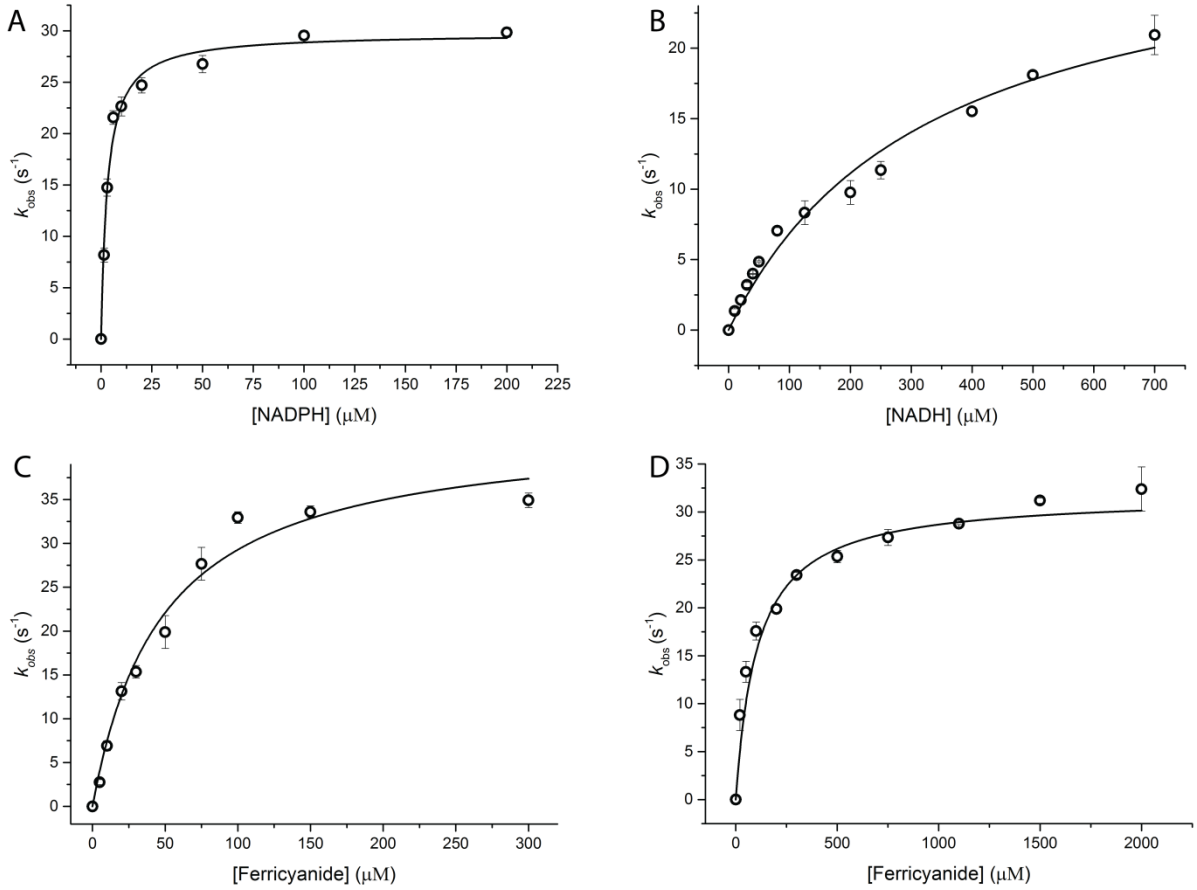

Figure 4.13 Selected steady-state kinetic data set for P450 MT1-dependent reduction of cytochrome c and ferricyanide electron acceptors. Reactions were carried out in 50 mM KPi (pH 7.0) buffer containing 200 mM KCl. Replicates of each assay were averaged, and fitted (black line) using a hyperbolic function (Equation 1). Error bars represent the standard deviation from the averaged data points. The steady-state data for the reduction of cyt *c* by P450 MT1 with varying [NADPH] (panel A) and [NADH] (panel B) concentrations were fitted to give k_{cat} = 29.7 s^{-1} and 29.5 s^{-1}, and K_M values of 3.12 μM and 330 μM, respectively. The steady-state kinetic data for varying ferricyanide concentrations are shown using the electron donor NADPH in panel C and NADPH in panel D. P450 MT1's steady-state kinetic parameters for the ferricyanide concentration-dependent

oxidation of NAD(P)H are: k_{cat} = 43.4 s^{-1} and K_M = 48.2 µM for panel C (NADPH); and k_{cat} = 31.7 s^{-1} and K_M = 106.9 µM for panel D (NADH).

The higher affinity of P450 MT1 for NADPH over NADH can be observed in the discrepancy between their K_M values. The K_M for NADPH at 3.12 ± 0.36 µM is ~100-fold tighter when compared to that for NADH (330.1 ± 56.4 µM) when measuring cytochrome *c* reduction. The same ~100-fold difference in K_M (within error) is also observed when comparing the relevant K_M values for ferricyanide reduction by P450 MT1. This trend suggests that NADPH is the preferred electron donor in P450 MT1. Examination of the 2nd order rate constants reporting on the catalytic efficiency (k_{cat}/K_M) of P450 MT1 also shows that these values are 100-fold lower for NADPH compared to NADH (Table 4.4).

Table 4.4 Steady-state kinetic parameters for P450 MT1 with the artificial electron acceptors cytochrome c and ferricyanide. The k_{cat}, K_M and k_{cat}/K_M values are presented for both potassium ferricyanide (top) and cytochrome *c* (bottom) electron acceptors, with electron donors NADPH (right) and NADH (left). Kinetic analyses were done at pH 7.0 and 20 °C in 50 mM KPi 200 mM KCl buffer.

		Ferricyanide		
Substrate varied:	**NADPH**	**KFeCN**	**NADH**	**KFeCN**
k_{cat} (s^{-1})	38.4 ± 1.8	43.4 ± 2.6	34.3 ± 2.4	31.7 ± 0.4
K_M (µM)	2.9 ± 0.4	48.2 ± 8.0	265.0 ± 38.0	106.9 ± 13.3
k_{cat}/K_M (μM^{-1} s^{-1})	13.4	0.9	0.13	0.3

		Cytochrome *c*		
Substrate varied:	**NADPH**	**Cyt *c***	**NADH**	**Cyt *c***
k_{cat} (s^{-1})	29.7 ± 0.7	27.6 ± 1.4	29.5 ± 2.4	24.2 ± 1.1
K_M (µM)	3.1 ± 0.4	79.3 ± 10.3	330.1 ± 56.4	50.0 ± 7.3
k_{cat}/K_M (μM^{-1} s^{-1})	9.5	0.34	0.09	0.48

4.5 Stopped-flow analysis of P450 MT1 electron transfer kinetics

Electron transfer kinetics of P450 MT1 were investigated using stopped-flow absorbance assays. Absorbance transients for flavin reduction in P450 MT1 were collected aerobically at 475 nm to allow for the observation of flavin cofactor reduction by NADPH and NADH at a wavelength with minimal contribution from the the heme Soret band (Section 3.3, Figure 3.12, Panel A).

Analysis of the kinetics of the first FMN-to-heme electron transfer step in P450 MT1 required more elaborate experimental conditions than those for flavin reduction previously mentioned. Oxygen binding to heme iron occurs following its reduction to the ferrous state (Section 1.11), and is preceded by substrate binding in P450 MT1 to provide the thermodynamic driving force for FMN-to-heme electron transfer. The heme absorbance changes associated with these steps are significant, but are partially obscured by the absorption contribution associated with the oxidation of FMN in the reductase domain during the electron transfer process. For this reason the absorption changes at 450 nm (following Fe^{2+}-CO complex formation) were followed. CO binds to ferrous heme with a rate constant of ~1000 s^{-1}, which is ~50-fold faster than the 1st FMN-to-heme electron transfer rate constant measured in P450 MT1 [116]. The experiments were carried out in anaerobic conditions to minimise oxygen binding to reduced heme in place of CO, and in the presence and absence of substrate to compare efficiencies of electron transfer.

4.5.1 Analysis of NAD(P)H-dependent electron transfer to P450 MT1 flavins

To investigate the kinetics of NAD(P)H-dependent flavin reduction in P450 MT1, the changes in flavin absorption associated with their reduction were monitored following the rapid mixture of enzyme with electron donor (either NADPH or NADH) in 50 mM KPi (pH 7.0) containing 200 mM KCl. Data were collected over 1 second to allow sufficient time for complete flavin reduction. All stopped-flow data collected for flavin reduction were fitted to a double exponential decay function (Methods 2.23.1), unless otherwise stated, and the faster rate constant observed, k_1 (accounting for >90% of the absorbance change in all cases Appendix 7.4 – 7.7), is attributed to the transfer of electrons (by hydride transfer) from the NAD(P)H electron donor to the FAD cofactor in the reductase domain of P450 MT1. The other rate constants obtained from these analyses (resulting from a double or triple exponential decay fit), k_2 and k_3, may be attributed to other events occurring that have smaller contributions to absorbance changes, e.g. absorbance change associated with the binding and dissociation of NAD(P)H and $NAD(P)^+$, including charge transfer species formation and decay. In addition the k_2 rate constant may also have absorbance contributions from FAD-to-FMN electron transfer [228]. Figure 4.14 shows an absorption transient measured at 475 nm following the reduction of flavins in P450 MT1 by 1 mM NADPH at 10 °C.

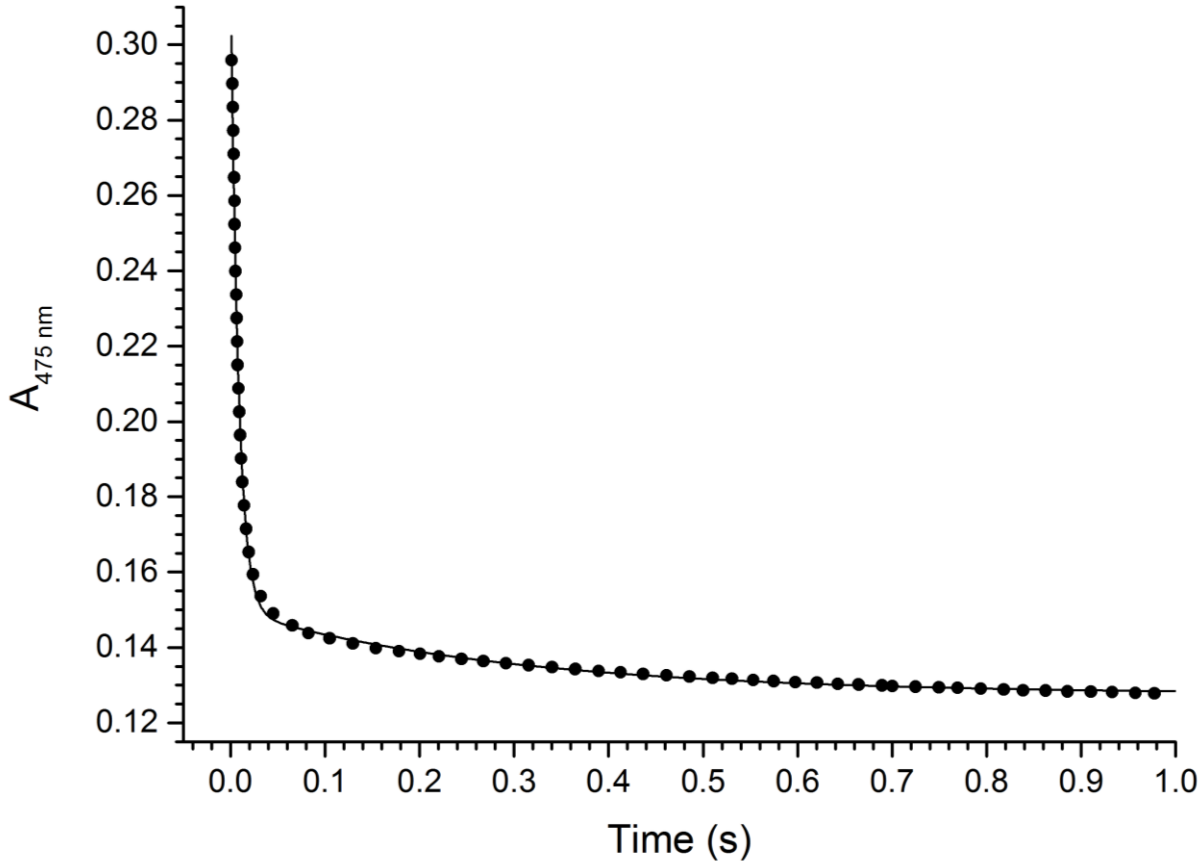

Figure 4.14 Single wavelength stopped-flow transient following flavin reduction in P450 MT1 by NADPH. Flavin reduction was followed at 475 nm for 1 second after the rapid mixture of 20 µM P450 MT1 with 2 mM NADPH in 50 mM KPi (pH 7.0) containing 200 mM KCl at 10 °C. The absorbance transient (full circles) was best fitted using a double exponential function (black line) which gives a k_1 of 92 ± 0.4 s^{-1} describing the rate constant electron transfer from NADPH to FAD under the conditions used. The k_2 rate constant is 4 ± 0.1 s^{-1}.

The k_1 rate constant obtained for flavin reduction in P450 MT1 was 92 s^{-1} ± 0.4 using 1 mM NADPH at 10 °C. Using the same experimental conditions, the effect of electron donor concentration on P450 MT1 flavin reduction was probed. The different k_{obs} rate constants obtained for NADPH- and NADH-dependent reduction of P450 MT1 at concentrations between 0 – 1.2 mM at 10 °C are plotted in Figure 4.15.

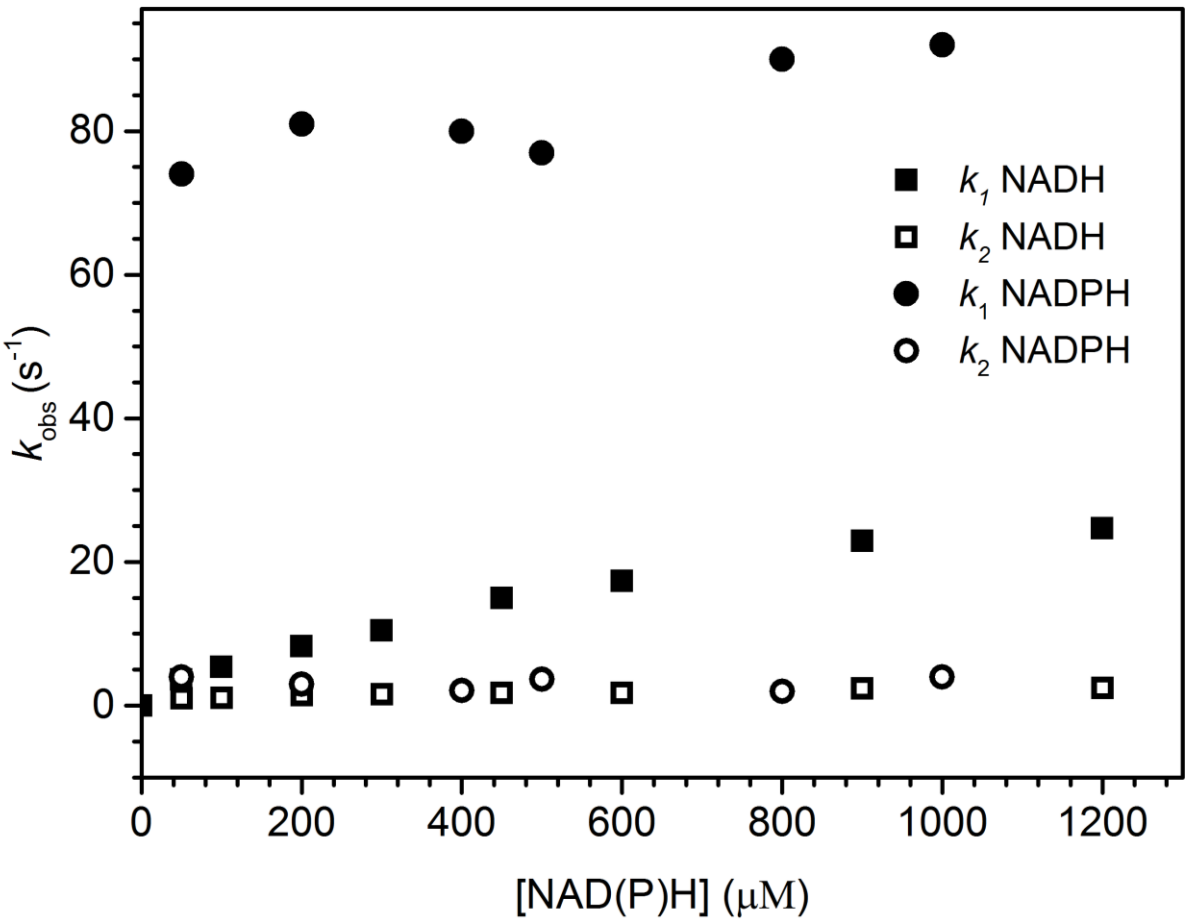

Figure 4.15 Stopped-flow analysis of the effects of NADPH and NADH concentration on P450 MT1 flavin reduction rate. Absorbance transients following P450 MT1 flavin reduction at 475 nm were obtained using a range of NAD(P)H concentrations between 0 – 1.2 mM. Absorption transients obtained for NADPH-dependent reduction of P450 MT1 flavins were fitted using a double exponential function, while NADH-dependent flavin reduction data were fitted using a triple exponential function. The k_1 and k_2 rate constant values were plotted against the relevant NADPH and NADH concentrations used. Stopped-flow reactions were done in 50 mM KPi buffer (pH 7.0) plus 200 mM KCl at 10 ˚C, using a final enzyme concentration of 10 μM. The k_3 rate constant values generated from the triple exponential fit of NADH-dependent flavin reduction data were omitted from this graph for clarity, but are shown in Figure 4.16.

The plot in Figure 4.15 shows the limiting rate constant (k_{lim}) of 92 ± 0.4 s^{-1} obtained for MT1 flavin reduction by NADPH at 10 °C. In Section 4.4 it was found that NADPH binds very tightly to P450 MT1, based on the K_M value obtained from steady-state data, and it seems that the binding of NADPH is sufficiently tight that NADPH concentrations of ~50 µM are high enough to satisfy pseudo first order conditions (5x the enzyme concentration at 10 µM). There is no substantial increase in the k_1 value for flavin reduction rate at higher NADPH concentrations, and linear fitting of the k_1 data set provides the k_{lim} value of 92 ± 0.4 s^{-1} for flavin reduction.

In contrast, there is a clear NADH concentration dependence on the fast rate constant (k_1) for flavin reduction with this coenzyme (Figure 4.16). A hyperbolic fit of k_1 values against the relevant NADH concentrations gave an apparent k_{lim} of 41.9 ± 3.1 s^{-1} for P450 MT1 flavin reduction by NADH at 10 °C, and a K_d value of 815.8 ± 113.4 µM. The k_{lim} of 92 s^{-1} for the NADPH-dependent flavin reduction at 10 °C is over two-fold that for NADH at 41.9 s^{-1} which, together with its 100-fold tighter binding (Table 4.2), is further evidence of P450 MT1's strong preference for NADPH over NADH.

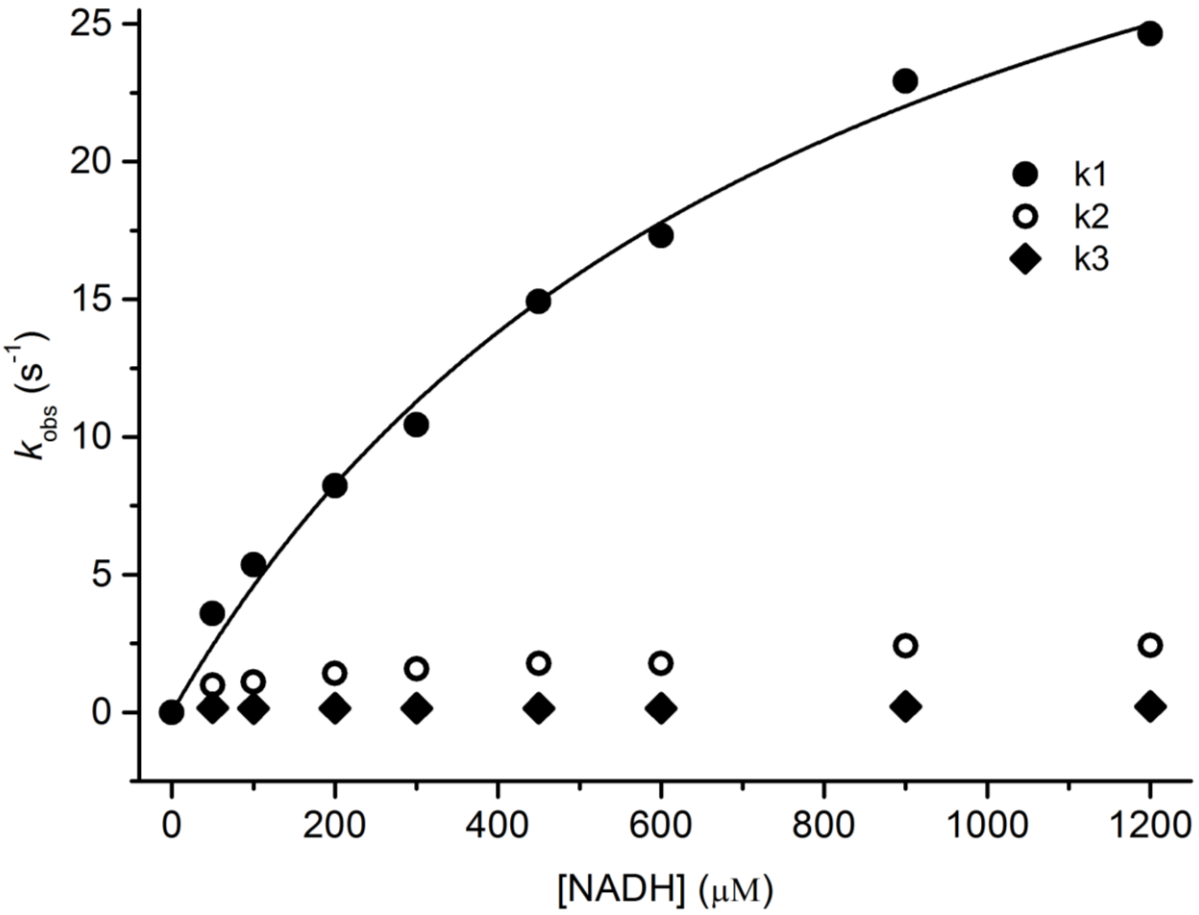

Figure 4.16 Stopped-flow analysis of NADH-dependent reduction of flavins in P450 MT1. Rate constants k_1 (full circle), k_2 (hollow circle) and k_3 (diamond) were obtained from the fitting of ΔA475 versus time transients using a triple exponential function for a range of NADH concentrations between 0 – 1.2 mM. There is an apparent hyperbolic dependence of *k*1 on NADH concentration and the data obtained were fitted (black line) to Equation 1 (hyperbolic function) to give limiting rates of reduction: *k*lim 1 = 41.9 ± 3.1 s^{-1} and *K*d = 815.8 ± 113.4 μM for NADH). There is no strong dependence of *k*2 or k_3 on NADH concentration, and the *k*lim values are 2.5 ± 0.1 s^{-1} and 0.24 ± 0.2 s^{-1} (hyperbolic function, fit not shown). Stopped-flow reactions were done using 50 mM KPi buffer (pH 7.0) containing 200 mM KCl at 10 ˚C, using 10 μM enzyme.

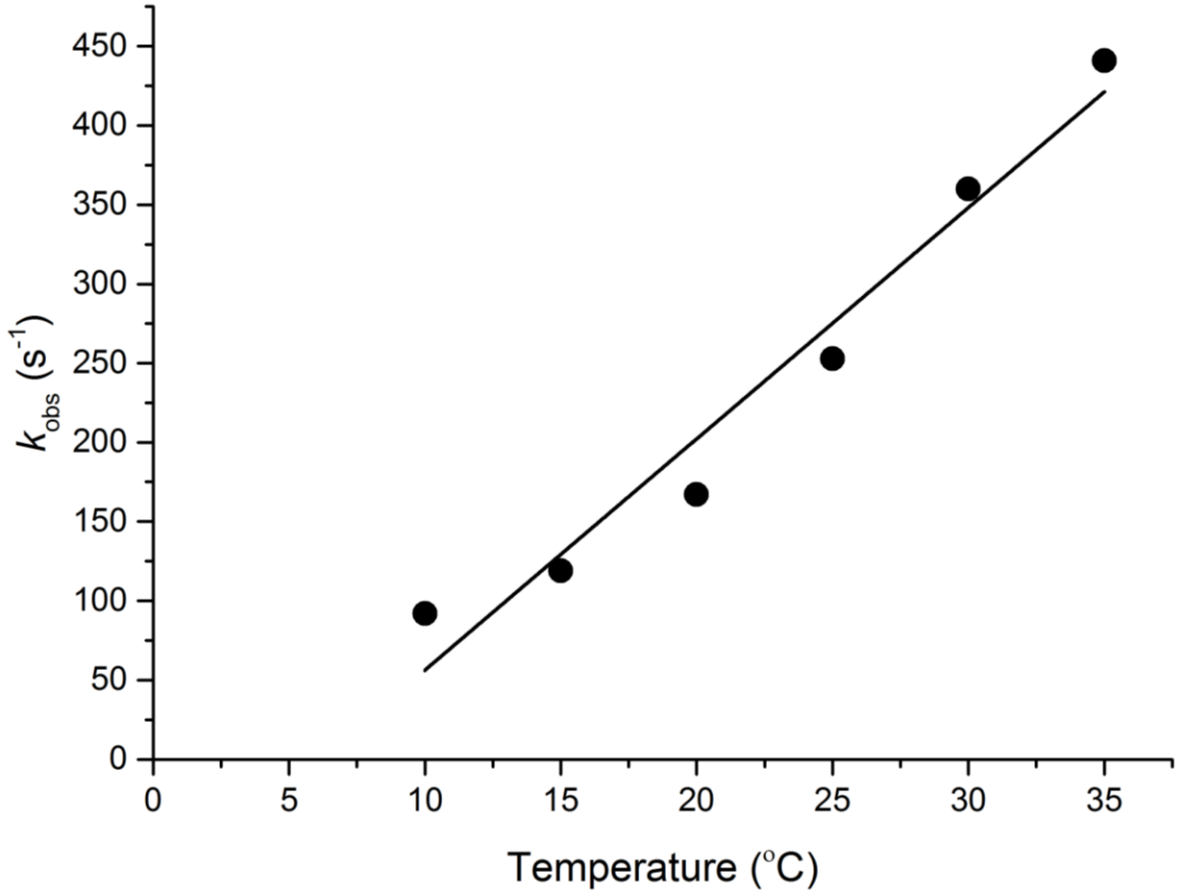

Figure 4.15 The effects of temperature on the kinetics of flavin reduction in P450 MT1. The major rate constant k_1 (k_{obs}, black circle) obtained from the fitting of biphasic absorbance transients using a double exponential function was plotted at each relevant temperature point. The k_{obs} values were fitted to a linear function (black line) to show the increase in rate with temperature, with a slope of 14.5 ± 1.5 s^{-1} $°C^{-1}$. Absorbance at 475 nm was monitored after the rapid mixture of 10 µM P450 MT1 with 1 mM NADPH in 50 mM KPi buffer (pH 7.0) plus 200 mM KCl at 5 °C intervals in the temperature range from 10 – 35 °C.

The effect of temperature on flavin reduction in P450 MT1 from the mesophilic thermophile *M. thermophila* was investigated using stopped-flow absorption kinetics. The rate constant for flavin reduction by NADPH approximately doubles every 10 °C in this temperature range, from 92 s^{-1} at 10 °C to 441 s^{-1} at 35 °C.

4.5.2 Investigating Flavin-to-Heme Electron Transfer

The rate constant for the first electron delivery from FMN to heme was investigated by monitoring the transient kinetics of absorbance change at 450 nm observed upon the binding of CO to reduced heme iron to form an Fe^{2+}-CO complex (Figure 4.18). 40 µM P450 MT1 was mixed with 500 µM NAD(P)H in CO-saturated 50 mM KPi (pH 7.0) containing 200 mM KCl, either with or without 0.5 mM arachidonic acid and under anaerobic conditions. Data were collected over 5 seconds to allow sufficient time for complete Fe^{2+}-CO complex formation. All stopped-flow absorption data collected for heme reduction were fitted using a double exponential decay function (Methods 2.23.2).

The initial spectrum (thick black line with highest intensity at 400 nm and 480 nm) in Figure 4.18 is typical of the near-fully oxidised, high-spin MT1. The progression of reduction of the enzyme through P450 MT1's domains is easily followed in the absorbance spectra. The flavins are the first to reduce with a decrease in absorbance over the range from 400 – 520 nm. The high-spin heme peak at 390 nm remains mainly oxidised at this stage, but as the oxidised flavins also absorb in this range, the peak decreases in intensity somewhat as the flavins become reduced. Subsequently, electron transfer from FMN-to-heme enables reduced heme iron to bind CO, and for the accumulation of the P450 complex. The rate of flavin reduction can be followed using this experimental set up in the initial stages of the reaction. By analysis of the absorbance change at 475 nm and fitting of the absorbance transients using a double exponential function, a consistent value of k_1 values = 167 ± 12 s^{-1} was obtained at 20 °C, and these data are concordant with the single wavelength data plotted in Figure 4.15. From the same experimental analysis, the value of k_2 was 80 ± 24 s^{-1}, and the relative contributions to the absorbance amplitude change at 475 nm were 84 and 16%, respectively.

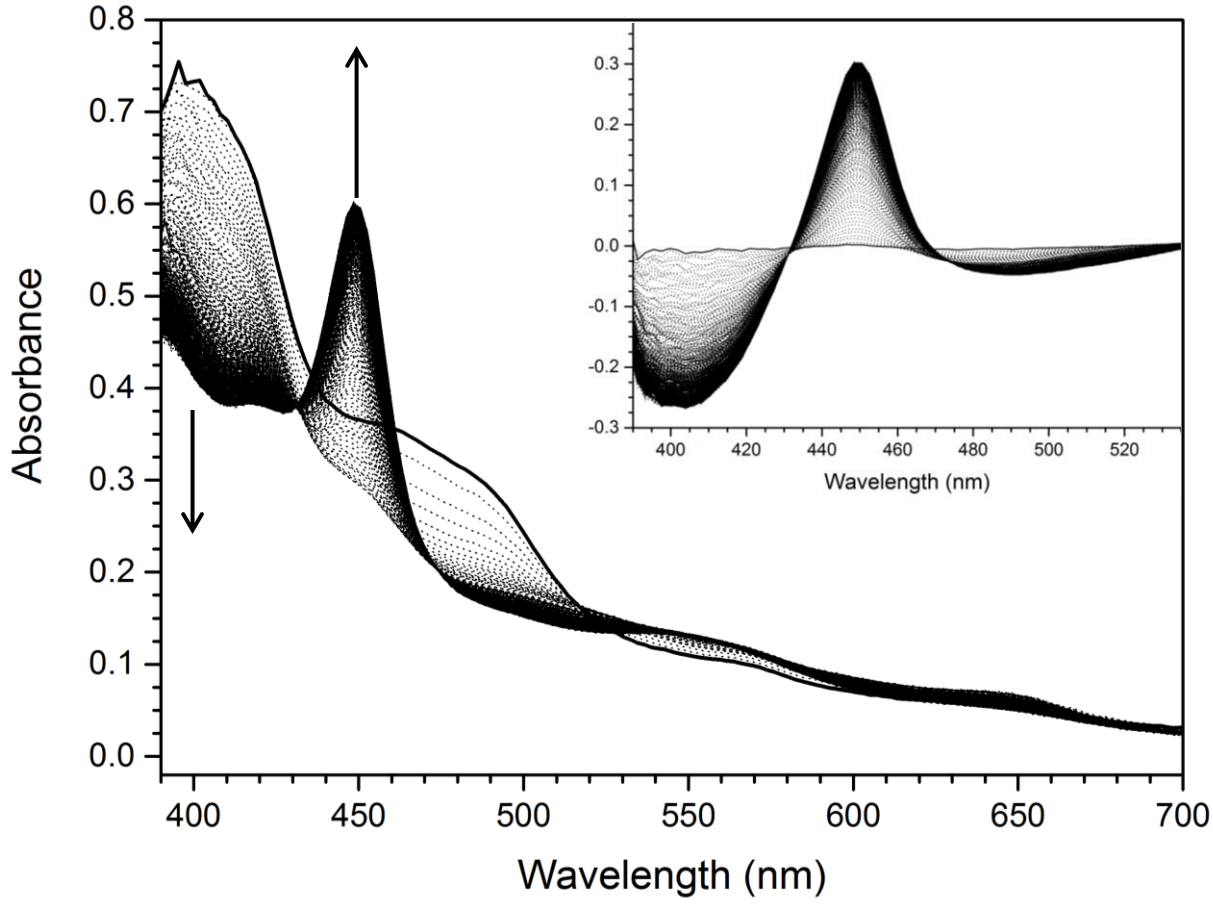

Figure 4.18 Photodiode array stopped flow analysis for Fe^{2+}-CO complex formation in P450 MT1. UV-visible spectral data from 390 nm to 700 nm were recorded after mixing (i) 40 µM P450 MT1 plus 500 µM arachidonic acid with (ii) 500 µM NADPH plus 500 µM arachidonic acid, with both samples in deaerated, CO-saturated 50 mM KPi (pH 7.0) containing 200 mM KCl. 1000 time point spectra were taken over 2 seconds. Near fully-oxidised, arachidonate-bound P450 MT1 is shown as a thick black line and the final, reduced CO-bound heme complex is shown a thick black line with maximal intensity at 450 nm (with all intermediate spectra displayed as dotted black lines). The evolution of the 450 nm peak associated with the binding of CO to reduced heme in P450 MT1 and concomitant decrease in the absorbance of the substrate-bound heme peak (arrows) can be better observed in the inset. The inset shows the difference spectra (from the point at which the flavins are mainly bleached) obtained by subtraction of the initial spectrum recorded for the mainly oxidised, substrate-bound enzyme from each of the successive spectra, in which the Fe^{2+}-CO complex of the P450 MT1 heme accumulates. In the main panel, the reductive bleaching of the P450 MT1 flavins is seen to occur over the first 20-25 spectra collected (seen most clearly in the region from ~450-520 nm), while the progression towards to the fully formed Fe^{2+}-CO complex at 450 nm takes considerably longer. The difference spectra in the inset show the development of a peak at 450 nm, a trough at 400 nm and 2 isosbestic points at 432 nm and 473 nm.

The inset in Figure 4.18 shows the difference spectra from the time point where flavins are mainly reduced and the Fe^{2+}- CO complex starts to evolve. An increase in the absorbance of the reduced heme Fe^{2+}-CO complex at 450 nm in observed, as is the concomitant decrease of oxidised, high-spin heme absorbance at 390 nm. There is a notable contribution from flavin absorbance changes (in the final stages of their reduction) after the isosbestic point at 473 nm. As indicated above, the vast majority of this change occurs prior to heme reduction, but these minor changes may contribute to a small extent to the heme absorbance changes fitted to define a rate constant for the FMN-to-heme electron transfer process.

The absorbance transients at 450 nm (Figure 4.19) for the FMN-to-heme electron transfer process and the concomitant evolution of the heme Fe^{2+}-CO complex in arachidonate-bound P450 MT1 were fitted using a double exponential function, giving a major rate constant, k_1 of 15.13 ± 0.1 s^{-1}. Using the same experimental conditions, the effects of different fatty acid substrates and electron donors (NADH and NADPH) on FMN-to-heme electron transfer were investigated, and the data are presented in Table 4.6.

Faster P450 MT1 heme iron reduction occurs with NADPH than with NADH, and this phenomenon is observed with both lauric acid and NPG substrates (Table 4.6). As the rate constant for NADH-dependent flavin reduction is substantially lower than that for NADPH-dependent (Figure 4.15), this might be expected to carry through into the rate constant for FMN-to-heme electron transfer (as measured by formation of the Fe^{2+}-CO complex). However the data shown in Table 4.6 suggest that the rate constant (k_1) values for FMN-to-heme electron transfer using NADH are ~60% those with NADPH as the donor. This suggests that FMN-to-heme electron transfer is rather slower than NAD(P)H-dependent flavin reduction, such that there is a much lower difference between NADH/NADPH-dependent heme reduction (Fe^{2+}-CO complex formation) rate constants than there is between NADH/NADPH-dependent flavin reduction rates in P450 MT1.

An interesting trend is observed in the rate constants for the first FMN-to-heme electron transfer across the different fatty acid substrates investigated with NADPH as the reductant (Table 4.6). The concentration of substrate used in these experiments was 500 µM, well above their K_d values by at least 100-fold. The amount of high-spin heme iron shift elicited by a particular substrate in P450 MT1 is correlated with the observed rate constants for the NADPH-dependent Fe^{2+}-CO complex formation in P450 MT1. The highest rate constant

achieved was with NPG substrate at 18.47 ± 0.8 s^{-1}. In the NPG-bound form, P450 MT1 is ~95% high-spin. Lauric acid had the lowest rate constant for NADPH-dependent flavin-to-heme electron transfer at 10.21 ± 0.1s^{-1}, and in this case only 10% of the P450 MT1 heme iron is in the high-spin state.

This trend can be explained by the relationship of substrate binding to the efficiency of the initial heme iron reduction step from FMN. During the catalytic cycle, heme iron reduction occurs only after the removal of the distal-ligated water molecule from the ferric heme iron, a process driven by substrate binding (though dependent on the mode of binding and affinity for the substrate) (Section 1.11). Substrate binding shifts the ferric heme iron from a hexacoordinated to a pentacoordinated state. This coordination change is responsible for an absorbance change in the Soret peak from ~418 nm to ~390 nm, known as type I (high-spin) shift. In this state, the heme iron's redox potential is increased sufficiently to allow efficient reduction by electron delivery from FMN. The substrate-controlled step has been observed previously in both BM3 and $P450_{cam}$ [27,215]. The amount of high-spin shift (Table 4.6) is directly related to the population of enzyme with a more positive redox potential in this pentacoordinated state. If only a fraction of the enzyme population is in a high-spin state at equilibrium, e.g. 10% for lauric acid, this proportion will have an effect on the flavin-to-heme transfer rate, as is clearly seen for lauric acid, which has the lowest rate constant for heme reduction among the fatty acids tested.

The steady-state rate constants measured for lauric acid- and arachidonic acid-dependent NADPH oxidation by P450 MT1 are 4.80 s^{-1} and 1.98 s^{-1} (Section 4.2), and these values are ~2-fold and ~7.5-fold lower than the observed flavin-to-heme electron transfer rates of 10.21 s^{-1} and 15.13 s^{-1}, respectively, measured with these substrates. This observation indicates that the flavin-to-heme electron transfer rate constant may not be the only contributor to rate limitation in steady-state. For instance, hydroxylated product release or the second FMN-to-heme electron transfer step could also be major factors limiting enzyme activity.

There is no observable rate for P450 MT1 heme iron reduction in the absence of substrates. A small amount (~0.02 absorbance units at 450 nm) of CO-bound heme was formed rapidly in the control experiments, but this proportion does not change further, suggesting that there may be small amount of fatty acid bound to the enzyme, and that only this proportion of the sample can be reduced to form the Fe^{2+}-CO complex.

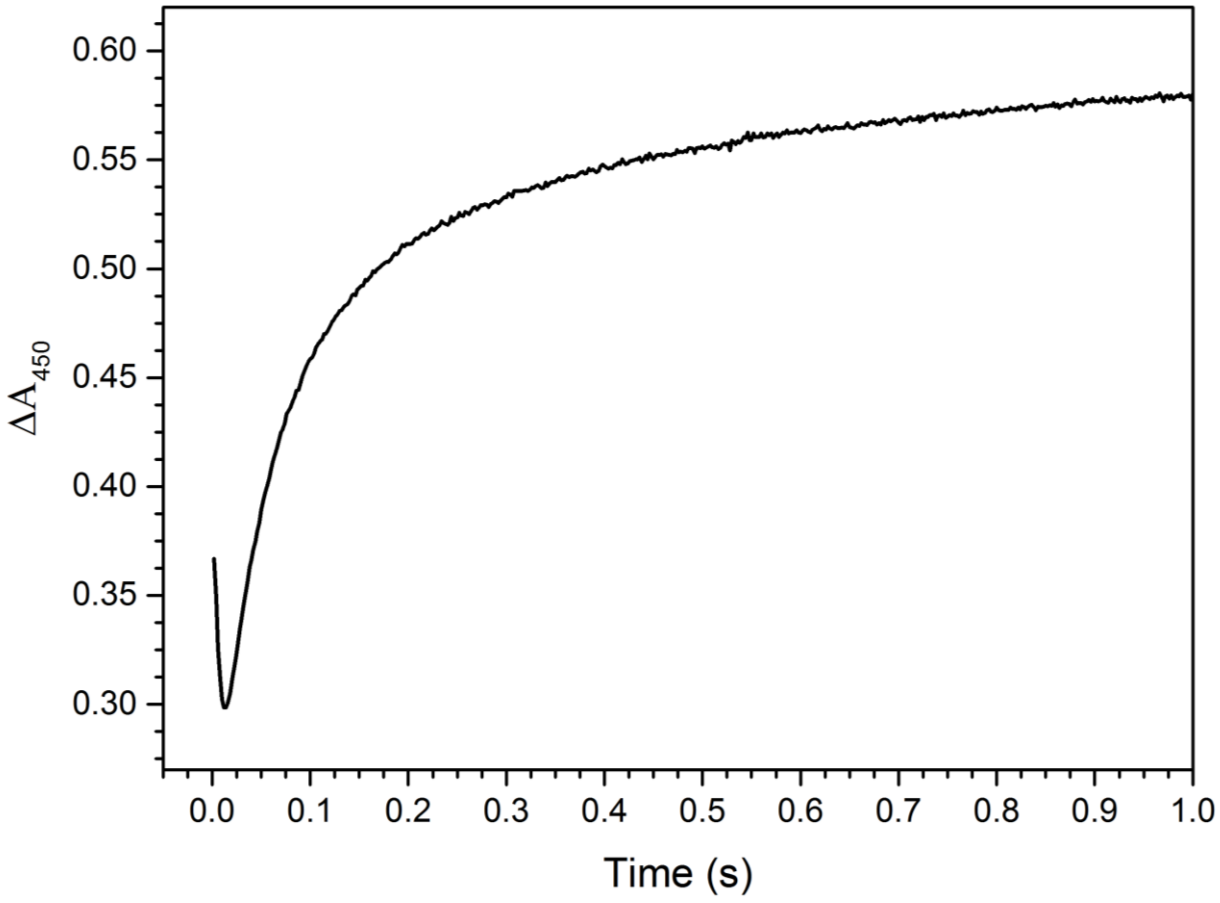

Figure 4.19 Single wavelength transient at 450 nm from a photodiode array stopped-flow experiment following Fe^{2+}-CO complex formation. 1000 data points were collected at each wavelength over 2 seconds (1 second shown in the figure) after the rapid mixing of 40 µM high-spin P450 MT1 with 2 mM NADPH. Entire spectral data sets were collected using the PDA stopped-flow set up. Heme reduction was measured by following Fe^{2+}-CO peak formation at 450 nm (black line), with data fitted using a double exponential function (fit not shown) to give a k_1 of 15.13 ± 0.13 s^{-1}. The absorbance transient (black line) shows an initial decrease in absorbance corresponding to flavin reduction, which was not included in the fit. Both (i) P450 MT1 and (ii) NADPH were in 50 mM KPi (pH 7.0) containing 200 mM KCl and 500 µM arachidonate at 20 °C and in anaerobic conditions. The fit is omitted from the graph as it overlaps with the transient completely. Parameters from the biphasic fit are A_1 = 0.25 ± 0.001, t_1 = 0.07 ± 0.001 s, A_2 = 0.1 ± 0.001, t_2 = 0.6 ± 0.006 s and k_2 = 1.56 ± 0.01 s^{-1}.

Table 4.6 Effect of substrate and electron donor on FMN-to-heme electron transfer rate constant. All rate constants shown are the major (k_1) rate constants from a single ΔA_{450} transient fitted using a double exponential function. The amount of high spin shift (%) was determined from substrate binding titrations in Section 3.3.1 and is included for comparison. N.D. stands for not determined. NAD(P)H and fatty acid substrate concentrations were 1 mM and 500 µM in the mixing chamber.

Substrate	Rate constant (k_1, s^{-1})		High-spin shift (%)
	NADPH	NADH	
Lauric acid	10.21 ± 0.11	6.34 ± 0.05	10
Arachidonic acid	15.13 ± 0.10	N.D.	60
NPG	18.47 ± 0.78	12.25 ± 0.32	95

4.6 Product determination by GCMS

Substrate candidates for product determination composed of both straight chain and branched chain fatty acids were identified from previous optical binding studies as well as from steady-state kinetic experiments (Sections 3.3.2 and 4.4) and are represented in Scheme 1. Reactions were set up as described in Methods (Section 2.24) for each of the substrates along with the appropriate controls, and an identical experimental was set up in the absence of enzyme. The reaction products were purified using solid phase extraction (SPE) columns and derivatised using BSTFA + TMCS (Materials, section 2.24). BSTFA + TCMS incorporate silyl groups ($Si(CH_3)_3$) into the hydroxyl groups of both alcohols and carboxylic acids. GCMS experiments were carried out with assistance from Sarah Matthews (Munro Group, University of Manchester) at the premises of her industrial (CASE) sponsor: Agilent Technologies Ltd, Cheadle, Manchester, UK.

Figure 4.20 Product identification from the P450 MT1-mediated oxidation of straight chain fatty acids from C12–16 (left, table) and branched chain fatty acids (right, table). The ω-1 to ω-3 positions on the left hand diagram indicate the sites of substrate oxidation on the carbon chain, and the *iso* and *anteiso* groups on the right hand diagram display the location of the methyl group on the branched chain fatty acid substrates.

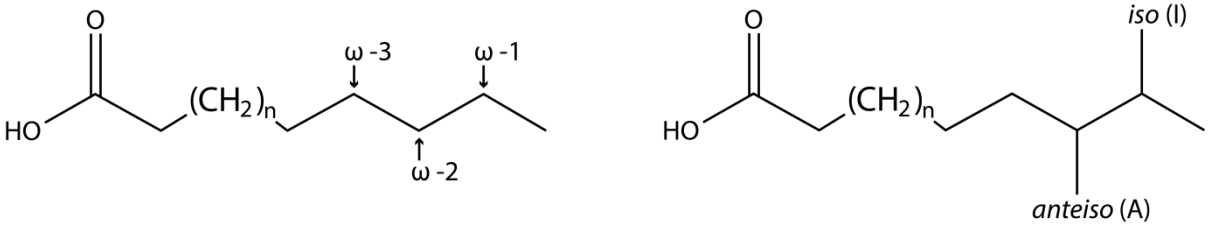

Number	Fatty acid	n (CH_2)	Number	Fatty acid	n (CH_2)
12	Lauric acid	5	**14**	*Iso* myristic acid	6
13	Tridecanoic acid	6	**14**	*Anteiso* myristic acid	6
14	Myristic acid	7	**15**	*Iso* pentadecanoic acid	7
15	Pentadecanoic acid	8	**15**	*Anteiso* pentadecanoic acid	7
16	Palmitic acid	9			

The GC traces for all the fatty acid substrates tested for product formation with P450 MT1 had 3 distinct peaks and analysis of their fragmentation by MS showed that these corresponded to the hydroxylated products at positions ω-1, ω-2 and ω-3, as is typical of BM3 [48,316]. Figure 4.20 shows the GC traces from the P450 MT1-dependent turnover of the saturated fatty acids lauric acid and tridecanoic acid. All other GC traces obtained for substrate turnover reactions are in Appendix 7.9.

The fragmentation pattern of peaks a (at 8.95 min) in the lauric acid trace (top) and b (at 9.35 min) in the tridecanoic acid trace (bottom) in Figure 4.21 are displayed in Figure 4.24.

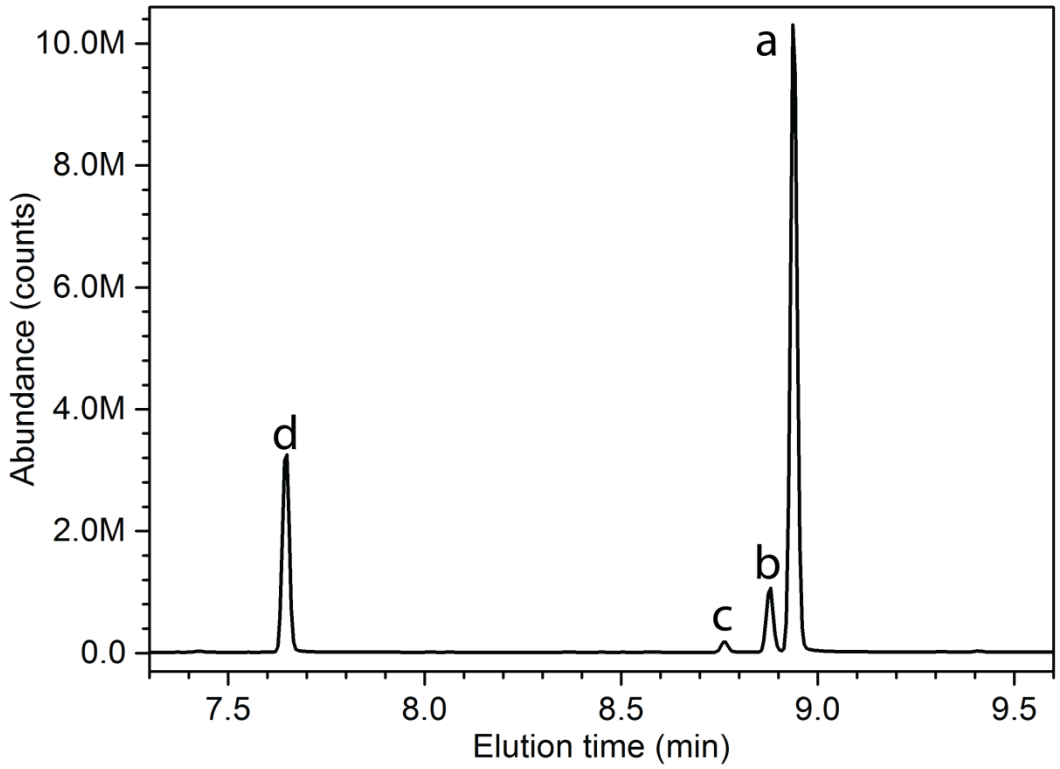
10.0M
8.0M
6.0M
4.0M
2.0M
0.0
Abundance (counts)
a
b
c
d
7.5
8.0
8.5
9.0
9.5
Elution time (min)

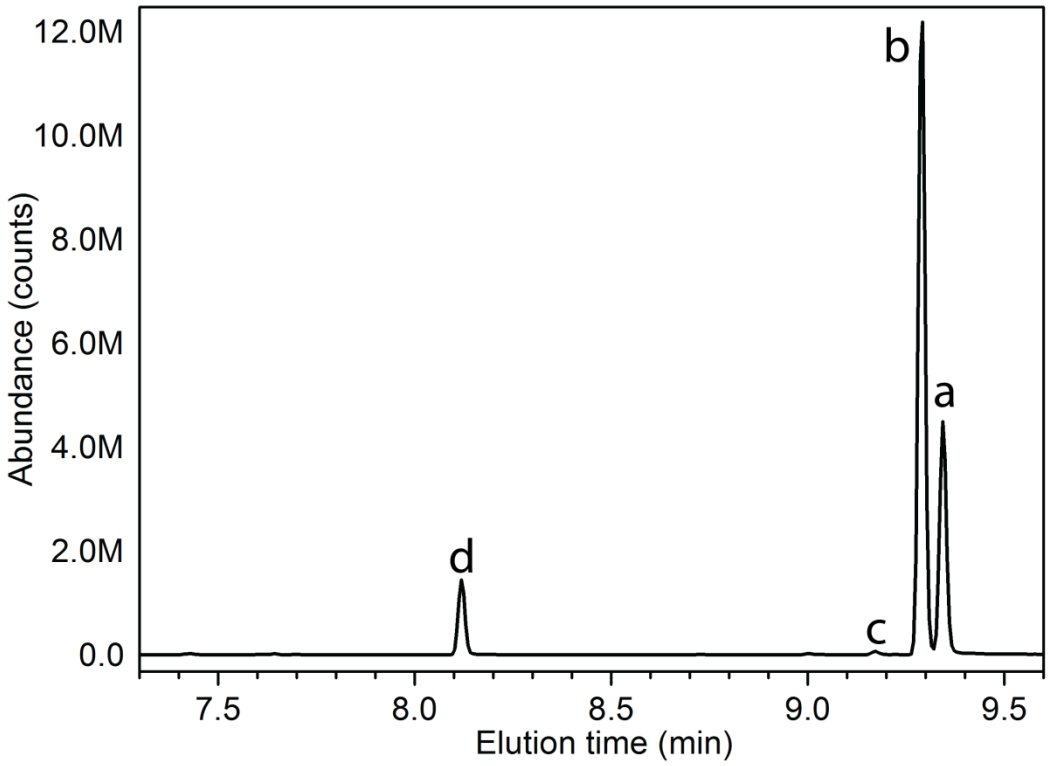
12.0M
10.0M
8.0M
6.0M
4.0M
2.0M
0.0
Abundance (counts)
b
a
d
c
7.5
8.0
8.5
9.0
9.5
Elution time (min)

Figure 4.21 GC traces showing the separated peaks of the hydroxylated products from P450 MT1 with lauric acid (top) and tridecanoic acid (bottom) substrates. The ω-1, ω-2, and ω-3 hydroxylated products are labelled ‘a’, ‘b’ and ‘c’ respectively for both lauric acid (top) and tridecanoic acid (bottom) traces. Peaks a, b and c have column retention times of 8.95 min, 8.8 min and 8.75 min for lauric acid (top) and 9.35 min, 9.3 min and 9.15 min for tridecanoic acid, respectively. Unconverted substrate is labelled ‘d’ in both traces and has a retention time of 7.65 min for lauric acid and 8.1 min for tridecanoic acid.

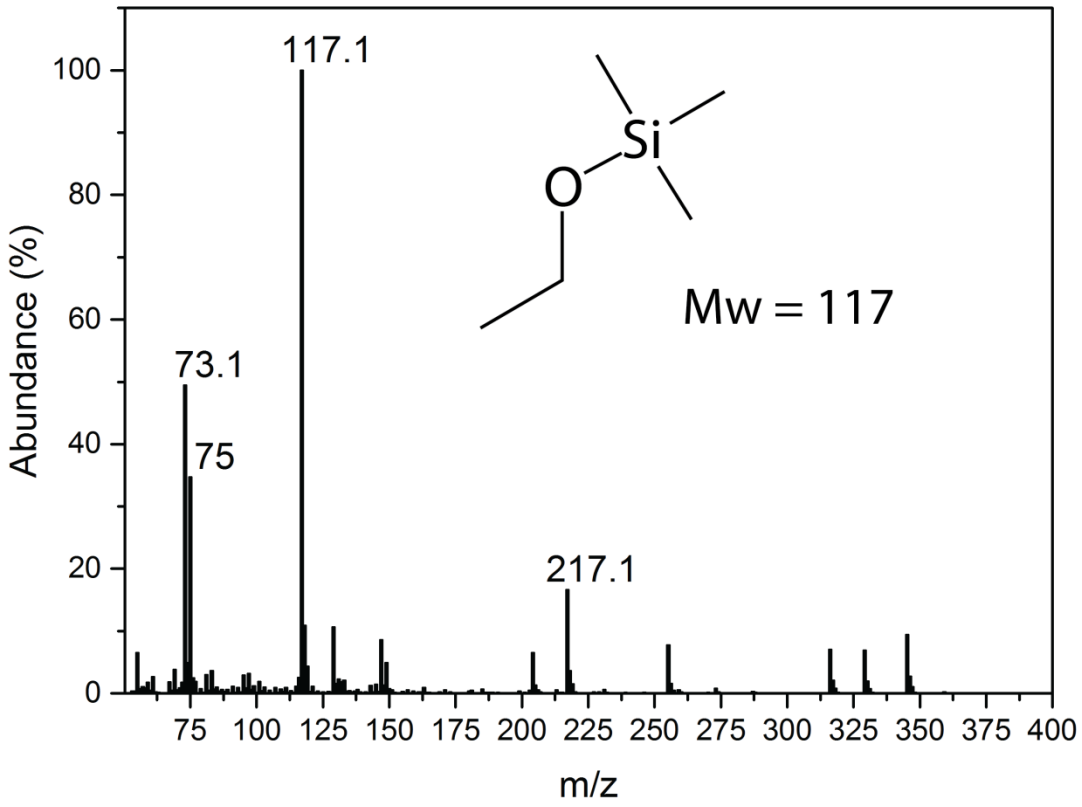
117.1
73.1
75
217.1
Mw = 117
Abundance (%)
m/z

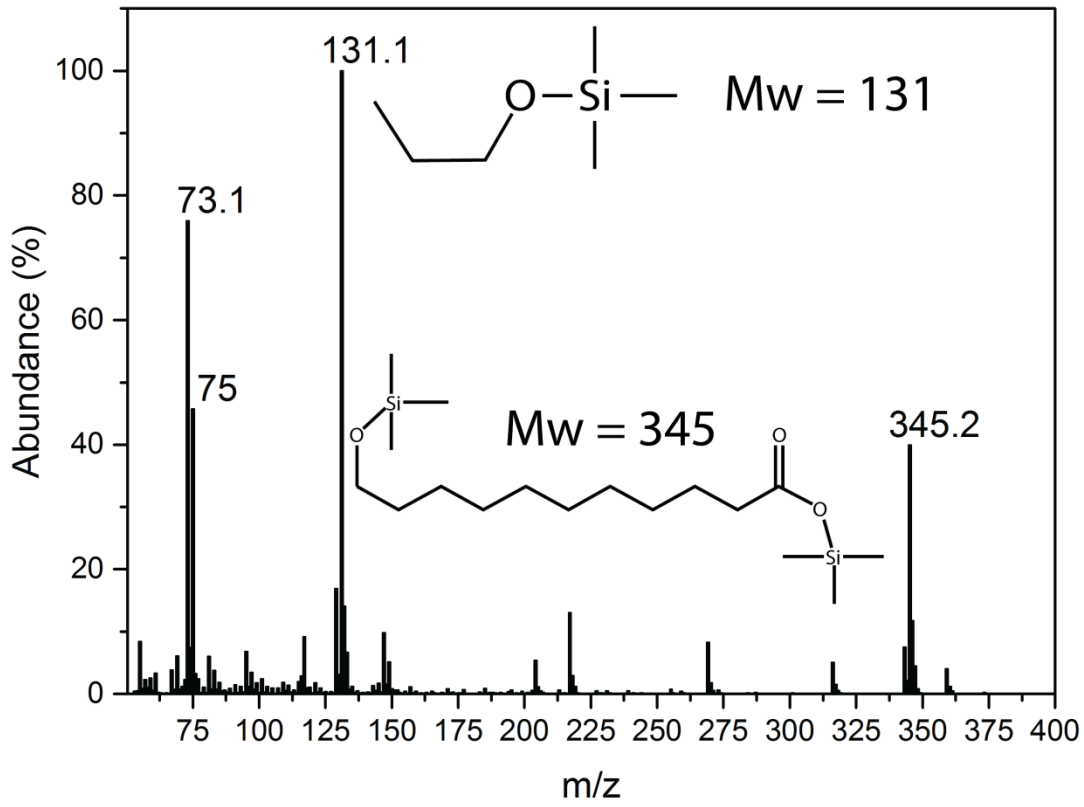
131.1
Mw = 131
73.1
75
Mw = 345
345.2
Abundance (%)
m/z

Figure 4.22 Mass spectral fragmentation of derivatised ω-1 hyroxylauric acid (top) and ω-2 hydroxytridecanoic acid (bottom). Traces show the fragmentation pattern of GC peaks observed in Figure 4.22 with the mass to charge (m/z) ratio on the x-axis and the abundance of fragments on the y-axis. The top panel shows the fragmentation pattern observed for the peak at the 8.85 min elution point of the lauric acid sample, showing a single peak belonging to a fragment with a molecular weight of 117. The inset shows the ω-1 hydroxylated fragment with a M_w of 117 that corresponds to the peak observed. Displayed in the bottom panel is the fragmentation pattern observed for peak at the 9.3 min elution point the tridecanoic acid sample, showing two distinct peaks with molecular weights of 131 and 345. The inset shows the ω-2 hydroxylated tridecanoic fragments with molecular weights of 131 and 345 that correspond to the peaks observed. Only significant peaks above an abundance of 20% are labelled with their corresponding molecular weight. Observed in both traces are peaks at 73 and 75, which originate from the derivatising agents BSTFA and TCMS and correspond to isolated silyl groups.

As is evident from the data in Figure 4.21, P450 MT1 preferentially hydroxylates lauric acid at the ω-1 position, as opposed to the ω-2 position in tridecanoic acid. This regioselectivity trend can be observed in all the straight chain fatty acids trialled and the relative amounts of hydroxylated products (ω-1, ω-2 and ω-3) formed are shown in Table 4.7. Another general trend in P450 MT1 with straight chain, saturated fatty acids is for hydroxylation regioselectivity not to follow a consistent pattern, with switching between ω-1 and ω-2 hydroxylated products as the major species as the lengths of the straight chain saturated fatty acids increase.

Table 4.7 The distribution of P450 MT1 hydroxylated products for saturated fatty acid substrates from C12 – C16. The preference for P450 MT1 to hydroxylate even chain fatty acids at the ω-1 position and odd chain fatty acids at the ω-2 position is evident from these data. The ω-3 hydroxylated fatty acid is the minor product in all cases.

Carbon no.	Substrate	Relative conversion (%)		
		ω-1	**ω-2**	**ω-3**
12	Lauric acid	90.0	9.7	2.3
13	Tridecanoic acid	20.5	73.0	1.5
14	Myristic acid	62.0	27.0	8.0
15	Pentadecacnoic acid	36.0	58.0	6.0
16	Palmitic acid	64.0	30.4	5.6

The same incubations were next carried out with branched chain fatty acids in order to observe the effects of the methyl groups on the regioselectivity observed for both odd and even chain fatty acids. For this reason, the separate *iso* and *anteiso* isomers in odd and even chain fatty acids were used (Figure 4.20, right).

The hydroxylation profiles for the four branched chain fatty acids also follow a trend. The *iso* fatty acids were preferentially oxidised at the ω-2 position while the *anteiso* fatty acids demonstrated a preference for hydroxylation at the ω-1 position.

Figure 4.23 shows the product profile of the straight chain fatty acid 'parent' molecules with their *iso* and *anteiso* branched chain isomers. For the *iso* branched chain fatty acid, oxidation at a single position (ω-1) accounted for 70-98% of the products, a higher extent of regioselectivity than is observed with *anteiso* branched chain fatty acids (54-70% of products at the ω-2 position), or with straight chain fatty acids, where 60-90% of products are hydroxylated at the ω-1 position in even chain fatty acids and 58-70% of products are hydroxylated at the ω-2 position in odd chain fatty acids. The highest extent of regioselectivity observed in BM3 towards branched chain fatty acids was with *iso* pentadecanoic acid, where 90% of the product was hydroxylated at the ω-2 position, compared with P450 MT1 where 97.5% of *iso* myristic acid was hydroxylated at the ω-2 position [350].

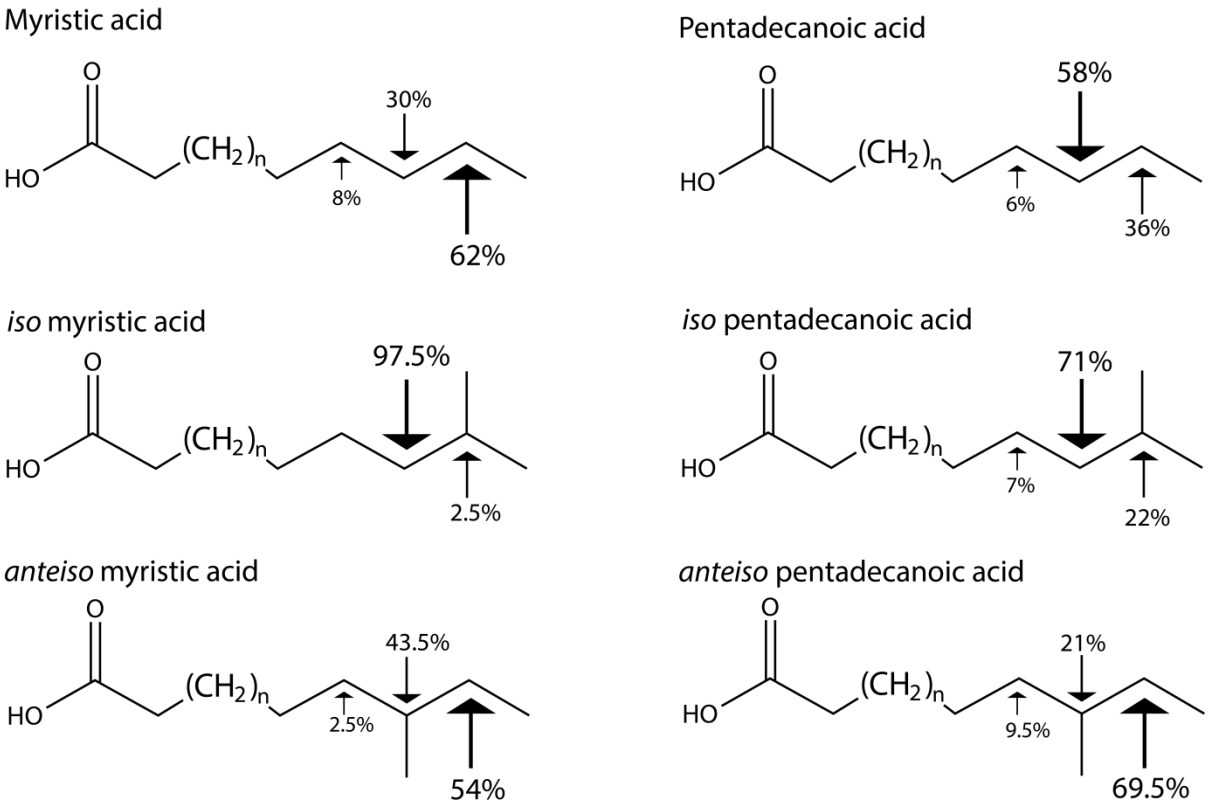

Figure 4.23 Comparison of P450 MT1-dependent hydroxylated product distribution in branched chain fatty acids and their straight chain parent molecules. The straight chain fatty acids myristic acid and pentadecanoic acid (labelled) are preferentially hydroxylated at the ω-1 (62%) and ω-2 (58%) positions, respectively, and are shown for comparison to the other data. The *iso* branched chain isomers both show preference for the ω-2 position, with 97.5% of the overall product in *iso* myristic acid and 71% for *iso* pentadecanoic acid being the ω-2 hydroxylated product. The *anteiso* branched chain fatty acids all show a preference for the ω-1 position. 54% of the overall product in *anteiso* myristic acid and 69.5% in *anteiso* pentadecanoic acid are hydroxylated at the ω-1 position. The ω-3 is a minor hydroxylation product in all cases and is never present at levels above 9.5% of the overall hydroxylated product.

4.7 Discussion

After the identification of P450 MT1 (CYP505A30) from *M. thermophila*, the gene was expressed in *E. coli* and the protein purified, leading to the confirmation of P450 MT1 as a P450-CPR fusion enzyme homologous to the *B. megaterium* P450 BM3. Work presented in this chapter has focussed on the elucidation of the fatty acid substrate and electron donor (NADPH versus NADH) preference, and on the determination of various kinetic and catalytic parameters for P450 MT1, as well as on investigation of selected biophysical properties of this catalytically self-sufficient enzyme.

EPR spectroscopy proved to be an excellent tool to study P450 MT1, as various states of its three cofactors (heme, FAD and FMN) are detectable using EPR spectroscopy. Importantly, EPR can identify and quantify the low-spin and high-spin ferric heme in the resting state of P450 MT1 and its heme domain. In the case of many P450s, the development of high-spin heme iron is observed by UV-Vis spectroscopy on addition of substrates at ambient temperature. However, P450 high-spin changes on substrate binding by EPR at low temperatures is often not seen, as substrate binding is an endothermic process and the low-spin form is probably favoured during EPR data collection at a temperature of 10 K (as required for heme EPR studies). Solubility of fatty acid substrates is also severely compromised at such temperatures, although it would be expected that fatty acids would remain bound to the P450 in these EPR experiments, since samples are prepared at ambient temperature before rapid freezing prior to EPR data collection. Interestingly, the MT1 HD showed a small proportion of a high-spin EPR spectral feature in both its substrate-free and substrate-bound forms (Figure 4.4). It is possible that the heme domain of MT1 has a hydrogen bonding network that readily enables displacement of the distal water ligand, allowing it to shift to high-spin readily. Potentially, the reductase domain interactions with the heme domain also influence the low-spin/high-spin equilibrium, as might the tight binding of a fatty acid substrate (retained through purification in the MT1 HD) close to the heme iron in a proportion of the P450 molecules [110].

Incubation of the P450 MT1 enzyme with sodium dithionite ($E°'$ = -420 mV) facilitates the reduction of the CPR domain of P450 MT1 to an EPR silent, 4-electron reduced state. This is not observed following enzymatic reduction using NADPH or NADH ($E°'$ = -340 mV), indicating that one of the P450 MT1 redox couples (likely the FAD semiquinone/hydroquinone) has a redox potential out of the range that would enable the complete reduction of the flavins by the physiological electron donor.

By comparison with P450 MT1, the incubation of substrate-free BM3 with excess NADPH in the absence of fatty acid substrate leads to its inactivation, which has been speculated to be a form of control to prevent the futile cycling of electrons and the generation of reactive oxygen intermediates in the absence of substrate [320]. The exact reduction state is probably a mixture of 3- and 4-electron reduced forms of the BM3 CPR domain in the inactive complex, and the generation of the fully reduced $FMNH_2$ hydroquinone species is responsible for the inactivation, due to an unfavourable redox potential for heme iron

reduction in this state [94,222]. In this state, the BM3 FAD remains in a mixture of semiquinone and hydroquinone states after NADPH reduction, and this likely also reflects the situation that occurs in P450 MT1, with semiquinone species also observed by EPR upon incubation of P450 MT1 with NAD(P)H. Both NADPH and NADH elicited the formation of a mixture of red and blue semiquinone, as observed by EPR in P450 MT1 after a 30 second incubation and with G values of 16.3 and 15.9 respectively. A similar phenomenon was seen for P450 BM3, where the EPR linewidth indicated a mixture of red (FMN) and blue (FAD) semiquinones present in the active form of BM3 under turnover conditions [226,354]. Using NADPH, this EPR linewidth value is blue-shifted to 16.8 G at 5 minutes, indicative of a larger proportion of blue semiquinone at this stage than at the 30 second incubation point. By 10 minutes incubation, it appeared that only blue semiquinone was present in the sample, with a flavin radical linewidth value of 19 G. These data represent the diminishing population of red semiquinone in P450 MT1 with increased NADPH incubation time and the concurrent relative increase of the blue semiquinone species. The abolished red anionic semiquinone signal is indicative of the formation of $FMNH_2$ hydroquinone in P450 MT1 on extended NADPH (and NADH) incubation, while the blue semiquinone present remains on the FAD (i.e. as FADH), forming the inactive 3-electron reduced form, as also seen in the BM3 reductase. Therefore it seems likely that $FMNH^-$ is responsible for the red, anionic semiquinone signal in in P450 MT1 and that FADH is responsible for the blue neutral semiquinone formation. The apparent extent of formation of blue semiquinone in P450 MT1 is a molar ratio of 0.6 after a 10 minute incubation with NADPH, and this points to some $FADH_2$ hydroquinone also being present, and thus the likelihood of a mixture of 3-electron (~60%) and 4-electron (~40%) reduced forms of P450 MT1.

Redox potentiometry (spectroelectrochemistry) studies showed that P450 MT1's flavin cofactors were reduced in a "monophasic" manner through analysis of the absorbance versus potential changes near the oxidised flavin peak absorbance at 460 nm (Figure 4.8). Reduction also occurs in quite a positive potential range (compared to P450 BM3). These data suggest that the redox potentials for the FAD and FMN cofactors are close to one another. As mentioned previously, it was shown that P450 MT1 contains substantial amounts of both FAD and FMN cofactors, and EPR studies (following reduction and freezing of samples over short time periods) showed the formation of two distinct semiquinone species formed in P450 MT1. Redox potentiometry studies done with

analysis at 600 nm show the formation and decay of a P450 MT1 blue (FAD) semiquinone within the same redox potential window in which full reduction of the flavins was observed (Figure 4.9). This is again consistent with the flavin cofactors becoming reduced in quite a narrow reduction potential window. The 4-electron flavin midpoint potential of P450 MT1 at -119 mV vs NHE is quite positive compared to the flavin potentials in P450 BM3. In P450 MT1, flavin reduction is essentially complete by -200 mV vs NHE, while in full length P450 BM3 the range of flavin midpoint potentials is -177 mV $FMN_{sq/hq}$ to -372 mV $FAD_{sq/hq}$ [27,228]. Thus, despite clear similarities in structure and substrate selectivity, the redox properties of P450 MT1 are quite distinct from those of P450 BM3.

Based on the assumption that the FAD cofactor stabilises the blue, neutral FADH semiquinone species in P450 MT1, as is the case in P450 BM3 and in eukaryotic CPR enzymes [27,218], the plot of ΔA_{600} (reflecting absorption specific to flavin blue semiquinone) against the applied reduction potential (mV vs NHE) was made and (as described above) enabled the deconvolution of the flavin midpoint potentials for the FAD (and possibly with some contribution from FMN) oxidised/semiquinone and semiquinone/hydroquinone transitions. The biphasic curve obtained, similar to that observed for FAD reduction in full length P450 BM3, gave two midpoint potentials which follow the rise and fall of semiquinone-specific absorbance at 600 nm, coinciding with the formation of the 1-electron reduced blue semiquinone and then its conversion to the fully reduced hydroquinone. The $FAD_{ox/sq}$ E'_1 of -110 mV and $FAD_{sq/hq}$ E'_2 of -178 mV vs. NHE (Figure 4.9) both fall within the redox potential limits of flavin reduction (-50 mV to -190 mV) observed in P450 MT1 (Figure 4.8). Further redox potentiometry experiments with P450 MT1's isolated FAD and FMN domains could enable more accurate determination of the individual midpoint potential value for the FAD and FMN cofactors. While the midpoint potentials for the isolated BM3 FAD and FMN domains do match quite well with the ones obtained from analysis of full length BM3; redox potentiometric analysis of the isolated BM3 reductase (CPR) domain suggested a 30 mV difference between their FAD oxidised/semiquinone couples and a 10 mV difference between their FMN semiquinone/hydroquinone couples, as reported in Daff et al. [27], although the latter value is essentially identical within error. Activity assays involving analysis of the interactions of NADP(H) and various analogues with the reductase domain of CPR, along with computational modelling techniques, have shown that NADP(H) binding induces conformational changes that affect the redox potential of the flavin cofactors by up to 58

mV [226]. Mutagenesis experiments altering the isoalloxazine ring environment of FMN through the introduction of a hydrophobic residue nearby resulted in even larger changes in redox potential of ~180 mV [364]. The proximity of the nicotinamide ring of NADPH to the FAD cofactor in P450 MT1 could affect its electronic environment enough to significantly alter its redox potential, and this effect would not be observed in typical redox potentiometry experiments involving sodium dithionite.

P450 MT1 has a complex absorption spectrum with 3 contributing redox-active species: cysteine thiolate-ligated heme iron, FMN and FAD. Attempts to follow only absorbance changes associated with heme reduction in the arachidonic acid-bound state were unsuccessful, as the substrate induces a positive shift in the heme iron midpoint potential that makes it difficult to isolate absorbance changes from those associated with the flavins, and also enables electron transfer from the P450 MT1 FMN to the substrate-bound heme iron. In order to obtain a MT1 heme domain construct that could be used to determine the potential for the heme iron Fe^{3+}/Fe^{2+} transition, a stop codon was inserted into the *CYP505A30* gene shortly before the linker region to the CPR domain, in order to generate the isolated heme domain of MT1 – MT1 HD (amino acid residues 1-463 of the intact P450 MT1).

P450 MT1's flavin cofactors with a midpoint potential at -119 mV cannot efficiently transfer electrons to the substrate-free P450 heme iron, as its midpoint potential is at -288 mV and electron transfer is thermodynamically hindered. However, substrate binding was shown to induce a large positive shift in reduction potential of 219 mV from -288 mV to -69 mV. This positive potential shift is much larger than that observed in P450 BM3 with arachidonic acid (129 mV) and in $P450_{cam}$ with camphor (167 mV), by almost 100 mV in the former case [27,358]. BM3 heme domain crystal structures and NMR data both show that fatty acid substrate is bound distal to the oxidised heme, and apparently too far from a reactive heme iron species for any chemical reaction to occur. It has been proposed that structural changes occur following reduction of the heme iron to the ferrous state, and that this enables motion of the fatty acid to a catalytically relevant position in which the ω-end of the substrate moves close enough to compound I for oxidation to occur at this region of the molecule [110,365]. While there is no explanation as to why a change in heme iron redox state would cause this substrate movement, it has been speculated that the heme domain structure is in equilibrium between conformational states and that the binding of

substrate and the interaction with the reductase domain push the equilibrium toward one or more particular conformational states that favours a productive substrate binding mode [94]. Figure 4.24 graphically represents the midpoint potentials and reduction windows of redox centres obtained in this chapter.

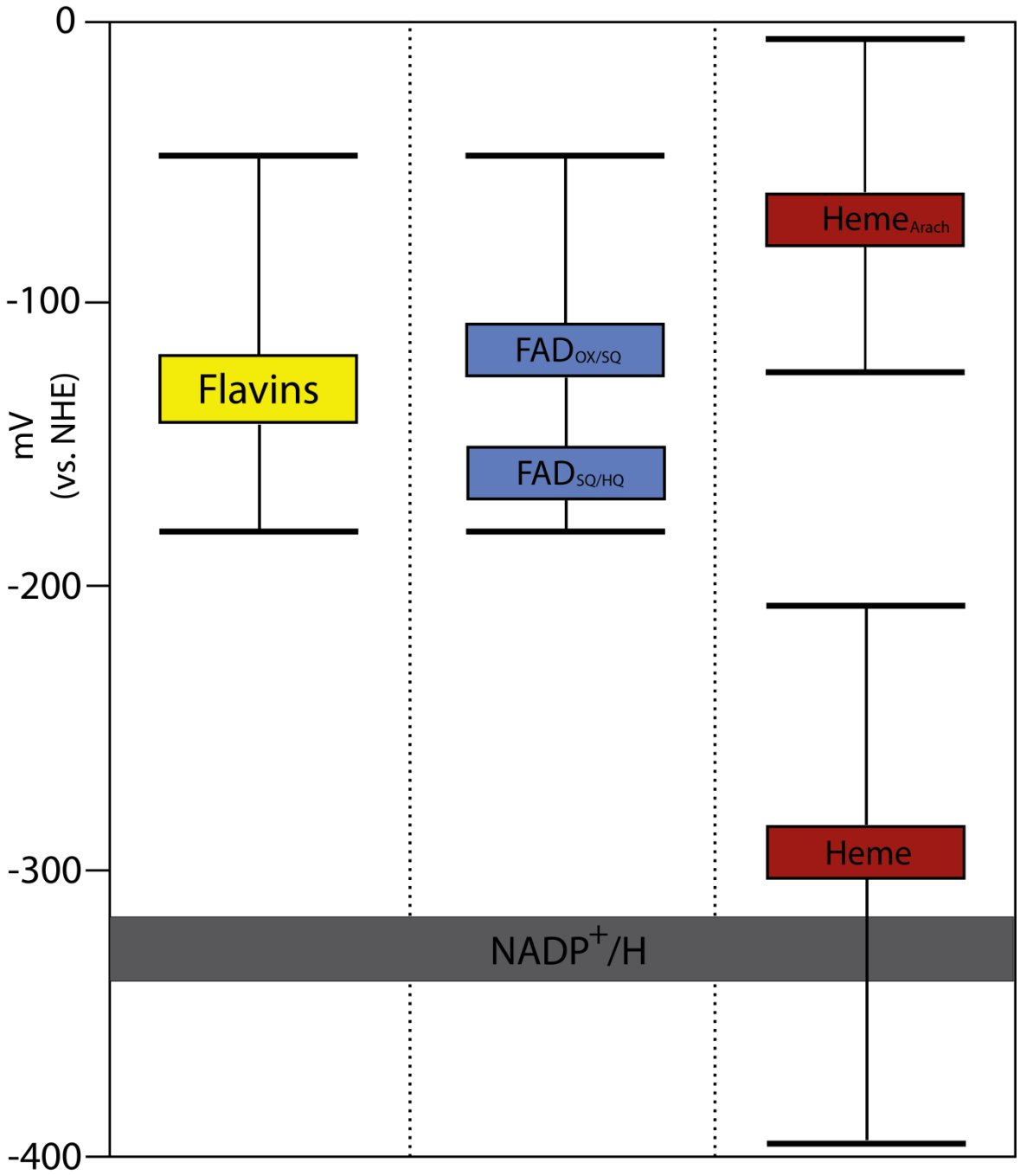

Figure 4.24 Comparison of the reduction potentials of MT1 redox centres. The y-axis shows the reduction potential (mV vs. NHE) and the x-axis arbitrarily divides the midpoint potentials measured for the flavins (left, yellow), FAD domains (middle, blue) and heme domain (right, red) in this chapter. The thick bars define the start and end of the absorbance changes associated with the midpoint potentials of each redox centre. The midpoint potential of NADPH at -320 mV is shown as a grey bar [218].

The apparent reduction potential difference between the flavin species responsible for heme reduction in BM3, the FMN_{sq}, and the arachidonic acid-bound heme iron is 49 mV, which was suggested to be close enough to support electron transfer, particularly in view of the fact that reduced heme iron should bind rapidly to dioxygen, with the potential of the ferrous-oxy heme species probably becoming considerably more positive [222]. Comparing midpoint potentials in P450 MT1, there would be no significant redox potential barriers for FMN electron transfer to substrate-bound heme. The flavins begin to reduce at approximately -60 mV vs NHE, a potential only ~9 mV more negative than that for the arachidonic acid-bound heme iron Fe^{3+}/Fe^{2+} midpoint potential in the MT1 HD (-69 mV vs NHE). Thus, from a redox potentiometry standpoint, it is clear that the high-spin P450 MT1 heme iron is poised to accept electrons from reduced FMN, probably from the semiquinone species, as is seen in the case of P450 BM3.

Steady-state kinetic assays using a variety of fatty acid substrates demonstrate P450 MT1's ability to oxidise NADPH at an enhanced rate in their presence. Substrate-dependent NADPH oxidation could be determined for all the lipid substrates tested, and catalytic parameters (k_{cat} and K_M values) are presented in Table 4.3. While the k_{cat} values were not as high as those observed for P450 BM3, it was found that all substrates produced rate constants in a similar range for NADPH oxidation (1 - 10 s^{-1}) and that the substrates in the higher bounds of this range were all branched chain fatty acids, indicating a preference for this type of substrate, as reported earlier in substrate-binding experiments (Section 3.3.2). Other steady-state kinetic assays involved the non-physiological electron acceptors potassium ferricyanide and cytochrome *c*, which are able to accept electrons near-exclusively from the FAD and FMN domains, respectively, of CPR enzymes [198,228]. The results show tighter binding (lower K_M values) and faster rate constants (higher k_{cat} values) with NADPH over NADH. P450 MT1's preference for NADPH is also evident

from the data collected in stopped-flow studies that measured P450 MT1 flavin reduction using various concentrations of NAD(P)H.

The steady-state rate constants for P450 MT1 NADPH oxidation with electron transfer from FAD to potassium ferricyanide (reported in Section 4.4) also fall within the limits defined by stopped-flow studies. The k_{lim} values for NADPH- and NADH-dependent flavin reduction at 10 °C were 92 s^{-1} and 42 s^{-1}, respectively. The highest steady-state kinetic rate constant for NADPH oxidation was determined as 43.4 ± 2.6 s^{-1}, observed upon varying ferricyanide substrate concentration at 20 °C, and is approximately half of the stopped-flow rate constant value obtained for P450 MT1 flavin reduction (92 s^{-1}) at 10 °C. The steady-state rate constant of 34 s^{-1} for ferricyanide reduction determined by varying NADH concentration at 20 °C does approach the limiting rate constant from stopped-flow studies (41.9 ± 3.1 s^{-1} at 10 °C), but further steady-state kinetic data obtained at 10 °C (Appendix Section 7.8) revealed much lower rate constants for ferricyanide reduction of >10 s^{-1}. Electron transfer reactions through the reductase domain of P450 MT1, measured by both stopped-flow and steady-state kinetic methods, are thus likely too rapid to contribute to be rate-limiting to any significant extent during fatty acid monooxygenation. The initial FMN-to-heme electron transfer rate constant (18.5 s^{-1}) is approximately double the highest rate constant observed for steady-state fatty acid-dependent NADPH oxidation. This suggests that this process may be a major rate-limiting step in steady-state catalysis of fatty acid oxidation, although, other factor(s) may also contribute to rate limitation, e.g. the delivery of the second electron from FMN-to-heme, or lipid product dissociation.

This apparent rate constant for FMN-to-heme electron transfer (18.5 s^{-1}) in P450 MT1 is substantially lower than that observed for myristate-bound P450 BM3 at 223.4 s^{-1} [198]. A potential source of error in this experimental measurement, aside from those associated with monitoring the binding of CO to reduced heme iron previously mentioned (Section 4.5.2), may be in the experimental set up. In the system used in my experiments, fully oxidised substrate-bound P450 MT1 in one syringe was mixed with NAD(P)H in the other, such that FAD and FMN both need to become reduced before the FMN can pass an electron to the high-spin ferric heme iron, as described by Hazzard et al [336]. An alternative set up would be to have substrate-free P450 MT1 in the same syringe as NAD(P)H in order to prime the reductase domain for electron transfer to the heme domain, before mixing with substrate in saturating CO conditions in the other syringe. Due to adverse redox potentials, FMN-to-heme electron transfer in P450 MT1 will only occur

efficiently on mixing with the fatty acid substrate, the binding of which shifts the heme iron spin-state equilibrium from low-spin to high-spin and increases the heme reduction potential substantially. The only significant issue with this experimental set up is that the incubation time of P450 MT1 with NAD(P)H may be extensive if several experiments are done with the same samples , and this might cause reductive "inactivation" of the reductase domain towards heme reduction if FMN hydroquinone accumulates (as seen with BM3) and is a less effective reductant for the heme iron [67].

Fatty acid product determination experiments confirmed that P450 MT1 is a catalytically self-sufficient P450/diflavin reductase fusion enzyme that catalyses the NADPH-dependent hydroxylation of various long chain fatty acids in the ω-1, ω-2 and ω-3 positions. Differences in the patterns of regioselectivity of hydroxylation of substrates were observed for even-chain, odd-chain and branched-chain fatty acid hydroxylation by P450 MT1. These data contrast somewhat with the behaviour observed in P450 BM3, where ω-2 hydroxylation usually predominates over hydroxylation at the other two positions [366].

P450 MT1 displayed a trend of substrate hydroxylation regiospecificity in which major product formation occurred at either the ω-1 and ω-2 positions in odd and even chain length fatty acids, respectively, a pattern which carried through the saturated fatty acid range from C12-C16. There was no such trend observed in the case of P450 BM3. It is notable that the BM3 heme domain has residues R47 and Y51 at the mouth of the active site, which are involved in positioning fatty acid substrates as they enter the active site through interactions with the substrate carboxylate group (Section 3.1.2) [110]. P450 MT1 lacks such carboxylate-orienting residues in a similar position, or apparently any other similar substitute amino acids that could help bind fatty acids in a "BM3-like" mode. This is one potential reason for differences in the pattern of regioselectivity of hydroxylation of straight chain fatty acids observed between P450 BM3 and P450 MT1, although it should be noted that both enzymes favour substrate hydroxylation at the ω-1 to ω-3 positions.

All P450s uncouple electron transfer to some extent – i.e. electrons lost in the reduction of oxygen to superoxide, peroxide or water (Figure 1.13), or through wastage of electrons through flavins in oxygen reduction and the degree of reaction uncoupling is another measure of enzyme efficiency. The GC traces in Figure 4.21 and Figure 7.9 show peaks of unconverted substrate which indicate some level of uncoupling in MT1 with the substrates trialled. Inaccuracies from substrate solubility and through formation of the previously

established, inactive 3-electron reduced form on NADPH incubation could account for the presence of unconverted substrate. This putative uncoupling of MT1 with these substrates should be tested by the measurement of the relative amounts of peroxide or superoxide formed compared to amount of fatty acid hydroxylated product formed. Alternatively, the absolute amount of NADPH oxidized could be directly compared to the amount of hydroxylated product formed using accurate LC/GC-MS or MS in combination with UV-vis spectroscopy measuring the amount NADPH oxidation.

The highest level of regioselectivity of substrate oxidation was observed with branched chain fatty acid substrates, e.g. 97.5% with *iso*-myristic acid at the ω-2 position, and this was higher than observed for BM3 in some cases, e.g. 90% with *iso*-pentadecanoic and 85% with *iso*-heptadecanoic acid at the ω-2 position [350]. These data, together with the relatively high catalytic rate constants for these substrates, indicate they are good substrates for P450 MT1. These findings complement the existing evidence seen from substrate binding titrations (Section 3.3.2) and steady-state kinetic data (Section 4.4.1). While the physiological role hasn't been proven here, a hypothesis based on these data from analyses using branched chain lipid substrates is that P450 MT1 may primarily be responsible for the oxidation of branched chain fatty acids in *M. thermophila*. The CYP102A P450 enzyme family's high regioselectivity towards branched chain fatty acids (over straight chain fatty acids) and the fatty acid content of *B. megaterium*, which is almost 90% branched chain fatty acids, also makes these molecules likely prime substrate candidates for P450 BM3 [317,350,351]. ω-oxidation is an alternative route to β-oxidation in fatty acid metabolism and particularly for branched chain fatty acids, e.g. phytanic acid, where a methyl group on the β carbon makes β-oxidation impossible. P450 MT1 is clearly a very efficient lipid hydroxylase which could indicate a role in transforming selected lipids at a high rate at a particular phase of the life cycle of the bacterium.

Following on from the work presented in this chapter are a number of additional experiments than could further our existing knowledge of P450 MT1. Separating P450 MT1 into its separate reductase, FMN- and FAD/NADPH-binding domains by genetic dissection of *CYP505A30* could allow the more accurate determination of the midpoint potentials for the flavin cofactors, including better description of the spectral properties of their semiquinone forms. In the absence of structural data on intact, full length P450 MT1, it is likely that these individual domains would be more amenable to crystallisation and to the determination of their 3-dimensional structures. Other spectroscopic analysis, including

resonance Raman experiments on the bound heme cofactor, would also be useful for the P450 MT1 heme domain. In the case of resonance Raman, data would be informative on the structure of the heme cofactor and the orientation of its peripheral groups, as well as on the heme iron oxidation-, spin- and coordination-states, and the influence of ligands (e.g. lipid substrates and inhibitors) on these properties.

P450 MT1's high level of regioselectivity in substrate hydroxylation is a valuable quality which may be useful for applications of this enzyme in synthetic chemistry and for the pharmaceutical industry. Aliphatic C-H bonds are notoriously hard to functionalise and the ability to specifically target them can be very useful. Further, the determination of the crystal structure of the P450 MT1 heme domain would identify several sites for rational mutagenesis in order to identify roles of various residues and potentially to allow binding to a broader array of substrates, and to enable their oxidation. Thus, there are exciting prospects for further research into P450 MT1.

Chapter 5: Structural studies on P450 BM3 and its reconstituted domains.

5.1 Introduction

At present the structure of full length P450 BM3 remains unsolved likely because its multidomain, dimeric nature has not proven amenable to resolution by conventional structural determination methods such as X-ray crystallography and NMR spectroscopy. However, other important outcomes have been achieved from the rational and directed evolution mutagenesis of P450 BM3, including altering its substrate preference from mid-chain length fatty acids towards novel substrates including alkanes, polycyclic aromatic hydrocarbons and pharmaceuticals including testosterone and omeprazole [93,250,252,367,368]. P450 BM3's dimeric nature (along with the rapid electron transfer kinetics within its reductase domain) is evidently an underlying cause of its high turnover rate compared to similar monooxygenase fusion enzymes and a crucial reason to obtain the structure of this 238 kDa homodimeric complex [240]. The determination of P450 BM3's complete dimeric structure would be an invaluable tool for identifying productive dimeric contacts and their influence on stability, structural dynamics and activity. These data could then influence approaches taken in redesigning and priming BM3's activity, as well as aiding in the design of other P450 fusion systems and the enhancement of their catalytic efficiency towards the oxidation of novel substrates. In this chapter, different approaches taken through the use structural techniques for the analysis of P450 BM3 are described.

Early analytical ultracentrifugation (AUC) and HPLC-SEC experiments on P450 BM3 first showed that the flavocytochrome enzyme could existed in various aggregated states in solution [237]. Mutagenesis experiments were used to make two inactive forms of BM3: the A264H mutant with an inactivated heme domain (with heme iron distally coordinated by His264) and the G570D mutant with an FMN-depleted reductase domain (through disruption of the FMN binding site) [240]. Independently, each P450 BM3 mutant failed to show any fatty acid hydroxylase activity. However, once combined this activity was reconstituted. This elegant experiment not only proved BM3 activity in its dimeric form, but also that electron transfer can occur in an inter-monomeric fashion, from the FMN domain of one monomer to the heme domain of the other.

The approach taken in the study of P450 BM3 was analogous to the mutagenesis and reconstitution experiments carried out on nitric oxide synthase (NOS), which led to the same conclusion [9]. The three isoforms: neuronal (nNOS), endothelial (eNOS) and inducible (iNOS) NOSs are homodimers with their monomers having a similar domain arrangement to that of P450 BM3 (Section x.xx), but with a calmodulin (CaM)-binding domain separating their N-terminal oxygenase and C-terminal reductase domains [369–371]. NOSs have a heme-containing oxygenase domain with overlapping β-wing sheets that are structurally distinct from the P450 domain fold [372]. However, they have an FAD- and FMN- containing reductase domain sharing 60% amino acid sequence identity with CPR and BM3. These findings suggests that the unique features of the CPR domain predetermine its function in the efficient electron transfer from NADPH to these two structurally distinct heme-containing monooxygenases [328]. Interestingly, while electron transfer is inter-monomeric in BM3 and NOSs their modes of dimerization are distinct from one another, which highlight differing adaptations for catalytic efficiency in this remarkable example of convergent evolution. Crystal structures and functional studies with deletion mutants identified 49 residues responsible for NOSs dimerization in the N-terminal of the oxygenase domain, specifically residues 65-114 in iNOS [373–376]. Initial characterisation by Black and Martin indicated the FAD domain as the dimerization site in P450 BM3 and later work associated with the crystallisation and structural analysis of P450 BM3's FAD domain complemented those findings [237,268]. The crystal structure of BM3's isolated FAD-binding domain was elucidated using a double cysteine mutant (DM) – the C773A/C999A FAD domain. The C773 residue is a surface exposed cysteine while C999 is a part of the catalytic triad involved in NADPH binding and electron transfer to the flavin. The structure of the DM FAD domain showed A773 to be 7.5 Å away from C810, another surface cysteine, suggesting either disulfide linkages between monomers or structural perturbations affecting crystal formation as possible reasons for failure of the WT FAD domain to crystallise. MALLS studies on the DM FAD domain showed that cysteine mutations affected dimerization, as the WT FAD domain was largely dimeric in solution [268]. Interestingly, NOSs lack the corresponding C773 cysteine and reductase domain associations in eNOS and nNOS are far weaker than their oxygenase domain interactions, while dimerization in iNOS arises solely from its oxygenase domain [377].

The first domain of P450 BM3 solved by X-ray crystallography was the P450 domain in 1992 by Boddupalli et al., and since this breakthrough there have been many more

contributions of BM3 P450 domain structures to the Protein Data Bank (PDB) at higher resolution (*21*, *22*). Crystal structures of substrate-bound BM3 P450 domains have also been published, but invariably show distances between the substrate and the heme that are too great to permit substrate oxidation [110,122]. Temperature-jump spectroscopy experiments indicated that substrate binding is dynamic and suggested that the substrate can occupy two distinct sites within the active site [111]. The substrate could occupy a distal site 7.5 Å away from the heme, similar to that observed from the crystallography data, and also a 'catalytically productive' site in close enough proximity to the heme to allow oxidation, as also predicted by molecular simulation dynamics (*24*, *26*, *27*). These data complement earlier computational modelling data that predict the effect that temperature has on the high-spin and low-spin state of P450 BM3 heme, and its implications for the mode of binding of substrate suggest that at the low temperatures experienced during crystallography the substrate adopts the distal site, away from the heme [380]. The P450 domain has also been crystallised in a form fused to the FMN-binding (flavodoxin-like) domain. However, the structure determined showed that the FMN domain was cleaved from the P450 domain, with a single FMN domain and two heme domains in the asymmetric unit. The separated FMN domain was also not located in a position (relative to the heme domains) that would be conducive to efficient electron transfer [223]. With all the structures of P450 BM3's individual domains now solved, other techniques should now be employed for further studies of P450 BM3, such as electron microscopy (EM), which routinely allows the visualisation of large protein complexes and should be appropriate for the investigation of P450 BM3's dimeric structural organization. Structural and dynamic experiments on P450 BM3 HD by NMR spectroscopy could also be employed to further our current understanding of redox states, substrate binding and conformational dynamics, and reductase partner interactions. The effects of temperature on P450 BM3's heme domain substrate binding and spin-state could also be measured in the same sample [381]. Conformational changes upon the binding of substrates as well as the orientation of binding of complex substrates within the active site could also be explored. The effect of the oxidation state of the heme iron on the overall enzyme conformation (if any) would also be interesting to examine as, for the crystal structure, the X-ray beam would be expected to reduce the heme iron during the collection of crystallography data. The identification of residues involved in the interaction of the isolated, labelled P450 domain with unlabelled reductase domain in isolation and with the unlabelled full length

enzyme (and any relevant conformational changes associated with these interactions) could also be probed using NMR spectroscopy [382].

5.2 Purification of WT P450 BM3

The pET14b/WTBM3 construct was previously worked on and showed good expression and solubility in a BL21-Gold (DE3) *E. coli* host strain. Expression and purification was carried out as in Methods 2.7.4 with a typical culture volume of 12 litres grown over a period of 20 hours. The resulting bacterial cell pellet was freeze-thawed prior to sonication. The soluble crude extract was applied to a nickel-NTA column after ammonium sulfate precipitation. Three column volumes (CV) of 20 mM imidazole in buffer C was a sufficient wash step before elution with 200 mM imidazole in buffer A. The purest factions were pooled and dialysed into 2 x 5 L buffer D before further purification involving ion exchange chromatography (IEC) with Q-Sepharose and size exclusion chromatography (SEC) with a Sephacryl S-200 column (Figure 5.1).

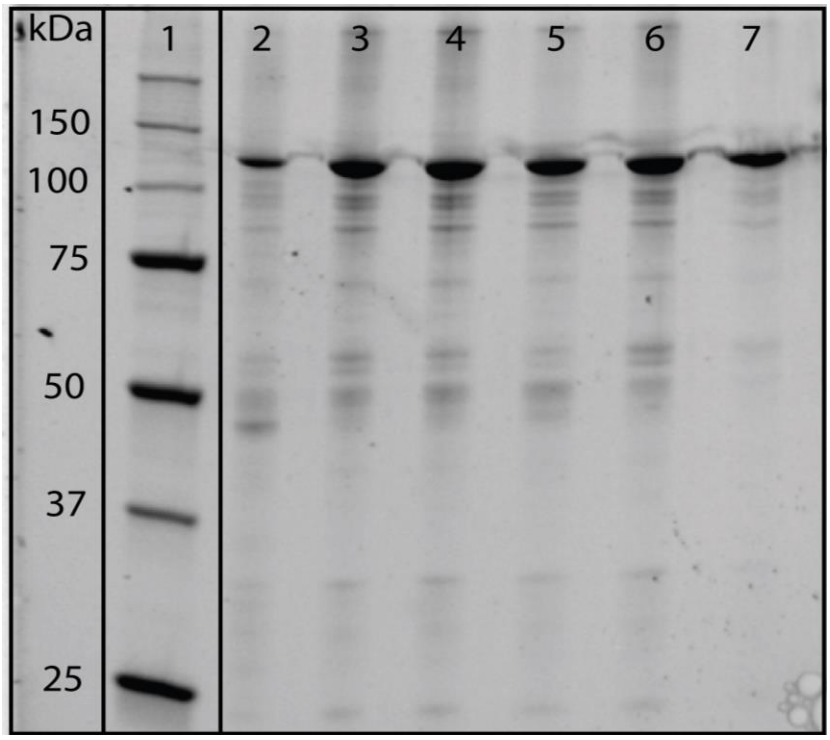

Figure 5.1 WT P450 BM3 purification by size-exclusion chromatography. SDS-PAGE analysis of BM3 fractions after purification using a Sephacryl S-200 SEC column shows a molecular weight ladder (lane 1, BIO-RAD Precision Plus^{TM} Unstained Standards 10-250 kDa) and fractions of purified BM3 at ~120 kDa (lanes 2-7) from the SEC column.

5.3 Purification of P450 BM3 heme domain (HD)

The pBM20/BM3HD construct was previously worked on and showed good expression and solubility in the BL21-Gold (DE3) *E. coli* host strain, which was used for expression (Methods 2.5.4) with a typical culture volume of 12 L of LB medium, and incubated after IPTG induction for 20 hours. The BM3HD construct was tag-less and so pure enzyme was achieved with 2 rounds of IEC purification followed by SEC column chromatography as detailed in Methods section 2.7.5. Figure 5.2 shows the purity of the BM3HD during the various steps involved in its purification.

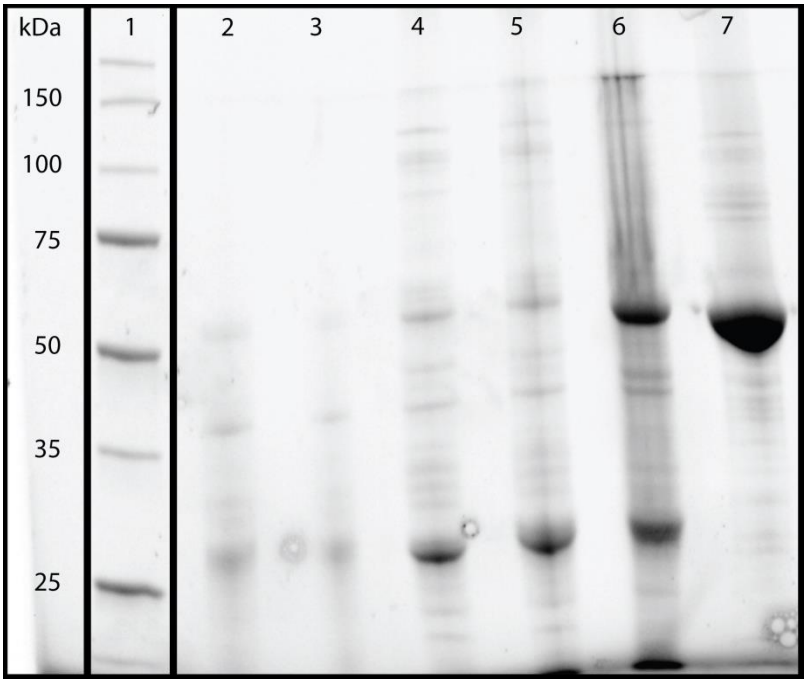

Figure 5.2 P450 BM3 HD purification steps. SDS-PAGE analysis of BM3 HD purification by DEAE and Q-Sepharose IEC columns shows a molecular weight ladder (lane 1, BIO-RAD Precision Plus^{TM} Unstained Standards 10-250 kDa), lanes 2+3 are the flow-through from the DEAE column, lanes 4+5 are eluted DEAE fractions. Lane 6 is a sample of the pooled fractions eluted from the DEAE column and Lane 7 is a sample of greater purity from the pooled fractions eluted from the Q-Sepharose column, showing the BM3HD at 55 kDa. The BM3 HD was subsequently purified to a homogeneity using SEC on a Sephacryl S-200 column.

5.4 WT P450 BM3 and P450 BM3 HD Multi-Angle Laser Light Scattering (MALLS)

MALLS is a structural technique that is able to determine the molecular mass and hydrodynamic radius of proteins and their complexes in solution. The effect of salt concentration on BM3's oligomerisation state was investigated by running 2 samples: one high salt sample in 50 mM KPi buffer (pH 7.0) containing 800 mM KCl, and one low salt sample in 50 mM KPi buffer (pH 7.0) containing 100 mM KCl. 200 µl of 1 mg/ml purified BM3 was needed per sample for each experiment. Each sample was run through a 8 ml SX200 SEC column pre-equilibrated in its relative buffer before entering the MALLS equipment for detection (Methods 2.15). The raw data collected were processed by Zimm fitting from the ASTRA v.6 software, giving values for the hydrodynamic radius (Rh) and molecular mass (M_r) for the WT P450 BM3.

WT P450 BM3 is predominantly a dimer of 247 kDa in the low salt solution of 50 mM KPi buffer (pH 7.0) plus 100 mM KCl (Figure 5.2). This apparent mass corresponds to approximately twice the molecular weight of the BM3 monomer as identified by SDS-PAGE (Figure 5.1). The dimer species had an apparent hydrodynamic radius (Rh) of 6.7 nm. A lower molecular weight species elutes just after the BM3 dimer, this probably being a smaller amount of a monomeric species. Its molecular weight corresponds to ~120 kDa, but the value is probably slightly inaccurate due to its proximity to the main peak and the low amount of the small species present in solution. For this reason, no accurate Rh could be calculated using the software.

This MALLS experiment was repeated using a buffer with higher ionic strength in order to probe its effects on P450 BM3's dimeric interactions. The conditions were kept identical to those used above, except for the use of 50 mM KPi buffer (pH 7.0) containing 800 mM KCl at pH 7.0 used for the MALLS experiment. Figure 5.4 shows the MALLS spectra of the high salt BM3 sample with a major peak at 11.8 mL with a corresponding molecular weight of 249 kDa and an Rh value of 6.8 nm, which corresponds exactly to the major peak in Figure 5.3 and is again indicative of the dimeric species of P450 BM3. A small shoulder of 0.2 RI on the right side of the major peak shows that a lower molecular weight species elutes just after the P450 BM3 dimer. Its molecular weight of 99.0 kDa and elution time of 14.5 mL also correspond with the same species in Figure 5.3, and while its apparent molecular weight value is slightly lower it clearly does indicate the monomer species. The Rh of the 99.0 kDa species could not be calculated for the same reasons as discussed for the species in Figure 5.3. There is a clear effect of salt concentration on BM3 dimerisation, as a higher amount of monomeric enzyme was present in the 800 mM KCl buffer sample compared to the 200 mM KCl sample. P450 BM3 was already shown to be functional as a dimer and both concentrations show P450 BM3 in a predominantly dimeric state (>90%) which is most likely its physiological oligomeric form [240]. Analytical ultracentrifugation (AUC) methods showed that a number of reagents could shift BM3's oligomerisation equilibrium towards either the monomer or the dimer species [237]. The Analytical ultracentrifugation (AUC) and HPLC-SEC techniques used on full length BM3 and its isolated domains showed a completely monomeric heme domain, while the BM3 FAD domain displayed higher aggregation species which pointed towards the role of the FAD domain as the site of dimerisation in the full length P450 BM3.

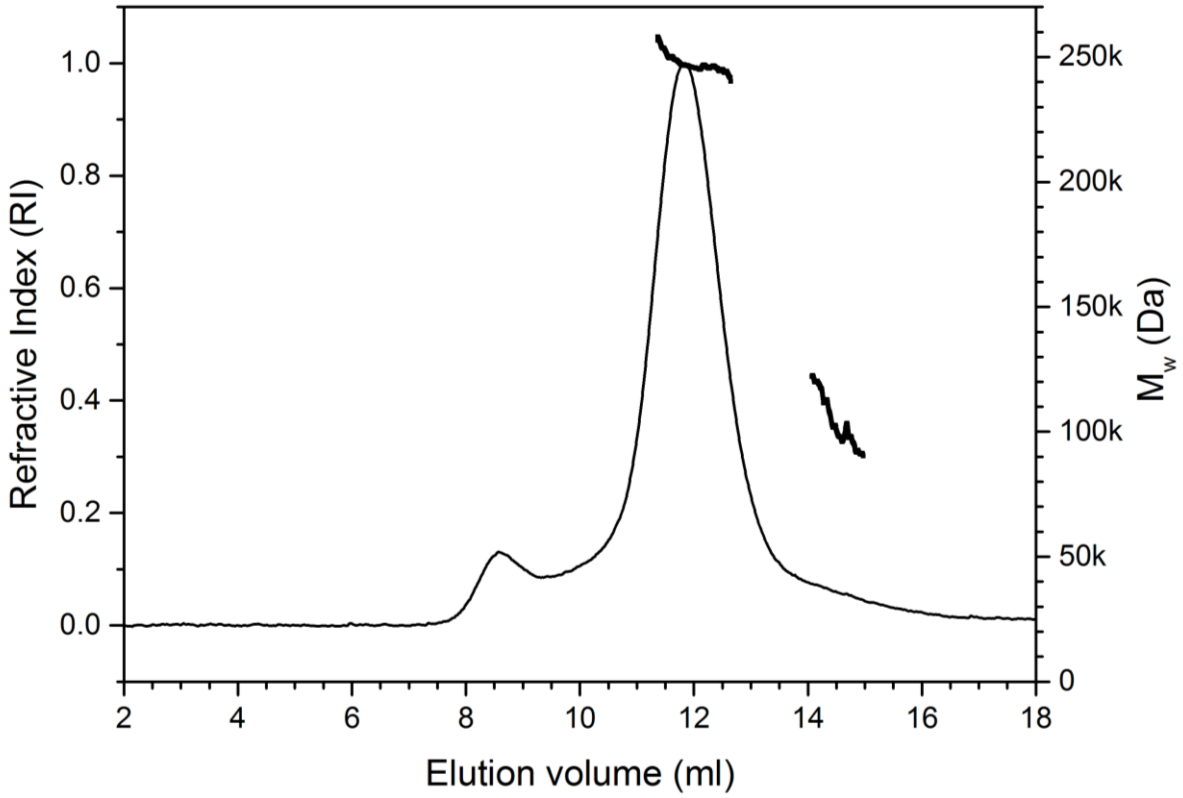

Figure 5.3 MALLS analysis of WT P450 BM3 oligomerisation state in low salt buffer. The x-axes show the elution volume of the low salt P450 BM3 sample from an 8 ml size exclusion column. The left hand side y-axes show the refractive index (RI) at 633 nm, a relative scale of the ability of light to propagate through the sample, plotted as a thin solid line. The right hand side y-axes show the molecular weight (Da) and Zimm fitting of the species in the sample, plotted as a thick solid line. The low salt P440 BM3 sample in 50 mM KPi buffer (pH 7.0) containing 100 mM KCl shows a single peak eluting at 11.8 mL with a mass of 247 kDa, indicative of a dimer species of P450 BM3. There is a minor peak at the 8.5 mL mark that corresponds to the void volume of the 8 mL SX200 SEC column. A slight shoulder is observable on the right hand side of the dimer species at ~14.5 mL which may correspond to the monomer species at ~120 kDa.

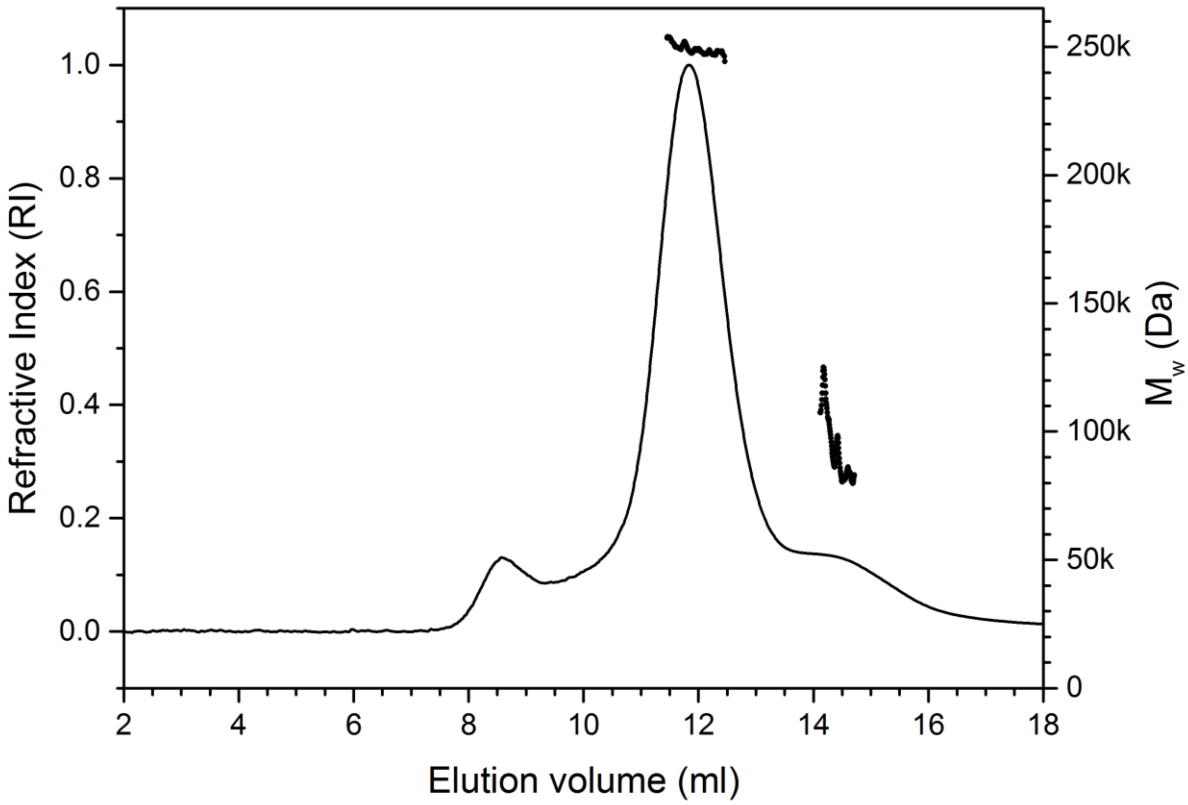

Figure 5.4 MALLS analysis of WT P450 BM3 oligomerisation state in high salt buffer. The x-axes show the elution volume of the high salt P450 BM3 sample from an 8 ml size exclusion column. The left hand side y-axes show the refractive index (RI) at 633 nm, a relative scale of the ability of light to propagate through the sample, plotted as a thin solid line. The right hand side y-axes show the molecular weight (Da) and Zimm fitting of the species in the sample, plotted as a thick solid line. The high salt BM3 sample in 50 mM KPi buffer (pH 7.0) containing 800 mM KCl shows a distinct peak eluting at 11.8 mL with a mass of 250 kDa, indicative of the dimer species. There is a minor peak at the 8.5 mL mark that corresponds to the void volume of the 8 mL SX200 SEC column. A visible shoulder is observable on the right hand side of the dimer species at ~14.5 mL with a molecular weight of 99 kDa, which roughly corresponds to the monomeric species.

Purified BM3 HD samples were also analysed by MALLS. The sample was run in 50 mM KPi buffer (pH 7.0) containing 200 mM KCl (Figure 5.5). The BM3 HD is visible as a completely monomeric species with a molecular weight of 62.5 kDa and Rh of 3.6 nm. Even though the full length protein is dimeric it is not implausible for an isolated domain to have a different solution state. In fact, other P450 heme domains from dimeric fusions been shown to be monomeric when isolated, e.g. P450 MT1 (Chapter 3.4), while the isolated BM3 reductase domain is present as a dimer in solution [331]. This growing body

of evidence points towards the reductase domain as the driving force behind WT BM3 dimerisation, which was examined in Section 5.6 with the WT FAD domain and cysteine knockout mutants thereof.

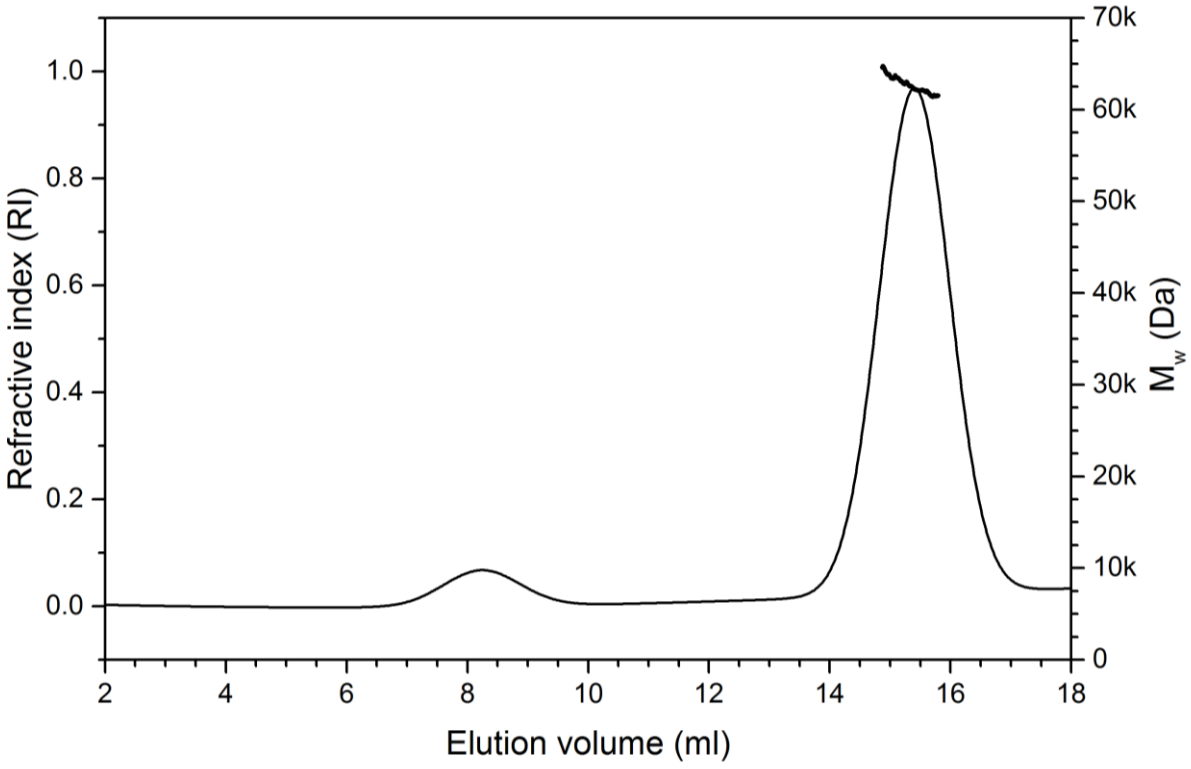

Figure 5.5 MALLS analysis of the P450 BM3 HD oligomerisation state. The x-axes show the elution volume of the BM3 HD sample. The left hand side y-axes show the refractive index (RI) at 633 nm, plotted as a thin solid line. The right hand side y-axes show the molecular weight (Da) and Zimm fitting of the species in the sample, plotted as a thick solid line. The BM3 HD sample in 50 mM KPi buffer (pH 7.0) containing 200 mM KCl shows a major peak eluting at 15.5 mL with a mass of 62.5 kDa, indicative of the monomer species. There is a minor peak at the 8.5 mL mark that corresponds to the void volume of the 8 mL SX200 SEC column.

5.5 Purification of WT, C773A and C773A/C999A BM3 FAD Domains.

Prior to use, the genes encoding the WT and different mutant forms of the BM3 FAD/NADPH binding (or FAD domain) were verified by sequencing with T7F/T7R primers from SourceBioscience (Nottingham). Once the sequencing results confirmed the

plasmid contained the correct gene insert and mutations, if present, the three constructs were transformed into competent *E. coli* BL21 (DE3) cells and transformants were grown in large scale cultures as described in the Methods (Section 2.5.4).

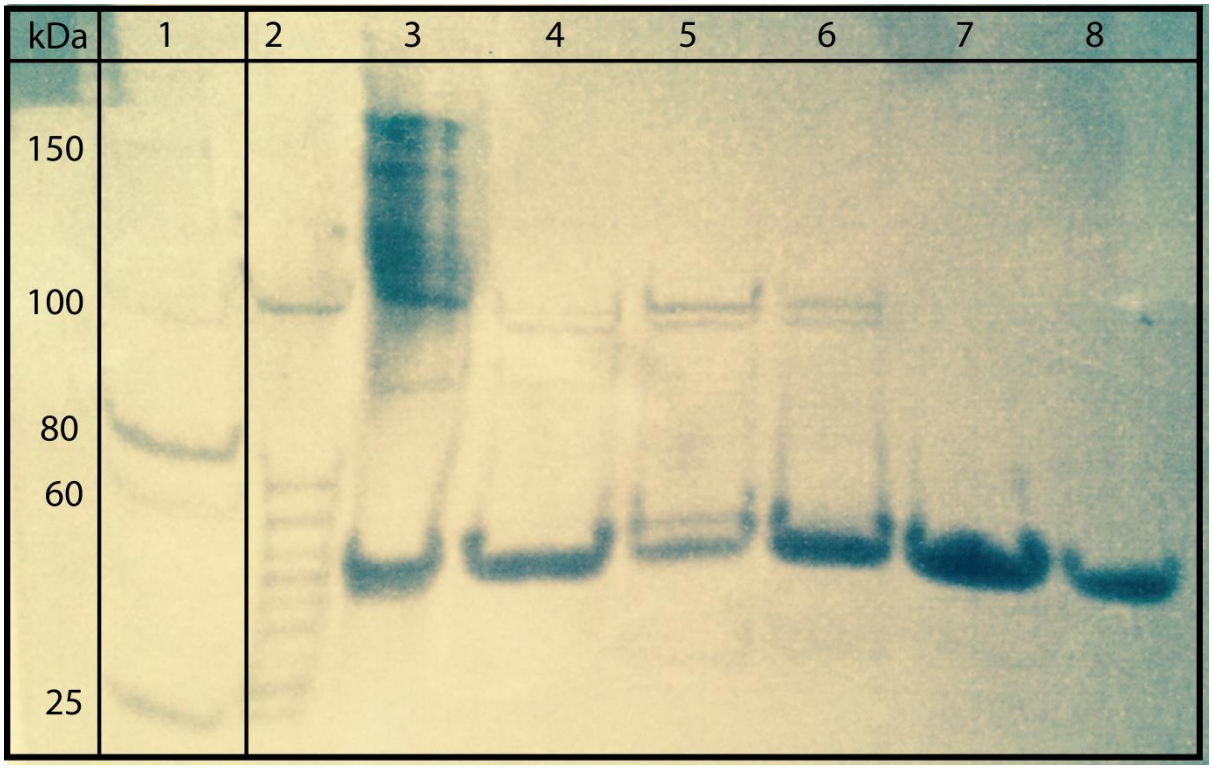

Figure 5.6 SDS-PAGE analysis of WT FAD domain purification stages. Lane 1 shows NEB Prestained Protein Ladder (10-230 kDa). Lanes 2 – 8 show WT FAD domain fractions after purification using a 2-step IEC purification process followed by IEC using a Sephacryl S200 SEC column. Lane 2 shows the Q-Sepharose wash flow-through, Lanes 3 and 4 are two Q-Sepharose fractions of varying purity. Lanes 5- 8 are fractions from the SEC column with the WT FAD domain at 47 kDa.

The purification strategy for WT, C773A (single mutant, SM) and C773A/C999A (double mutant, DM) BM3 FAD domains was identical. The bacterial cell pellet was freeze-thawed prior to sonication. A 2-step IEC purification was needed to obtain enzyme pure enough for SEC in the absence of a His-Tag suitable for nickel affinity purification. Extensive dialysis with 3 x 5 L of buffer D was used to desalt the enzyme solution before loading the sample onto the DEAE and Q-Sepharose columns in succession. The IEC columns were pre-equilibrated in 50 mM Tris-EDTA buffer (pH 7.2) and elution was achieved by a linear

gradient of 0 – 500 mM KCl in this Tris-EDTA buffer. Pure FAD domain fractions eluted from the Q-Sepharose IEC column were pooled and further purified using a Sephacryl S-200 SEC column, as described in Methods 2.7.6. SDS-PAGE analysis (Figure 5.6) showed that the FAD domains were of a high purity and absorption studies (Figure 5.7) demonstrated both the SM and DM FAD has stoichiometric amount of bound FAD, as also found in the WT FAD domain.

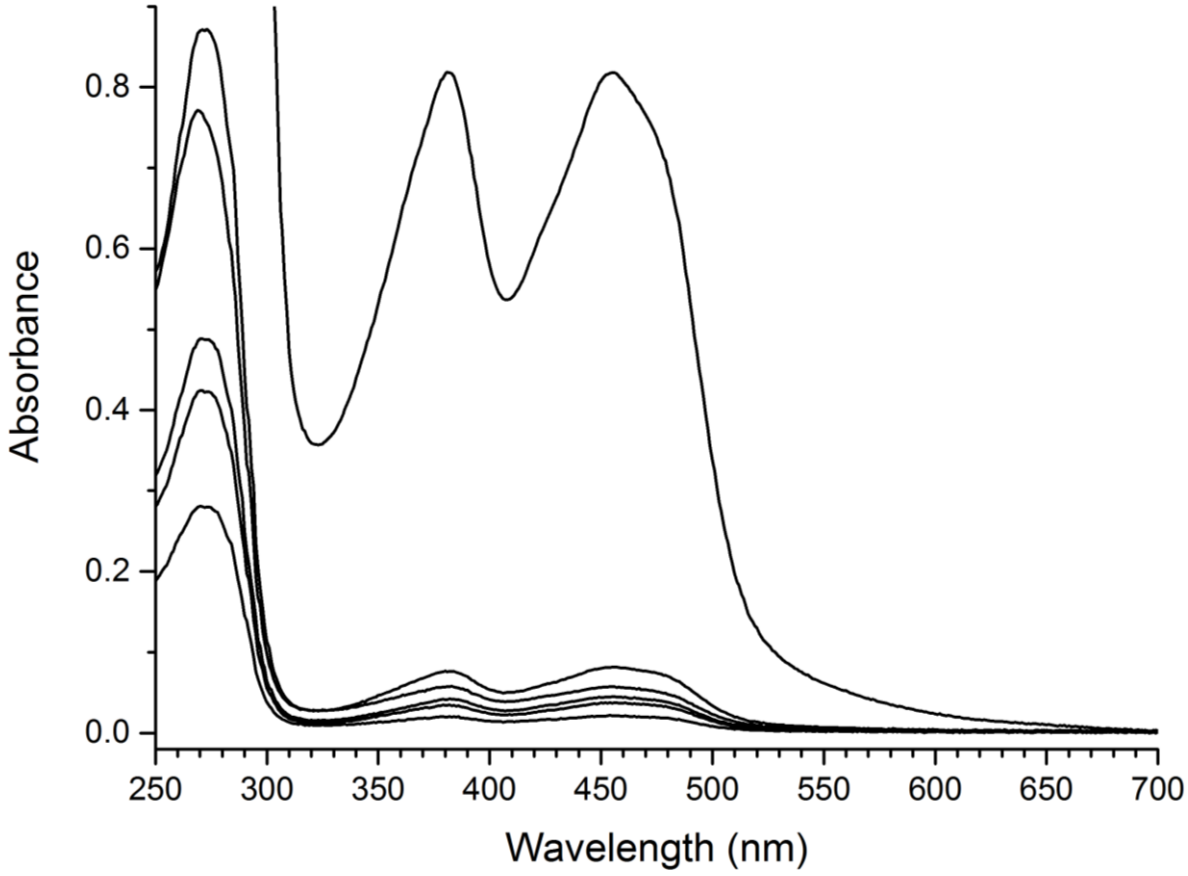

Figure 5.7 UV-visible spectra of WT FAD domain fractions eluted from a Q-Sepharose column. All lines represent individual fractions and had an $A_{280/450}$ value range between 10 and 13. All purification fractions with an $A_{280/450}$ value below 13 were pooled and prepared for the next column chromatography stage. The flavin spectral features are clearly seen, with absorption maxima at 457 nm and 384 nm.

5.6 Structural analysis of the WT, C773A and C773A/C999A BM3 FAD domains by MALLS

WT P450 BM3 is functional as a dimer in solution with inter-monomeric electron transfer occurring from the FMN of one monomer to the heme domain of the other. (Introduction, section 1.13). Early studies showed that both the intact reductase domain and the FAD domain dimerise when isolated from intact BM3 [331]. Dimeric interactions for these domains were shown to be due to contacts/bonds arising between surface cysteine residues from each monomer. Using MALLS, the solution states of the WT FAD, C773A (SM) and C773A/C999A (DM) FAD domains were investigated under different conditions. It was the inclusion of these mutations in the DM FAD domain that led to its crystallisation and the determination of the FAD domain crystal structure, and in the following studies they are investigated by MALLS along with the WT and C773A SM FAD domains [268].

Two MALLS experiments were carried out per FAD domain, one sample in either Tris Buffer (50 mM Tris, 1 mM EDTA, pH 7.2 at 4 °C) or 1 mM dithiothreitol (DTT)-supplemented Tris buffer of the same composition. Samples were loaded onto the Superdex 200 SEC column and all data collected are tabulated in Table 5.1. Samples to be run in Tris buffer containing 1 mM DTT were incubated with 10 mM DTT prior to loading on the column (Methods, section 2.14). Incubation in the reductant DTT reduces cysteine residues from their disulfide bonds to their protonated thiol form.

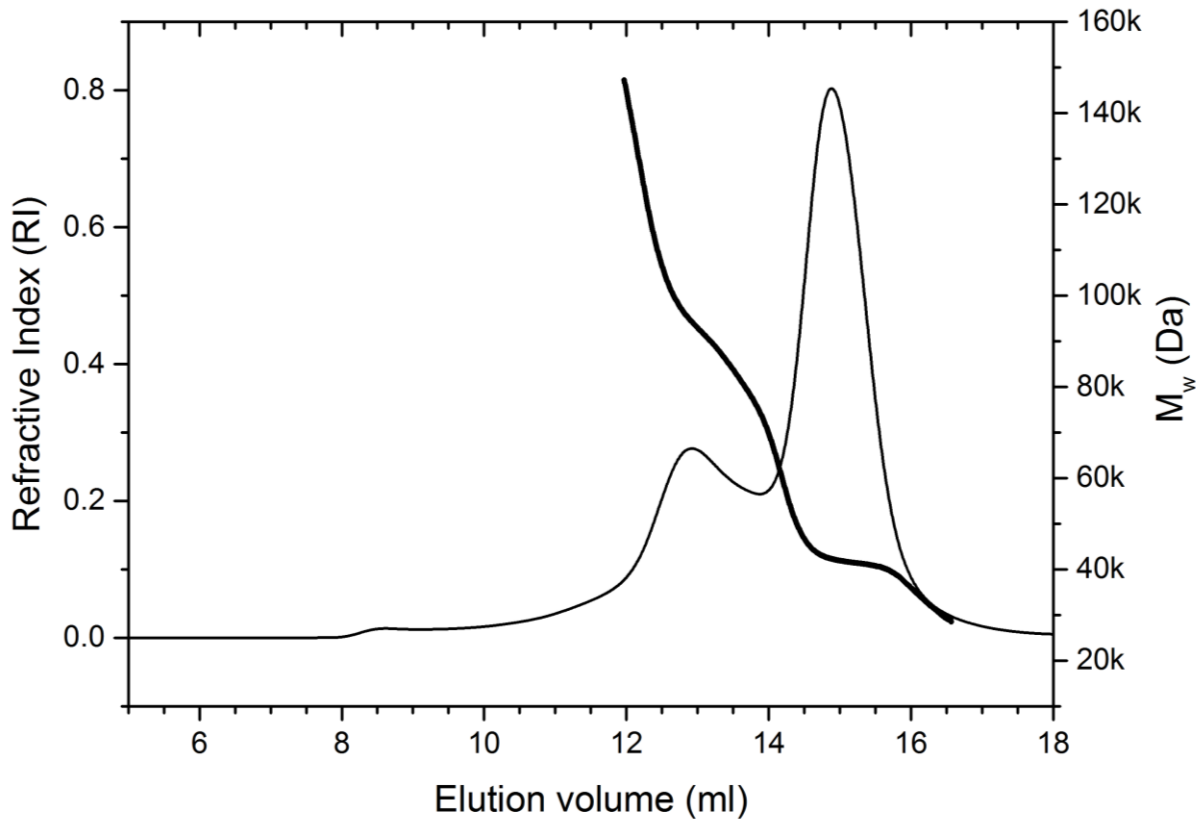

Figure 5.8 MALLS analysis of the WT FAD domain oligomerisation state. The x-axes show the elution volume of the low salt FAD domain sample from an 8 ml size exclusion column. The left hand side y-axes show the refractive index (RI) at 633 nm, a relative scale of the ability of light to propagate through the sample, plotted as a thin solid line. The right hand side y-axes show the molecular weight (Da) and Zimm fitting of the species in the sample, plotted as a thick solid line. The FAD domain sample in 50 mM Tris (pH 7.2) plus 1 mM EDTA shows two peaks with elution volumes of 13 mL and 15 mL. The major peak at 15 mL has a molecular weight of 42.2 kDa, which corresponds to the monomeric FAD domain species. The minor peak at 13 mL has a molecular weight of 94.5 kDa, and likely represents the FAD domain dimer at roughly twice the size of the monomeric FAD domain species.

The WT FAD domain is largely monomeric in solution but ~25% w/w of its population in solution is present as a dimer (Figure 5.8, Table 5.1). The monomeric FAD domain species has a M_w of 42.2 kDa, which corresponds to the apparent M_w of 47 kDa obtained from SDS-PAGE analysis (Figure 5.7) and to data from bioinformatics tools. The large amount of monomer present in the 15 ml fraction allowed the QELS detector to obtain a stable reading seen by the M_w value over that elution range. The M_w for the dimer species at 13 mL is 94.5 kDa, which is slightly above twice that of the monomer mass. This small inaccuracy is probably due to the 8 mL SEC column's inability to completely separate

monomer and dimer species, resulting in a varied signal from the QELS detector over this elution range.

One way to overcome this limitation is by re-running the individual elution fractions of each species. Figure 5.9 shows the monomer (dotted line) and dimer (solid line) fractions from the WT FAD domain sample (Figure 5.8) re-run through the SX200 SEC column and MALLS instrumentation.

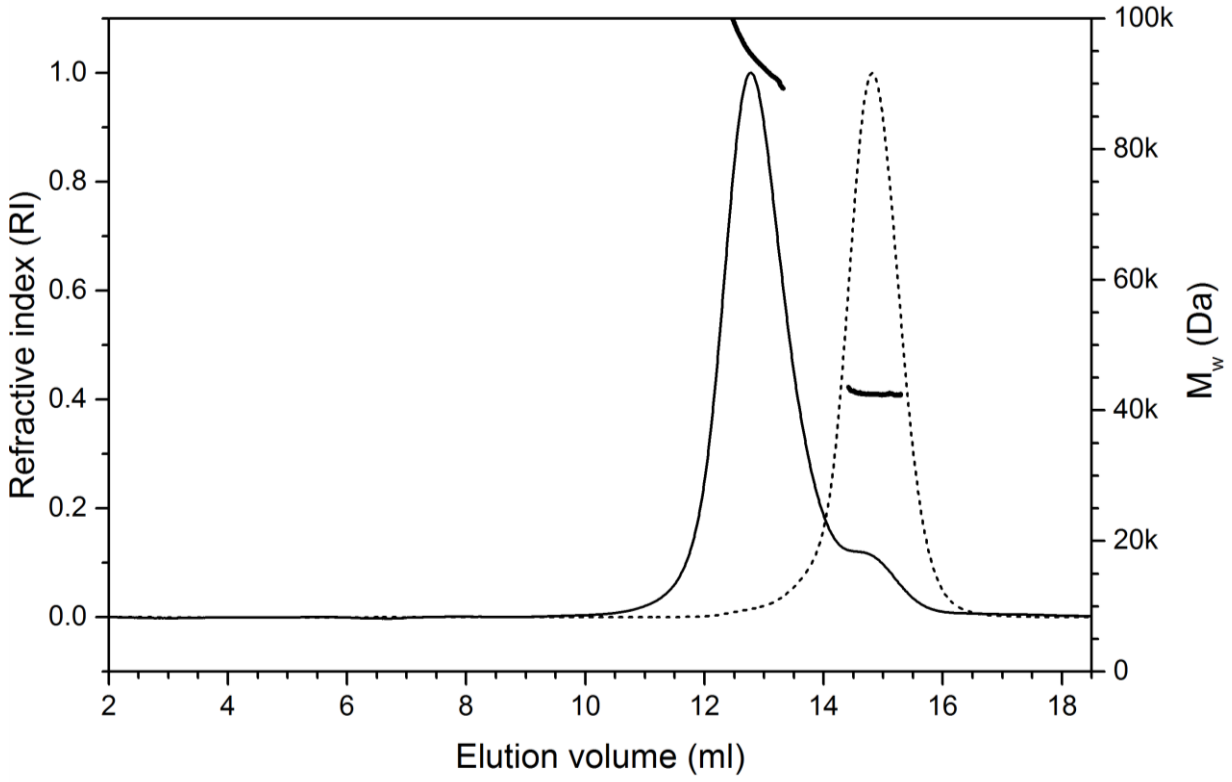

Figure 5.9 Overlaid MALLS re-run spectra for the dimer and monomer fractions from the WT FAD domain. The monomer and dimer fractions at the 15 mL and 13 mL elution points from the MALLS run of WT FAD domain in 50 mM Tris (pH 7.2) plus 1 mM EDTA were re-run in the same buffer. The left hand side y-axes show the refractive index (RI) at 633 nm plotted as a thin solid line for the dimer re-run fraction and as a dotted line for the monomer re-run fraction. The right hand side y-axes show the molecular weight (Da) plotted as a thick solid line. The re-run FAD dimer fraction (solid line) shows one major peak at an elution volume of 13 mL with a predicted molecular weight of 95.9 kDa, corresponding to the dimeric FAD domain species. The shoulder at 15 mL corresponds to the monomeric FAD domain species. The re-run FAD domain monomer fraction (dotted line) has one major peak at 15 ml which has a predicted molecular weight of 42.5 kDa.

The re-run FAD monomer fraction (dotted line) was completely separated from the dimer form, and visible as a single peak at 15 mL with a molecular weight of 42.5 kDa and a Rh of 3.1 nm. The FAD domain dimer fraction (solid line) had a major peak at 13 mL with a molecular weight of 95.9 kDa and Rh of 4.5 nm, and a shoulder at 15 mL which corresponds to the FAD domain monomer species. The monomer present in this fraction is most likely from incomplete FAD monomer/dimer separation from the first SX200 SEC run. However, there could be some contribution from dimer dissociation. In either case, there is a substantial proportion of FAD domain dimer still present in the re-run fraction (94% w/w) which implies that the intact FAD domain dimer formed is a stable species.

The FAD domain monomer re-run has a stable, flat M_w reading (thick solid line) at 42.5 kDa, while that of the FAD domain dimer is not as consistent. The RI values are relative and do not reflect the amount (mg) of protein in the sample, and the major peak will always have an RI of 1.0. As the re-run dimer (solid line) was the minor fraction in the original sample, there is about 6x less FAD domain dimer (0.2 mg) as monomer (1.3 mg, dotted line) in Figure 5.9. This factor and the small amount of FAD domain monomer still present in the sample account for the difference in M_w reading quality for the re-run monomer and dimer fractions.

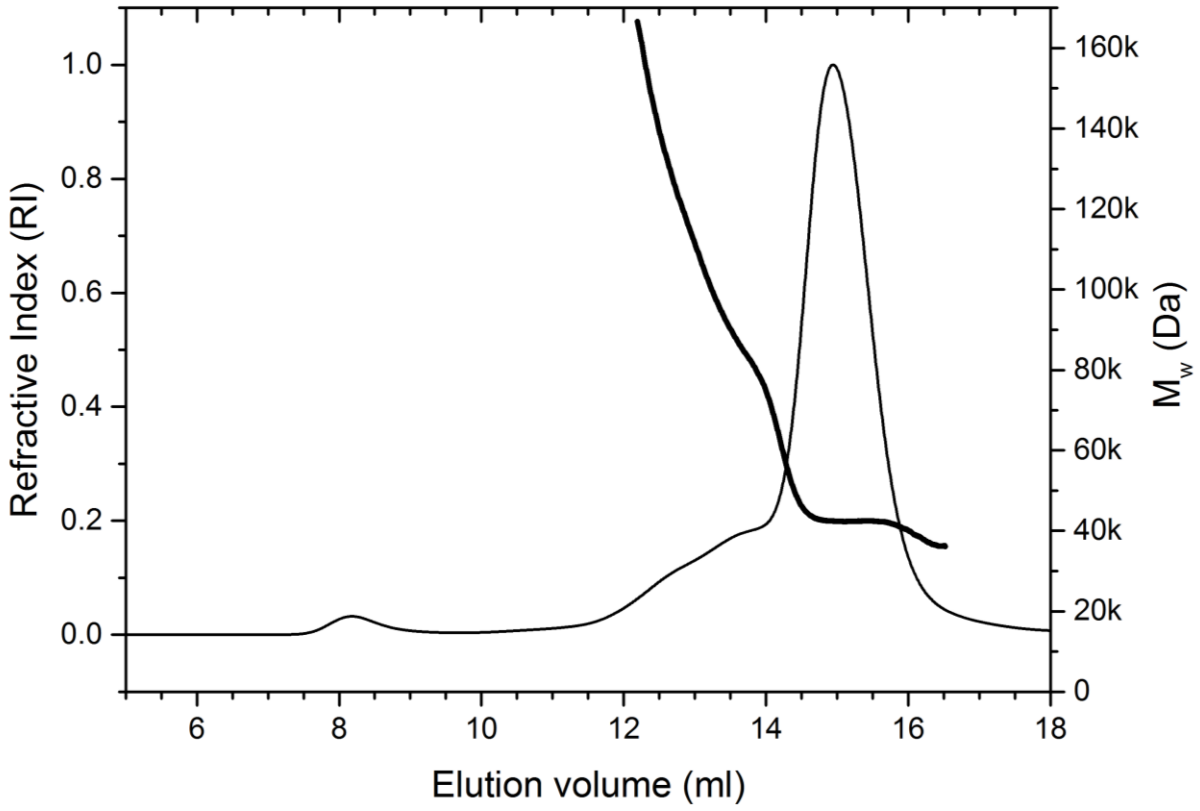

Figure 5.10 MALLS analysis of the effect of dithiothreitol on the WT FAD domain oligomerisation state. The x-axes show the elution volume of the low salt BM3 sample from an 8 ml size exclusion column. The left hand side y-axes show the refractive index (RI) at 633 nm, a relative scale of the ability of light to propagate through the sample, plotted as a thin solid line. The right hand side y-axes show the molecular weight (Da) and Zimm fitting of the species in the sample, plotted as a thick solid line. The WT FAD domain sample in 50 mM Tris (pH 7.2) plus 1 mM EDTA and 1 mM DTT shows one major peak at an elution volume of 15 mL with a molecular weight of 42.2 kDa, corresponding to the monomeric FAD domain species. The shoulder at 13 mL has a molecular weight of ~95 kDa, likely representing the dimer at roughly twice the size of the monomeric FAD domain species.

The incubation of the WT FAD domain with DTT considerably reduced the amount of dimer present in solution compared to the sample without DTT addition. In Figure 5.10, there is a single major RI peak at the 15 mL elution point, which corresponds to monomeric FAD domain with a M_w of 42.2 kDa. There is still some dimer present in solution at ~13 mL, visible as a shoulder on the left of both the major RI peak and in the M_w trace over that elution point. These data show that the dimeric associations in WT FAD can be disrupted by the effects of DTT and suggest that the dimeric associations between WT FAD arise from disulphide bonds between cysteine residues residing on each monomeric domain that are reduced on DTT exposure. Another possibility is that electrostatic interactions between charged amino acids on the surface of the FAD domains causes dimerisation and that the added DTT is able to disrupt these dimeric interactions. Early work on the dimerization state of BM3 showed that treatment with DTT did affect the oligomerisation state of the enzyme and shifted the equilibrium towards the monomer, but concluded that the origin of the dimeric associations were not through disulfide bonds [237]. Reagents such as sodium dithionite were also seen to shift the equilibrium towards the monomeric state, while a shift towards the dimer was seen with detergent molecules such as octyl glucoside [237].

The exact conditions described above were repeated with MALLS studies of the SM FAD domain and DM FAD domain to observe the effects of cysteine mutations on the oligomerisation state of these mutant FAD domains. The SM FAD domain has a C773A mutation, replacing a surface cysteine, while the DM FAD domain has both the C773A mutation and a C999A mutation. C999 is a cysteine that is functionally important as part of the ‘catalytic triad’ in the FAD domain involved in both NADP(H) cofactor binding and in electron transfer from the electron donor NADPH to the FAD flavin cofactor (Chapter 3.1.3).

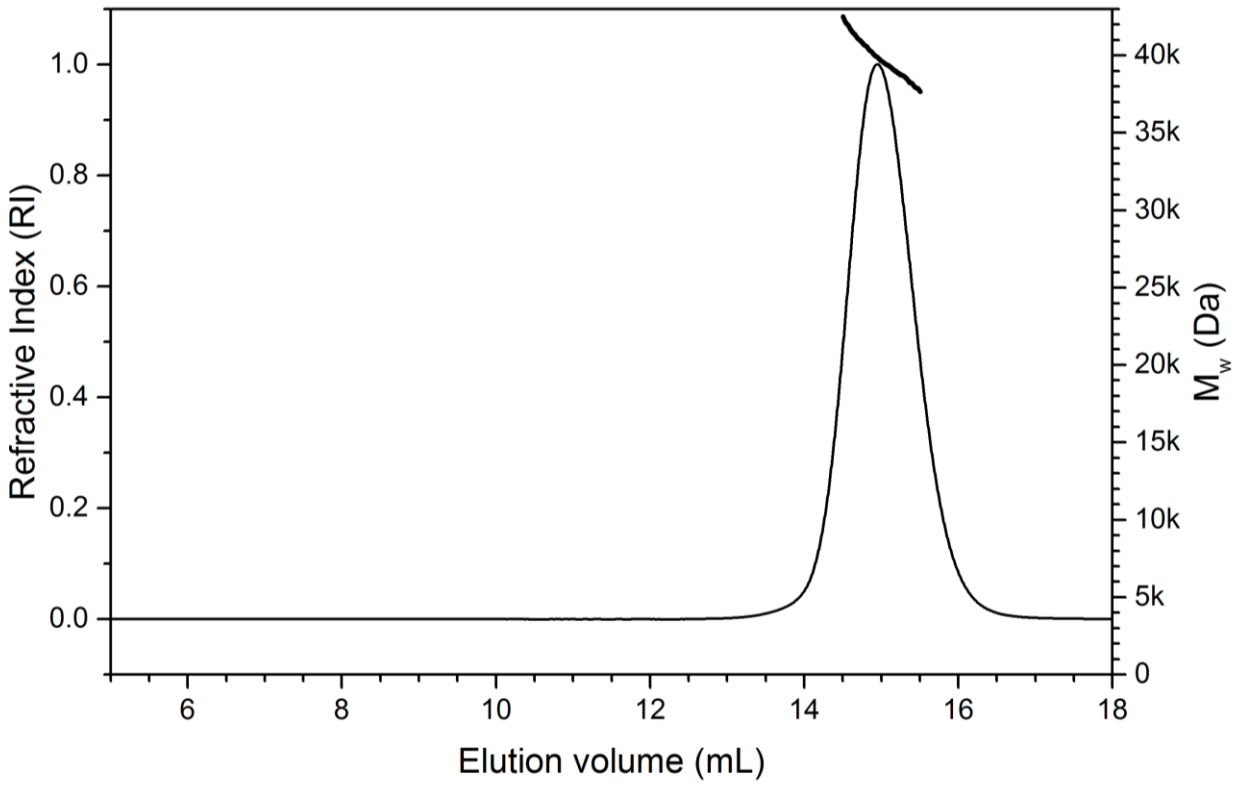

Figure 5.11 MALLS analysis of the SM FAD domain oligomerisation state. The x-axes show the elution volume of the low salt SM FAD domain sample from an 8 ml size exclusion column. The left hand side y-axes show the refractive index (RI) at 633 nm, a relative scale of the ability of light to propagate through the sample, plotted as a thin solid line. The right hand side y-axes show the molecular weight (Da) and Zimm fitting of the species in the sample, plotted as a thick solid line. The SM FAD domain sample in 50 mM Tris (pH 7.2) plus 1 mM EDTA shows a single peak at 15 mL with a molecular weight of 41.1 kDa, which corresponds to the monomeric SM FAD domain species.

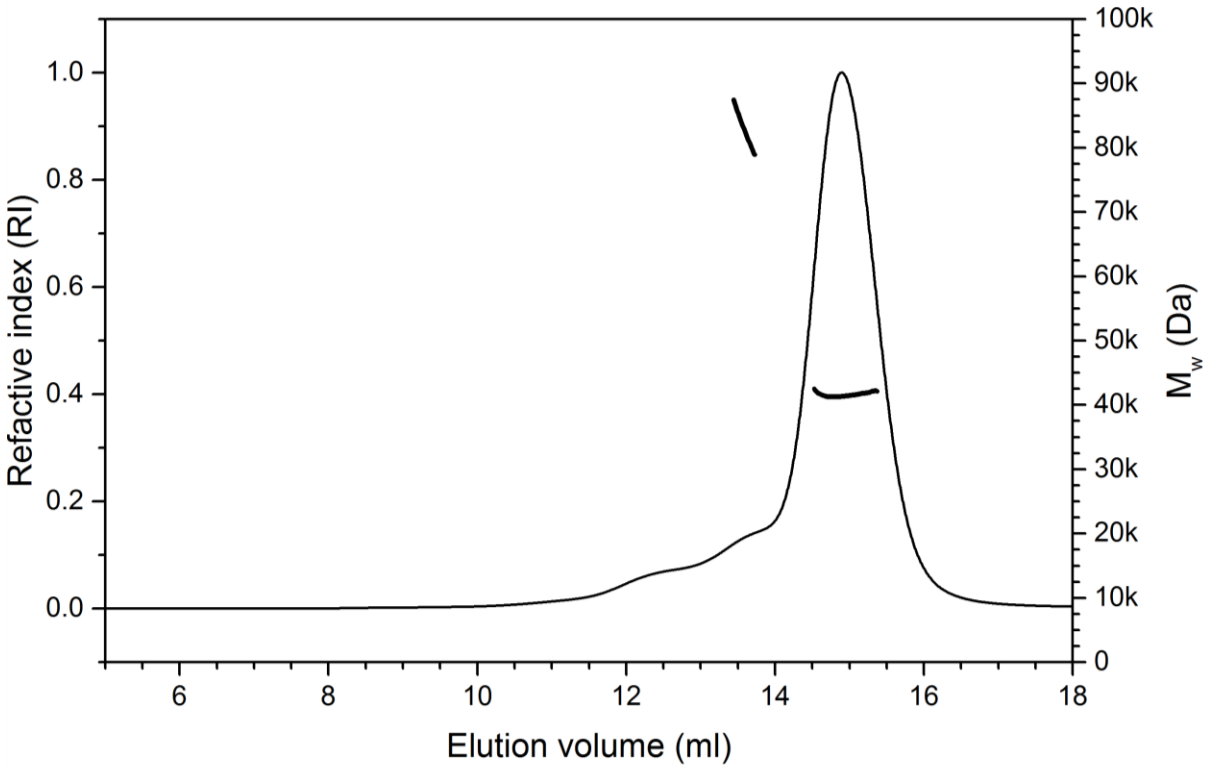

Figure 5.12 MALLS analysis of DM FAD domain oligomerisation state. The x-axes show the elution volume of the low salt DM FAD domain sample from an 8 ml size exclusion column. The left hand side y-axes show the refractive index (RI) at 633 nm, a relative scale of the ability of light to propagate through the sample, plotted as a thin solid line. The right hand side y-axes show the molecular weight (Da) and Zimm fitting of the species in the sample, plotted as a thick solid line. The DM FAD domain sample 50 mM Tris (pH 7.2) plus 1 mM EDTA shows a major peak at 15 mL with a molecular weight of 41.4 kDa, which corresponds to the monomeric DM FAD domain species. A small amount of a higher molecular species is present at 13.5 mL, likely corresponding to the dimer at ~83.1 kDa and a smaller amount of an even higher M_w species at 151.5 kDa (at 12 mL) is roughly equal to twice the dimer weight, perhaps indicating a tetramer form.

The mutation of a single surface cysteine at position 773 to alanine in the SM FAD domain completely eliminated any dimeric association that was seen in the WT FAD domain. The SM FAD domain sample is completely monomeric in 50 mM Tris (pH 7.2) plus 1 mM EDTA (Figure 5.11). The SM FAD domain has a M_w of 41.1 kDa and an Rh of 3.1 nm, which corresponds well to the size of the WT FAD domain monomer. This result is consistent with either disulphide bonds (or possibly electrostatic interactions) involving the surface cysteine at the C773 position being responsible for the observed dimerization in the

isolated WT FAD domain protein. While DTT is able to significantly reduce the amount of FAD domain dimer species in the WT FAD domain, the C773A mutation completely abolishes its formation.

The MALLS analysis of the DM FAD domain in Figure 5.12 had some curious features aside from the major peak of the FAD domain monomer at 15 mL, which has an apparent molecular weight of 41.4 kDa and an Rh of 3.2 nm and which accounts for 92% w/w of the total protein in the sample. Also present in equal proportions (4% each) were apparent dimer and tetramer species, with M_ws of 83.1 kDa and 151.5 kDa, and Rh values of 4.0 nm and 4.9 nm, respectively. As the SM FAD domain sample was completely monomeric (Figure 5.10) it would follow that the DM FAD domain with the same C773A mutation would also be completely monomeric. The DM FAD domain also has the C999A mutation, replacing a cysteine residue involved in NADP(H) binding and electron transfer from this cofactor to the FAD flavin. The additional C999A mutation in the DM FAD domain could possibly account for a perturbation in structure which would favour some aggregation of the mutant FAD domain and the formation of the higher molecular weight species seen in Figure 5.12. Incubation of a DM FAD domain sample in 10 mM DTT and then repeating the MALLS experiment in the same buffer containing 1 mM DTT did not significantly affect the proportion (w/w) of higher molecular weight species observed in the DM FAD domain sample without DTT (Table 5.1). Thus, the protein-protein interactions observed that form likely dimer and tetramer species in the DM FAD domain likely arise from a greater propensity of this double mutant to self-interact as a result of protein structural perturbations caused by the C999A mutation (or the combination of the C773A/C999A mutations), rather than through disulphide bonds as formed in the WT FAD domain dimer.

Table 5.1 Molecular weight (M_w) and hydrodynamic radius (Rh) parameters for WT, SM and DM FAD domains obtained from MALLS analysis. Each run is separated by horizontal dividing lines. The WT, SM (C773A) and DM (C773A and C999A) FAD domain samples were run with and without DTT incubation and the M_w (kDa), Rh (nm) and proportion by weight (w/w) of each species in solution is tabulated. The individual WT dimer (re-run) and WT monomer (re-run) samples were fractions of the previously run WT FAD sample corresponding to the FAD dimer and monomer fractions, respectively. The '/' denotes hydrodynamic radii that could not be resolved by the Wyatt MALLS software program.

FAD domain species	DTT	Proportion by weight	M_w (kDa)	Rh (nm)
WT monomer	-	75%	42.2 ± 2	3.2 ± 0.02
WT dimer	-	25%	94.5 ± 5	4.5 ± 0.05
WT dimer (re-run)	-	94%	95.9 ± 5	4.5 ± 0.05
WT monomer (re-run)	-	100%	42.5 ± 2	3.1 ± 0.01
WT monomer	+	96%	42.2 ± 2	3.1 ± 0.02
WT dimer	+	4%	95.0 ± 5	/
SM monomer	-	100%	41.1 ± 2	3.1 ± 0.02
SM monomer	+	100%	41.0 ± 2	3.2 ± 0.02
DM monomer	-	92%	41.4 ± 2	3.1 ± 0.02
DM dimer	-	4%	83.1 ± 4	4.0 ± 0.04
DM tetramer	-	4%	151.5 ± 8	4.9 ± 0.05
DM monomer	+	90%	41.0 ± 2	3.2 ± 0.01
DM dimer	+	6%	79.2 ± 4	4.3 ± 0.04
DM tetramer	+	4%	148.0 ± 8	/

5.7 Functional studies of the DM FAD domain

The FAD domain of P450 BM3 is able to oxidise NADPH much faster than do eukaryotic CPR enzymes and other diflavin reductases, despite their relatively high amino acid sequence and three dimensional structural similarities [198,383]. This rapid hydride transfer reaction from NADPH to FAD allows similarly fast FAD-to-FMN electron transfer, and these steps help contributes to the rapid FMN-to-heme electron transfer step in P450 BM3, which occurs substantially faster (10-100 fold) than is seen in non-fusion P450/redox partner systems [197]. P450 BM3 is also able to catalyse the reduction of several non-physiological electron acceptors faster than do other diflavin reductases.

Combined CPR crystallographic and mutagenesis studies suggest that NADPH-binding disrupts hydrogen bonding between the catalytic triad residues, which is then reformed on the release of $NADP^+$ product [384]. C999 is one residue of the catalytic triad (comprising C999, S830 and D1044 in P450 BM3), which is highly conserved throughout the diflavin reductase family. Mutagenesis studies in rat CPR have shown than in C630A (BM3's C999A counterpart in CPR) the rate of flavin reduction is compromised and that the cysteine residue may be involved in proton delivery to the N5 atom of the FAD molecule [384]. Thermodynamic and kinetic studies on BM3's C999A FAD mutant have already been investigated, and show a trend of reduced hydride transfer rate constant and increased K_M consistent with the C630A FAD mutant in rat CPR. Here, the thermodynamic and catalytic properties of the C773A/C999A FAD domain, the double mutant responsible for the only resolved BM3 FAD domain crystal structure, are investigated [268].

5.7.1 DM BM3 FAD domain incubation with NADPH

The WT BM3 FAD domain forms a blue semiquinone species on the FAD cofactor upon reduction with NADPH. The flavin then reoxidises slower on incubation in aerobic buffer. This was shown to occur in the C999A FAD domain, and is reinvestigated here with the C773A/C999A DM FAD domain.

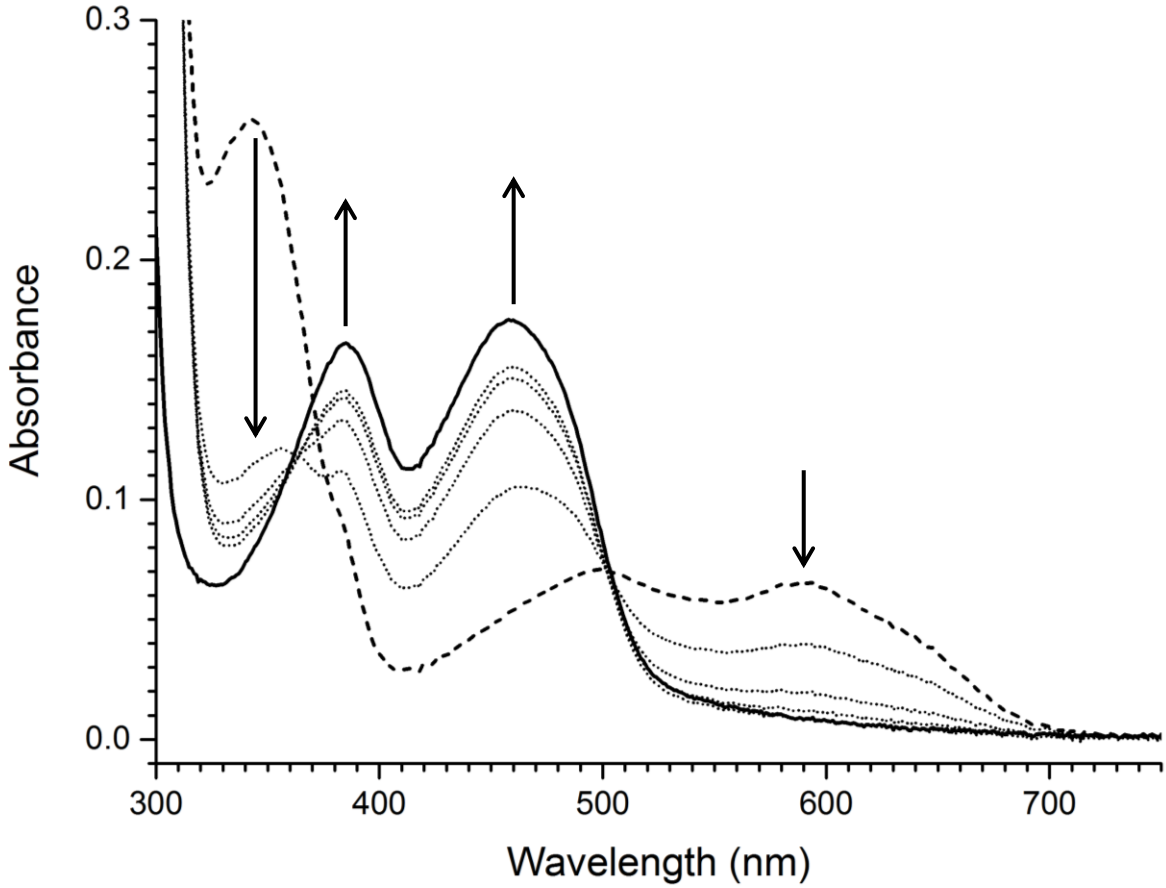

Figure 5.13 Spectral changes associated with BM3 DM FAD domain incubation with NADPH. Oxidised DM FAD domain (16 µM) is shown as a thick solid line with absorbance maxima at 384 nm and 457 nm. Incubation with 60 µM NADPH reduced the DM FAD domain to form the semiquinone species (dashed line) with absorbance maxima at 500 nm and 590 nm. The DM FAD domain near-completely oxidised over a period of 30 minutes when incubated in aerobic buffer, during which time it reoxidised the remaining NADPH and then reduced available O_2 to return to its initial, oxidised state. The spectra shown as dotted lines represent intermediate spectra during the flavin reoxidation process, and the directions of absorbance change during flavin reoxidation at different parts of the flavin spectrum are depicted with arrows (with NADPH oxidation also evident at 340 nm).

The oxidised DM FAD domain UV-visible spectrum was shown to be indistinguishable from that of the C999A and WT FAD domain spectra [301]. Oxidised DM FAD domain (thick solid line) in Figure 5.13 has absorbance maxima at 384 nm and 457 nm, as in the WT and C999A FAD domains. Incubation with NADPH also partially reduces the DM FAD domain to (mainly) a 1-electron reduced blue semiquinone state, with absorbance maxima at 500 nm and 590 nm. Upon aerobic incubation, the DM FAD domain slowly oxidises the remaining NADPH and returns back to its oxidised (quinone) resting state. This behaviour suggests that the electronic environment around the C773A/C999A DM FAD cofactor is not significantly perturbed compared to the C999A FAD and WT FAD domain, and that it retains ability to form the neutral FAD semiquinone species.

2.7.2 Steady-state kinetics of the DM and SM FAD domain mutants

The steady-state kinetics of C773A SM FAD and C773A/C999A DM FAD domains were investigated to determine if surface cysteine mutation in SM FAD altered hydride transfer compared to the WT FAD domain and if the combination of mutations in the DM FAD resulted in similar steady state rates to a previously characterised single mutant C999A FAD domain.

Ferricyanide has been shown to accept electrons from the FAD domain and the NADPH-concentration dependant reduction of potassium ferricyanide was followed in SM FAD and DM FAD (Figure 5.13) and the kinetic parameters recorded in Table 5.2. The C999 has already been identified as part of the catalytic triad with a major role in hydride transfer from the NADPH cofactor to FAD coenzyme in both BM3 and CPR [301,384]. Compared to the WT BM3 FAD domain the rate of hydride transfer (k_{cat}) is 17.6-fold less in C999A and the K_M with NADPH is 4-fold lower (Table 5.2).

The significantly lowered k_{cat} for ferricyanide reduction in DM FAD compared to WT FAD is consistent with C999A as is its larger $K_{M.}$ The rates measured for DM FAD in this study of 18.3 s^{-1} and K_M of 160.9 μM for the NADPH-dependent ferricyanide reduction were consistent with the ones previously published [268]. The weaker apparent binding (K_M) arises from the slower hydride transfer from NADPH to the FAD cofactor in mutants lacking the critical C999 residue. This suggests there is no cumulative effect of the C773A mutation on the electron transfer rate of DM FAD which is expected as C773 is a surface

cysteine residue. In addition the steady state parameters obtained for C773A were comparable to WT FAD domain with a k_{cat} of 303 s^{-1} and a K_M of 10.9 µM.

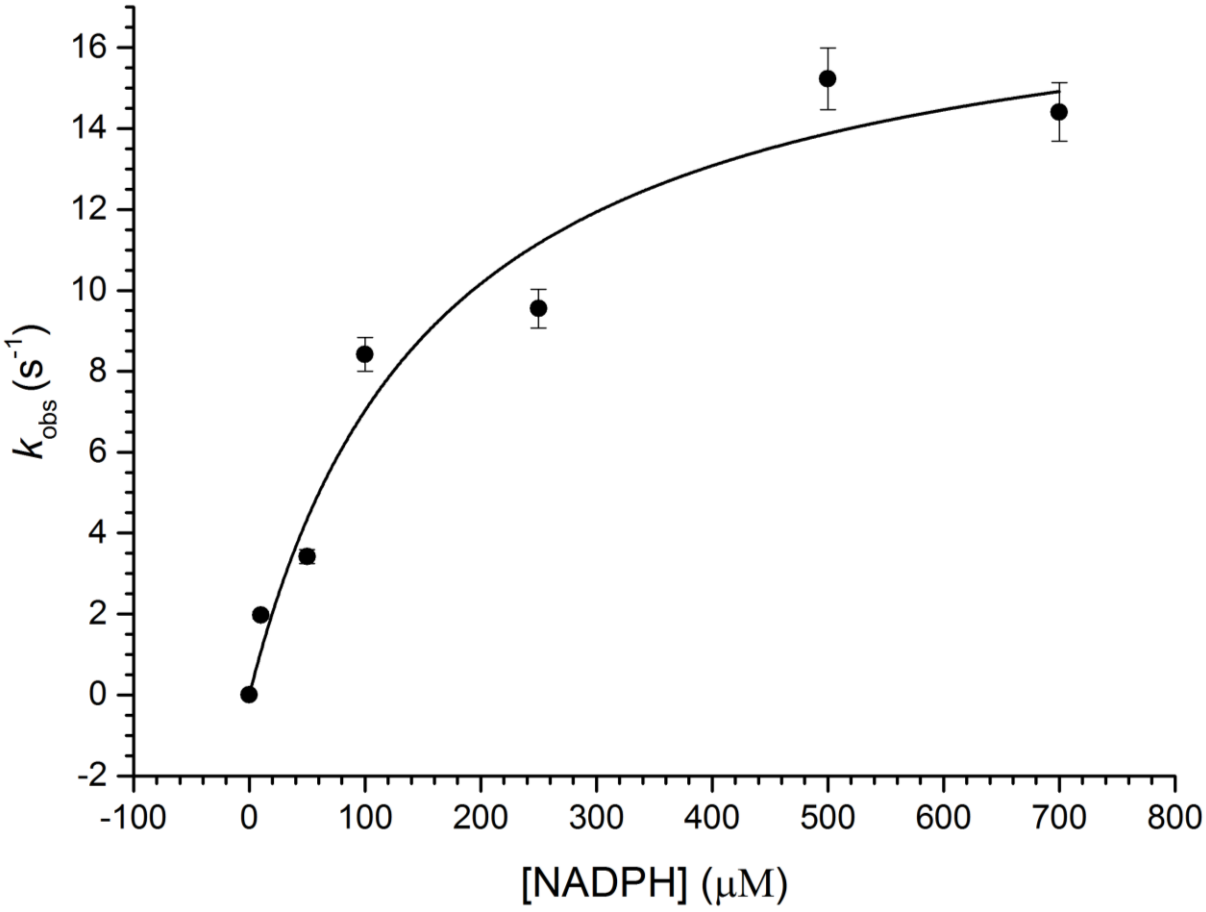

Figure 5.14 BM3 DM FAD domain steady-state kinetic plot showing the dependence of ferricyanide reduction rate on NADPH concentration. The averaged data points for three assays per concentration point were fitted (black line) using a hyperbolic function (Equation 2). Error bars represent the standard deviation from the averaged data points. The k_{cat} is 18.3 ± 2.1 s^{-1} and the K_M is 160.9 ± 55.6 µM. Reactions were carried out in 50 mM KPi buffer(pH 7.0) containing 200 mM KCl buffer.

Table 5.2 Steady-state kinetic parameters for ferricyanide reduction by WT BM3 FAD domain and its C773A (SM), C773A/C999A (DM) and C999A FAD domain mutants. The results reported in this study were from the SM and DM FAD domain mutants. The data denoted by an asterisk (*) were taken from literature values. Kinetic parameters (k_{cat} and K_M) were determined by varying NADPH concentration with a near-saturating concentration of potassium ferricyanide (2 mM). Reactions were carried out in 50 mM KPi buffer (pH 7.0) plus 200 mM KCl at 25 °C.

BM3 FAD domain species	k_{cat} (s^{-1})	K_M (μM)
WT FAD*	360.0 ± 4.0	6.5 ± 1.3
SM FAD	303.8 ± 8.1	10.9 ± 5.5
DM FAD	18.3 ± 2.1	160.9 ± 55.6
DM FAD**	16.3 ± 1.3	160.3 ± 31.0
C999A FAD*	23.1 ± 0.7	55.4 ± 11.7

*taken from Roitel et al. [301]

**taken from Joyce et al. [268]

5.8 BM3 HD Extinction Coefficient Determination

Experiments were set up to accurately determine the heme Soret extinction coefficient of the BM3 heme domain to enabling simple and precise quantification of the protein. Electron Paramagnetic Resonance (EPR) heme quantification (Methods, 2.17.1) and pyridine hemochromagen determination (Methods, 2.11) were both used to determine the concentration of a pure sample of the BM3 HD protein. These analyses in turn led to the calculation of two different extinction coefficients for each absorbance feature shown in Figure 5.15. Spectra for the BM3 heme domain complexed with N-palmitoylgycine (NPG), as its pyridine adduct, and when complexed with NO and CO were also obtained, and the changes in absorbance induced by the binding of each of the specific ligands were determined, and the calculated extinction coefficients tabulated in Table 5.3.

X-band EPR was used to quantify the concentration of thiolate-ligated ferric heme in the same P450 heme domain sample that was used for the UV-visible spectral analyses shown in Figure 5.15. The heme concentration determined by EPR was done with reference to the doubly integrated area of its g-factor to those of a set of copper solution concentration standards. Using the Beer-Lambert law and with reference to the absorbance difference changes in Table 5.3, heme absorbance difference extinction coefficients were also re-determined based on the heme concentration established from the EPR experiment.

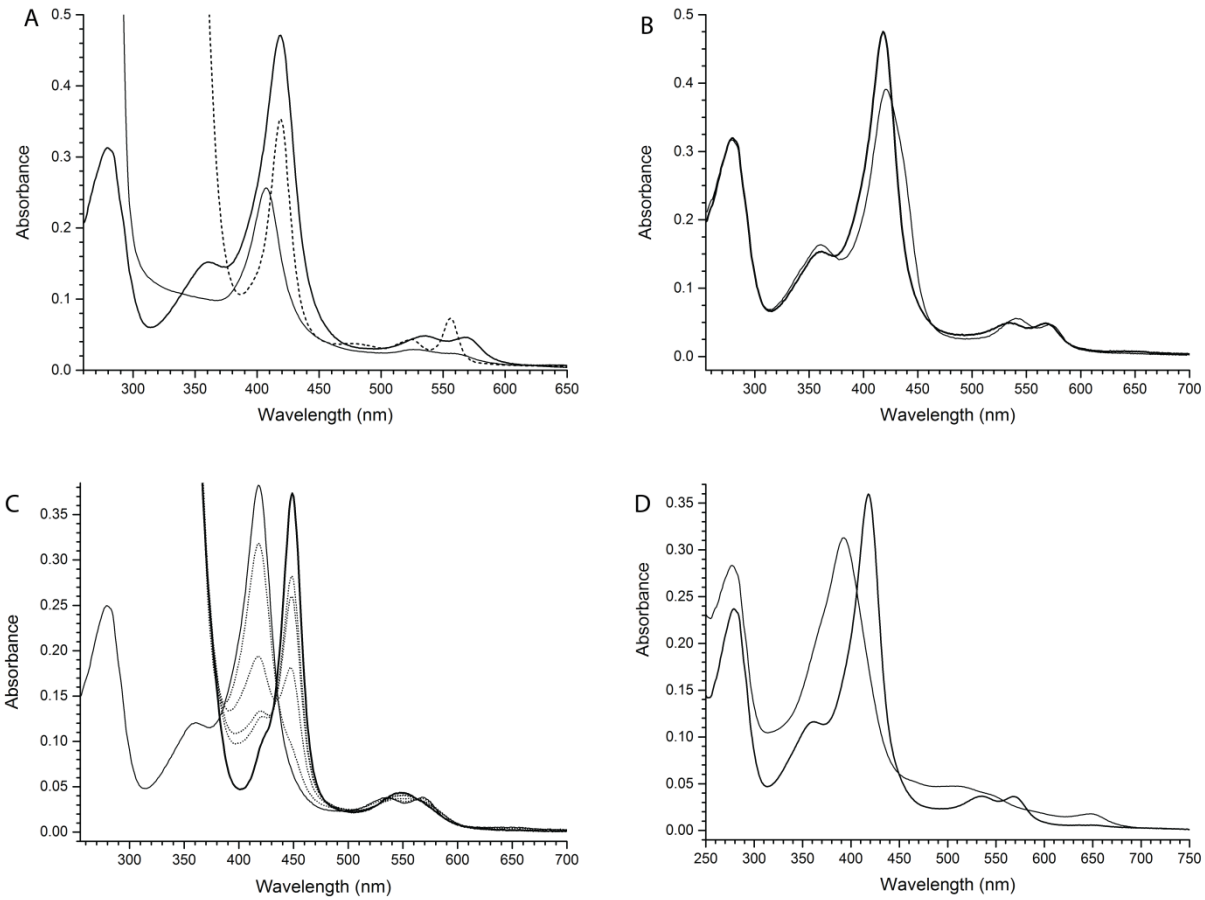
A
B
C
D
Absorbance
Wavelength (nm)

Figure 5.15 Ligand binding to the BM3 HD for extinction coefficient determination from EPR and pyridine hemochromagen methods. Panel A: UV-visible spectrum of the heme moiety complexed with pyridine. The thick solid line shows the heme domain (~4.9 μM based on ε_{418} = 95 mM^{-1} cm^{-1}) with A_{max} at 419 nm, while the thin solid line shows the end spectrum for the titration of pyridine against oxidised heme with A_{max} at 407 nm. The dotted line shows the end spectrum for the titration of pyridine against sodium dithionite-reduced heme, with A_{max} returned to 419 nm. Once the difference spectrum was calculated (reduced minus oxidised), the $\Delta A_{556-540}$ was used to calculate the extinction coefficient of pyridine-bound, reduced heme. The extinction coefficient of 23.9 mM^{-1} cm^{-1} was then used to determine the concentration of heme in the sample [56]. Panel B: UV-visible spectrum of the BM3 heme domain complexed with NO. The thick line shows the heme domain with A_{max} at 418 nm. The thin line shows the partially-formed spectrum for the NO-heme complex with A_{max} at 420 nm. The heme-NO complex however was not fully formed and the $\Delta A_{568-500}$ value of 0.004424 was used to calculate the extinction coefficient. Panel C: UV-visible spectrum of BM3 heme domain complexed with CO. The thin solid line shows the heme domain with A_{max} at 418 nm while the thick solid line shows the end spectrum for the titration of the dithionite-reduced heme domain with CO, with A_{max} at 450 nm. Intermediate spectra collected during the conversion of the oxidised heme to its reduced, CO-bound complex are shown as dotted lines. Panel D: UV-visible spectrum of BM3 heme domain complexed with NPG. The thin line shows the oxidised, low-spin heme domain with A_{max} at 418 nm, while the thick line shows the end spectrum for the titration with NPG with A_{max} at 392 nm for the near-fully high-spin heme iron. The 392 nm absorbance of 0.483 was used to calculate the extinction coefficient of NPG-bound BM3 HD heme.

The discrepancies in extinction coefficients obtained from these two heme quantification methods likely highlights mainly the inaccuracies involved with pyridine hemochromagen methodology, as EPR quantification is the more accurate and consistent technique, though requires much higher concentrations of P450 sample. The extinction coefficients for each ligand in Table 5.3 vary consistently by a factor of ~1.2 between the different quantification methods meaning that provided the spectra are reproducible, any of the extinction coefficients can be used to quantify the amount of BM3 HD in a given solution. In the case of the reaction of NO with the BM3 HD, the instability of the Fe^{3+}-NO complex to oxidation prevented the complete formation of this species. A coefficient for the partially formed complex was determined as $\Delta A_{568-500}$ = 11.7 mM^{-1} cm^{-1}. Based on previous data for an apparent fully formed BM3 HD Fe^{3+}-NO complex (ε_{435} = 86 mM^{-1} cm^{-1}) and by comparison of the spectrum for this sample with that for the BM3 HD Fe^{3+}-NO complex in Figure 5.15 panel B, it can be estimated that there is ~35% formation of the

Fe^{3+}-NO complex in the latter [385]. Assuming this to be an accurate estimate, the absorbance difference coefficients ($\Delta A_{568-500}$) for a fully formed BM3 HD Fe^{3+}-NO complex would be increased to 39.49 and 33.43 mM^{-1} cm^{-1} for the pyridine and EPR determinations, respectively.

Table 5.3 Extinction coefficients determined for the P450 BM3 Heme domain from EPR and pyridine hemochromagen methods. Both EPR and pyridine hemochromagen methods were used to determine the concentration of a pure sample of BM3 HD from which the UV-Vis spectra collected from ligand binding was used to determine the extinction coefficients.

			Extinction Coefficient (mM^{-1} cm^{-1})	
Ligand	Wavelength (nm)	ΔA value	Pyridine determination	EPR quantification
Pyridine	$A_{556\ nm\ (red)} - A_{540\ nm\ (ox)}$	0.0451	23.9*	28.2
NPG	$A_{392\ nm} - A_{418\ nm}$	0.351	109.7	93.4
NO	$A_{568\ nm} - A_{500\ nm}$	0.044	13.82	11.7
CO	$A_{450\ nm} - A_{490\ nm}$	0.348	108.8	92.7

*Obtained from literature [275].

5.9 P450 BM3 Structural Analysis by Transmission Electron Microscopy (TEM)

While the individual P450, FMN and FAD domain structures of BM3 have been solved by protein crystallisation and X-ray diffraction studies, the structure of the intact, dimeric P450 BM3 structure remains elusive despite numerous attempts to crystallise the protein [109,223,268]. This is possibly due to the dynamic nature of the protein, where individual domains may be highly mobile within the multidomain dimeric complex. Electron microscopy (EM) is an attractive technique for examining the P450 BM3 structure, as it allows the generation of structural data from proteins and complexes in their physiological environment, without the need for crystallography. However, its resolution limit is currently not as high as that for crystallography at <2.0 Å [386]. However, in recent years there have been improvements in resolutions levels for EM, which can now reach up to 2.2 Å, in addition to being successfully applied to the structural analysis of lower molecular weight species than previously were possible [387].

Negative stain Cryo-EM was used in efforts to elucidate the dimeric structure of P450 BM3. SEC-MALLS was employed to obtain a homogeneous sample of dimeric P450 BM3. After resolving a sample of purified P450 BM3 in 100 mM Tris buffer (pH 7.0) using SEC, a fraction containing only the P450 BM3 dimer was used to make samples for analysis by EM. To ensure that the P450 BM3 sample used was completely dimeric, i.e. that there was no monomer and that the dimer did not dissociate over the time course of the EM sample preparation, the sample was re-run on the SEC-MALLS instrumentation in the same buffer to confirm that a homogeneous dimer was present (Figure 5.16).

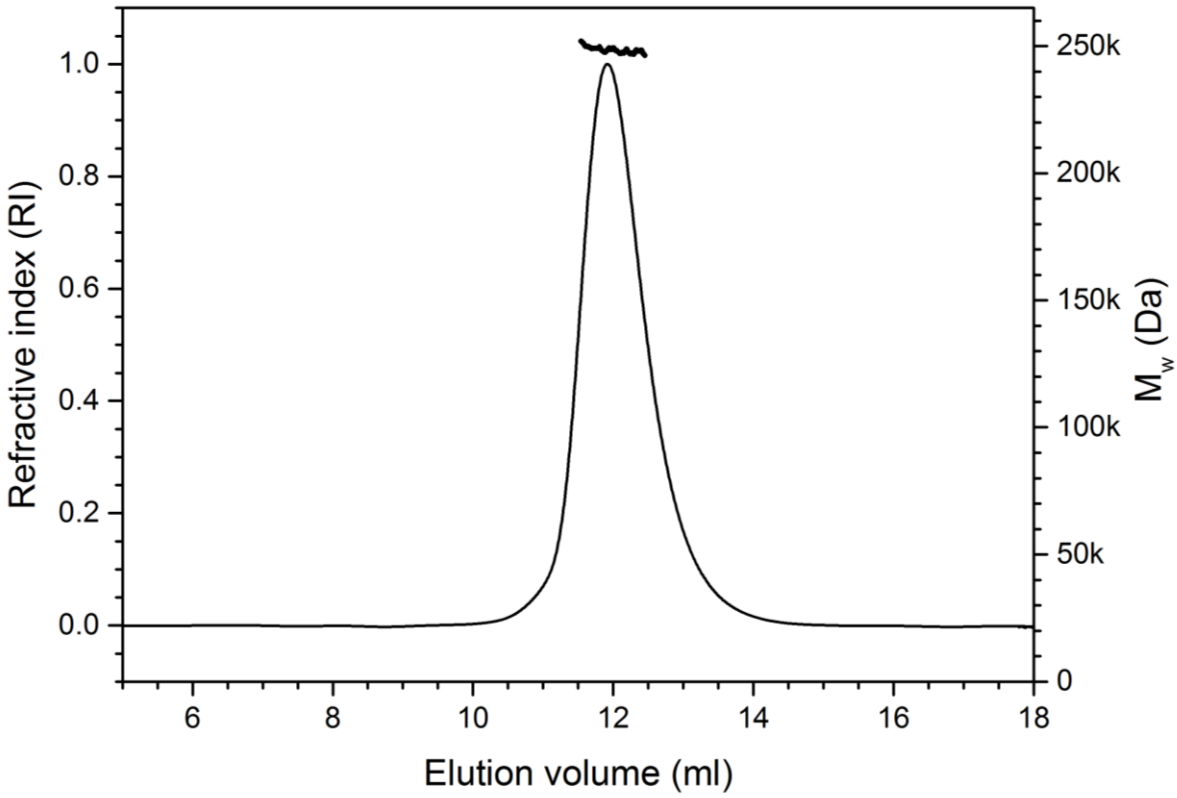

Figure 5.16 MALLS analysis of P450 BM3 dimer fraction re-run. The x-axes show the elution volume of the BM3 HD sample. The left hand side y-axes show the refractive index (RI) at 633 nm, plotted as a thin solid line. The right hand side y-axes show the molecular weight (Da) and Zimm fitting of the species in the sample, plotted as a thick solid line. The P450 BM3 sample in 100 mM Tris buffer (pH 7.0) shows a single major peak eluting at 12 mL with an apparent molecular weight of 249.3 kDa, indicative of a homogeneous dimeric species.

Quantifoil grids were prepared by ionisation and by washing in 100 mM Tris buffer (pH 7.0) before they were incubated in P450 BM3 dimer solution. Different concentrations of BM3 were trialled and it was found that 7 µg/mL P450 BM3 populated the grids adequately and without overcrowding. After negative staining with 2% aqueous uranyl acetate, grids were incubated further in wash buffer to remove excess stain (Methods 2.25).

The grids were screened on a Tecnai Bio-Twin Transmission Electron Microscope (FEI Company, OR, USA). The data were generated from 21K particles and were processed with applied C2 (dyad) symmetry (Figure 5.17). The class averages fit to a single coherent and feasible 3-D solution with a resolution of 20 Angstroms (Figure 5.19).

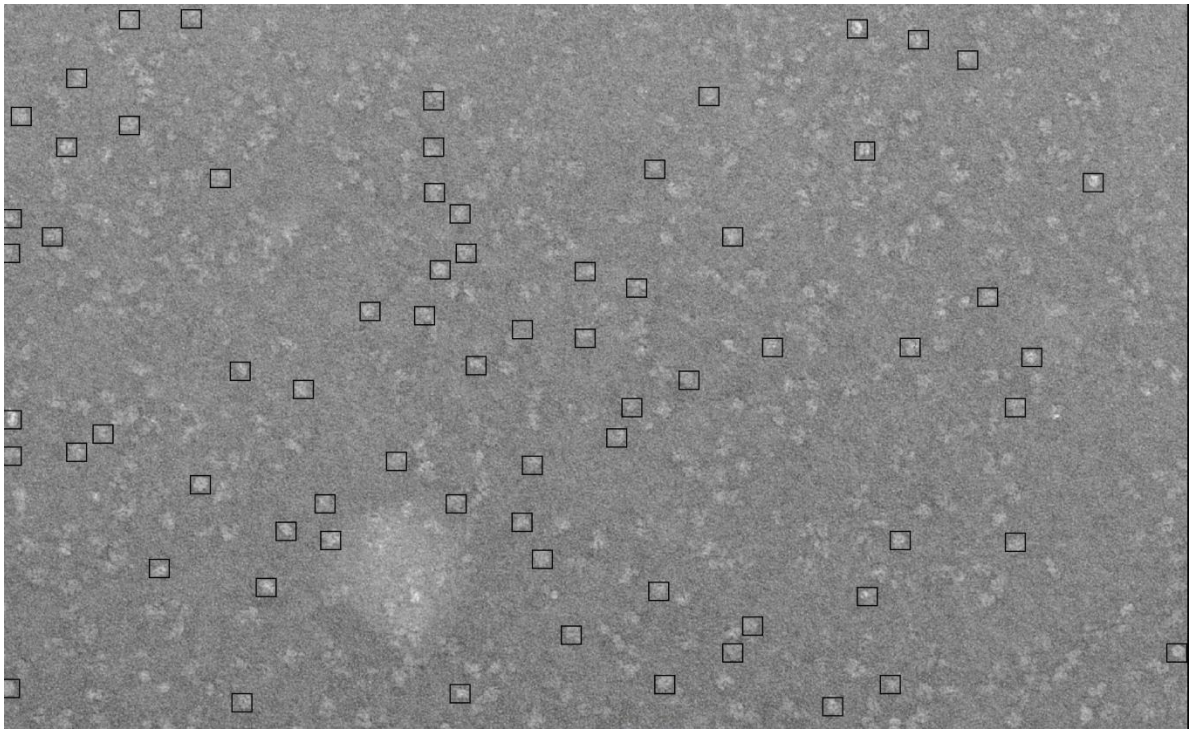

Figure 5.17 TEM of P450 BM3 dimer particles visualised under negative stain. Each square box surrounds a single P450 BM3 dimer. These particles were all sampled, arranged and used to compile the different representations of BM3 orientations shown in Figure 5.18.

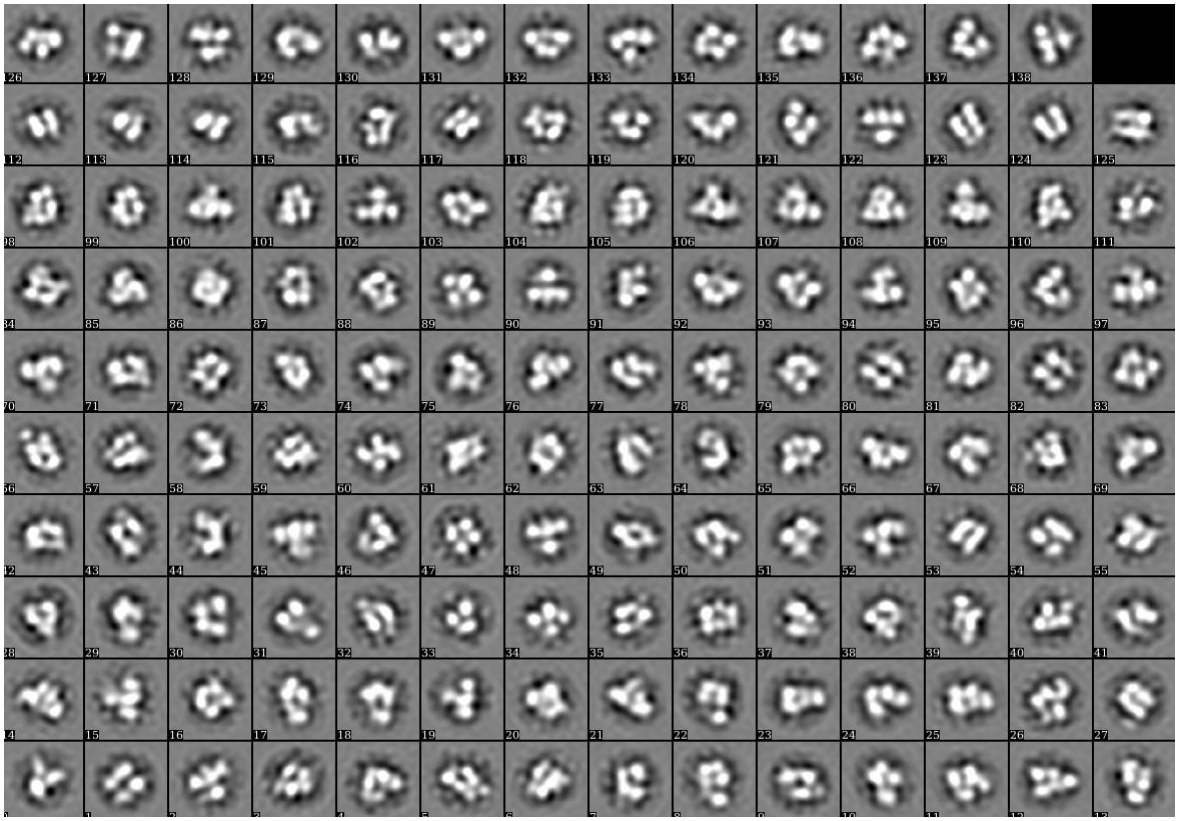

Figure 5.18 A montage of different orientations representing the P450 BM3 dimer. The projection averages of all the three-dimensional orientations sampled are shown.

At 20 Å, the P450 BM3 structure lacks the definition of distinct features such as α-helices and β-sheets that would come with a higher resolution structure (<4 Å). However, the three domain volumes belonging to the P450, FMN and FAD domains within each P450 BM3 monomer are clearly visible, as are the orientation of the dimer and the various inter-monomer domain associations.

The three domains within each monomer are organised in a twisting 'L' shape and the full complex is shaped like a mushroom with two very strong protein-protein contacts at the bottom of the mushroom stem (Figure 5.19, panel B), these likely being from the FAD domains.

Of all the possible random orientations with which the dimer could adhere to the grids, all were sampled, resulting in a well-defined Euler space. In the resulting structure we can see a cavity between the dimer interface in looking from the top into the structure (Figure 5.19, panel A) and a space between monomers (Figure 5.19, panel B).

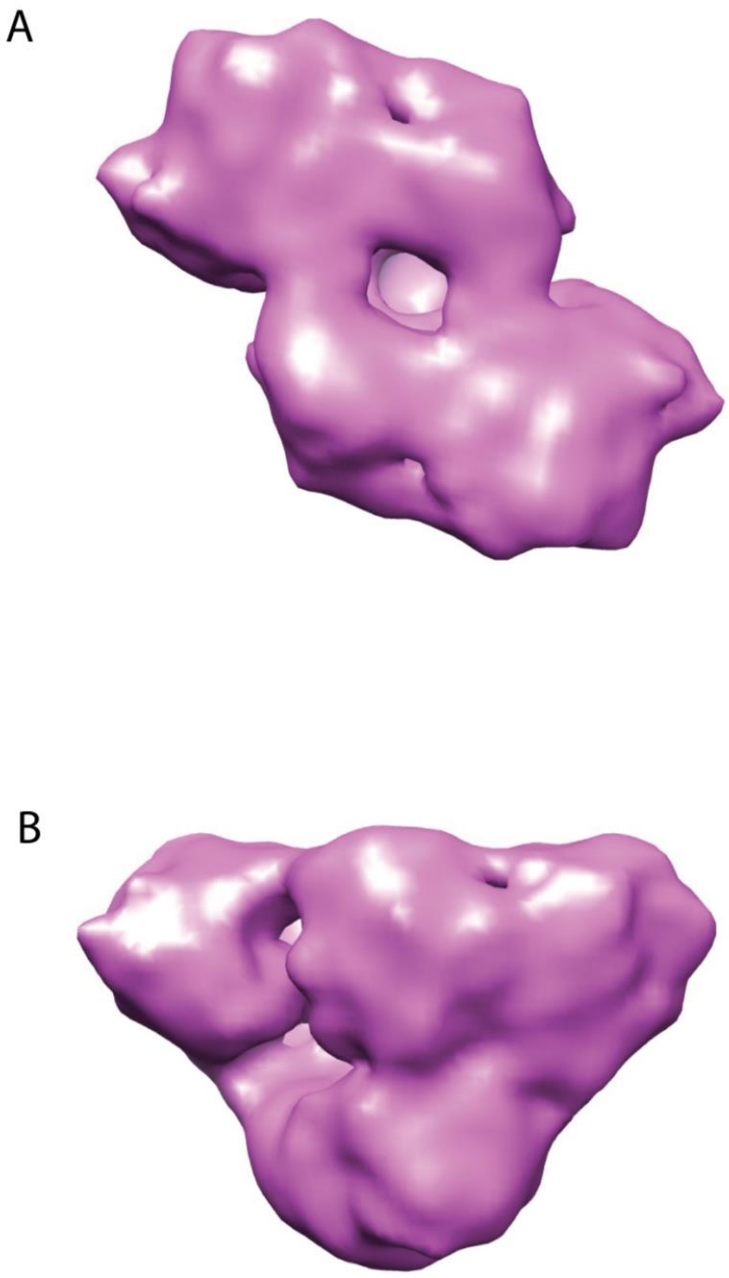

Figure 5.19 Three-dimensional structure of the BM3 dimer at 20 Å resolution. Panel A shows the surface render from the top view of the complex (purple). Panel B shows the surface render from side view of the complex.

All the regular error contributions from negative staining techniques (e.g. potential for shrinkage, contrast transfer function (CTF) artefacts and dehydration) exist and contribute a degree of error, such as the apparent space between the heme and FMN domain dimeric interface evident.

5.10 P450 BM3 HD analysis using Nuclear Magnetic Resonance (NMR) Spectroscopy

NMR is a structural biology technique often applied to proteins to resolve their three-dimensional structures. It has an advantage over X-ray crystallography in that experiments are carried out on proteins in their solution state, which allows a variety of dynamic processes to be investigated. NMR spectroscopy, however, is not without its challenges. A variety of multidimensional NMR experiments involving the double and triple-labelling of the protein sample with isotopes are needed to collect the different spectra used to ultimately assign a protein structure. A variety of temperature, pH, oxidations states, ligand and redox partner effects can be used to probe the structural dynamics of a protein in solution, and these properties can measured by NMR techniques to shed new light on protein dynamic processes and how they are influenced by environmental changes. Detailed below is the approach taken for the P450 BM3 HD, the P450 domain of the fusion enzyme flavocytochrome P450 BM3.

5.10.1 1D NMR

The size of the BM3 HD is 62.5 kDa, which is on the upper limits of resolution of protein structure by conventional NMR techniques. To check the feasibility of these studies on the BM3 HD, a set of 1D NMR spectra were collected. ^{1}H nuclei have a spin number of ½ and are therefore observable by NMR spectroscopy. Other nuclei abundant in proteins like ^{14}N and ^{12}C have a spin number of 0 and are NMR silent, which makes the acquisition of 1D ^{1}H NMR spectra relatively easy as no labelling is required. However, the ferric, low-spin heme iron in the oxidised BM3 HD is paramagnetic (spin = ½) and therefore detectable by NMR spectroscopy. Paramagnetic species such as ferric heme and FeS clusters (in appropriate redox states) are known to affect the mapping of chemical shifts up to 20 Å away from the paramagnetic centre in more complex 2D and 3D NMR experiments [388]. The ferrous heme in reduced BM3 HD, however, is diamagnetic with a spin number of 0 and is therefore NMR silent.

Unlabelled BM3 HD was expressed and purified as described in Methods 2.5.4/2.7.5. Two 500 µl NMR samples of 500 µM BM3 HD were prepared, one oxidised the other reduced.

The BM3 HD sample was made ferrous in an anaerobic glove box, using sodium dithionite to reduce the heme iron in the concentrated sample. A 0.1 mm pathlength cuvette was used to measure the absorbance of the reduced sample without dilution in a spectrophotometer contained within the glovebox, as detailed in Methods section 2.26.1. A layer of mineral oil over the sample in a parafilm-sealed Shigemi tube prepared in anaerobic conditions ensured that the ferrous sample remained reduced over the time for collection of data. The ferric and ferrous samples of BM3 HD were run on a Bruker 800 MHz spectrophotometer to produce the one dimensional ^{1}H spectrum in Figure 5.20.

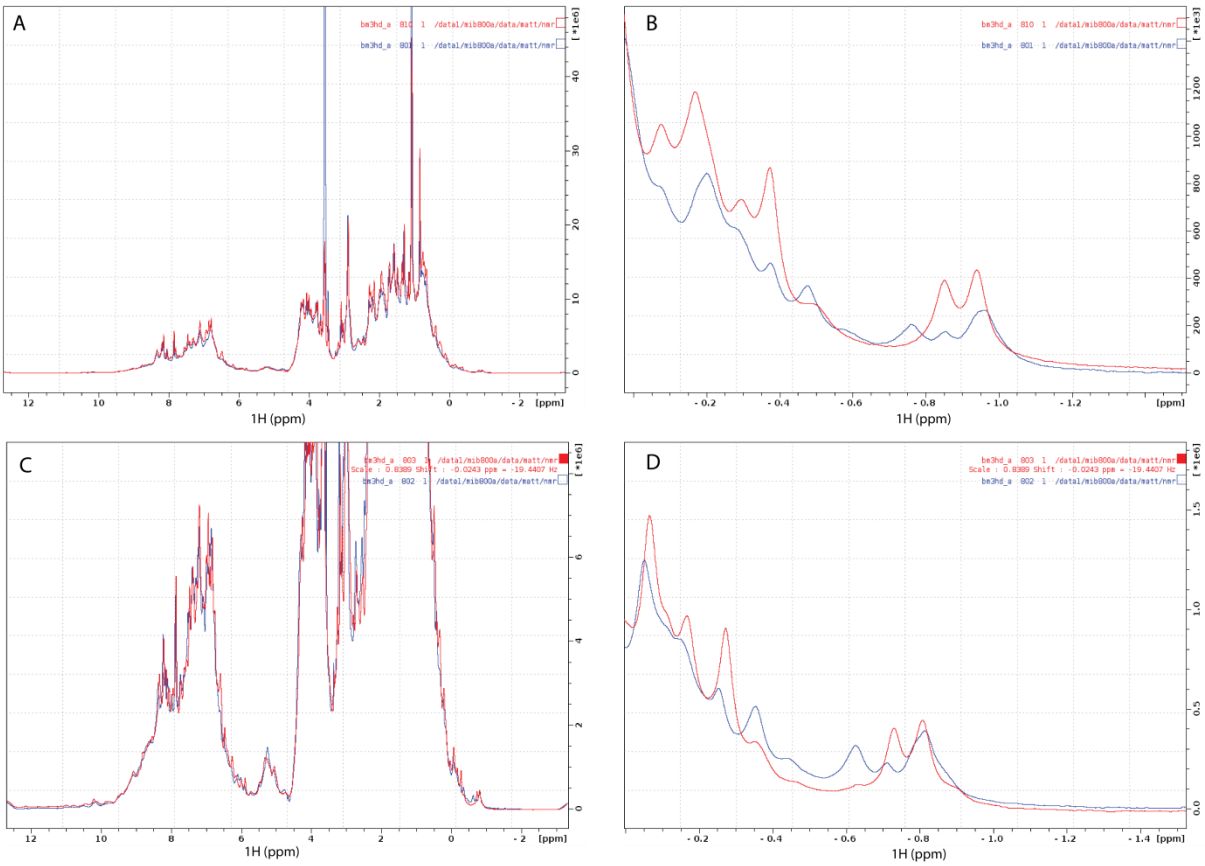

Figure 5.20 Comparison of the 1D ^{1}H spectra of the ferric (oxidised) BM3 HD and the ferrous (reduced) BM3 HD. Panel A shows overlaid spectra of ferric (red) and ferrous (blue) BM3 HD, and panel B is a zoomed in portion of the panel A. Panel C shows the same ferrous sample (blue) spectrum overlaid with a spectrum taken of the same sample after 10 days (red) and panel D is shows a portion of those spectra zoomed in.

The 1D, ^{1}H spectra of even small proteins are impossible to interpret in a comprehensive manner and the complexity 1D ^{1}H NMR spectra of P450 BM3 HD is typical of a large protein with many overlapping proton peaks. Even a protein of 100 amino acids would have ~800 protons, and thus the situation is much more complex for the BM3 HD.

However, a gross analysis of secondary and tertiary structure can be made from the 1D spectrum. The range between 6-9 ppm shows the chemical shift values of the amide backbone and is most indicative of a correctly folded secondary structure. These are the protons that will be correlated with the resonances of their bound ^{15}N in the HSQC spectra in Section 5.10.2. The full spectra of the ferric (red) and ferrous (blue) forms of the BM3 HD in Figure 5.20, Panel A have sharp distinct peaks between 6 and 9 ppm that are indicative of folded protein. After 10 days the peaks of the spectra for both ferrous and ferric BM3 HD (Panel C) are relatively unchanged, illustrating the stability of the BM3 HD sample, even in excess dithionite reductant.

Interestingly, the oxidation state of the P450 heme iron appears to have an effect on the chemical shifts values at certain positions, as highlighted in Panel B (Figure 5.20). This region is typical of methyl groups shielded by the aromatic side chains. Panels C and D show the ^{1}H NMR spectrum of the reduced sample overlaid with a spectrum of the same sample taken after 10 days. This discrepancy between the spectra is due to the reoxidation of the BM3 HD in the 10 day old reduced sample, which closely (but not completely) overlays with the oxidised BM3 HD sample.

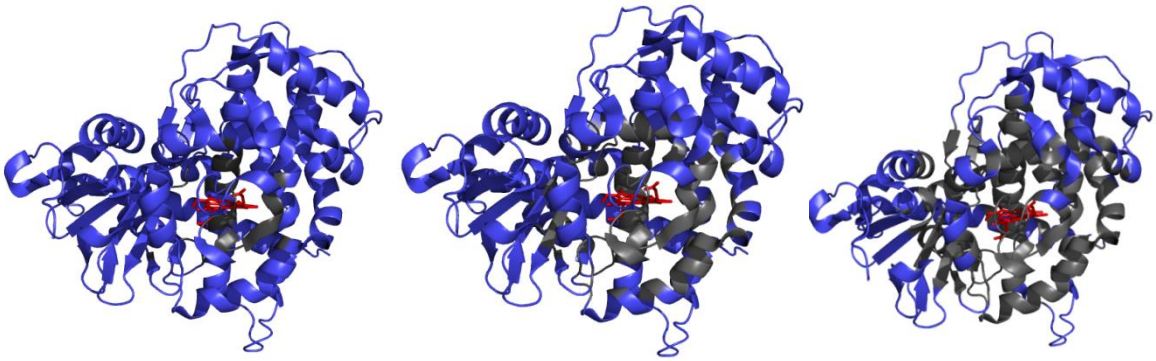

Figure 5.21 BM3 HD structure highlighting the paramagnetic effects of the ferric heme on nearby residues. The 1JPZ PDB entry was used in this model. The heme cofactor (red) is displayed in the centre and unaffected residues are in blue. The left hand image shows amino acid residues up to 10 Å away from the heme coloured grey. The middle and right hand images show residues 15 Å and 20 Å away from the heme cofactor coloured grey, respectively.

The paramagnetic effects of the heme iron have been reported to affect the chemical shifts of nuclei between 10 - 20 Å away from the paramagnetic centre and Figure 5.21 shows the difference in amino acids affected in this range [389–391]. Comparing the overlaid ^{1}H

spectra in Panel B (Figure 5.20), most of the peaks seem to be affected. This area of the spectrum is typically populated by methyl group protons shielded by aromatic residues and represents buried residues which should be the least affected by conformational change. The discrepancy in chemical shift could be represented by minor changes in protein conformation with large contributions from the paramagnetic heme iron [392]. However, it has been reported that large changes in structural dynamics are seen upon redox-linked changes in heme-containing enzymes using 2D NMR techniques [393,394]. To better understand the effects of the paramagnetic heme and to achieve better resolution, multidimensional experiments involving isotope labels needed to be employed, as described below.

5.10.2 2D NMR

The Heteronuclear Single Quantum Coherence (HSQC) spectra are two-dimensional, with the proton chemical shift on one axis and the ^{15}N chemical shift on the other axis. This is a highly sensitive experiment that involves the transfer of magnetisation from the proton to the ^{15}N on amide N-H bonds, followed by the detection of nucleic spin relaxation times. Each residue is observable in the HSQC spectra by correlating the proton chemical shift with the resonance of the nitrogen atom. HSQC spectra act as a unique fingerprint for each protein and are usually trialled before moving on to triple resonance experiments involving both ^{15}N and ^{13}C isotopic labels.

HSQC experiments require the protein to be isotopically labelled as the naturally occurring ^{14}N and ^{12}C have a spin number of 0 and are NMR silent. ^{15}N in usually used first over ^{13}C as it is far cheaper. The expression of the desired protein in carried out in cells grown in minimal medium, supplemented with a ^{15}N salt to ensure that the only source of nitrogen available is the isotope. Initially, M9 minimal medium was trialled with BL21-Gold (DE3) expressing the pBM20 vector for BM3 HD production (Section 2.26.2). Overnight LB cultures were used to inoculate 2L of M9 medium distributed in 0.2 L per flask. From this point on the expression protocol was unchanged, with induction with IPTG done once the cells reached an OD_{600} of 0.6 and cells harvested after 24 hours growth time. While the BL21-Gold (DE3) cells did express the BM3 HD protein, there was a consistent low yield compared to many of the other bacterial enzymes expressed in the same cell sample, and

when grown in the volumes used for the large scale preparations (200 mL). Purification of labelled protein was carried out exactly as for the unlabelled BM3 HD (Methods, section 2.7.5). However, due to the low yield of labelled protein obtained, this approach proved very inefficient.

The BL21-Gold (DE3) strain expressed the BM3 HD well when grown in regular LB large scale trials using BL21-Gold (DE3) and BL21-CodonPlus (DE3) transformant strains grown in 200 mL cultures (2 flasks x 0.1 L) of M9 and Enpresso media (Figure 5.21). BL21-CodonPlus (DE3) strains have extra genes encoding rare tRNAs which aid protein expression. BL21-CodonPlus (DE3) is often employed when expressing protein in minimal medium as expression is often hampered in the low nutrient environment of minimal medium. Enpresso B Defined Nitrogen-free (Biosilta, Cambridgeshire, UK) medium was obtained as pre-prepared tablets that only require the addition of water, labelled nitrogen salt and ‘Reagent A’ before inoculation. Reagent A is likely an amylase enzyme that breaks down the unusable complex starch into a steady supply of glucose, which is attributed to the high yields associated with this product.

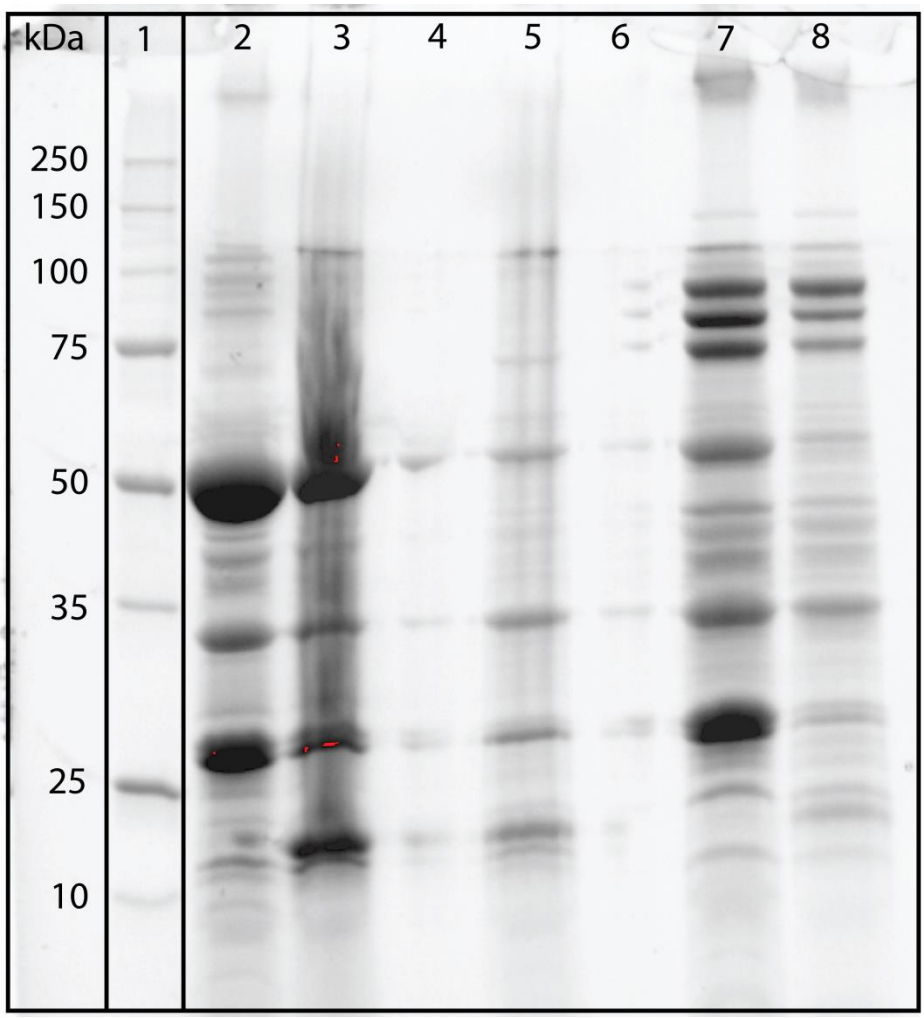

Figure 5.22 SDS-PAGE analysis of ^{15}N-labelled BM3 HD expression in different strains and growth media. Lane 1, BIO-RAD Precision Plus^{TM} Unstained Standards, 10-250 kDa). Lanes 2 and 3 show BL21-Gold (DE3) and BL21-CodonPlus (DE3) expression of the BM3 HD in Enpresso B medium, respectively. Lanes 7 and 8 show BL21-Gold (DE3) and BL21-CodonPlus (DE3) expression of BM3 HD in M9 medium, respectively. Lanes 4 and 6 are blank, while lane 5 is a replicate of lane 3 (BL21-CodonPlus (DE3)/BM3 HD transformants grown in Enpresso medium) at a lower concentration.

Expression of the BM3 HD in both *E. coli* strains is evidently better in EnPresso B Defined medium than in M9 medium (Figure 5.22). BL21-Gold (DE3) was chosen over BL21-CodonPlus (DE3) as the yield of the BM3 HD was greater. The cell pellet weights also differed considerably: 7.2 g/L in M9 medium for both BL21-Gold (DE3) and BL21-CodonPlus (DE3) transformants, but only 2 g/L in EnPresso medium for both BL21-Gold (DE3) and BL21-CodonPlus transformants. This may provide some insight into the success of EnPresso, where the controlled growth by steady glucose release allows for better protein expression and caps the cell density to avoid resource depletion. The colour of the EnPresso pellets were also a dark brown compared to much paler M9 cell pellets.

Once BL21-Gold (DE3) grown in Enpresso B medium was established as the best route to production of ^{15}N labelled protein, 2 L of BM3 HD transformant culture was grown in this medium, as described in the Methods (section 2.26.2). The purification of isotopically labelled proteins was done exactly the same as for unlabelled proteins. The untagged BM3 HD was purified as described in the Methods (section 2.7.5) with two rounds of ion exchange column chromatography before a final SEC column step to achieve pure BM3 HD. A 500 µl sample of 500 µM BM3 HD was prepared in 10% D_2O and transferred to a Shigemi tube for spectral collection as described in the Methods (section 2.26.3). A ^{15}N HSQC (TROSY) spectrum was acquired for the oxidised sample (Figure 5.23, top). As the fast relaxation time of paramagnetic ferric heme has been shown interfere with the resonances of backbone amides within 10 Å of the paramagnetic centre, the same BM3 HD sample was reduced to the ferrous state under anaerobic conditions [395]. A layer of mineral oil over the sample in a parafilm sealed Shigemi tube prepared in anaerobic conditions ensured the ferrous sample remained reduced over the time course required for the data collection. The ^{15}N spectrum of the reduced BM3 HD sample is shown in Figure 5.23 (lower panel).

Unfortunately, the chemical shifts of the backbone amides did not resolve well in the ferrous sample, which is common for larger proteins (>50 kDa). Some peaks are distinct, but the large majority are too closely spaced to be properly assigned. The ferric sample looks to be better resolved, possibly due to the occlusion of residues from detection between 10-20 Å away from the paramagnetic heme iron [389]. There are a few shifted peaks in the HSQC spectra of the ferric (top) sample compared to the ferrous (bottom) BM3 HD in Figure 5.23, which is indicative of oxidation-state induced structural changes. However, without their assignment nothing else can be deduced at this stage.

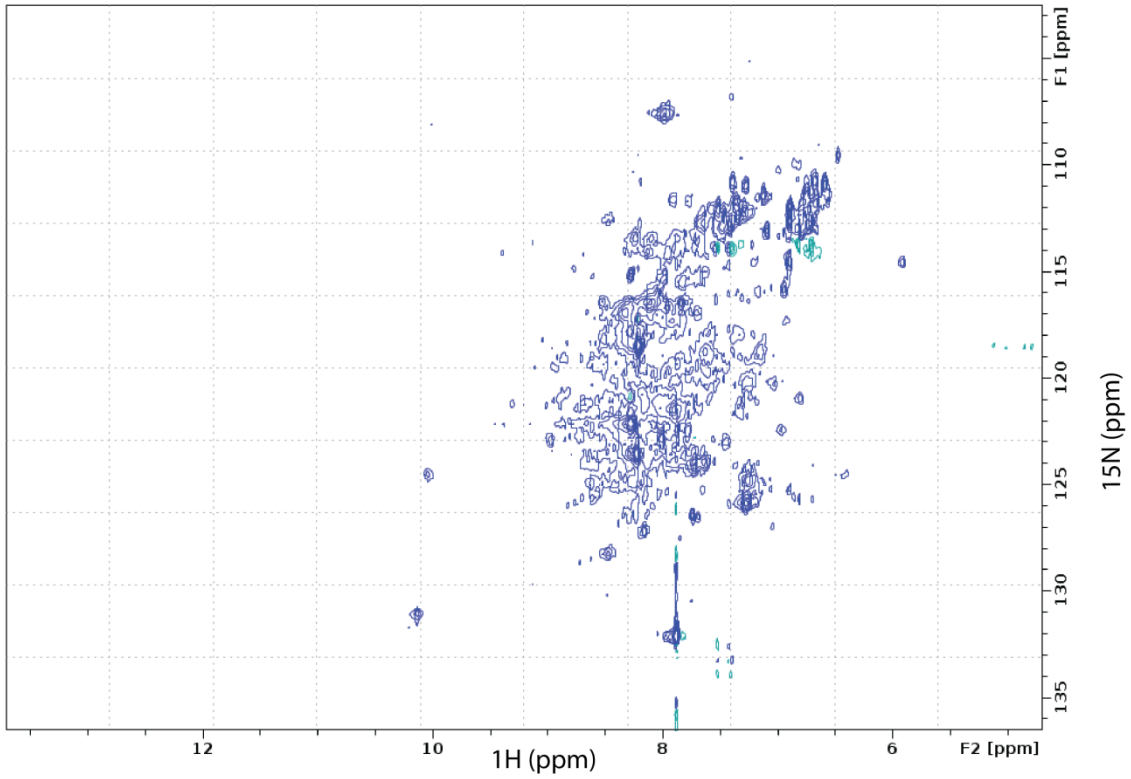
F1 [ppm]
110
115
120
125
130
135
15N (ppm)
12
10
8
6
F2 [ppm]
1H (ppm)

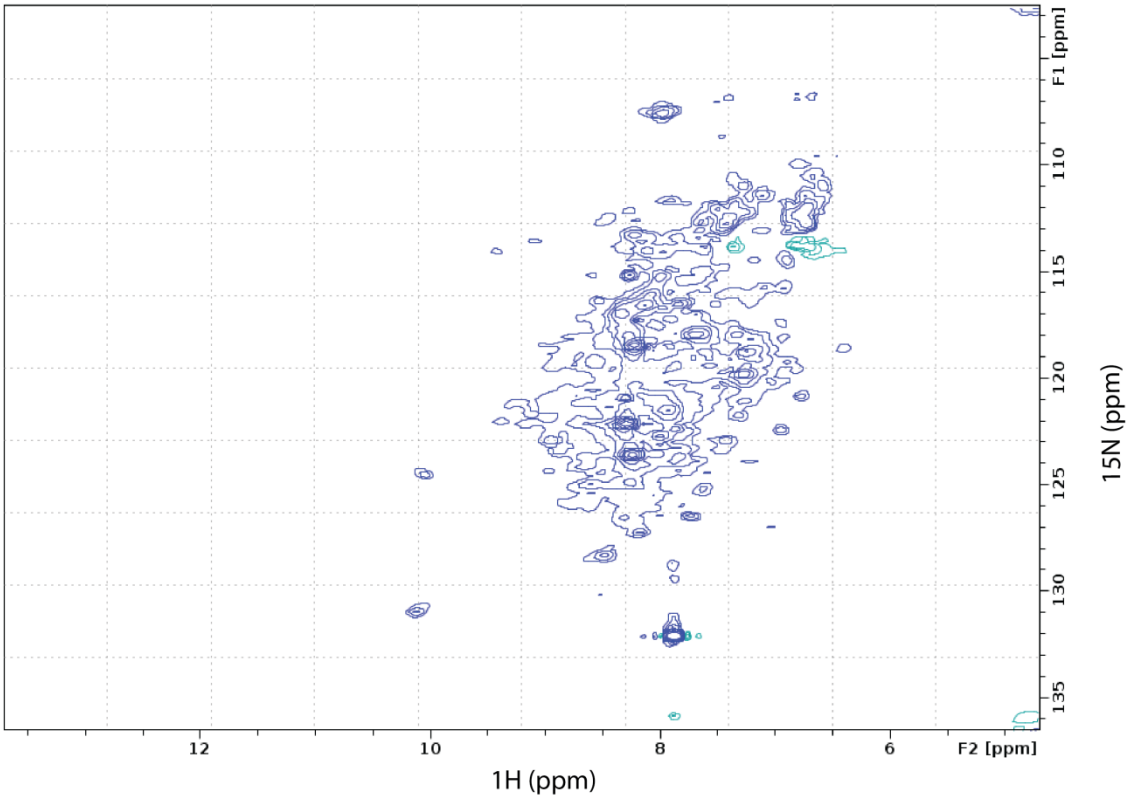
F1 [ppm]
110
115
120
125
130
135
15N (ppm)
12
10
8
6
F2 [ppm]
1H (ppm)

Figure 5.23 Comparison of the 2D ^{15}N-HSQC spectra of the ferric (oxidised) BM3 HD and the ferrous (reduced) BM3 HD. The y-axis show the ^{15}N chemical shift (ppm) and the x-axis the ^{1}H chemical shift (ppm). The amide (N-H) of each residue is visible as a spot on the spectrum as the HSQC experiments correlate the resonances of protons bonded to nitrogen by magnetisation transfer. The ferric BM3 HD sample data (top) are better resolved than those for the ferrous BM3 HD sample (bottom).

5.11 Discussion

Full length P450 BM3 was analysed by MALLS and these studies have shown that it is present as a highly monodisperse dimer of 249 kDa, in accordance with previous structural and functional work [237,240]. The isolated heme domain of BM3 (BM3 HD) is completely monomeric in solution, which identifies the reductase domain of BM3 as the likely source of Fanalysis of P450 MT1 in Section 3.4, where the full length enzyme was also shown to be completely dimeric and the isolated heme domain completely monomeric in solution.

The MALLS analysis of the WT BM3 FAD domain showed that ~25% of the enzyme was in a dimeric state in solution. It is therefore likely that other protein interactions present in the full length enzyme can also aid in its dimerisation. The dimerisation of the FAD domain is completely abolished in a surface cysteine mutant (C773A) of the BM3 FAD domain. The crystal structure of the BM3 FAD domain places C773 next to another surface cysteine (C810) positioned near the crystal contact interface between FAD domains [268]. These data are indicative of the potential for interactions between these residues, particular in the formation of disulfide bonds.

It has been reported that the stability of the naturally dimeric forms of nitric oxide synthase (NOS) enzymes is enhanced by a single zinc ion that coordinates four cysteine thiolate residues at the dimer interface [396]. While these cysteines are conserved throughout the NOS isoforms, dimerization in the iNOS crystal structure was also reported to occur through disulfide bonds across those same conserved cysteines in the absence of zinc [397]. The dimerization of NOSs is multifaceted, with an N-terminal “hook” domain known to help dimerization, as are reductase domain interactions in the eNOS and nNOS isoforms [377,398]. Given the convergent evolution of BM3 and NOSs, as described in Section 5.1, it would be interesting to examine the effect of zinc on the C773 and C810

surface cysteines in the FAD domain of BM3, in order to determine any resemblance in binding mode to the oxygenase domains of NOSs. Their proximity and the effect of the C773A mutation on dimerization are likely more than coincidental. Incubation of the WT FAD domain with dithiothreitol (DTT) does affect the oligomerisation state of the protein in solution (i.e. disrupts the dimer by reducing disulfide bonds), which would be consistent with the aforementioned theory. DTT would reduce cysteine residues in disulphide bonds to their thiol form, rendering them unable to form disulfide bonds or to coordinate Zn^{2+} ions. The DM FAD domain mutant carries the surface cysteine mutation C773A, and also a mutation to a "catalytic triad" cysteine residue (C999A). C999 is crucial for effective binding and orientating NADPH, and in the catalysis of hydride ion transfer from NADPH to the FAD cofactor. MALLS analysis showed that the DM FAD domain was an almost completely monodisperse monomer, similar to the SM (C773A) FAD domain, as expected. Thus, the C773 residue is implicated in the formation of inter-molecular (and possibly also intra-molecular) disulfide bonds that help to stabilise an FAD domain dimer. Very small amounts of higher molecular weight species, consistent with the formation of dimeric and tetrameric forms of the DM FAD domain, are also observed by MALLS analysis. These species remain unchanged upon DTT incubation of the protein and are likely a result of structural changes induced by the C999A mutation or resulting from the combined effects of the C773A/C999A mutations in promoting aggregation between molecules of the DM FAD domain.

The effects of the C773A and C999A mutations on the DM BM3 FAD domain flavin cofactor's electronic environment were also investigated. The incubation of the DM FAD domain with NADPH resulted in the extensive reduction of the FAD cofactor and substantial amounts of a neutral blue semiquinone form were observed, consistent with the properties of the WT BM3 reductase and FAD domains. The failure of NADPH to completely reduce the FAD cofactor to its 2-electron (hydroquinone) state results from the negative potential of the FAD semiquinone/hydroquinone couple [27]. Under aerobic conditions, the BM3 DM FAD domain gradually reoxidised through a process of enzymatic oxidation of remaining NADPH cofactor, and reduction of oxygen (to superoxide) by electron transfer from the FAD cofactor [27,228]. Steady-state kinetics were also employed to examine the effects of decreased hydride transfer rates (caused by the C999A mutation) on FAD domain-dependent ferricyanide reduction using NADPH. The DM FAD domain had severely reduced catalytic rates (Table 5.2), consistent with

those previously published, while the SM FAD domain had a high catalytic activity, comparable with that of the WT FAD domain, consistent with the C773A surface residue mutation not affecting NADPH binding or the ferricyanide substrate binding site [268].

Finally, a negative-stain EM structure was obtained for the P450 BM3 enzyme at a moderate resolution level of 20 Å. Further studies using cryo-EM could possibly achieve a higher resolution (e.g. to less than 10 Å), and even near-atomic resolution at 2.2 Å was shown to be possible for the protein β-galactosidase with current EM instrumentation and techniques [387]. Despite the resolution and sources of error associated with the negative stain approach (e.g. the appearance of the P450 BM3 protein being 'squashed' under the weight of the stain, or due to local dehydration), there is still much to be deduced from the structural data for the individual monomers and their domains, and their relative orientations and interactions in the homodimeric flavocytochrome P450 BM3 complex. The structural model obtained appears to show BM3 domain associations that are consistent with the functional model of inter-monomeric electron transfer from the flavodoxin module of the reductase domain of one of the monomers (FMN_1) to the P450 domain of the other ($heme_2$). The negative stain procedure globally affects the structure, although the looser dimeric association of the heme and FMN domains (compared to the FAD domain associations) observed remains a consequence of their weaker relative affinities relative to the FAD domains. It is likely that strong FAD domain associations are crucial in allowing the dimer to form, while the P450 and FMN domains are allowed a more conformational freedom for inter-monomeric electron transfer.

In summary, data presented in this chapter provide novel quantitative and structural data describing the properties of the intact P450 BM3 and its component domains. Important inroads were made into the analysis of the structure of the BM3 HD using NMR methods. Further work is needed using triple (^{2}H, ^{13}C, ^{15}N) labelled protein, along with application of 3-dimensional techniques (e.g. NOESY and TROESY methods) in order to obtain useful structural data for e.g. studies of the dynamic properties of the BM3 HD. Data obtained from EM studies of the intact P450 BM3 are very promising with respect to enabling the determination of a medium resolution structure of the flavocytochrome. These initial EM studies using the negative staining method pave the way to further research (e.g. using cryo-EM techniques) that could enable the first determination of the structure of the intact P450 BM3 enzyme.

Chapter 6: Conclusions and future work

6.1 Summary

The work detailed in this thesis describes the first detailed analysis of the flavocytochrome P450 BM3 (CYP102A1) enzyme homologue P450 MT1 (CYP505A30), a cytochrome P450-cytochrome P450 reductase (CPR) fusion enzyme from the fungus *Myceliophthora thermophila*, along with additional structural characterisation of P450 BM3 and its isolated domains. All the work on novel fusion enzyme P450 MT1 presented here is currently unpublished. Interest in the characterisation of P450 MT1 arose from its host organism (*M. thermophila*) being a moderately thermophilic fungus, and due to its relatively high sequence similarity to the model P450-CPR fusion enzyme P450 BM3 (BM3), with which it shares 36% amino acid sequence identity. In light of the recent confirmation that the WT BM3 is functional as a dimer, different structural approaches were undertaken in order to gain greater insights into its dimeric association, which is believed to underpin its extremely high monooxygenase activity.

6.2 Cytochrome P450 MT1 from *Myceliophthora thermophila*

A key objective of the project at its outset was the structural characterisation of the full length protein by X-ray crystallography. Its solved structure could have potentially provided much insight into BM3's dynamic structure. This approach (unpublished work) proved unsuccessful, likely for the same reasons that have prevented the successful crystallisation of the full length BM3 since its discovery in 1974. Thermostability studies with the full length P450 MT1 from *M. thermophila* proved that the enzyme had an incremental increase in stability over P450 BM3, but the increased stability was not as great as that observed for many of the fungus' various secreted enzymes [397]. While P450 MT1's stability did fall within the natural growth temperature range of its moderately thermophilic fungal host, its thermal stability was not high enough such that protein dynamics were sufficiently diminished to allow its crystallisation at 4 °C. In scope of the

EM results achieved with BM3 in Chapter 5, this technique should be adopted over Xray crystallography for structural determination of the dimeric 250 kDa MT1 complex.

After structural characterisation the second most pressing question is the elucidation of the function of MT1. The true substrates of P450 MT1 are likely to be branched chain fatty acids. The binding titrations reported in this thesis, together with kinetic data and product analysis from turnover reactions all point to branched chain fatty acids as being favoured substrates; since these molecules elicit the largest heme iron equilibrium shift towards high-spin, the fastest rates of lipid-dependent oxidation of NADPH, and the highest extent of regioselectivity observed with P450 MT1. This pattern of behaviour is also consistent with that observed for P450 BM3, albeit with higher catalytic rates seen in P450 BM3, and some differences in the patterns of regioselectivity of substrate hydroxylation between these enzymes. While branched chain fatty acids also appear likely to be BM3's favoured substrates, the physiological roles of both P450 BM3 and P450 MT1 are still uncertain. The analysis of *CYP505A30* mRNA expression levels in *Myceliophthora thermophila* in different growth conditions, combined with studies comparing the viability of both WT and *CYP505A30* gene deletion mutant strains of *M. thermophila* (again in a variety of different environmental conditions, and preferably with parallel studies of the microbial metabolome) could help elucidate the physiological function of P450 MT1 and also contribute towards more clearly defining the role of P450 BM3 in *Bacillus megaterium*.

Much work has already been done on P450 BM3 (and its bacterial homologues) to make the enzyme more attractive for industrial applications. Examples include the previously mentioned generation of CYP102A chimeras, where increased stability and diversification of substrate diversity were observed in various chimeras compared to the parent enzymes (CYP102A1 [BM3] and CYPs 102A2 and A3 from *Bacillus subtilis*) [241]. Similar approaches could be taken with P450 MT1, either by creating chimeras with other fungal enzymes (e.g. P450foxy) or with members of the CYP102A P450 subfamily (including P450 BM3). According to the choice of P450-CPR fusion enzymes used to make chimeras with P450 MT1, variants with increased thermostability and/or substantially diversified substrate selectivity and regioselectivity of lipid substrate oxidation may be obtained.

Thanks to the common P450 and CPR fold shared by P450 MT1 and P450 BM3, and to the number of P450s, CPR and CPR's constituent ferredoxin and ferredoxin reductase domains already crystallised and structurally determined; homology modelling did provide key

insights into the structural properties of the individual domains of P450 MT1. Some inferences could also be made from the amino acid sequence of P450 MT1, including identifying the lack of likely fatty acid carboxylate tail orienting residues (R47 and Y51 in BM3), which could account for some of the differences observed in P450 MT1 fatty acid binding compared to BM3. However, altered structural properties that might account for the differences observed in regioselectivity of hydroxylation of various different fatty acids were not clear. While the trend for oxidation of branched chain fatty acids follows that of BM3, P450 MT1 appears uniquely to show a high level of regioselectivity of substrate oxidation with unsaturated fatty acids. In these types of reactions, there lies potential of BM3 and P450 MT1 for synthetic biology application for industrial and pharmaceutical use. There are several benefits in using enzymes for industrial synthesis reactions: including their being less harmful environmentally, often showing faster and more specific catalysis, and the possibility of better yield and purity of products [398].

One route for future efforts on P450 MT1 characterisation should be an attempt at the crystallisation of its heme domain (MT1 HD). Preliminary work was already done in this thesis with the G463X variant of the MT1 HD. However, this proved unsuccessful (unpublished work). Bioinformatics revealed regions of instability at both the N- and C-termini of G463X. However, there were no predictions for transmembrane (TM) domains, consistent with the ability to express the MT1 HD (and P450 MT1) in a soluble form. Therefore, a future approach to MT1 HD crystallisation should involve the generation of various N-terminal and C-terminal truncations of the protein, and the removal of the N-terminal His-tag, which might contribute to a lower resolution of X-ray diffraction data from MT1 HD crystals due to its effect on crystal packing and/or disordered nature. Once these truncated constructs have been made, expressed and purified, stability screens such as the ones used in Chapter 3 (Section 3.6) could identify the most stable mutants in order to rationally select these forms for crystal trials. A heme domain structure would provide further insights into P450 MT1's substrate selectivity and its unusual regioselectivity properties regarding unsaturated fatty acids, compared to those of P450 BM3. This could pave the way for rational mutagenesis and *in silico* modelling, akin to what has been performed on BM3, in order to facilitate protein engineering to enable re-design of the substrate binding cavity and the "opening up" of its active site in order to allow P450 MT1 to accept and oxidise a more diverse pool of substrates with greater pharmaceutical/biotechnological value. P450 MT1 was found to bind tightly to the steroid

cholestenone (K_d = 265 nM), but with a relatively low conversion to high-spin heme iron at ~5% (Chapter 3.3.2, Table 3.3), although no high-spin shift was observed with testosterone (unpublished work). Thus, there is already evidence that P450 MT1 may have a spectrum of substrates that is rather different from those for P450 BM3. In P450 BM3, so-called 'gatekeeper' mutations (such as I401P, A82F and F87V) resulted in changes to the P450 structural organization and facilitated the binding of novel substrate types. A similar approach may facilitate a portfolio of human P450-like compounds (such as other steroids and diverse lipids, or human pharmaceuticals including gastric proton-pump inhibitors [PPIs] such as omeprazole) to be oxidised by similarly "conformationally destabilised" P450 MT1 mutants [88,280]. With P450 MT1's altered regioselectivity in hydroxylation of saturated fatty acids compared to the pattern seen in P450 BM3 it would clearly be interesting to observe the differences in the properties of these two enzymes and their mutated forms in the binding and oxidation of a range of its pharmaceutical compounds.

Steady-state and stopped-flow kinetic studies established P450 MT1's preference for NADPH over NADH, consistent with the properties displayed by P450 BM3. Studies have already been done to alter P450 BM3's pyridine nucleotide cofactor preference through the generation of W1046 mutants. A similar strategy could also be explored in P450 MT1 with a view to generating variants that can use the cheaper NADH cofactor more efficiently [399]. While P450 MT1 has an otherwise conserved amino acid sequence binding the *re-face* of the FAD molecule, it lacks the P450 BM3 Trp1046 residue, instead having a similarly hydrophobic phenylalanine in this position. For P450 BM3, replacement of W1046 with smaller, non-aromatic residues resulted in a substantial switch in cofactor specificity from NADPH towards NADH. NADH is much cheaper than NADPH, and a cofactor specificity switch towards NADH in P450 MT1 would have cost benefits and could lead to its application for industrial scale enzymatic reactions.

The stabilisation of a functional dimer of P450 MT1 would also be beneficial for its industrial application. This could be approached through directed evolution studies, although identification of a truly thermostable P450 BM3 homologue from a thermophilic bacterium or archaeon might provide a better route to an industrially useful catalyst. In many cases aimed at biotechnological applications of P450 enzymes, these enzymes have been fused to reductase modules, including the phthalate dioxygenase reductase (PDOR) domains from the monomeric CYP116B family P450-PDOR fusion enzymes, or in some cases the BM3 reductase [293,294]. The inter-monomer electron transfer process central to

BM3's function (and apparently the same as that seen for its non-P450 homologue nitric oxide synthase) could be explored in P450 MT1 in the same way as has been done already in P450 BM3 and NOS enzymes; i.e. through the reconstitution of activity by the mixing of inactive P450 MT1 mutants with defective (i) heme domains (e.g. heme iron distally coordinated by an engineered active site amino acid, such as histidine) and (ii) FMN domains (e.g. mutated to remove an aromatic residue shielding the isoalloxazine ring and resulting in FMN dissociation). The formation of an active heterodimer enabling electron transfer from the functional reductase domain of mutant (i) to the functional heme domain of monomer (ii) would confirm that P450 MT1 shares the inter-monomer electron transfer properties seen in P450 BM3 and NOS. If P450 MT1 was shown to be able to transfer electrons from one of its reductase domain to both the fused heme domain and the partner monomer heme domain, then this might be beneficial for practical applications of P450 MT1 and give it some advantages over P450 BM3.

The properties of the individual domains of P450 MT1 have been characterised in terms of their cofactor content. Studies of cofactors and their binding sites in their respective heme, FMN and FAD domains have been done using EPR (for their radical forms, where feasible), and HPLC analysis also confirmed that near-stoichiometric amounts of FAD and FMN were bound in the reductase domain. The generation of isolated P450 MT1 reductase, FAD and FMN domains might allow for a much clearer understanding of the properties of these domains, the environments of the flavin cofactors, and the overall electron transfer mechanism in P450 MT1. Single electron midpoint potentials (oxidised/semiquinone and semiquinone/hydroquinone) for both flavin cofactors could be determined in this way, and these data could would give further insights into the coupling of these redox potentials and how electron transfer is regulated in this enzyme. Potentiometric studies using both EPR and spectroelectrochemical methods on the individual FAD and FMN domains should also be done in order to unequivocally attribute the formation of blue and red semiquinones, respectively, to the FAD or FMN species.

Once initial expression and purification strategies for P450 MT1 had been worked out and made more efficient, further spectroscopic characterisation was carried out to ensure that the purified P450 MT1 enzyme was in fact a cytochrome P450. Its absorption spectra showed a peak at 420 nm in the resting, ferric state, and this Soret band feature was shifted to 450 nm upon reduction and the binding of CO to the ferrous heme iron. This spectral property confirms that P450 MT1 is a *bona fide* cytochrome P450 enzyme which retains

cysteine thiolate coordination in its reduced/CO-bound form. Similarly, its EPR spectrum had a characteristic rhombic trio of g-tensors typical of P450 enzymes. Although P450 MT1 was expressed from a pET15b vector that encoded an N-terminal His_6-tag on the enzyme, P450 MT1 failed to bind to nickel resins, likely as the His-tag was either buried within the heme domain of the protein, or possibly reflecting that both His-tags in a P450 MT1 dimer are buried in a domain interface of the dimeric protein. Future work should include trying to achieve a simpler and more efficient P450 MT1 purification process by nickel chromatography, possibly through the lengthening or shortening of the unstructured sequence of amino following the His_6-tag, or by swapping it for a C-terminal tag instead.

Resonance Raman spectroscopy is a useful technique for studying hemoproteins, but one which has not yet been used for the study of P450 MT1. Raman spectroscopy is a derivative technique of IR spectroscopy that measures the inelastic scattering of IR light, which can then be used to probe intramolecular motions through bond vibrations and rotations [400]. The resonance Raman technique uses laser excitation focused at a wavelength specific for the excitation of a particular molecular structure – and in the case of P450s this is typically done with laser excitation of heme in the Soret absorption range. The data collected can reveal useful information on e.g. changes in heme porphyrin ring conformation, heme-iron oxidation and spin state properties, the nature of axial ligands to the heme iron, and the relative conformations of peripheral substituents on the heme ring (e.g. vinyl and propionate groups). Resonance Raman spectroscopy of P450 MT1 could also be used to examine the heme-thiolate bond distance and strength, and how this is influenced by heme iron redox state and ligand binding. These studies should give further insights into heme binding, which would be important in view of the P450 MT1 heme incorporation issues identified in Chapter 3.

Table 6.1 Notable similarities and differences between MT1 and BM3.

Technique	Similarities	Differences
Binding (UV/Vis)	Tight binding (>20 μM) of saturated and branched chain fatty acids in range of C12-18.	MT1 bind to larger molecules like cholestenone and bifonazole.
MALLS	Both form dimeric complexes of >240 kDa.	MT1 has larger H_r.
HPLC	FAD and FMN stoichiometrically bound.	MT1 shows tighter FMN binding.
Thermostability studies		MT1 has a higher T_m.
EPR	Rhombic trio of *g*-values indicative of heme, red and blue forms of flavin semiquinone develop.	No notable differences.
Redox	Substrate modulation of heme potential.	MT1 displays more positive flavin and HS heme midpoint potentials.
Steady state	Each show substrate dependent NADPH- and NADH- oxidation and a preference of NADPH over NADH.	Slower NADPH- and NADH-oxidation of substrates by MT1.
Stopped-flow	NADPH- and NADH- dependant flavin and heme reduction.	Electron transfer rates lower in MT1.
GC-MS	Hydroxylation of fatty acids at positions ω-1, ω-2 and ω-3.	MT1 and BM3 show differences in regioselectivity.

6.3 Cytochrome P450 BM3 from *Bacillus megaterium*

The work featured in Chapter 5 was a foray into alternative structural techniques to crystallography that were available for use in structural analysis of P450 BM3. The electron microscopy (EM) work carried out on the full length P450 BM3 enzyme proved far more promising than NMR with respect to successful structure determination. The negative stain structure shows the first ever three-dimensional rending of full length BM3 in its functionally active form. The resolution is low, however it is high enough to visualise the position of each domain within the dimeric structure. Moreover, these data fit together logically with what we currently know about P450 BM3's domain structure and function. The next logical step is further work using cryo-EM techniques which should allow the

imaging of BM3 dimer at an even higher resolution, and these data would considerably further our knowledge of the structure-function relationships of this model P450-CPR fusion enzyme.

Once high resolution imagining of BM3 dimer is achieved through EM, much would be learned about its domain movement during catalysis through structural dynamic studies using NMR. The NMR work presented was ultimately unsuccessful and the assignment of the 2D HSQC spectra proved impossible, partly due to the size of the protein examined, but also in part due to the P450 paramagnetic heme iron. What has come from this work is an efficient protocol for the ^{15}N labelling of the P450 BM3 heme domain, which sets the groundwork for possible future triple labelling experiments. The determination of NMR structures of paramagnetic proteins and proteins larger than the BM3 HD has certainly been achieved, and so future work should consider alternative NMR experiments. Nuclear Overhauser Effect SpectroscopY (NOESY) measures the phenomenon of nuclear spin polarisation through space, and not bonds as in residual dipolar coupling experiments, e.g. HSQC, and is less prone to adverse effects from the paramagnetic centre during spectral collection. NOESY on paramagnetic proteins is not straightforward and requires a triple labelled sample. Its assignment would require a variety of spectra to be collected and would need their fine-tuned refinement. Any future protein solution-structure work done using NMR for the BM3 heme domain should probably involve this route [401].

Even though BM3's individual domain structures have been structurally elucidated, there are still important insights to be gained from the successful crystallisation and of BM3's CPR domain. The same mutations that led to the crystallisation of the FAD domain could also be used in this approach to prevent non-specific inter- and/or intra-domain disulfide/electrostatic bond formation between the FAD domains which might prevent crystal formation, as was found with the WT BM3 FAD domain. A BM3 CPR structure could establish the organization of the intra-monomer FAD/FMN domain interface which would complement a potential EM structure of the BM3 dimer and, potentially, if a similar dimeric interface to that seen in the FAD domain crystal structure exists between CPR domain monomers, the importance of C773 and C810 surface cysteine residues in domain interactions could also be revealed.

The C773A/C999A double mutant FAD domain was the last of the individual P450 BM3 domains to be crystallised for determination of the FAD domain structure. The work was

carried out to catalytically and structurally characterise the C773A and C773A/C999A mutants, and to enable the first description of the structure of the BM3 FAD/NADPH-binding domain of P450 BM3. This outcome was achieved by the mutation of peripheral cysteine residues on the FAD domain (to alanine(s)) in order to prevent the non-specific formation of intra- and inter-molecular disulphide bridges within and between FAD domains that compromise the crystallisation of the WT FAD domain. Studies to compare the properties of the mutants with those of the WT FAD domain were described in Chapter 5, and were done in part to provide additional data accompanying the publication of the crystal structure of the BM3 FAD domain. MALLS studies established the dimeric nature of WT FAD, and highlighted this property as being a potential driving force for the dimerization of full-length P450 BM3, especially in light of the monomeric nature of the BM3 HD in solution. The crystal structure compounded the pre-existing evidence for the role of the C773 surface cysteine in dimerization of the FAD domain, but also pointed towards another surface cysteine in close proximity, C810, as another possible contributor to intra- and inter-domain disulphide bond formation. It remains uncertain whether inter-/intra- molecular disulfide bonds or electrostatic interactions involving C773 and C810 are primarily responsible for the dimerization observed in the BM3 FAD domain, but these surface cysteine resides certainly play an important role from *in vitro* studies. Further work involving the C810A mutation could establish its involvement in FAD dimeric association more clearly. Zinc coordination by two cysteine residues on each oxygenase domain is responsible for heme domain dimerization in certain isoforms of NOS. The possibility of metal ion coordination by these cysteine residues in BM3's FAD domain might also be also explored, although as yet there is no evidence for any role of a metal ion in the formation of dimeric structures for the BM3 FAD domain or reductase domain (Chapter 5.1).

References:

[1] Lewis, C. A., and Wolfenden, R. (2008) Uroporphyrinogen decarboxylation as a benchmark for the catalytic proficiency of enzymes. *Proc. Natl. Acad. Sci. U. S. A.* **105**, 17328–17333.

[2] Schomburg, I., Chang, A., Placzek, S., Söhngen, C., Rother, M., Lang, M., Munaretto, C., Ulas, S., Stelzer, M., Grote, A., Scheer, M., and Schomburg, D. (2013) BRENDA in 2013: Integrated reactions, kinetic data, enzyme function data, improved disease classification: New options and contents in BRENDA. *Nucleic Acids Res.* **41**, 764–772.

[3] Enzyme Nomenclature: Recommendations of the Nomenclature Committee of the International Union of Biochemistry and Molecular Biology on the Nomenclature and Classification of Enzymes by the Reactions they Catalyse. *http://www.chem.qmul.ac.uk/iubmb/enzyme/index.htm*

[4] Xu, F. (2005) Applications of oxidoreductases: Recent progress. *Ind. Biotechnol.* **1**, 38–50.

[5] Solomon, E. I., Xie, X., and Dey, A. (2008) Mixed valent sites in biological electron transfer. *Chem. Soc. Rev.* **37**, 623–638.

[6] Butler, C. S., and Mason, J. R. (1997) Structure-function analysis of the bacterial aromatic ring-hydroxylating dioxygenases. *Adv. Microb. Physiol.* **38**, 47–84.

[7] Moser, C. C., Keske, J. M., Warncke, K., Farid, R. S., and Dutton, P. L. (1992) Nature of biological electron transfer. *Nature*. **355**, 796–802.

[8] Page, C. C., Moser, C. C., Chen, X., and Dutton, P. L. (1999) Natural engineering principles of electron tunnelling in biological oxidation-reduction. *Nature*. **402**, 47–52.

[9] Siddhanta, U., Presta, A., Fan, B., Wolan, D., Rousseau, D. L., and Stuehr, D. J. (1998) Domain swapping in inducible nitric-oxide synthase: Electron transfer occurs between flavin and heme groups located on adjacent subunits in the dimer. *J. Biol. Chem.* **273**, 18950–18958.

[10] Girvan, H. M., Dunford, A. J., Neeli, R., Ekanem, I. S., Waltham, T. N., Joyce, M. G., Leys, D., Curtis, R. a., Williams, P., Fisher, K., Voice, M. W., and Munro, A. W. (2011) Flavocytochrome P450 BM3 mutant W1046A is a NADH-dependent fatty acid hydroxylase: Implications for the mechanism of electron transfer in the P450 BM3 dimer. *Arch. Biochem. Biophys.* **507**, 75–85.

[11] Foote, C. S. (1968) Mechanisms of Photosensitized Oxidation. *Science (80-.).* **162**, 963–970.

[12] Hamza, I., and Dailey, H. A. (2012) One ring to rule them all: Trafficking of heme and heme synthesis intermediates in the metazoans. *Biochim. Biophys. Acta - Mol. Cell Res.* **1823**, 1617–1632.

[13] Palmer, D. J., Schroeder, S., Lawrence, A. D., Deery, E., Lobo, S. A., Saraiva, L. M., McLean, K. J., Munro, A. W., Ferguson, S. J., Pickersgill, R. W., Brown, D. G., and Warren, M. J. (2014) The structure, function and properties of sirohaem decarboxylase - an enzyme with structural homology to a transcription factor family that is part of the alternative haem biosynthesis pathway. *Mol. Microbiol.* **93**, 247–261.

[14] Dionysius, D. A., Grieve, P. A., and Vos, A. C. (1992) Studies on the lactoperoxidase system: reaction kinetics and antibacterial activity using two methods for hydrogen peroxide generation. *J. Appl. Bacteriol.* **72**, 146–153.

[15] Singh, A. K., Singh, N., Sharma, S., Singh, S. B., Kaur, P., Bhushan, A., Srinivasan, A., and Singh, T. P. (2008) Crystal Structure of Lactoperoxidase at 2.4Å Resolution. *J. Mol. Biol.* **376**, 1060–1075.

[16] Weidinger, I. M. (2015) Analysis of structure-function relationships in cytochrome *c* oxidase and its biomimetic analogs via resonance Raman and surface enhanced resonance Raman spectroscopies. *Biochim. Biophys. Acta*. **1847**, 119–25.

[17] Hendler, R. W., Sidhu, G. S., and Pardhasaradhi, K. (1990) High voltage redox properties of cytochrome *c* oxidase. *Biophys. J.* **58**, 957–967.

[18] Gao, Y. T., Smith, S. M. E., Weinberg, J. B., Montgomery, H. J., Newman, E., Guillemette, J. G., Ghosh, D. K., Roman, L. J., Martasek, P., and Salerno, J. C. (2004) Thermodynamics of Oxidation-Reduction Reactions in Mammalian Nitric-oxide Synthase Isoforms. *J. Biol. Chem.* **279**, 18759–18766.

[19] Faulkner, K. M., Bonaventura, C., and Crumbliss, A. L. (1995) A spectroelectrochemical method for differentiation of steric and electronic effects in hemoglobins and myoglobins. *J. Biol. Chem.* **270**, 13604–13612.

[20] Yeh, S. R., and Rousseau, D. L. (1998) Folding intermediates in cytochrome *c*. *Nat. Struct. Biol.* **5**, 222–228.

[21] Bowman, S. E. J., and Bren, K. L. (2008) The chemistry and biochemistry of heme *c*: functional bases for covalent attachment. *Nat. Prod. Rep.* **25**, 1118–1130.

[22] Lamb, D. C., Lei, L., Warrilow, A. G. S., Lepesheva, G. I., Mullins, J. G. L., Waterman, M. R., and Kelly, S. L. (2009) The first virally encoded cytochrome P450. *J. Virol.* **83**, 8266–8269.

[23] Nelson, D. R. (2009) The Cytochrome P450 Homepage. *Hum. Genomics*. **4**, 59–65.

[24] Yosca, T. H., Rittle, J., Krest, C. M., Onderko, E. L., Silakov, A., Calixto, J. C., Behan, R. K., and Green, M. T. (2013) Iron(IV)hydroxide pK(a) and the role of thiolate ligation in C-H bond activation by cytochrome P450. *Science*. **342**, 825–9.

[25] Guengerich, F. P., Tang, Z., Cheng, Q., and Salamanca-Pinzón, S. G. (2011) Approaches to deorphanization of human and microbial cytochrome P450 enzymes. *Biochim. Biophys. Acta - Proteins Proteomics*. **1814**, 139–145.

[26] Brodhun, F., Schneider, S., Göbel, C., Hornung, E., and Feussner, I. (2010) PpoC from *Aspergillus nidulans* is a fusion protein with only one active haem. *Biochem. J.* **425**, 553–565.

[27] Daff, S. N., Chapman, S. K., Turner, K. L., Holt, R. A., Govindaraj, S., Poulos, T. L., and Munro, A. W. (1997) Redox control of the catalytic cycle of flavocytochrome P-450 BM3. *Biochemistry*. **36**, 13816–13823.

[28] Klingenberg, M. (1958) Pigments of Rat Liver Microsomes. *Arch. Biochem. Biophys.* **75**, 376–386.

[29] Garfinkel, D. (1958) Studies on pig liver microsomes. I. Enzymatic and pigment composition of different microsomal fractions. *Arch. Biochem. Biophys.* **77**, 493–509.

[30] Hanson, L. K., Eaton, W. A., Sligar, S. G., Gunsalus, I. C., Gouterman, M., and Connell, C. R. (1976) Origin of the Anomalous Soret Spectra of Carboxy-Cytochrome P-450. *J. Am. Chem. Soc.* **98**, 2672–2674.

[31] Wang, J., Stuehr, D. J., Ikeda-Saito, M., and Rousseau, D. L. (1993) Heme Coordination and Structure of the Catalytic Site in Nitric Oxide Synthase. *Biol. Chem.* **268**, 22255–22258.

[32] Sono, M., Smith, K., Dawsonsli, J. H., and Hagerji, L. P. (1985) Preparation and Properties of Ferrous Chloroperoxidase Complexes with Dioxygen , Nitric Oxide, and an Alkyl Isocyanide; Spectroscopic Dissimilarities Between the Oxygenated Forms of Chloroperoxidase and Cytochrome P450. *J. Biol. Chem.* **260**, 15530–15535.

[33] Kim, I. C., and Deal, W. C. J. (1976) Isolation and properties of a new, soluble, hemoprotein

(H-450) from pig liver. *Biochemistry*. **15**, 4925–30.

[34] Sezutsu, H., Le Goff, G., and Feyereisen, R. (2013) Origins of P450 diversity. *Philos. Trans. R. Soc. Lond. B. Biol. Sci.* **368**, 20120428.

[35] Nelson, D. R., Kamataki, T., Waxman, D. J., Guengerich, F. P., and Estabrook, R.W. Feyereisen, R., Gonzalez, F.J., Coon, M.J., Gunsalus, I.C., Gotoh, O., Okuda, K., and Nebert, D. W. (1993) The P450 superfamily: update on new sequences, gene mapping, accession numbers, early trivial names of enzymes and nomenclature. *DNA Cell Biol.* **12**, 1–51.

[36] Nebert, D. W., and Feyereisen, R. (1994) Cytochrome P450. in *Cytochrome P450, Biochemistry, Biophysics and Molecular Biology* (Lechner, M. C. ed), pp. 3–13, Libbey Eurotext, London

[37] Lewis, D. F., and Sheridan, G. (2001) Cytochromes P450, oxygen, and evolution. *Sci. World J.* **1**, 151–167.

[38] Nelson, D. R., and Strobe, H. W. (1987) Evolution of Cytochrome P-450 Proteins. *Mol. Biol. Evol.* **4**, 572–593.

[39] Gonzalez, F. J., and Nebert, D. W. (1990) Evolution of the P450 gene superfamily: animal-plant "warfare", molecular drive and human genetic differences in drug oxidation. *Trends Genet.* **6**, 182–186.

[40] Nelson, D. R. (2013) Cytochrome P450 Homepage. *Hum. Gen.* **4**, 59–60.

[41] Nebert, D. W., Adesik, M., Coon, M. J., Estabrook, R. W., Gonzalez, F. J., Guegenrich, F. P., Gunsalus, I. C., Johnson, E. F., Kemper, B., and Levin, W. (1987) The P450 gene superfamily: recommended nomenclature. *DNA*. **6**, 1–11.

[42] Porter, T. D., and Coon, M. J. (1991) Minireview: Cytochrome P-450. *J. Biol. Chem.* **266**, 13469–13472.

[43] Gustafsson, M. C. U., Roitel, O., Marshall, K. R., Noble, M. A., Chapman, S. K., Pessegueiro, A., Fulco, A. J., Cheesman, M. R., Von Wachenfeldt, C., and Munro, A. W. (2004) Expression, Purification, and Characterization of *Bacillus subtilis* Cytochromes P450 CYP102A2 and CYP102A3: Flavocytochrome Homologues of P450 BM3 from *Bacillus megaterium*. *Biochemistry*. **43**, 5474–5487.

[44] Turpeinen, M., Hofmann, U., Klein, K., Murdter, T., Schwab, M., and Zanger, U. M. (2009) A Predominate Role of CYP1A2 for the Metabolism of Nabumetone to the Active Metabolite, 6-Methoxy-2-naphthylacetic Acid, in Human Liver Microsomes. *Drug Metab. Dispos.* **37**, 1017–1024.

[45] Lee, D. S., Yamada, A., Sugimoto, H., Matsunaga, I., Ogura, H., Ichihara, K., Adachi, S. ichi, Park, S. Y., and Shiro, Y. (2003) Substrate recognition and molecular mechanism of fatty acid hydroxylation by cytochrome P450 from *Bacillus subtilis*: Crystallographic, spectroscopic, and mutational studies. *J. Biol. Chem.* **278**, 9761–9767.

[46] Fujishiro, T., Shoji, O., Nagano, S., Sugimoto, H., Shiro, Y., and Watanabe, Y. (2011) Crystal Structure of H2O2-dependent Cytochrome P450SPα with Its Bound Fatty Acid Substrate: Insight into the regioselective hydroxylation of fatty acids at the alpha position. *J. Biol. Chem.* **286**, 29941–29950.

[47] Guengerich, F. P. (2001) Common and uncommon cytochrome P450 reactions related to metabolism and chemical toxicity. *Chem. Res. Toxicol.* **14**, 611–650.

[48] Miura, Y., and Fulco, A. J. (1974) (omega - 2) Hydroxylation of Fatty Acids by a Soluble System from *Bacillus megaterium*. *J. Biol. Chem.* **249**, 1880–1888.

[49] Okazaki, O., and Guengerich, F. P. (1993) Evidence for specific base catalysis in N-dealkylation reactions catalyzed by cytochrome P450 and chloroperoxidase: Differences in

rates of deprotonation of aminium radicals as an explanation for high kinetic hydrogen isotope effects observed with peroxid. *J. Biol. Chem.* **268**, 1546–1552.

[50] Yun, C. H., Shimada, T., and Guengerich, F. P. (1992) Contributions of human liver cytochrome P450 enzymes to the N-oxidation of 4,4'-methylene-bis(2-chloroaniline). *Carcinogenesis*. **13**, 217–222.

[51] Vaz, A. D., McGinnity, D. F., and Coon, M. J. (1998) Epoxidation of olefins by cytochrome P450: evidence from site-specific mutagenesis for hydroperoxo-iron as an electrophilic oxidant. *Proc. Natl. Acad. Sci. U. S. A.* **95**, 3555–3560.

[52] Helvig, C., Alayrac, C., Mioskowski, C., Koop, D., Poullain, D., Durst, F., and Salaün, J. P. (1997) Suicide inactivation of cytochrome P450 by midchain and terminal acetylenes: A mechanistic study of inactivation of a plant lauric acid ω- hydroxlyase. *J. Biol. Chem.* **272**, 414–421.

[53] Song, W. C., and Brash, A. R. (1991) Purification of an allene oxide synthase and identification of the enzyme as a cytochrome P-450. *Science*. **253**, 781–784.

[54] Podust, L. M., Poulos, T. L., and Waterman, M. R. (2001) Crystal structure of cytochrome P450 14alpha -sterol demethylase (CYP51) from *Mycobacterium tuberculosis* in complex with azole inhibitors. *Proc. Natl. Acad. Sci. U. S. A.* **98**, 3068–3073.

[55] Wójcikowski, J., and Daniel, W. A. Perazine at therapeutic drug concentrations inhibits human cytochrome P450 isoenzyme 1A2 (CYP1A2) and caffeine metabolism: an in vitro study. *Pharmacol. Rep.* **61**, 851–858.

[56] Yamada, H., Shiiyama, S., Soejima-Ohkuma, T., Honda, S., Kumagai, Y., Cho, A. K., Oguri, K., and Yoshimura, H. (1997) Deamination of amphetamines by cytochromes P450: studies on substrate specificity and regioselectivity with microsomes and purified CYP2C subfamily isozymes. *J. Toxicol. Sci.* **22**, 65–73.

[57] Shimada, T., and Fujii-Kuriyama, Y. (2004) Metabolic activation of polycyclic aromatic hydrocarbons to carcinogens by cytochromes P450 1A1 and 1B1. *Cancer Sci.* **95**, 1–6.

[58] Oritz de Montellano, P. R., and Correia, M. A. (1983) Suicidal destruction of cytochrome P-450 during oxidative drug metabolism. *Annu. Rev. Pharmacol. Toxicol.* **23**, 481–503.

[59] Munro, A. W., Girvan, H. M., and McLean, K. J. (2007) Variations on a (t)heme--novel mechanisms, redox partners and catalytic functions in the cytochrome P450 superfamily. *Nat. Prod. Rep.* **24**, 585–609.

[60] Waterman, M. R., and Lepesheva, G. I. (2005) Sterol 14 alpha-demethylase, an abundant and essential mixed-function oxidase. *Biochem. Biophys. Res. Commun.* **338**, 418–422.

[61] Yu, A.-M., Idle, J. R., Herraiz, T., Küpfer, A., and Gonzalez, F. J. (2003) Screening for endogenous substrates reveals that CYP2D6 is a 5-methoxyindolethylamine O-demethylase. *Pharmacogenetics*. **13**, 307–319.

[62] Guengerich, F. P. (2005) Human cytochrome P450 enzymes. in *Cytochrome P450: Structure, Mechanism and Biochemistry* (Ortiz De Montellano, P. R. ed), pp. 377–530, Kluwer Academic/Plenum Publishers, New York.

[63] Cryle, M. J., and De Voss, J. J. (2004) Carbon-carbon bond cleavage by cytochrome P450(BioI)(CYP107H1). *Chem. Commun. (Camb).* 10.1039/b311652b

[64] Kashiyama, E., Yokoi, T., Odomi, M., Funae, Y., Inoue, K., and Kamataki, T. (1997) Cytochrome P450 responsible for the stereoselective S-oxidation of flosequinan in hepatic microsomes from rats and humans. *Drug Metab. Dispos.* **25**, 716–724.

[65] Hakki, T., and Bernhardt, R. (2006) CYP17- and CYP11B-dependent steroid hydroxylases as drug development targets. *Pharmacol. Ther.* **111**, 27–52.

[66] Hanna, I. H., Roberts, E. S., and Hollenberg, P. F. (1998) Molecular basis for the differences in lidocaine binding and regioselectivity of oxidation by cytochromes P450 2B1 and 2B2. *Biochemistry*. **37**, 311–318.

[67] Narhi, L. O., and Fulco, A. J. (1986) Characterization of a catalytically self-sufficient 119,000-dalton cytochrome P-450 monooxygenase induced by barbiturates in *Bacillus megaterium*. *J. Biol. Chem.* **261**, 7160–7169.

[68] Okita, R. T., and Okita, J. R. (2001) Cytochrome P450 4A fatty acid omega hydroxylases. *Curr. Drug Metab.* **2**, 265–281.

[69] Nebert, D. W., Wikvall, K., and Miller, W. L. (2013) Human cytochromes P450 in health and disease. *Philos. Trans. R. Soc. Lond. B. Biol. Sci.* **368**, 20120431.

[70] Williams, P. A., Cosme, J., Sridhar, V., Johnson, E. F., and McRee, D. E. (2000) Mammalian microsomal cytochrome P450 monooxygenase: structural adaptations for membrane binding and functional diversity. *Mol. Cell*. **5**, 121–131.

[71] Wang, B., Yang, L.-P., Zhang, X.-Z., Huang, S.-Q., Bartlam, M., and Zhou, S.-F. (2009) New insights into the structural characteristics and functional relevance of the human cytochrome P450 2D6 enzyme. *Drug Metab. Rev.* **41**, 573–643.

[72] Wu, J.-J., Ge, G.-B., He, Y.-Q., Wang, P., Dai, Z.-R., Ning, J., Hu, L.-H., and Yang, L. (2015) Gomisin A is a Novel Isoform-Specific Probe for the Selective Sensing of Human Cytochrome P450 3A4 in Liver Microsomes and Living Cells. *AAPS J.* 10.1208/s12248-015-9827-4

[73] Betts, S., Björkhem-Bergman, L., Rane, A., and Ekström, L. (2015) Expression of CYP3A4 and CYP3A7 in Human Foetal Tissues and its Correlation with Nuclear Receptors. *Basic Clin. Pharmacol. Toxicol.* 10.1111/bcpt.12392

[74] Kakehashi, A., Hagiwara, A., Imai, N., Wei, M., Fukushima, S., and Wanibuchi, H. (2015) Induction of cell proliferation in the rat liver by the short-term administration of ethyl tertiary-butyl ether. *J. Toxicol. Pathol.* **28**, 27–32.

[75] Sun, X., Ai, M., Wang, Y., Shen, S., Gu, Y., Jin, Y., Zhou, Z., Long, Y., and Yu, Q. (2013) Selective induction of tumor cell apoptosis by a novel P450-mediated reactive oxygen species (ROS) inducer methyl 3-(4-nitrophenyl) propiolate. *J. Biol. Chem.* **288**, 8826–8837.

[76] Dey, A., and Nebert, D. W. (1998) Markedly increased constitutive CYP1A1 mRNA levels in the fertilized ovum of the mouse. *Biochem. Biophys. Res. Commun.* **251**, 657–661.

[77] Beckman, M. J., Tadikonda, P., Werner, E., Prahl, J., Yamada, S., and DeLuca, H. F. (1996) Human 25-hydroxyvitamin D3-24-hydroxylase, a multicatalytic enzyme. *Biochemistry*. **35**, 8465–8472.

[78] Yoshimoto, F. K., and Auchus, R. J. (2015) The diverse chemistry of cytochrome P450 17A1 (P450c17, CYP17A1). *J. Steroid Biochem. Mol. Biol.* **151**, 52–65.

[79] Nelson, D., and Werck-Reichhart, D. (2011) A P450-centric view of plant evolution. *Plant J.* **66**, 194–211.

[80] Chapple, C. (1998) Molecular-genetic analysis of plant cytochome P450-dependent monooxygenases. *Annu. Rev. Plant Physiol. Plant Mol. Biol.* **49**, 311–343.

[81] Werck-Reichhart, D., Hehn, A., and Didierjean, L. (2000) Cytochromes P450 for engineering herbicide tolerance. *Trends Plant Sci.* **5**, 116–123.

[82] Cabello-Hurtado, F., Taton, M., Forthoffer, N., Kahn, R., Søren, B., Rahier, A., and Werck-Reichhart, D. (1999) Optimized expression and catalytic properties of a wheat obtusifoliol 14α-demethylase (CYP51) expressed in yeast complementation of erg11Δ yeast mutants by plant CYP51. *Eur. J. Biochem.* **262**, 435–446.

[83] Van Bogaert, I. N. A., Groeneboer, S., Saerens, K., and Soetaert, W. (2011) The role of cytochrome P450 monooxygenases in microbial fatty acid metabolism. *FEBS J.* **278**, 206–221.

[84] Rylott, E. L., Jackson, R. G., Edwards, J., Womack, G. L., Seth-Smith, H. M. B., Rathbone, D. A., Strand, S. E., and Bruce, N. C. (2006) An explosive-degrading cytochrome P450 activity and its targeted application for the phytoremediation of RDX. *Nat. Biotechnol.* **24**, 216–219.

[85] Warman, A. J., Robinson, J. W., Luciakova, D., Lawrence, A. D., Marshall, K. R., Warren, M. J., Cheesman, M. R., Rigby, S. E. J., Munro, A. W., and McLean, K. J. (2012) Characterization of *Cupriavidus metallidurans* CYP116B1 - A thiocarbamate herbicide oxygenating P450-phthalate dioxygenase reductase fusion protein. *FEBS J.* **279**, 1675–1693.

[86] Omura, T., and Sato, R. (1962) A New Cytochrome in Liver Microsomes. *J. Biol. Chem.* **237**, 1375–1376.

[87] World Health Organisation (2014) WHO Model List of Essential Medicines. *http://apps.who.int/iris/bitstream/10665/93142/1/EML_18_eng.pdf*

[88] Andersen, J. F., Tatsuta, K., Gunji, H., Ishiyama, T., and Hutchinson, C. R. (1993) Substrate specificity of 6-deoxyerythronolide B hydroxylase, a bacterial cytochrome P450 of erythromycin A biosynthesis. *Biochemistry*. **32**, 1905–1913.

[89] Poulos, T. L., Finzel, B. C., Gunsalus, I. C., Wagner, G. C., and Kraut, J. (1985) The 2.6-Å crystal structure of *Pseudomonas putida* cytochrome P-450. *J. Biol. Chem.* **260**, 16122–16130.

[90] Gunsalus, I. C., Meeks, J. R., and Lipscomb, J. D. (1973) Cytochrome P-450cam substrate and effector interactions. *Ann. N. Y. Acad. Sci.* **212**, 107–121.

[91] Xu, F., Bell, S. G., Rao, Z., and Wong, L. L. (2007) Structure-activity correlations in pentachlorobenzene oxidation by engineered cytochrome P450cam. *Protein Eng. Des. Sel.* **20**, 473–480.

[92] Di Nardo, G., and Gilardi, G. (2012) Optimization of the bacterial cytochrome P450 BM3 system for the production of human drug metabolites. *Int. J. Mol. Sci.* **13**, 15901–15924.

[93] Butler, C. F., Peet, C., Mason, A. E., Voice, M. W., Leys, D., and Munro, A. W. (2013) Key mutations alter the cytochrome P450 BM3 conformational landscape and remove inherent substrate bias. *J. Biol. Chem.* **288**, 25387–25399.

[94] Warman, A. J., Roitel, O., Neeli, R., Girvan, H. M., Seward, H. E., Murray, S. A., McLean, K. J., Joyce, M. G., Toogood, H., Holt, R. A., Leys, D., Scrutton, N. S., and Munro, A. W. (2005) Flavocytochrome P450 BM3: an update on structure and mechanism of a biotechnologically important enzyme. *Biochem. Soc. Trans.* **33**, 747–753.

[95] Hirosue, S., Tazaki, M., Hiratsuka, N., Yanai, S., Kabumoto, H., Shinkyo, R., Arisawa, A., Sakaki, T., Tsunekawa, H., Johdo, O., Ichinose, H., and Wariishi, H. (2011) Insight into functional diversity of cytochrome P450 in the white-rot basidiomycete *Phanerochaete chrysosporium*: Involvement of versatile monooxygenase. *Biochem. Biophys. Res. Commun.* **407**, 118–123.

[96] Ichinose, H. (2012) Molecular and Functional Diversity of Fungal Cytochrome P450s. *Biol. Pharm. Bull.* **35**, 833–837.

[97] Amborabé, B.-E., Fleurat-Lessard, P., Chollet, J.-F., and Roblin, G. (2002) Antifungal effects of salicylic acid and other benzoic acid derivatives towards *Eutypa lata*: structure–activity relationship. *Plant Physiol. Biochem.* **40**, 1051–1060.

[98] Harwood, C. S., and Parales, R. E. (1996) The β-ketoadipate pathway and the biology of

self-identity. *Annu. Rev. Microbiol.* **50**, 553–590.

[99] Barriuso, J., Nguyen, D. T., Li, J. W. H., Roberts, J. N., MacNevin, G., Chaytor, J. L., Marcus, S. L., Vederas, J. C., and Ro, D. K. (2011) Double oxidation of the cyclic nonaketide dihydromonacolin L to monacolin J by a single cytochrome P450 monooxygenase, LovA. *J. Am. Chem. Soc.* **133**, 8078–8081.

[100] Petrič., Š., Hakki, T., Bernhardt, R., Žigon, D., and Črešnar, B. (2010) Discovery of a steroid 11α-hydroxylase from *Rhizopus oryzae* and its biotechnological application. *J. Biotechnol.* **150**, 428–437.

[101] Aoyama, Y., Yoshida, Y., and Sato, R. (1984) Yeast cytochrome P-450 catalyzing lanosterol 14 alpha-demethylation. II. Lanosterol metabolism by purified P-450(14)DM and by intact microsomes. *J. Biol. Chem.* **259**, 1661–1666.

[102] Črešnar, B., and Petrič, S. (2011) Cytochrome P450 enzymes in the fungal kingdom. *Biochim. Biophys. Acta - Proteins Proteomics*. **1814**, 29–35.

[103] Kelly, S. L., Arnoldi, A., and Kelly, D. E. (1993) Molecular genetic analysis of azole antifungal mode of action. *Biochem. Soc. Trans.* **21**, 1034–1038.

[104] Raoult, D., Audic, S., Robert, C., Abergel, C., Renesto, P., Ogata, H., La Scola, B., Suzan, M., and Claverie, J.-M. (2004) The 1.2-megabase genome sequence of *Mimivirus*. *Science*. **306**, 1344–1350.

[105] Viral Genomes listed on the NCBI *http://www.ncbi.nlm.nih.gov/genomes/GenomesGroup.cgi?taxid=10239*

[106] Moreira, D., and Brochier-Armanet, C. (2008) Giant viruses, giant chimeras: the multiple evolutionary histories of *Mimivirus* genes. *BMC Evol. Biol.* **8**, 12.

[107] Dus, K., Katagiri, M., Yu, C. A., Erbes, D. L., and Gunsalus, I. C. (1970) Chemical characterization of cytochrome P-450cam. *Biochem. Biophys. Res. Commun.* **40**, 1423–1430.

[108] Hedegaard, J., and Gunsalus, I. C. (1965) Mixed function oxidation. IV. An induced methylene hydroxylase in camphor oxidation. *J. Biol. Chem.* **240**, 4038–4043.

[109] Ravichandran, K. G., Boddupalli, S. S., Hasermann, C. A., Peterson, J. A., and Deisenhofer, J. (1993) Crystal structure of hemoprotein domain of P450BM-3, a prototype for microsomal P450's. *Science*. **261**, 731–736.

[110] Li, H., and Poulos, T. L. (1997) The structure of the cytochrome P450BM-3 haem domain complexed with the fatty acid substrate, palmitoleic acid. *Nat. Struct. Biol.* **2**, 140–6.

[111] Brenner, S., Hay, S., Girvan, H. M., Munro, A. W., and Scrutton, N. S. (2007) Conformational dynamics of the cytochrome P450 BM3/N-palmitoylglycine complex: The proposed "proximal-distal" transition probed by temperature-jump spectroscopy. *J. Phys. Chem. B*. **111**, 7879–7886.

[112] Hasemann, C. A., Kurumbail, R. G., Boddupalli, S. S., Peterson, J. A., and Deisenhofer, J. (1995) Structure and function of cytochromes P450: a comparative analysis of three crystal structures. *Structure*. **3**, 41–62.

[113] Graham, S. E., and Peterson, J. A. (1999) How similar are P450s and what can their differences teach us? *Arch. Biochem. Biophys.* **369**, 24–29.

[114] Groves, J. T., and Subramanian, D. V (1984) Hydroxylation by Cytochrome P-450 and Metalloporphyrin Models. Evidence for Allylic Rearrangement. *J. Am. Chem. Soc.* **106**, 2177–2181.

[115] Munro, A. W., Leys, D. G., McLean, K. J., Marshall, K. R., Ost, T. W. B., Daff, S., Miles, C. S.,

Chapman, S. K., Lysek, D. A., Moser, C. C., Page, C. C., and Dutton, P. L. (2002) P450 BM3: The very model of a modern flavocytochrome. *Trends Biochem. Sci.* **27**, 250–257.

[116] Ost, T. W. B., Clark, J., Mowat, C. G., Miles, C. S., Walkinshaw, M. D., Reid, G. A., Chapman, S. K., and Daff, S. (2003) Oxygen Activation and Electron Transfer in Flavocytochrome P450 BM3. *J. Am. Chem. Soc.* **125**, 15010–15020.

[117] Ortiz De Montellano, P. R. (2005) Chapter 4: Substrate Oxidation by Cytochrome P450 Enzymes. in *Cytochrome P450: Structure, Mechanism and Biochemistry*, 2nd Ed., pp. 115–148

[118] Sono, M., Stuehr, D. J., Ikeda-Saito, M., and Dawson, J. H. (1995) Identification of nitric oxide synthase as a thiolate-ligated heme protein using magnetic circular dichroism spectroscopy. Comparison with cytochrome P-450-CAM and chloroperoxidase. *J. Biol. Chem.* **270**, 19943–19948.

[119] Fann, Y., Gerber, N., Osmulski, P., Sligar, S. G., and Hoffman, B. M. (1994) ENDOR Determination of Heme Ligation in Chloroperoxidase and Comparison with Cytochrome P-450. *J. Am. Chem. Soc.* **116**, 5989–5990.

[120] Chang, Y.-T., and Loew, G. H. (1999) Molecular Dynamics Simulations of P450 BM3; Examination of Substrate-Induced Conformational Change. *J. Biomol. Struct. Dyn.* **16**, 1189–1203.

[121] Li, H., and Poulos, T. L. (1994) Structural variation in heme enzymes: a comparative analysis of peroxidase and P450 crystal structures. *Structure*. **2**, 461–464.

[122] Haines, D. C., Tomchick, D. R., Machius, M., and Peterson, J. A. (2001) Pivotal role of water in the mechanism of P450BM-3. *Biochemistry*. **40**, 13456–13465.

[123] Poulos, T. L., Finzel, B. C., and Howard, A. J. (1987) High-resolution crystal structure of cytochrome P450cam. *J. Mol. Biol.* **195**, 687–700.

[124] Ost, T. W. B., Miles, C. S., Munro, A. W., Murdoch, J., Reid, G. A., and Chapman, S. K. (2001) Phenylalanine 393 exerts thermodynamic control over the heme of flavocytochrome P450 BM3. *Biochemistry*. **40**, 13421–13429.

[125] Schlichting, I., Berendzen, J., Chu, K., Stock, A. M., Maves, S. A., Benson, D. E., Sweet, R. M., Ringe, D., Petsko, G. A., and Sligar, S. G. (2000) The catalytic pathway of cytochrome p450cam at atomic resolution. *Science*. **287**, 1615–1622.

[126] Tripathi, S., Li, H., and Poulos, T. L. (2013) Structural basis for effector control and redox partner recognition in cytochrome P450. *Science*. **340**, 1227–30.

[127] Graham-Lorence, S., Truant, G., Peterson, J. A., Falck, J. R., Wei, S., Helvig, C., and Capdevila, J. H. (1997) An active site substitution, F87V, converts cytochrome P450 BM-3 into a regio- and stereoselective (14S,15R)-arachidonic acid epoxygenase. *J. Biol. Chem.* **272**, 1127–1135.

[128] Shimura, Y. (1988) A quantitative scale of the spectrochemical series for the mixed ligand complexes of d6 metals. *Bull. Chem. Soc. Jpn.* **63**, 693–698.

[129] Guengerich, F. P. (1983) Oxidation-reduction properties of rat liver cytochromes P-450 and NADPH-cytochrome P-450 reductase related to catalysis in reconstituted systems. *Biochemistry*. **22**, 2811–2820.

[130] Tsai, R., Yu, C. A., Gunsalus, I. C., Peisach, J., Blumberg, W., Orme-Johnson, W. H., and Beinert, H. (1970) Spin-state changes in cytochrome P-450cam on binding of specific substrates. *Proc. Natl. Acad. Sci. U. S. A.* **66**, 1157–1163.

[131] Luthra, A., Denisov, I. G., and Sligar, S. G. (2011) Spectroscopic features of cytochrome P450 reaction intermediates. *Arch. Biochem. Biophys.* **507**, 26–35.

[132] Sharrock, M., Münck, E., Debrunner, P. G., Marshall, V., Lipscomb, J. D., and Gunsalus, I. C. (1973) Mössbauer studies of cytochrome P-450 cam. *Biochemistry*. **12**, 258–265.

[133] Lipscomb, J. D. (1980) Electron paramagnetic resonance detectable states of cytochrome P-450cam. *Biochemistry*. **19**, 3590–3599.

[134] Kumaki, K., Sato, M., Kon, H., and Nebert, D. W. (1978) Correlation of type I, type II, and reverse type I difference spectra with absolute changes in spin state of hepatic microsomal cytochrome P-450 iron from five mammalian species. *J. Biol. Chem.* **253**, 1048–1058.

[135] Denisov, I. G., Makris, T. M., Sligar, S. G., and Schlichting, I. (2005) Structure and chemistry of cytochrome P450. *Chem. Rev.* **105**, 2253–2277.

[136] Gibson, G. G., and Tamburini, P. P. (1984) Cytochrome P-450 spin state: inorganic biochemistry of haem iron ligation and functional significance. *Xenobiotica.* **14**, 27–47.

[137] Reed, C. A., and Cheung, S. K. (1977) On the bonding of FeO2 in hemoglobin and related dioxygen complexes. *Proc. Natl. Acad. Sci. U. S. A.* **74**, 1780–1784.

[138] Tovrog, B. S., Kitko, D. J., and Drago, R. S. (1976) Nature of the bound oxygen in a series of cobalt dioxygen adducts. *J. Am. Chem. Soc.* **98**, 5144–5153.

[139] Bertini, I., Gray, H. B., Lippard, S. J., and Valentine, J. S. (1994) Bioinorganic Chemistry. Chapter 4: Biological and Synthetic Dioxygen Carriers, pp. 167–253, University Science Books, Mill Valley, California.

[140] Meunier, B., and Bernadou, J. (2000) Active Iron-Oxo and Iron-Peroxo Species in Cytochromes P450 and Peroxidases; Oxo-Hydroxo Tautomerism with Water-Soluble Metalloporphyrins. in *Metal-Oxo and Metal-Peroxo Species in Catalytic Oxidations SE - 1* (Meunier, B. ed), pp. 1–35, Structure and Bonding, Springer Berlin Heidelberg, **97**, 1–35.

[141] Denisov, I. G., Mak, P. J., Makris, T. M., and Sligar, S. G. (2008) The peroxo intermediates in P450 catalysis: Characterisation of Compound 0 by resonance Raman spectroscopy. *J. Phys. Chem. A*. **112**, 13172–13179.

[142] Nagano, S., and Poulos, T. L. (2005) Crystallographic study on the dioxygen complex of wild-type and mutant cytochrome P450cam: Implications for the dioxygen activation mechanism. *J. Biol. Chem.* **280**, 31659–31663.

[143] Cryle, M. J., and De Voss, J. J. (2006) Is the ferric hydroperoxy species responsible for sulfur oxidation in cytochrome P450s? *Angew. Chemie - Int. Ed.* **45**, 8221–8223.

[144] Clark, J. P., Miles, C. S., Mowat, C. G., Walkinshaw, M. D., Reid, G. a., Daff, S. N., and Chapman, S. K. (2006) The role of Thr268 and Phe393 in cytochrome P450 BM3. *J. Inorg. Biochem.* **100**, 1075–1090.

[145] Yeom, H., and Sligar, S. G. (1997) Oxygen activation by cytochrome P450BM-3: effects of mutating an active site acidic residue. *Arch. Biochem. Biophys.* **337**, 209–216.

[146] Rittle, J., and Green, M. T. (2010) Cytochrome P450 compound I: capture, characterization, and C-H bond activation kinetics. *Science*. **330**, 933–937.

[147] Groves, J. T. (2006) High-valent iron in chemical and biological oxidations. *J. Inorg. Biochem.* **100**, 434–447.

[148] Groves, J. T., and McClusky, G. A. (1978) Aliphatic hydroxylation by highly purified liver microsomal cytochrome P-450. Evidence for a carbon radical intermediate. *Biochem. Biophys. Res. Commun.* **81**, 154–160.

[149] Hersleth, H. P., Ryde, U., Rydberg, P., Görbitz, C. H., and Andersson, K. K. (2006) Structures of the high-valent metal-ion haem-oxygen intermediates in peroxidases, oxygenases and catalases. *J. Inorg. Biochem.* **100**, 460–476.

[150] Groves, J. T. (1975) A Stereochemical Probe of the Fate of Carbon Radicals Oxidised by Metals. *Tetrahedron Lett.* **36**, 3113–3116.

[151] Ogliaro, F., Harris, N., Cohen, S., Filatov, M., De Visser, S. P., and Shaik, S. (2000) A model "rebound" mechanism of hydroxylation by cytochrome P450: Stepwise and effectively concerted pathways, and their reactivity patterns. *J. Am. Chem. Soc.* **122**, 8977–8989.

[152] Rutter, R., and Hager, L. P. (1982) The detection of two electron paramagnetic resonance radical signals associated with chloroperoxidase compound I. *J. Biol. Chem.* **257**, 7958–7961.

[153] Newcomb, M., Zhang, R., Chandrasena, R. E. P., Halgrimson, J. A., John, H., Makris, T. M., and Sligar, S. G. (2006) Cytochrome P450 Compound I. *J. Am. Chem. Soc.* **128**, 4580–4581.

[154] Yuan, X., Wang, Q., Horner, J. H., Sheng, X., and Newcomb, M. (2009) Kinetics and Activation Parameters for Oxidations of Styrene by Compounds I from Cytochrome P450BM3 (CYP102A1) Heme Domain and from CYP119. *J. Biochem.* **29**, 997–1003.

[155] Behan, R. K., Hoffart, L. M., Stone, K. L., Krebs, C., and Green, M. T. (2007) Reaction of cytochrome P450BM3 and peroxynitrite yields nitrosyl complex. *J. Am. Chem. Soc.* **129**, 5855–5859.

[156] Krest, C. M., Onderko, E. L., Yosca, T. H., Calixto, J. C., Karp, R. F., Livada, J., Rittle, J., and Green, M. T. (2013) Reactive intermediates in cytochrome P450 catalysis. *J. Biol. Chem.* **288**, 17074–17081.

[157] Berglund, G. I., Carlsson, G. H., Smith, A. T., Szöke, H., Henriksen, A., and Hajdu, J. (2002) The catalytic pathway of horseradish peroxidase at high resolution. *Nature*. **417**, 463–468.

[158] Gigon, P. L., Gram, T. E., and Gillette, J. R. (1969) Studies on the rate of reduction of hepatic microsomal cytochrome P-450 by reduced nicotinamide adenine dinucleotide phosphate: effect of drug substrates. *Mol. Pharmacol.* **5**, 109–122.

[159] Ullrich, V. (1969) On the hydroxylation of cyclohexane in rat liver microsomes. *Hoppe. Seylers. Z. Physiol. Chem.* **350**, 357–365.

[160] Eyer, C. S., and Backes, W. L. (1992) Relationship between the rate of reductase-cytochrome P450 complex formation and the rate of first electron transfer. *Arch. Biochem. Biophys.* **293**, 231–240.

[161] Sem, D. S., and Kasper, C. B. (1995) Effect of ionic strength on the kinetic mechanism and relative rate limitation of steps in the model NADPH-cytochrome P450 oxidoreductase reaction with cytochrome *c*. *Biochemistry*. **34**, 12768–12774.

[162] Nordblom, G. D., White, R. E., and Coon, M. J. (1976) Studies on hydroperoxide-dependent substrate hydroxylation by purified liver microsomal cytochrome P-450. *Arch. Biochem. Biophys.* **175**, 524–533.

[163] Rude, M. A., Baron, T. S., Brubaker, S., Alibhai, M., Del Cardayre, S. B., and Schirmer, A. (2011) Terminal olefin (1-alkene) biosynthesis by a novel P450 fatty acid decarboxylase from *Jeotgalicoccus species*. *Appl. Environ. Microbiol.* **77**, 1718–1727.

[164] Nakahara, K., Tanimoto, T., Hatano, K. I., Usuda, K., and Shoun, H. (1993) Cytochrome P-450 55A1 (P-450dNIR) acts as nitric oxide reductase employing NADH as the direct electron donor. *J. Biol. Chem.* **268**, 8350–8355.

[165] Oshima, R., Fushinobu, S., Su, F., Zhang, L., Takaya, N., and Shoun, H. (2004) Structural evidence for direct hydride transfer from NADH to cytochrome P450nor. *J. Mol. Biol.* **342**, 207–217.

[166] Kudo, T., Takaya, N., Park, S. Y., Shiro, Y., and Shoun, H. (2001) A Positively Charged Cluster Formed in the Heme-distal Pocket of Cytochrome P450nor Is Essential for Interaction with

NADH. *J. Biol. Chem.* **276**, 5020–5026.

[167] Barry, S. M., Kers, J. A., Johnson, E. G., Song, L., Aston, P. R., Patel, B., Krasnoff, S. B., Crane, B. R., Gibson, D. M., Loria, R., and Challis, G. L. (2012) Cytochrome P450–catalyzed L-tryptophan nitration in thaxtomin phytotoxin biosynthesis. *Nat. Chem. Biol.* **8**, 814–816.

[168] Sen, K., and Hackett, J. C. (2010) Peroxo-iron mediated deformylation in sterol 14α-demethylase catalysis. *J. Am. Chem. Soc.* **132**, 10293–10305.

[169] Castro, C. E., Wade, R. S., and Belser, N. O. (1985) Biodehalogenation: reactions of cytochrome P-450 with polyhalomethanes. *Biochemistry*. **24**, 204–210.

[170] Delaforge, M., Servent, D., Wirsta, P., Ducrocq, C., Mansuy, D., and Lenfant, M. (1993) Particular ability of cytochrome P-450 CYP3A to reduce glyceryl trinitrate in rat liver microsomes: Subsequent formation on nitric oxide. *Chem. Biol. Interact.* **86**, 103–117.

[171] Dijkman, W. P., de Gonzalo, G., Mattevi, A., and Fraaije, M. W. (2013) Flavoprotein oxidases: classification and applications. *Appl. Microbiol. Biotechnol.* **97**, 5177–5188.

[172] Orru, R., Dudek, H. M., Martinoli, C., Torres Pazmiño, D. E., Royant, A., Weik, M., Fraaije, M. W., and Mattevi, A. (2011) Snapshots of enzymatic Baeyer-Villiger catalysis: Oxygen activation and intermediate stabilization. *J. Biol. Chem.* **286**, 29284–29291.

[173] Wang, M., Roberts, D. L., Paschke, R., Shea, T. M., Masters, B. S., and Kim, J. J. (1997) Three-dimensional structure of NADPH-cytochrome P450 reductase: prototype for FMN- and FAD-containing enzymes. *Proc. Natl. Acad. Sci. U. S. A.* **94**, 8411–8416.

[174] Correll, C. C., Batie, C. J., Ballou, D. P., and Ludwig, M. L. (1992) Phthalate dioxygenase reductase: a modular structure for electron transfer from pyridine nucleotides to [2Fe-2S]. *Science*. **258**, 1604–1610.

[175] Achary, V. M. M., Reddy, C. S., Pandey, P., Islam, T., Kaul, T., and Reddy, M. K. (2015) Glutathione reductase a unique enzyme: molecular cloning, expression and biochemical characterization from the stress adapted C4 plant, *Pennisetum glaucum* (L.) R. Br. *Mol. Biol. Rep.* **42**, 947–62.

[176] Nojiri, M., Xie, Y., Inoue, T., Yamamoto, T., Matsumura, H., Kataoka, K., Deligeer, Yamaguchi, K., Kai, Y., and Suzuki, S. (2007) Structure and function of a hexameric copper-containing nitrite reductase. *Proc. Natl. Acad. Sci. U. S. A.* **104**, 4315–4320.

[177] Ostrowski, J., Barber, M. J., Rueger, D. C., Miller, B. E., Siegel, L. M., and Kredich, N. M. (1989) Characterization of the flavoprotein moieties of NADPH-sulfite reductase from *Salmonella typhimurium* and *Escherichia coli*. Physicochemical and catalytic properties, amino acid sequence deduced from DNA sequence of cysJ, and comparison with N. *J. Biol. Chem.* **264**, 15796–15808.

[178] Sridhar Prasad, G., Kresge, N., Muhlberg, A. B., Shaw, A., Jung, Y. S., Burgess, B. K., and Stout, C. D. (1998) The crystal structure of NADPH:ferredoxin reductase from *Azotobacter vinelandii*. *Protein Sci.* **7**, 2541–2549.

[179] Leadbeater, C., McIver, L., Campopiano, D. J., Webster, S. P., Baxter, R. L., Kelly, S. M., Price, N. C., Lysek, D. A., Noble, M. A., Chapman, S. K., and Munro, A. W. (2000) Probing the NADPH-binding site of *Escherichia coli* flavodoxin oxidoreductase. *Biochem. J.* **352**, 257–266.

[180] Karplus, P. A., Daniels, M. J., and Herriott, J. R. (1991) Atomic structure of ferredoxin-NADP+ reductase: prototype for a structurally novel flavoenzyme family. *Science*. **251**, 60–66.

[181] Marcus, R. A. (2012) Electron transfer theory and its inception. *Phys. Chem. Chem. Phys.* **14**, 13729–30.

[182] Fujii, K., and Huennekens, F. M. (1974) Activation of methionine synthetase by a reduced triphosphopyridine nucleotide dependent flavoprotein system. *J. Biol. Chem.* **249**, 6745–6753.

[183] Blaschkowski, H. P., Neuer, G., Ludwig-Festl, M., and Knappe, J. (1982) Routes of flavodoxin and ferredoxin reduction in *Escherichia coli*. CoA-acylating pyruvate: flavodoxin and NADPH: flavodoxin oxidoreductases participating in the activation of pyruvate formate-lyase. *Eur. J. Biochem.* **123**, 563–569.

[184] Bianchi, V., Reichard, P., Eliasson, R., Pontis, E., Krook, M., Jornvall, H., and Haggard-Ljungquist, E. (1993) *Escherichia coli* ferredoxin NADP+ reductase: Activation of E. coli anaerobic ribonucleotide reduction, cloning of the gene (fpr), and overexpression of the protein. *J. Bacteriol.* **175**, 1590–1595.

[185] Birch, O. M., Fuhrmann, M., and Shaw, N. M. (1995) Biotin synthase from *Escherichia coli*, an investigation of the low molecular weight and protein components required for activity in vitro. *J. Biol. Chem.* **270**, 19158–19165.

[186] Jenkins, C. M., and Waterman, M. R. (1998) NADPH-flavodoxin reductase and flavodoxin from *Escherichia coli*: Characteristics as a soluble microsomal P450 reductase. *Biochemistry*. **37**, 6106–6113.

[187] Sevrioukova, I. F., Poulos, T. L., and Churbanova, I. Y. (2010) Crystal Structure of the Putidaredoxin Reductase/Putidaredoxin Electron Transfer Complex. *J. Biol. Chem.* **285**, 13616–13620.

[188] Hiruma, Y., Hass, M. A. S., Kikui, Y., Liu, W. M., Ölmez, B., Skinner, S. P., Blok, A., Kloosterman, A., Koteishi, H., Löhr, F., Schwalbe, H., Nojiri, M., and Ubbink, M. (2013) The structure of the cytochrome P450cam-putidaredoxin complex determined by paramagnetic NMR spectroscopy and crystallography. *J. Mol. Biol.* **425**, 4353–4365.

[189] Porter, T. D., and Kasper, C. B. (1986) NADPH-cytochrome P-450 oxidoreductase: flavin mononucleotide and flavin adenine dinucleotide domains evolved from different flavoproteins. *Biochemistry*. **25**, 1682–1687.

[190] Oster, T., Boddupalli, S. S., and Peterson, J. A. (1991) Expression, purification, and properties of the flavoprotein domain of cytochrome P-450(BM-3): Evidence for the importance of the amino-terminal region for FMN binding. *J. Biol. Chem.* **266**, 22718–22725.

[191] Marletta, M. A. (1993) Nitric oxide synthase structure and mechanism. *J. Biol. Chem.* **268**, 12231–12234.

[192] Hawkes, D. B., Slessor, K. E., Bernhardt, P. V., and De Voss, J. J. (2010) Cloning, expression and purification of cindoxin, an unusual FMN-containing cytochrome P450 redox partner. *ChemBioChem*. **11**, 1107–1114.

[193] Lawson, R. J., Von Wachenfeldt, C., Haq, I., Perkins, J., and Munro, A. W. (2004) Expression and characterization of the two flavodoxin proteins of *Bacillus subtilis*, YkuN and YkuP: Biophysical properties and interactions with cytochrome P450 BioI. *Biochemistry*. **43**, 12390–12409.

[194] Cryle, M. J., and Schlichting, I. (2008) Structural insights from a P450 Carrier Protein complex reveal how specificity is achieved in the P450BioI ACP complex. *Proc. Natl. Acad. Sci.* **105**, 15696–15701.

[195] Hu, M. C., Hsu, H. J., Guo, I. C., and Chung, B. C. (2004) Function of Cyp11a1 in animal models. *Mol. Cell. Endocrinol.* **215**, 95–100.

[196] Hannemann, F., Bichet, A., Ewen, K. M., and Bernhardt, R. (2007) Cytochrome P450

systems—biological variations of electron transport chains. *Biochim. Biophys. Acta - Gen. Subj.* **1770**, 330–344.

[197] Capdevila, J. H., Wei, S., Helvig, C., Falck, J. R., Belosludtsev, Y., Truan, G., Graham-Lorence, S. E., and Peterson, J. A. (1996) The highly stereoselective oxidation of polyunsaturated fatty acids by cytochrome P450BM-3. *J. Biol. Chem.* **271**, 22663–22671.

[198] Munro, A. W., Daff, S., Coggins, J. R., Lindsay, J. G., and Chapman, S. K. (1996) Probing electron transfer in flavocytochrome P-450 BM3 and its component domains. *Eur. J. Biochem.* **239**, 403–409.

[199] Kent, U. M., Pascual, L., Roof, R. A., Ballou, D. P., and Hollenberg, P. F. (2004) Mechanistic studies with N-benzyl-1-aminobenzotriazole-inactivated CYP2B1: Differential effects on the metabolism of 7-ethoxy-4-(trifluoromethyl)coumarin, testosterone, and benzphetamine. *Arch. Biochem. Biophys.* **423**, 277–287.

[200] Kitazume, T., Takaya, N., Nakayama, N., and Shoun, H. (2000) *Fusarium oxysporum* fatty-acid subterminal hydroxylase (CYP505) is a membrane-bound eukaryotic counterpart of *Bacillus megaterium* cytochrome P450BM3. *J. Biol. Chem.* **275**, 39734–39740.

[201] Seo, J. A., Proctor, R. H., and Plattner, R. D. (2001) Characterization of four clustered and coregulated genes associated with fumonisin biosynthesis in *Fusarium verticillioides*. *Fungal Genet. Biol.* **34**, 155–165.

[202] De Mot, R., and Parret, A. H. A. (2002) A novel class of self-sufficient cytochrome P450 monooxygenases in prokaryotes. *Trends Microbiol.* **10**, 502–508.

[203] Gassner, G. T., Ludwig, M. L., Gatti, D. L., Correll, C. C., and Ballou, D. P. (1995) Structure and mechanism of the iron-sulfur flavoprotein phthalate dioxygenase reductase. *FASEB J.* **9**, 1411–1418.

[204] Nagy, I., Schoofs, G., Compernolle, F., Proost, P., Vanderleyden, J., and De Mot, R. (1995) Degradation of the thiocarbamate herbicide EPTC (S-ethyl dipropylcarbamothioate) and biosafening by *Rhodococcus sp.* Strain NI86/21 involve an inducible cytochrome P-450 system and aldehyde dehydrogenase. *J. Bacteriol.* **177**, 676–687.

[205] Munro, A. W., Girvan, H. M., and McLean, K. J. (2007) Cytochrome P450-redox partner fusion enzymes. *Biochim. Biophys. Acta - Gen. Subj.* **1770**, 345–359.

[206] Lamb, D. C., Jackson, C. J., Warrilow, A. G. S., Manning, N. J., Kelly, D. E., and Kelly, S. L. (2007) Lanosterol biosynthesis in the prokaryote *Methylococcus Capsulatus*: Insight into the evolution of sterol biosynthesis. *Mol. Biol. Evol.* **24**, 1714–1721.

[207] Seth-Smith, H. M. B., Rosser, S. J., Basran, A., Travis, E. R., Dabbs, E. R., Nicklin, S., and Bruce, N. C. (2002) Cloning, sequencing, and characterization of the hexahydro-1,3,5-trinitro-1,3,5-triazine degradation gene cluster from *Rhodococcus rhodochrous*. *Appl. Environ. Microbiol.* **68**, 4764–4771.

[208] Puchkaev, A. V., Wakagi, T., and Ortiz de Montellano, P. R. (2002) CYP119 Plus a *Sulfolobus t okodaii* Strain 7 Ferredoxin and 2-Oxoacid:Ferredoxin Oxidoreductase Constitute a High-Temperature Cytochrome P450 Catalytic System. *J. Am. Chem. Soc.* **124**, 12682–12683.

[209] Puchkaev, A. V., and Ortiz de Montellano, P. R. (2005) The *Sulfolobus solfataricus* electron donor partners of thermophilic CYP119: an unusual non-NAD(P)H-dependent cytochrome P450 system. *Arch. Biochem. Biophys.* **434**, 169–177.

[210] Luciakova, D. (2014) *Characterisation of Novel Cytochrome P450-fusion enzymes*. Ph.D. thesis, University of Manchester

[211] Reipa, V., Holden, M. J., and Vilker, V. L. (2007) Association and redox properties of the putidaredoxin reductase-nicotinamide adenine dinucleotide complex. *Biochemistry*. **46**,

13235–13244.

[212] Huang, H., Wang, S., Moll, J., and Thauer, R. K. (2012) Electron bifurcation involved in the energy metabolism of the acetogenic bacterium *Moorella thermoacetica* growing on glucose or H2 plus CO2. *J. Bacteriol.* **194**, 3689–3699.

[213] Lambeth, D. J., and Kamin, H. (1976) Adrenodoxin Reductase: Properties of the complexes of reduced enzyme with NADP+ and NADPH. *J. Biol. Chem.* **251**, 4299–4306.

[214] Batie, C. J., and Kamin, H. (1986) Association of ferredoxin-NADP+ reductase with NADP(H) specificity and oxidation-reduction properties. *J. Biol. Chem.* **261**, 11214–11223.

[215] Gunsalus, I. C., and Sligar, S. G. (1976) Redox regulation of cytochrome P450cam mixed function oxidation by putidaredoxin and camphor ligation. *Biochimie*. **58**, 143–147.

[216] Gutierrez, A., Doehr, O., Paine, M., Wolf, C. R., Scrutton, N. S., and Roberts, G. C. K. (2000) Trp-676 facilitates nicotinamide coenzyme exchange in the reductive half-reaction of human cytochrome P450 reductase: Properties of the soluble W676H and W676A mutant reductases. *Biochemistry*. **39**, 15990–15999.

[217] Döhr, O., Paine, M. J., Friedberg, T., Roberts, G. C., and Wolf, C. R. (2001) Engineering of a functional human NADH-dependent cytochrome P450 system. *Proc. Natl. Acad. Sci. U. S. A.* **98**, 81–86.

[218] Munro, A. W., Noble, M., Robledo, L., Daff, S. N., and Chapman, S. K. (2001) Determination of the redox properties of human NADPH-cytochrome P450 reductase. *Biochemistry*. **40**, 1956–1963.

[219] Modi, S., Sutcliffe, M. J., Primrose, W. U., Lian, L. Y., and Roberts, G. C. (1996) The catalytic mechanism of cytochrome P450 BM3 involves a 6 Å movement of the bound substrate on reduction. *Nat. Struct. Biol.* **3**, 414–417.

[220] Das, A., and Sligar, S. G. (2009) Modulation of the cytochrome P450 reductase redox potential by the phospholipid bilayer. *Biochemistry*. **48**, 12104–12112.

[221] Sevrioukova, I. F., and Peterson, J. A. (1995) NADPH-P-450 reductase: Structural and functional comparisons of the eukaryotic and prokaryotic isoforms. *Biochimie*. **77**, 562–572.

[222] Hanley, S. C., Ost, T. W. B., and Daff, S. (2004) The unusual redox properties of flavocytochrome P450 BM3 flavodoxin domain. *Biochem. Biophys. Res. Commun.* **325**, 1418–1423.

[223] Sevrioukova, I. F., Li, H., Zhang, H., Peterson, J. A., and Poulos, T. L. (1999) Structure of a cytochrome P450-redox partner electron-transfer complex. *Proc. Natl. Acad. Sci. U. S. A.* **96**, 1863–1868.

[224] Zhao, Q., Modi, S., Smith, G., Paine, M., McDonagh, P. D., Wolf, C. R., Tew, D., Lian, L. Y., Roberts, G. C., and Driessen, H. P. (1999) Crystal structure of the FMN-binding domain of human cytochrome P450 reductase at 1.93 Å resolution. *Protein Sci.* **8**, 298–306.

[225] Paine, M., Scrutton, N. S., Munro, A. W., Gutierrez, A., Roberts, G. C. K., and Wolf, C. R. (2005) Electron Transfer Partners of Cytochrome P450. in *Cytochrome P450 Structure, Mechanism, and Biochemistry* (Ortiz de Montellano, P. R. ed), pp. 115–138, Kluwer Academic/Plenum Publishers, New York.

[226] Murataliev, M. B., and Feyereisen, R. (2000) Interaction of NADP(H) with oxidized and reduced P450 reductase during catalysis. Studies with nucleotide analogues. *Biochemistry*. **39**, 5066–5074.

[227] Narhi, L. O., and Fulco, A. J. (1987) Identification and characterization of two functional domains in cytochrome P-450BM-3, a catalytically self-sufficient monooxygenase induced

by barbiturates in *Bacillus megaterium*. *J. Biol. Chem.* **262**, 6683–6690.

[228] Dunford, A. J., Girvan, H. M., Scrutton, N. S., and Munro, A. W. (2009) Probing the molecular determinants of coenzyme selectivity in the P450 BM3 FAD/NADPH domain. *Biochim. Biophys. Acta - Proteins Proteomics*. **1794**, 1181–1189.

[229] Gutierrez, A., Lian, L. Y., Wolf, C. R., Scrutton, N. S., and Roberts, G. C. K. (2001) Stopped-flow kinetic studies of flavin reduction in human cytochrome P450 reductase and its component domains. *Biochemistry*. **40**, 1964–1975.

[230] Xia, C., Hamdane, D., Shen, A. L., Choi, V., Kasper, C. B., Pearl, N. M., Zhang, H., Im, S. C., Waskell, L., and Kim, J. J. P. (2011) Conformational changes of NADPH-cytochrome P450 oxidoreductase are essential for catalysis and cofactor binding. *J. Biol. Chem.* **286**, 16246–16260.

[231] Bhattacharyya, A. K., Lipka, J. J., Waskell, L., and Tollin, G. (1991) Laser flash photolysis studies of the reduction kinetics of NADPH:cytochrome P-450 reductase. *Biochemistry*. **30**, 759–765.

[232] Gutierrez, A., Paine, M., Wolf, C. R., Scrutton, N. S., and Roberts, G. C. K. (2002) Relaxation Kinetics of Cytochrome P450 Reductase: Internal Electron Transfer Is Limited by Conformational Change and Regulated by Coenzyme Binding †. *Biochemistry*. **41**, 4626–4637.

[233] Brenner, S., Hay, S., Munro, A. W., and Scrutton, N. S. (2008) Inter-flavin electron transfer in cytochrome P450 reductase - Effects of solvent and pH identify hidden complexity in mechanism. *FEBS J.* **275**, 4540–4557.

[234] Hedison, T. M., Hay, S., and Scrutton, N. S. (2015) Real time analysis of conformational control in electron transfer reactions of human cytochrome P450 reductase with cytochrome *c*. *FEBS J.*

[235] Aigrain, L., Pompon, D., Moréra, S., and Truan, G. (2009) Structure of the open conformation of a functional chimeric NADPH cytochrome P450 reductase. *EMBO Rep.* **10**, 742–747.

[236] Simtchouk, S., Eng, J. L., Meints, C. E., Makins, C., and Wolthers, K. R. (2013) Kinetic analysis of cytochrome P450 reductase from *Artemisia annua* reveals accelerated rates of NADH-dependent flavin reduction. *FEBS J.* **280**, 6627–6642.

[237] Black, S. D., and Martin, S. T. (1994) Evidence for conformational dynamics and molecular aggregation in cytochrome P450 102 (BM-3). *Biochemistry*. **33**, 12056–12062.

[238] Stuehr, D. J. (1999) Mammalian nitric oxide synthases. *Biochim. Biophys. Acta - Bioenerg.* **1411**, 217–230.

[239] Stuehr, D. J., Santolini, J., Wang, Z. Q., Wei, C. C., and Adak, S. (2004) Update on mechanism and catalytic regulation in the NO synthases. *J. Biol. Chem.* **279**, 36167–36170.

[240] Neeli, R., Girvan, H. M., Lawrence, A., Warren, M. J., Leys, D., Scrutton, N. S., and Munro, A. W. (2005) The dimeric form of flavocytochrome P450 BM3 is catalytically functional as a fatty acid hydroxylase. *FEBS Lett.* **579**, 5582–5588.

[241] Gustafsson, M. C., Palmer, C. N., Wolf, R. C., and Von Wachenfeldt, C. (2001) Fatty-acid-displaced transcriptional repressor, a conserved regulator of cytochrome P450 102 transcription in *Bacillus* species. *Arch. Microbiol.* **176**, 459–464.

[242] Lentz, O., Urlacher, V., and Schmid, R. D. (2004) Substrate specificity of native and mutated cytochrome P450 (CYP102A3) from *Bacillus subtilis*. *J. Biotechnol.* **108**, 41–49.

[243] Eiben, S., Bartelmäs, H., and Urlacher, V. B. (2007) Construction of a thermostable cytochrome P450 chimera derived from self-sufficient mesophilic parents. *Appl. Microbiol.*

Biotechnol. **75**, 1055–1061.

[244] Nakayama, N., Takemae, A., and Shoun, H. (1996) Cytochrome P450foxy, a catalytically self-sufficient fatty acid hydroxylase of the fungus *Fusarium oxysporum*. *J. Biochem.* **119**, 435–440.

[245] Rambaut, A. http://tree.bio.ed.ac.uk/software/figtree/

[246] Bernhardt, R., and Urlacher, V. B. (2014) Cytochromes P450 as promising catalysts for biotechnological application: Chances and limitations. *Appl. Microbiol. Biotechnol.* **98**, 6185–6203.

[247] Urlacher, V. B., Lutz-Wahl, S., and Schmid, R. D. (2004) Microbial P450 enzymes in biotechnology. *Appl. Microbiol. Biotechnol.* **64**, 317–325.

[248] Whitehouse, C. J. C., Bell, S. G., and Wong, L.-L. (2012) P450BM3 (CYP102A1): connecting the dots. *Chem. Soc. Rev.* **41**, 1218.

[249] Lewis, J. C., Mantovani, S. M., Fu, Y., Snow, C. D., Komor, R. S., Wong, C. H., and Arnold, F. H. (2010) Combinatorial alanine substitution enables rapid optimization of cytochrome P450BM3 for selective hydroxylation of large substrates. *ChemBioChem*. **11**, 2502–2505.

[250] Kille, S., Zilly, F. E., Acevedo, J. P., and Reetz, M. T. (2011) Regio- and stereoselectivity of P450-catalysed hydroxylation of steroids controlled by laboratory evolution. *Nat. Chem.* **3**, 738–743.

[251] Peters, M. W., Meinhold, P., Glieder, A., and Arnold, F. H. (2003) Regio- and Enantioselective Alkane Hydroxylation with Engineered Cytochromes P450 BM-3. *J. Am. Chem. Soc.* **125**, 13442–13450.

[252] Meinhold, P., Peters, M. W., Chen, M. M. Y., Takahashi, K., and Arnold, F. H. (2005) Direct conversion of ethane to ethanol by engineered cytochrome P450 BM3. *ChemBioChem*. **6**, 1765–1768.

[253] Buriek, M., and Bernhardt, R. (2007) Steroid hydroxylation: Microbial steroid biotransformations using Cytochrome P450 enzymes. in *Modern Biooxidation*, pp. 155–176

[254] DeLoache, W. C., Russ, Z. N., Narcross, L., Gonzales, A. M., Martin, V. J. J., and Dueber, J. E. (2015) An enzyme-coupled biosensor enables (*S*)-reticuline production in yeast from glucose. *Nat. Chem. Biol.* **11**, 465–471.

[255] Fossati, E., Narcross, L., Ekins, A., Falgueyret, J.-P., and Martin, V. J. J. (2015) Synthesis of Morphinan Alkaloids in *Saccharomyces cerevisiae*. *PLoS One*. **10**, e0124459.

[256] Hagel, J. M., and Facchini, P. J. (2013) Benzylisoquinoline alkaloid metabolism: A century of discovery and a brave new world. *Plant Cell Physiol.* **54**, 647–672.

[257] Winzer, T., Kern, M., King, A. J., Larson, T. R., Teodor, R. I., Donninger, S. L., Li, Y., Dowle, A. A., Cartwright, J., Bates, R., Ashford, D., Thomas, J., Walker, C., Bowser, T. A., and Graham, I. A. (2015) Morphinan biosynthesis in opium poppy requires a P450-oxidoreductase fusion protein. *Plant Sci.* **349**, 309–312.

[258] Farrow, S. C., Hagel, J. M., Beaudoin, G. A. W., Burns, D. C., and Facchini, P. J. (2015) Stereochemical inversion of (S)-reticuline by a cytochrome P450 fusion in opium poppy. *Nat. Chem. Biol.* 10.1038/nchembio.1879

[259] WHO (2014) *World Malaria Report: http://apps.who.int/iris/bitstream/10665/160458/1/WHO_HTM_GMP_2015.2_eng.pdf?ua=1&ua=1*

[260] Ro, D.-K., Paradise, E. M., Ouellet, M., Fisher, K. J., Newman, K. L., Ndungu, J. M., Ho, K. a, Eachus, R. A., Ham, T. S., Kirby, J., Chang, M. C. Y., Withers, S. T., Shiba, Y., Sarpong, R., and

Keasling, J. D. (2006) Production of the antimalarial drug precursor artemisinic acid in engineered yeast. *Nature*. **440**, 940–943.

[261] Paddon, C. J., Westfall, P. J., Pitera, D. J., Benjamin, K., Fisher, K., McPhee, D., Leavell, M. D., Tai, a, Main, a, Eng, D., Polichuk, D. R., Teoh, K. H., Reed, D. W., Treynor, T., Lenihan, J., Fleck, M., Bajad, S., Dang, G., Dengrove, D., Diola, D., Dorin, G., Ellens, K. W., Fickes, S., Galazzo, J., Gaucher, S. P., Geistlinger, T., Henry, R., Hepp, M., Horning, T., Iqbal, T., Jiang, H., Kizer, L., Lieu, B., Melis, D., Moss, N., Regentin, R., Secrest, S., Tsuruta, H., Vazquez, R., Westblade, L. F., Xu, L., Yu, M., Zhang, Y., Zhao, L., Lievense, J., Covello, P. S., Keasling, J. D., Reiling, K. K., Renninger, N. S., and Newman, J. D. (2013) High-level semi-synthetic production of the potent antimalarial artemisinin. *Nature*. **496**, 528–32.

[262] Westfall, P. J., Pitera, D. J., Lenihan, J. R., Eng, D., Woolard, F. X., Regentin, R., Horning, T., Tsuruta, H., Melis, D. J., Owens, A., Fickes, S., Diola, D., Benjamin, K. R., Keasling, J. D., Leavell, M. D., McPhee, D. J., Renninger, N. S., Newman, J. D., and Paddon, C. J. (2012) Production of amorphadiene in yeast, and its conversion to dihydroartemisinic acid, precursor to the antimalarial agent artemisinin. *Proc. Natl. Acad. Sci.* **109**, E111–E118.

[263] Barrios-González, J., and Miranda, R. U. (2010) Biotechnological production and applications of statins. *Appl. Microbiol. Biotechnol.* **85**, 869–883.

[264] Matsuoka, T., Miyakoshi, S., Tanzawa, K., Nakahara, K., Hosobuchi, M., and Serizawa, N. (1989) Purification and characterization of cytochrome P-450sca from Streptomyces carbophilus. *Eur. J. Biochem.* **184**, 707–713.

[265] McLean, K. J., Hans, M., Meijrink, B., van Scheppingen, W. B., Vollebregt, A., Tee, K. L., van der Laan, J.-M., Leys, D., Munro, A. W., and van den Berg, M. A. (2015) Single-step fermentative production of the cholesterol-lowering drug pravastatin via reprogramming of *Penicillium chrysogenum*. *Proc. Natl. Acad. Sci.* **112**, 2847–2852.

[266] Belcher, J., McLean, K. J., Matthews, S., Woodward, L. S., Fisher, K., Rigby, S. E. J., Nelson, D. R., Potts, D., Baynham, M. T., Parker, D. A., Leys, D., and Munro, A. W. (2014) Structure and biochemical properties of the alkene producing cytochrome P450 OleTJE (CYP152l1) from the *Jeotgalicoccus* sp. 8456 bacterium. *J. Biol. Chem.* **289**, 6535–6550.

[267] Dennig, A., Kuhn, M., Tassoti, S., Thiessenhusen, A., Gilch, S., Bülter, T., Haas, T., Hall, M., and Faber, K. (2015) Oxidative Decarboxylation of Short-Chain Fatty Acids to 1-Alkenes. *Angew. Chemie Int. Ed.* **54**, 8819–8822.

[268] Joyce, M. G., Ekanem, I. S., Roitel, O., Dunford, A. J., Neeli, R., Girvan, H. M., Baker, G. J., Curtis, R. A., Munro, A. W., and Leys, D. (2012) The crystal structure of the FAD/NADPH-binding domain of flavocytochrome P450 BM3. *FEBS J.* **279**, 1694–1706.

[269] Maniatis, T., Fritsch, E. F., and Sambrook, J. (1982) *Molecular Cloning: A Laboratory Manual*, Cold Spring Harbor Laboratory, N.Y.

[270] Chapman, S. K., and Reid, G. A. (1999) *Methods in Molecular Biology: Flavoprotein Protocols*, Humana Press Inc.

[271] Noble, M. A., Miles, C. S., Chapman, S. K., Lysek, D. A., MacKay, A. C., Reid, G. A., Hanzlik, R. P., and Munro, A. W. (1999) Roles of key active-site residues in flavocytochrome P450 BM3. *Biochemistry*. **339**, 371–379.

[272] French, J. S., and Coon, M. J. (1979) Properties of NADPH-cytochrome P-450 reductase purified from rabbit liver microsomes. *Arch. Biochem. Biophys.* **195**, 565–577.

[273] Light, D. R., Walsh, C., and Marletta, M. A. (1980) Analytical and preparative high-performance liquid chromatography separation of flavin and flavin analog coenzymes. *Anal. Biochem.* **109**, 87–93.

[274] Hausinger, R. P., Honek, J. F., and Walsh, C. (1986) Separation of flavins and flavin analogs by high-performance liquid chromatography. *Methods Enzymol.* **122**, 199–209.

[275] Berry, E. A., and Trumpower, B. L. (1987) Simultaneous determination of hemes *a*, *b*, and *c* from pyridine hemochrome spectra. *Anal. Biochem.* **161**, 1–15.

[276] Collins, R. F., Ford, R. C., Kitmitto, A., Olsen, R. O., Tønjum, T., and Derrick, J. P. (2003) Three-dimensional structure of the *Neisseria meningitidis* secretin PilQ determined from negative-stain transmission electron microscopy. *J. Bacteriol.* **185**, 2611–2617.

[277] Scheres, S. H. W. (2012) RELION: Implementation of a Bayesian approach to cryo-EM structure determination. *J. Struct. Biol.* **180**, 519–530.

[278] Tang, G., Peng, L., Baldwin, P. R., Mann, D. S., Jiang, W., Rees, I., and Ludtke, S. J. (2007) EMAN2: An extensible image processing suite for electron microscopy. *J. Struct. Biol.* **157**, 38–46.

[279] Schulte-Herbrüggen, T., and Sorensen, O. W. (2000) Clean TROSY: compensation for relaxation-induced artifacts. *J. Magn. Reson.* **144**, 123–128.

[280] Boddupalli, S. S., Hasemann, C. A., Ravichandran, K. G., Lu, J. Y., Goldsmith, E. J., Deisenhofer, J., and Peterson, J. A. (1992) Crystallization and preliminary x-ray diffraction analysis of P450terp and the hemoprotein domain of P450BM-3, enzymes belonging to two distinct classes of the cytochrome P450 superfamily. *Proc. Natl. Acad. Sci. U. S. A.* **89**, 5567–5571.

[281] Girvan, H. M., Seward, H. E., Toogood, H. S., Cheesman, M. R., Leys, D., and Munro, A. W. (2007) Structural and spectroscopic characterization of P450 BM3 mutants with unprecedented P450 heme iron ligand sets: New heme ligation states influence conformational equilibria in P450 BM3. *J. Biol. Chem.* **282**, 564–572.

[282] Whitehouse, C. J. C., Yang, W., Yorke, J. A., Rowlatt, B. C., Strong, A. J. F., Blanford, C. F., Bell, S. G., Bartlam, M., Wong, L. L., and Rao, Z. (2010) Structural basis for the properties of two single-site proline mutants of CYP102A1 (P450BM3). *ChemBioChem*. **11**, 2549–2556.

[283] Park, S.-Y., Yamane, K., Adachi, S., Shiro, Y., Weiss, K. E., Maves, S. A., and Sligar, S. G. (2002) Thermophilic cytochrome P450 (CYP119) from *Sulfolobus solfataricus*: high resolution structure and functional properties. *J. Inorg. Biochem.* **91**, 491–501.

[284] Brewer, C. B., and Peterson, J. A. (1988) Single turnover kinetics of the reaction between oxycytochrome P-450(cam) and reduced putidaredoxin. *J. Biol. Chem.* **263**, 791–798.

[285] Sibbesen, O., De Voss, J. J., and Ortiz de Montellano, P. R. (1996) Putidaredoxin reductase-putidaredoxin-cytochrome P450(cam) triple fusion protein. Construction of a self-sufficient *Escherichia coli* catalytic system. *J. Biol. Chem.* **271**, 22462–22469.

[286] Boddupalli, S. S., Oster, T., Estabrook, R. W., and Peterson, J. A. (1992) Reconstitution of the fatty acid hydroxylation function of cytochrome P-450BM-3 utilizing its individual recombinant hemo- and flavoprotein domains. *J. Biol. Chem.* **267**, 10375–10380.

[287] Munro, A. W., Lindsay, J. G., Coggins, J. R., Kelly, S. M., and Price, N. C. (1996) Analysis of the structural stability of the multidomain enzyme flavocytochrome P-450 BM3. *Biochim Biophys Acta.* **1296**, 127–37.

[288] Rentmeister, A., Brown, T. R., Snow, C. D., Carbone, M. N., and Arnold, F. H. (2011) Engineered Bacterial Mimics of Human Drug Metabolizing Enzyme CYP2C9. *ChemCatChem*. **3**, 1065–1071.

[289] Misawa, N., Nodate, M., Otomatsu, T., Shimizu, K., Kaido, C., Kikuta, M., Ideno, A., Ikenaga, H., Ogawa, J., Shimizu, S., and Shindo, K. (2011) Bioconversion of substituted naphthalenes and β-eudesmol with the cytochrome P450 BM3 variant F87V. *Appl. Microbiol. Biotechnol.*

90, 147–157.

[290] Otey, C. R., Landwehr, M., Endelman, J. B., Hiraga, K., Bloom, J. D., and Arnold, F. H. (2006) Structure-guided recombination creates an artificial family of cytochromes P450. *PLoS Biol.* **4**, 789–798.

[291] Li, Y., Drummond, D. A., Sawayama, A. M., Snow, C. D., Bloom, J. D., and Arnold, F. H. (2007) A diverse family of thermostable cytochrome P450s created by recombination of stabilizing fragments. *Nat. Biotechnol.* **25**, 1051–1056.

[292] Landwehr, M., Carbone, M. N., Otey, C. R., Li, Y., and Arnold, F. H. (2007) Diversification of catalytic function in a synthetic family of chimeric cytochrome P450s. *Chem. Biol.* **14**, 269–278.

[293] Jamakhandi, A. P., Jeffus, B. C., Dass, V. R., and Miller, G. P. (2005) Thermal inactivation of the reductase domain of cytochrome P450 BM3. *Arch. Biochem. Biophys.* **439**, 165–174.

[294] Eiben, S., Kaysser, L., Maurer, S., Kühnel, K., Urlacher, V. B., and Schmid, R. D. (2006) Preparative use of isolated CYP102 monooxygenases-A critical appraisal. *J. Biotechnol.* **124**, 662–669.

[295] Schückel, J., Rylott, E. L., Grogan, G., and Bruce, N. C. (2012) A Gene-Fusion Approach to Enabling Plant Cytochromes P450 for Biocatalysis. *ChemBioChem*. **13**, 2758–2763.

[296] Guengerich, F. P., and Munro, A. W. (2013) Unusual cytochrome P450 enzymes and reactions. *J. Biol. Chem.* **288**, 17065–17073.

[297] Geer, L. Y., Domrachev, M., Lipman, D. J., and Bryant, S. H. (2002) CDART : Protein Homology by Domain Architecture CDART : Protein Homology by Domain Architecture. 10.1101/gr.278202

[298] Kasim, M., Chen, H. C., and Swenson, R. P. (2009) Functional Characterisation of the re-Face Loop Spanning Residues 536 to 541 and its Interactions with the Cofactor in the Flavin Mononucleotide-Binding Domain of the Flavocytochrome P450 from *Bacillus megaterium*. *Biochemistry*. **48**, 5131–5141.

[299] Murray, T. A., and Swenson, R. P. (2003) Mechanism of Flavin Mononucleotide Cofactor Binding to the Desulfovibrio vulgaris Flavodoxin. 1. Kinetic Evidence for Cooperative Effects Associated with the Binding of Inorganic Phosphate and the 5‘-Phosphate Moiety of the Cofactor. *Biochemistry*. **42**, 2307–2316.

[300] Maheshwari, R., Bharadwaj, G., and Bhat, M. K. (2000) Thermophilic fungi: their physiology and enzymes. *Microbiol. Mol. Biol. Rev.* **64**, 461–488.

[301] Roitel, O., Scrutton, N. S., and Munro, A. W. (2003) Electron transfer in flavocytochrome P450 BM3: Kinetics of flavin reduction and oxidation, the role of cysteine 999, and relationships with mammalian cytochrome P450 reductase. *Biochemistry*. **42**, 10809–10821.

[302] Simon, M., and Hancock, J. M. (2009) Tandem and cryptic amino acid repeats accumulate in disordered regions of proteins. *Genome Biol.* **10**, R59.

[303] Dunker, A. K., Silman, I., Uversky, V. N., and Sussman, J. L. (2008) Function and structure of inherently disordered proteins. *Curr. Opin. Struct. Biol.* **18**, 756–764.

[304] Dunker, A. K., and Uversky, V. N. (2010) Drugs for “protein clouds”: Targeting intrinsically disordered transcription factors. *Curr. Opin. Pharmacol.* **10**, 782–788.

[305] Kelley, L. A., Mezulis, S., Yates, C. M., Wass, M. N., and Sternberg, M. J. E. (2015) The Phyre2 web portal for protein modeling , prediction and analysis. *Nat. Protoc.* **10**, 845–858.

[306] Kanehisa, M., Goto, S., Sato, Y., Kawashima, M., Furumichi, M., and Tanabe, M. (2014)

Data, information, knowledge and principle: back to metabolism in KEGG. *Nucleic Acids Res.* **42**, D199–D205.

[307] Medema, M. H., Blin, K., Cimermancic, P., De Jager, V., Zakrzewski, P., Fischbach, M. A., Weber, T., Takano, E., and Breitling, R. (2011) AntiSMASH: Rapid identification, annotation and analysis of secondary metabolite biosynthesis gene clusters in bacterial and fungal genome sequences. *Nucleic Acids Res.* **39**, 339–346.

[308] Wawrik, B., Kerkhof, L., Zylstra, G. J., Jerome, J., and Kukor, J. J. (2005) Identification of Unique Type II Polyketide Synthase Genes in Soil. *Appl. Environ. Microbiol.* **71**, 2232–2238.

[309] Cortes, J., Haydock, S. F., Roberts, G. A., Bevitt, D. J., and Leadlay, P. F. (1990) An unusually large multifunctional polypeptide in the erythromycin-producing polyketide synthase of *Saccaropolyspora erythraea*. *Nature*. **348**, 176–178.

[310] Donadio, S., Staver, Micheal, J., McAlpine, James, B., Swanson, Susan, J., and Katz, L. (1991) Modular Organization of Genes Required for Complex Polyketide Biosynthesis. *Science (80-.).* **252**, 675–679.

[311] Jenke-Kodama, H., Sandmann, A., Müller, R., and Dittmann, E. (2005) Evolutionary implications of bacterial polyketide synthases. *Mol. Biol. Evol.* **22**, 2027–2039.

[312] Khosla, C., Gokhale, R. S., Jacobsen, J. R., and Cane, D. E. (1999) Tolerance and Specificity of Polyketide Synthases. *Annu. Rev. Biochem.* **68**, 219–253.

[313] Gasteiger, E., Hoogland, C., Gattiker, A., Duvaud, S., Wilkins, M. R., Appel, R. D., and Bairoch, A. (2005) Protein Identification and Analysis Tools on the ExPASy Server. in *The Proteomics Protocols Handbook, Humana Press*, pp. 571–607

[314] Sligar, S. G. (1976) Coupling of spin, substrate, and redox equilibria in cytochrome P450. *Biochemistry*. **15**, 5399–406.

[315] Morrison, J. F. (1969) Kinetics of the reversible inhibition of enzyme-catalysed reactions by tight-binding inhibitors. *Biochim. Biophys. Acta*. **185**, 269–286.

[316] Boddupalli, S. S., Estabrook, R. W., and Peterson, J. A. (1990) Fatty acid monooxygenation by cytochrome P-450BM-3. *J. Biol. Chem.* **265**, 4233–4239.

[317] Budde, M., Morr, M., Schmid, R. D., and Urlacher, V. B. (2006) Selective hydroxylation of highly branched fatty acids and their derivatives by CYP102A1 from *Bacillus megaterium*. *ChemBioChem*. **7**, 789–794.

[318] Sevrioukova, I., Truan, G., and Peterson, J. A. (1997) Reconstitution of the fatty acid hydroxylase activity of cytochrome P450BM-3 utilizing its functional domains. *Arch. Biochem. Biophys.* **340**, 231–238.

[319] Li, H., and Poulos, T. L. (1999) Fatty acid metabolism, conformational change, and electron transfer in cytochrome P-450(BM-3). *Biochim. Biophys. Acta*. **1441**, 141–149.

[320] Murataliev, M. B., and Feyereisen, R. (1996) Functional interactions in cytochrome P450BM3. Fatty acid substrate binding alters electron-transfer properties of the flavoprotein domain. *Biochemistry*. **35**, 15029–15037.

[321] Harris, D. L., Chang, Y. T., and Loew, G. H. (1995) Molecular dynamics simulations of phenylimidazole inhibitor complexes of cytochrome P450cam. *Mol. Eng.* **5**, 143–156.

[322] Dawson, J. H., Andersson, L. A., and Sono, M. (1981) Spectroscopic Investigations of Ferric Cytochrome P-450-CAM Ligand Complexes. *J. Biol. Chem.* **257**, 3606–3617.

[323] Poulos, T. L., and Howard, A. J. (1987) Crystal structures of metyrapone- and phenylimidazole-inhibited complexes of cytochrome P-450cam. *Biochemistry*. **26**, 8165–8174.

[324] Ouellet, H., Johnston, J. B., and Montellano, P. R. O. De (2011) The *Mycobacterium tuberculosis* Cytochrome P450 System. *System*. **493**, 82–95.

[325] McLean, K. J., Carroll, P., Lewis, D. G., Dunford, A. J., Seward, H. E., Neeli, R., Cheesman, M. R., Marsollier, L., Douglas, P., Smith, W. E., Rosenkrands, I., Cole, S. T., Leys, D., Parish, T., and Munro, A. W. (2008) Characterization of active site structure in CYP121: A cytochrome P450 essential for viability of *mycobacterium tuberculosis* H37Rv. *J. Biol. Chem.* **283**, 33406–33416.

[326] Girvan, H. M., Toogood, H. S., Littleford, R. E., Seward, H. E., Smith, W. E., Ekanem, I. S., Leys, D., Cheesman, M. R., and Munro, A. W. (2009) Novel haem co-ordination variants of flavocytochrome P450BM3. *Biochem. J.* **417**, 65–76.

[327] Girvan, H. M., Marshall, K. R., Lawson, R. J., Leys, D., Joyce, M. G., Clarkson, J., Smith, W. E., Cheesman, M. R., and Munro, A. W. (2004) Flavocytochrome P450 BM3 mutant A264E undergoes substrate-dependent formation of a novel heme iron ligand set. *J. Biol. Chem.* **279**, 23274–23286.

[328] Gorren, A. C. F., and Mayer, B. (2007) Nitric-oxide synthase: A cytochrome P450 family foster child. *Biochim. Biophys. Acta - Gen. Subj.* **1770**, 432–445.

[329] Iyanagi, T., Xia, C., and Kim, J. P. (2012) NADPH-Cytochrome P450 Oxidoreductase: Prototypic Member of the Diflavin Reductase Family. *Arch. Biochem. Biophys.* **528**, 72–89.

[330] Porter, T. D., Wilson, T. E., and Kasper, C. B. (1987) Expression of a Functional 78,000 Dalton Mammalian Flavoprotein, NADPH-Cytochrome P-450 Oxidoreductase, in *Escherchia coli*. *Arch. Biochem. Biophys.* **254**, 353–367.

[331] Govindaraj, S., and Poulos, T. L. (1997) The domain architecture of cytochrome P450BM-3. *J. Biol. Chem.* **272**, 7915–7921.

[332] Kleine, M. L., and Fulco, A. J. (1993) Critical residues involved in FMN binding and catalytic activity in cytochrome P450BM-3. *J. Biol. Chem.* **268**, 7553–7561.

[333] Harvey, R. A. (1980) Flavin 1, N6-ethaneoadenine dinucleotide. *Methods Enzymol.* **66**, 290–294.

[334] Harris, D. A., and Bashford, C. L. (1987) *Spectra, in Spectrophotometry and Spectrofluorimetry: A Practical Approach*, IRL Press, Oxford

[335] Koga, Y. (2012) Thermal Adaptation of the Archaeal and Bacterial Lipid Membranes. *Archaea*. **2012**, 6 pages.

[336] Hazzard, J. T., Govindaraj, S., Poulos, T. L., and Tolling, G. (1997) Electron transfer between the FMN and heme domains of cytochrome P450BM- 3: Effects of substrate and CO. *J. Biol. Chem.* **272**, 7922–7926.

[337] Ruettinger, R. T., Wen, L. P., and Fulco, A. J. (1989) Coding nucleotide, 5’ regulatory, and deduced amino acid sequences of P-450(BM-3), a single peptide cytochrome P-450:NADPH-P-450 reductase from *Bacillus megaterium*. *J. Biol. Chem.* **264**, 10987–10995.

[338] Sevrioukova, I., Shaffer, C., Ballou, D. P., and Peterson, J. A. (1996) Equilibrium and transient state spectrophotometric studies of the mechanism of reduction of the flavoprotein domain of P450BM-3. *Biochemistry*. **35**, 7058–7068.

[339] Sevrioukova, I. F., Hazzard, J. T., Tollin, G., and Poulos, T. L. (1999) The FMN to Heme Electron Transfer in Cytochrome P450BM-3. *J. Biol. Chem.* **274**, 36097–36106.

[340] Vermilion, J. L., Ballou, D. P., Massey, V., and Coon, M. J. (1981) Separate roles for FMN and FAD in catalysis by liver microsomal NADPH-cytochrome P-450 reductase. *J. Biol. Chem.* **256**, 266–277.

[341] Ludwig, M. L., Pattridge, K. a., Metzger, A. L., Dixon, M. M., Eren, M., Feng, Y., and Swenson, R. P. (1997) Control of oxidation-reduction potentials in flavodoxin from *Clostridium beijerinckii*: The role of conformation changes. *Biochemistry*. **36**, 1259–1280.

[342] Chen, H. C., and Swenson, R. P. (2008) Effect of the Insertion of a Glycine Residue into the Loop Spanning Residues 536-541 on the Semiquinone State and Redox Properties of the Flavin Mononucleotide-binding Domain of Flavocytochrome P450BM-3 from Bacillus megaterium. *Biochemistry*. **47**, 13788–13799.

[343] Li, H., Das, A., Sibhatu, H., Jamal, J., Sligar, S. G., and Poulos, T. L. (2008) Exploring the electron transfer properties of neuronal nitric-oxide synthase by reversal of the FMN redox potential. *J. Biol. Chem.* **283**, 34762–34772.

[344] Pochapsky, S. S., Pochapsky, T. C., and Wei, J. W. (2003) A model for effector activity in a highly specific biological electron transfer complex: The cytochrome P450cam-putidaredoxin couple. *Biochemistry*. **42**, 5649–5656.

[345] English, N., Palmer, C. N., Alworth, W. L., Kang, L., Hughes, V., and Wolf, C. R. (1997) Fatty Acid Signals in *Bacillus megaterium* are Attenuated by Cytochrome P-450-mediated Hydroxylation. *Biochem. J.* **327**, 363–368.

[346] Narhi, L. O., and Fulco, A. J. (1982) Phenobarbital induction of a soluble cytochrome P-450-dependent fatty acid monooxygenase in *Bacillus megaterium*. *J. Biol. Chem.* **257**, 2147–2150.

[347] Govindaraj, S., and Poulos, T. L. (1995) Role of the linker region connecting the reductase and heme domains in cytochrome P450(BM-3). *Biochemistry*. **34**, 11221–11226.

[348] English, N., Hughes, V., and Wolf, C. R. (1994) Common pathways of cytochrome P450 gene regulation by peroxisome proliferators and barbiturates in *Bacillus megaterium* ATCC14581. *J. Biol. Chem.* **269**, 26836–26841.

[349] Palmer, C. N. A., Axen, E., Hughes, V., and Wolf, C. R. (1998) The repressor protein, Bm3R1, mediates an adaptive response to toxic fatty acids in *Bacillus megaterium*. *J. Biol. Chem.* **273**, 18109–18116.

[350] Cryle, M. J., Espinoza, R. D., Smith, S. J., Matovic, N. J., and De Voss, J. J. (2006) Are branched chain fatty acids the natural substrates for P450BM3? *Chem. Commun.* **14**, 2353–2355.

[351] Kaneda, T. (1991) Iso- and anteiso-fatty acids in bacteria: biosynthesis, function, and taxonomic significance. *Microbiol. Rev.* **55**, 288–302.

[352] Cryle, M. J., Matovic, N. J., and De Voss, J. J. (2007) The stereochemistry of fatty acid hydroxylation by cytochrome P450BM3. *Tetrahedron Lett.* **48**, 133–136.

[353] McKnight, J., Cheeseman, M. R., Thomson, A. J., Miles, J. S., and Munro, A. W. (1993) Identification of charge-transfer transitions in the optical spectrum of low-spin ferric cytochrome P-450 *Bacillus megaterium*. *Eur. J. Biochem.* **213**, 683–687.

[354] Murataliev, M. B., Klein, M., Fulco, A., and Feyereisen, R. (1997) Functional interactions in cytochrome P450BM3: Flavin semiquinone intermediates, role of NADP(H), and mechanism of electron transfer by the flavoprotein domain. *Biochemistry*. **36**, 8401–8412.

[355] Sligar, S. G., and Gunsalus, I. C. (1976) A thermodynamic model of regulation: modulation of redox equilibria in camphor monoxygenase. *Proc. Natl. Acad. Sci. U. S. A.* **73**, 1078–1082.

[356] Driscoll, M. D., McLean, K. J., Levy, C., Mast, N., Pikuleva, I. A., Lafite, P., Rigby, S. E. J., Leys, D., and Munro, A. W. (2010) Structural and biochemical characterization of *Mycobacterium tuberculosis* CYP142: evidence for multiple cholesterol 27-hydroxylase activities in a

human pathogen. *J. Biol. Chem.* **285**, 38270–38282.

[357] McLean, K. J., Warman, A. J., Seward, H. E., Marshall, K. R., Girvan, H. M., Cheesman, M. R., Waterman, M. R., and Munro, A. W. (2006) Biophysical characterization of the sterol demethylase P450 from *Mycobacterium tuberculosis*, its cognate ferredoxin, and their interactions. *Biochemistry*. **45**, 8427–8443.

[358] Martinis, S. A., Blanke, S. R., Hager, L. P., and Sligar, S. G. (1996) Probing the Heme Iron Coordination Structure of Pressure-Induced Cytochrome P420cam. *Biochemistry*. **35**, 14539–14536.

[359] Das, A., Grinkova, Y. V, and Sligar, S. G. (2007) Redox Potential Control by Drug Binding to Cytochrome P450 3A4. *J Am Chem Soc*. **129**, 13778–13779.

[360] Lewis, D. F., Ioannides, C., and Parke, D. V (1986) Molecular dimensions of the substrate binding site of cytochrome P-448. *Biochem. Pharmacol.* **35**, 2179–2185.

[361] Light, D. R., and Orme-Johnson, N. R. (1981) Beef adrenal cortical cytochrome P-450 which catalyzes the conversion of cholesterol to pregnenolone. Oxidation-reduction potentials of the free, steroid-complexed, and adrenodoxin-complexed P-450. *J. Biol. Chem.* **256**, 343–350.

[362] Masters, B. S., Nelson, E. B., Schacter, B. A., Baron, J., and Isaacson, E. L. (1973) NADPH-cytochrome *c* reductase and its role in microsomal cytochrome P-450-dependent reactions. *Drug Metab. Dispos.* **1**, 121–128.

[363] Coon, M. J., van der Hoeven, A., Haugen, D. A., Guengerich, F. P., Vermilion, J. L., and Ballou, D. P. (1975) Biochemical characterization of highly purified cytochrome P-450 and other components of the mixed function oxidase system of liver microsomal membranes. *Adv. Exp. Med. Biol.* **58**, 25–46.

[364] O'Farrell, P. A., Walsh, M. A., McCarthy, A. A., Higgins, T. M., Voordouw, G., and Mayhew, S. G. (1998) Modulation of the redox potentials of FMN in *Desulfovibrio vulgaris* flavodoxin: Thermodynamic properties and crystal structures of glycine-61 mutants. *Biochemistry*. **37**, 8405–8416.

[365] Modi, S., Primrose, W. U., Boyle, J. M., Gibson, C. F., Lian, L., and Roberts, G. (1995) NMR studies of substrate binding to cytochrome P450 BM3: comparisons to cytochrome P450 cam. *Biochemistry*. **34**, 8982–8.

[366] Hare, R. S., Matson, R. S., and Fulco, A. J. (1977) Characteristics of a Cytochrome P-450-Dependent Fatty Acid Omega-2 Hydoxylase from *Bacillus megaterium*. *Biochim. Biophys. Acta*. **487**, 487–494.

[367] Ost, T. W. B., Miles, C. S., Murdoch, J., Cheung, Y. F., Reid, G. A., Chapman, S. K., and Munro, A. W. (2000) Rational re-design of the substrate binding site of flavocytochrome P450 BM3. *FEBS Lett.* **486**, 173–177.

[368] Whitehouse, C. J. C., Bell, S. G., and Wong, L. L. (2008) Desaturation of alkylbenzenes by cytochrome P450BM3 (CYP102A1). *Chem. - A Eur. J.* **14**, 10905–10908.

[369] Masters, B. S., McMillan, K., Sheta, E. A., Nishimura, J. S., Roman, L. J., and Martasek, P. (1996) Neuronal nitric oxide synthase, a modular enzyme formed by convergent evolution: structure studies of a cysteine thiolate-liganded heme protein that hydroxylates L-arginine to produce NO. as a cellular signal. *FASEB J.* **10**, 552–558.

[370] Hemmens, B., and Mayer, B. (1998) Enzymology of nitric oxide synthases. *Methods Mol. Biol.* **100**, 1–32.

[371] Stuehr, D. J. (1997) Structure-function aspects in the nitric oxide synthases. *Annu. Rev. Pharmacol. Toxicol.* **37**, 339–359.

[372] Crane, B. R., Arvai, A. S., Gachhui, R., Wu, C., Ghosh, D. K., Getzoff, E. D., Stuehr, D. J., and Tainer, J. A. (1997) The structure of nitric oxide synthase oxygenase domain and inhibitor complexes. *Science*. **278**, 425–431.

[373] McMillan, K., and Masters, B. S. (1995) Prokaryotic expression of the heme- and flavin-binding domains of rat neuronal nitric oxide synthase as distinct polypeptides: identification of the heme-binding proximal thiolate ligand as cysteine-415. *Biochemistry*. **34**, 3686–3693.

[374] Boyhan, A., Smith, D., Charles, I. G., Saqi, M., and Lowe, P. N. (1997) Delineation of the arginine- and tetrahydrobiopterin-binding sites of neuronal nitric oxide synthase. *Biochem. J.* **323**, 131–139.

[375] Ghosh, D. K., Wu, C., Pitters, E., Moloney, M., Werner, E. R., Mayer, B., and Stuehr, D. J. (1997) Characterization of the inducible nitric oxide synthase oxygenase domain identifies a 49 amino acid segment required for subunit dimerization and tetrahydrobiopterin interaction. *Biochemistry*. **36**, 10609–10619.

[376] Rodríguez-Crespo, I., Moënne-Loccoz, P., Loehr, T. M., and Ortiz de Montellano, P. R. (1997) Endothelial nitric oxide synthase: Modulations of the distal heme site produced by progressive N-terminal deletions. *Biochemistry*. **36**, 8530–8538.

[377] Venema, R. C., Ju, H., Zou, R., Ryan, J. W., and Venema, V. J. (1997) Subunit interactions of endothelial nitric-oxide synthase: Comparisons to the neuronal and inducible nitric-oxide synthase isoforms. *J. Biol. Chem.* **272**, 1276–1282.

[378] Ravindranathan, K. P., Gallicchio, E., Friesner, R. A., McDermott, A. E., and Levy, R. M. (2006) Conformational equilibrium of cytochrome P450 BM-3 complexed with N -palmitoylglycine: A replica exchange molecular dynamics study. *J. Am. Chem. Soc.* **128**, 5786–5791.

[379] Ravindranathan, K. P., Gallicchio, E., Mcdermott, A. E., and Levy, R. M. (2007) Conformational dynamics of substrate in the active site of cytochrome P450 BM-3 / NPG complex : Insights from NMR order parameters. *J Am Chem Soc*. **129**, 474–475.

[380] Jovanovic, T., Farid, R., Friesner, R. A., and McDermott, A. E. (2005) Thermal equilibrium of high- and low-spin forms of cytochrome P450 BM-3: Repositioning of the substrate? *J. Am. Chem. Soc.* **127**, 13548–13552.

[381] Estrada, D. F., Skinner, A. L., Laurence, J. S., and Scott, E. E. (2014) Human cytochrome P450 17A1 conformational selection: Modulation by ligand and cytochrome *b*5. *J. Biol. Chem.* **289**, 14310–14320.

[382] Zhang, W., Pochapsky, S. S., Pochapsky, T. C., and Jain, N. U. (2008) Solution NMR structure of putidaredoxin-cytochrome P450cam complex via a combined residual dipolar coupling-spin labeling approach suggests a role for Trp106 of putidaredoxin in complex formation. *J. Mol. Biol.* **384**, 349–363.

[383] Guengerich, F. P., and Johnson, W. W. (1997) Kinetics of ferric cytochrome P450 reduction by NADPH-cytochrome P450 reductase: Rapid reduction in the absence of substrate and variations among cytochrome P450 systems. *Biochemistry*. **36**, 14741–14750.

[384] Shen, A. L., Sem, D. S., and Kasper, C. B. (1999) Mechanistic studies on the reductive half-reaction of NADPH-cytochrome P450 oxidoreductase. *J. Biol. Chem.* **274**, 5391–5398.

[385] Quaroni, L. G., Seward, H. E., McLean, K. J., Girvan, H. M., Ost, T. W. B., Noble, M. A., Kelly, S. M., Price, N. C., Cheesman, M. R., Smith, W. E., and Munro, A. W. (2004) Interaction of nitric oxide with cytochrome P450 BM3. *Biochemistry*. **43**, 16416–16431.

[386] Vojtechovský, J., Chu, K., Berendzen, J., Sweet, R. M., and Schlichting, I. (1999) Crystal

structures of myoglobin-ligand complexes at near-atomic resolution. *Biophys. J.* **77**, 2153–2174.

[387] Bartesaghi, A., Merk, A., Banerjee, S., Matthies, D., Wu, X., Milne, J. L. S., and Subramaniam, S. (2015) 2.2 Å resolution cryo-EM structure of β-galactosidase in complex with a cell-permeant inhibitor. *Science (80-.).* **48**, 826–840.

[388] Machonkin, T. E., Westler, W. M., and Markley, J. L. (2004) Strategy for the study of paramagnetic proteins with slow electronic relaxation rates by NMR spectroscopy: Application to oxidized human [2Fe-2S] ferredoxin. *J. Am. Chem. Soc.* **126**, 5413–5426.

[389] Machonkin, T. E., Westler, W. M., and Markley, J. L. (2005) Paramagnetic NMR spectroscopy and density functional calculations in the analysis of the geometric and electronic structures of iron−sulfur proteins. *Inorg. Chem.* **44**, 779–797.

[390] Vathyam, S., Byrd, R. A., and Miller, A. F. (2000) Mapping the effects of metal ion reduction and substrate analog binding to Fe-superoxide dismutase by NMR spectroscopy. *Magn. Reson. Chem.* **38**, 536–542.

[391] Bertini, I., Luchinat, C., and Parigi, G. (2002) Magnetic susceptibility in paramagnetic NMR. *Prog. Nucl. Magn. Reson. Spectrosc.* **40**, 249–273.

[392] Blanchard, L., Blackledge, M. J., Marion, D., and Guerlesquin, F. (1996) Investigation of oxidation state-dependent conformational changes in Desulfovibrio vulgaris Hildenborough cytochrome *c*553 by two-dimensional 1H-NMR spectra. *FEBS Lett.* **389**, 203–209.

[393] Paixão, V. B., Vis, H., and Turner, D. L. (2010) Redox linked conformational changes in cytochrome *c*3 from *Desulfovibrio desulfuricans* ATCC 27774. *Biochemistry*. **49**, 9620–9629.

[394] Morgado, L., Bruix, M., Londer, Y. Y., Pokkuluri, P. R., Schiffer, M., and Salgueiro, C. A. (2007) Redox-linked conformational changes of a multiheme cytochrome from *Geobacter sulfurreducens*. *Biochem. Biophys. Res. Commun.* **360**, 194–198.

[395] Cheng, H., and Markley, J. L. (1995) NMR spectroscopic studes of paramagnetic proteins: Iron-sulfur proteins. *Annu. Rev. Biophys. Biomol. Struct.* **24**, 209–37.

[396] Chen, P. F., Tsai, A. L., and Wu, K. K. (1995) Cysteine 99 of endothelial nitric oxide synthase (NOS-III) is critical for tetrahydrobiopterin-dependent NOS-III stability and activity. *Biochem. Biophys. Res. Commun.* **215**, 1119–1129.

[397] Li, H., Raman, C. S., Glaser, C. B., Blasko, E., Young, T. A., Parkinson, J. F., Whitlow, M., and Poulos, T. L. (1999) Crystal structures of zinc-free and -bound heme domain of human inducible nitric-oxide synthase. Implications for dimer stability and comparison with endothelial nitric-oxide synthase. *J. Biol. Chem.* **274**, 21276–21284.

[398] Crane, B. R., Rosenfeld, R. J., Arvai, A. S., Ghosh, D. K., Ghosh, S., Tainer, J. A., Stuehr, D. J., and Getzoff, E. D. (1999) N-terminal domain swapping and metal ion binding in nitric oxide synthase dimerization. *EMBO J.* **18**, 6271–6281.

[399] Berka, R. M., Grigoriev, I. V., Otillar, R., Salamov, A., Grimwood, J., Reid, I., Ishmael, N., John, T., Darmond, C., Moisan, M.-C., Henrissat, B., Coutinho, P. M., Lombard, V., Natvig, D. O., Lindquist, E., Schmutz, J., Lucas, S., Harris, P., Powlowski, J., Bellemare, A., Taylor, D., Butler, G., de Vries, R. P., Allijn, I. E., van den Brink, J., Ushinsky, S., Storms, R., Powell, A. J., Paulsen, I. T., Elbourne, L. D. H., Baker, S. E., Magnuson, J., LaBoissiere, S., Clutterbuck, A. J., Martinez, D., Wogulis, M., de Leon, A. L., Rey, M. W., and Tsang, A. (2011) Comparative genomic analysis of the thermophilic biomass-degrading fungi *Myceliophthora thermophila* and *Thielavia terrestris*. *Nat. Biotechnol.* **29**, 922–927.

[400] Koeller, K. M., and Wong, C.-H. (2001) Enzymes for chemical synthesis. *Nature*. **409**, 232–

240.

[401] Neeli, R., Roitel, O., Scrutton, N. S., and Munro, A. W. (2005) Switching pyridine nucleotide specificity in P450 BM3: Mechanistic analysis of the W1046H and W1046A enzymes. *J. Biol. Chem.* **280**, 17634–17644.

[402] Atkins, P. W. (2006) *Atkins' Physical Chemistry*, 8th Ed., Oxford University Press, Oxford.

[403] Bertini, I., Luchinat, C., Parigi, G., and Pierattelli, R. (2008) Perspectives in paramagnetic NMR of metalloproteins. *Dalton Trans.* 10.1039/b719526e

[404] Katagiri, M., Ganguli, B. N., and Gunsalus, I. C. (1968) A soluble cytochrome P-450 functional in methylene hydroxylation. *J. Biol. Chem.* **243**, 3543–3546.

[405] Groves, J. T., and McClusky, G. A. (1976) Aliphatic Hydroxylation Via Oxygen Rebound - Oxygen-Transfer Catalyzed By Iron. *J. Am. Chem. Soc.* **98**, 859–861.

Chapter 7 Appendix

7.1 *CYP505A30* gene sequence and translated protein sequence.

```
   1 H  M  A  D  K  T  T  E  T  V  P  I  P  G  P  P  G  L  P  L  V  G  N  A  L  A  F  D  S  E
   1 CATATGGCCGACAAGACGACCGAAACGGTGCCGATTCCGGGTCCGCCGGGCCTGCCGCTGGTTGGTAATGCCCTGGCTTTTGATTCTGAA
  31 L  P  L  R  T  F  Q  E  F  A  E  E  Y  G  E  I  Y  R  L  T  L  P  T  G  T  T  L  V  V  S
  91 CTGCCGCTGCGCACCTTTCAGGAATTCGCGGAAGAATATGGTGAAATTTACCGTCTGACCCTGCCGACGGGTACCACCCTGGTGGTGTCT
  61 S  Q  A  L  V  H  E  L  C  D  D  K  R  F  K  K  P  V  A  A  A  L  A  E  V  R  N  G  V  N
 181 TCTCAAGCCCTGGTTCATGAACTGTGCGATGACAAACGCTTTAAAAAGCCGGTCGCAGCAGCACTGGCAGAAGTCCGTAACGGTGTGAAT
  91 D  G  L  F  T  A  R  E  E  E  P  N  W  G  I  A  H  R  I  L  M  P  A  F  G  P  A  S  I  Q
 271 GATGGCCTGTTCACGGCCCGCGAAGAAGAACCGAACTGGGGTATTGCACACCGTATCCTGATGCCGGCATTTGGTCCGGCTTCGATCCAG
 121 G  M  F  T  E  M  H  E  I  A  S  Q  L  A  L  K  W  A  R  H  G  P  D  T  P  I  F  V  T  D
 361 GGCATGTTCACCGAAATGCATGAAATTGCGAGCCAACTGGCCCTGAAATGGGCACGTCACGGCCCGGATACGCCGATCTTTGTTACCGAT
 151 D  F  T  R  L  T  L  D  T  L  A  L  C  T  M  N  F  R  F  N  S  Y  Y  H  D  E  L  H  P  F
 451 GACTTCACCCGCCTGACGCTGGATACCCTGGCCCTGTGTACCATGAACTTCCGTTTCAACAGTTACTACCATGATGAACTGCACCCGTTT
 181 I  N  A  M  G  N  F  L  T  E  S  G  A  R  A  M  R  P  A  I  T  S  I  F  H  Q  A  A  N  R
 541 ATTAACGCGATGGGTAATTTCCTGACGGAATCCGGTGCACGTGCAATGCGTCCGGCCATTACCTCAATCTTTCATCAGGCTGCGAACCGT
 211 K  Y  W  E  D  I  E  V  L  R  K  T  A  Q  G  V  L  D  T  R  R  K  H  P  T  N  R  K  D  L
 631 AAATATTGGGAAGATATCGAAGTGCTGCGCAAGACCGCGCAAGGCGTTCTGGATACGCGTCGCAAACACCCGACCAATCGCAAGGACCTG
 241 L  S  A  M  L  D  G  V  D  A  K  T  G  Q  K  L  S  D  S  S  I  I  D  N  L  I  T  F  L  I
 721 CTGTCTGCTATGCTGGATGGTGTGGACGCGAAAACGGGCCAGAAGCTGAGTGATAGTTCCATTATCGACAACCTGATTACCTTTCTGATC
 271 A  G  H  E  T  T  S  G  L  L  S  F  A  F  Y  L  L  I  K  H  Q  D  A  Y  R  K  A  Q  E  E
 811 GCCGGTCATGAAACCACGTCGGGCCTGCTGAGCTTTGCATTCTATCTGCTGATCAAACACCAGGATGCTTACCGTAAGGCGCAAGAAGAA
 301 V  D  R  V  I  G  K  G  P  I  K  V  E  H  I  K  K  L  P  Y  I  A  A  V  L  R  E  T  L  R
 901 GTTGACCGCGTCATTGGCAAAGGTCCGATCAAGGTGGAACATATTAAAAAGCTGCCGTATATTGCCGCAGTTCTGCGTGAAACGCTGCGC
 331 L  C  P  T  I  P  I  I  N  R  A  A  K  Q  D  E  V  I  G  G  K  Y  A  V  A  K  D  Q  R  L
 991 CTGTGCCCGACCATCCCGATTATCAATCGCGCTGCGAAACAGGATGAAGTTATTGGCGGTAAATATGCAGTCGCTAAGGACCAGCGTCTG
 361 A  L  L  L  A  Q  S  H  L  D  P  A  V  Y  G  E  T  A  K  Q  F  I  P  E  R  M  L  D  E  N
1081 GCCCTGCTGCTGGCACAAAGCCACCTGGACCCGGCCGTGTACGGTGAAACCGCAAAACAGTTTATCCCGGAACGTATGCTGGATGAAAAC
 391 F  E  R  L  N  R  E  Y  P  D  C  W  K  P  F  G  T  G  M  R  A  C  I  G  R  P  F  A  W  Q
1171 TTCGAACGTCTGAATCGCGAATACCCGGACTGCTGGAAACCGTTTGGCACCGGTATGCGTGCATGTATTGGTCGTCCGTTCGCTTGGCAG
 421 E  A  V  L  V  M  A  M  L  L  Q  N  F  D  F  V  L  H  D  P  Y  Y  E  L  H  Y  K  Q  T  L
1261 GAAGCGGTGCTGGTTATGGCGATGCTGCTGCAAAACTTTGATTTCGTTCTGCATGACCCGTATTACGAACTGCACTATAAACAGACCCTG
 451 T  T  K  P  K  D  F  Y  M  R  A  I  L  R  D  G  L  T  A  T  E  L  E  H  R  L  A  G  N  A
1351 ACCACGAAACCGAAGGATTTTTACATGCGTGCTATTCTGCGCGACGGTCTGACCGCGACGGAACTGGAACATCGTCTGGCCGGTAACGCA
 481 A  S  V  A  R  S  G  G  G  G  G  G  P  S  K  P  T  A  Q  K  T  S  P  A  E  A  K  P  M  S
1441 GCATCTGTGGCACGTAGTGGCGGTGGCGGTGGCGGTCCGTCGAAACCGACGGCACAGAAGACCAGCCCGGCAGAAGCCAAACCGATGTCG
 511 I  F  Y  G  S  N  T  G  T  C  E  S  L  A  Q  R  L  A  T  D  A  A  S  H  G  Y  A  A  A  A
1531 ATCTTCTATGGTAGCAATACCGGCACGTGCGAATCGCTGGCACAACGTCTGGCAACCGATGCTGCAAGCCACGGTTACGCAGCAGCTGCA
 541 V  E  P  L  D  T  A  T  E  K  L  P  T  D  R  P  V  V  I  I  T  A  S  F  E  G  Q  P  P  D
1621 GTGGAACCGCTGGATACCGCCACGGAAAAACTGCCGACGGACCGTCCGGTCGTGATTATCACCGCATCTTTTGAAGGCCAGCCGCCGGAT
 571 N  A  A  K  F  C  G  W  L  K  N  L  E  G  D  E  L  K  N  V  S  Y  A  V  F  G  C  G  H  H
1711 AATGCCGCAAAATTCTGCGGTTGGCTGAAGAACCTGGAAGGCGATGAACTGAAAAATGTTTCCTATGCGGTCTTTGGCTGTGGTCATCAC
 601 D  W  S  Q  T  F  H  R  I  P  K  L  V  H  Q  T  M  K  A  H  G  A  S  P  I  C  D  E  G  L
1801 GATTGGTCACAGACGTTCCATCGCATCCCGAAACTGGTTCATCAAACCATGAAGGCGCACGGTGCCTCCCCGATTTGTGATGAAGGTCTG
 631 T  D  V  A  E  G  N  M  F  T  D  F  E  Q  W  E  D  D  V  F  W  P  A  V  R  A  R  Y  G  A
1891 ACGGACGTGGCCGAAGGCAACATGTTTACCGATTTCGAACAGTGGGAAGATGACGTCTTTTGGCCGGCAGTGCGTGCTCGTTACGGTGCT
 661 A  G  A  V  A  E  T  E  D  A  P  G  S  D  G  L  N  I  H  F  S  S  P  R  S  S  T  L  R  Q
1981 GCGGGCGCAGTTGCTGAAACGGAAGATGCGCCGGGTAGTGACGGCCTGAATATTCATTTCTCATCGCCGCGTAGCTCTACCCTGCGTCAG
 691 D  V  R  E  A  T  V  V  G  E  A  L  L  T  A  P  D  A  P  P  K  K  H  I  E  V  Q  L  P  D
2071 GATGTGCGCGAAGCTACGGTTGTCGGTGAAGCACTGCTGACCGCACCGGATGCACCGCCGAAAAAGCACATCGAAGTCCAACTGCCGGAT
 721 G  A  T  Y  K  V  G  D  Y  L  A  V  L  P  V  N  S  K  E  S  I  G  R  V  M  R  K  F  Q  L
2161 GGTGCCACCTATAAAGTGGGCGACTACCTGGCAGTGCTGCCGGTTAATTCGAAAGAAAGCATCGGCCGTGTCATGCGCAAGTTTCAGCTG
 751 S  W  D  S  H  V  T  I  A  S  D  R  W  T  A  L  P  T  G  T  P  V  P  A  Y  D  V  L  G  S
2251 TCTTGGGATAGTCATGTGACGATTGCAAGCGACCGTTGGACCGCACTGCCGACCGGTACGCCGGTTCCGGCGTATGATGTCCTGGGCTCT
 781 Y  V  E  L  S  Q  P  A  T  K  R  G  I  L  R  L  A  D  A  A  E  D  E  A  T  K  A  E  L  Q
2341 TACGTGGAACTGAGTCAGCCGGCTACCAAACGTGGTATTCTGCGCCTGGCGGATGCCGCAGAAGACGAAGCAACGAAAGCTGAACTGCAA
 811 K  L  A  G  D  L  Y  T  S  E  I  S  L  K  R  A  S  V  L  D  L  L  D  R  F  P  S  I  S  L
2431 AAGCTGGCGGGCGATCTGTATACCTCCGAAATCTCACTGAAACGTGCCTCTGTGCTGGATCTGCTGGACCGCTTTCCGTCTATTAGTCTG
 841 P  F  G  T  F  L  S  L  L  P  P  I  R  P  R  Q  Y  S  I  S  S  S  P  L  N  D  P  S  R  A
2521 CCGTTTGGCACCTTCCTGTCTCTGCTGCCGCCGATCCGTCCGCGCCAGTATAGTATTAGTTCCTCACCGCTGAACGATCCGTCCCGTGCA
 871 T  L  T  Y  S  L  L  D  S  P  S  L  A  N  P  S  R  R  F  V  G  V  A  T  S  Y  L  S  S  L
2611 ACCCTGACGTACTCACTGCTGGACTCCCCGTCACTGGCTAATCCGTCTCGTCGCTTTGTCGGTGTGGCGACCAGTTATCTGTCGAGCCTG
 901 V  R  G  D  K  L  L  V  S  V  R  P  T  H  T  A  F  R  L  P  D  E  D  K  M  G  E  T  A  I
2701 GTTCGTGGCGATAAACTGCTGGTTTCGGTCCGTCCGACCCATACGGCATTCCGCCTGCCGGATGAAGACAAGATGGGTGAAACGGCGATT
 931 I  C  V  G  A  G  S  G  L  A  P  F  R  G  F  I  Q  E  R  A  A  L  L  A  K  G  T  Q  L  A
2791 ATCTGCGTGGGTGCTGGTTCAGGTCTGGCACCGTTTCGTGGCTTCATTCAGGAACGCGCTGCGCTGCTGGCGAAAGGTACCCAACTGGCC
 961 A  A  L  L  F  Y  G  C  R  S  P  E  K  D  D  L  Y  R  D  E  F  D  K  W  Q  E  S  G  A  V
2881 GCAGCTCTGCTGTTTTATGGCTGTCGTTCCCCGGAAAAAGATGACCTGTACCGCGATGAATTTGACAAGTGGCAGGAATCAGGTGCTGTG
 991 D  V  R  R  A  F  S  R  V  D  S  D  D  T  E  A  R  G  C  R  H  V  Q  D  R  L  W  H  D  R
2971 GATGTTCGTCGCGCGTTCTCCCGTGTTGACTCAGATGACACCGAAGCCCGTGGCTGCCGCCATGTTCAGGATCGTCTGTGGCACGACCGC
1021 E  E  V  K  A  L  W  D  R  G  A  R  V  Y  V  C  G  S  R  Q  V  G  E  G  V  K  T  A  M  G
3061 GAAGAAGTCAAAGCCCTGTGGGATCGTGGTGCACGCGTCTATGTGTGTGGCAGCCGCCAAGTGGGTGAAGGCGTTAAAACCGCGATGGGT
1051 R  I  V  L  G  E  E  D  A  E  D  A  I  S  K  W  Y  E  T  V  R  N  D  R  Y  A  T  D  V  F
3151 CGTATTGTGCTGGGCGAAGAAGATGCGGAAGACGCCATCTCCAAGTGGTATGAAACCGTCCGTAATGACCGTTATGCGACCGATGTCTTT
1081 D
3241 GAC
```

7.2 Trace Elements (100 ml)

The following salts were used:

- 550 mg $CaCl_2.2H_2O$ (add last)
- 140 mg $MnSO_4.H_2O$
- 40 mg $CuSO_4.5H_2O$
- 220 mg $ZnSO_4.7H_2O$
- 45 mg $CoCl_2.6H_2O$
- 26 mg $Na_2MoO_4.2H_2O$
- 40 mg H_3BO_4
- 26 mg KI

These were weighed out and dissolved in 70 ml dH_2O and the solution adjusted to pH 8.0. 500 mg of EDTA was then added and the pH was readjusted to pH 8.0. 375 mg $FeSO_4.7H_2O$ was then added before the solution was made up to 100 ml.

7.3 Melting temperatures for P450 MT1 and MT1HD under different conditions using Differential Scanning Fluorimetry.

Buffer	pH	P450 MT1 Tm (°C)	MT1 HD Tm (°C)
CAPS	10	/	/
CHES	9.5	/	/
CHES	9	48.6	/
TRIS	8.5	47.3	45.0
BICINE	8.5	47.9	46.3
EPPS	8	49.6	47.2
TRIS	7.5	49.8	46.9
HEPES	7.5	/	46.5
MOPS	7	51.5	46.6
Na/K Pi	7	58.0	48.0
NH_4Ac	7	51.7	43.5
BisTris	6.5	52.1	46.3
ADA	6.5	52.2	47.4
MES	6.2	52.2	44.1
BisTris	6	50.7	46.7
Na/K Pi	6	52.8	47.0
NaCit	5.5	54.5	43.3
Na/K Pi	5	54.0	/
NaAc	4.5	55.1	/
Citric Acid	4	41.2	/
PIPPS	3.7	51.8	/
Citric Acid	3.2	/	/
Glycine	3	53.4	/

Appendix

Salt conditions	P450 MT1 Tm (°C)
500 mM NaCl	52.5
1 M NaCl	53.4
1.5 M NaCl	53.4
500 mM KCl	51.5
1 M KCl	51.4
1.5 M KCl	51.4
500 mM NH_4SO_4	53.1
1 M NH_4SO_4	55.0
1.5 M NH_4SO_4	57.2
10% Glycerol	52.3
20% Glycerol	53.5
30% Glycerol	56.8
5 mM Glucose	52.3
5 mM Proline	52.3
15 mM NaAc	52.4
15 mM MgAc	54.1
15 mM MnCl	51.8
15 mM KAc	/
8 mM Lauric	46.9
15 mM NAD^+	/
15 mM $NADP^+$	/

7.4 Stopped-flow parameters for P450 MT1 flavin reduction by NADH. Flavin reduction was followed at 475 nm for 1 second after the rapid mixing of 20 µM P450 MT1 with varying concentrations of NADH in 50 mM KPi (pH 7.0) buffer containing 200 mM KCl at 10 °C. Absorbance transients were fitted using a triple exponential function and the parameters are tabulated below (k_1-k_3 are the rate constants and a_1-a_3 the respective amplitudes of absorbance changes of in the different phases).

[NADH] (µM)	k_1 (s^{-1})	k_2 (s^{-1})	k_3 (s^{-1})	a_1	a_2	a_3
50	3.59 ± 0.01	1.0 ± 0.1	0.16 ± 0.01	0.0498 ± 0.0001	0.049 ± 0.001	0.039 ± 0.001
100	5.36 ± 0.02	1.1 ± 0.1	0.14 ± 0.01	0.0693 ± 0.0001	0.049 ± 0.001	0.034 ± 0.001
200	8.22 ± 0.02	1.4 ± 0.1	0.15 ± 0.01	0.082 ± 0.001	0.041 ± 0.001	0.027 ± 0.001
300	10.44 ± 0.03	1.6 ± 0.1	0.15 ± 0.01	0.089 ± 0.001	0.038 ± 0.001	0.026 ± 0.001
450	14.92 ± 0.04	1.8 ± 0.1	0.15 ± 0.01	0.098 ± 0.001	0.031 ± 0.001	0.025 ± 0.001
600	17.32 ± 0.05	1.8 ± 0.1	0.15 ± 0.01	0.10 ± 0.01	0.028 ± 0.001	0.024 ± 0.001
900	22.93 ± 0.06	2.4 ± 0.1	0.21 ± 0.01	0.10 ± 0.01	0.026 ± 0.001	0.024 ± 0.001
1200	24.65 ± 0.06	2.4 ± 0.1	0.21 ± 0.01	0.10 ± 0.01	0.025 ± 0.001	0.024 ± 0.001

7.5 Stopped flow parameters for P450 MT1 flavin reduction by NADPH. Flavin reduction was followed at 475 nm for 1 second after the rapid mixing of 20 µM P450 MT1 with varying concentrations of NADPH in 50 mM KPi (pH 7.0) buffer containing 200 mM KCl at 10 °C. Absorbance transients were fitted using a double exponential function and the parameters are tabulated below (k_1-k_2 are the rate constants and a_1-a_2 the respective amplitudes of absorbance changes of in the different phases).

[NADPH] (µM)	k_1 (s^{-1})	k_2 (s^{-1})	a_1	a_2
50	90 ± 1	6.6 ± 0.1	0.056 ± 0.006	0.0058 ± 0.0002
200	81 ± 1	7.1 ± 0.1	0.17 ± 0.01	0.021 ± 0.001
400	80 ± 1	2.1 ± 0.1	0.15 ± 0.01	0.021 ± 0.001
500	77 ± 1	3.7 ± 0.1	0.048 ± 0.005	0.0054 ± 0.0002
800	90 ± 1	2.6 ± 0.1	0.17 ± 0.01	0.021 ± 0.001
1000	92 ± 1	4.1 ± 0.1	0.028 ± 0.003	0.0027 ± 0.0002

7.6 Stopped flow parameters for MT1 flavin reduction by NADPH with varying temperature. Flavin reduction was followed at 475 nm for 1 second after the rapid mixing of 20 µM P450 MT1 with 1 mM NADPH in 50 mM KPi (pH 7.0) buffer containing 200 mM KCl at 10 °C, over a range of temperatures between 10-35 °C. Absorbance transients were fitted using a double exponential function and the parameters are tabulated below.

Temperature (°C)	k_1 (s^{-1})	k_2 (s^{-1})	a_1	a_2
10	95 ± 2	9.7 ± 0.5	0.02 ± 0.01	0.0025 ± 0.0001
15	119 ± 3	3.5 ± 0.3	0.02 ± 0.01	0.0002 ± 0.0001
20	167 ± 4	2.0 ± 0.1	0.02 ± 0.01	0.0023 ± 0.0001
25	253 ± 4	0. 7 ± 0.1	0.016 ± 0.001	0.003 ± 0.001
30	360 ± 6	1.8 ± 0.1	0.019 ± 0.001	0.003 ± 0.001
35	441 ± 8	1.1 ± 0.1	0.027 ± 0.001	0.0036 ± 0.0001

7.7 Stopped flow parameters for MT1 FMN-to-heme electron transfer. Heme reduction was followed by Fe^{2+}-CO complex formation ay 450 nm. Both P450 MT1 and NADPH were in 500 µM substrate, 50 mM KPi (pH 7.0) buffer containing 200 mM KCl, CO-saturated buffer at 20 °C and under anaerobic conditions. Transients were fitted using a double exponential function and parameters are tabulated below.

Substrate	k_1 (s^{-1})	k_2 (s^{-1})	a_1	a_2
Lauric	10.21 ± 0.08	0.72 ± 0.06	0.23 ± 0.01	0.11 ± 0.01
AA	15.13 ± 0.02	0.6 ± 0.06	0.22 ± 0.01	0.11 ± 0.01
NPG	18.47 ± 0.02	0.66 ± 0.05	0.24 ± 0.01	0.11 ± 0.01

7.8 Steady-state kinetic parameters for P450 MT1 flavin reduction by NADH at 10 °C. Reactions were carried out in 50 mM KPi (pH 7.0) buffer containing 200 mM KCl. Replicates of each assay were fitted using a hyperbolic function (Equation 1) and the data are tabulated below.

Substrate varied	k_{cat} (s^{-1})	K_M (µM)
KFeCN	6.3 ± 0.5	22 ± 3
NADH (KFeCN)	6.2 ± 0.6	190 ± 21
Cyt *c*	4.1 ± 0.3	15 ± 2
NADH (Cyt *c*)	4.4 ± 0.4	185 ± 17

7.9 GC-MS traces of fatty acid substrates. A, myristic acid. **B**, pentadecanoic acid. **C**, palmitic acid. **D**, *iso*-pentadecanoic acid. **E**, *anteiso*-pentadecanoic acid. **F**, *iso*-myristic acid. **G**, *anteiso*-myristic acid. **H**, heptadecanoic acid. Turnover reactions with these fatty acids substrates were prepared, products derivatised and GC-MS samples run as outlined in Methods 2.24. Substrate peaks are labelled as are the ω-1, ω-2 and ω-3 hydroxylated products in each panel. The 'U' denotes unidentified peaks. The column retention time of each peak is tabulated in the table below.

Panel	Substrate	ω-1	ω-2	ω-3	U
A	8.57	9.73	9.68	9.57	10.05
B	9.01	10.11	10.01	9.94	9.82, 9.84
C	9.42	10.47	10.42	10.32	10.21, 10.23
D	8.83	9.93	9.87	9.70	/
E	8.87	9.95	9.94	9.85	9.61
F	/	/	9.06	8.96	/
G	8.24	9.38	9.35	9.23	/
H	9.81	10.85, 11.44	10.79, 11.36	10.67, 11.25	11.56, 11.68

Appendix

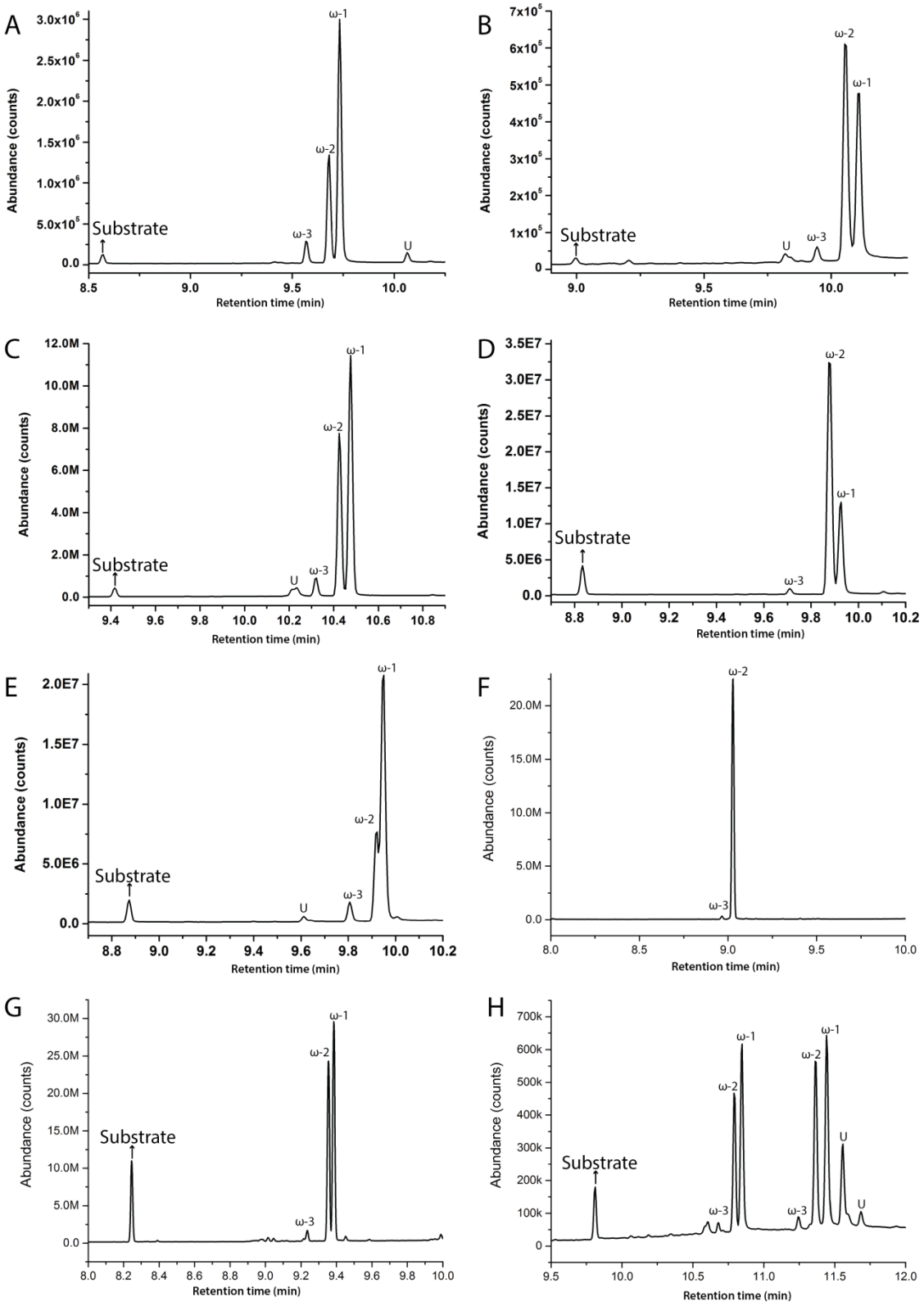
A
Abundance (counts)
Retention time (min)
Substrate
ω-1
ω-2
ω-3
U
B
C
D
E
F
G
H